Radiopharmaceuticals

A Guide to PET/CT and PET/MRI

Ferdinando Calabria
Orazio Schillaci
Editors

Second Edition

Springer

Radiopharmaceuticals

Ferdinando Calabria • Orazio Schillaci
Editors

Radiopharmaceuticals

A Guide to PET/CT and PET/MRI

Second Edition

Springer

Editors
Ferdinando Calabria
Department of Nuclear Medicine and Theranostics
Mariano Santo Hospital
Cosenza
Italy

Orazio Schillaci
Department of Biomedicine and Prevention
University of Rome Tor Vergata
Rome
Italy

ISBN 978-3-030-27778-9 ISBN 978-3-030-27779-6 (eBook)
https://doi.org/10.1007/978-3-030-27779-6

This Springer imprint is published by the registered company Springer Nature Switzerland AG
The registered company address is: Gewerbestrasse 11, 6330 Cham, Switzerland

To Nicoletta, Maria Beatrice and Agnese Felicia.
O.S.
To my father, my principal sponsor.
F.C.

Preface

Two years have elapsed since the publication of the book *Radiopharmaceuticals*, a well-received volume reflecting the state of the art in hybrid PET/CT and PET/MR imaging with novel radiopharmaceuticals. Since its publication, the necessity to cover a larger spectrum of PET tracers has emerged, allowing physicians, residents, and students to deepen their knowledge about PET molecular imaging in a single volume.

Therefore, this edition is enriched by two new chapters, respectively, that focus on prostate cancer imaging with ^{68}Ga-PSMA and imaging of tau pathology. Previous chapters are also updated by new interesting clinical cases and novel applications.

The *panorama* of PET molecular imaging has been improved in the last decades by the development of several novel radiopharmaceuticals; some of them play an established role while other tracers are showing interesting preliminary results.

In this scenario, the most useful PET tracer, the ^{18}F-FDG, shows a limited role in several diseases due to its intrinsic molecular properties while PET imaging is increasingly changing into a diagnostic technique, where the radiopharmaceuticals rather than the scanner can help clinicians in reaching the diagnostic goal. Therefore, amino acid tracers, radiolabeled choline, amyloid tracer, and other radiopharmaceuticals are becoming a valid alternative to ^{18}F-FDG in specific clinical settings.

Nevertheless, all PET tracers do not completely satisfy an important characteristic of the "*ideal tracer*": the capability to be largely, quickly, and selectively taken up at the target site.

Moreover, the PET imaging has been rapidly improved by the development and commercial availability of hybrid PET/CT and, more lately, PET/MRI scanners, which afford us to enlarge our understanding on the applications of molecular imaging, taking advantage of the concurrent functional and anatomical depiction of the human body.

For the reasons above expressed, the aim of our work is to describe the most common tracers actually used in PET imaging. An essential, synthetic chapter is still targeted on the ^{18}F-FDG, the "*milestone*" among radiopharmaceuticals, in order to describe its actual applications, with a specific paragraph focused on ^{18}F-FDG PET/MRI.

Thereafter, several novel tracers are presented in each chapter. For all of them, we have described bio-distribution, physiopathology, and kinetics, aiming to describe their specific "*molecular pathways.*" For all tracers, we have tried to provide the essential diagnostic features and the most common clinical indications. Moreover, a special paragraph in each chapter describes and comments some diagnostic pitfalls which can occur in clinical practice, while another paragraph describes the most used PET/CT acquisition protocols.

A special interest is given to a large number of clinical cases (more than 170 figures in this new edition), in order to get the reader close to the typical imaging features, pathologic findings, or to the diagnostic pitfalls of all radiopharmaceuticals.

Figures of our book (with several multimodal imaging pictures) also try to achieve different goals, as follows:

- Compare potential differences between SPECT and PET imaging
- Show the importance of the hybrid-integrated evaluation of PET/CT imaging with the expertise on CT diagnostic criteria
- Describe the added value of contrast-enhanced PET/CT in some limited cases
- Explain mismatches or overlapping among two different radiopharmaceuticals in the same patient
- Realize all the potentiality of correlative MRI and of the hybrid PET/MRI evaluation

Considering the continuous innovation process of nuclear medicine, all chapters are focused on the role of a single tracer or few radiopharmaceuticals. Actually, some chapters are focused on the amino acid radiopharmaceuticals, such as ^{11}C-methionine, ^{18}F-DOPA, and ^{18}F-FET. All these tracers are useful for brain tumor imaging with some analogies, but we have also tried to describe some peculiar applications beyond neuro-oncology.

A specific chapter is focused on "*radiolabeled choline,*" including all variants of this useful tracer: ^{11}C-choline, ^{18}F-methylcholine, and ^{18}F-ethylcholine. This chapter is also enriched by new interesting cases, bibliography, and applications other than prostate cancer.

Other important chapters concern imaging of the skeletal system by ^{18}F-NaF, the myocardial perfusion imaging with ^{82}Rb, and the β-amyloid imaging of dementia.

Considering the importance of targeted radionuclide therapy, two chapters, respectively, regard PET/CT imaging with ^{68}Ga-labeled *somatostatin receptors analogs* and the therapy with ^{223}Ra.

A special section is also focused on the ^{64}Cu as a versatile nuclide for PET imaging, its possible ligands PSMA, ATSM, and DOTATOC, and their *potential* clinical applications.

As in the previous edition, particular mention is given to fields other than oncology. In fact, new approaches are described in the study of brain tumors, urological malignancies, functional imaging, forensic use, and the evaluation of phlogosis and inflammation.

Humbly, we still hope to have centered our ambitious and arduous scope, without exceeding technical aspects, trying to give the readers (clinicians, nuclear medicine physicians, radiologists, and young colleagues or students) an easy-to-consult, practical and concise atlas guide to the PET, PET/CT, and PET/MR molecular imaging with novel radiopharmaceuticals.

Cosenza, Italy — Ferdinando Calabria
Rome, Italy — Orazio Schillaci

Contents

^{18}F-FDG

1

Ferdinando Calabria, Andrea Cimini, Antonio Bagnato, Domenico Gullà, Giuseppe L. Cascini, Nicoletta Urbano, and Orazio Schillaci

Contents

Authors declare they have obtained permission for any previously published material used in their chapter.

F. Calabria (✉) · A. Bagnato
Department of Nuclear Medicine and Theranostics, "Mariano Santo" Hospital, Cosenza, Italy
e-mail: ferdinandocalabria@hotmail.it

A. Cimini
Department of Diagnostic Imaging, Molecular Imaging, Interventional Radiology and Radiotherapy, University Hospital Tor Vergata, Rome, Italy

D. Gullà
Neuroimaging PET/MRI Research Unit, Institute of Molecular Bioimaging and Physiology, Italian National Research Council, IBFM-CNR, Catanzaro, Italy

G. L. Cascini
Nuclear Medicine Unit, Department of Diagnostic Imaging, Magna Graecia University, Catanzaro, Italy

N. Urbano
Nuclear Medicine Unit, University Hospital "Tor Vergata", Rome, Italy

O. Schillaci
Department of Biomedicine and Prevention, University "Tor Vergata", Rome, Italy

Department of Nuclear Medicine and Molecular Imaging, IRCCS Neuromed, Pozzilli, IS, Italy

F. Calabria, O. Schillaci (eds.), *Radiopharmaceuticals*,
https://doi.org/10.1007/978-3-030-27779-6_1

Abbreviations

^{18}F-FDG	^{18}F-Fluoro-deoxyglucose
BOLD	Blood oxygenation level dependent
FLAIR	Fluid attenuation inversion recovery
MIP	Maximum intensity projection
MRI	Magnetic resonance imaging
PET/CT	Positron emission tomography/computed tomography
ROI	Region of interest
SPECT/CT	Single photon emission computed tomography/computed tomography
SUVmax	Maximum standardized uptake value

1.1 Synthesis

^{18}F-FDG is a glucose analog with the hydroxyl group on the 2-carbon of a glucose molecule replaced by ^{18}F, a β+ emitter isotope of Fluorine. ^{18}F-FDG can be synthesized by either electrophilic or nucleophilic fluorination reactions. The first synthesis of 1^{8}F-FDG was obtained in 1976 by electrophilic fluorination [1]. Instead, the chemical reaction of nucleophilic substitution involves the addition of a nucleophilic molecule (a negatively charged molecule) into a molecule with a leaving group (electron drawing group attached to the parent molecule through an unstable chemical bond). Nucleophilic fluorination, using mannose triflate as precursor and tetrabutylammonium salts, is largely used because of the high yield and short reaction time [2]. The main quality control requirements of ^{18}F-FDG regard the identity of radionuclide, radiochemical purity, pH, residual solvent, sterility, and the level of bacterial endotoxin. These tests should be finished after the tracer can be released [2].

1.2 Pharmacokinetics

Being an analog of glucose, the ^{18}F-FDG plays an undisputed role in PET imaging, due to its versatility as marker of cellular metabolism. ^{18}F-FDG enters the cell by the same membrane transport mechanism as glucose. After penetration of the cellular membrane via glucose transporters [3], both ^{18}F-FDG and glucose are phosphorylated by hexokinase. Unlike glucose-6-phosphate, ^{18}F-FDG-6-phosphate is not a substrate of glucose-6-phosphate isomerase and does not undergo further metabolism in the glucose pathway. Therefore, ^{18}F-FDG remains trapped within cells (Fig. 1.1). The increased glucose utilization in tumor cells is due to three main reasons: overexpression of membrane glucose transporters, increased hexokinase activity, and decreased levels of glucose-6-phosphatase [4].

Physiologically, the tracer is taken up in cells with high metabolism or gradient of glucose uptake, as in the brain. First studies on ^{14}C-deoxgyglucose as imaging agent well displayed that synapses metabolism is strictly related with neuronal cells metabolism [5].

Subsequently, the ^{18}F-FDG has been successfully employed as tumor imaging marker, since it provides useful functional information based on the increased glucose uptake and glycolysis of cancer cells. Moreover, after the antiblastic therapy, this tracer can be considered as marker of response to therapy, owing to show the decrease of glucose metabolism in cancer cells, after therapy.

The clearance of ^{18}F-FDG is rapid and involves the renal system, through a filtration process of

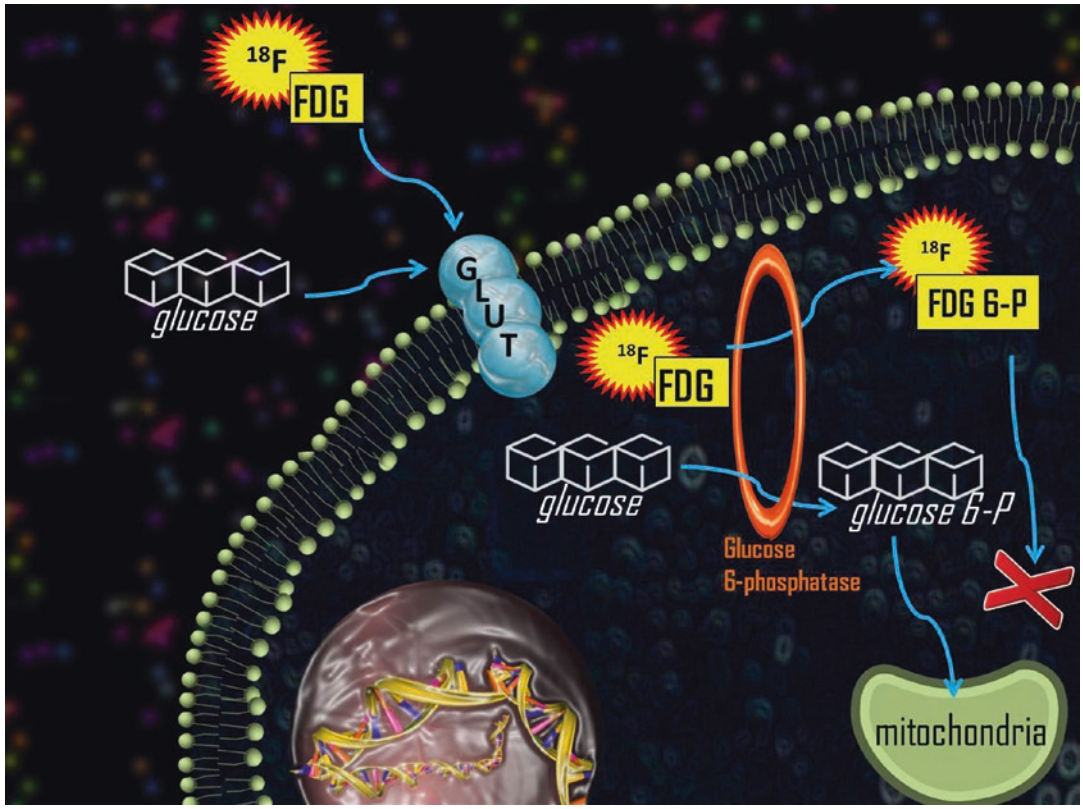

Fig. 1.1 Being an analog of glucose, the ^{18}F-FDG is internalized in cells and phosphorylated

^{18}F-FDG from blood pool into kidneys and a rapid production of radioactive urine, starting few minutes after the intravenous administration.

1.3 Physiological Distribution

The physiological distribution of ^{18}F-FDG concerns organs or tissues with high rate of glucose metabolism: in the brain, this radiopharmaceutical is normally taken up in the normal structures of gray matter, basal ganglia, cerebellum, and thalamus. A lower uptake gradient can be observed in the glial cells of the white matter, rectus muscle of the eye, medial and lateral, can show tracer uptake due to physiologic activity.

The myocardium normally can show high ^{18}F-FDG uptake, with a certain variability, since glucose is not the primary metabolic substrate of the myocardium. Due to the high affinity of the reticuloendothelial cells, spleen and bone marrow are usually characterized by mild uptake. The liver usually shows high gradient of uptake while kidneys, ureters, and bladder are normally visualized at PET imaging, due to the tracer renal excretion (Fig. 1.2). A certain grade of vascular activity can also be observed, especially for early imaging, in mediastinal vascular structures or in the iliac arteries. Finally, other sites of mild uptake are salivary and lachrymal glands, pancreas, stomach, and, due to the peristaltic activity, the intestinal loops, with large intra-individual variability.

Among some physiopathological features of bio-distribution of the ^{18}F-FDG should be primarily considered the possibility of a diffuse homogeneous bone marrow uptake, which usually reflects hyperplastic bone marrow which can be documented in patients undergoing chemotherapy (Fig. 1.3).

Several methods are available for measuring the rate of ^{18}F-FDG accumulation in tissues. PET

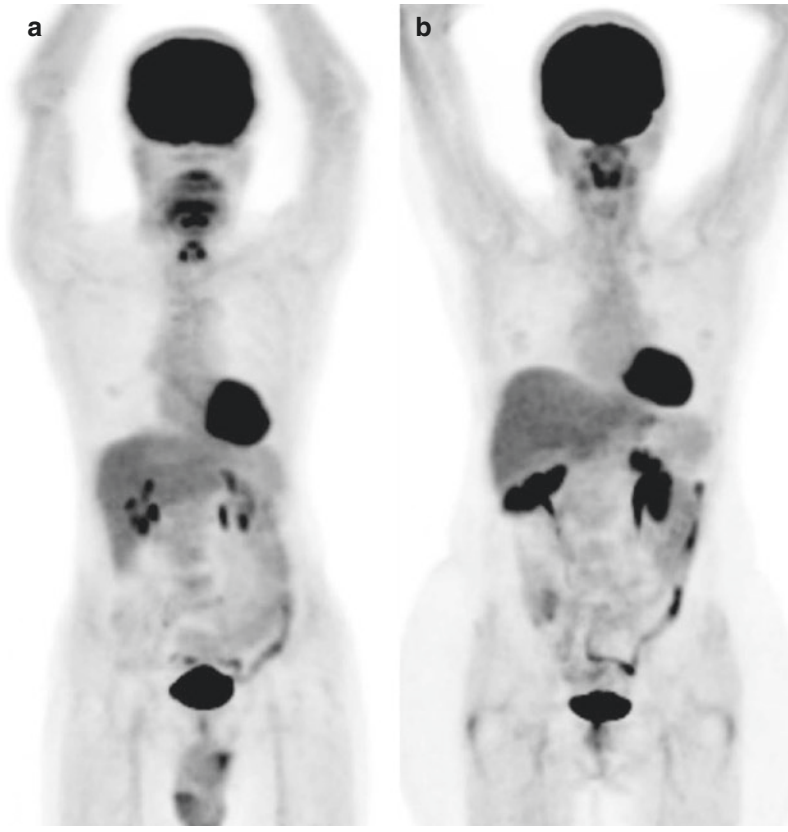

Fig. 1.2 Physiological whole body ^{18}F-FDG bio-distribution in a 42-year-old male subject (**a**) and a 36-year-old female subject (**b**)

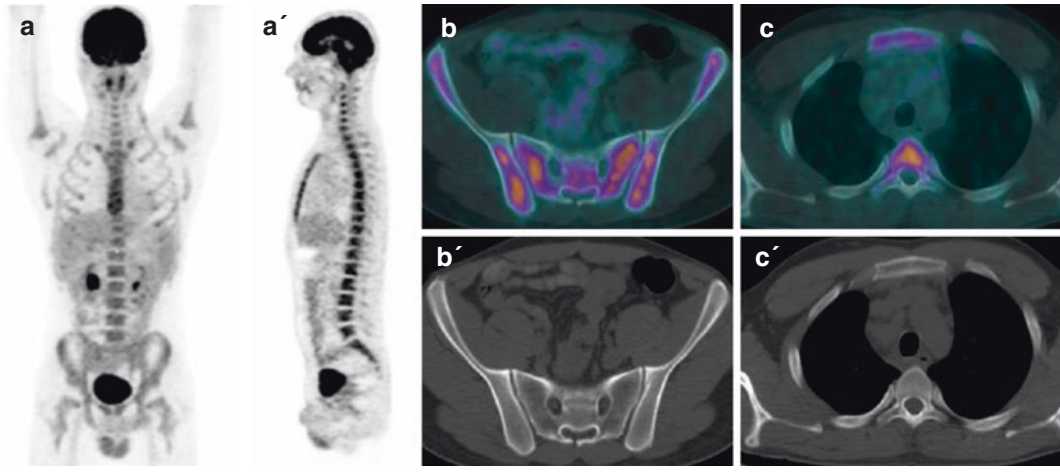

Fig. 1.3 ^{18}F-FDG 3D PET maximum intensity projection in coronal (**a**) and lateral (**a'**) views shows diffuse physiological uptake in the skeleton of a 45-year-old woman, due to bone marrow activation, 15 days after the end of chemotherapy. As evident in axial PET/CT (**b**, **c**) and CT (**b'**, **c'**) details, no morphological abnormalities are associated with functional findings

scanners are designed to measure the in vivo radioactivity concentration [kBq/mL], which is directly linked to the tracer concentration. However, it is the relative tissue uptake of ^{18}F-FDG that is of interest. The two most significant sources of variation that occur in practice are the amount of injected ^{18}F-FDG and the patient size. To compensate for these variations, the standardized uptake value (SUV) is used as a relative measure of ^{18}F-FDG uptake as it represent the most commonly used semiquantitative parameter for analysis of oncology PET studies.

The SUV is a semiquantitative value expressing degree of metabolic activity in selected tissues [6], by using a region of interest (ROI), and can be obtained by the following formula:

$$\mathrm{SUV} = r\left(a' / w\right)$$

where r is the radioactivity activity concentration [kBq/mL] measured by the PET scanner within a ROI, a' is the decay-corrected amount of injected radiolabeled FDG [kBq], and w is patient weight [7]. Moreover, the maximum standardized uptake value (SUVmax) is the maximum number of counts within the pixels in a ROI and can be considered the actual semiquantitative measure useful in assessing ^{18}F-FDG rate of uptake in tissues.

A SUVmax cutoff value of 2.5 is commonly used to differentiate between benign and malignant lesions in PET/CT [8]; however, there are a significant number of false positives (due to inflammatory diseases) and false negatives (due to low-grade malignancies) [9]. It is necessary to state that, in oncology ^{18}F-FDG PET is generally assessed using visual criteria, looking for a focal area of increased uptake that can be compatible with malignancy, in the clinical context [10].

1.4 Clinical Indications

1.4.1 Differentiation Between Benign and Malignant Lesions

For its peculiar molecular properties, the ^{18}F-FDG is successfully employed in the differential diagnosis between malignant and benign lesions, or in assessing the metabolism of uncertain findings at conventional radiologic imaging. ^{18}F-FDG PET/CT can be useful for the characterization of enlarged lymph nodes, in the differential diagnosis among benign and malignant lesions of the bones and soft tissues. One of the most important field of applications of ^{18}F-FDG PET is the evaluation of solitary lung node: to date, the ^{18}F-FDG PET/CT allows to simultaneously evaluate the metabolism of the lung nodes and to depict, by the measurement of the SUVmax, which can improve the visual assessment of PET data in a clinical context [11]. In particular, it has been showed that a SUVmax > 2.5 is frequently associated with a possibility of malignant nature of lung nodules. However, correlative CT imaging can also improve the specificity of PET imaging, allowing the concurrent possibility to describe morphologic findings as size, margins, eccentric calcifications or to ensure the contrast enhancement, when administered [9]. Anyway, the metabolic depiction of the pulmonary lesion is a significant information, especially for those lung nodes without evident radiographic characteristics of malignancy (Fig. 1.4). On the other hand, nuclear medicine physicians cannot exclude the possibility of malignancy in some histological types of lung cancer, without significant glucose metabolism, as for bronco-alveolar carcinoma [12]: the accurate knowledge of the CT diagnostic criteria is of the utmost importance, allowing to consider the PET/CT as an unique, hybrid, single session, whole body imaging modality with an useful overall diagnostic accuracy.

1.4.2 Unknown Primary Tumor

Unknown primary tumors are a heterogeneous group of metastatic malignancies in which the primary tumor could not be detected despite diagnostic evaluation. Generally, these tumors are characterized by the presence of a metastatic lymph nodal disease, evident at conventional imaging (CT and/or MRI), with positive histological exam for malignant cells and no evidence of the primitive lesion [10]. The unknown primary tumors are aggressive diseases, with a

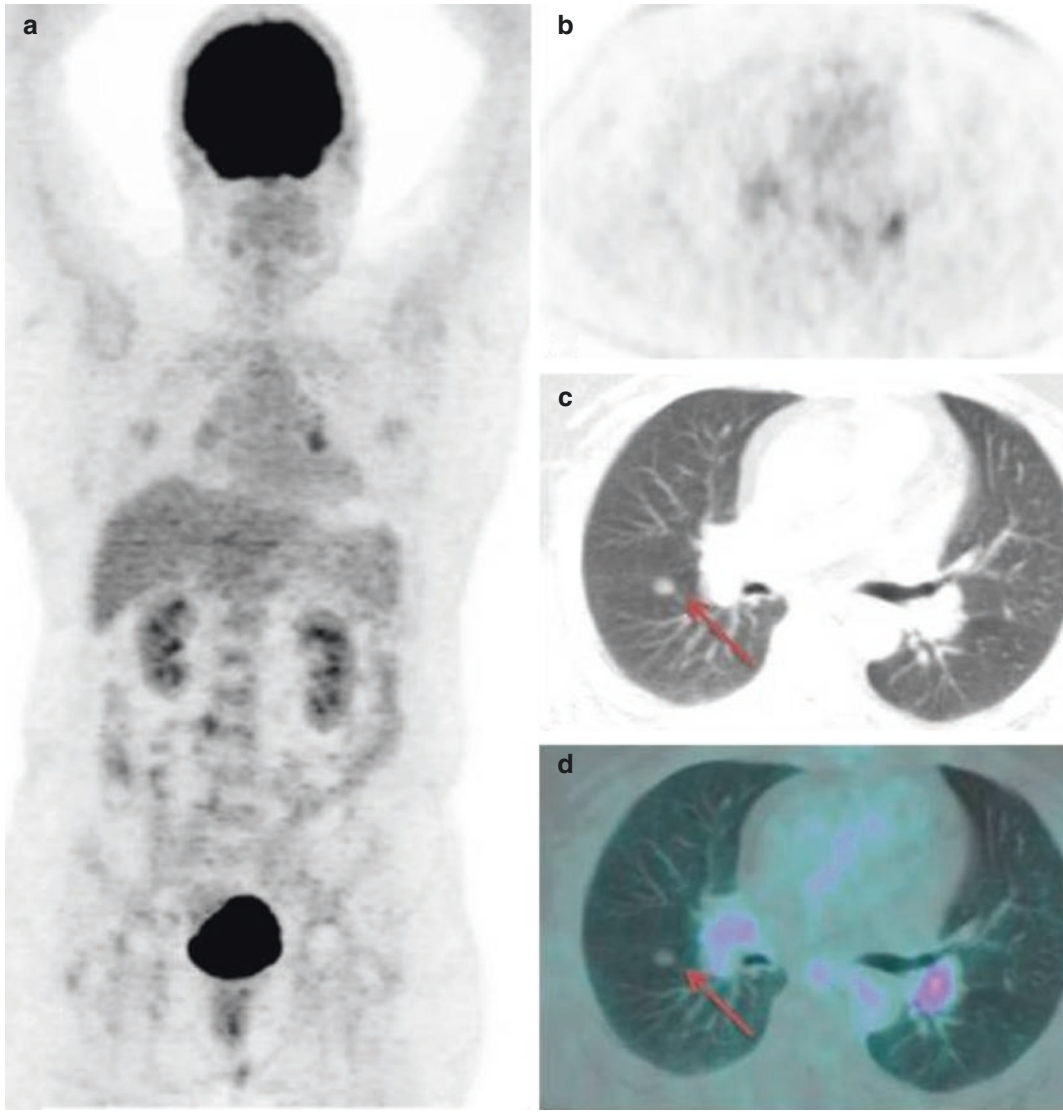

Fig. 1.4 Metabolic evaluation of a node in the right lung. PET 3D maximum intensity projection (**a**) and corresponding axial PET view (**b**) do not show significant uptake in the lesion. Axial CT (**c**) and PET/CT (**d**) views display a 1-cm wide node with regular margins and without characteristics of malignancy

poor survival, ranging from only 2 to 10 months from the diagnosis. Anyway, it can be hypothesized that the detection of the primary tumor may optimize treatment planning and, therefore, patient prognosis [13]. Despite a low diagnostic performance of ^{18}F-FDG PET/CT in detecting unknown primary tumors (Fig. 1.5), ranging from 25% to 43% in several meta-analysis [14], this diagnostic tool should be considered as first-line imaging method, due to the challenge to ensure the diagnosis with CT and to the very poor diagnostic accuracy of conventional imaging on this topic.

1.4.3 Staging

One of the main indications for ^{18}F-FDG PET/CT is the staging of patients with known malignancies, due to the capability in assessing tumor

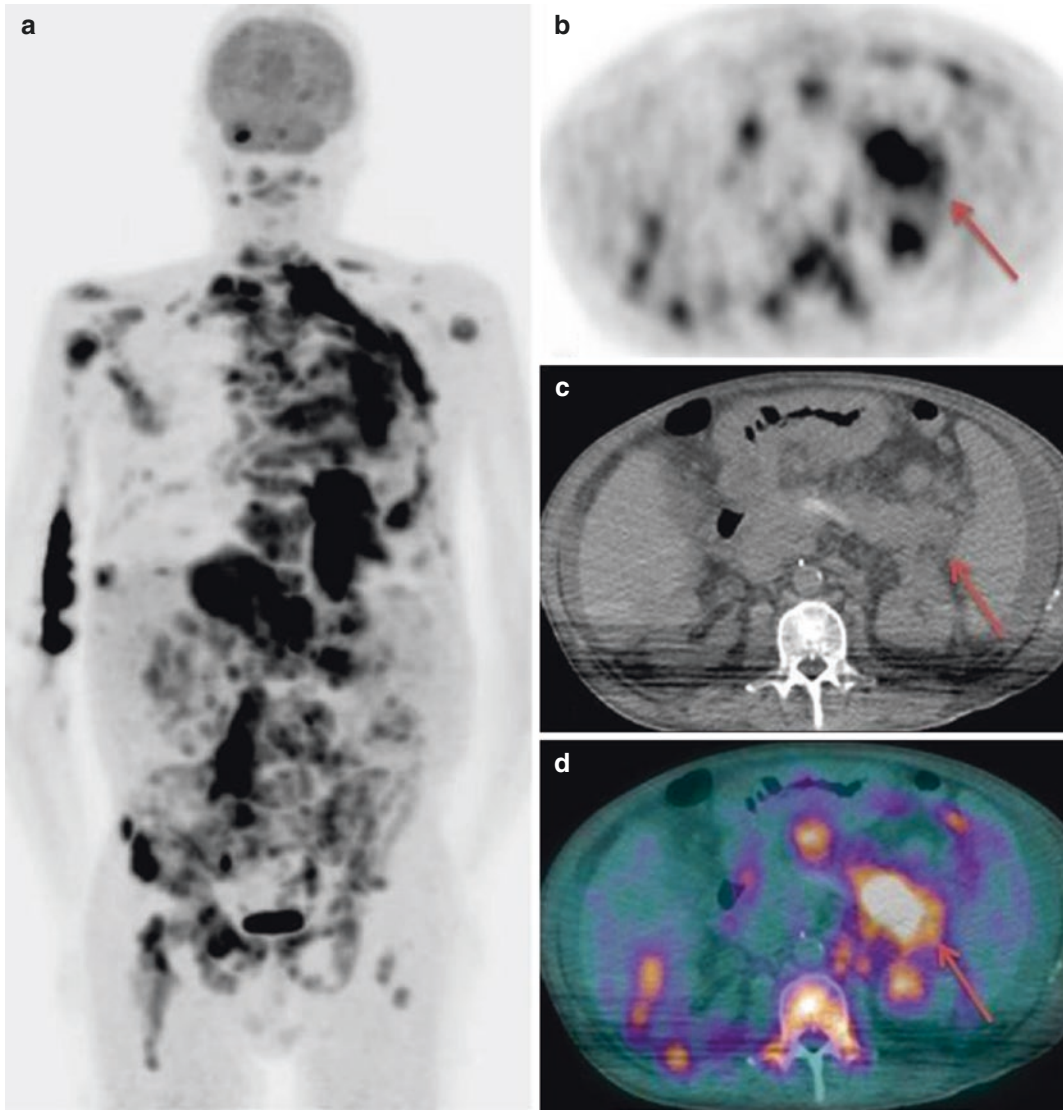

Fig. 1.5 Patient with multiple metastases of unknown primary tumor. ^{18}F-FDG 3D PET Maximum intensity projection (**a**) shows multiple areas of pathologic tracer uptake in the brain, lungs, skeleton, thorax, and abdomen. Axial PET (**b**), CT (**c**), and PET/CT (**d**) views show focal and intense uptake in the tail of the pancreas (*final histological diagnosis: pancreas carcinoma*)

extension, lymph node metastases, and bone secondary lesions [15]. In fact, the hybrid PET/CT evaluation, with and without contrast media administration, also provides in a single whole body scan to rapidly obtain information regarding the primitive tumor and metastases, in order to choice the best therapeutic approach.

Indications for ^{18}F-FDG PET/CT during the staging of solid tumors include, but are not limited to, the following: lung cancer [16], locally advanced breast cancer (Fig. 1.6) [17], sarcoma [18], lymphomas (Fig. 1.7) [19], colon cancer [20], gynecological malignancies [21], and other kinds of tumor with high grade of glucose metabolism which potentially can be radically treated. ^{18}F-FDG PET-CT can also be used as a problem-solving tool to establish the baseline staging before commencing treatment in

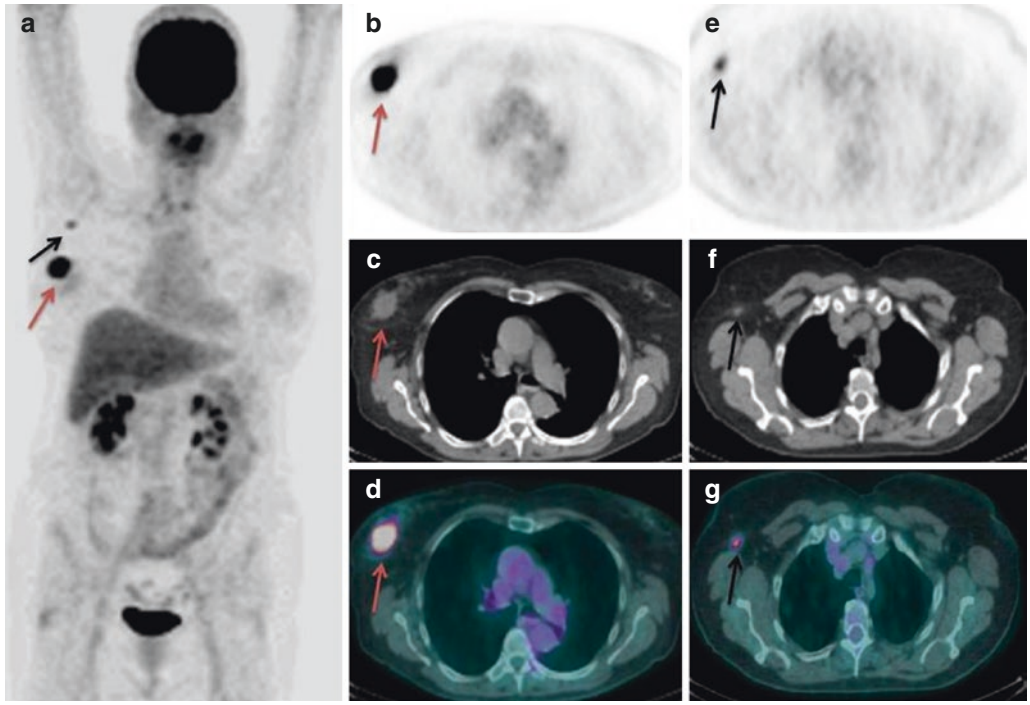

Fig. 1.6 A 56-year-old woman examined for staging locally advanced breast cancer. PET 3D maximum intensity projection (**a**) shows pathologic uptake in the upper outer quadrant of the right breast (*red arrow*) and a further area of uptake in the ipsilateral axilla (*black arrow*), as evident in corresponding axial PET views (**b**, **e**). The uptake was linked to a 3.2-cm-wide node in the breast and to a 1-cm-wide metastatic lymph node, as showed in corresponding CT (**c**, **f**) and PET/CT views (**d**, **g**)

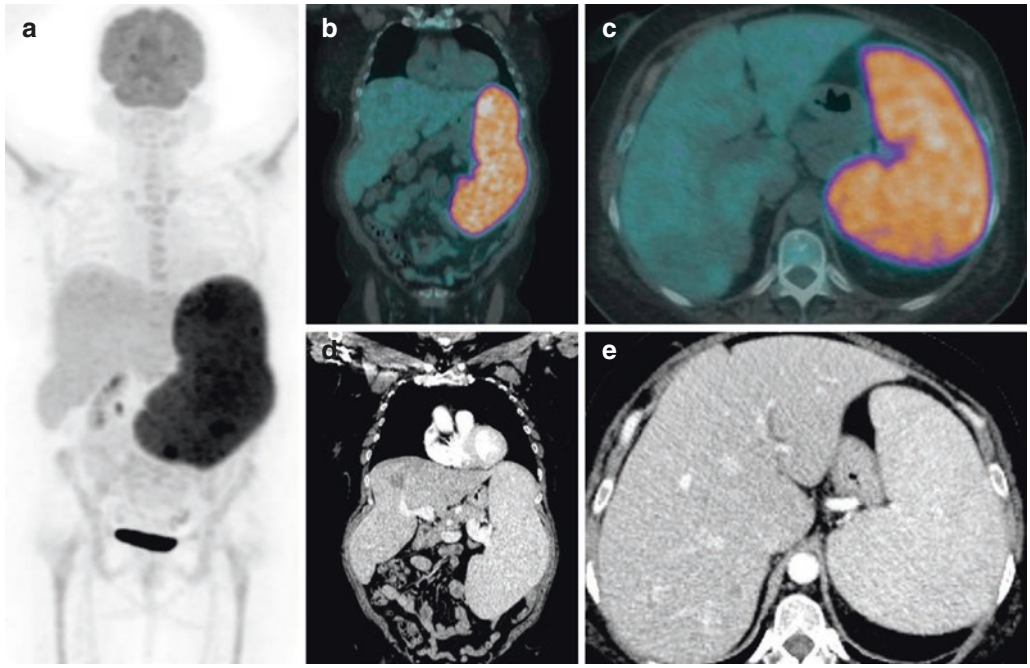

Fig. 1.7 In a patient with splenic lymphoma, PET 3D maximum intensity projection (**a**) shows abnormal tracer uptake in the spleen, in association with splenomegaly, as evident in PET/CT (**b**, **c**) and contrast-enhanced CT (**d**, **e**) coronal and axial views

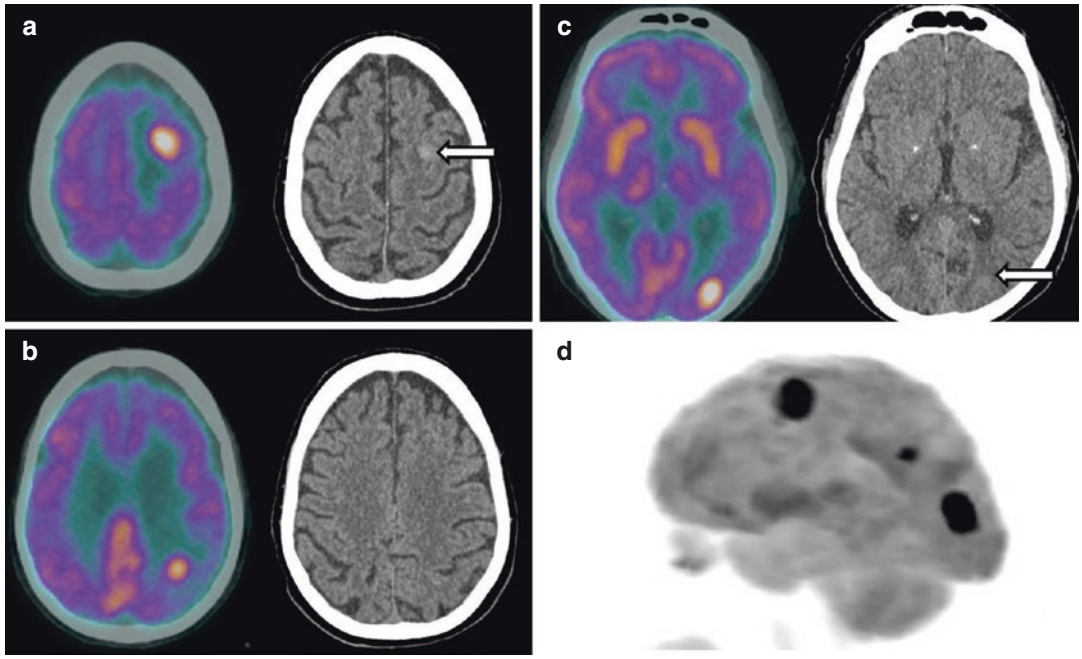

Fig. 1.8 In a patient with dorsal melanoma, axial PET/CT and CT views (**a**, **b,** and **c**) show three foci of abnormal ^{18}F-FDG uptake in subcortical frontal, parietal, and occipital regions of the left cerebral hemisphere, due to hyperdense lesions (arrows), also evident in PET 3D maximum intensity projection of the brain (**d**)

gastro-intestinal stromal tumors [22] and in head and neck cancer and prior to radical nodal resection in patients with suspicion of metastatic melanoma (Fig. 1.8) [23].

^{18}F-FDG PET/CT is also a valid guide to biopsy of suspected secondary bone lesions from somatic tumors [24] or in detecting the best site to perform biopsy. In fact, ^{18}F-FDG PET/CT has the advantage to accurately differentiate viable from nonviable tissues. This feature can reduce inconclusive biopsy results by specifically targeting areas of viability showing high rate of glucose metabolism [25].

1.4.4 Restaging

^{18}F-FDG PET/CT is also useful in detecting tumor recurrence in patients with solid tumors previously treated for curative intent. The diagnostic performance of the exam is accurate especially in patients with rising tumor markers [26], suggestive for tumor relapse. Other tumors which can be evaluated during this phase are urological malignancies [27] and ovarian (Fig. 1.9) and esophageal cancer [28]. Also in this clinical setting, ^{18}F-FDG PET/CT has proven to be more accurate modality than CT for assessment of recurrence [29]**.**

1.4.5 Assessment of Response to Therapy

Being an in vivo marker of tumor growth and vitality, the ^{18}F-FDG is useful for characterization of cancer cells metabolism during the time, especially for evaluating the response to therapy (chemotherapy and/or radiotherapy). In oncology, this approach can be directly applied in evaluating disease progression or in detecting the reduction of tumor metabolism [30], allowing to exceed limits of conventional anatomical imaging (Fig. 1.10).

On this topic, the "*interim PET*" with ^{18}F-FDG, and its comparison with the "*baseline PET,*" has become a milestone for the imaging of lymphomas. In particular, in patients with Hodgkin lymphoma,

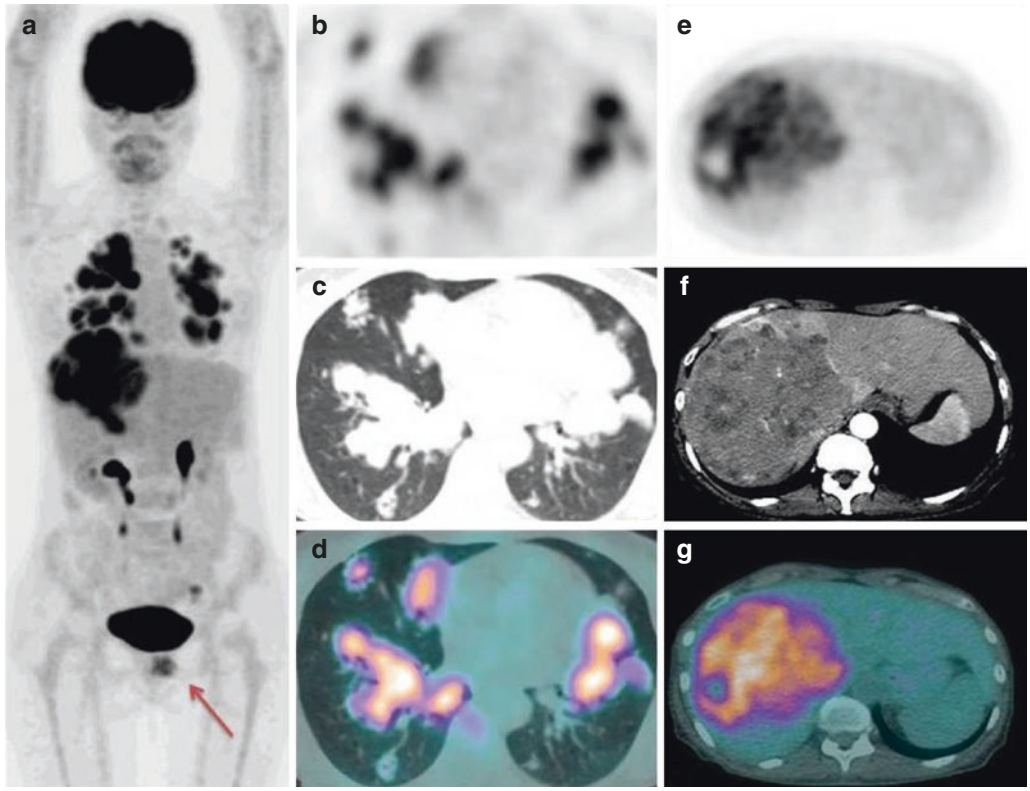

Fig. 1.9 Restaging in a 55-year-old patient with ovarian cancer and rising level of Ca-125, previously submitted to surgical intervention of isteroannessiectomy. PET 3D maximum intensity projection (**a**) shows pathologic uptake in the pelvis (*red arrow*) with multiple metastases in lungs (**b**, **c**, **d**) and liver (**e**, **f**, **g**), as evident in axial PET, CT, and PET/CT details

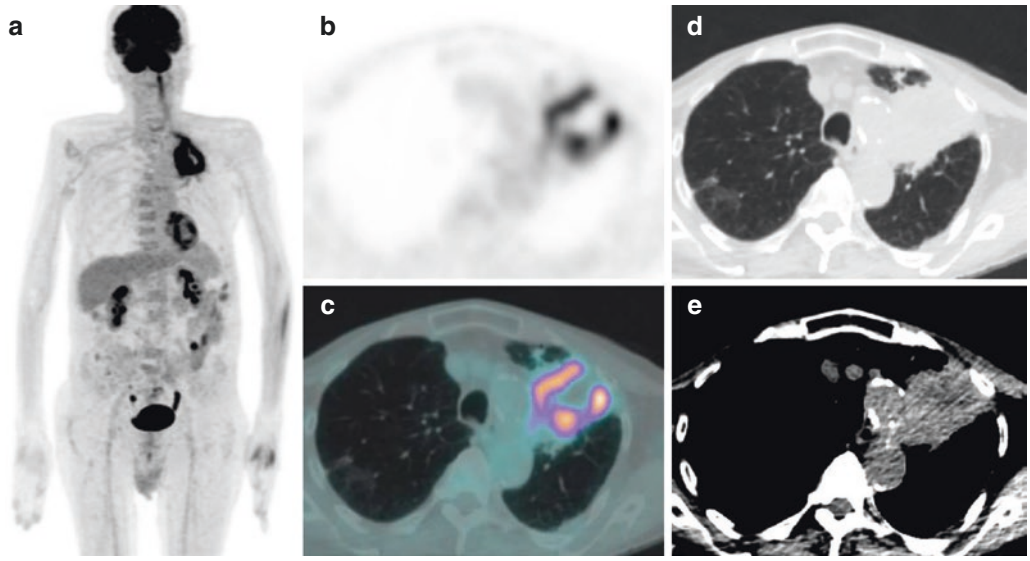

Fig. 1.10 A patient examined 3 months after radiotherapy for lung cancer. PET 3D maximum intensity projection (**a**) shows pathologic tracer uptake in the upper lobe of left lung, with internal core of hypometabolism due to post-actinic necrosis, as evident in axial ^{18}F-FDG PET (**b**) and PET/CT (**c**) views. Relative CT views (**d**, **e**) confirm a lung lesion with irregular borders and pleural infiltration

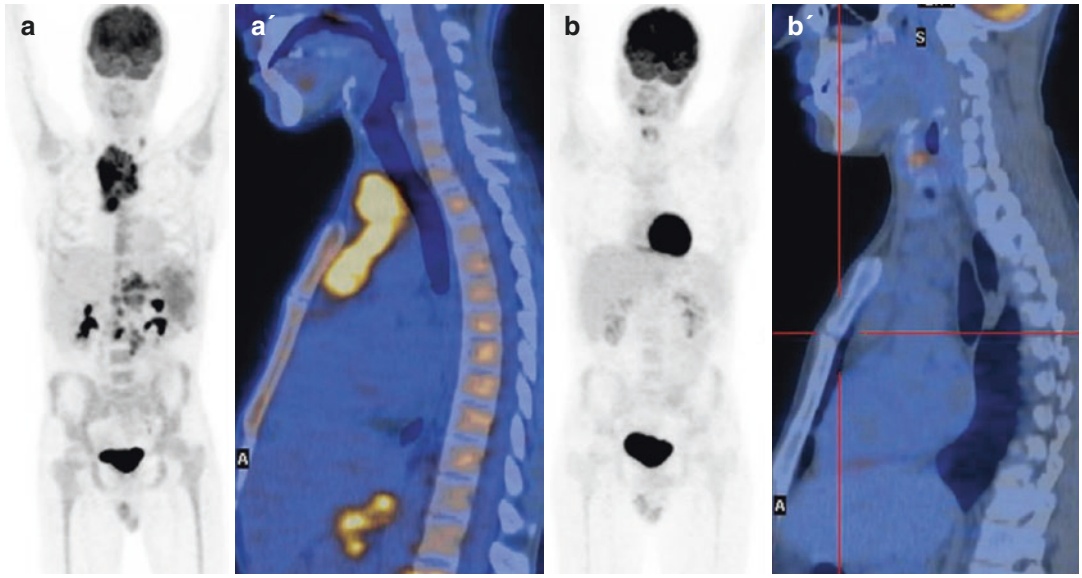

Fig. 1.11 "*Baseline*" (**a**, **a'**) and "*interim* (**b**, **b'**) *^{18}F-FDG PET/CT*" showing a patient with mediastinal bulky Hodgkin lymphoma before and after two cycles of *Adriamycin-Bleomycin-Vinblastine-Dacarbazine* (ABVD). The complete absence of uptake in the mediastinum in the *interim PET* (**b**, **b'**), assessed by visual analysis, allows to diagnose early response to therapy and to predict a complete remission of lymphoma. Interestingly, a residual hypodense tissue is still evident in the upper mediastinum in sagittal PET/CT view of the *interim PET/CT* (**b'**), not expressing metabolic activity

the *interim PET* after two courses of standard therapy allows to ensure the response to therapy and to predict the survival-free progression of patients. For example, a negative "*interim PET*" determines the prosecution of the standard therapy and is associated with a complete remission of the disease (Figs. 1.11 and 1.12). Instead, the minority of patients with Hodgkin lymphoma presenting a positive "*interim PET*" need intensification of second-line chemotherapy with the eventual addition of radiotherapy [31] and present a poor prognosis (Fig. 1.13).

Beyond hematology, the principle of using the molecular properties of ^{18}F-FDG as marker of chemosensitivity can be applied to all solid tumors with high rate of glucose metabolism (Fig. 1.14). Moreover, this diagnostic tracer can also be useful in assessing response to radiotherapy (Fig. 1.15) [32].

1.4.6 Detection of Tumor Recurrence

An important feature of ^{18}F-FDG PET/CT is the capability to detect tumor recurrence of all tumors with high rate of glucose metabolism. The added value provided by the molecular properties of ^{18}F-FDG is the early diagnosis of local relapse or the identification of secondary metastases which can lead in an optimal assessment of small secondary lymph node lesions or bone metastases, also before the osseous remodeling.

This property can help clinicians in the early diagnosis of tumor recurrence and in promptly planning the best therapeutic approach, before these lesions can be detected at conventional imaging (Fig. 1.16).

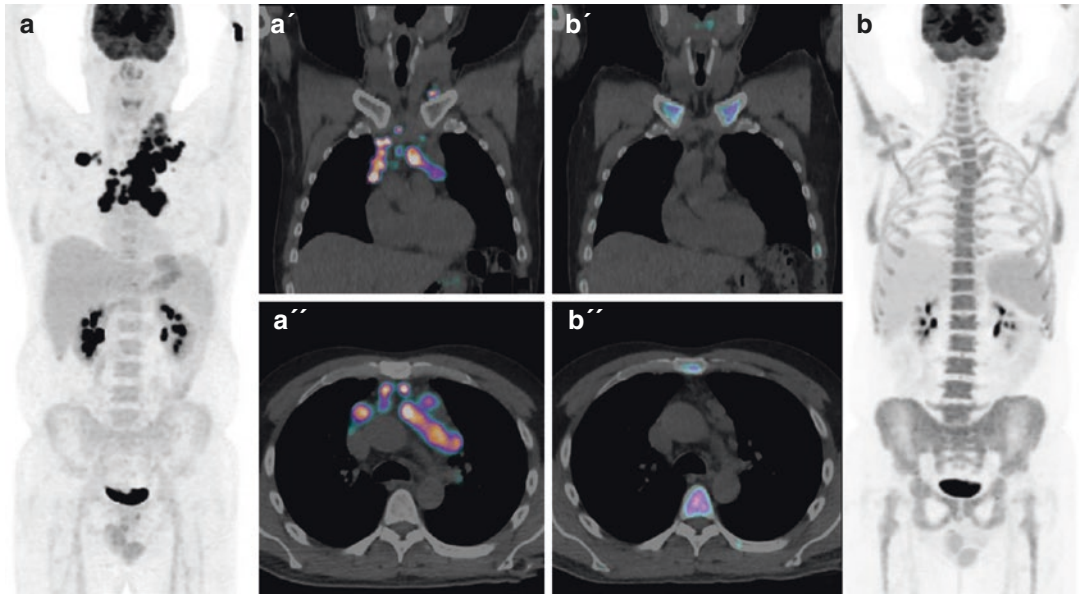

Fig. 1.12 In a patient with Hodgkin lymphoma, "*Baseline*" ^{18}F-FDG PET/CT (**a**, **a'**, **a"**) shows pathologic tracer uptake in cervical and mediastinal lymph nodes. After two cycles of *Adriamycin-Bleomycin-Vinblastine-Dacarbazine* (ABVD), the "*interim*" ^{18}F-FDG PET/CT (**b**, **b'**, **b"**) shows residual lymph nodes in mediastinum, without significant metabolic activity, diagnosing early response to therapy

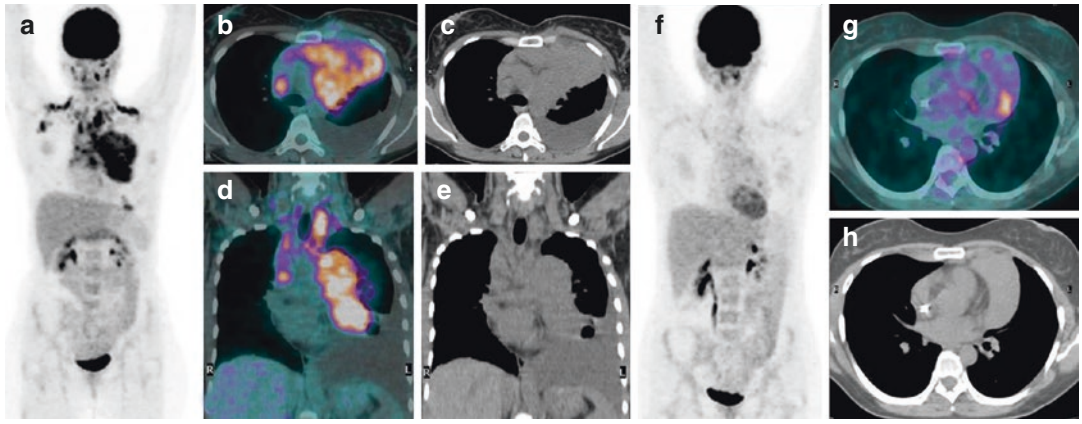

Fig. 1.13 "*Baseline* (**a**–**e**) *PET/CT*" of a patient with Hodgkin lymphoma showing a bulky mediastinal mass with other cervical lymph nodes, expressing pathologic tracer uptake. Despite the significant reduction of the volume lesion after two cycles of *Adriamycin-Bleomycin-Vinblastine-Dacarbazine* (ABVD), the "*interim PET/CT"* (**f–h**) displays a single area of focal uptake in the residual lesion of upper mediastinum, indicative of failed response to therapy

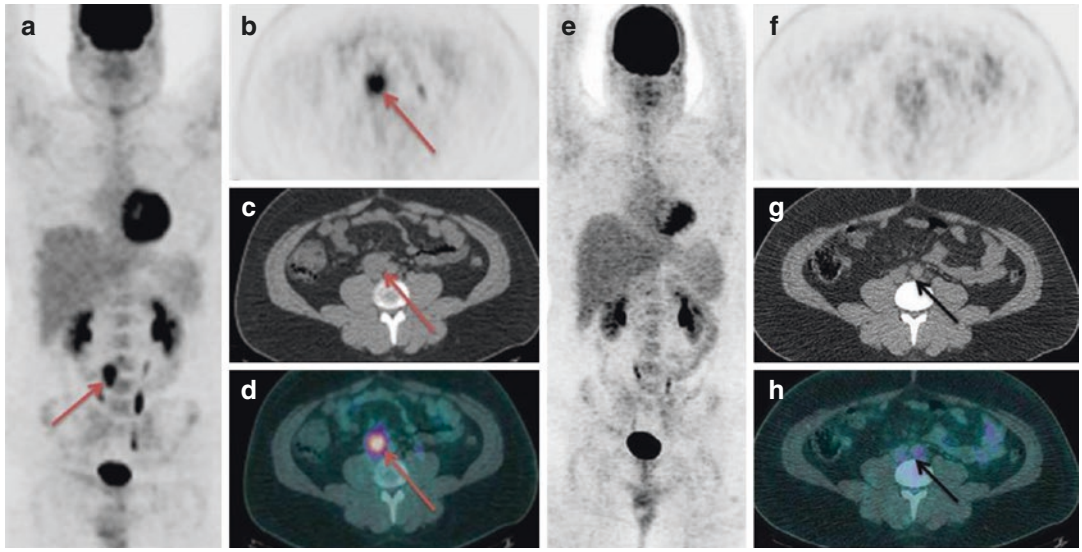

Fig. 1.14 A 23-year-old patient previously submitted to excision of seminoma of the right testicle was examined by PET/CT, showing pathologic tracer uptake in a 2.8-cm-wide abdominal, retrocaval lymphadenopathy (red arrow), evident in MIP (**a**) and axial PET (**b**), CT (**c**), and PET/CT (**d**) views. After the end of chemotherapy, a further exam allowed to diagnose a residual lymphatic tissue without meaningful metabolic activity, indicative of response to therapy, as evident in MIP (**e**) and axial PET (**f**), CT (**g**), and PET/CT (**h**) views

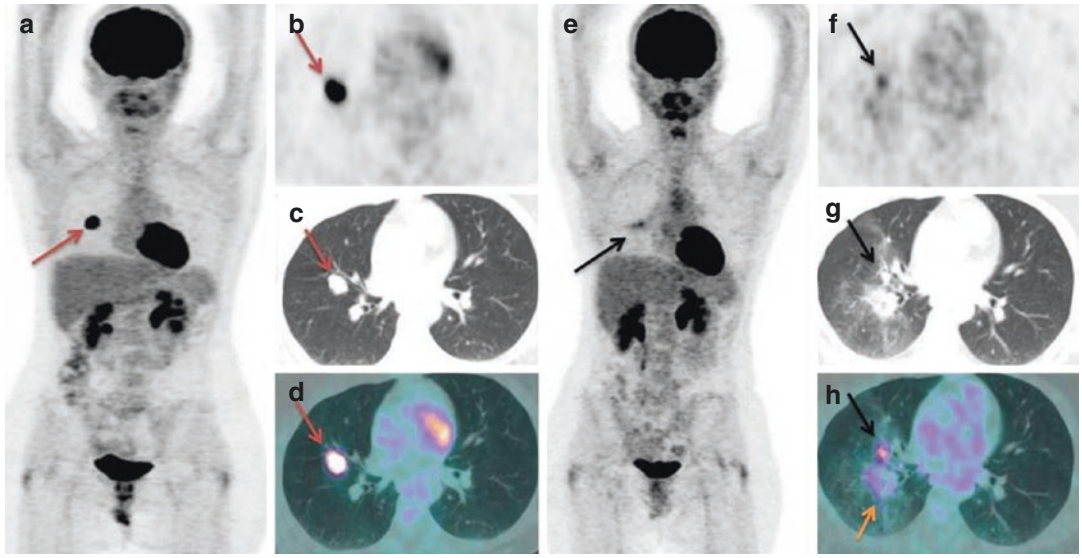

Fig. 1.15 PET 3D maximum intensity projection (**a**) shows pathologic tracer uptake in a lung node, 2.8 cm wide (*red arrow*), better displayed on correlative axial PET (**b**), CT (**c**), and PET/CT (**d**) views. Histological exam diagnosed lung carcinoma. Six months after radiotherapy (**e–h**), the volume lesion was considerably reduced with mild metabolic activity, indicative of residual tumor (*black arrow*). The *yellow arrow* in axial PET/CT view (**h**) shows low, physiological uptake in radiation-induced lung inflammation

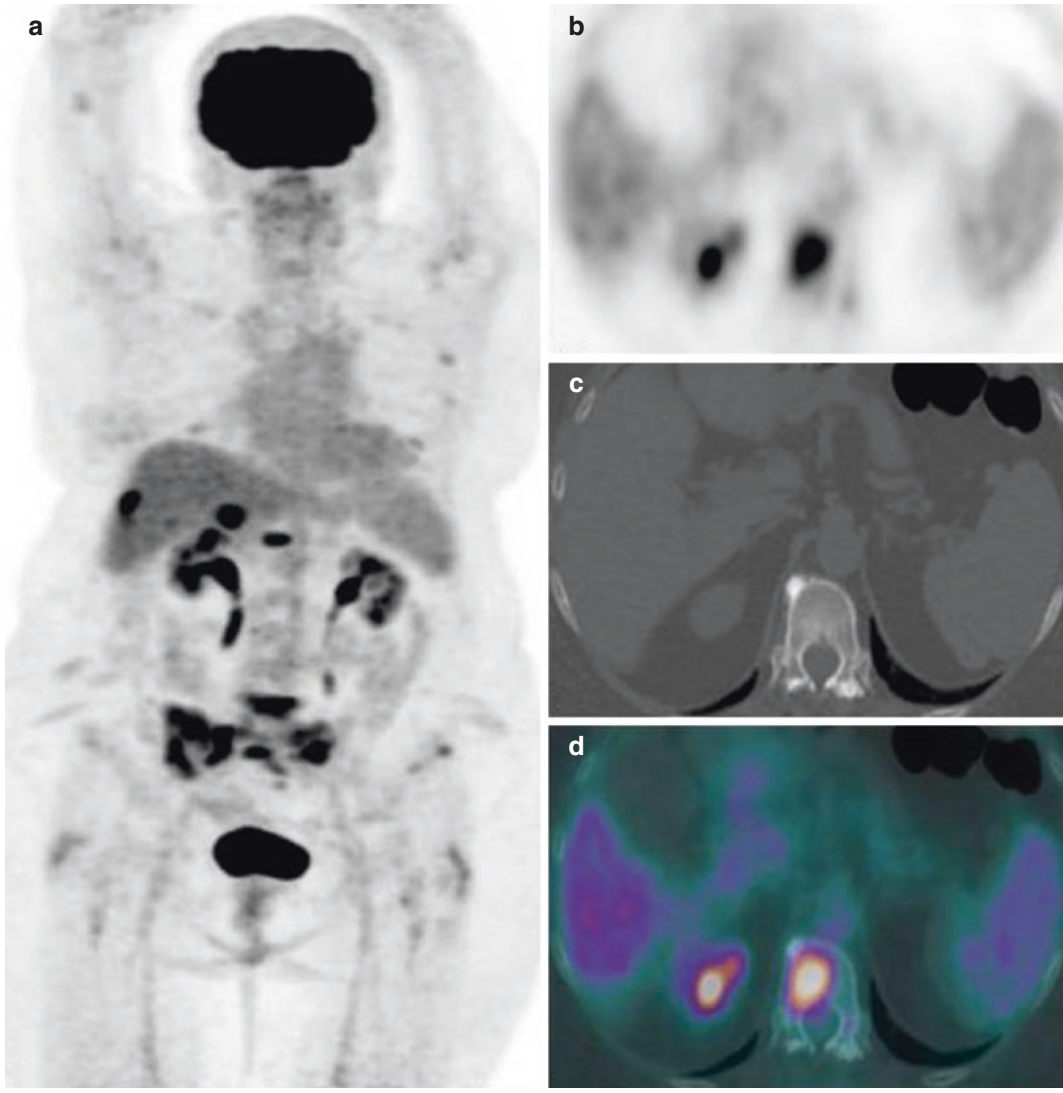

Fig. 1.16 ^{18}F-FDG PET 3D maximum intensity projection (**a**) shows several bone metastases and a hepatic lesion in a 61-year-old woman examined for restaging breast cancer. Axial PET detail (**b**) shows focal uptake in the 11th thoracic vertebra, without morphological alterations on the CT component of the exam (**c**, **d**)

1.4.7 Radiation Therapy Planning

The appropriate selection and delineation of target volumes prior to perform radiotherapy in oncology, generally performed with contrast-enhanced CT or MRI, is of the utmost importance. The intrinsic advantage of PET imaging is the possibility to delineate the metabolically active part of tumors, improving the choice and the extension of the radiotherapy field. Naturally, limits of this tool are the low spatial resolution, which has been recently considerably improved by the development of novel PET/CT and hybrid PET/MRI scanners.

For lung cancer, the ^{18}F-FDG PET/CT for radiation planning has added biological information in defining the gross tumor volume and the eventual concomitant nodal disease. For example, the accurate target delineation between tumor and atelectasis is achievable by using PET and CT imaging simultaneously [33]. Several articles recently published propose the use of PET/CT for radiotherapy planning in esophageal cancer, head and neck carcinoma, and anal tumors [34–36].

1.4.8 Inflammation and Infection

In addition to its established role in oncological imaging, ^{18}F-FDG PET/CT can also have clinical utility in evaluating infection and inflammation. In fact, this diagnostic tool can identify the source of inflammation (Fig. 1.17) or infection (Fig. 1.18), more accurately than conventional anatomical imaging techniques, such as CT and MRI. Moreover, ^{18}F-FDG PET/CT could map the extent of disease: for example, the involvement of bone tissue in case of osteomyelitis or *Charcot foot* (Fig. 1.19). Consecutive exams help to assess therapy response [37].

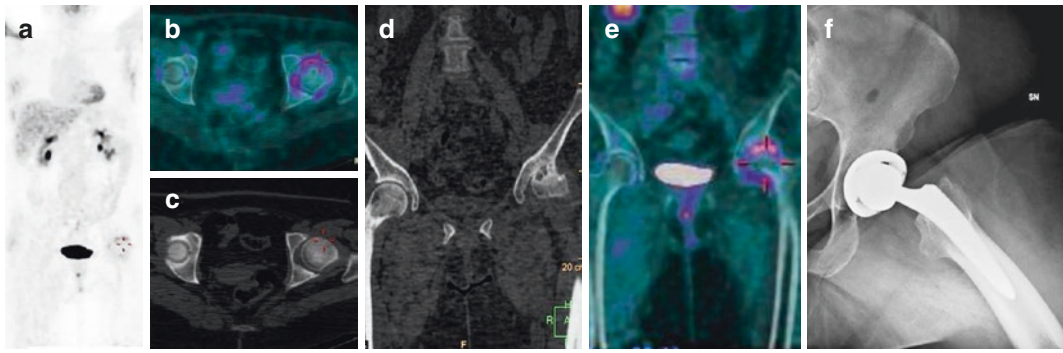

Fig. 1.17 ^{18}F-FDG PET 3D maximum intensity projection (**a**) shows diffuse uptake surrounding the head of left femur, due to inflammation, as evident in corresponding axial (**b**, **c**) and coronal (**d**, **e**) CT and PET/CT views. In particular, in coronal CT view (**d**) are evident the geodic lesions due to arthrosis. *X* rays (**f**), performed after surgical intervention, confirm the correct femoral prosthesis insertion

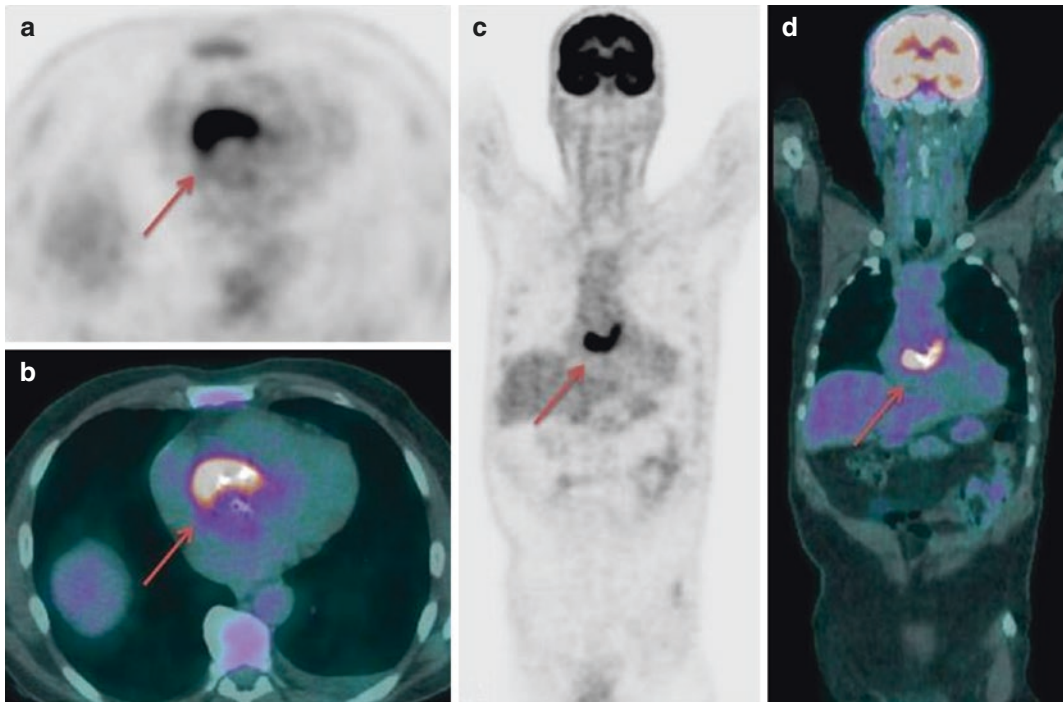

Fig. 1.18 A 57-year-old patient with prosthetic valve endocarditis: axial PET (**a**) and PET/CT (**b**) views, coronal PET (**c**) and PET/CT (**d**) views show high ^{18}F-FDG uptake around prosthetic aortic valve, indicative of infective endocarditis

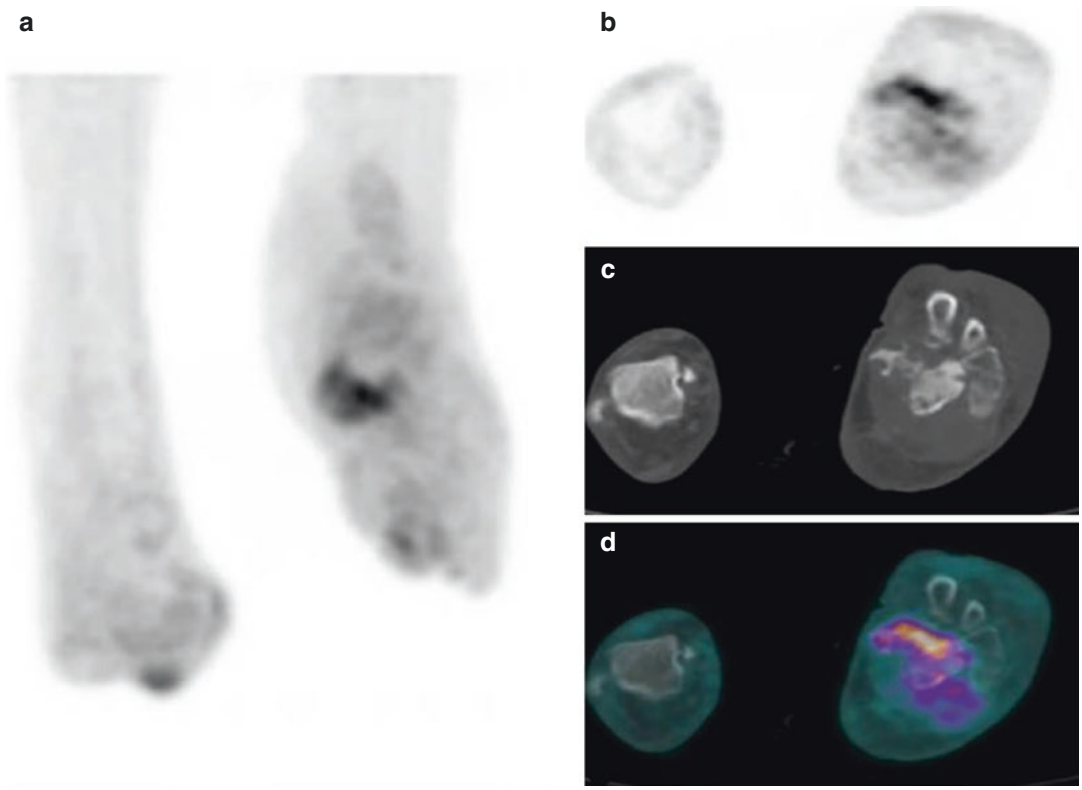

Fig. 1.19 ^{18}F-FDG PET/CT imaging in a diabetic foot: PET 3D maximum intensity projection (**a**) and PET axial view (**b**) show intense tracer uptake in the left tarsal region, with partial bone involvement, as evident in correlative axial CT (**c**) and PET/CT (**d**) views

The advantages of PET/CT technology, in comparison with conventional SPECT or SPECT/CT imaging with ^{99m}Tc-labeled leukocytes [38], are due to a shorter duration of examination, higher spatial resolution, and noninvasive nature of scan (Fig. 1.20) [39]. Anyway, due to the lack of specificity of ^{18}F-FDG, recent studies are examining ^{18}F-FDG-labeled leukocytes PET/CT as a useful diagnostic tool to investigate inflammation and infection in soft-tissues imaging [40].

^{18}F-FDG PET/CT can show inflammatory activity in the aorta and major arteries in patients with active Takayasu arteritis (Fig. 1.21). The intensity of accumulation may decrease in response to therapy [41, 42].

Under study is the potential usefulness of ^{18}F-FDG PET/CT in the assessment of activity, staging, follow-up and prognosis estimation of patients with chronic intestinal inflammatory disease as Crohn's disease [43] and ulcerative colitis [44].

Finally, ^{18}F-FDG PET/CT can be of help in diagnosis and assessment of response to therapy of invasive fungal infections [45, 46], tuberculosis [47], and other thoracic granulomatous diseases [48, 49].

1.4.9 Neuroimaging

^{18}F-FDG PET is able to visualize a *map* of the whole brain glucose metabolism, being normally enhanced in normal structures of white and gray matter.

In fact, the bio-distribution of ^{18}F-FDG in the brain regards gray and white matters, thalamus, caudate nuclei, and cerebellum. The reduction of the uptake in these structures allows to recognize some neurodegenerative diseases, characterized by a typical pattern of deficit extension, generally before morphologic abnormalities can be observed on MRI. For the same reason, the CT

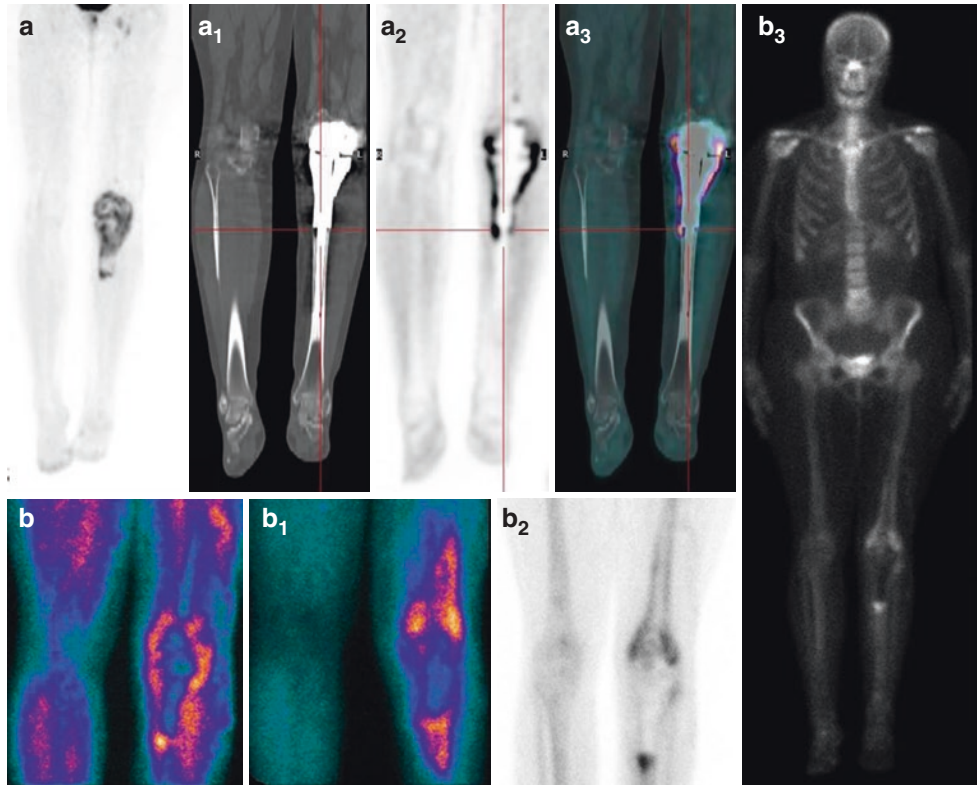

Fig. 1.20 ^{18}F-FDG PET 3D maximum intensity projection (**a**), coronal CT (**a$_1$**), PET (**a$_2$**), and PET/CT (**a$_3$**) views show intense pathologic tracer uptake surrounding a prosthesis of the left knee. Triphasic planar scintigraphy with ^{99m}Tc-labeled leukocytes (**b**, **b$_1$**, **b$_2$**, and **b$_3$**) confirms the diagnosis of soft tissue infection around the prosthetic joint. This case summarizes the better power resolution limit of PET/CT in comparison with a higher specificity of scintigraphic imaging with ^{99m}Tc-labeled leukocytes

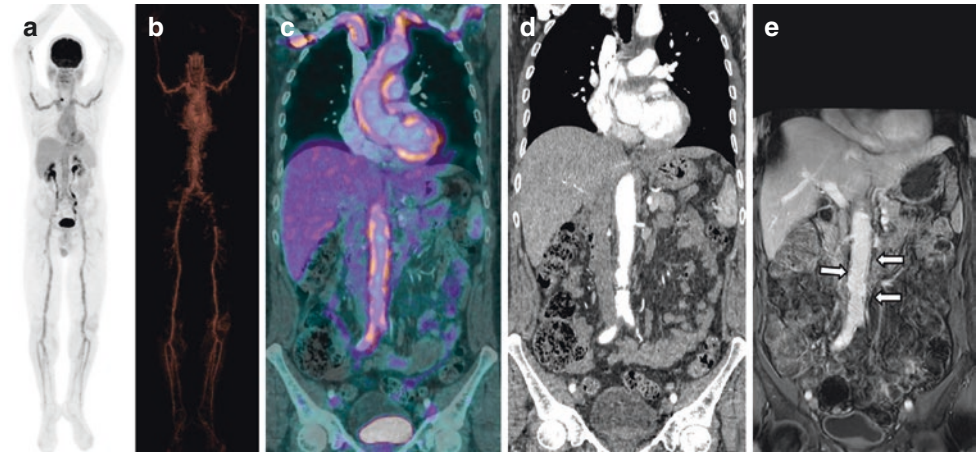

Fig. 1.21 Patient with Takayasu arteritis. ^{18}F-FDG PET 3D maximum intensity projection (**a**) and PET 3D volume rendering (**b**) show intense and pathologic tracer uptake in vascular structures of mediastinum and major arteries of the body. Coronal PET/CT (**c**) and contrast-enhanced CT (**d**) display the uptake in the abdominal aorta and iliac arteries. MRI (**e**) show abdominal aortic wall thickening (*arrows*). *Credits to Rosanna Tavolaro (MD) and Mario Leporace (MD), Department of Nuclear Medicine and Theranostics, Mariano Santo Hospital, Cosenza.*

component of the PET/CT, in neurological studies, is generally not useful, excepting data for attenuation correction and anatomical landmarks.

^{18}F-FDG PET can be a valid tool, according to clinical examination, in discriminating between several kinds of dementia: Alzheimer disease (AD) generally shows hypometabolism in the parietotemporal association area, posterior cingulate, and precuneus (Fig. 1.22); hypometabolism in the inferior parietal lobe and posterior cingulate/precuneus is a predictor of cognitive decline from mild cognitive impairment to AD dementia. On the other hand, a deficit of uptake in frontotemporal region is indicative of frontotemporal dementia. Moreover, seriate scans can offer the possibility to evaluate the disease progression and its evolution.

On the other hand, we must also consider the recent development and commercial availability of β-amyloid specific tracers (see Chap. 8), which are replacing ^{18}F-FDG scans in patients with suspicion of AD or mild cognitive impairment, due

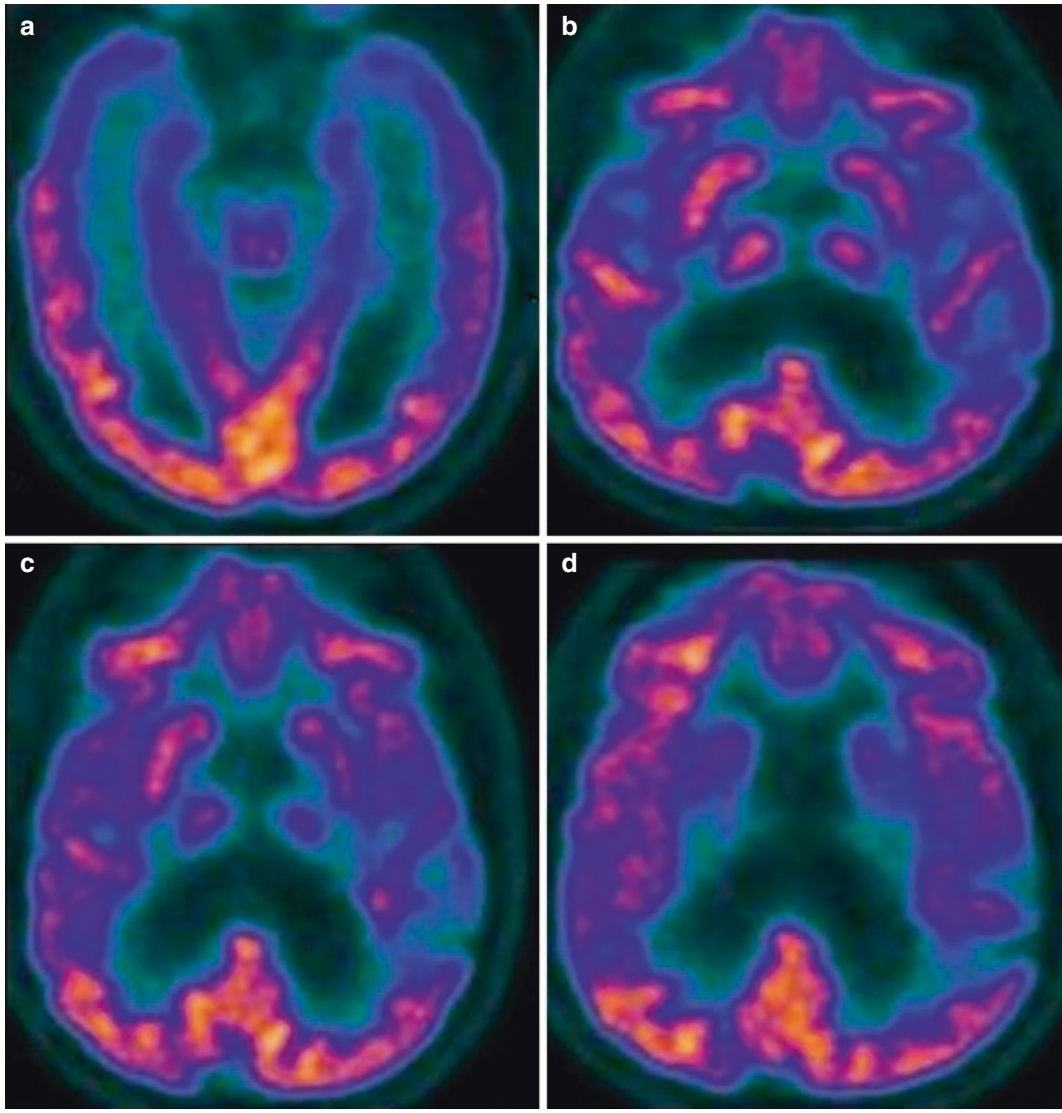

Fig. 1.22 Axial PET views (**a**–**d**) showing bilateral parietotemporal deficit of glucose metabolism in a patient examined for suspicion of Alzheimer's Disease

to the better tracer specificity and predictive value. However, brain ^{18}F-FDG PET still plays a role in the management of patients with dementia, also allowing global evaluation of cortical, cerebellar, and subcortical regions of the brain (Fig. 1.23).

Concerning the imaging of movement disorders, ^{18}F-FDG cannot easily detect the reduction of metabolism in the striatum, due to its high rate of physiological bio-distribution in this structure, also in comparison with ^{18}F-DOPA (see Chap. 2) [50]. ^{18}F-FDG PET can only support the clinical diagnosis of Parkinsonian syndromes, allowing the characterization of specific uptake patterns when the differential diagnosis between supranuclear progressive palsy, multisystemic atrophy, and cortico-basal degeneration is uncertain [51]. Consequently, the attention of the researchers is focused on the potential usefulness of brain ^{18}F-FDG PET in the differential diagnosis of Parkinsonian syndromes or in detecting, in a minority of patients with Parkinson's disease, the related *dementia complex* [52].

Other potential applications of brain ^{18}F-FDG PET are linked to its capability to detect epileptogenic foci. In particular, *ictal* ^{18}F-FDG PET, with tracer administration occurring during the crisis, has proven to be very sensitive in identifying the temporal or extra-temporal epileptogenic focus, despite its difficult reproducibility [53].

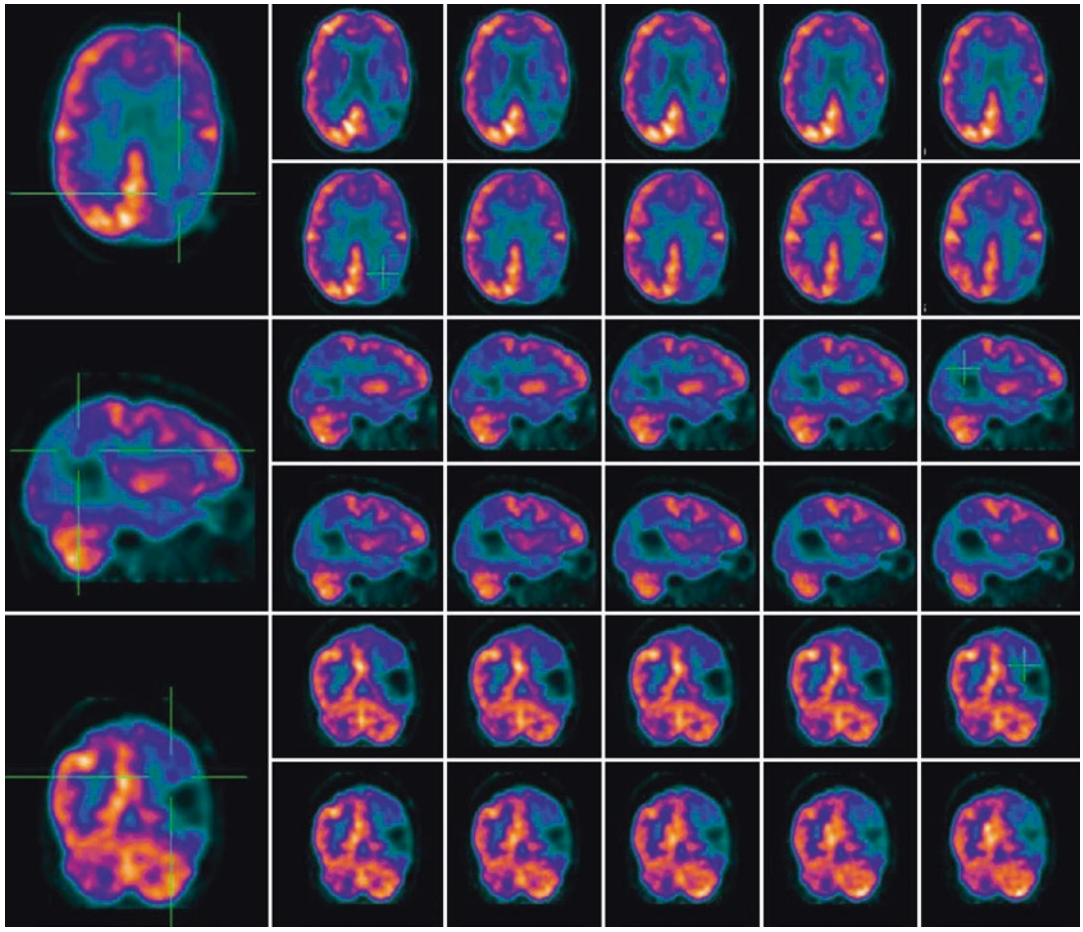

Fig. 1.23 Multiplanar PET evaluation of a patient with a past history of stroke in the left parietal region. The brain ^{18}F-FDG PET was performed 2 years after the ischemic injury and shows deficit of glucose metabolism in the left parietal region, in association with deficit of ^{18}F-FDG uptake in the contralateral cerebellar hemisphere (*crossed cerebellar diaschisis*)

As a future trend, due to the versatility of the tracer, we can consider an emerging indication of ^{18}F-FDG PET the study of autoimmune encephalitis, due to the challenge to depict the site of neuronal inflammation (Fig. 1.24) and to monitor the response to therapy [54].

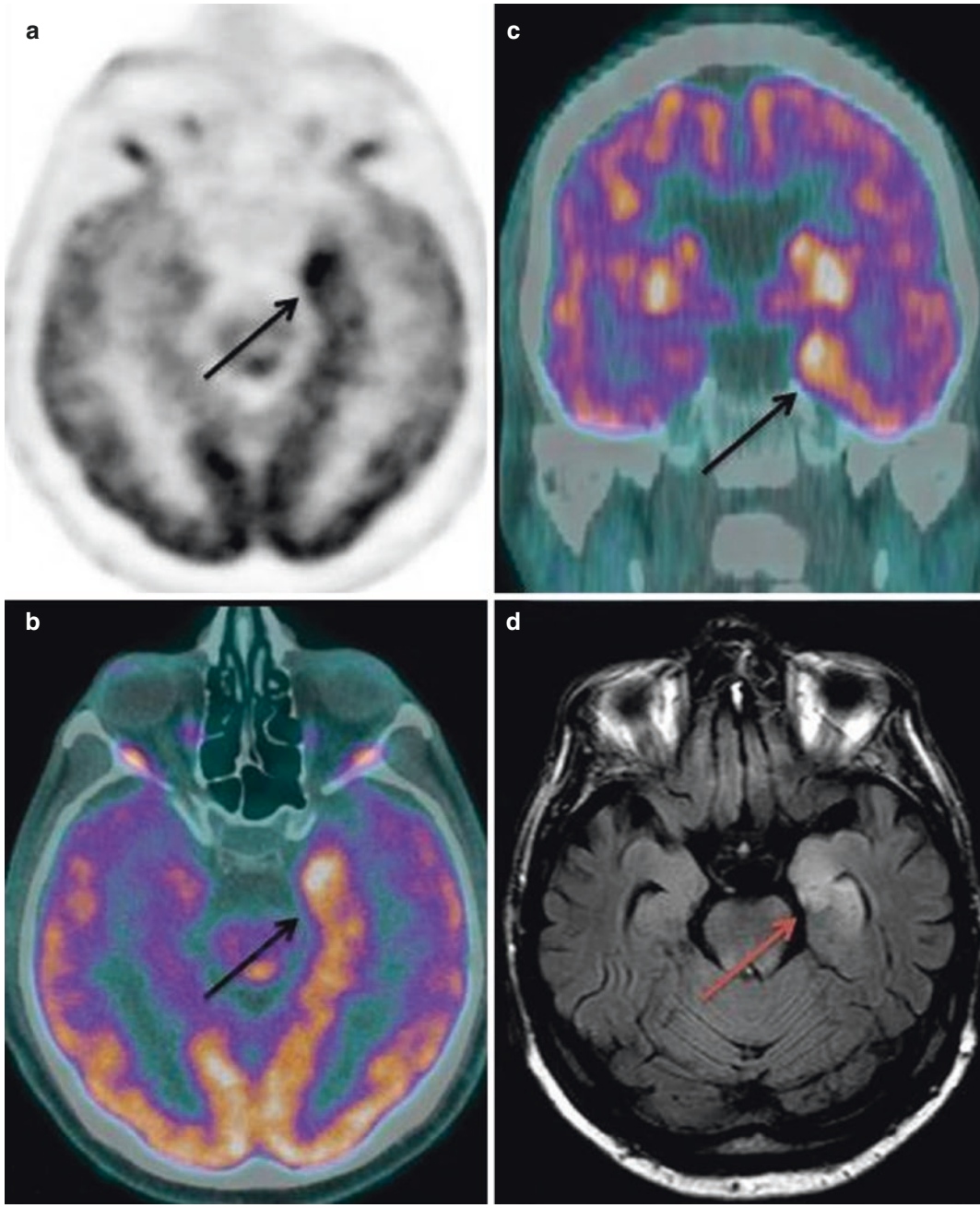

Fig. 1.24 In a 56-year-old patient with autoimmune encephalitis, axial ^{18}F-FDG PET view (**a**, black arrow) shows hypermetabolism in the left temporal lobe, as evident also in axial (**b**) and coronal (**c**) PET/CT views. Axial T2 FLAIR MRI (**d**) displays hyperintensity in the left hippocampus, due to the condition of encephalitis

1.4.10 Myocardial Viability

The assessment of myocardial viability has become an important investigation in the management of patients with ventricular dysfunction following an ischemic event. The assessment of residual myocardial viability can be useful to individualize the management of patients and can help in deciding whether patients should receive surgical or medical treatment based on PET data or, alternatively, need to undergone revascularization. The ^{18}F-FDG "*myocardial"* PET is performed after a rest injection of the tracer, followed by a PET scan triggered with cardiac cycle, in order to avoid motion artifacts of the heart (see also Chap. 9). Anyway, for nuclear medicine physicians experienced in this field, the cornerstone to evaluate PET data is the myocardial perfusion imaging with SPECT, which is necessary to individuate regional myocardial hypoperfusion which can display ^{18}F-FDG uptake, and therefore be susceptible of revascularization (Fig. 1.25).

1.5 PET/CT Acquisition Protocols

- Whole Body PET/CT: from the vertex of the skull to the upper thighs, 60 min following the ^{18}F-FDG administration (300–400 Mbq; 2–3 min per bed position, depending on the PET scanner). The low-dose CT for the anatomical localization of functional findings is sufficient, also in order to reduce radiation exposure for patients. A full-dose contrast-enhanced CT can be normally omitted from ^{18}F-FDG PET/CT oncologic studies [55]. This option can be reserved, to ensure the diagnosis (*surgical resectability, disease extension, peritoneal carcinomatosis,* etc.*)*.
- Dynamic PET/CT: during the tracer administration, a dynamic segmental PET scan can be added to the standard whole body imaging, to ensure a peculiar finding, in example by avoiding the urinary activity of the bladder in the late scan or to evaluate the vascular activity after the bolus injection. In these cases generally a low-dose CT is associated to PET imaging for the attenuation correction and to obtain anatomical landmarks.
- Brain PET/CT: A specific, one bed position acquisition of the brain is the method of choice for PET imaging. A low-dose CT of the brain, with the head of the patient in the center of the scanner field of view, is necessary for attenuation correction and anatomical reference. Thereafter, a 10 min PET, following 45–60 min the tracer administration (≈180 MBq), is sufficient for the functional imaging. Lately, additional brain CT with contrast agent can follow the standard imaging for a better depiction of encephalic structures or for the detection of brain metastases.

1.6 PET/MRI

The emergence of combined PET/CT scanners was at the basis of the success of PET imaging and of hybrid imaging, which allows in a single session the simultaneous evaluation of metabolic and morphological data, with an overall diagnostic impact superior to that of both modalities separately performed. On this basis, the emergence and commercial availability of hybrid PET/MRI scanners will improve the diagnosis in specific fields of oncology and neurology in the next future.

The main technical advantage of PET/MRI, regarding PET/CT, is the simultaneous acquisition of PET and MRI data, rather than the sequential PET/CT scan (Fig. 1.26): in our experience, we perform the standard PET imaging simultaneously with *Blood Oxygenation Level Dependent* (BOLD) MRI sequences, which offer the possibility of motion correction during the acquisition and in the post processing. As for PET/CT, the PET/MRI scanner allows the possibility to obtain

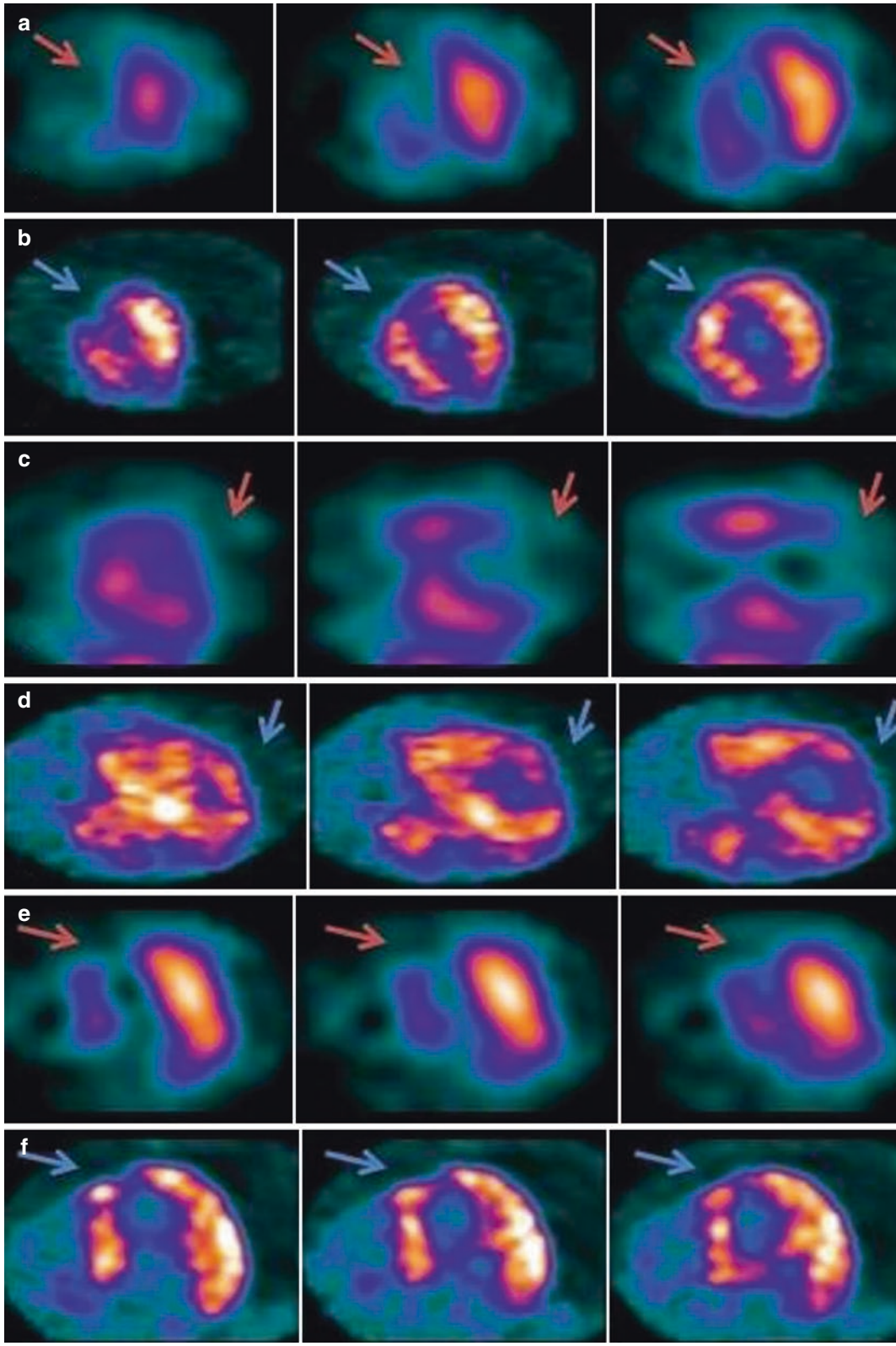

Fig. 1.25 Myocardial SPECT (**a**, **c**, **e**) shows perfusion deficit in the apex of the left ventricle; correlative myocardial PET with ^{18}F-FDG (**b**, **d**, **f**) displays tracer uptake in the apex, indicative of myocardial viability

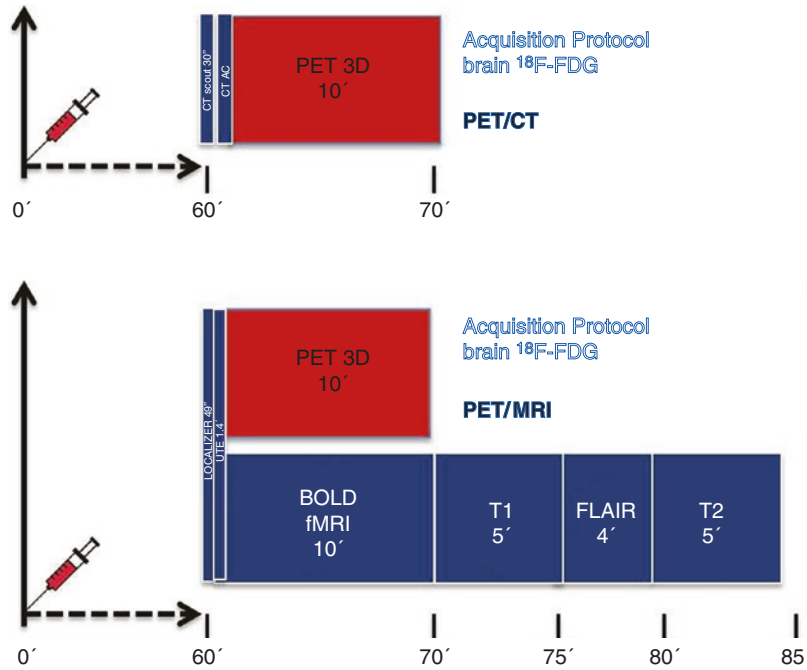

Fig. 1.26 Differences between the sequential ^{18}F-FDG brain PET/CT acquisition protocol and a proposal of simultaneous ^{18}F-FDG brain PET/MRI scan, for imaging dementia

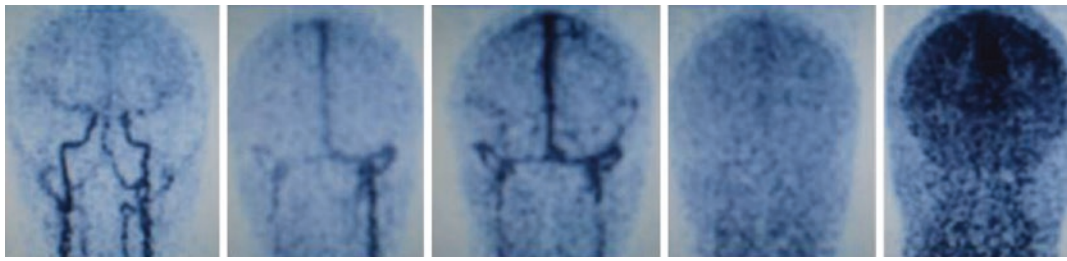

Fig. 1.27 In these selected frames of a dynamic ^{18}F-FDG brain PET are recognizable the arterial phase, rapidly following the tracer administration, and the venous phases while, 5 min after the injection, the last image shows the beginning of tracer accumulation in the brain

dynamic or static PET data (Fig. 1.27) but with a large series of morphological and functional MRI sequences. T1, T2, and *Fluid Attenuation Inversion Recovery* (FLAIR) sequences are the basis for morphological imaging and represent the substratum for PET/MRI image fusion, especially for neurodegenerative diseases (Fig. 1.28). Depending on the clinical indications, other functional MRI sequences can be added to the imaging, in order to deep the knowledge of catabolites with MR spectroscopy or to assess other functional features, as for diffusion tensor imaging, which can give additional information to PET/MRI data (Fig. 1.29).

Therefore, concerning simultaneous PET/MRI system workflows, the main issues, also in comparison to the era of "*post processing PET/MRI fusion imaging*" (Fig. 1.30) regard capability to simultaneously depict the disease for many points of views, also needing for this reasons the collaboration of nuclear medicine physicians and radiologists with skill in this field, being the *holistic* evaluation of hybrid imaging at the basis of the PET/MRI clinical output.

Despite these premises, it is also necessary to state that MRI sequences should be not too long. In whole body imaging with ^{18}F-FDG, the MRI displays a better soft tissue contrast than CT,

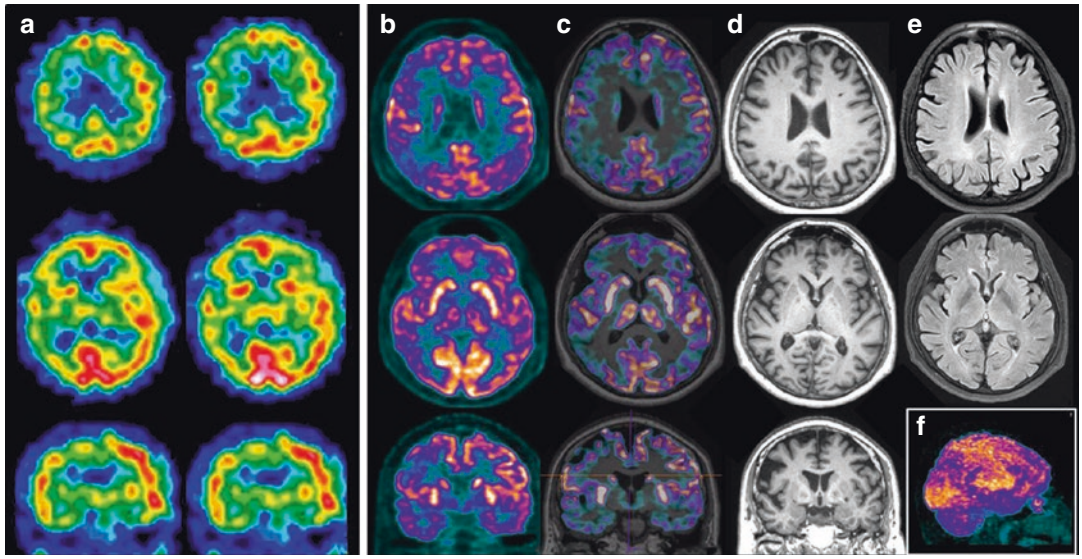

Fig. 1.28 In the left column (**a**), axial and coronal SPECT views of a 65-year-old woman examined for suspicion of Alzheimer disease, showing perfusion deficit in right frontal and parietal regions. ^{18}F-FDG PET (**b**) and PET/MRI (**c**) better displays a deficit of glucose metabolism in the same areas with further hypometabolism in left parietal region. Correlative T1-weighted (**d**) and FLAIR (**e**) MRI images display a condition of ventricular enlargement with prevalent atrophy in the right hemisphere. ^{18}F-FDG PET 3D maximum intensity projection of the brain (**f**) summarizes the right parieto-frontal deficit

without using ionizing radiations, which can lead in better diagnostic accuracy in oncologic studies (Fig. 1.31).

PET/MRI will become an important tool in the prognostic stratification of prostate cancer patients, due to the possibility to depict in a single whole body imaging tool primary tumor (Fig. 1.32) and distant bone and/or lymph node metastases [56]. However, rather than ^{18}F-FDG, other tracers are showing more interesting results in this specific clinical setting [57].

In neuro-oncology, PET/MRI can provide simultaneous evaluation of brain tumors, depicting both functional processes at the basis of neoplastic proliferation and morphological abnormalities with the high-power resolution (Fig. 1.33) and the possibility of multiplanar evaluation [58].

In neurology, the ^{18}F-FDG PET/MRI can play a specific role in the depiction of functional and anatomical processes at the basis of the developing of neurodegenerative diseases, due the extreme versatility of this tracer in the evaluation of brain metabolism and the challenge to accurately investigate all the anatomical brain structures, provided by MRI (Fig. 1.34).

In fact, considering the large amount of neuro-oncologic amino acid PET tracers (also see Chaps. 2, 4 and 11) and the limits of ^{18}F-FDG in neuro-oncological imaging as analog of glucose, we must also state that this tracer is still the most useful in the evaluation of all metabolic changes and disorders that can occur in the human brain.

From ^{18}F-FDG PET/CT imaging, the transitive property holds true also for the study of epilepsy by means of ^{18}F-FDG PET/MRI. In fact, this diagnostic tool is potentially more useful than PET/CT in identifying epileptogenic foci during the ictal phase, with the added value of the optimal spatial resolution limit of MRI (Fig. 1.35) [59]. The ultimate goal in neurology is to establish combined PET/MRI as the first-line imaging technique to provide in a single session all biomarker information required to increase diagnostic confidence toward specific diagnoses, in dementia, movement disorders,

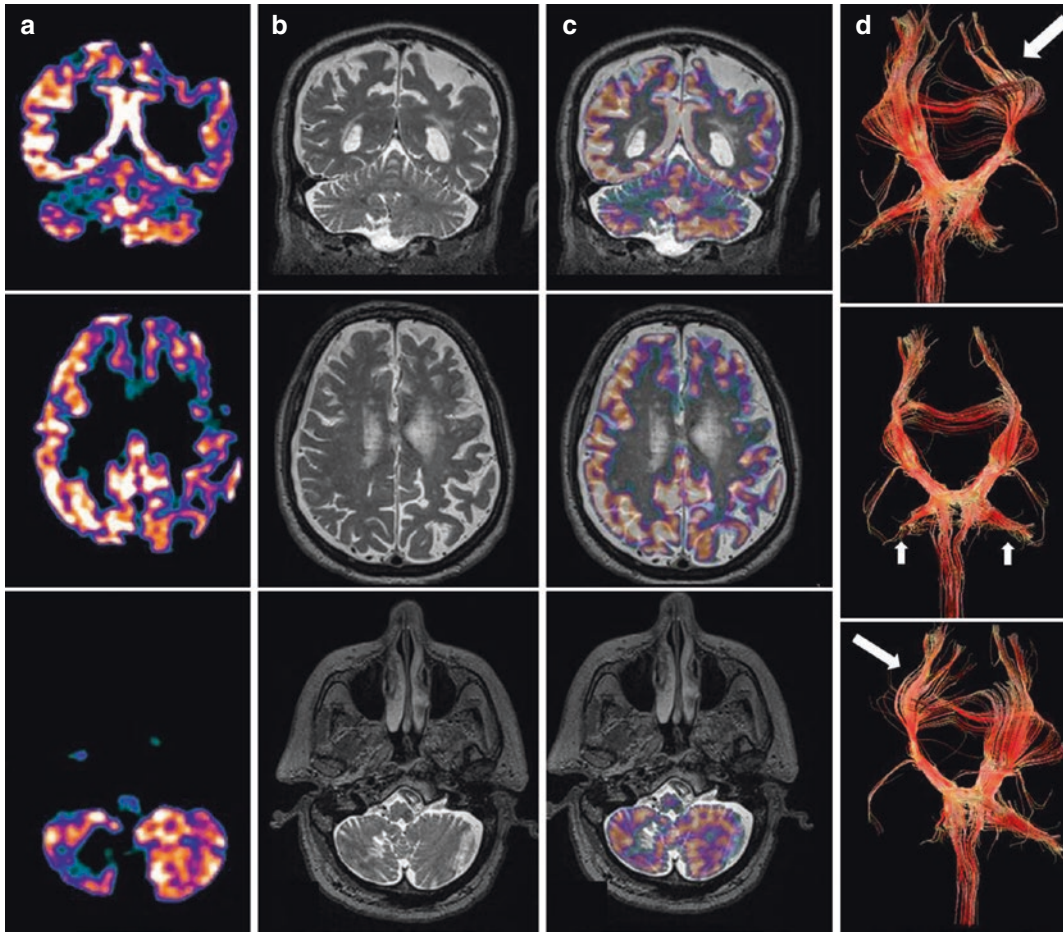

Fig. 1.29 In a patient with cortico-basal degeneration ^{18}F-FDG PET (**a**) displays diffuse hypometabolism in the left hemisphere of the brain and in the right cerebellar hemisphere (*crossed cerebellar diaschisis*); T1 weighted MRI views (**b**) well show a condition of diffuse atrophy, prevalent on the left hemisphere. PET/MRI (**c**) summarizes all these findings while the analysis of tractography (**d**), obtained by diffusion tensor imaging, improves the display of decreased fibers in the left brain hemisphere and in the right cerebellar hemisphere *(white arrows)*

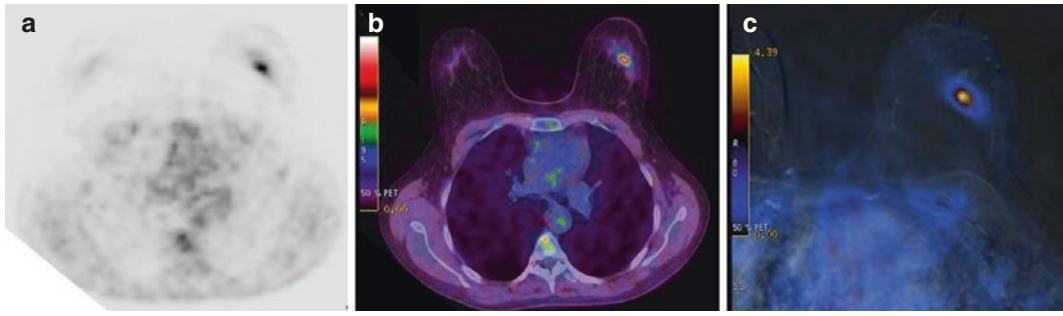

Fig. 1.30 Example of PET/MRI fusion imaging before the development of hybrid scanners. ^{18}F-FDG axial PET (**a**) and PET/CT (**b**) views of a patient with locally advanced breast cancer. Following the anatomical landmarks of co-registered CT it is possible to fuse, during the post-processing, PET and MRI data of the breast (**c**), only by using a unique breast coil in the two acquisition steps

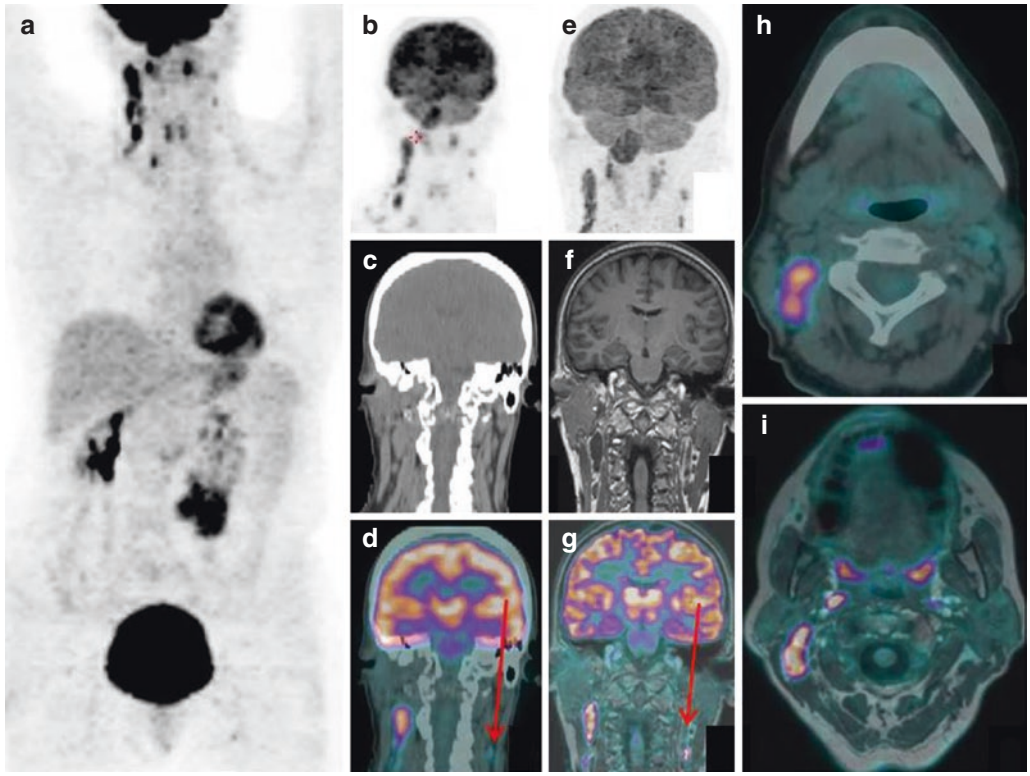

Fig. 1.31 ^{18}F-FDG PET 3D whole body maximum intensity projection (**a**) and detail (**b**) of a patient examined for staging non-Hodgkin lymphoma of the neck. Correlative coronal CT (**c**) and PET/CT (**d**) views show several right cervical lymphadenopathies with a further area of uptake in the contralateral side of the neck (*red arrow*). ^{18}F-FDG PET 3D maximum intensity projection of the brain and neck (**e**), obtained with hybrid PET/MRI scanner, allows to better display all the cervical lesion and a further subcentimetric left cervical lymph node, eloquently showed in coronal T1 weighted view (**f**) and coronal PET/MRI view (**g**). Finally, axial PET/CT (**h**) and PET/MRI (**i**) details of the neck eloquently show different power resolution limits

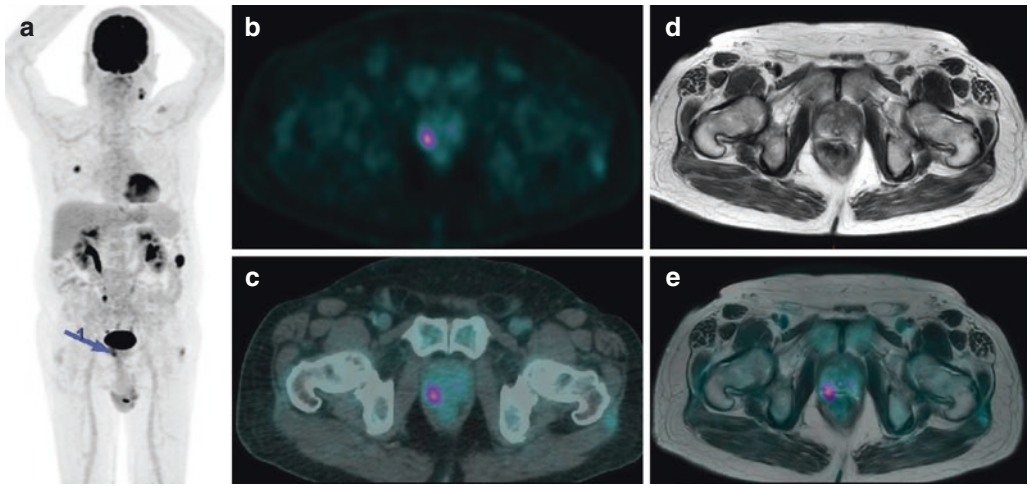

Fig. 1.32 The patient was examined for restaging colon cancer. Beyond abdominal and lung metastases of colon cancer (Maximum PET Intensity Projection, **a**), incidentally, an area of focal ^{18}F-FDG uptake was detected in the right prostate lobe, as evident in MIP (**a**, arrow) and axial PET (**b**) and PET/CT (**c**) views. Patient also undergone MRI of the pelvis, showing a hyperintense node in the peripheral portion of the right prostate lobe (**d**), corresponding to the focus of tracer uptake in PET/MRI axial view (**e**)

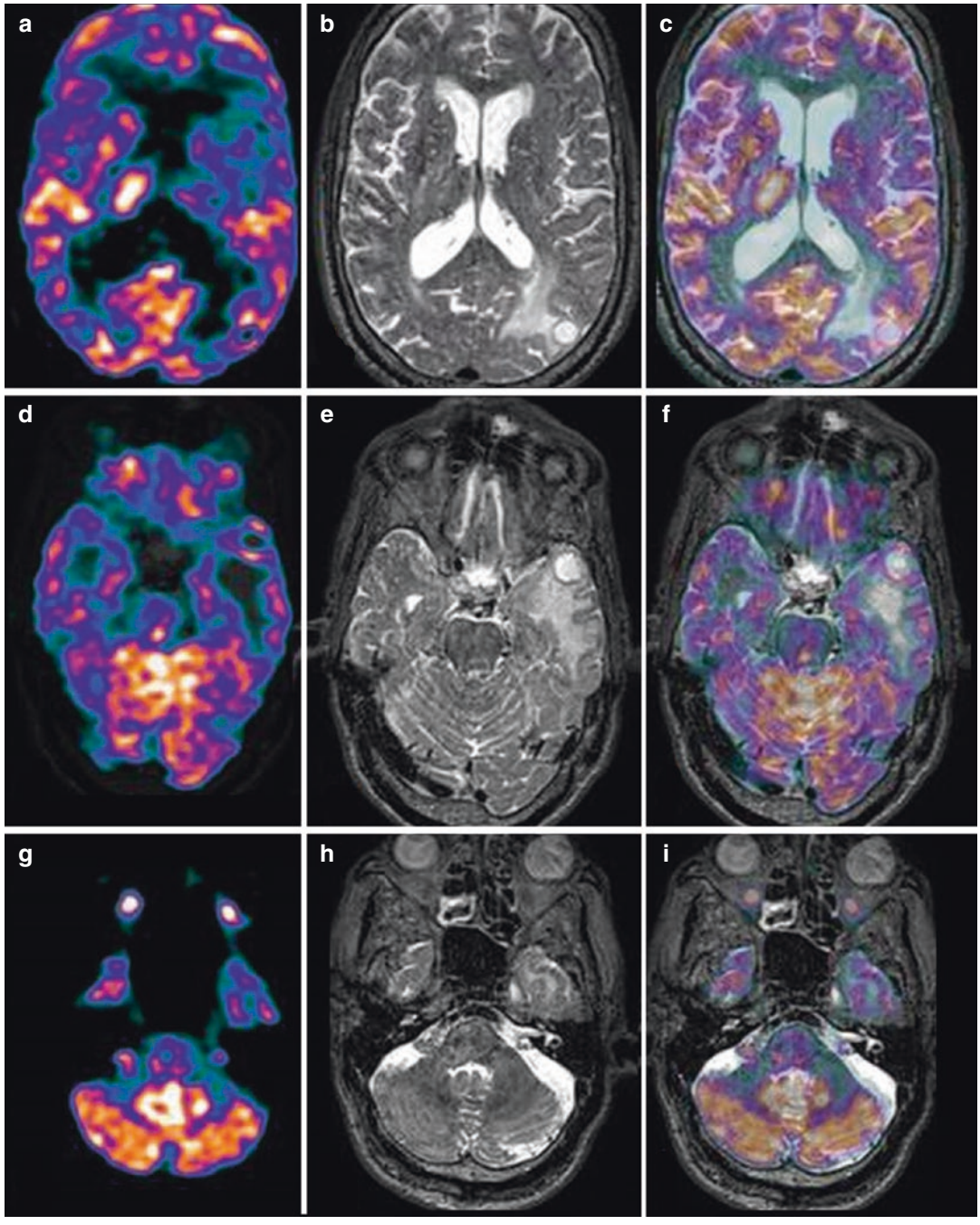

Fig. 1.33 Multiple brain metastases from melanoma. In particular, an area of hypometabolism is evident in axial PET view (**a**) in left occipital region, in association with 1-cm-wide hyperintense lesion, with surrounding edema, in corresponding MRI (**b**) and PET/MRI (**c**) views. Similar findings are displayed in left temporal region in axial PET (**d**), MRI (**e**), and PET/MRI (**f**) views and in the left cerebellar lobe in axial PET (**g**), MRI (**h**), and PET/MRI (**i**) views

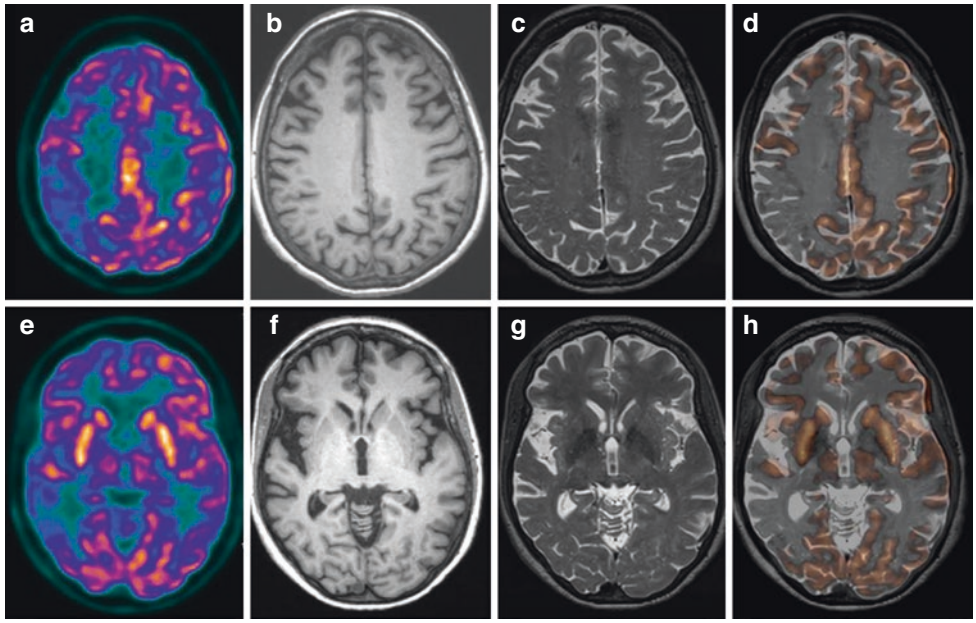

Fig. 1.34 In a patient examined for suspicion of Alzheimer's disease with hybrid PET/MRI scanner, axial PET (**a**, **e**), T1 (**b**, **f**) and T2 (**c**, **g**) weighted MRI images show hypometabolism in right parietotemporal regions, in the ipsilateral frontal lobe and in the left temporal lobe, without meaningful morphological abnormalities. Fused PET/MRI well summarize this findings (**d**, **h**)

Fig. 1.35 In a 24-year-old patient with epilepsy, examined during the ictal phase by hybrid PET/MRI scanner, the T1 weighted MRI image (**a**) shows cortical heterotopy in the white matter of the left frontal lobe, characterized by high glucose metabolism in correlative PET (**b**) and PET/MRI (**c**) views (*arrows*). The analysis of tractography displays lack of fibers in the epileptogenic focus (**d**)

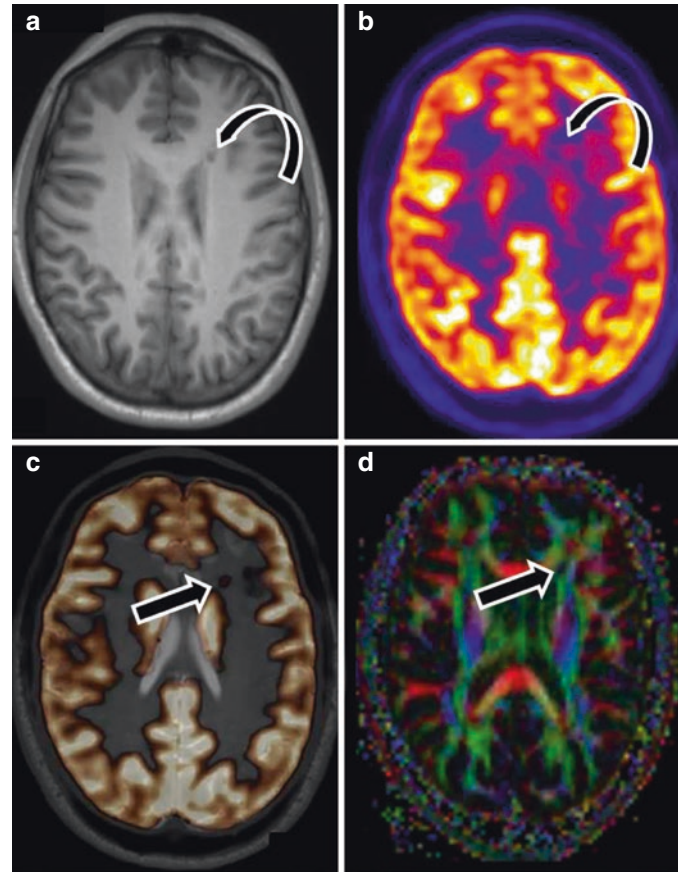

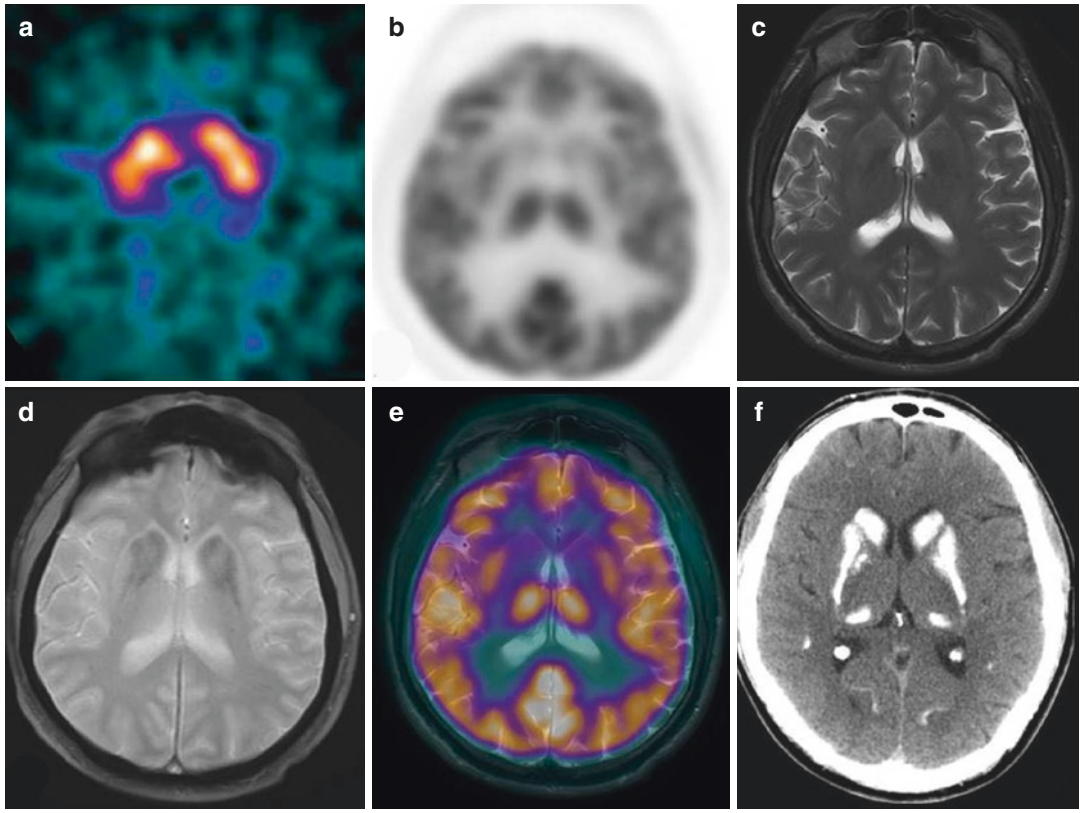

Fig. 1.36 In a patient with ataxia and chronic headache, axial SPECT view with ^{123}I-ioflupane (**a**) shows regular tracer activity in the basal ganglia. The axial ^{18}F-FDG PET view (**b**) displays hypometabolism in both caudate nuclei, in association with calcifications on T2 weighted (**c**) and FLAIR (**d**) MRI images. Fused PET/MRI view (**e**) summarizes these findings while correlative CT (**f**) better shows diffuse calcifications in the basal ganglia. The final diagnosis was *Fahr's disease*

and other neurodegenerative diseases (Fig. 1.36) [60], with improved patient comfort.

1.7 Variants and Pitfalls

The bio-distribution of ^{18}F-FDG can vary according to fasting state, level of muscular exertion, various drugs, and the length of the uptake period after injection. Incidental pathologies with high tracer uptake can be found in 25% of PET studies [61] performed for several indications while, being the ^{18}F-FDG the first and more used PET tracer, several studies in literature have been well described the possibility of uptake of this tracer in inflammation, benign lesions (Fig. 1.37), malignancies concomitant to the disease under study or consequences of surgical procedures such as chemical *pleurodesis* [62, 63].

Concerning the molecular processes at the basis of ^{18}F-FDG cellular uptake, it is also necessary to consider the possibility of uptake in some physiopathological conditions which are not strictly related to a specific disease but can mimic a neoplasm, as in the case of thymic hyperplasia, occurring in a significant minority amount of young adults (Fig. 1.38) [64].

Splenosis is a further peculiar condition, defined as an autotransplantation of the splenic tissue after splenic rupture or splenectomy; it occurs most frequently in the peritoneal cavity and is usually asymptomatic. However, multiple

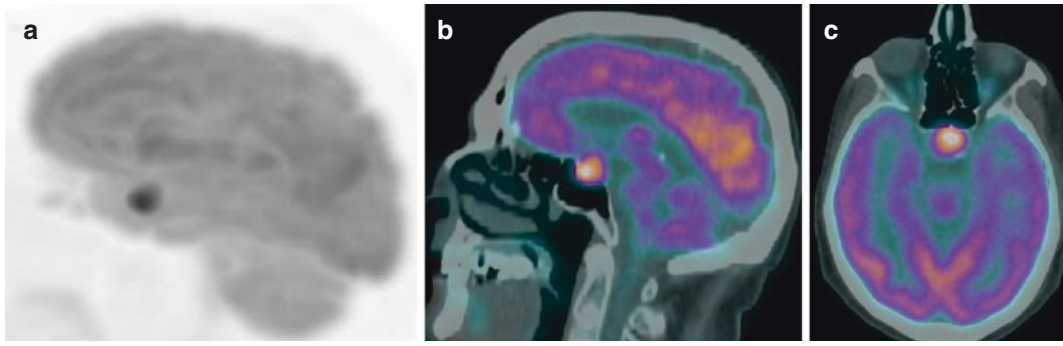

Fig. 1.37 ^{18}F-FDG uptake can be incidentally detected in association with pituitary adenoma, as evident in PET 3D maximum intensity projection of the brain (**a**) and relative axial (**b**) and sagittal (**c**) PET/CT views

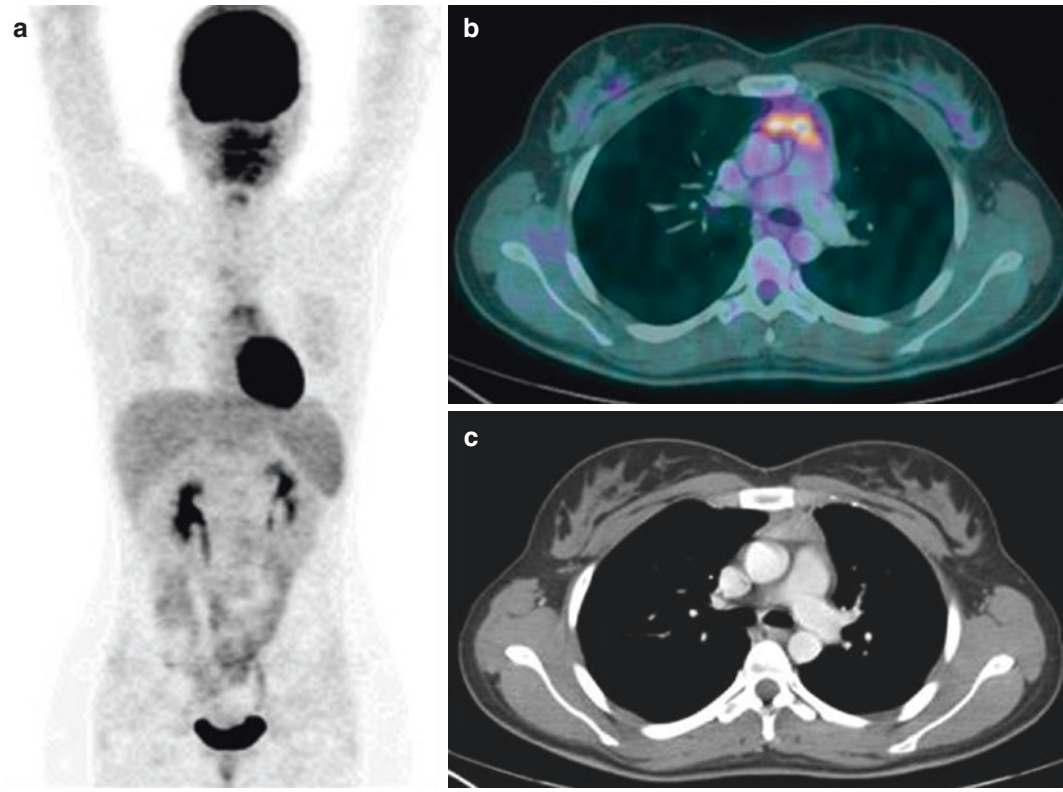

Fig. 1.38 A case of thymic hyperplasia after chemotherapy. ^{18}F-FDG PET 3D whole body maximum intensity projection (**a**) of a young female patient following chemotherapy for inguinal non-Hodgkin lymphoma, showing mild uptake in the upper mediastinum. PET/CT axial view (**b**) confirms the uptake in hypodense tissue in the upper mediastinum, without meaningful contrast enhancement at CT (**c**)

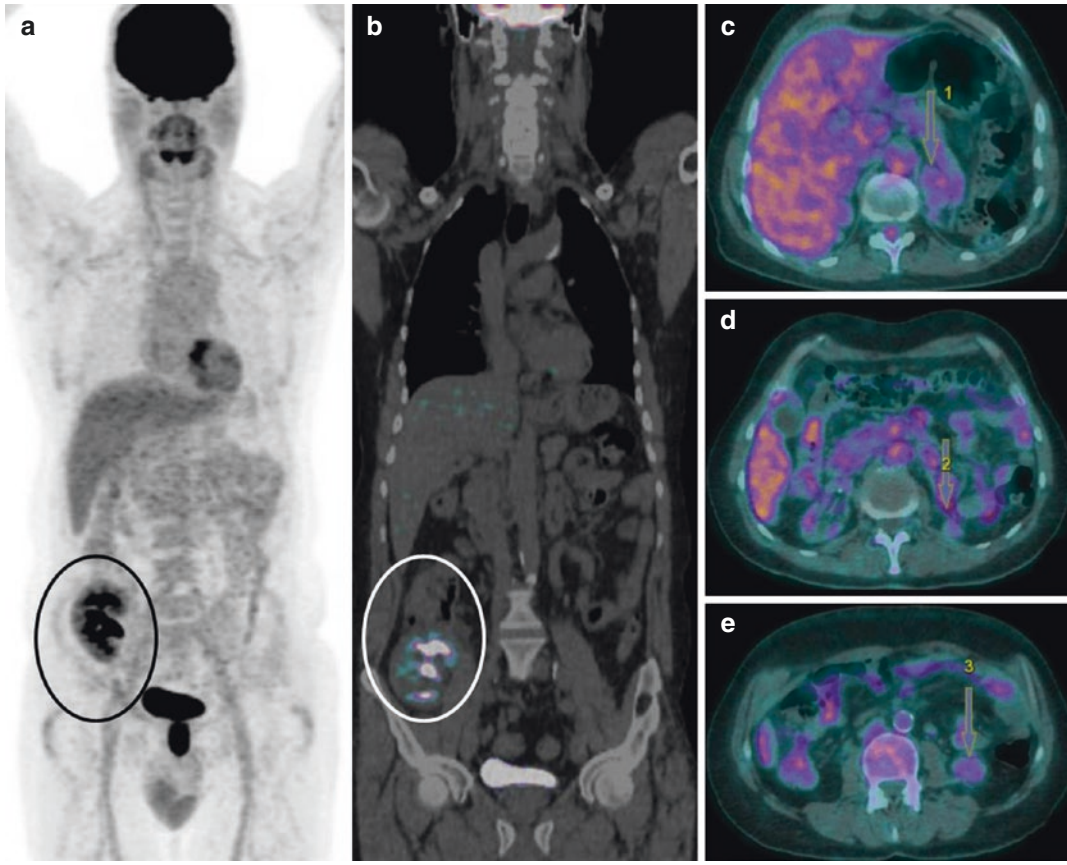

Fig. 1.39 [18]F-FDG PET maximum intensity projection (**a**) and coronal PET/CT view (**b**) show transplanted kidney in right iliac fossa (*circles*). In the same patient, arrows in axial PET/CT views (**c**, **d**, **e**) show hypodense lesions with moderate tracer uptake in the abdomen, due to a condition of splenosis

accessory spleens, showing moderate tracer uptake, can represent a diagnostic dilemma in patients examined by [18]F-FDG PET/CT for somatic tumors (Fig. 1.39) [65].

On the other hand, it is also mandatory to consider the possibility of faint [18]F-FDG uptake in malignant disease with low rate of glucose metabolism, as for bronco-alveolar carcinoma (Fig. 1.40) and some kinds of renal cells carcinoma (Fig. 1.41). Furthermore, in the urinary tract, some lesions can be also not easily recognizable due the high gradient of tracer urinary excretion.

In the field of neuro-oncological imaging, some novel radiopharmaceuticals are replacing the [18]F-FDG, due to the lack of specificity of this tracer and high rate of false negative cases that can occur, especially when evaluating patients with brain tumors or suspicion of brain tumor relapse (Fig. 1.42).

Beyond pitfalls linked to the tracer biodistribution, for [18]F-FDG PET/CT and PET/MRI,

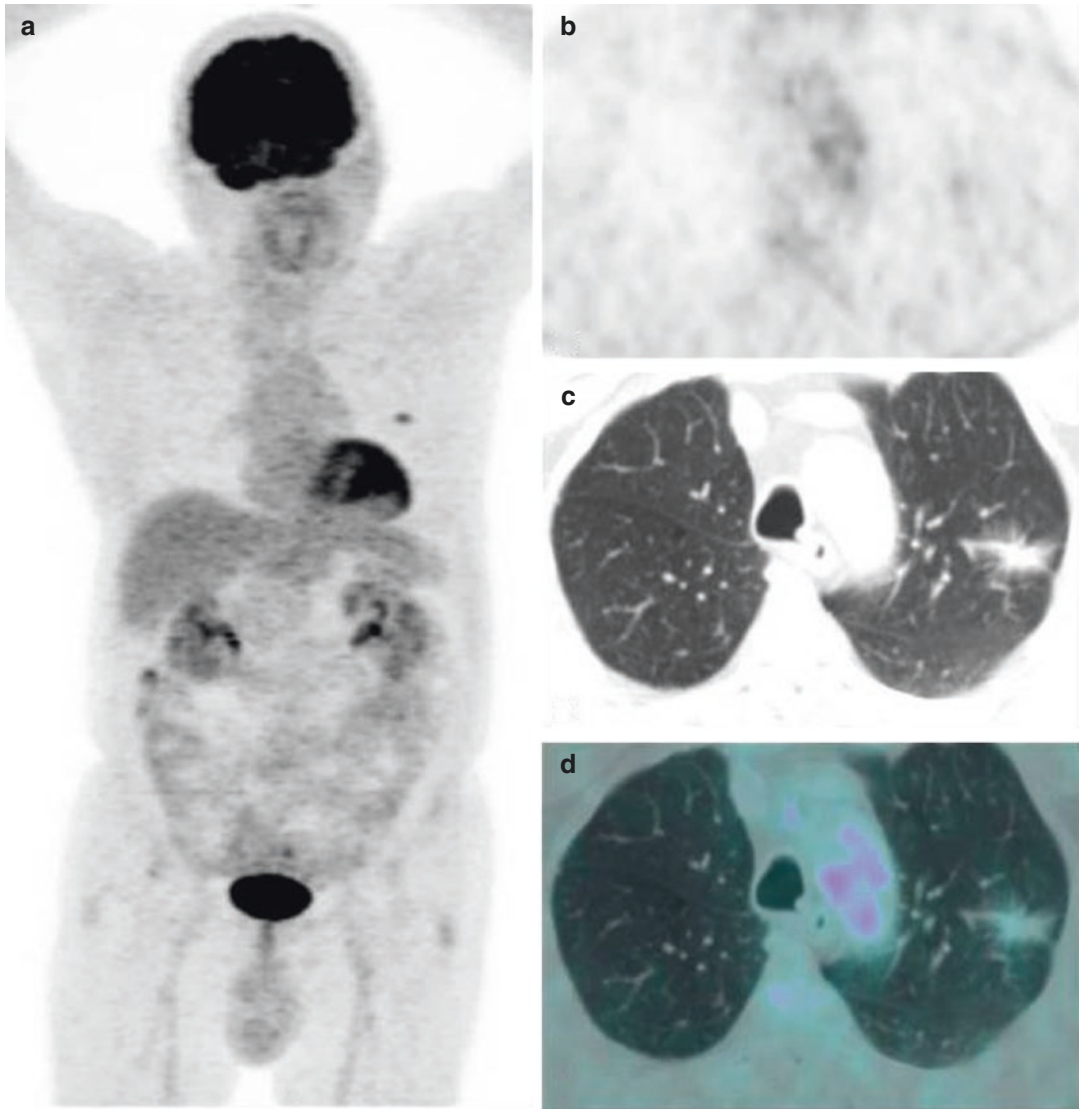

Fig. 1.40 In a patient examined for staging histologically proven bronco-alveolar carcinoma, ^{18}F-FDG PET 3D whole body maximum intensity projection (**a**) and axial PET view (**b**) show very low uptake in the lesion in the left lung, with spiculate margins at correlative CT (**c**) and PET/CT (**d**) views

several studies or reports well described the possibility of technical artifacts, mostly related to the movement of patient among the two scans (Fig. 1.43), as known for intestinal loops, lungs during respiration, and head and neck, generally due to the rotation of the neck of patients from the PET scan and the CT or MRI scan. To date, with the development of novel software for PET/MRI image processing, this frequent artifact can be satisfactorily managed (Fig. 1.44).

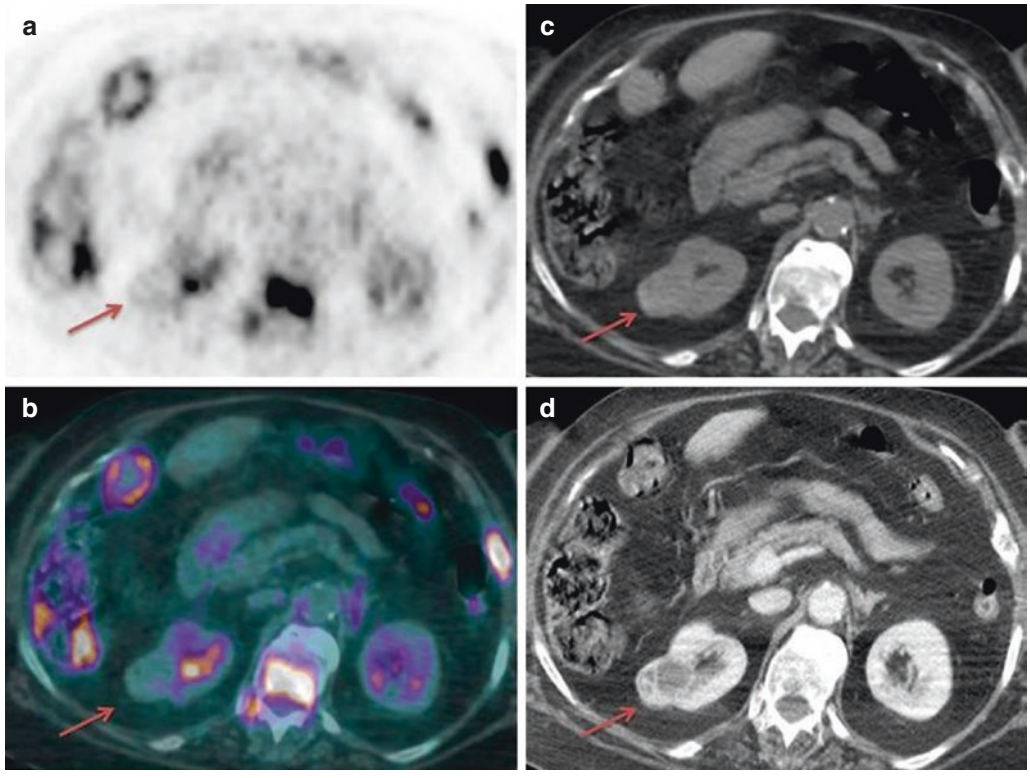

Fig. 1.41 A patient with metastatic lung cancer examined by contrast-enhanced ^{18}F-FDG PET/CT: axial PET (**a**), PET/CT (**b**), CT (**c**), and contrast-enhanced CT (**d**) show a neoformation in the right kidney, without significant tracer uptake and non-homogeneous contrast enhancement (*red arrows*). Final histological diagnosis was renal carcinoma

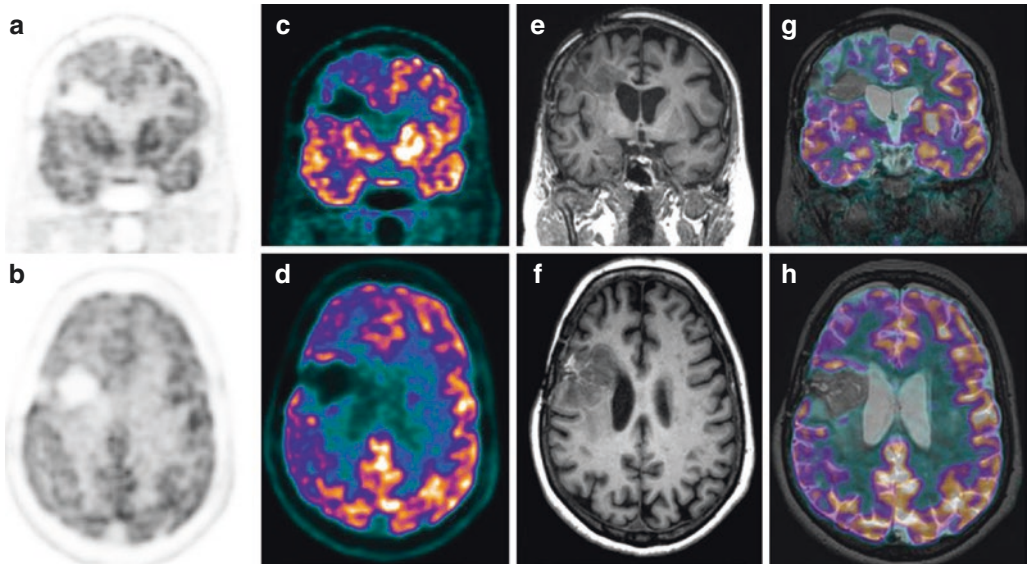

Fig. 1.42 Coronal (**a**, **c**, **e**, **g**) and axial (**b**, **d**, **f**, **h**) PET, MRI, and PET/MRI views of a patient with histologically proven glioblastoma relapse in the site of previous surgical excision. ^{18}F-FDG PET/MRI, developed on a hybrid scanner, displays aspecific findings as reduction of uptake in the surgical lacuna and ventricular enlargement but no findings indicative of tumor relapse

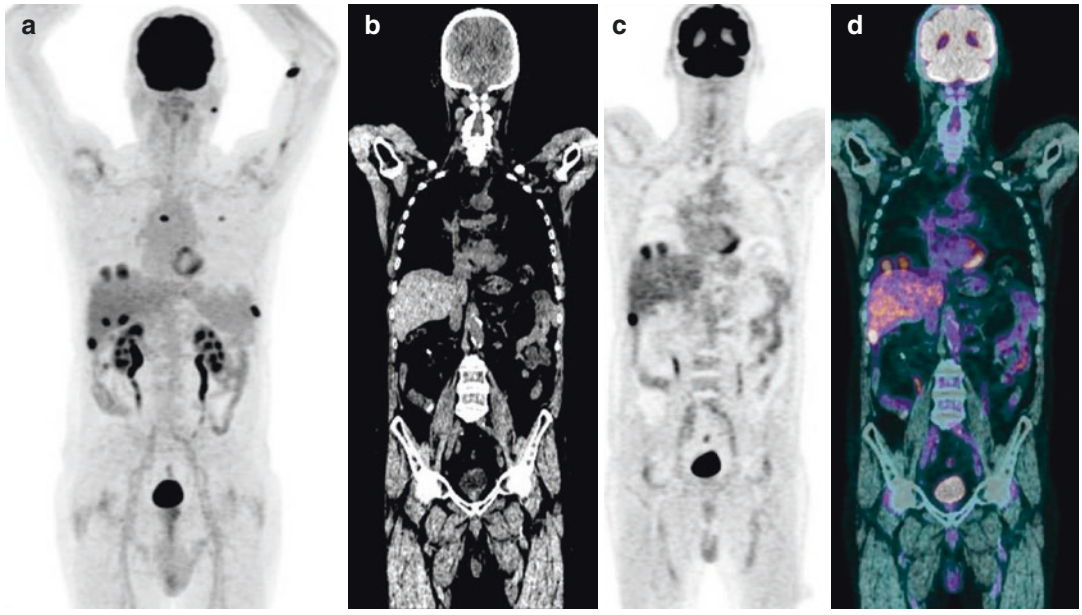

Fig. 1.43 Patient with several metastases of colon cancer, evident in ^{18}F-FDG PET maximum intensity projection (**a**). As motion artifacts due to respiration during the PET acquisition, hepatic ^{18}F-FDG-avid lesions are not correctly detectable on fusion imaging, due to different position among CT (**b**) and PET (**c**) coronal views, and abnormal PET/CT fusion (**d**)

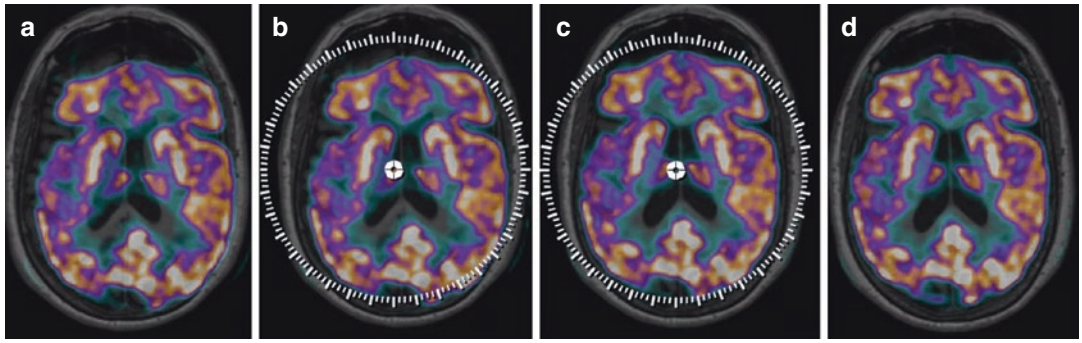

Fig. 1.44 Brain ^{18}F-FDG PET/MRI with motion artifacts. During the post-processing is possible to correctly fuse PET and MRI data in few steps (**a**, **b**, **c**) in order to obtain an optimal realignment of both scans (**d**)

References

1. Fowler JS, Ido T. Initial and subsequent approach for the synthesis of 18FDG. Semin Nucl Med. 2002;32:6–12.
2. Hamacher K, Coenen HH, Stocklin G. Efficient stereospecific synthesis of no-carrier-added 2-[18F]-fluoro-2-deoxy-D-glucose using aminopolyether supported nucleophilic substitution. J Nucl Med. 1986;27:235–8.
3. Mochizuki T, Tsukamoto E, Kuge Y, et al. FDG uptake and glucose transporter subtype expressions in experimental tumor and inflammation models. J Nucl Med. 2001;42:1551–5.
4. Buck AK, Reske SN. Cellular origin and molecular mechanisms of 18F-FDG uptake: is there a contribution of the endothelium? J Nucl Med. 2004;45:461–3.
5. Sokoloff L, Reivich M, Kennedy C, et al. The [14C] deoxyglucose method for the measurement of local cerebral glucose utilization: theory, procedure, and normal values in the conscious and anesthetized albino rat. J Neurochem. 1977;28:897–916.
6. Nguyen NC, Kaushik A, Wolverson MK, et al. Is there a common SUV threshold in oncological FDG PET/CT, at least for some common indications? A retrospective study. Acta Oncol. 2011;50:670–7.
7. Weber WA, Grosu AL, Czernin J. Technology insight: advances in molecular imaging and an

appraisal of PET/CT scanning. Nat Clin Pract Oncol. 2008;5:160–70.
8. Kinahan PE, Fletcher JW. Positron emission tomography-computed tomography standardized uptake values in clinical practice and assessing response to therapy. Semin Ultrasound CT MR. 2010;31:496–505.
9. Schillaci O, Travascio L, Bolacchi F, et al. Accuracy of early and delayed FDG-PET/CT and of contrast enhanced CT in the evaluation of lung nodules: a preliminary study on 30 patients. Radiol Med. 2009;114:890–906.
10. Boellaard R, Delgado-Bolton R, Oyen WJ, et al. FDG PET/CT: EANM procedure guidelines for tumour imaging: version 2.0. Eur J Nucl Med Mol Imaging. 2015;42:238–354.
11. Orlacchio A, Schillaci O, Antonelli L, et al. Solitary pulmonary nodules: morphological and metabolic characterization by FDG-PET-MDCT. Radiol Med. 2007;112:157–73.
12. Bhure UN, Lardinois D, Kalff V, et al. Accuracy of CT parameters for assessment of tumour size and aggressiveness in lung adenocarcinoma with bronchoalveolar elements. Br J Radiol. 2010;89:841–9.
13. Pavlidis N, Fizazi K. Carcinoma of unknown primary (CUP). Crit Rev Oncol Hematol. 2009;69:271–8.
14. Kwee TC, Basu S, Cheng G, et al. FDG PET/CT in carcinoma of unknown primary. Eur J Nucl Med Mol Imaging. 2010;37:635–44.
15. Antoch G, Saoudi N, Kuehl H, et al. Accuracy of whole-body dual-modality fluorine-18-2-fluoro-2-deoxy-D-glucose positron emission tomography and computed tomography (FDG-PET/CT) for tumor staging in solid tumors: comparison with CT and PET. J Clin Oncol. 2004;22:4357–68.
16. Fernández-Pérez G, Sánchez-Escribano R, García-Vicente AM, et al. SEOM-SERAM-SEMNIM guidelines on the use of functional and molecular imaging techniques in advanced non-small-cell lung cancer. Clin Transl Oncol. 2018;20:837–52.
17. Orsaria P, Chiaravalloti A, Caredda E, et al. Evaluation of the usefulness of FDG-PET/CT for nodal staging of breast cancer. Anticancer Res. 2018;38:6639–52.
18. Macpherson RE, Pratap S, Tyrrell H, et al. Retrospective audit of 957 consecutive 18F-FDG PET-CT scans compared to CT and MRI in 493 patients with different histological subtypes of bone and soft tissue sarcoma. Clin Sarcoma Res. 2018;8:9.
19. Panebianco M, Bagni O, Cenfra N, et al. Comparison of 18F FDG PET-CT AND CECT in pretreatment staging of adults with Hodgkin's lymphoma. Leuk Res. 2018;5:48–52.
20. Shim JR, Lee SD, Han SS, et al. Prognostic significance of 18F-FDG PET/CT in patients with colorectal cancer liver metastases after hepatectomy. Eur J Surg Oncol. 2018;44:670–6.
21. Narayanan P, Sahdev A. The role of 18F-FDG PET CT in common gynaecological malignancies. Br J Radiol. 2017;90:20170283.
22. Ronellenfitsch U, Wängler B, Niedermoser S, et al. Importance of PET for surgery of gastrointestinal stromal tumors. Chirurg. 2014;85:493–9.
23. Frary EC, Gad D, Bastholt T, et al. The role of FDG-PET/CT in preoperative staging of sentinel lymph node biopsy-positive melanoma patients. EJNMMI Res. 2016;6:73.
24. Guo W, Hao B, Chen H-j, et al. PET/CT-guided percutaneous biopsy of FDG-avid metastatic bone lesions in patients with advanced lung cancer: a safe and effective technique. Eur J Nucl Med Mol Imaging. 2017;44:25–32.
25. Radhakrishnan RK, Mittal BR, Gorla AKR, et al. Real-time intraprocedural 18F-FDG PET/CT-guided biopsy using automated robopsy arm (ARA) in the diagnostic evaluation of thoracic lesions with prior inconclusive biopsy results: initial experience from a tertiary health care centre. Br J Radiol. 2017;90:20170258.
26. Chiaravalloti A, Fiorentini A, Palombo E, et al. Evaluation of recurrent disease in the re-staging of colorectal cancer by 18F-FDG PET/CT: use of CEA and CA 19-9 in patient selection. Oncol Lett. 2016;12:4209–13.
27. Soubra A, Gencturk M, Froelich J, et al. FDG-PET/CT for assessing the response to neoadjuvant chemotherapy in bladder cancer patients. Clin Genitourin Cancer. 2018;16:360–4.
28. Findlay JM, Bradley KM, Wang LM, et al. Predicting pathologic response of esophageal cancer to neoadjuvant chemotherapy: the implications of metabolic nodal response for personalized therapy. J Nucl Med. 2017;58:266–75.
29. Kitajima K, Yamamoto S, Fukushima K, et al. FDG-PET/CT as a post-treatment restaging tool in urothelial carcinoma: comparison with contrast-enhanced CT. Eur J Radiol. 2016;85:593–8.
30. Wahl RL, Jacene H, Kasamon Y, et al. From RECIST to PERCIST: evolving considerations for PET response criteria in solid tumors. J Nucl Med. 2009;50:122s–50s.
31. Rigacci L, Puccini B, Zinzani PL, et al. The prognostic value of positron emission tomography performed after two courses (INTERIM-PET) of standard therapy on treatment outcome in early stage Hodgkin lymphoma: a multicentric study by the fondazione italiana linfomi (FIL). Am J Hematol. 2015;90:499–503.
32. Rudžianskas V, Korobeinikova E, Rudžianskienė M, et al. Use of 18F-FDG PET/CT imaging for radiotherapy target volume delineation after induction chemotherapy and for prognosis of locally advanced squamous cell carcinoma of the head and neck. Medicina (Kaunas). 2018;10:6.
33. Lee P, Kupelian P, Czernin J, et al. Current concepts in F18 FDG PET/CT-based radiation therapy planning for lung cancer. Front Oncol. 2012;11:71.
34. Moule RN, Kayani I, Moinuddin SA, et al. The potential advantages of (18)FDG PET/CT-based target volume delineation in radiotherapy planning of head and neck cancer. Radiother Oncol. 2010;97:189–93.
35. Muijs CT, Beukema JC, Pruim J, et al. A systematic review on the role of FDG-PET/CT in tumour delineation and radiotherapy planning in patients with esophageal cancer. Radiother Oncol. 2010;97:165–71.

36. Nguyen BT, Joon DL, Khoo V, et al. Assessing the impact of FDG-PET in the management of anal cancer. Radiother Oncol. 2008;87:376–82.
37. Vaidyanathan S, Patel CN, Scarsbrook AF, et al. FDG PET/CT in infection and inflammation--current and emerging clinical applications. Clin Radiol. 2015;70:787–800.
38. Filippi L, Uccioli L, Giurato L, et al. Diabetic foot infection: usefulness of SPECT/CT for 99mTc-HMPAO-labeled leukocyte imaging. J Nucl Med. 2009;50:1042–6.
39. Petruzzi N, Shanthly N, Thakur M. Recent trends in soft-tissue infection imaging. Semin Nucl Med. 2009;39:115–23.
40. Rastogi A, Bhattacharya A, Prakash M, et al. Utility of PET/CT with fluorine-18-fluorodeoxyglucose-labeled autologous leukocytes for diagnosing diabetic foot osteomyelitis in patients with Charcot's neuroarthropathy. Nucl Med Commun. 2016;37:1253–9.
41. Kobayashi Y, Ishii K, Oda K, et al. Aortic wall inflammation due to Takayasu arteritis imaged with 18F-FDG PET coregistered with enhanced CT. J Nucl Med. 2005;46:917–22.
42. Slart RHJA; Writing group; Reviewer group; Members of EANM Cardiovascular; Members of EANM Infection & Inflammation; Members of Committees, SNMMI Cardiovascular, et al. FDG-PET/CT(A) imaging in large vessel vasculitis and polymyalgia rheumatica: joint procedural recommendation of the EANM, SNMMI, and the PET Interest Group (PIG), and endorsed by the ASNC. Eur J Nucl Med Mol Imaging. 2018;45:1250–69.
43. Palatka K, Kacska S, Lovas S, et al. The potential role of FDG PET-CT in the characterization of the activity of Crohn's disease, staging follow-up and prognosis estimation: a pilot study. Scand J Gastroenterol. 2018;53:24–30.
44. Berry N, Sinha SK, Bhattacharya A, et al. Role of positron emission tomography in assessing disease activity in ulcerative colitis: comparison with biomarkers. Dig Dis Sci. 2018;63:1541–50.
45. Ankrah AO, Span LFR, Klein HC, et al. Role of FDG PET/CT in monitoring treatment response in patients with invasive fungal infections. Eur J Nucl Med Mol Imaging. 2019;46:174–83.
46. Leroy-Freschini B, Treglia G, Argemi X, et al. 18F-FDG PET/CT for invasive fungal infection in immunocompromised patients. QJM. 2018;111:613–22.
47. Sathekge M, Maes A, Van de Wiele C. FDG-PET imaging in HIV infection and tuberculosis. Semin Nucl Med. 2013;43:349–66.
48. Akaike G, Itani M, Shah H, et al. PET/CT in the diagnosis and workup of sarcoidosis: focus on atypical manifestations. Radiographics. 2018;38:1536–49.
49. Imperiale A, Riehm S, Braun JJ. Interest of [18F]FDG PET/CT for treatment efficacy assessment in aggressive phenotype of sarcoidosis with special emphasis on sinonasal involvement. Q J Nucl Med Mol Imaging. 2013;57:177–86.
50. Calabria FF, Calabria E, Gangemi V, et al. Current status and future challenges of brain imaging with 18F-DOPA PET for movement disorders. Hell J Nucl Med. 2016;19:33–41.
51. Garraux G, Phillips C, Schrouff J, et al. Multiclass classification of FDG PET scans for the distinction between Parkinson's disease and atypical parkinsonian syndromes. Neuroimage Clin. 2013;14:883–93.
52. Yoon RG, Kim SJ, Kim HS, et al. The utility of susceptibility-weighted imaging for differentiating Parkinsonism-predominant multiple system atrophy from Parkinson's disease: correlation with 18F-flurodeoxyglucose positron-emission tomography. Neurosci Lett. 2015;1:296–301.
53. Meltzer CC, Adelson PD, Brenner RP, et al. Planned ictal FDG PET imaging for localization of extratemporal epileptic foci. Epilepsia. 2000;41:193–200.
54. Morbelli S, Djekidel M, Hesse S, et al. Role of (18) F-FDG-PET imaging in the diagnosis of autoimmune encephalitis. Lancet Neurol. 2016;15:1009–10.
55. van Hamersvelt HP, Kwee TC, Fijnheer R, et al. Can full-dose contrast-enhanced CT be omitted from an FDG-PET/CT staging examination in newly diagnosed FDG-avid lymphoma? J Comput Assist Tomogr. 2014;38:620–5.
56. Rosenkrantz AB, Friedman K, Chandarana H, et al. Current status of hybrid PET/MRI in oncologic imaging. AJR Am J Roentgenol. 2016;206:162–72.
57. Ferda J, Ferdová E, Baxa J, et al. 18F-Fluorocholine PET/MRI in restaging of prostatic carcinoma in relation to PSA level and detection of active disease. Anticancer Res. 2018;38:4139–43.
58. Leiva-Salinas C, Muttikkal TJE, Flors L, et al. FDG PET/MRI Coregistration helps predict response to gamma knife radiosurgery in patients with brain metastases. AJR Am J Roentgenol. 2018;13:1–6.
59. Seniaray N, Jain A. PET MRI Coregistration in intractable epilepsy and gray matter heterotopia. Clin Nucl Med. 2017;42:e171–2.
60. Barthel H, Schroeter ML, Hoffmann KT, et al. PET/MR in dementia and other neurodegenerative diseases. Semin Nucl Med. 2015;45:224–33.
61. Corrigan AJ, Schleyer PJ, Cook GJ. Pitfalls and artifacts in the use of PET/CT in oncology imaging. Semin Nucl Med. 2015;45:481–99.
62. Vandemoortele T, Laroumagne S, Roca E, et al. Positive FDG-PET/CT of the pleura twenty years after talc pleurodesis: three cases of benign talcoma. Respiration. 2014;87:243–8.
63. Purohit BS, Ailianou A, Dulguerov N, et al. FDG-PET/CT pitfalls in oncological head and neck imaging. Insights Imaging. 2014;5:585–602.
64. Priola AM, Priola SM. Chemical-shift MRI of rebound thymic hyperplasia with unusual appearance and intense (18)F-FDG uptake in adulthood: report of two cases. Clin Imaging. 2014;38:739–42.
65. Martínez Lorca A, Coronado Poggio M, Hernández Pérez I, et al. Utility of (^{99}m)Tc-labelled heat-denatured erythrocyte scintigraphy and ^{18}F-FDG PET-CT to differentiate accessory spleens from tumoral metastases. A case report. Rev Esp Med Nucl Imagen Mol. 2015;34:68–9.

^{18}F-DOPA

2

Ferdinando Calabria and Orazio Schillaci

Contents

Abbreviations

18F-DOPA	18F-Diidrossiphenilalanine
^{18}F-FDG	18F-Fluorodeoxyglucose
^{18}F-FET	^{18}F-Fluoroethyltirosine
^{18}F-FLT	^{18}F-Fluorothymidine
AAAD	Aromatic amino acid decarboxylase
CBD	Cortico-basal degeneration
COMT	Catechol-o-methyl transferase
LAT1 and LAT2	L-Type amino acid transporter 1 and 2
L-DOPA	L-3,4-Dihydroxyphenylalanine
MSA	Multiple systemic atrophy
NET	Neuroendocrine tumors
PET/CT	Positron emission tomography/computed tomography
PET/MRI	Positron emission tomography/magnetic resonance imaging

Authors declare they have obtained permission for any previously published material used in their chapter.

F. Calabria (✉)
Department of Nuclear Medicine and Theranostics, "Mariano Santo" Hospital, Cosenza, Italy
e-mail: ferdinandocalabria@hotmail.it

O. Schillaci
Department of Biomedicine and Prevention, University "Tor Vergata", Rome, Italy

Department of Nuclear Medicine and Molecular Imaging, IRCCS Neuromed, Pozzilli, IS, Italy

F. Calabria, O. Schillaci (eds.), *Radiopharmaceuticals*,
https://doi.org/10.1007/978-3-030-27779-6_2

PSP	Progressive supranuclear palsy
SPECT	Single photon emission computed tomography

2.1 Synthesis

The ^{18}F-diidrossiphenilalanine (^{18}F-DOPA) is an amino acid PET tracer and can be synthetized by either an electrophilic or nucleophilic process. The electrophilic radiofluorination by destannylation of ^{18}F-DOPA precursor has emerged as the synthesis method of choice. The fluorination of L-3-(3-hydroxy-4-pivaloyloxyphenyl)-alanine (4-*O*-pivaloyl-r-dopa, mPDOPA) with ^{18}F-acetyl hypofluorite in acetic acid, followed by HCl hydrolysis and high-performance liquid chromatography, has proved to be the recommended method for routine production of ^{18}F-DOPA, allowing a radiochemical yield of 17.0 ± 1.9% and a radiochemical purity of more than 97% [1].

2.2 Pharmacokinetics

The ^{18}F-DOPA has been introduced in clinical practice to investigate the in vivo transport of dopamine precursor from plasma to basal ganglia in the dopaminergic system of *substantia nigra*, in order to ensure the metabolism of the basal ganglia in movement disorders [2]. In oncology, ^{18}F-DOPA PET/CT is proposed to evaluate neuroendocrine tumors (NET) and brain tumors [3]. In fact, in cancer cells, the malignant growth is linked to an increased use of amino acids for energy, protein synthesis, and cell proliferation, in association with an overexpression of amino acid cellular transport system. Similar to other amino acid radiopharmaceuticals, as ^{11}C-Methionine and ^{18}F-fluorethyltirosine (^{18}F-FET), the uptake of ^{18}F-DOPA in NET and brain tumors is linked to the increased cell proliferation and protein synthesis.

Being the precursor of L-DOPA, the ^{18}F-DOPA follows *in vivo* the same metabolic pathway. Both molecules penetrate inside the cells carried by the L-type amino acid transporter 1 and 2 (LAT1 and LAT2). These transporters are also enrolled in the permeability of the blood brain barrier to ^{18}F-DOPA. The ^{18}F-DOPA is converted into ^{18}F-dopamine in peripheral tissues, by the aromatic amino acid decarboxylase (AAAD), and the ^{18}F-dopamine, converted by decarboxylation, cannot be taken up in the brain [2] (Fig. 2.1). The tracer can be also metabolized in several peripheral tissues by catechol-O-methyl transferase (COMT), before crossing the blood brain barrier, with a reduction of brain availability. The premedication of patients before tracer administration with carbidopa can reduce the COMT peripheral activity, enhancing the availability of the ^{18}F-DOPA in the brain [4]. No adverse reactions are reported in literature, with the exception of a short, transient mild pain and/or irritation at the site of the intravenous administration of the radiopharmaceutical. Therefore, it appears necessary to slowly administer the tracer through a venous catheter [5].

2.3 Physiological Distribution

The most prominent and intense tracer uptake is documented in exocrine glands as pancreas, liver, and gallbladder. Other organs with moderate-to-high uptake are spleen and lachrymal and salivary glands, with a common embryologic origin with pancreas [6]. Low uptake is normally detected in bone marrow. Kidneys and bladder can present high radioactivity concentration due to the tracer urinary excretion (Fig. 2.2). In the brain, the normal distribution is negligible, with the exception of basal ganglia [7].

Considering the rapid peak of the tracer uptake in brain tumor cells, all researchers agree about the usefulness of an early PET scan, few minutes after tracer administration. In particular, basal ganglia show faint uptake of ^{18}F-DOPA at 20 min after injection while tumor visualization is more pronounced at this time [8]. Therefore, an early acquisition, following 20 min the tracer administration, is the best time to perform the scan in patients with brain tumors [9, 10]. Conversely, a late scan at 70–90 min is associated

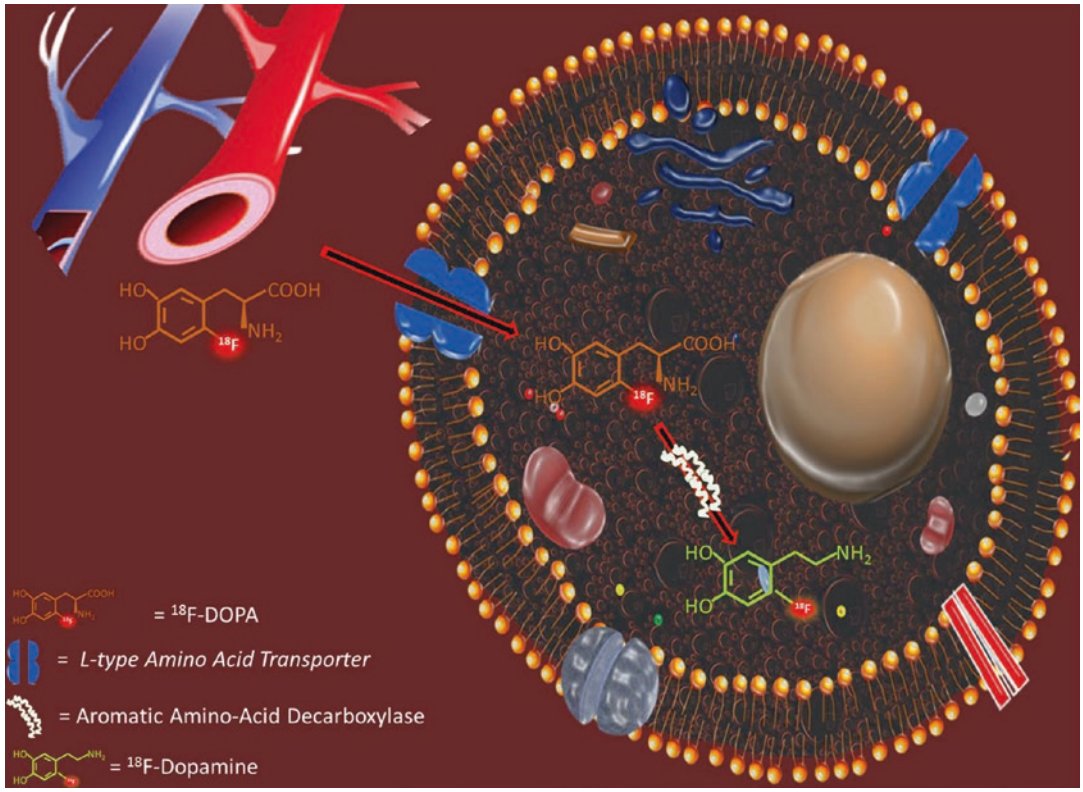

Fig. 2.1 The ^{18}F-DOPA is the precursor of L-*DOPA* and follows *"in vivo"* the same metabolic pathway. This radiopharmaceutical penetrates inside the cells carried by the L-type amino acid transporters and then is converted into ^{18}F-dopamine by the aromatic amino acid decarboxylase

with a better visualization of the basal ganglia and should be considered for imaging patients with movement disorders [8].

2.4 Clinical Indications

2.4.1 Neuroendocrine Tumors

Dopamine receptors have been found to be expressed in NET, the tumors which arise from the diffuse neuroendocrine cells. The dopamine receptors in these cells exhibit cytoplasmic or nuclear localizations, the latter being possibly linked to a higher grade of malignancy, and are often co-expressed with somatostatin receptors [11]. Usually, NET are relatively slowly growing tumors with low malignant potential but can produce pronounced endocrine-related symptoms despite their small size. NET are mainly located in the gastrointestinal tract and in the pancreas but can also origin from other sites such as the neck (medullary thyroid cancer), the bronchopulmonary system, the adrenal glands (pheochromocytoma), and the extra-adrenal paraganglia (paraganglioma) [12]. ^{18}F-DOPA PET/CT actually plays an interesting role in detection and monitoring of paraganglioma and pheochromocytoma [13]; several studies have demonstrated a good diagnostic accuracy of ^{18}F-DOPA PET/CT both in the staging (88%) and restaging (92%) of other NET. In particular, it has been showed a feasible role of ^{18}F-DOPA in the monitoring of patients with biochemical proof of disease, also with negative conventional imaging methods [12]. The usefulness of ^{18}F-DOPA has been also investigated in detecting primary NET occult on morphologic and functional imaging [14]: patients with negative conventional and somatostatin receptor scintigraphy results were stud-

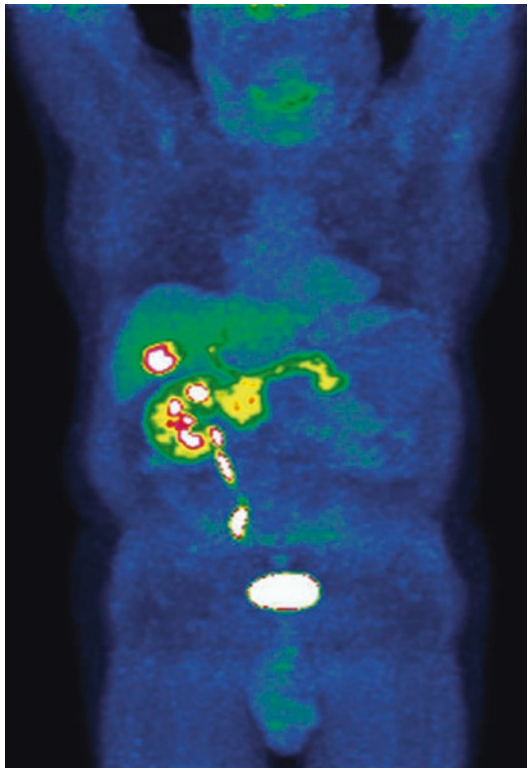

Fig. 2.2 Whole body ^{18}F-DOPA PET maximum intensity projection in a male patient shows the physiological distribution of the tracer in the human body. Pancreas, liver, kidneys, and ureters are the sites of higher physiological tracer uptake. The uptake in the brain is negligible, with the exception of the basal ganglia

ied by means of ^{18}F-DOPA PET/CT. The primary occult NET was localized in 12/27 patients (sensitivity, 44%), leading to tumor resection in all cases. In particular, there were correctly diagnosed tumors with a well-differentiated pattern and serotonin secretion [15]. Despite ^{18}F-DOPA PET/CT appears to be a sensitive functional imaging tool for the detection of primary NET, especially tumors with a well-differentiated pattern and serotonin secretion, the potential applications of ^{18}F-DOPA in the management of NET have been partially replaced by the recent commercial availability of ^{68}Ga labeled somatostatin receptors analogs, also allowing the possibility to plan the therapy with radiolabeled *somatostatin analogs as* ^{111}In-Octreotide or ^{177}Lu-DOTATATE [16, 17] (see Chap. 6).

On the other hand, ^{18}F-DOPA PET/CT seems to play a crucial role in the restaging of patients with recurrent medullary thyroid cancer (Fig. 2.3). In fact, some papers well described ^{18}F-DOPA PET/CT as a useful imaging method to detect recurrent medullary thyroid lesions, performing better than ^{18}F-FDG and ^{68}Ga-somatostatin analogs PET/CT [18], in this specific clinical setting. Following literature data, ^{18}F-FDG may complement ^{18}F-DOPA in patients with aggressive tumors while ^{68}Ga-somatostatin analogs PET/CT may be useful to select patients who could benefit from radioreceptor therapy [19]. In particular, in patients in restaging of medullary thyroid cancer and rise of CEA and calcitonin, it has been showed that ^{18}F-DOPA PET/CT may have an important prognostic value in predicting disease progression and mortality rate [20].

The molecular properties of the tracer and the higher availability of hybrid PET/CT scanners, rather than SPECT/CT devices, allow to still consider the ^{18}F-DOPA a useful tracer in the diagnosis and monitoring of pheochromocytoma and paraganglioma [21].

2.4.2 Neuro-oncological Imaging

Brain PET imaging with amino acid tracers is being increasingly used to supplement MRI in the clinical management of glioma. Several limitations are linked to the use of ^{18}F-FDG in brain tumor imaging, due to the intrinsic properties of this tracer, an analog of glucose with high rate of physiological distribution in the normal structures of white and gray matters [22]. The ^{11}C-Methionine has a high degree of uptake in brain neoplastic tissue due to its role as an essential amino acid form, necessary for protein synthesis (see Chap. 11). Unfortunately, the short half-life of ^{11}C (20 min) [23] limits its availability. Therefore, several fluorinated amino acid tracers as ^{18}F-FET [24] (see Chap. 4), ^{18}F-fluorothymidine (^{18}F-FLT) [9], and ^{18}F-DOPA [25] are currently used for brain tumor staging and restaging [26]. These fluorinated tracers present a longer half-life that makes them clini-

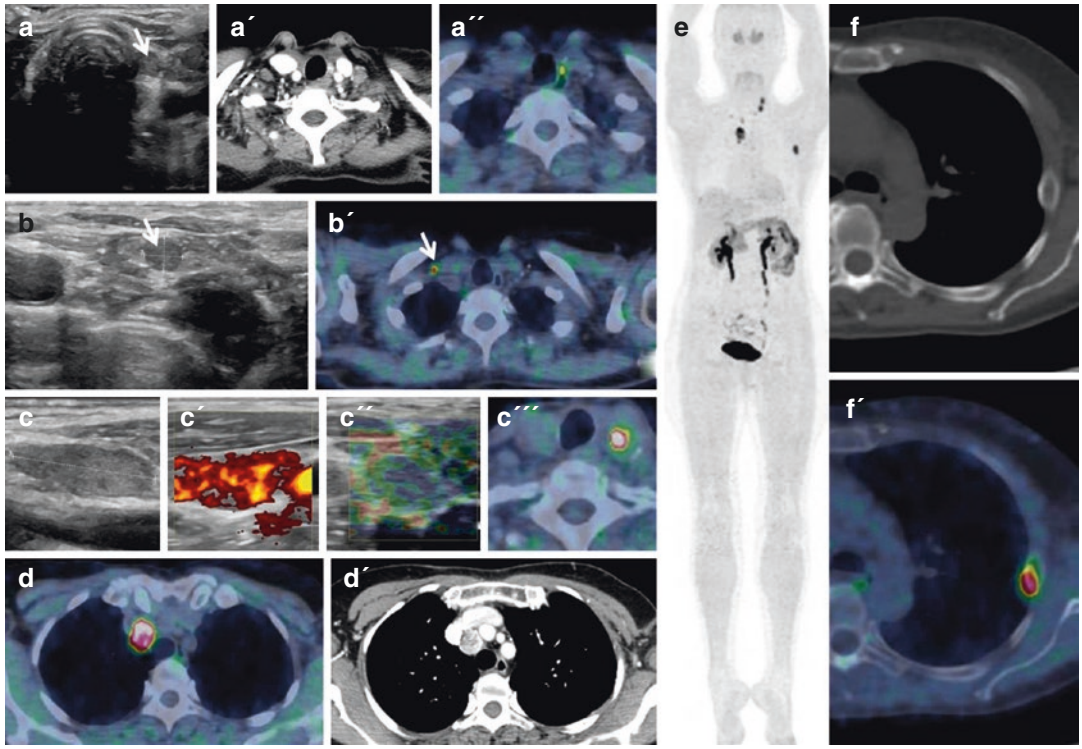

Fig. 2.3 A 49-year-old male patient examined by ultrasonography, contrast enhanced CT, and ^{18}F-DOPA PET/CT, due to rise of calcitonin, 2 years after radical thyroidectomy for medullary thyroid cancer. Axial ultrasound (**a**), contrast enhanced CT (**a'**), and PET/CT (**a"**) show a 1-cm-wide para-tracheal lymph node with pathologic tracer uptake. Axial ultrasound (**b**) and PET/CT (**b'**) display a further right retro-clavicular lymph node (*arrows*). Axial ultrasound (**c**) shows tumor relapse in the left thyroid bed with intense blood flow in Doppler (**c'**), ample areas of hard strain, prevalently arranged in a constant manner at the periphery or at the center of the nodule, as assessed by elastography (**c"**), and pathologic ^{18}F-DOPA uptake in corresponding axial PET/CT detail (**c"'**). Moreover, axial PET/CT (**d**) and CT (**d'**) show further pathologic mediastinal lymphadenopathy, with high tracer uptake and intense contrast enhancement. These findings, due to secondary localizations of medullary thyroid cancer, are summarized in *Maximum Intensity Projection* ^{18}F-DOPA PET (**e**), also showing an area of uptake in a rib of the left hemithorax, in association with lytic lesion, as evident in CT (**f**) and PET/CT (**f'**) details. *Credits to Mario Leporace (MD) Department of Nuclear Medicine and Theranostics, Mariano Santo Hospital, Cosenza, Italy*

cally available in many diagnostic centers, not provided by a cyclotron.

In the brain, the ^{18}F-DOPA is normally enhanced in the brain in the *substantia nigra* and in the caudate and putamen nuclei, which are similar in structure and have a common embryologic origin [27]. Due to the very low rate of physiological uptake in the other structures of the brain, the ^{18}F-DOPA has been proposed for brain lesions detection, especially because of its high uptake in tumors [28]. Several studies have described the potential role of ^{18}F-DOPA in the management of newly diagnosed brain tumors [9], even with PET/MRI combined fusion imaging [10] (Fig. 2.4): however, in this field the ^{18}F-DOPA PET/CT should not be considered as a first-line imaging method, due to the possibility of tracer uptake that can occur in some benign conditions [3].

On the other hand, in patients with suspected recurrent low-grade brain tumors, ^{18}F-DOPA shows good diagnostic accuracy in the identification of brain tumor relapse and in differentiating recurrent low-grade tumors from necrotic tissues after radiotherapy [28], especially in comparison with ^{18}F-FDG [9, 10]. The ^{18}F-DOPA PET/CT can be also useful in detecting brain metastases

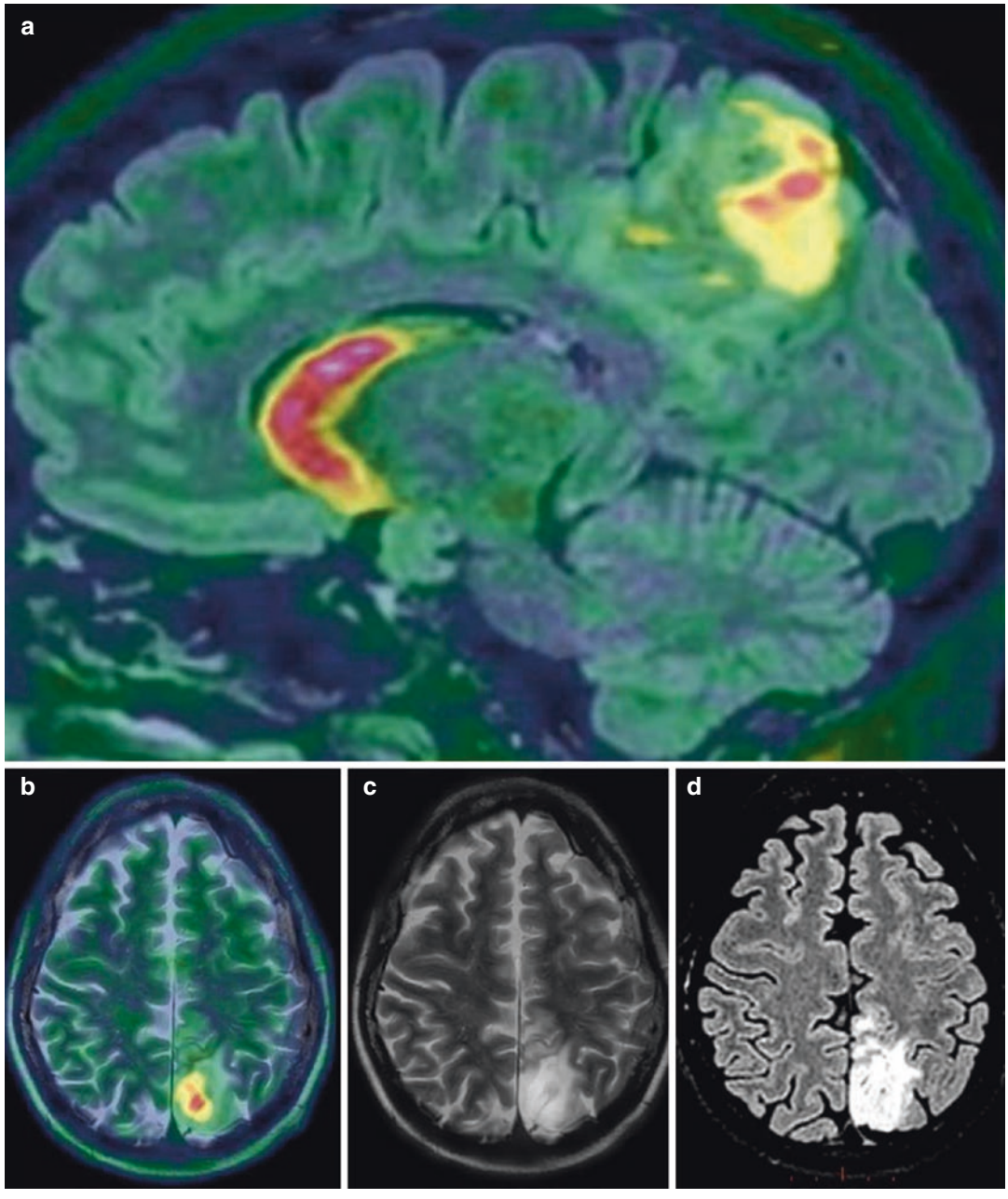

Fig. 2.4 Patient in staging for glioma. Sagittal PET/MRI (**a**) shows intense ^{18}F-DOPA uptake in a hyperintense lesion in left parietal region, also evident in axial PET/CT (**b**), T2-weighted (**c**) and *Fluid Attenuated Inversion Recovery* (**d**) MRI

of somatic tumors, even if few data on poor populations are available on this topic [8].

In comparison to other amino acid tracers, in several studies a substantial overlapping is reported, in terms of sensitivity and specificity, among ^{11}C-Methionine, ^{18}F-FLT, ^{18}F-FET, and ^{18}F-DOPA [24, 29], while all these tracers have been proven substantially superior to ^{18}F-FDG in detecting residual brain tumors [9, 27, 30].

In conclusion, the ^{18}F-DOPA PET/CT seems to be useful in the diagnosis of patients with suspected brain tumor recurrence, because of low signal ratio in normal brain white and gray matter, similar to other amino acid tracers and in contrast to ^{18}F-FDG PET/CT low performance. MRI still remains the gold standard tool but ^{18}F-DOPA PET/CT is adjuvant to diagnosis. Simultaneous PET/MRI will play in the next future a crucial role in the field of brain tumor imaging [31].

2.4.3 Functional Neuroimaging

Since 1996, it has been demonstrated that in Parkinson's disease the ^{18}F-DOPA uptake in the basal ganglia is reduced, compared to controls [32]. Moreover, during the time it has emerged that in parkinsonian patients the rate of loss of dopaminergic neurons is faster than controls [33]. The mean annual rate of decreased ^{18}F-DOPA uptake in Parkinson's disease patients is reported to be 8–12% in the putamen and 4–6% in the caudate while in healthy volunteers is less than 1% in both structures [34, 35], following the Braak's hypothesis [36]. In patients with a positive ^{18}F-DOPA PET scan of the brain, the tracer uptake is more decreased in the putamen nuclei rather than in the caudate nuclei indicating that, during the natural history of the disease, putamens show earlier involvement in respect to caudate nuclei. In healthy controls a minimal uptake difference is known between putamen and caudate. Moreover, in patients affected by Parkinson's disease the striatal uptake is decreased on the brain side contralateral to symptoms.

Deficit of ^{18}F-DOPA uptake in the basal ganglia can be also documented in other forms of Parkinson's disease, as in its juvenile form, due to the rapid loss of striatal neurons [37].

One of the most important goals in the early diagnosis and identification of Parkinson's disease patients is the differential diagnosis with the Parkinsonian syndromes, as progressive supranuclear palsy (PSP), multiple systemic atrophy (MSA), cortico-basal degeneration (CBD). In fact, only Parkinson's disease patients clinically respond to anti-Parkinson drugs therapy. Unfortunately, in this field, minimal differences are reported in reduction of ^{18}F-DOPA uptake in the basal ganglia between Parkinson's disease patients and patients with parkinsonian syndromes. The overlapping between these populations is too much for a meaningful differentiation [38–41]. In this specific field, especially for CBD, the ^{18}F-FDG PET/CT still could play a crucial role, allowing the depiction of the hypometabolism that can occur in specific cortical regions [39].

However, ^{18}F-DOPA PET has shown a similar diagnostic accuracy in the diagnosis of Parkinson's disease, in comparison with the actual gold standard imaging, the single photon emission computed tomography (SPECT) with cocaine analogs [42, 43].

More recently, researchers recently focused the attention on the possible role of an integrated, multi-modal evaluation of Parkinson's disease by means of both MRI and PET in a double session [44]. On this topic, the potential usefulness of MRI can allow to exclude symptomatic parkinsonism due to structural basal ganglia cells loss,

by analysis of morphologic images and MR spectroscopy [45]. Correlative imaging with MRI can be also useful in discriminating between vascular parkinsonism or rare tremor syndromes and Parkinson's disease, allowing the recognition of the anatomical alterations at the basis of the symptomatology, as post-hemorrhagic lacunar areas or calcifications in the basal ganglia. Moreover, other motor disorders characterized by subcortical alterations could be better discriminated by MRI.

Recent studies supported the usefulness of an integrated PET/MRI scan to ensure the diagnosis of Parkinson's disease by the depiction of glucose metabolism with ^{18}F-FDG PET [46] or the metabolism of the striatum provided by ^{18}F-DOPA PET [47] and the morphological imaging provided by MRI. Furthermore, an advantage of a hybrid PET/MRI evaluation in patients with movement disorders could be the possibility of an advanced head movement correction, actually not fully available with PET/CT scanners.

2.5 Clinical Cases

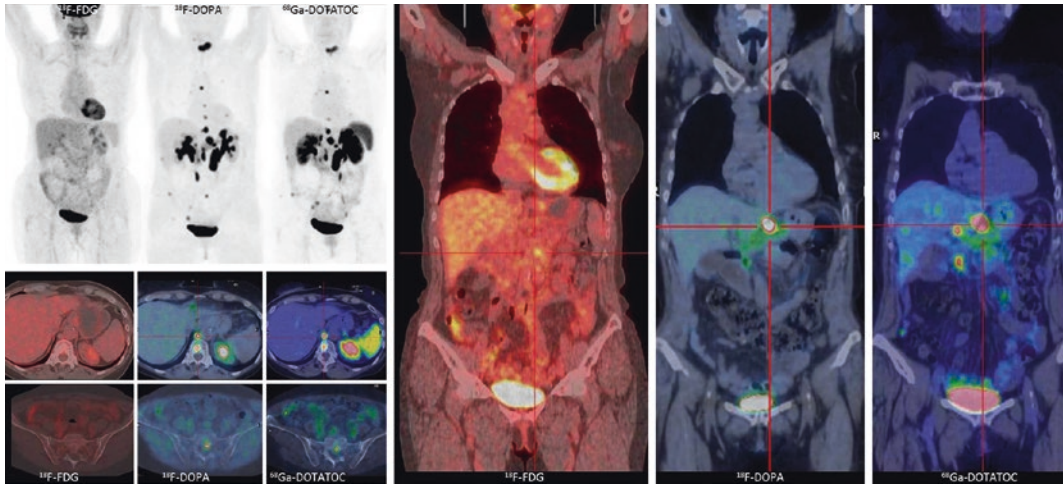

Fig. 2.5 This picture summarizes ^{18}F-FDG, ^{18}F-DOPA, and ^{68}Ga-DOTATOC PET/CT findings in a patient with multiple secondary localizations and rise of *Chromogranine A* serum level, 2 years after surgical excision of a cecal carcinoid. The PET maximum intensity projections (MIP) (*in gray scale*) of the ^{18}F-FDG PET/CT is negative while the ^{18}F-DOPA and ^{68}Ga-DOTATOC MIP display numerous sites of pathologic tracer uptake in liver, bones, and multiple lymph nodes. On a per lesion analysis, a substantial overlapping was recorded between ^{18}F-DOPA and ^{68}Ga-DOTATOC PET/CT. The axial PET/CT details show a retro-diaphragmatic lymph node and a sacral lesion without meaningful ^{18}F-FDG uptake (*in red scale*) and high ^{18}F-DOPA (*in green scale*) and ^{68}Ga-DOTATOC (*in blue/red scale*) uptake. Coronal views confirm very low ^{18}F-FDG uptake (*in red scale*) in an infra-diaphragmatic lymph node with high uptake gradient of ^{18}F-DOPA (*in green scale*) and ^{68}Ga-DOTATOC (*in blue/red scale*)

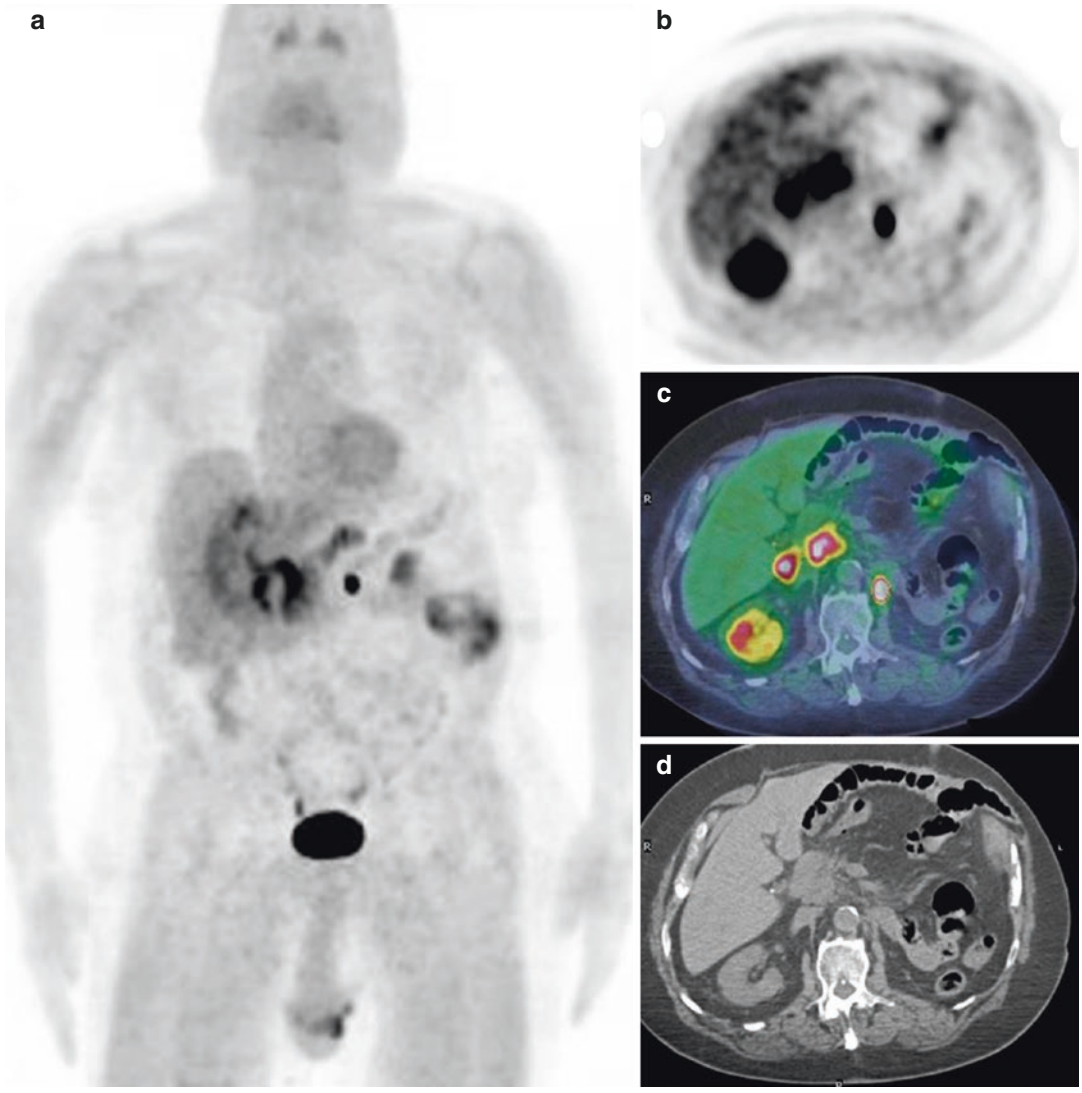

Fig. 2.6 In a patient with a NET of the head of the pancreas, the ^{18}F-DOPA PET maximum intensity projection (**a**) shows pathologic tracer uptake in the primary lesion. Axial PET (**b**) and PET/CT (**c**) views display a further area of pathologic tracer uptake in a thickening of the left diaphragmatic crus, evident on corresponding CT view (**d**)

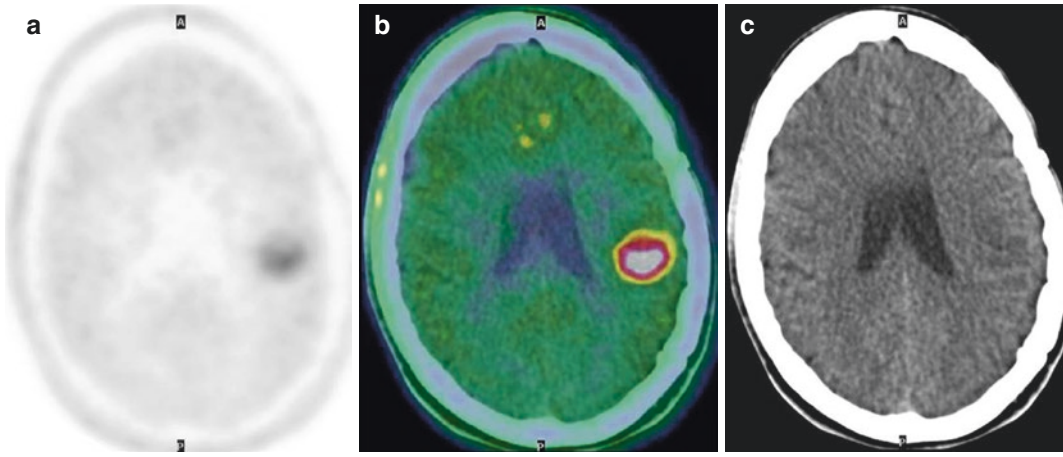

Fig. 2.7 In a patient with glioma, axial ^{18}F-DOPA PET (**a**) and PET/CT (**b**) views show intense uptake in the lesion in left parietal region, with mild surrounding edema in the corresponding CT view (**c**)

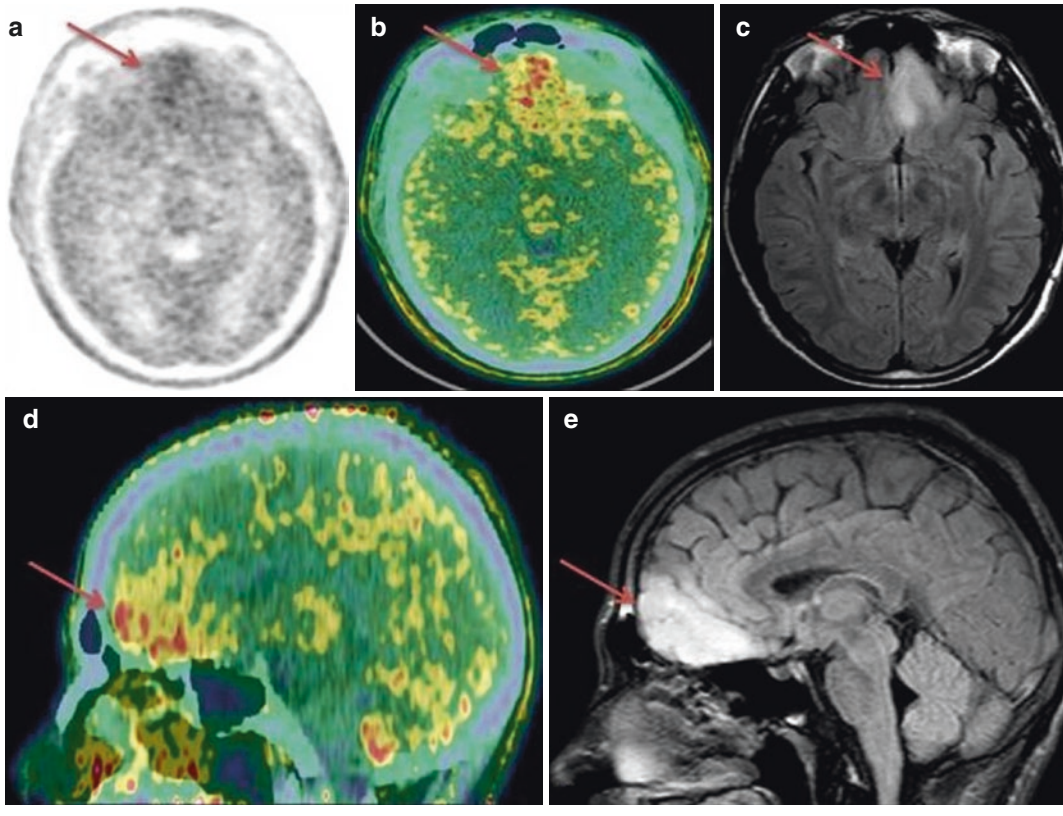

Fig. 2.8 Patient with astrocytoma. Axial PET (**a**) and PET/CT (**b**) views and sagittal PET/CT views (**d**) show intense ^{18}F-DOPA uptake in the left frontal region, in correspondence of a hyperintense lesion on related axial (**c**) and sagittal (**e**) *Fluid Attenuated Inversion Recovery* MRI views

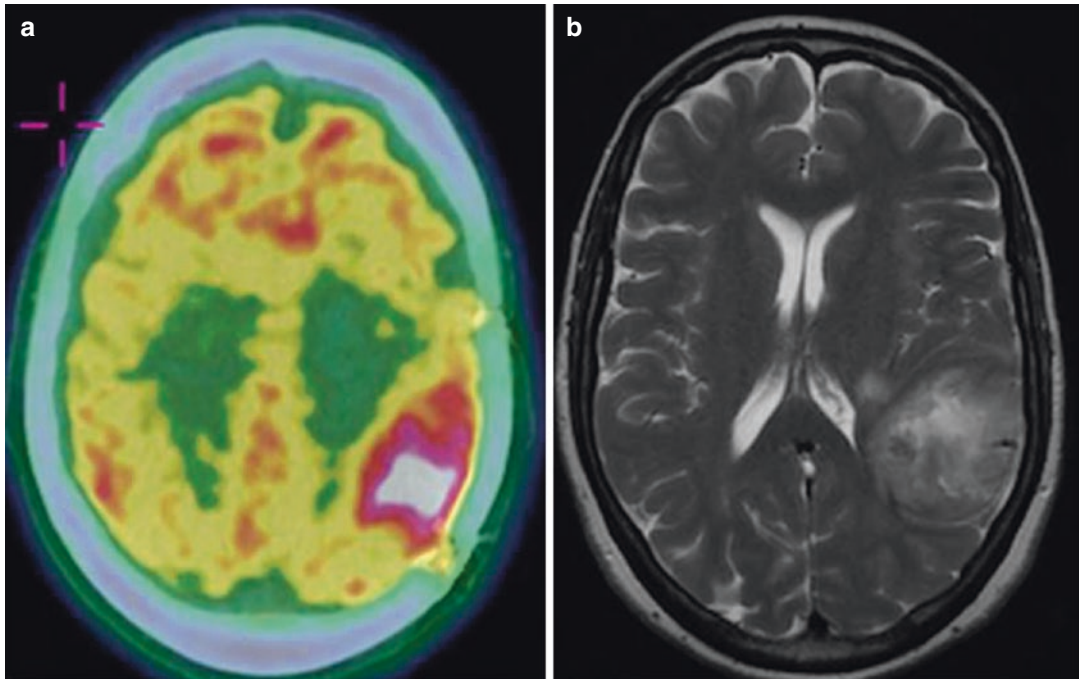

Fig. 2.9 Axial ^{18}F-DOPA PET/CT (**a**) shows intense uptake in the left parietal region, with abnormal signal intensity and surrounding edema in related T2-weighted MRI view (**b**), in a patient with glioblastoma

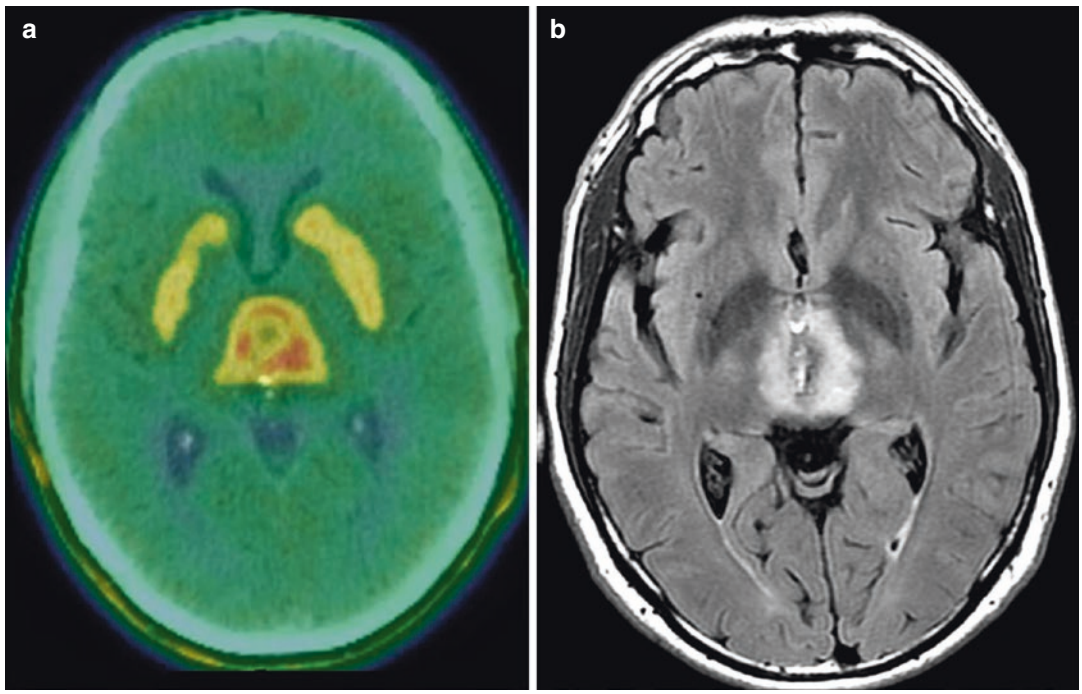

Fig. 2.10 Axial ^{18}F-DOPA PET/CT (**a**) shows intense uptake in the thalamus, higher than the physiologic uptake of the basal ganglia, due to glioma relapse, as evident in related fluid attenuated inversion recovery MRI view (**b**), showing a high signal intensity lesion

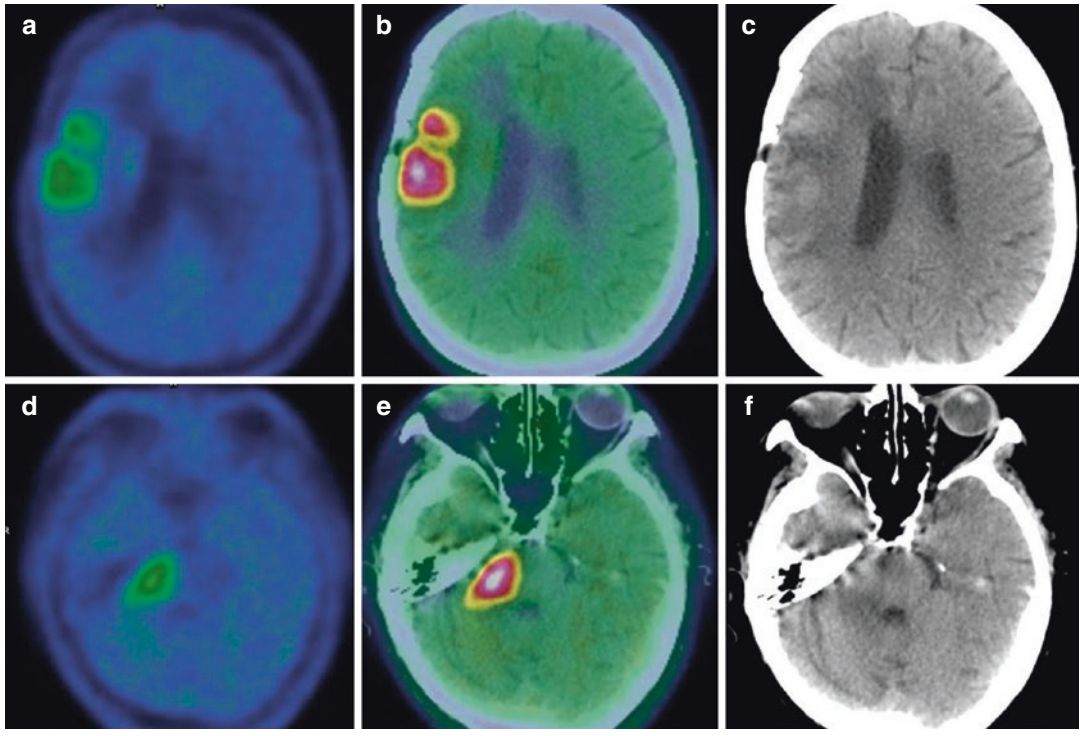

Fig. 2.11 Axial ^{18}F-DOPA PET (**a**, **d**) and PET/CT (**b**, **e**) views show two areas of diffuse tracer uptake, due to glioblastoma relapse, respectively, in the right frontotemporal region and ipsilateral temporal lobe. Related axial CT views (**c**, **f**) display the enlargement of the right ventricle and surrounding edema

Fig. 2.12 Example of a *dual phase* ^{18}F-DOPA PET/CT. In a patient examined for staging a low-grade brain tumor of the left frontal region, axial PET and PET/CT views in the left column show intense pathologic uptake in the lesion (SUVmax 4.8) in the early PET/CT scan, 20 min after the tracer administration. At the late scan, following 60 min the injection, the lesion presents reduced uptake (SUVmax 2.4) as evident in corresponding PET and PET/CT view in the right column

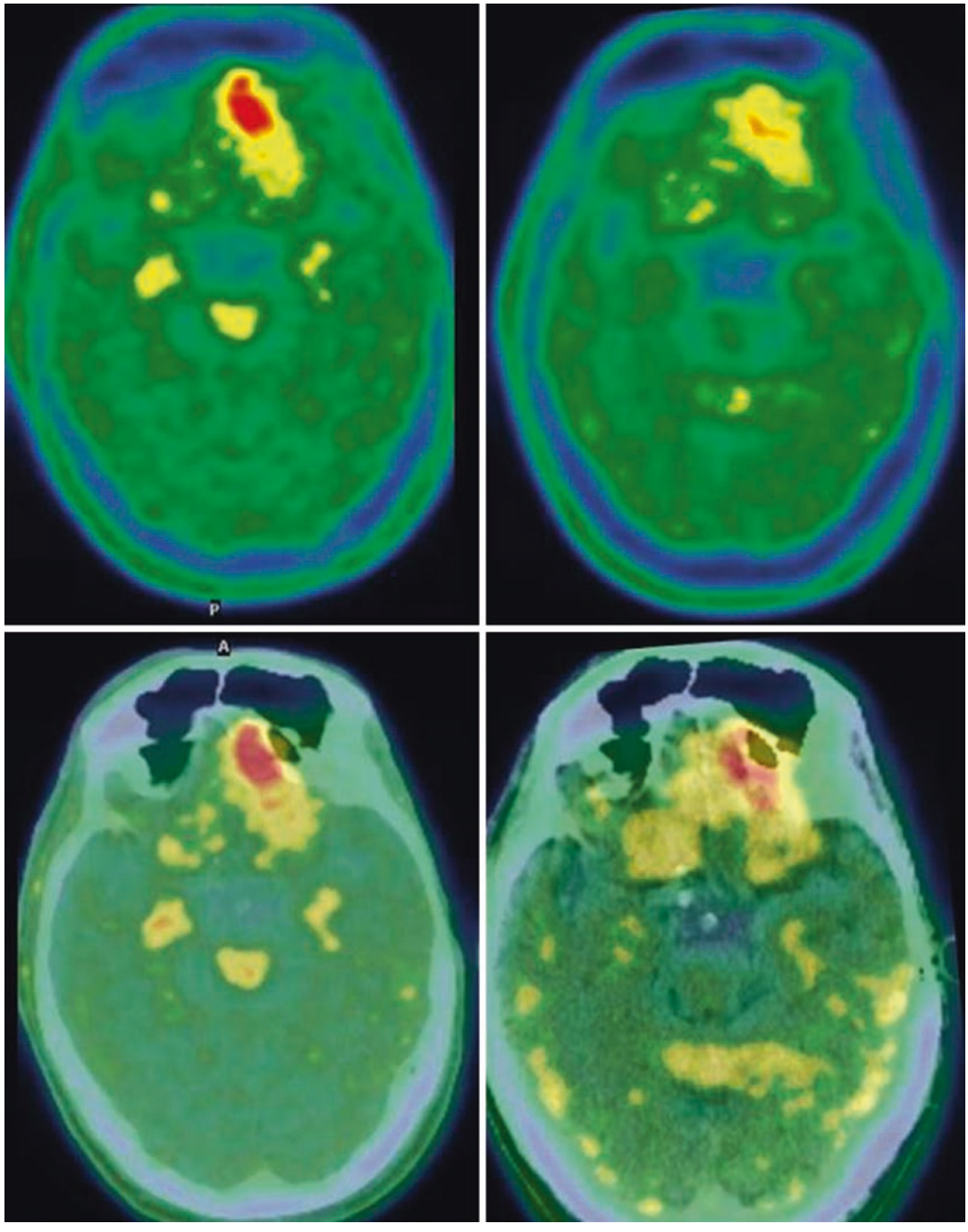
P
A

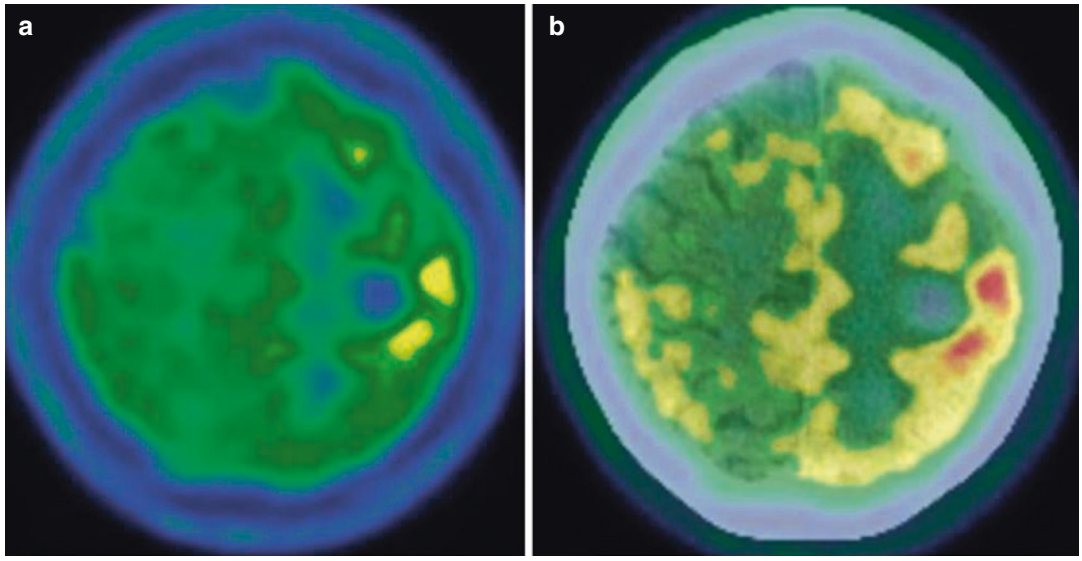

Fig. 2.13 In a patient submitted to radiotherapy on a brain metastasis of lung cancer in left parietal region, axial PET (**a**) and PET/CT (**b**) views show residual tumor activity

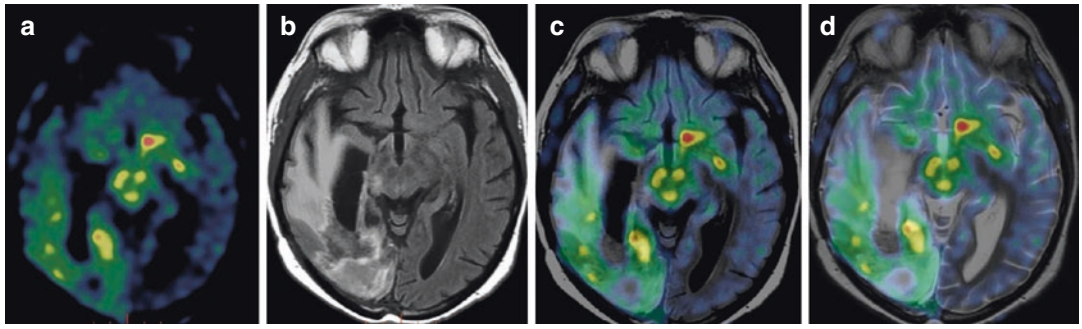

Fig. 2.14 Patient previously submitted to surgical intervention for glioblastoma. Axial PET (**a**) and T1 weighted MRI (**b**) show pathologic tracer uptake in a hyperintense lesion of the right temporal lobe, in association with edema and enlargement of the ipsilateral ventricle. These findings are well summarized in related T1 (**c**) and T2 (**d**) PET/MRI views

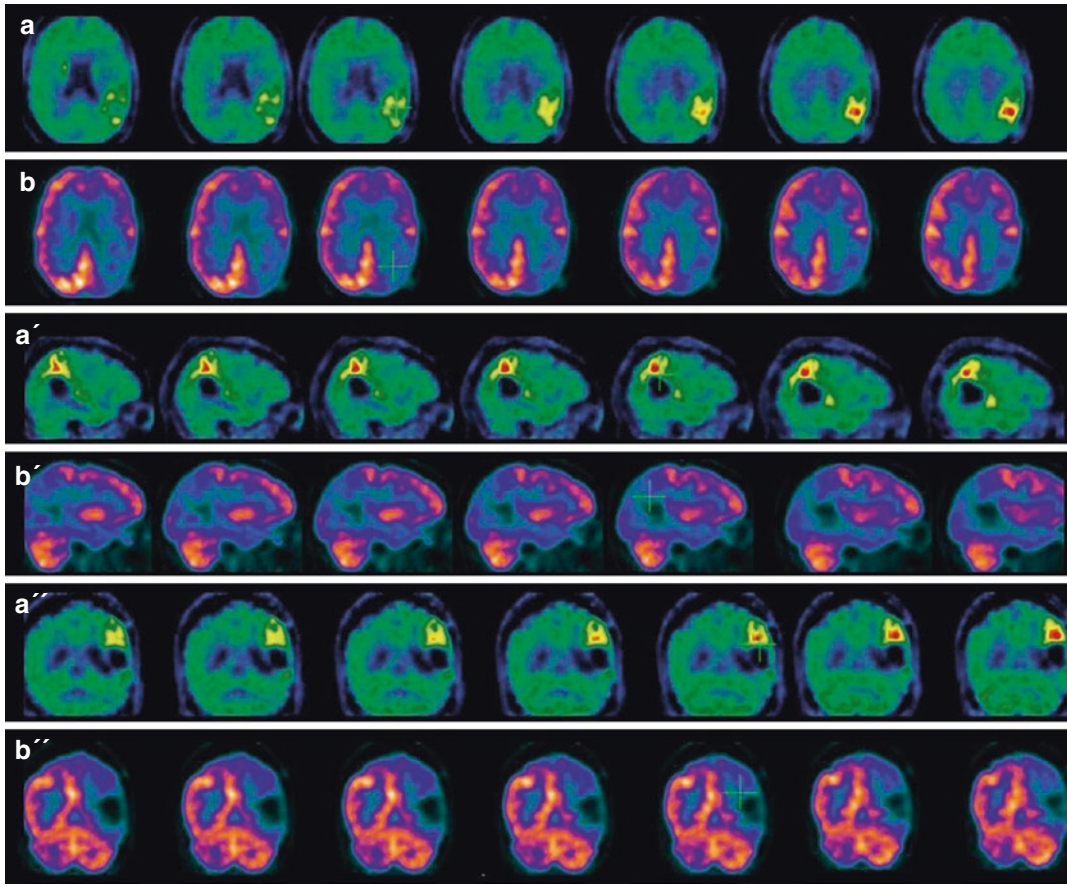

Fig. 2.15 A patient was previously submitted to surgical excision of a left parietal glioma. Two years after, axial (**a**), sagittal (**a'**), and coronal (**a''**) ^{18}F-DOPA PET views (*in green scale*) show tracer uptake in the left parietal region, linked to tumor recurrence, as confirmed by histological exam. The patient was also submitted to brain ^{18}F-FDG PET/CT. ^{18}F-FDG PET (*in purple scale*) only showed hypometabolism in the left, parietal, post-surgical lacunar area, as evident in axial (**b**) and sagittal (**b'**) ^{18}F-FDG PET views. A further area of hypometabolism was detected in the right cerebellar hemisphere, contralateral to the lacunar area, as shown in coronal ^{18}F-FDG PET views (**b''**), indicative of crossed cerebellar diaschisis. ^{18}F-DOPA PET allowed to diagnose tumor relapse; ^{18}F-FDG PET was not able to identify tumor recurrence but displayed a functional disorder

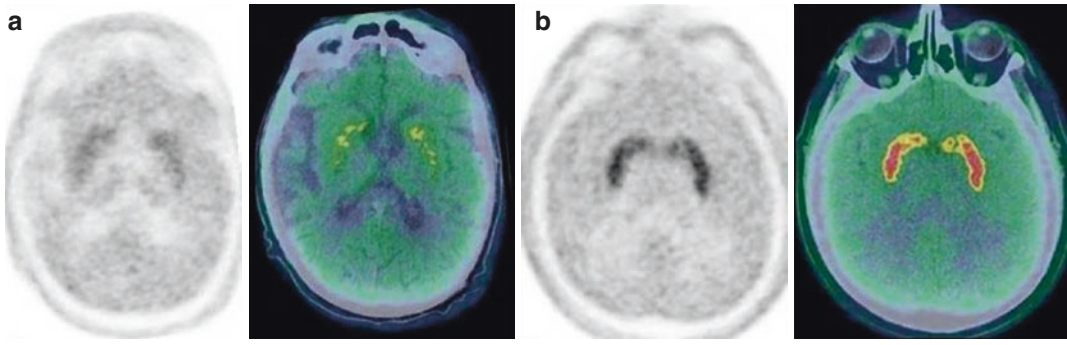

Fig. 2.16 In a 60-year-old patient with Parkinson's disease, axial ^{18}F-DOPA PET and PET/CT views (**a**) show diffuse reduction of the uptake in putamen and caudate nuclei. In a healthy 62-year-old case control, axial ^{18}F-DOPA PET and PET/CT views (**b**) show homogeneous tracer uptake in the basal ganglia

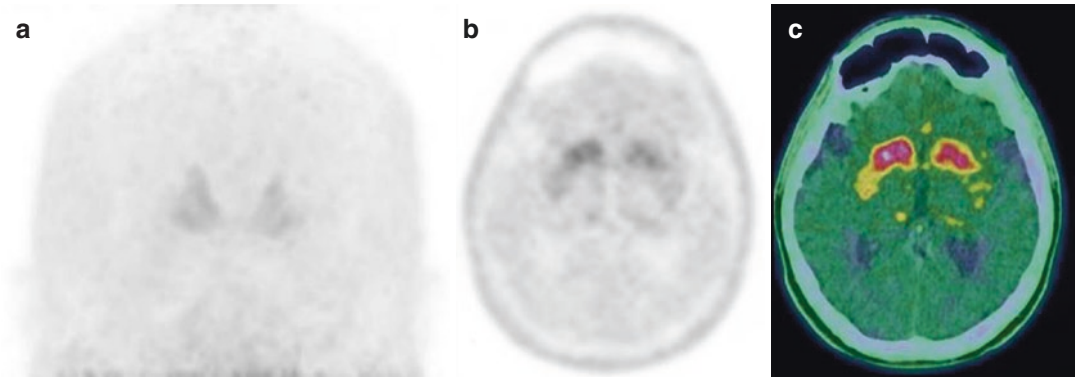

Fig. 2.17 In a patient with Parkinson's disease and predominant right side tremor, PET maximum intensity projection of the brain (**a**), axial PET (**b**), and PET/CT (**c**) views show reduction of ^{18}F-DOPA uptake in both putamen nuclei and in the left caudate

2.6 PET/CT Acquisition Protocols

- Whole body PET/CT: from the vertex of the skull to the upper thighs, 45–60 min following the tracer administration (≈300 MBq; 2–3 min per bed position). A low-dose CT is sufficient, for the anatomical localization of functional findings, such as primary NET, in order to reduce radiation exposure for patients. Additional segmentary scans, if requested. Routinely iodinate contrast media administration during the CT seem to be unnecessary.
- Brain PET/CT: A low-dose CT of the brain, with the head of the patient in the center of the scanner field of view, is necessary for attenuation correction and anatomical reference. The 10 min PET scan should be performed 20 min after the ^{18}F-DOPA injection (≈180 MBq) for brain tumor imaging while a late scan (90 min after the injection) is the optimal timing to image basal ganglia in patients with movement disorders. Contrast enhanced CT can be associated with PET in brain tumor imaging but correlative imaging with MRI still remains of the utmost importance.

2.7 Variants and Pitfalls

As for other PET and SPECT radiopharmaceuticals, the in vivo bio-distribution of ^{18}F-DOPA can present physiological variants and sites of abnormal uptake not related to the disease under study.

In whole body standard imaging, the gallbladder can be a site of intense physiological uptake that may simulate a liver metastasis from a primary NET [48]: the knowledge of the normal biliary tracer excretion and the hybrid PET/CT imaging help to avoid this common pitfall [49]. Occasionally, the adrenal glands can show mild uptake: this feature is normally linked to the physiologic functional activity but, when in association with a hypodense node at the CT component of the scan, could be related to an adrenal adenoma [3, 48]. However, nuclear physicians should take into account the possibility of faint ^{18}F-DOPA uptake in malignant conditions which can have origin from adrenal glands, such as lymphomas [50] (Fig. 2.18).

For brain imaging, the main potential false positive finding can be the ^{18}F-DOPA uptake in granulation tissues, due to the activation of monocyte-macrophages and fibroblasts in the site of a recent surgical intervention [3]: anyway, this feature can be observed when the scan

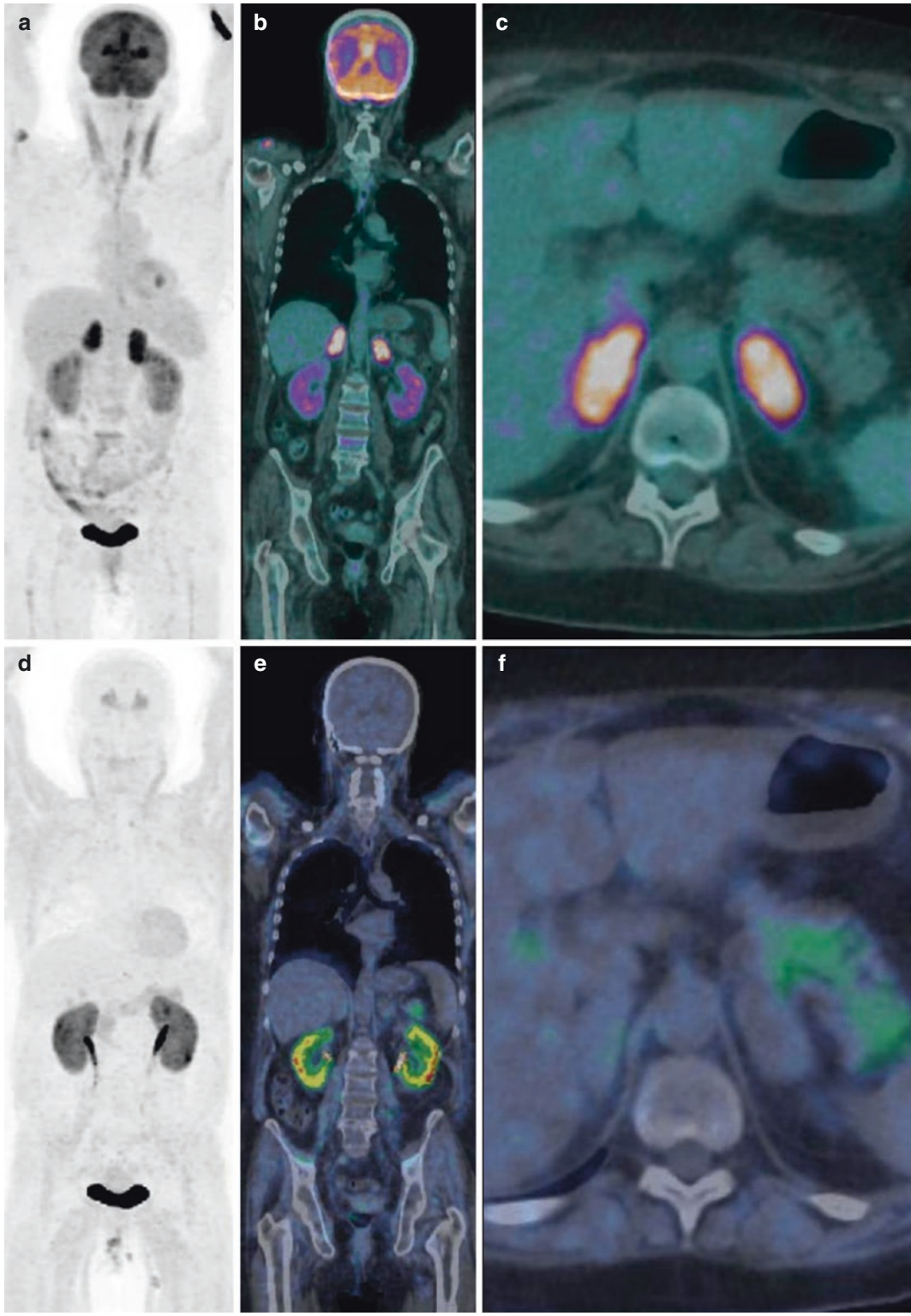

Fig. 2.18 Patient with bilateral adrenal lymphoma. ^{18}F-FDG maximum intensity projection (**a**) shows intense tracer uptake in both adrenal glands, in association with enlargement of both glands, as evident in coronal (**b**) and axial (**c**) PET/CT views. No uptake was documented on ^{18}F-DOPA PET, as showed in maximum intensity projection (**d**), coronal (**e**), and axial (**f**) PET/CT views

is performed few days following surgery; the hybrid PET/MRI could help in managing this findings [51].

When approaching with newly diagnosed brain tumors, it is mandatory to consider that ^{18}F-DOPA uptake can occur in some benign brain lesions as meningiomas [52], ependymomas, benign lesions of the pineal gland [3], focal encephalomyelitis, and neurosarcoidosis [53].

References

1. Lemaire C, Libert L, Franci X, et al. Automated production at the curie level of no-carrier-added 6-[(18)F]fluoro- l-dopa and 2-[(18) F]fluoro- l-tyrosine on a FASTlab synthesizer. J Labelled Comp Radiopharm. 2015;58:281–90.
2. Calabria FF, Calabria E, Gangemi V, et al. Current status and future challenges of brain imaging with 18F-DOPA PET for movement disorders. Hell J Nucl Med. 2016;19:33–41.
3. Calabria FF, Chiaravalloti A, Jaffrain-Rea ML, et al. 18F-DOPA PET/CT physiological distribution and pitfalls: experience in 215 patients. Clin Nucl Med. 2016;41:753–60.
4. Melega WP, Hoffman JM, Luxen A, et al. The effects of carbidopa on the metabolism of 6-[18F] fluoro-L-dopa in rats, monkeys and humans. Life Sci. 1990;47:149–57.
5. Doudet DJ, Dejesus OT, Chan GLY et al. Quantitative functional brain Imaging with Positron Emission Tomography. Chapter 58. Imaging of the dopamine presynaptic system by PET: 6-[18F]-L-DOPA versus 6-[F]Fluoro-l-m-tyrosine. 1998.
6. Hisatomi Y, Okumura K, Nakamura K, et al. Flow cytometric isolation of endodermal progenitors from mouse salivary gland differentiate into hepatic and pancreatic lineages. Hepatology. 2004;39:667–75.
7. Chiaravalloti A, Fiorentini A, Villani V, et al. Factors affecting ^{18}F FDOPA standardized uptake value in patients with primary brain tumors after treatment. Nucl Med Biol. 2015;42:355–99.
8. Becherer A, Karanikas G, Szabó M, et al. Brain tumour imaging with PET: a comparison between [18F]fluorodopa and [11C]methionine. Eur J Nucl Med Mol Imaging. 2003;30:1561–7.
9. Tripathi M, Sharma R, D'Souza M, et al. Comparative evaluation of F-18 FDOPA, F-18 FDG, and F-18 FLT-PET/CT for metabolic imaging of low grade gliomas. Clin Nucl Med. 2019;34:878–83.
10. Ledezma CJ, Chen W, Sai V, et al. 18F-FDOPA PET/MRI fusion in patients with primary/recurrent gliomas: initial experience. Eur J Radiol. 2009;71:242–8.
11. Minn H, Kemppainen J, Kauhanen S, et al. 18F-fluorodihydroxyphenylalanine in the diagnosis of neuroendocrine tumors. PET Clin. 2014;9:27–36.
12. Kauhanen S, Seppänen M, Ovaska J, et al. The clinical value of [18F]fluoro-dihydroxyphenylalanine positron emission tomography in primary diagnosis, staging, and restaging of neuroendocrine tumors. Endocr Relat Cancer. 2009;16:255–65.
13. Taïeb D, Timmers HJ, Hindié E, et al. EANM 2012 guidelines for radionuclide imaging of phaeochromocytoma and paraganglioma. Eur J Nucl Med Mol Imaging. 2012;39:1977–95.
14. Gornes H, Vaysse C, Deslandres M, et al. Discovery of a neuroendocrine tumor of the caecum by mammary metastasis using 18F-DOPA-PET. J Obstet Gynaecol Res. 2018;44:2195–8.
15. Imperiale A, Rust E, Gabriel S, et al. 18F-fluorodihydroxyphenylalanine PET/CT in patients with neuroendocrine tumors of unknown origin: relation to tumor origin and differentiation. J Nucl Med. 2014;55:367–72.
16. Filippi L, Scopinaro F, Pelle G, et al. Molecular response assessed by (68)Ga-DOTANOC and survival after (90)Y microsphere therapy in patients with liver metastases from neuroendocrine tumours. Eur J Nucl Med Mol Imaging. 2016;43:432–40.
17. Hofman MS, Lau WF, Hicks RJ. Somatostatin receptor imaging with 68Ga DOTATATE PET/CT: clinical utility, normal patterns, pearls, and pitfalls in interpretation. Radiographics. 2015;35:500–16.
18. Treglia G, Castaldi P, Villani MF, et al. Comparison of different positron emission tomography tracers in patients with recurrent medullary thyroid carcinoma: our experience and a review of the literature. Recent Results Cancer Res. 2013;194:385–93.
19. Slavikova K, Montravers F, Treglia G, et al. What is currently the best radiopharmaceutical for the hybrid PET/CT detection of recurrent medullary thyroid carcinoma? Curr Radiopharm. 2013;6:96–105.
20. Caobelli F, Chiaravalloti A, Evangelista L, et al. Predictive and prognostic value of 18F-DOPA PET/CT in patients affected by recurrent medullary carcinoma of the thyroid. Ann Nucl Med. 2018;32:7–15.
21. Chondrogiannis S, Grassetto G, Marzola MC, et al. 18F-DOPA PET/CT biodistribution consideration in 107 consecutive patients with neuroendocrine tumours. Nucl Med Commun. 2012;33:179–84.
22. Huang Z, Zuo C, Guan Y, et al. Misdiagnoses of 11C-choline combined with 18F-FDG PET imaging in brain tumours. Nucl Med Commun. 2008;29:354–8.
23. Utriainen M, Komu M, Vuorinen V, et al. Evaluation of brain tumor metabolism with [11C]choline PET and 1H-MRS. J Neurooncol. 2003;62:329–38.
24. Lapa C, Linsenmann T, Monoranu CM, et al. Comparison of the amino acid tracers 18F-FET and 18F-DOPA in high-grade glioma patients. J Nucl Med. 2014;55:1611–6.
25. Morana G, Puntoni M, Garrè ML, et al. Ability of (18)F-DOPA PET/CT and fused (18)F-DOPA PET/MRI to assess striatal involvement in paediatric glioma. Eur J Nucl Med Mol Imaging. 2016;43:1664–472.
26. Law I, Albert NL, Arbizu J, et al. Joint EANM/EANO/RANO practice guidelines/SNMMI procedure

standards for imaging of gliomas using PET with radiolabelled amino acids and [18F]FDG: version 1.0. Eur J Nucl Med Mol Imaging. 2019;6(3):540–57.
27. Tripathi M, Sharma R, Jaimini A, et al. Striatal "function-metabolism" mismatch on F-18 FDG/F-18 FDOPA PET/CT. Clin Nucl Med. 2009;34:703–5.
28. Fueger BJ, Czernin J, Cloughesy T, et al. Correlation of 6-18F-fluoro-L-dopa PET uptake with proliferation and tumor grade in newly diagnosed and recurrent gliomas. J Nucl Med. 2010;51:1532–8.
29. Kratochwil C, Combs SE, Leotta K, et al. Intra-individual comparison of ^{18}F-FET and ^{18}F-DOPA in PET imaging of recurrent brain tumors. Neuro Oncol. 2014;16:434–40.
30. Calabria F, Schillaci O. Recurrent glioma and crossed cerebellar diaschisis in a patient examined with 18F-DOPA and 18F-FDG PET/CT. Clin Nucl Med. 2012;37:878–9.
31. Fraioli F, Shankar A, Hargrave D, et al. 18F-fluoroethylcholine (18F-Cho) PET/MRI functional parameters in pediatric astrocytic brain tumors. Clin Nucl Med. 2015;40:e40–5.
32. Morrish PK, Sawle GV, Brooks DJ. An [18F]dopa-PET and clinical study of the rate of progression in Parkinson's disease. Brain. 1996;119(2):585–91.
33. Morrish PK, Rakshi JS, Bailey DL, et al. Measuring the rate of progression and estimating the preclinical period of Parkinson's disease with [18F]dopa PET. J Neurol Neurosurg Psychiatry. 1998;64:314–9.
34. Vingerhoets FJ, Snow BJ, Lee CS, et al. Longitudinal fluorodopa positron emission tomographic studies of the evolution of idiopathic parkinsonism. Ann Neurol. 1994;36:759–64.
35. Nurmi E, Ruottinen HM, Bergman J, et al. Rate of progression in Parkinson's disease: a 6-[18F]fluoro-L-dopa PET study. Mov Disord. 2001;16:608–15.
36. Braak H, Del Tredici K, Rüb U, et al. Staging of brain pathology related to sporadic Parkinson's disease. Neurobiol Aging. 2003;24:197–211.
37. Pal PK, Leung J, Hedrich K, et al. [18F]-Dopa positron emission tomography imaging in early-stage, non-parkin juvenile parkinsonism. Mov Disord. 2002;17:789–94.
38. Burn DJ, Sawle GV, Brooks DJ. Differential diagnosis of Parkinson's disease, multiple system atrophy, and Steele-Richardson-Olszewski syndrome: discriminant analysis of striatal 18F-dopa PET data. J Neurol Neurosurg Psychiatry. 1994;57:278–584.
39. Nagasawa H, Tanji H, Nomura H, et al. PET study of cerebral glucose metabolism and fluorodopa uptake in patients with corticobasal degeneration. J Neurol Sci. 1996;139:210–7.
40. Eidelberg D, Dhawan V, Moeller JR, et al. The metabolic landscape of cortico-basal ganglionic degeneration: regional asymmetries studied with positron emission tomography. J Neurol Neurosurg Psychiatry. 1991;54:856–62.
41. Sawle GV, Brooks DJ, Marsden CD, et al. Corticobasal degeneration. A unique pattern of regional cortical oxygen hypometabolism and striatal fluorodopa uptake demonstrated by positron emission tomography. Brain. 1991;114:541–6.
42. Eshuis SA, Maguire RP, Leenders KL, et al. Comparison of FP-CIT SPECT with F-DOPA PET in patients with de novo and advanced Parkinson's disease. Eur J Nucl Med Mol Imaging. 2006;33:200–9.
43. Eshuis SA, Jager PL, Maguire RP, et al. Direct comparison of FP-CIT SPECT and F-DOPA PET in patients with Parkinson's disease and healthy controls. Eur J Nucl Med Mol Imaging. 2009;36:454–62.
44. Heiss WD, Hilker R. The sensitivity of 18-fluorodopa positron emission tomography and magnetic resonance imaging in Parkinson's disease. Eur J Neurol. 2004;11:5–12.
45. Ciurleo R, Di Lorenzo G, Bramanti P, et al. Magnetic resonance spectroscopy: an in vivo molecular imaging biomarker for Parkinson's disease? Biomed Res Int. 2014;2014:519816.
46. Teune LK, Renken RJ, de Jong BM, et al. Parkinson's disease-related perfusion and glucose metabolic brain patterns identified with PCASL-MRI and FDG-PET imaging. Neuroimage Clin. 2014;3:240–4.
47. Struck AF, Hall LT, Kusmirek JE, et al. (18)F-DOPA PET with and without MRI fusion, a receiver operator characteristics comparison. Am J Nucl Med Mol Imaging. 2012;2:475–82.
48. Chondrogiannis S, Marzola MC, Al-Nahhas A, et al. Normal biodistribution pattern and physiologic variants of 18F-DOPA PET imaging. Nucl Med Commun. 2013;34:1141–9.
49. Balan KK. Visualization of the gall bladder on F-18 FDOPA PET imaging: a potential pitfall. Clin Nucl Med. 2005;30:23–4.
50. Okada M, Shimono T, Komeya Y, et al. Adrenal masses: the value of additional fluorodeoxyglucose-positron emission tomography/computed tomography (FDG-PET/CT) in differentiating between benign and malignant lesions. Ann Nucl Med. 2009;23:349–54.
51. Hernández Pinzón J, Mena D, Aguilar M, et al. Radionecrosis versus disease progression in brain metastasis. Value of (18)F-DOPA PET/CT/MRI. Rev Esp Med Nucl Imagen Mol. 2016;35:332–5.
52. Calabria FF, Chiaravalloti A, Calabria EN, et al. 18F-DOPA PET/CT and MRI findings in a patient with multiple meningiomas. Clin Nucl Med. 2016;41:636–7.
53. Sala Q, Metellus P, Taieb D, et al. 18F-DOPA, a clinically available PET tracer to study brain inflammation? Clin Nucl Med. 2014;39:e283–5.

3 Lipogenesis Pathway: Radiolabeled Choline

Ferdinando Calabria, Marzia Colandrea, Giuseppe L. Cascini, and Orazio Schillaci

Contents

Authors declare they have obtained permission for any previously published material used in their chapter.

F. Calabria (✉)
Department of Nuclear Medicine and Theranostics, "Mariano Santo" Hospital, Cosenza, Italy
e-mail: ferdinandocalabria@hotmail.it

M. Colandrea
Division of Nuclear Medicine, European Institute of Oncology, Milan, Italy

G. L. Cascini
Nuclear Medicine Unit, Department of Diagnostic Imaging, Magna Graecia University, Catanzaro, Italy

O. Schillaci
Department of Biomedicine and Prevention, University "Tor Vergata", Rome, Italy

Department of Nuclear Medicine and Molecular Imaging, IRCCS Neuromed, Pozzilli, IS, Italy

F. Calabria, O. Schillaci (eds.), *Radiopharmaceuticals*,
https://doi.org/10.1007/978-3-030-27779-6_3

Abbreviations

^{18}F-DOPA	18F-Diidrossiphenil-alanine
^{18}F-FDG	^{18}F-Fluorodeoxyglucose
^{18}F-FECH	^{18}F-Ethylcholine
^{18}F-FET	18F-Fluoroethyltirosine
^{18}F-FLT	18F-Fluorothymidine
^{18}F-FMC	^{18}F-Methylcholine
^{68}Ga-PSMA	^{68}Ga-Prostate-specific membrane antigen
ADC	Apparent diffusion coefficient
FDA	Food and Drug Administration
MRI	Magnetic resonance imaging
MRS	Magnetic resonance spectroscopy
PSA	Prostate-specific antigen
SPECT	Single photon emission tomography/computed tomography
SUVmax	Maximum standardized uptake value

3.1 Synthesis

The choline can be labeled with ^{11}C, in those PET centers provided by a cyclotron, or with ^{18}F, with a longer half time decay, allowing a better availability during the time of PET/CT scan.

The carbon is a ubiquitous element in a large series of molecules; consequently, ^{11}C can be considered useful to label radiopharmaceuticals since it does not change their chemical structures. The short half time decay (20 min) of ^{11}C is strongly attractive for PET imaging in order to reduce the dosimetry exposure. For this reason, the ^{11}C-choline was the first radiolabeled choline proposed and approved by the United States *Food and Drug Administration* (FDA) in 2012 [1].

Generally, the synthesis of ^{11}C-choline begins with the reaction of ^{11}C-methylation with ^{11}C-CH3I and 11C-CH3OTf. The choice of methodology is still yet not standardized [2] and, considering the short half time decay, the production process of this tracer should be as fast as possible to reduce the loss of radioactivity during the time.

Conversely, the fluorinated kinds of choline, ^{18}F-methylcholine (^{18}F-FMC) and ^{18}F-ethylcholine (^{18}F-FECH) could be obtained by different synthesis protocols. The ^{18}F-FECH is the first example of fluorinated choline. Authors from Japan suggested a synthesis protocol for ^{18}F-FECH, in which as first, tetrabutylammonium-^{18}F-fluoride was reacted with 1,2-bis(tosyloxy)ethane to yield 2-^{18}F-fluoroethyltosylate and, subsequently, the obtained 2-^{18}F-fluoroethyltosylate was reacted with N-dimethyl-ethanolamine to reach ^{18}F-FEC, which was then purified by chromatograph for final human use [3]. More recently, in Germany it has been developed a new synthesis method, allowing a purity of the ^{18}F-FECH of 95% [4]. Similarly, a radiochemical purity of 98% for ^{18}F-FMC can be obtained, in a synthesis time of 40 min, where the radiochemical yield was determined primarily by the yield of the intermediate synthon, 4′-[(2-^{18}F-fluoroethyl)(methyl)amino]-4-phenyl-3-buten-2-malonitrile [5].

3.2 Pharmacokinetics

Choline metabolism plays a significant role in tumor imaging because the choline is an amino acid, precursor of phosphatidyl-choline, an important element of the lipid bilayer structure of cellular wall. Several tumors show a high rate of cell membrane synthesis due to increased proliferation; attempts were made to synthesize a choline analogue labeled with a radioactive nuclide as imaging agent for tumor detection and localization. In particular, the choline, labeled with ^{11}C or ^{18}F, can be a useful tracer especially for those neoplastic tissues not showing high rate of glucose metabolism, not detectable with ^{18}F-fluorodeoxyglucose (^{18}F-FDG).

Biosynthesis of the cell membrane is very fast in tumor tissues, and the upregulation of choline kinase enzyme, particularly increased in prostate cancer cells, induces an in vivo higher uptake of choline.

The mechanisms of choline transport in tumor cells have been elucidated and described using first ^{3}H-choline and ^{14}C-choline. When the amount of choline is increased in tumor cells, it incorporates into the cells by an active-transport

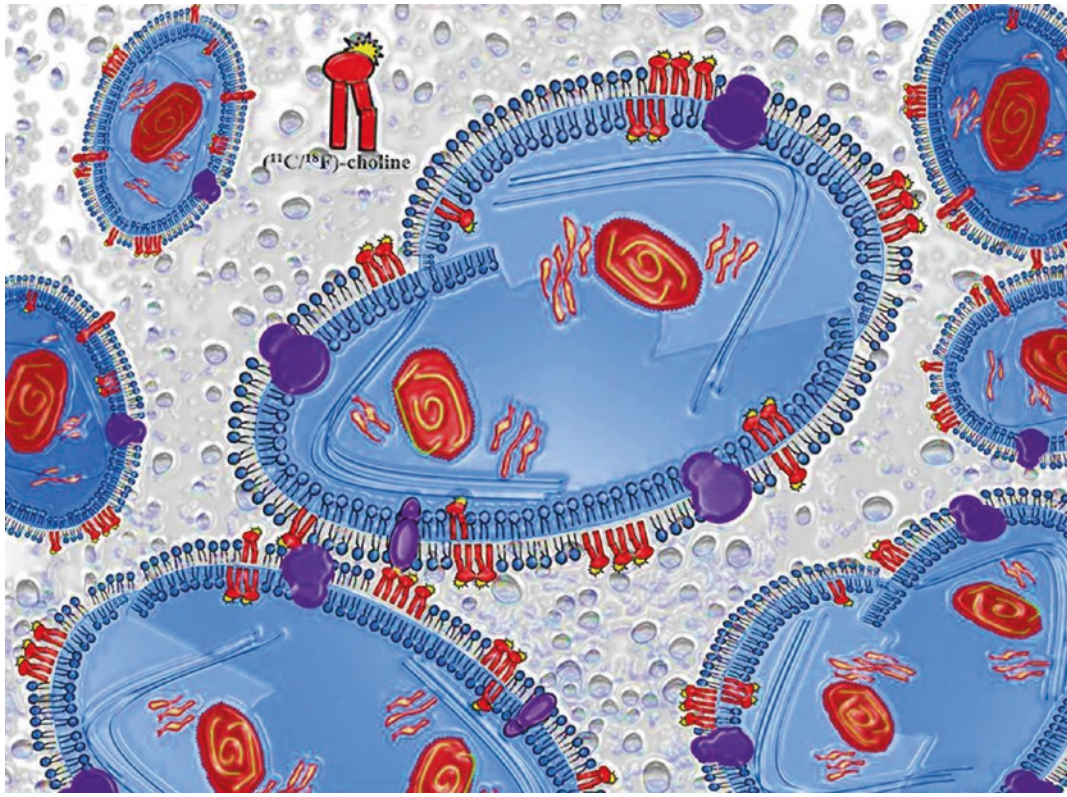

Fig. 3.1 The (^{11}C/^{18}F)-choline follows, in vivo, the metabolic pathway of lipogenesis and cell membrane synthesis. Consequently, the tracer is enhanced in cells with high rate of mitosis

mechanism, and then converted into phosphorylcholine within 1 h; finally, it transforms into phosphatidylcholine [6] as a part of the cellular wall (Fig. 3.1). The process of choline metabolism is dynamic and balanced by influx and efflux of choline in the cells. On a theoretical basis, a diet avoid of food containing high levels of choline (*asparagus, beans, soya, carrots, egg yolk, lamb, pig and calf liver, skimmed milk, peanuts, peanut butter, peas, spinach, turnip*) should be recommended for patients, in the days preceding the PET/CT scan [7].

Therefore, tracking the in vivo molecular pathway of radiolabeled choline could help in depicting cells with high mitosis and, consequently, high rates of lipogenesis and synthesis of cell membrane, as documented for prostate cancer [8], bronchioloalveolar carcinoma [9], and urothelial carcinoma [10].

3.3 Physiological Distribution

The physiological distribution is similar for all three kinds of tracer, beyond few differences as the prevalent renal excretion of ^{18}F-FMC and ^{18}F-FECH and the prevalent hepatic metabolism of ^{11}C-choline. In particular, a faster urinary excretion is documented for ^{18}F-FECH: some authors have hypothesized the routine administration of furosemide prior to the exam, to reduce the urinary activity in order to better evaluate the pelvis [11]. On the other hand, the relatively higher uptake of ^{11}C-choline in the liver could lead a misdiagnosis of rare hepatic metastases from prostate cancer or the detection of hepatocellular carcinoma [12]. Furthermore, whereas the urinary excretion of ^{18}F-FMC and ^{18}F-FECH seems to exceed that of ^{11}C-choline, the latter tracer also shows early, intense uptake in the

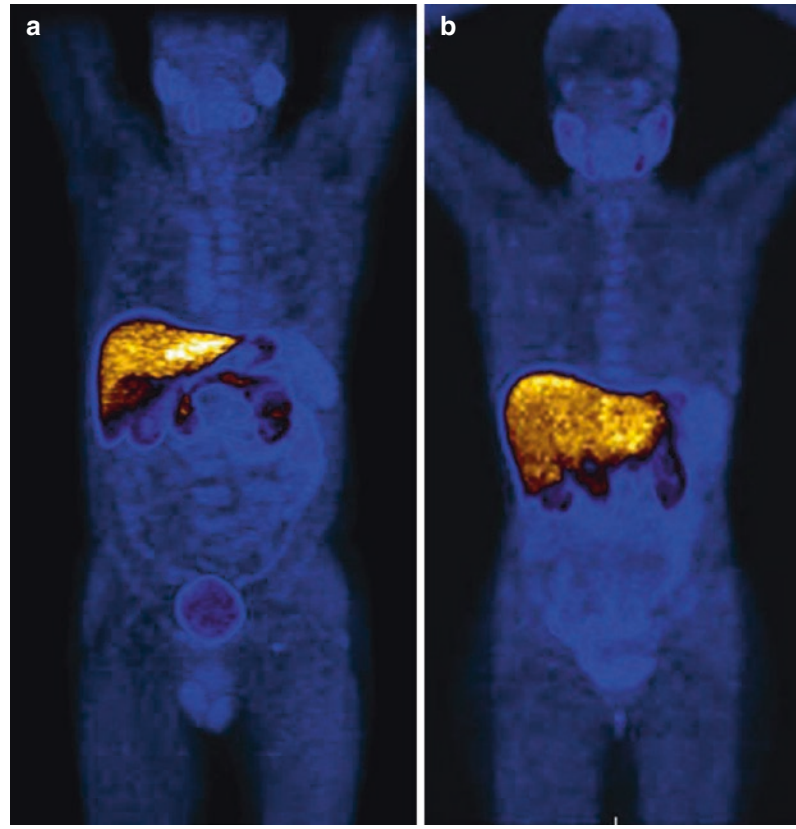

Fig. 3.2 Whole body ^{18}F-FMC PET maximum intensity projections, respectively, in male (**a**) and female (**b**) patients, showing the tracer physiological distribution in the human body. Liver, pancreas, spleen, ureters and kidneys, exocrine glands and bone marrow are the sites of higher, physiological tracer uptake. The uptake in the brain is negligible, with the exception of the pineal gland and choroid plexus

bowel, which may also interfere with the visualization of the abdomen.

All these variants of radiolabeled choline are enhanced and metabolized in cells with high lipogenesis. The physiological distribution generally regards kidneys, liver, spleen, bone marrow and all exocrine glands such as salivary and lacrimal glands and testicles [13]. A common element of the choline in vivo distribution is the high rate of uptake in liver, pancreas, and salivary glands, perhaps due to the common embryologic origin of these organs [14] (Fig. 3.2).

For all variants of labeled choline, it could be difficult to detect neoplastic lesions in the pancreas, showing high gradient of physiological uptake.

Interestingly, the uptake of radiolabeled choline in the brain is usually negligible, with the exception of the pineal gland [13] and the choroid plexus [15]. This could justify its possible role in brain tumor imaging.

3.4 Clinical Indications

3.4.1 Prostate Cancer

Prostate cancer is a malignant neoplasm that cannot be adequately investigated by ^{18}F-FDG PET/CT because of the low-grade glucose metabolism expressed. Since first years of this century, preliminary studies demonstrated ^{18}F-FMC and ^{18}F-FECH as nontoxic, useful oncologic probes for metabolic characterization of prostate cancer and brain tumors [8]. However, the evidence of elevated levels of endogenous choline in prostate cancer cells was previously provided by MRS.

During the staging of prostate cancer it has been emerged that, being a non-tumor-specific tracer, the radiolabeled choline can be enhanced in primary tumors (Fig. 3.3) rather than conditions of prostatitis and benign prostate hyperplasia [16]. For these reasons, this tracer seems to

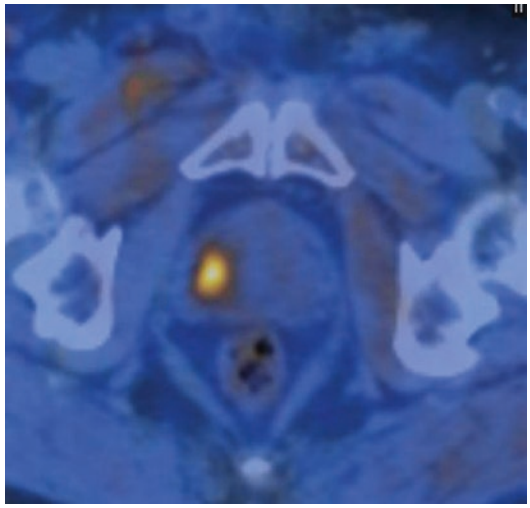

Fig. 3.3 In a patient examined for early staging of prostate cancer Gleason 7 (4 + 3), with PSA 12 ng/mL, axial PET/CT detail shows focal, pathologic uptake in the right prostate lobe, corresponding to the primary tumor

play a limited role in the characterization of the primitive tumor, even considering the low resolution limit of PET/CT scanners, not allowing a meaningful characterization of small prostatic nodes. Moreover, the rise of PSA serum levels during the early staging can be partially related to other concurrent benign conditions, which can affect its reliability in selecting patients for prostate biopsy or further diagnostic protocols.

Some studies have described the potential role of radiolabeled choline PET/CT in the detection of secondary localizations of prostate cancer in lymph nodes [17] but, globally, the detection rate of radiolabeled choline PET/CT in identifying secondary metastases of prostate cancer is significant only in patients with high-to-intermediate risk and high PSA serum levels [18].

On the other hand, the radiolabeled choline PET/CT is a very useful diagnostic tool in restaging prostate cancer after therapy, in patients with high Gleason score. After radical prostatectomy for curative intent, the detection of serum PSA using standard immunoassays is considered indicative of residual prostatic tissue, presumably representing loco-regional or systemic cancer. Therefore, in this clinical setting, the PSA can be considered a marker of biochemical relapse or disease progression. Sensitivity and specificity of radiolabeled choline PET/CT are considerably improved in this setting. Numerous studies have demonstrated an important diagnostic accuracy of radiolabeled choline PET/CT in detecting local relapse of prostate cancer, even with the help of further dynamic scans of the pelvis, performed during the tracer administration, in order to avoid the urinary radioactivity in the evaluation of the prostatic bed [19, 20].

Being a rapid whole body scan, PET/CT with radiolabeled choline is a powerful diagnostic tool for the diagnosis of lymph node and bone metastases of prostate cancer after radical prostatectomy [21] or radiotherapy [22]. Naturally, the exam is usually performed when a condition of biochemical relapse is diagnosed by laboratory data. Following the current guidelines, biochemical relapse is diagnosed when PSA is higher than 0.2 ng/mL in patients after radical prostatectomy and 1.5 ng/mL after radiotherapy [23].

Sensitivity and specificity of radiolabeled choline PET/CT in detecting metastases of prostate cancer after radical prostatectomy range from 64% to 100% and from 57% to 99%, respectively; similar data are reported for ^{11}C-choline, ^{18}F-FMC, and ^{18}F-FECH [7]. However, in patients submitted to surgical intervention of radical prostatectomy, the detection rate of radiolabeled choline PET/CT is linked to the PSA values. Several studies demonstrated a strict relationship between the PSA at the time of the scan and the diagnosis of metastases by PET/CT: generally, PET/CT with radiolabeled choline is more useful in identifying tumor relapse when PSA serum level is higher than 1–2 ng/mL [23–26] while the global diagnostic accuracy is more trusty when *PSA doubling time* is lower than 6 months [24, 27] and *PSA velocity* is more rapid than 1 ng/mL/year [27, 28]. In fact, these two PSA kinetics values are indicative of the overall aggressiveness of the disease and its progression during the time. Two absolute consecutive PSA values are necessary to calculate these parameters: the *PSA doubling time*, expressed in months, is found to be a reliable tool to distin-

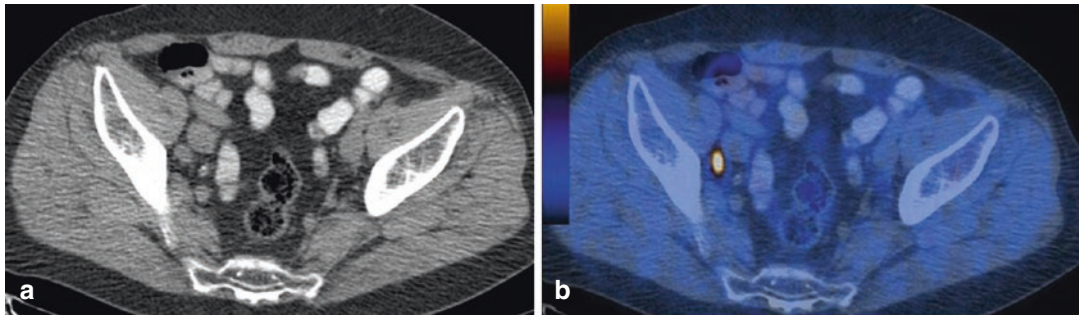

Fig. 3.4 Axial CT (**a**) and PET/CT (**b**) views of a whole body ^{18}F-FMC scan performed for biochemical relapse (PSA 1.1 ng/mL), in a patient previously submitted to radical prostatectomy for prostate cancer. A focal area of uptake is evident in a 1-cm-wide right iliac lymph node, without morphological characteristics of malignancy at the CT component of the exam. Anyway, in this patient, the oral contrast agent administration, prior to the exam, allowed to better discriminate the lymph node from intestinal loops

guish which patients have prolonged innocuous PSA levels after therapy from those who are at great risk for prostate cancer relapse and is defined as the duration for PSA levels in the blood to increase by 100 percent; the *PSA velocity*, expressed in ng/mL/year, is determined as linear regression of the PSA values over time [23, 29].

However, in our opinion, the best added value of radiolabeled choline PET/CT, in comparison to conventional imaging (bone scan, CT and MRI and ^{18}F-FDG PET/CT) [30], is due to its capability in early detection of oligo-metastatic patients, allowing clinicians to plan more rapidly the best treatment approach (Fig. 3.4). Consequently, the radiolabeled choline PET/CT is also an accurate whole body exam to evaluate response to therapy [31].

On the other hand, in patients undergoing antiandrogenic therapy for secondary bone metastases of prostate cancer, PET/CT with radiolabeled choline cannot replace the bone scan or CT [32] due to the effects of therapy on skeletal sclerotic lesions, which can interfere with choline uptake. In fact, as sclerotic changes are the most dominant morphological pattern in bone metastases of prostate cancer, probably because of the proliferation of osteoblasts and apoptosis of osteoclasts induced by PSA, it is possible to find some sclerotic lesions that are non-choline avid (Fig. 3.5) [24]. In this selected cases, an alternative tracer could be the ^{18}F-NaF (see also Chap. 5) [33].

Recently, novel PET radiopharmaceuticals have been developed to investigate prostate cancer patients in biochemical relapse after therapy: *Prostate-Specific Membrane Antigen* (PSMA), labeled with ^{68}Ga (see also Chap. 12), is becoming a valid alternative to radiolabeled choline. Several papers demonstrated good diagnostic accuracy of ^{68}Ga-PSMA in identification of oligo-metastatic patients during early phase of biochemical relapse. ^{68}Ga- PSMA PET/CT is effective for imaging disease in the prostate, lymph nodes, soft tissue, and bone in a single session scan [34]. There is emerging evidence for its clinical value in staging of high-risk primary prostate cancer [35, 36] and localization of distant metastases [37] or local recurrence [38], in biochemical relapse. The high sensitivity provided by PSMA PET/CT, with frequent identification of small-volume disease, is redefining patterns of disease spread; some studies are showing a better diagnostic accuracy of ^{68}Ga-PSMA PET/CT, rather than radiolabeled choline PET/CT, in detection of lymph nodes or bone metastases, especially in very early phase of biochemical relapse of prostate cancer [39].

Similar results are emerging for PET/CT studies with PSMA labeled with ^{64}Cu [40, 41] or ^{18}F [42]. These nuclides could provide, respectively, a better power resolution imaging and possibility of late scans, due to characteristics of ^{64}Cu, or larger availability and standardization imaging, due to the widespread distribution of ^{18}F.

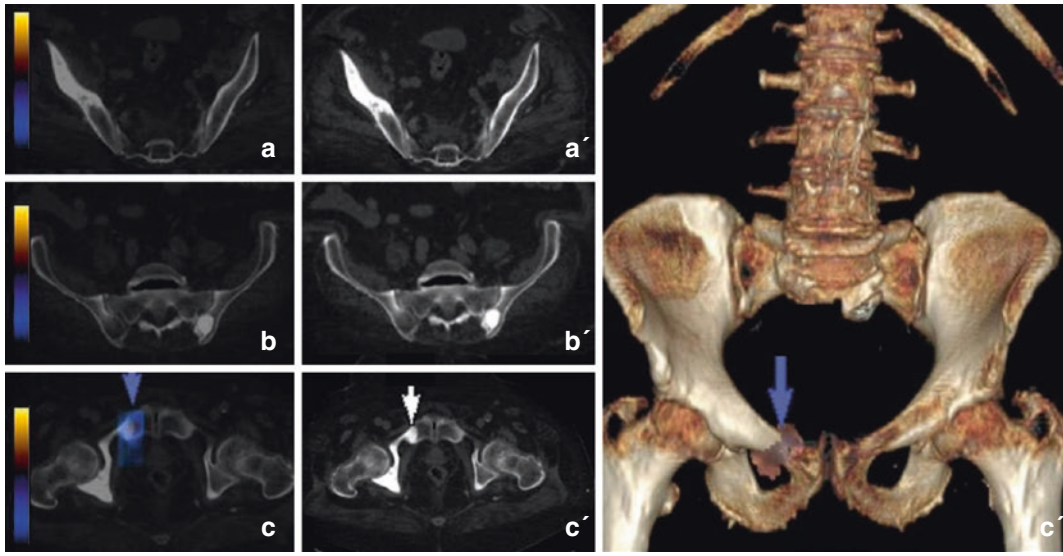

Fig. 3.5 Axial PET/CT views showing sclerotic lesions of the pelvis without significant ^{18}F-FMC uptake (**a**, **a'**, **b**, **b'**), in a patient with prostate cancer undergoing hormonal therapy (PSA 33 ng/mL at the time of the scan). Only a lesion in the right pubic bone displays residual tracer uptake in axial PET/CT views (arrow, **c**, **c'**) and in coronal 3D CT volume rendering fused with coronal 3D PET volume rendering (arrow, **c''**)

However, despite the term "*prostate specific*," PSMA is also expressed in normal tissues and in benign and malignant processes. As well as for other tracers in prostate cancer imaging, some studies well described a lack of specificity of PSMA, due to the possibility of uptake in Paget's disease, renal cell cancer, neuroendocrine tumors [43], and meningioma [44, 45].

3.4.2 Malignancies with High Lipogenesis Rate

Due to the intrinsic molecular properties, is currently under study the feasibility of radiolabeled choline PET/CT in the management of malignant tumors other than prostate cancer, characterized by high synthesis of cell membrane.

The bronchioloalveolar carcinoma is a tumor with malignant behavior and low metabolic uptake of ^{18}F-FDG. In the early stage of this disease, in some patients ^{18}F-FMC PET/CT allowed to detect primary pulmonary lesions with good accuracy, in comparison to ^{18}F-FDG PET/CT [9].

Preliminary studies also support the usefulness of radiolabeled choline PET/CT in detecting hepatocellular carcinoma with a better accuracy than ^{18}F-FDG PET/CT, especially in well to moderately differentiated lesions [46]. The liver is an organ with high physiological uptake gradient of choline: for this reason, other authors hypothesized the potential role of the semiquantitative assessment of radiolabeled choline SUVmax in the differential diagnosis between hepatocellular carcinoma and the condition of hepatic focal nodular hyperplasia [47].

Few other studies proposed a possible role of ^{11}C-choline PET/CT in depicting lytic, non ^{18}F-FDG-avid lesions of multiple myeloma [48].

Due to the incidental evidence of radiolabeled choline uptake in male breast cancer, in populations of prostate cancer patients [49, 50], some preclinical [51] and clinical [52] studies are describing a potential usefulness of ^{18}F-FMC PET/CT in management of female breast cancer.

However, all cited studies are linked to preliminary results and the possible applications of radiolabeled choline PET/CT, in malignancies other than prostate cancer, need to be considered under investigation.

Similarly, limited experience exists about the role of radiolabeled choline PET/CT in patients with head and neck malignant tumors and bladder cancer [10, 53].

3.4.3 Neuro-oncological Imaging

Beyond the undisputed role of ^{18}F-FDG in the management of a large amount of malignant tumors, this tracer presents a high rate of physiological distribution in the normal structures of the brain, not allowing its use in imaging brain tumors. As above reported, the radiolabeled choline offers a very low distribution in the normal structures of white and grey matter, suggesting a role as tracer of brain tumor vitality. Uptake of ^{11}C-choline and ^{18}F-FMC is reported as incidental finding in meningiomas and gliomas during a whole body examination for prostate cancer [13, 54]. Subsequently, various group of authors tried to depict brain tumors with the help of radiolabeled choline PET/CT. In fact, primary brain tumors and metastases of somatic cancer present a high rate of synthesis of cellular wall and, therefore, high uptake of radiolabeled choline. Numerous papers support the usefulness of (^{11}C/^{18}F) radiolabeled choline PET/CT in the diagnosis of primary brain tumors [55] and brain metastases [56] with accuracy superior to ^{18}F-FDG PET/CT [57, 58] and similar to other PET tracers, the ^{11}C-Methionine [59] and the ^{18}F-FET [60] (see Chaps. 4 and 11).

An interesting study supports the usefulness of ^{11}C-methionine and ^{11}C-choline PET/CT in distinguishing glioma relapse from radiation necrosis after radiotherapy, showing a good diagnostic accuracy of both tracers, better than ^{18}F-FDG PET/CT [61].

However, caution is needed when observing abnormal radiolabeled choline uptake in the brain, especially in the early characterization of brain lesions, due to the possibility of choline uptake in demyelinating foci [62] and vascular brain lesions [63]. Correlative imaging of the brain with MRI, with or without co-registration, is of the utmost importance.

3.4.4 Functional Imaging

From the evidence that parathyroid adenoma can show ^{11}C-choline uptake [64], the attempts of researchers have been largely investigated the usefulness of the radiolabeled choline PET/CT in order to diagnose parathyroid adenomas [65]. In patients with secondary and primary hyperparathyroidism, the accurate localization of hyperfunctioning parathyroid glands is critical to plan the correct surgical intervention. In particular, ^{18}F-FMC choline PET/CT is able in identifying the parathyroid adenoma as well as ^{123}I/^{99m}Tc-sestaMIBI SPECT and both are superior to conventional ultrasound [66]. For other authors, PET/CT with ^{18}F-FMC is superior to ^{99m}Tc-sestaMIBI SPECT/CT, ^{99m}Tc-sestaMIBI/pertechnetate subtraction imaging, and ^{99m}Tc-sestaMIBI dual-phase imaging, due to the better PET power resolution and the large availability of hybrid PET/CT scanners rather than hybrid SPECT/CT scanners [67]. Radiolabeled choline PET/CT should be considered as a new imaging modality for localizing parathyroid adenomas and enabling minimal invasive parathyroidectomy when conventional imaging fails.

Other applications of radiolabeled choline PET/CT in non-oncological field are linked to the property of the tracer to be enhanced in inflammation and benign tumors [13]. Therefore, some further field of interest of these diagnostic tools is under study. Limited experiences report its possible role in depicting pulmonary granulomatous diseases as active sarcoidosis [68] and tuberculosis [69].

3.4.5 PET/MRI

One of the potential main fields of application of hybrid PET/MRI should be prostate cancer imaging. In fact, the hybrid simultaneous functional and anatomical evaluation of prostate cancer patients can depict in a single, whole body imaging step the primary lesions and assess the presence and extension of lymph node (Fig. 3.6) and bone metastases, combining the high spatial resolution of MRI on prostate gland and the high sensitivity of radiolabeled choline PET in detecting secondary lymph node and bone localizations [70]. Probably, in the future, this diagnostic tool will replace several diagnostic procedures actually employed in prostate cancer imaging, as bone scan, contrast enhanced CT, MRI, PET/CT, and trans-rectal-ultrasonography [71].

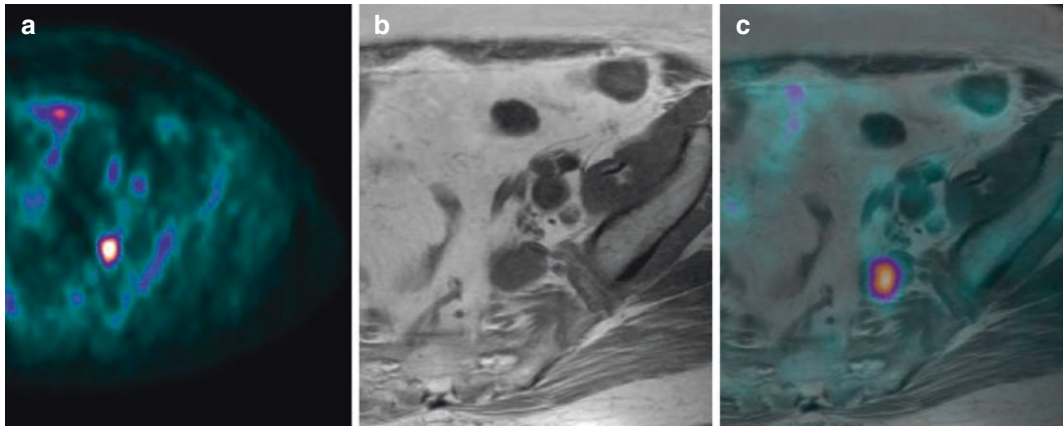

Fig. 3.6 Axial PET (**a**), T1-weighted MRI (**b**), and PET/MRI (**c**) views showing focal, pathologic ^{18}F-FMC uptake in a left iliac lymph node, 2 cm wide

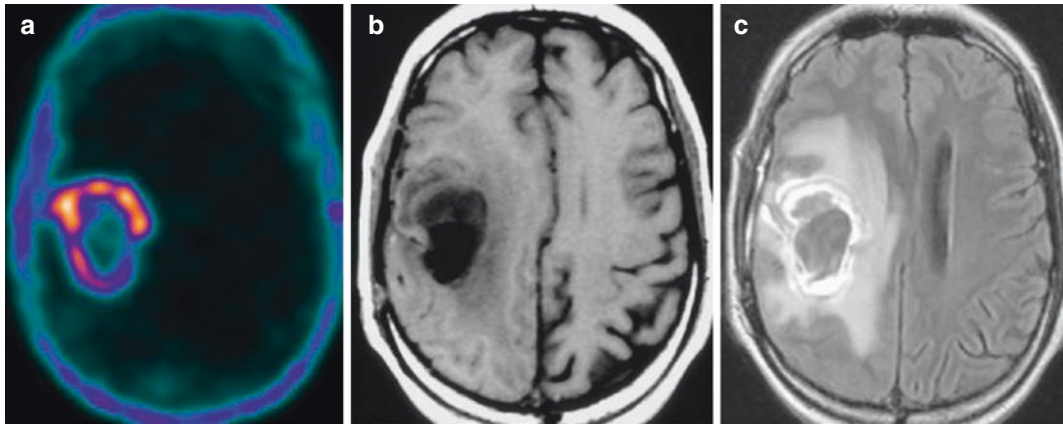

Fig. 3.7 A 64-year-old patient undergone surgical excision of a right frontotemporal glioblastoma. One year after, the PET/MRI showed diffused ^{18}F-FMC uptake along the margins of the postsurgical hypointense lacunar area, as showed in axial PET (**a**) and T1-weighted MRI (**b**) views. Intense gadolinium enhancement was also observed in the site of ^{18}F-FMC uptake, with surrounding edema in post-contrast FLAIR axial view (**c**). Histological exam diagnosed glioblastoma relapse

Regarding the semiquantitative analysis potentially provided by the calculation of SUVmax and ADC in hybrid PET/MRI scanners, literature data on a population with primary prostate cancer suggest a feasible role of SUVmax in depicting tracer uptake in bone metastases, while the contemporary evaluation of the apparent diffusion coefficient (ADC), provided by MRI, also can help in discriminating benign and malignant bone lesions. Anyway, no significant correlation between these two parameters is actually demonstrated [70].

Some authors also support the usefulness of bimodal radiolabeled choline PET/MRI fusion in depicting the early stage of biochemical relapse of prostate cancer after radiation therapy or radical prostatectomy, since combined imaging allows all morphological, functional, and metabolic information, thereby overcoming the limitations of each separate scan [71].

Starting by the experience with radiolabeled choline PET/CT in management of brain tumors [17], some authors support the usefulness of choline PET/MRI in the diagnosis of primary brain tumors. A potential use of this diagnostic tool could be the differential diagnosis between radiation necrosis and brain tumors relapse [15] (Fig. 3.7).

Anyway, few data are actually available on this topic, being limited to the experience of few groups, while the use of radiolabeled choline on this field is actually limited by the contemporary use of other radiopharmaceuticals as ^{18}F-FET (see also Chap. 4), ^{18}F-DOPA (see also Chap. 2), ^{11}C-Methionine (see also Chap. 11), and ^{18}F-FLT in the management of patients with brain tumors, all showing similar diagnostic accuracy [61, 72, 73].

3.5 Clinical Cases

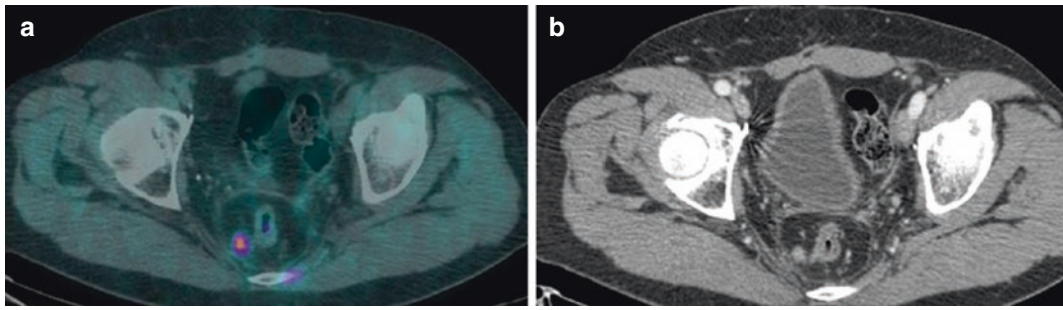

Fig. 3.8 In a patient undergoing ^{18}F-FMC PET/CT for biochemical relapse of prostate cancer (PSA 0.9 ng/mL at the time of the scan), following 2 years the radical prostatectomy, axial PET/CT view (**a**) shows focal, pathologic tracer uptake in a sub-centimeter lymph node, without meaningful contrast enhancement in the CT with iodinated contrast agent (**b**). As evident, in the CT view after contrast administration, the bladder presents a different volume

Fig. 3.9 A patient with ataxia and headache was examined by ^{18}F-FMC whole body PET/CT (**a**, PET maximum intensity projection) for increasing PSA serum levels (2.4 ng/mL at the time of the scan), 1 year after radiotherapy on the prostate gland, due to prostate carcinoma Gleason 9 (5 + 4). Focal tracer uptake was detected in the right cerebellar hemisphere, as evident in PET (**b**), PET/CT (**c**), and CT (**d**) axial details. A suspicion of rare brain prostate cancer metastasis was done. Neurological symptoms partially resolved after antiandrogenic treatment. The inclusion of the whole skull in the acquisition protocol should be considered to exclude rare brain metastases or secondary bony localizations in the skull

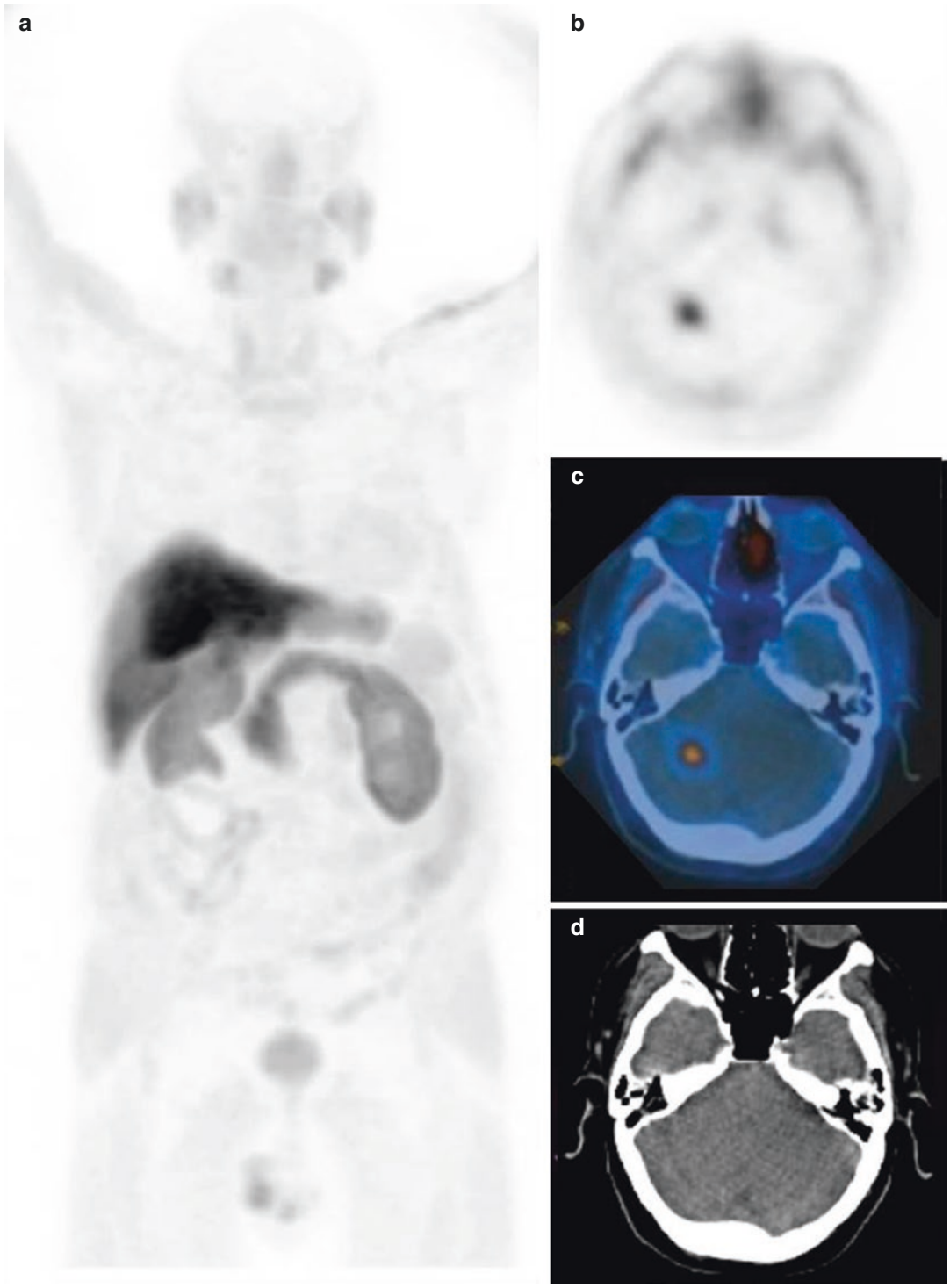
a
b
c
d

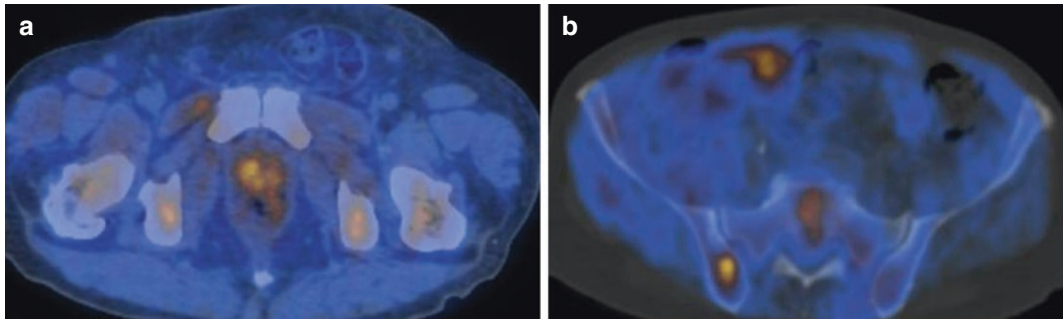

Fig. 3.10 In a patient examined for staging prostate cancer Gleason 8 (5 + 3), axial ^{18}F-FMC PET/CT views show pathologic tracer uptake in the right lobe of prostate gland (**a**) and a secondary localization in right ileum (**b**). PSA at the time of the scan was 22 ng/mL

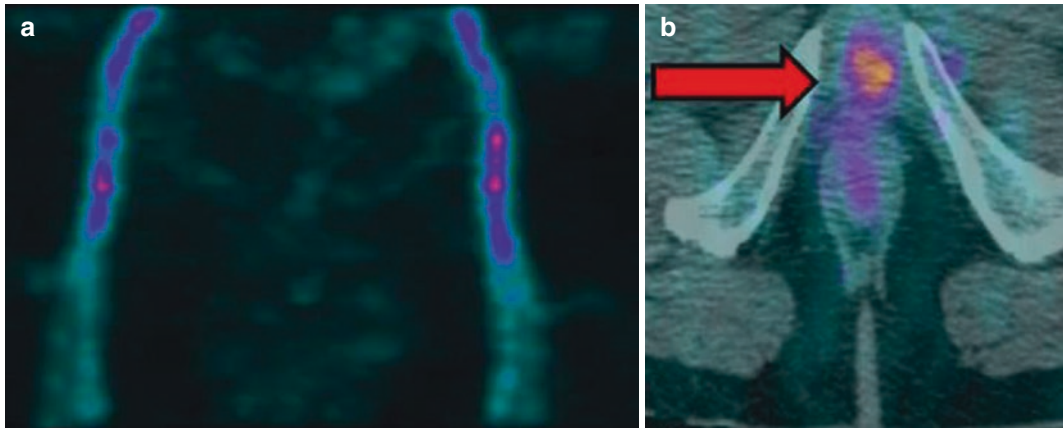

Fig. 3.11 The early dynamic ^{18}F-FMC PET/CT of the pelvis can help nuclear medicine physicians in detecting local relapse, by avoiding the interference with bladder physiologic radioactivity in the late, standard whole body imaging. The patient was examined for biochemical relapse of prostate cancer (PSA 0.6 ng/mL at the time of the scan), 16 months after radical prostatectomy. The dynamic PET scan (**a**) shows the tracer vascular phase in the iliac arteries, few seconds following the injection. The axial PET/CT detail of the pelvis (**b**) shows focal uptake in the prostatic bed, suspicious for local relapse (*red arrow*). Histological exam confirmed the diagnosis

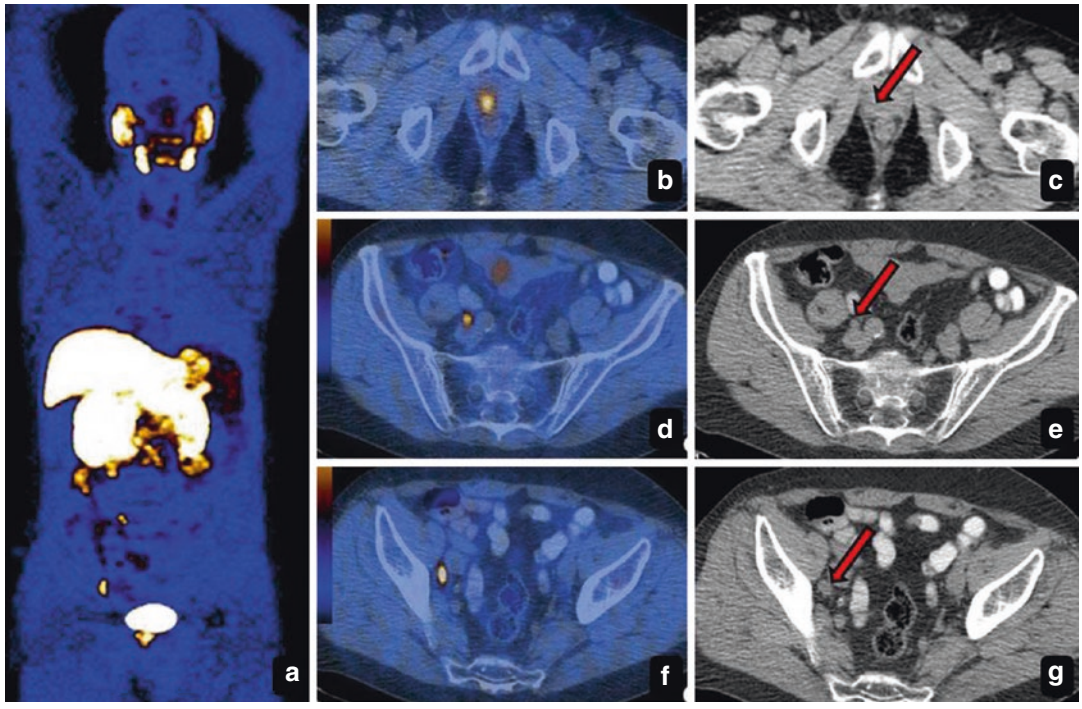

Fig. 3.12 High-risk prostate cancer patients can be examined during the early staging of disease, especially when absolute PSA values are considerably high. This patient was examined for prostate cancer Gleason 9 (5 + 4) and high PSA serum level (26 ng/mL). PET maximum intensity projection (**a**) shows focal uptake in the prostate gland and further areas in the pelvis. PET/CT axial views confirm three area of pathologic uptake, respectively, in the right prostate lobe (**b**) and in two right iliac lymph nodes (**d**, **f**). These findings are displayed by red arrows in corresponding axial CT views (**c**, **e**, **g**)

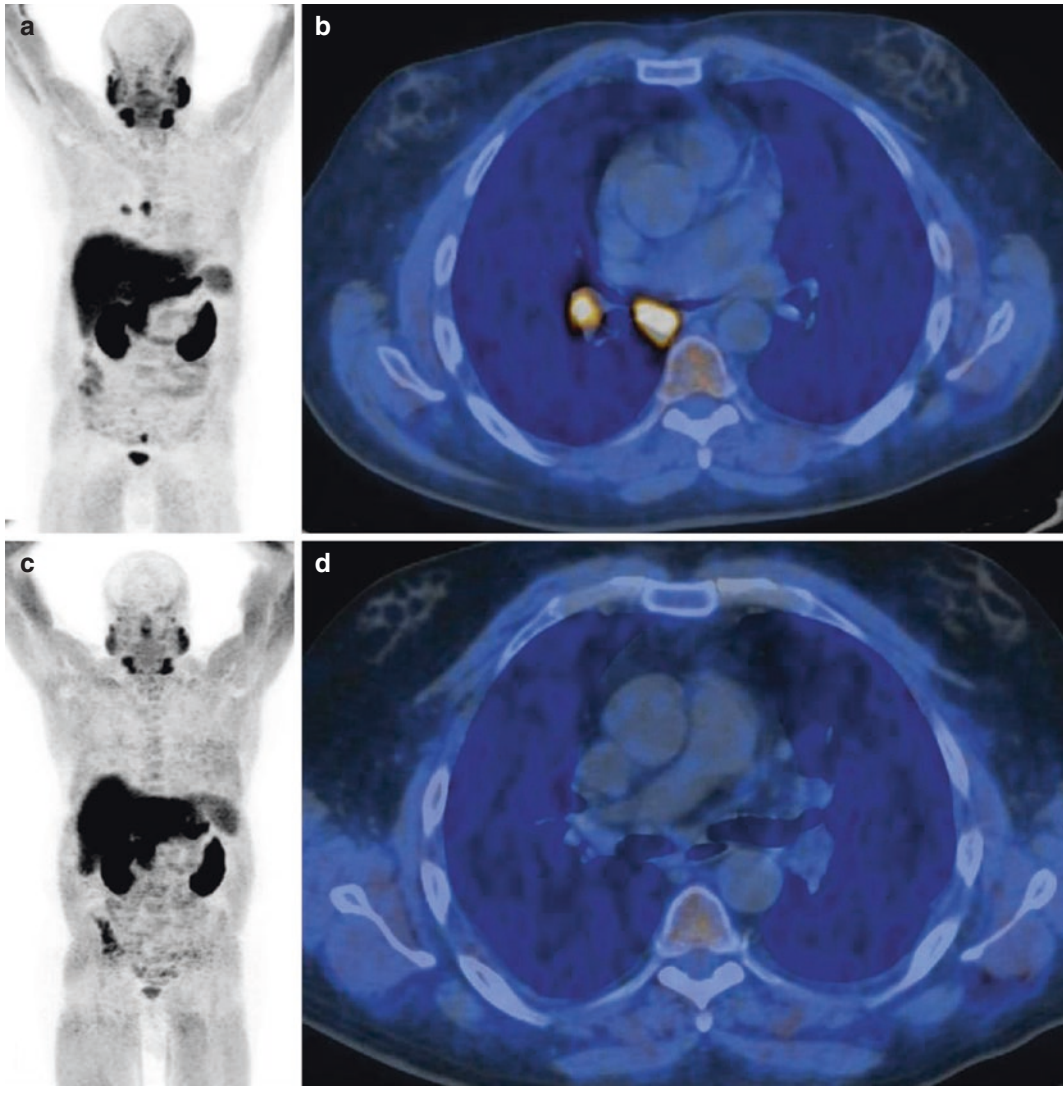

Fig. 3.13 Radiolabeled choline PET/CT can be useful in monitoring the response to therapy. Maximum intensity projection of ^{18}F-FMC PET/CT (**a**) shows intense pathologic tracer uptake in two mediastinal lymphadenopathies, respectively, in right hilar pulmonary region and sub-carinal region, as evident in axial PET/CT view (**b**). PSA value at the time of the scan was 6.5 ng/mL. The antiandrogenic treatment was started by clinicians and a further PET/CT was done: no areas of pathologic tracer uptake are visible in the maximum intensity projection of the second ^{18}F-FMC PET/CT (**c**): moreover, axial PET/CT view (**d**) shows significant volume reduction of the two metastatic lymph nodes. PSA value was considerably reduced at the time of the second PET/CT scan (0.8 ng/mL). PSA values can improve confidence in diagnosis

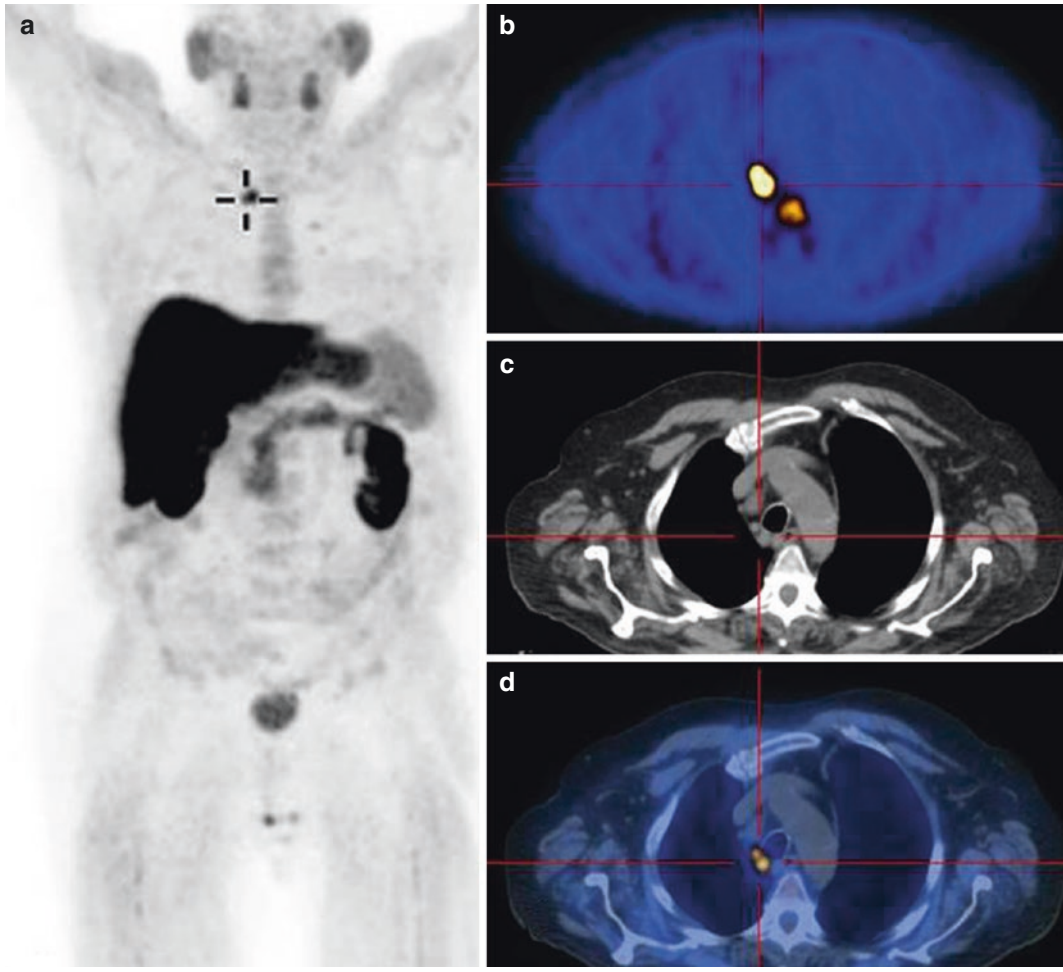

Fig. 3.14 A patient examined for restaging prostate cancer 1 year after radical prostatectomy. PSA value at the time of the scan was 2.5 ng/mL. ^{18}F-FMC PET maximum intensity projection (**a**) and axial PET view (**b**) show focal uptake in the upper mediastinum, corresponding to two sub-centimeter para-tracheal lymph nodes in related CT (**c**) and PET/CT (**d**) views

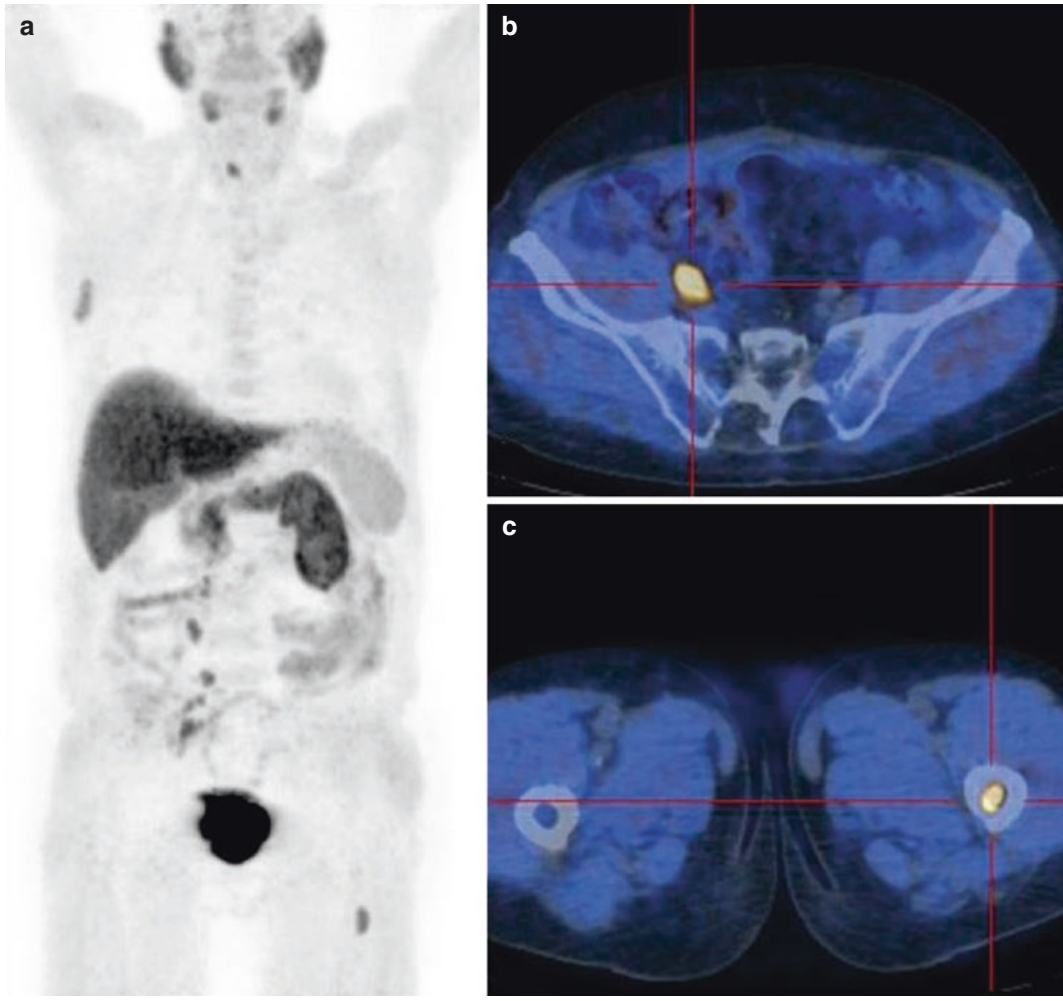

Fig. 3.15 A patient was submitted to radical prostatectomy for prostate cancer Gleason 8 (5 + 3). Subsequently, radiotherapy on the prostatic bed was also administered due to early biochemical relapse. At the time of the ^{18}F-FMC PET/CT scan, PSA was rapidly rising (PSA 16 ng/mL; PSA*dt* 4 months; PSA*ve* 1.5 ng/mL/year). The PET maximum intensity projection (**a**) shows several areas of pathologic uptake in the abdomen, in the right scapula, and in the contralateral femur. Axial PET/CT views (**b**, **c**) confirm a pathologic lymphadenopathy in the right iliac region and in the left femoral diaphysis

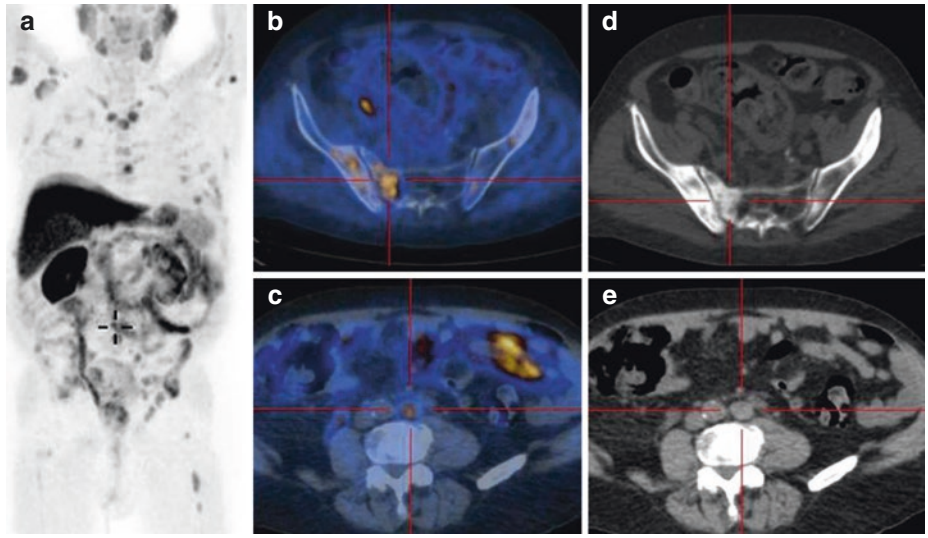

Fig. 3.16 A patient examined by ^{18}F-FMC PET/CT for high PSA value (68 ng/mL), prior to undergone antiandrogenic therapy. PET maximum intensity projection (**a**) shows pathologic tracer uptake in multiple bone lesions. Axial PET/CT views show a lesion in the right sacrum (**b**) and a further area of uptake in the pelvis (**c**), corresponding, respectively, to a sclerotic lesion (**d**) and a left iliac lymphadenopathy (**e**) in CT

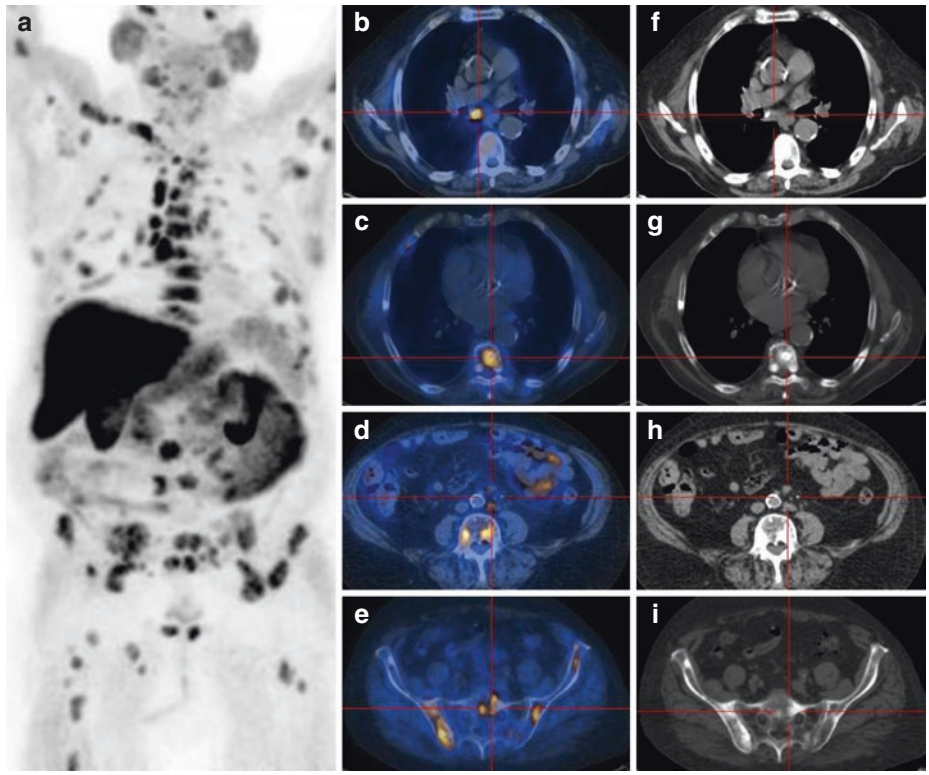

Fig. 3.17 A patient evaluated due to high PSA serum level (118 ng/mL) 6 years after radical prostatectomy for prostate carcinoma Gleason 9 (5 + 4). The ^{18}F-FMC PET maximum intensity projection (**a**) show multiple areas of pathologic tracer uptake, corresponding to superior diaphragmatic lymphadenopathies, multiple vertebral lesions, infra-diaphragmatic lymph nodes, and sacral sclerotic lesions in axial PET/CT views (**b**, **c**, **d**, **e**). All these findings are more clearly evident in related axial CT views, where it is also possible to observe the sclerotic lesions, typical of prostate cancer (**f**, **g**, **h**, **i**)

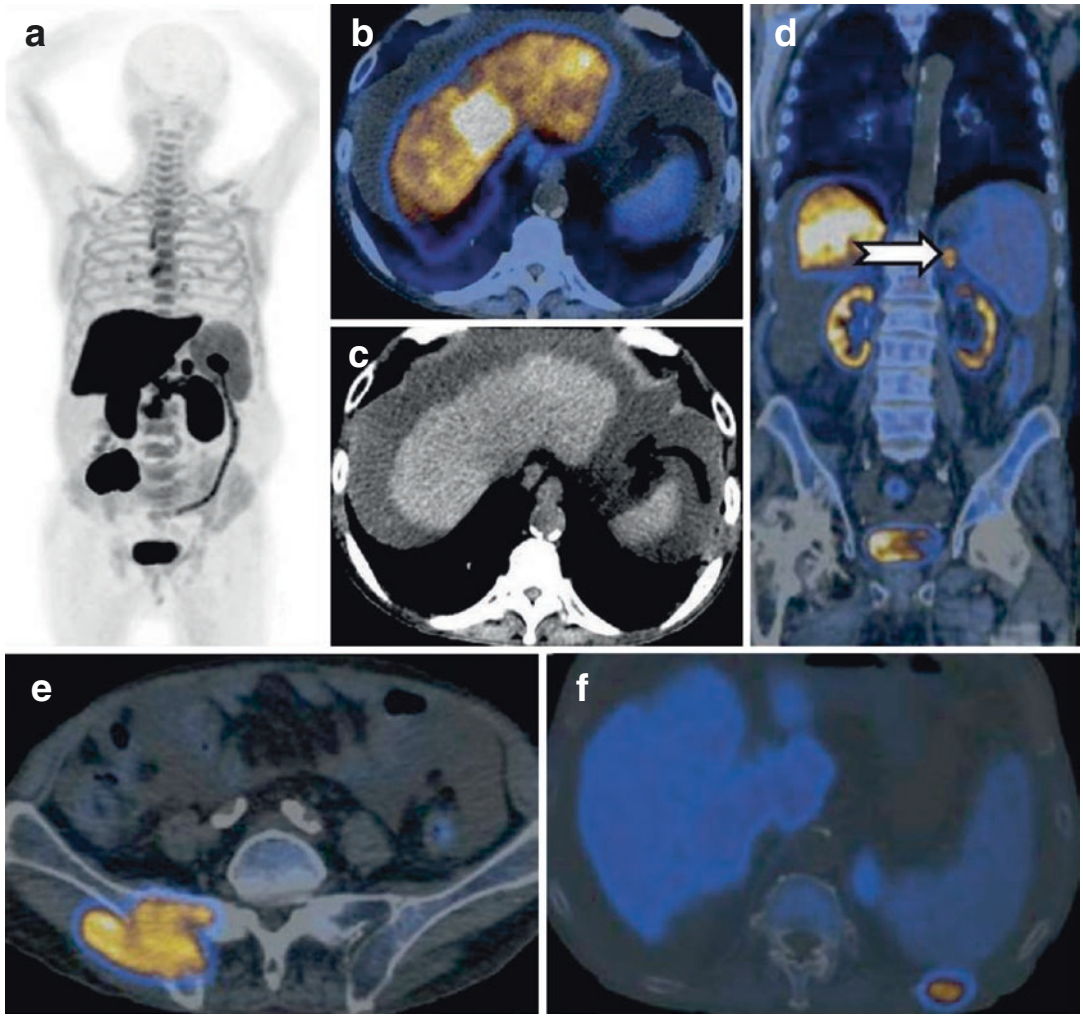

Fig. 3.18 A 71-year-old patient was examined by means of ^{18}F-FMC PET/CT. Four years before, he was submitted to radical prostatectomy for prostate cancer Gleason 8 (4 + 4); PSA at the time of the scan was 61 ng/mL. PET maximum intensity projection (**a**) shows multiple areas of pathologic tracer uptake, corresponding to a hepatic lesion of the VIII segment in axial PET/CT and CT views (**b**, **c**), a metastasis in the left adrenal gland in coronal PET/CT detail (arrow, **d**) and two tracer avid bone lesions in PET/CT views in the right iliac bone (**e**) and 11th left rib (**f**)

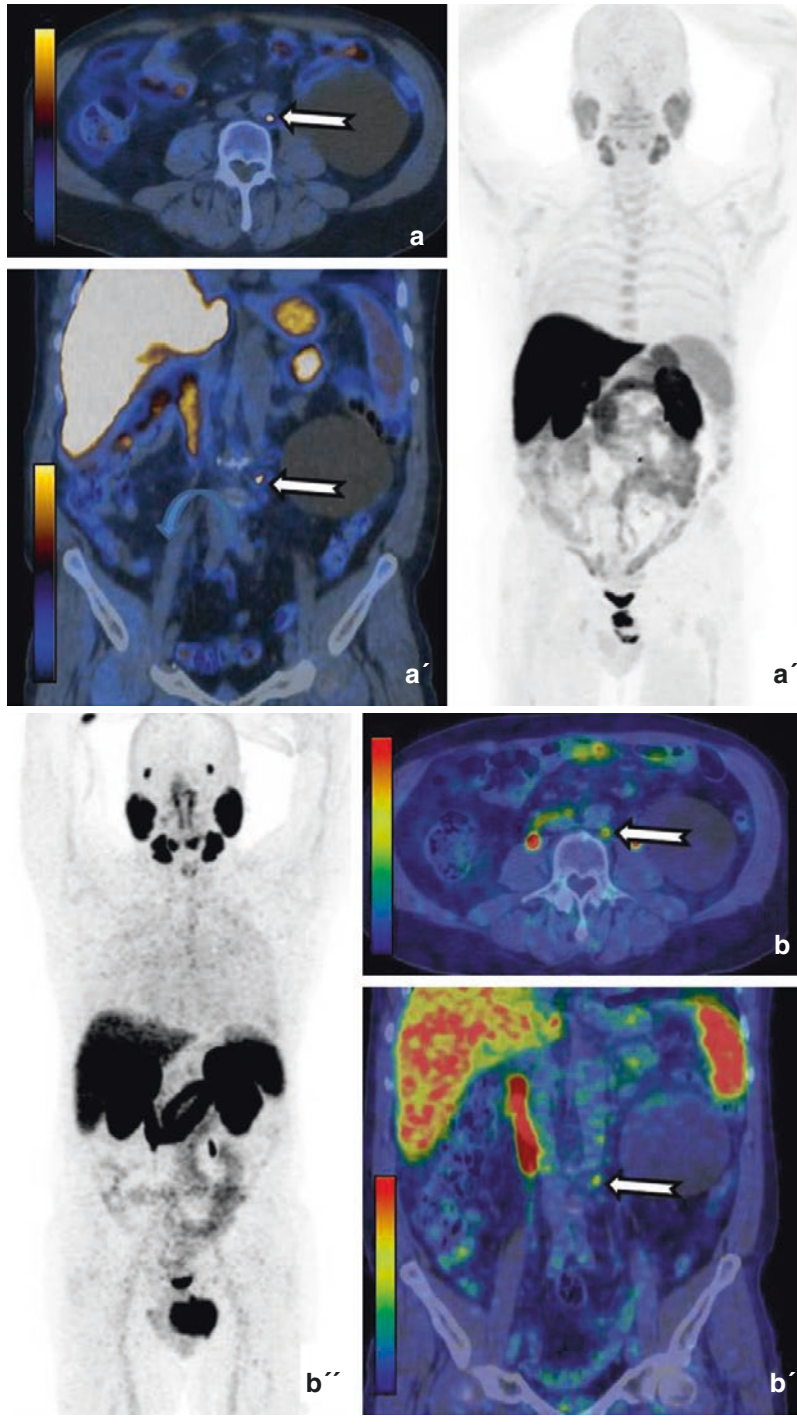

Fig. 3.19 This figure displays a 64-year-old patient, during early biochemical relapse (PSA 0.3 ng/mL) 1 year after radical prostatectomy for prostate cancer; patient was examined with ^{18}F-FMC and ^{68}Ga-PSMA PET/CT. Axial (**a**) and coronal (**a'**) ^{18}F-FMC PET/CT views show pathologic tracer uptake in a single para-aortic lymph node (arrows), also evident in ^{18}F-FMC PET maximum intensity projection (**a''**). Two months later, this finding was confirmed by ^{68}Ga-PSMA PET/CT. Axial (**b**), coronal (**b'**) PET/CT views and ^{68}Ga-PSMA PET maximum intensity projection (**b''**) confirm a tracer avid para-aortic lymph node. The comparison between two maximum intensity projection (**a''**, **b''**) can synthesize differences and similarities between two tracers (see also Chap. 12)

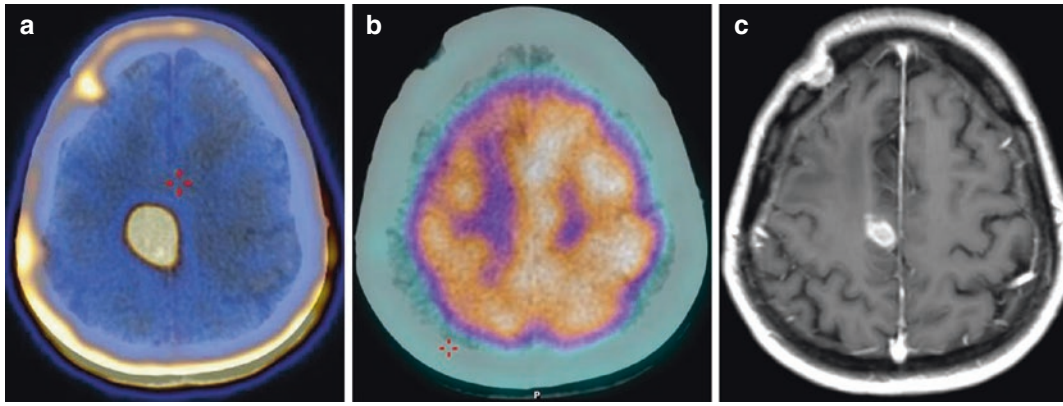

Fig. 3.20 A patient was examined by means of both ^{18}F-FMC and ^{18}F-FDG brain PET/CT for suspicion of astrocytoma relapse, 2 years after surgical tumor excision in the right parietal region. Axial ^{18}F-FMC PET/CT (**a**) shows focal uptake in the right, subcortical, parietal region. Conversely, no abnormal foci were detected in corresponding axial ^{18}F-FDG PET/CT view (**b**), probably due to the high physiological brain glucose metabolism. Post-contrast, T1-weighted MRI view (**c**) displays a 1-cm-wide nodular area in the site of ^{18}F-FMC uptake, with evident gadolinium enhancement, indicative of tumor relapse

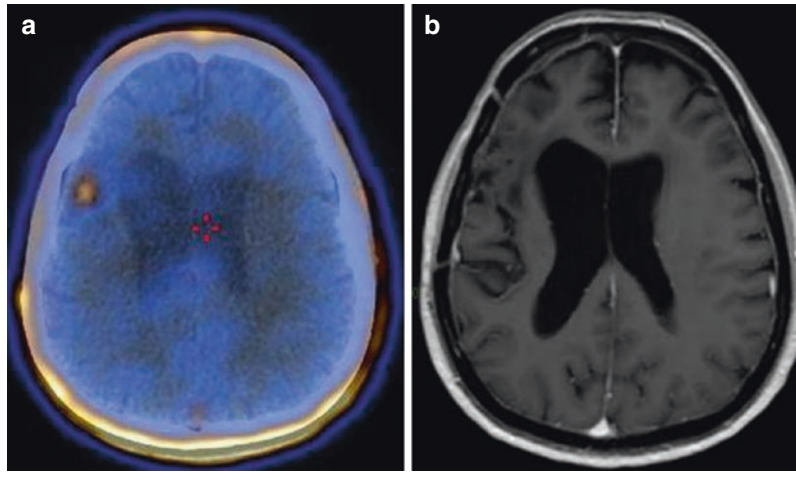

Fig. 3.21 In a patient previously submitted to surgical excision of a low-grade glioma, axial ^{18}F-FMC PET/CT view (**a**) shows pathologic tracer uptake in the postsurgical lacunar area in right temporal region. No meaningful morphological abnormalities were detected in corresponding post-contrast T1-weigted MRI (**b**). In both axial views is evident the right ventricle enlargement, consequent to the surgical intervention

3.6 PET/CT Acquisition Protocols

- Whole body PET/CT: from the vertex of the skull to the upper thighs, 45 min following tracer administration for fluorinated kinds of choline (≈300 Mbq; 2–3 min per bed position). Some scans with ^{11}C-choline are performed from the skull base (due to the faster half time decay of ^{11}C) but this can be not sufficient in order to exclude metastases in the skull or, more rarely, in the brain. Generally, is sufficient a low dose CT for the anatomical localization of functional findings, in order to reduce radiation exposure. Correlative good quality *low-dose* CT, as a part of the whole body PET/CT exam, is essential for the identification of sclerotic secondary bony metastases of prostate cancer, which can be non-choline avid, especially after antiandrogenic therapy. Routinely contrast media administration during the CT seems to be unnecessary [24].
- Dynamic or early PET/CT of the pelvis: during the tracer administration, a dynamic scan of the pelvis can improve the diagnosis of local recurrence of PC, in selected patients with early biochemical relapse, after radical prostatectomy, generally with PSA serum level lower than 2 ng/mL [23]. The acquisition protocol allows to avoid the interference to the urinary excretion of all kinds of radiolabeled choline tracers. The scan starts with the injection and is carried on for 3 min. A low-dose CT of the pelvis is necessary for the attenuation correction and to obtain anatomical landmarks.
- Brain PET/CT: the brain should be normally included in the whole body scan for oncologic patients. Some authors propose an acquisition of the brain for patients with brain tumors, brain tumor relapse, or brain metastases [74, 75]. A low-dose CT of the brain, with the head of the patient in the center of the scanner field of view, is necessary for attenuation correction and anatomical reference. Thereafter, a 10 min PET is performed for functional imaging. Finally, CT contrast agent can be administered for a better depiction of pathologic findings but correlative imaging with MRI or simultaneous PET/MRI should be preferable [55].

3.7 Variants and Pitfalls

Despite recent new development of new prostate radiopharmaceutical as the ^{68}Ga-PSMA, radiolabeled choline still plays an important role on prostate cancer imaging, being widely used in Western Europe and the USA, also supported by data of large amount of studies [76]. These studies also well described potential variants of physiological distribution and false positive cases or diagnostic pitfalls that can occur in clinical practice, not linked to prostate cancer. On the other hand, these features are still to be addressed for the other novel PC imaging radiopharmaceuticals [77, 78].

As known, the ideal tracer in nuclear medicine should demonstrate a specific affinity only for the neoplastic process under study, also in order to choose the better therapeutic approach. All the common nuclear medicine radiopharmaceuticals, probably with the exception of ^{131}I, can present physiological variants of bio-distribution and diagnostic pitfalls that need to be known in order to potentiate the confidence of nuclear physicians in images interpretation and avoiding misdiagnoses.

Specifically, the radiolabeled choline can be enhanced in inflammatory tissues, due to the high lipogenesis rate of the activated monocytes and macrophages [79] (Fig. 3.22). Other physiological variants of bio-distribution are linked to the possibility of tracer uptake in some conditions of "*functional activity*" in a specific organ or tissue, as in thyroiditis, hyperthyroidism, and adrenal adenomas [13]. The acquisition of this knowledge allowed to enlarge the use of radiolabeled choline to further fields as the imaging of hyperparathyroidism [80].

Tracer uptake can be also documented in benign thoracic lesions such as thymoma [81, 82] and sarcoidosis [68], due to the relatively high rate of cellular wall synthesis expressed.

The possibility of incidental detection of radiolabeled choline uptake in malignant diseases

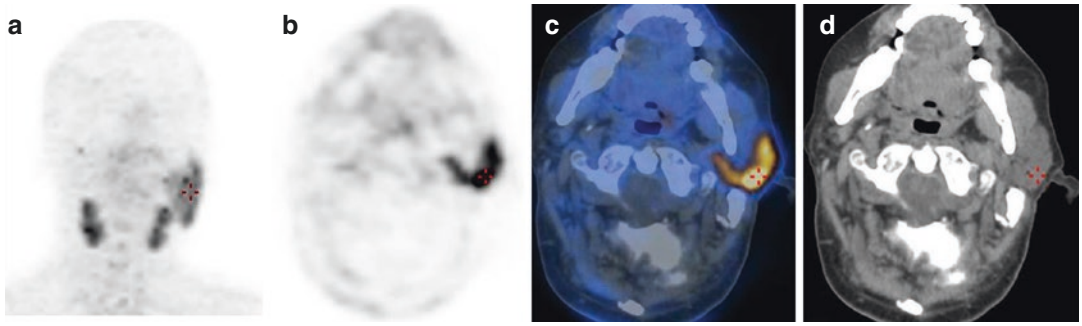

Fig. 3.22 In a patient examined with whole body ^{18}F-FMC PET/CT for restaging prostate cancer, diffuse tracer uptake was detected in the left parotid loggia, as evident in PET maximum intensity projection of the brain and neck (**a**) and axial PET view (**b**). The uptake was associated to subcutaneous hypodense tissue in corresponding PET/CT (**c**) and CT (**d**) views. The patient anamnesis was positive for an abscess following a tooth extraction procedure in left mandible. In this case, the radiolabeled choline uptake was absolutely nonspecific and linked to the increased monocytes and macrophages turnover in the infectious site

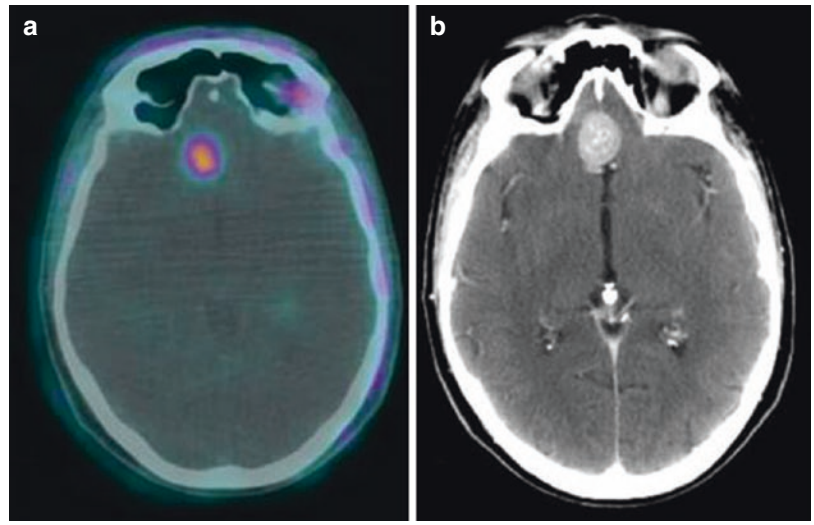

Fig. 3.23 In a patient examined for restaging prostate cancer, focal ^{18}F-FMC uptake was detected in the brain, in right frontal region, as evident in PET/CT axial view (**a**). The enhanced CT of the brain, consensually performed in the patient as a part of the exam, showed a hyperdense, 1.5 cm wide lesion in the same area (**b**), with mild iodinate contrast enhancement. The final diagnosis was meningioma

other than prostate cancer has been eloquently documented in several articles, as reports of a case or as a series, for both ^{11}C-choline and fluorinated choline: colon cancer [83, 84], multiple myeloma, bladder carcinoma [14], and plasma cell neoplasm [85] are rare, incidental findings that can be observed during a whole body PET/CT scan performed for prostate cancer [86, 87]. In these cases, laboratory data can help in correct diagnosis.

As incidental finding in prostate cancer patients is not rare to observe incidental radiolabeled choline uptake in meningiomas [88, 89]. Meningiomas can be documented in the co-registered CT as hyperdense areas with mild contrast enhancement, when administered (Fig. 3.23). In our experience, a PET/MRI of the brain, performed in addition to the standard whole body ^{18}F-choline PET/CT, can be a necessary step to depict sites of abnormal tracer uptake in the brain (Fig. 3.24). The possibility of choline uptake in meningioma must be known, especially considering that in prostate cancer patients these benign tumors can grow and become symptomatic, as a consequence of the antiandrogenic therapy [54].

Standing to our experience, false positive findings due to the nonspecific uptake of radiolabeled choline can occur in 17% of patients examined

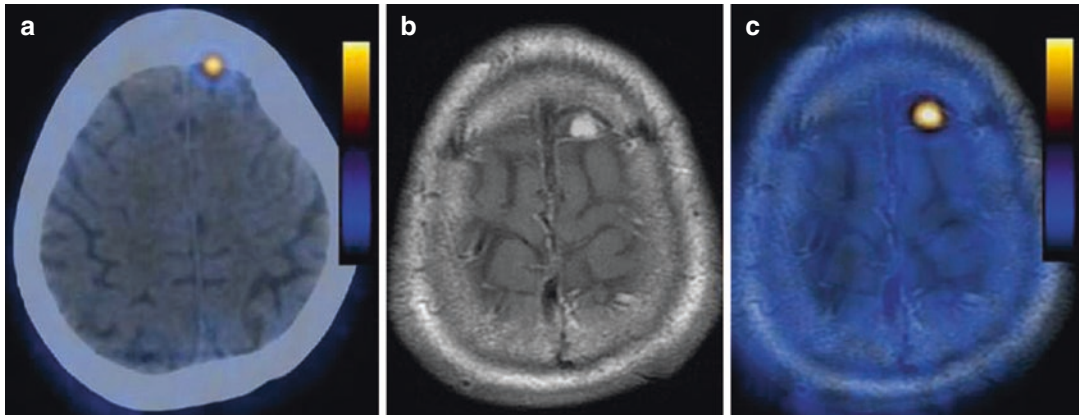

Fig. 3.24 A patient was examined by means of whole body ^{18}F-FMC PET/CT for restaging prostate cancer. A focal area of uptake was detected in left frontal region, evident in axial PET/CT view (**a**). The lesion was diagnosed as meningioma with MRI. Axial, post-contrast T1-weighted MRI view (**b**) shows the lesion with mild and uniform gadolinium enhancement. PET/MRI (**c**) confirms the morphologic and functional features of the lesion

for PC [14, 90]: anyway, the most part of these findings is easily recognizable as due to inflammation. The accurate collection of anamnestic data and the appropriate knowledge of the semeiotic CT diagnostic criteria can help nuclear physicians in correct identification of pitfalls.

The correlation with multimodal imaging still remains of the utmost importance to reach the correct diagnosis and identify the rare concomitant malignant lesions that can be observed as radiolabeled choline-avid.

References

1. No Authors listed. FDA approves 11C-choline for PET in prostate cancer. J Nucl Med. 2012;53(12):11N.
2. Lodi F, Malizia C, Castellucci P, et al. Synthesis of oncological [11C]radiopharmaceuticals for clinical PET. Nucl Med Biol. 2012;39:447–60.
3. Hara T, Kosaka N, Kishi H. Development of (18) F-fluoroethylcholine for cancer imaging with PET: synthesis, biochemistry, and prostate cancer imaging. J Nucl Med. 2002;13:187–99.
4. Schmaljohann J, Schirrmacher E, Wängler B, et al. Fully automated SPE-based synthesis and purification of 2-[18F]fluoroethyl-choline for human use. Nucl Med Biol. 2011;38:165–70.
5. DeGrado TR, Baldwin SW, Wang S, et al. Synthesis and evaluation of (18)F-labeled choline analogs as oncologic PET tracers. J Nucl Med. 2001;42:1805–14.
6. Haeffner EW. Studies on choline permeation through the plasma membrane and its incorporation into phosphatidyl choline of Ehrlich-Lettré-ascites tumor cells in vitro. Eur J Biochem. 1975;3:219–28.
7. Calabria F, Gallo G, Schillaci O, et al. Biodistribution, imaging protocols and diagnostic accuracy of PET with tracers of lipogenesis in imaging prostate cancer: a comparison between 11C-choline, 18F-fluoroethylcholine and 18F-methylcholine. Curr Pharm Des. 2015;21:4738–47.
8. DeGrado TR, Coleman RE, Wang S, et al. Synthesis and evaluation of 18F-labeled choline as an oncologic tracer for positron emission tomography: initial findings in prostate cancer. Cancer Res. 2001;1:110–7.
9. Balogova S, Huchet V, Kerrou K, et al. Detection of bronchioloalveolar cancer by means of PET/CT and 18F-fluorocholine, and comparison with 18F-fluorodeoxyglucose. Nucl Med Commun. 2010;31:389–97.
10. Sassa N, Kato K, Abe S, et al. Evaluation of 11C-choline PET/CT for primary diagnosis and staging of urothelial carcinoma of the upper urinary tract: a pilot study. Eur J Nucl Med Mol Imaging. 2014;41:2232–341.
11. Rischke HC, Beck T, Vach W, et al. Furosemide diminishes ^{18}F-fluoroethylcholine uptake in prostate cancer in vivo. Eur J Nucl Med Mol Imaging. 2014;41:2074–82.
12. Castilla-Lièvre MA, Franco D, Gervais P, et al. Diagnostic value of combining (11)C-choline and (18)F-FDG PET/CT in hepatocellular carcinoma. Eur J Nucl Med Mol Imaging. 2016;43:852–9.
13. Schillaci O, Calabria F, Tavolozza M, et al. 18F-choline PET/CT physiological distribution and pitfalls in image interpretation: experience in 80 patients with prostate cancer. Nucl Med Commun. 2010;31:39–45.
14. Calabria F, Chiaravalloti A, Schillaci O. (18)F-choline PET/CT pitfalls in image interpretation: an update on

300 examined patients with prostate cancer. Clin Nucl Med. 2014;39:122–30.
15. Mertens K, Ham H, Deblaere K, et al. Distribution patterns of 18F-labelled fluoromethylcholine in normal structures and tumors of the head: a PET/MRI evaluation. Clin Nucl Med. 2012;37:196–203.
16. Schwarzenböck S, Souvatzoglou M, Krause BJ. Choline PET and PET/CT in primary diagnosis and staging of prostate cancer. Theranostics. 2012;2:318–30.
17. Mertens K, Slaets D, Lambert B, et al. PET with (18) F-labelled choline-based tracers for tumour imaging: a review of the literature. Eur J Nucl Med Mol Imaging. 2010;37:2188–93.
18. Calabria F, Chiaravalloti A, Tavolozza M, et al. Evaluation of extraprostatic disease in the staging of prostate cancer by F-18 choline PET/CT: can PSA and PSA density help in patient selection? Nucl Med Commun. 2013;34:733–40.
19. Di Biagio D, Chiaravalloti A, Tavolozza M, et al. Detection of local recurrence of prostate cancer after radical prostatectomy: is there a role for early (18) F-FCH PET/CT? Ann Nucl Med. 2015;29:861–9.
20. Poncet D, Arnoux V, Descotes JL, et al. Biochemical recurrence after curative treatment for localized prostate cancer: performance of choline PET/CT in the assessment of local recurrence. Prog Urol. 2015;25:325–30.
21. Cimitan M, Bortolus R, Morassut S, et al. [18F]fluorocholine PET/CT imaging for the detection of recurrent prostate cancer at PSA relapse: experience in 100 consecutive patients. Eur J Nucl Med Mol Imaging. 2006;33:1387–98.
22. Quero L, Vercellino L, de Kerviler E, et al. 18F-choline PET/CT and prostate MRI for staging patients with biochemical relapse after irradiation for prostate cancer. Clin Nucl Med. 2015;40:e492–5.
23. Calabria F, Rubello D, Schillaci O. The optimal timing to perform 18F/11C-choline PET/CT in patients with suspicion of relapse of prostate cancer: trigger PSA versus PSA velocity and PSA doubling time. Int J Biol Markers. 2014;29:423–30.
24. Schillaci O, Calabria F, Tavolozza M, et al. Influence of PSA, PSA velocity and PSA doubling time on contrast-enhanced 18F-choline PET/CT detection rate in patients with rising PSA after radical prostatectomy. Eur J Nucl Med Mol Imaging. 2012;39:589–96.
25. Castellucci P, Ceci F, Graziani T, et al. Early biochemical relapse after radical prostatectomy: which prostate cancer patients may benefit from a restaging 11C-choline PET/CT scan before salvage radiation therapy? J Nucl Med. 2014;55:1424–9.
26. Vagnoni V, Brunocilla E, Bianchi L, et al. State of the PET/CT with 11-choline and 18F-fluorocholine in the diagnosis and follow-up of localized and locally advanced prostate cancer. Arch Esp Urol. 2015;68(3):354–70.
27. Marzola MC, Chondrogiannis S, Ferretti A, et al. Role of 18F-choline PET/CT in biochemically relapsed prostate cancer after radical prostatectomy: correlation with trigger PSA, PSA velocity, PSA doubling time, and metastatic distribution. Clin Nucl Med. 2013;38:e26–32.
28. Chiaravalloti A, Di Biagio D, Tavolozza M, et al. PET/CT with 18F-choline after radical prostatectomy in patients with PSA ≤2 ng/ml. Can PSA velocity and PSA doubling time help in patient selection? Eur J Nucl Med Mol Imaging. 2016;43:1418–24.
29. Svatek R, Karakiewicz PI, Shulman M, et al. Pretreatment nomogram for disease-specific survival of patients with chemotherapy-naive androgen independent prostate cancer. Eur Urol. 2006;49:666–74.
30. Jadvar H. Prostate cancer: PET with 18F-FDG, 18F- or 11C-acetate, and 18F- or 11C-choline. J Nucl Med. 2011;52:81–9.
31. Evangelista L, Bombardieri E. Prostate-specific antigen and radiolabelled choline PET/CT for the assessment of response to therapy: synergy or conflicting? Eur J Nucl Med Mol Imaging. 2016;43:200–11.
32. Picchio M, Spinapolice EG, Fallanca F, et al. [11C] Choline PET/CT detection of bone metastases in patients with PSA progression after primary treatment for prostate cancer: comparison with bone scintigraphy. Eur J Nucl Med Mol Imaging. 2012;39:13–26.
33. Koo PJ, David Crawford E. ^{18}F-NaF PET/CT and ^{11}C-choline PET/CT for the initial detection of metastatic disease in prostate cancer: overview and potential utilization. Oncology (Williston Park). 2014;28:1057–62.
34. Hofman MS, Hicks RJ, Maurer T, et al. Prostate-specific membrane antigen PET: clinical utility in prostate cancer, normal patterns, pearls, and pitfalls. Radiographics. 2018;38:200–17.
35. Smith CP, Laucis A, Harmon S, et al. Novel imaging in detection of metastatic prostate cancer. Curr Oncol Rep. 2019;5:31.
36. Kuten J, Mabjeesh NJ, Lerman H, et al. Ga-PSMA PET/CT staging of newly diagnosed intermediate- and high-risk prostate cancer. Isr Med Assoc J. 2019;21:100–4.
37. Evangelista L, Bonavina MG, Bombardieri E. Clinical results and economic considerations of 68Ga-PSMA and radiolabeled choline in prostate cancer. Nucl Med Biol. 2017;50:47–9.
38. Sachpekidis C, Pan L, Hadaschik BA, et al. 68Ga-PSMA-11 PET/CT in prostate cancer local recurrence: impact of early images and parametric analysis. Am J Nucl Med Mol Imaging. 2018;8:351–9.
39. Schwenck J, Rempp H, Reischl G, et al. Comparison of 68Ga-labelled PSMA-11 and 11C-choline in the detection of prostate cancer metastases by PET/CT. Eur J Nucl Med Mol Imaging. 2017;44:92–101.
40. Cantiello F, Gangemi V, Cascini GL, et al. Diagnostic accuracy of 64Copper prostate-specific membrane antigen positron emission tomography/computed tomography for primary lymph node staging of intermediate- to high-risk prostate cancer: our preliminary experience. Urology. 2017;106:139–45.
41. Cantiello F, Crocerossa F, Russo GI, et al. Comparison between 64Cu-PSMA-617 PET/CT and 18F-choline

PET/CT imaging in early diagnosis of prostate cancer biochemical recurrence. Clin Genitourin Cancer. 2018;16:385–91.
42. Giesel FL, Knorr K, Spohn F, et al. Detection efficacy of 18F-PSMA-1007 PET/CT in 251 patients with biochemical recurrence of prostate cancer after radical prostatectomy. J Nucl Med. 2019;60:362–8.
43. Shetty D, Patel D, Le K, et al. Pitfalls in gallium-68 PSMA PET/CT interpretation-A pictorial review. Tomography. 2018;4:182–93.
44. Calabria F, Gangemi V, Gullà D, et al. 64Cu-PSMA uptake in meningioma: a potential pitfall of a promising radiotracer. Rev Esp Med Nucl Imagen Mol. 2017;36:335–6.
45. Sheikhbahaei S, Afshar-Oromieh A, Eiber M, et al. Pearls and pitfalls in clinical interpretation of prostate-specific membrane antigen (PSMA)-targeted PET imaging. Eur J Nucl Med Mol Imaging. 2017;44:2117–36.
46. Bertagna F, Bertoli M, Bosio G, et al. Diagnostic role of radiolabelled choline PET or PET/CT in hepatocellular carcinoma: a systematic review and meta-analysis. Hepatol Int. 2014;8:493–500.
47. Bieze M, Bennink RJ, El-Massoudi Y, et al. The use of 18F-fluoromethylcholine PET/CT in differentiating focal nodular hyperplasia from hepatocellular adenoma: a prospective study of diagnostic accuracy. Nucl Med Commun. 2013;34:146–54.
48. Nanni C, Zamagni E, Cavo M, et al. 11C-choline vs. 18F-FDG PET/CT in assessing bone involvement in patients with multiple myeloma. World J Surg Oncol. 2007;20:68.
49. Vadrucci M, Gilardi L, Grana CM. Breast cancer incidentally detected by 18F-choline PET/CT in a patient with recurrent prostate carcinoma. Clin Nucl Med. 2016;41:892–3.
50. Hugentobler A, Gilbeau L, Talbot JN, et al. 18F-fluorocholine PET/CT of incidental male breast cancer. Clin Nucl Med. 2017;42:e56–7.
51. de Almeida Schirmer BG, de Araujo MR, Silveira MB, et al. Comparison of [18F]Fluorocholine and [18F]Fluordesoxyglucose for assessment of progression, lung metastasis detection and therapy response in murine 4T1 breast tumor model. Appl Radiat Isot. 2018;140:278–88.
52. Ahmad Saad FF, Zakaria MH, Appanna B. PET/CT analysis of 21 patients with breast cancer: physiological distribution of 18F-choline and diagnostic pitfalls. J Int Med Res. 2018;46:3138–48.
53. Treglia G, Giovannini E, Di Franco D, et al. The role of positron emission tomography using carbon-11 and fluorine-18 choline in tumors other than prostate cancer: a systematic review. Ann Nucl Med. 2012;26:451–61.
54. Fallanca F, Giovacchini G, Picchio M, et al. Incidental detection by [11C]choline PET/CT of meningiomas in prostate cancer patients. Q J Nucl Med Mol Imaging. 2009;53:417–21.
55. Fraioli F, Shankar A, Hargrave D, et al. 18F-fluoroethylcholine (18F-Cho) PET/MRI functional parameters in pediatric astrocytic brain tumors. Clin Nucl Med. 2015;40:e40–5.
56. Imperiale A, Bergerat JP, Saussine C, et al. Isolated cerebellar metastasis from prostate adenocarcinoma diagnosed by 18F-fluorocholine PET/CT: a rare but not impossible complication. Eur J Nucl Med Mol Imaging. 2014;41:397–8.
57. Narayanan TK, Said S, Mukherjee J, et al. A comparative study on the uptake and incorporation of radiolabeled methionine, choline and fluorodeoxyglucose in human astrocytoma. Mol Imaging Biol. 2002;4:147–56.
58. Ohtani T, Kurihara H, Ishiuchi S, et al. Brain tumour imaging with carbon-11 choline: comparison with FDG PET and gadolinium-enhanced MR imaging. Eur J Nucl Med. 2001;28:1664.
59. Rottenburger C, Hentschel M, Kelly T, et al. Comparison of C-11 methionine and C-11 choline for PET imaging of brain metastases: a prospective pilot study. Clin Nucl Med. 2011;36:639–42.
60. Roelcke U, Bruehlmeier M, Hefti M, et al. F-18 choline PET does not detect increased metabolism in F-18 fluoroethyltyrosine-negative low-grade gliomas. Clin Nucl Med. 2012;37:e1–3.
61. Takenaka S, Asano Y, Shinoda J, et al. Comparison of (11)C-methionine, (11)C-choline, and (18) F-fluorodeoxyglucose-PET for distinguishing glioma recurrence from radiation necrosis. Neurol Med Chir (Tokyo). 2014;54:280–9.
62. Takenaka S, Shinoda J, Asano Y, et al. Metabolic assessment of monofocal acute inflammatory demyelination using MR spectroscopy and (11)C-methionine-, (11)C-choline-, and (18)F-fluorodeoxyglucose-PET. Brain Tumor Pathol. 2011;28:229.
63. Cascini GL, Restuccia A, De Vincenti T, et al. A vascular lesion mimicking a primitive brain tumour in a patient examined by (18)F-choline PET/CT and MRI. Rev Esp Med Nucl Imagen Mol. 2015;34:335–6.
64. Mapelli P, Busnardo E, Magnani P, et al. Incidental finding of parathyroid adenoma with 11C-choline PET/CT. Clin Nucl Med. 2012;37:593–5.
65. Quak E, Lheureux S, Reznik Y, et al. F18-choline, a novel PET tracer for parathyroid adenoma? J Clin Endocrinol Metab. 2013;98:3111–2.
66. Michaud L, Balogova S, Burgess A, et al. A pilot comparison of 18F-fluorocholine PET/CT, ultrasonography and 123I/99mTc-sestaMIBI dual-phase dual-isotope scintigraphy in the preoperative localization of hyperfunctioning parathyroid glands in primary or secondary hyperparathyroidism: influence of thyroid anomalies. Medicine (Baltimore). 2015;94:e1701.
67. Lezaic L, Rep S, Sever MJ, et al. ^{18}F-Fluorocholine PET/CT for localization of hyperfunctioning parathyroid tissue in primary hyperparathyroidism: a pilot study. Eur J Nucl Med Mol Imaging. 2014;41:2083–9.
68. Takesh M, Haberkorn U, Strauss LG, et al. Incidental detection and monitoring of spontaneous recovery of sarcoidosis via fluorine-18-fluoroethyl-choline

positron emission tomography/computed tomography. Hell J Nucl Med. 2012;15:63–5.
69. Ankrah AO, van der Werf TS, de Vries EF, et al. PET/CT imaging of Mycobacterium tuberculosis infection. Clin Transl Imaging. 2016;4:131–44.
70. Wetter A, Lipponer C, Nensa F, et al. Quantitative evaluation of bone metastases from prostate cancer with simultaneous [18F] choline PET/MRI: combined SUV and ADC analysis. Ann Nucl Med. 2014;28:405–10.
71. Paparo F, Piccardo A, Bacigalupo L, et al. Value of bimodal (18)F-choline-PET/MRI and trimodal (18)F-choline-PET/MRI/TRUS for the assessment of prostate cancer recurrence after radiation therapy and radical prostatectomy. Abdom Imaging. 2015;40:1772–87.
72. Lapa C, Linsenmann T, Monoranu CM, et al. Comparison of the amino acid tracers 18F-FET and 18F-DOPA in high-grade glioma patients. J Nucl Med. 2014;55:1611–6.
73. Tripathi M, Sharma R, D'Souza M, et al. Comparative evaluation of F-18 FDOPA, F-18 FDG, and F-18 FLT-PET/CT for metabolic imaging of low grade gliomas. Clin Nucl Med. 2009;34:878–83.
74. Calabria FF, Barbarisi M, Gangemi V, et al. Molecular imaging of brain tumors with radiolabeled choline PET. Neurosurg Rev. 2016;41:67–76.
75. Gizewska A, Witkowska-Patena E, Stembrowicz-Nowakowska Z, et al. Brain metastases in patient with prostate cancer found in 18F-choline PET/CT. Nucl Med Rev Cent East Eur. 2015;18:39–41.
76. Evangelista L, Cimitan M, Hodolič M, et al. The ability of 18F-choline PET/CT to identify local recurrence of prostate cancer. Abdom Imaging. 2015;40:3230–7.
77. Krohn T, Verburg FA, Pufe T, et al. [(68)Ga] PSMA-HBED uptake mimicking lymph node metastasis in coeliac ganglia: an important pitfall in clinical practice. Eur J Nucl Med Mol Imaging. 2015;42:210–4.
78. Verburg FA, Pfister D, Heidenreich A, et al. Extent of disease in recurrent prostate cancer determined by [(68)Ga]PSMA-HBED-CC PET/CT in relation to PSA levels, PSA doubling time and Gleason score. Eur J Nucl Med Mol Imaging. 2016;43:397–403.
79. Calabria F, Schillaci O. The biodistribution of the radiolabeled kinds of choline in male patients, assessed by PET/CT. Nucl Med Commun. 2016;37:329–30.
80. van Raalte DH, Vlot MC, Zwijnenburg A, et al. F18-choline PET/CT: a novel tool to localize parathyroid adenoma. Clin Endocrinol (Oxf). 2015;82:910–2.
81. Fallanca F, Picchio M, Spinapolice EG, et al. Imaging of a thymoma incidentally detected by C-11 choline PET/CT. Clin Nucl Med. 2011;36:134–5.
82. Calabria F, D'Auria S, Sannino P, Schillaci O. A case of thymoma detected by 18F-choline positron emission tomography/computed tomography. Eur J Nucl Med Mol Imaging. 2011;38(3):602.
83. Calabria FF, Crusco S, Cicciò C, et al. A case of colon cancer incidentally detected by 18F-choline PET/CT. Clin Nucl Med. 2013;38:982–3.
84. Bagni O, Filippi L, Schillaci O. Incidental detection of colorectal cancer via 18F-choline PET/CT in a patient with recurrent prostate cancer: usefulness of early images. Clin Nucl Med. 2015;40:328–30.
85. Paudel J, Singla N, Bhattacharya A, et al. Incidental detection of plasma cell neoplasm on 18F-choline PET/CT imaging. Clin Nucl Med. 2019;44:140–1.
86. García Vicente AM, Núñez García A, Soriano Castrejón AM, et al. Pitfalls with 18F-choline PET/CT in patients with prostate cancer. Rev Esp Med Nucl Imagen Mol. 2013;32:37–9.
87. Beheshti M, Haroon A, Bomanji JB, et al. Fluorocholine PET/computed tomography: physiologic uptake, benign findings, and pitfalls. PET Clin. 2014;9:299–306.
88. Calabria F, Calabria E, Chiaravalloti A, et al. A case of intracranial meningioma detected by ^{18}F-choline PET/CT and examined by PET/MRI fusion imaging. Rev Esp Med Nucl Imagen Mol. 2014;33:306–7.
89. Calabria F. Fifty shades of meningioma: challenges and perspectives of different PET molecular probes. Clin Transl Imaging. 2017;5:403–5.
90. Calabria F, Chiaravalloti A, Cicciò C, et al. PET/CT with 18F-choline: physiological whole body biodistribution in male and female subjects and diagnostic pitfalls on 1000 prostate cancer patients: 18F-choline PET/CT bio-distribution and pitfalls. A southern Italian experience. Nucl Med Biol. 2017;51:40–54.

^{18}F-FET

4

Giorgio Treglia, Barbara Muoio, and Luca Giovanella

Contents

Abbreviations

^{18}F-FDG	Fluorine-18 fluorodeoxyglucose
^{18}F-FDOPA	Fluorine-18 fluorodihydroxyphenylalanine
^{18}F-FET	Fluorine-18 fluoroethyltyrosine
^{18}F-FLT	Fluorine-18 fluorothymidine
CT	Computed tomography
EANO	European Association for Neuro-Oncology
LBR	Lesion-to-background ratio
MBq	MegaBecquerel
MRI	Magnetic resonance imaging
PET	Positron emission tomography
RANO	Response Assessment in Neuro-Oncology (RANO)
Sv	Sievert

Authors declare they have obtained permission for any previously published material used in their chapter.

G. Treglia (✉)
Imaging Institute of Southern Switzerland, Ente Ospedaliero Cantonale, Bellinzona and Lugano, Switzerland

Health Technology Assessment Unit, General Directorate, Ente Ospedaliero Cantonale, Bellinzona, Switzerland

Department of Nuclear Medicine and Molecular Imaging, University Hospital of Lausanne and University of Lausanne, Lausanne, Switzerland
e-mail: giorgio.treglia@eoc.ch

B. Muoio
Oncology Institute of Southern Switzerland, Ente Ospedaliero Cantonale, Bellinzona, Switzerland

L. Giovanella
Imaging Institute of Southern Switzerland, Ente Ospedaliero Cantonale, Bellinzona and Lugano, Switzerland

F. Calabria, O. Schillaci (eds.), *Radiopharmaceuticals*,
https://doi.org/10.1007/978-3-030-27779-6_4

4.1 Synthesis, Pharmacokinetics and Biodistribution of ^{18}F-FET

^{18}F-FET is a radiolabelled amino acid, tyrosine analogue, which can be used to visualize brain tumours by using positron emission tomography (PET) [1]. The results of the first human study using ^{18}F-FET PET in a patient with brain tumour have been reported in 1999 [2]. ^{18}F-FET was synthesized by a direct alkylation of tyrosine with ^{18}F-fluoroethyltosylate as previously reported by Wester et al. [2]. An automated synthesis of ^{18}F-FET was then reported [1]. The specific activity of ^{18}F-FET was 18 GBq/μmol (0.49 Ci/μmol) with a total synthesis time of 80 min and a radiochemical yield of 55–60%. This method provided a radiochemical purity >99% [1].

Characteristics of this amino acid radiopharmaceutical are the high in vivo stability, the fast brain and tumour uptake kinetics, the usually low accumulation in non-tumour tissue and its ease of synthesis [2]. ^{18}F-FET penetrates the blood-brain barrier by a specific amino acid transport system and it is not incorporated into proteins [2]. Its uptake mechanism in tumour cells is mediated by the L-type amino acid transport system [3]. Several factors influence the increased amino acid uptake in brain tumour cells including the overexpression of the amino acid transport systems in tumour cells, alterations in the tumour vasculature and tumour cell proliferation [1, 2].

About dosimetry of ^{18}F-FET PET, the highest absorbed dose was found for the bladder. The effective dose is 16.5 microSv/MBq for adults, which would lead to an effective dose of 6.1 mSv in a PET study using 370 MBq [4]. The potential radiation risks associated with this functional imaging method are well within accepted limits [5].

4.2 ^{18}F-FET PET Acquisition Protocols

About the ^{18}F-FET PET imaging procedure [6] patients should be fasting for more than 4 h before the radiopharmaceutical injection. A mean dose of 200–250 MBq is intravenously injected in adult patients. Hybrid PET/CT or PET/MRI are used for brain image acquisition. Some centres start a 40 min dynamic acquisition just after the radiopharmaceutical injection. In other centres static PET image acquisition from 20 to 40 min post-injection is performed [6]. ^{18}F-FET PET image interpretation is usually performed by using visual (qualitative) and semi-quantitative criteria such as lesion-to-background uptake ratios [6].

Contraindications for ^{18}F-FET PET are only pregnancy and lack of patient cooperation [6].

4.3 Indications of ^{18}F-FET PET

4.3.1 Evaluation of Brain Tumours by ^{18}F-FET PET

MRI is the standard neuroimaging method to diagnose neoplastic brain lesions, as well as to perform stereotactic biopsy and surgical planning in neuro-oncology. MRI has the advantage of providing structural anatomical details with high sensitivity, though histological specificity is limited. Functional imaging by using radiolabelled amino acids may be useful in the diagnostic evaluation of brain lesions providing significant information compared to conventional morphological imaging techniques such as CT or MRI (Figs. 4.1, 4.2, and 4.3) (see also Chap. 2, 11) [7].

From the past decade to date several studies about ^{18}F-FET PET in brain tumours have been published in the literature. Recommendations for the clinical use of PET in neuro-oncology were recently published by the Response Assessment in Neuro-Oncology (RANO) working group and the European Association for Neuro-Oncology (EANO) taking into account available literature data. As stated by these recommendations, ^{18}F-FET PET is of additional value beyond MRI in glioma management [8].

In cases of diagnostic uncertainty, ^{18}F-FET PET improves the differential diagnosis between brain tumours and non-neoplastic lesions [8, 9].

Although ^{18}F-FET PET uptake is usually higher in high-grade gliomas compared to low-grade

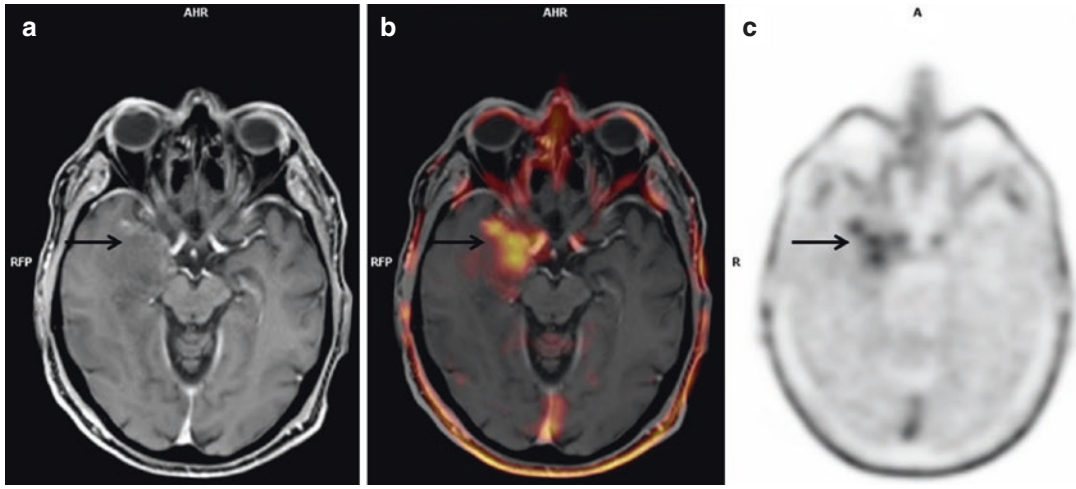

Fig. 4.1 Axial MRI (**a**), fused ^{18}F-FET PET/MRI (**b**) and ^{18}F-FET PET (**c**) images in a 54 y.o. female patient with a suspicious right temporal glioma (arrows). ^{18}F-FET PET shows an area of increased radiopharmaceutical uptake corresponding to the anterior portion of the cerebral lesion and suggesting a high-grade glioma, as confirmed by ^{18}F-FET PET-guided biopsy

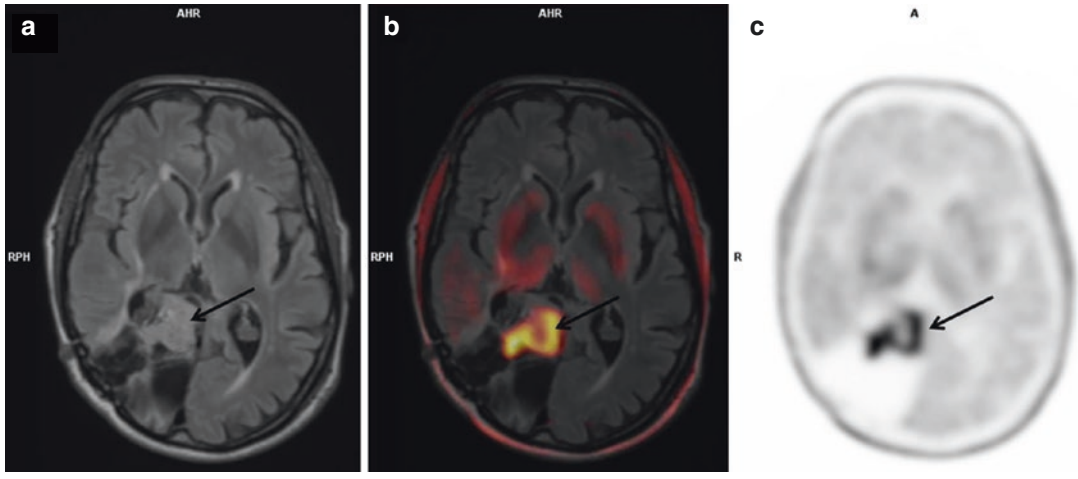

Fig. 4.2 Axial MRI (**a**), fused ^{18}F-FET PET/MRI (**b**) and ^{18}F-FET PET (**c**) images in a 64 y.o. female patient treated with surgery and radiochemotherapy for a right temporal-occipital high-grade glioma and with a contrast-enhanced area suspicious for disease relapse or radionecrosis at MRI (arrows). ^{18}F-FET PET shows increased radiopharmaceutical uptake corresponding to the MRI abnormality, suggesting a disease relapse as confirmed by histology

gliomas [9], tumour grading may be limited using static PET parameters, such as maximum and mean lesion-to-background ratio (LBR) due to significant overlap in uptake values. Nevertheless dynamic analysis of ^{18}F-FET PET uptake significantly improves differential diagnosis between low-grade and high-grade gliomas [8].

Delineation of tumour borders by ^{18}F-FET PET is superior to standard MRI both in contrast-enhancing and in non-contrast-enhancing gliomas. Integration of ^{18}F-FET PET into surgical planning allows better delineation of the extent of resection beyond margins visible with standard MRI. For biopsy planning, ^{18}F-FET PET is particularly helpful in identifying malignant foci within non-contrast-enhancing gliomas [8, 10].

^{18}F-FET PET may improve the delineation of a biological tumour volume beyond conventional

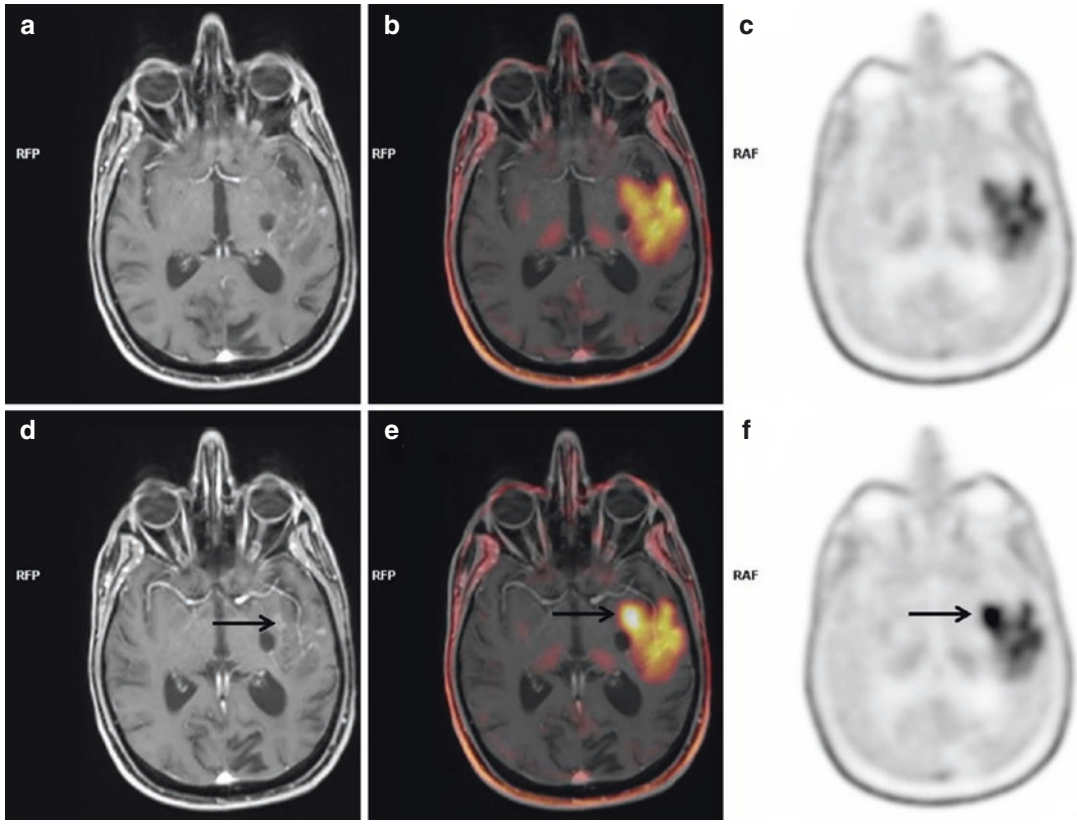

Fig. 4.3 Axial MRI (**a**, **d**), fused ^{18}F-FET PET/MRI (**b**, **e**) and ^{18}F-FET PET (**c**, **f**) images in a 58 y.o. male patient with a recurrent left temporal high-grade glioma post-radiochemotherapy, before (**a**–**c**) and after (**d**–**f**) antiangiogenic therapy. ^{18}F-FET PET after antiangiogenic therapy shows an area of increasing radiopharmaceutical uptake in the left temporal lobe (arrows) compared to the pre-treatment PET scan, suggesting disease progression

MRI and identify aggressive tumour subregions that may be targeted by radiation therapy. Radiation therapy planning using ^{18}F-FET PET appears feasible, with preliminary evidence of potential benefit [8, 11].

^{18}F-FET PET may be useful to evaluate treatment response in patients with high-grade gliomas because a decrease in ^{18}F-FET uptake and/or volume is associated with treatment response in these tumours. Furthermore ^{18}F-FET PET improves the differential diagnosis between brain tumours recurrence and non-neoplastic post-treatment changes [8, 12].

^{18}F-FET uptake is associated with outcome in high-grade gliomas both in a pre-treatment setting and following therapy. Biological tumour volume at ^{18}F-FET PET is associated with survival following therapy in glioblastoma. Dynamic ^{18}F-FET PET provides prognostic information within all grades of glioma prior to treatment [8, 13].

Future perspectives are represented by the standardization of PET acquisition protocols and the more widely diffusion of hybrid imaging techniques such as PET/MRI [14].

4.3.2 Comparison of ^{18}F-FET with Other PET Radiopharmaceuticals for Brain Tumour Imaging

Several PET radiopharmaceuticals may be used in neuro-oncology and some of them were recently compared with ^{18}F-FET.

PET using ^{11}C-methionine, a radiolabelled amino acid tracer, has high sensitivity and specificity for imaging of gliomas and brain

metastases. The short half-life of ^{11}C (20 min) limits the use of ^{11}C-methionine PET to institutions with onsite cyclotron. ^{18}F-FET is labelled with ^{18}F (half-life: 110 min) and could be used much more broadly. Based on literature data ^{18}F-FET PET and ^{11}C-methionine PET provided comparable diagnostic information on gliomas and brain metastases [15].

For brain tumour diagnosis radiolabelled choline PET was not found superior to ^{18}F-FET PET, in particular in low-grade gliomas [16].

^{18}F-FET PET has shown higher sensitivity in detection of gliomas than proliferation imaging with ^{18}F-fluorothymidine (^{18}F-FLT) PET [17]. In high-grade gliomas ^{18}F-FET PET but not ^{18}F-FLT PET was able to detect metabolic active tumour tissue beyond contrast-enhancing tumour on MRI. In contrast to ^{18}F-FET, blood-brain barrier breakdown seems to be a prerequisite for ^{18}F-FLT uptake [18].

In evaluating brain tumours ^{18}F-fluorodihydroxyphenylalanine (^{18}F-FDOPA) PET demonstrated superior contrast ratios for lesions outside the striatum compared to ^{18}F-FET PET, but ^{18}F-FDOPA uptake values did not correlate with grading. Compared to ^{18}F-FDOPA, ^{18}F-FET-PET can provide additional information on tumour grading and benefits from lower striatal uptake [19]. Whereas visual analysis revealed no significant differences in uptake pattern for ^{18}F-FET and ^{18}F-DOPA in patients with primary or recurrent high-grade gliomas, both maximum lesion-to-background uptake ratio (LBR) and mean LBR were significantly higher for ^{18}F-FET PET. However, regarding tumour delineation, both tracers performed equally well and seem equally feasible for imaging of primary and recurrent high-grade gliomas [20].

A recent meta-analysis demonstrated that for brain tumour diagnosis, ^{18}F-FET PET performed much better than ^{18}F-fluorodeoxyglucose (^{18}F-FDG) PET and should be preferred when assessing a new isolated brain tumour. For glioma grading, however, both tracers showed similar performances [21].

Unfortunately the availability of ^{18}F-FET as radiopharmaceutical is limited to some countries. This is the main limitation that hampers the widespread use of ^{18}F-FET PET.

Acknowledgements *Conflicts of Interest*: The authors declare that they have no conflicts of interest.

References

1. Hamacher K, Coenen HH. Efficient routine production of the 18F-labelled amino acid O-2-18F fluoroethyl-L-tyrosine. Appl Radiat Isot. 2002;57(6):853–6.
2. Wester HJ, Herz M, Weber W, et al. Synthesis and radiopharmacology of O-(2-[18F]fluoroethyl)-L-tyrosine for tumor imaging. J Nucl Med. 1999;40(1):205–12.
3. Heiss P, Mayer S, Herz M, et al. Investigation of transport mechanism and uptake kinetics of O-(2-[18F] fluoroethyl)-L-tyrosine in vitro and in vivo. J Nucl Med. 1999;40(8):1367–73.
4. Pauleit D, Floeth F, Herzog H, et al. Whole-body distribution and dosimetry of O-(2-[18F]fluoroethyl)-L-tyrosine. Eur J Nucl Med Mol Imaging. 2003;30(4):519–24.
5. Tang G, Wang M, Tang X, et al. Pharmacokinetics and radiation dosimetry estimation of O-(2-[18F] fluoroethyl)-L-tyrosine as oncologic PET tracer. Appl Radiat Isot. 2003;58(2):219–25.
6. Vander Borght T, Asenbaum S, Bartenstein P, et al. EANM procedure guidelines for brain tumour imaging using labelled amino acid analogues. Eur J Nucl Med Mol Imaging. 2006;33(11):1374–80.
7. Muoio B, Giovanella L, Treglia G. Recent developments of 18F-FET PET in neuro-oncology. Curr Med Chem. 2018;25(26):3061–73.
8. Albert NL, Weller M, Suchorska B, et al. Response Assessment in Neuro-Oncology Working Group and European Association for Neuro-Oncology recommendations for the clinical use of PET imaging in gliomas. Neuro Oncol. 2016;18(9):1199–208.
9. Dunet V, Rossier C, Buck A, et al. Performance of 18F-fluoro-ethyl-tyrosine (18F-FET) PET for the differential diagnosis of primary brain tumor: a systematic review and metaanalysis. J Nucl Med. 2012;53(2):207–14.
10. Heinzel A, Stock S, Langen KJ, et al. Cost-effectiveness analysis of FET PET-guided target selection for the diagnosis of gliomas. Eur J Nucl Med Mol Imaging. 2012;39(7):1089–96.
11. Munck Af Rosenschold P, Costa J, Engelholm SA, et al. Impact of [18F]-fluoro-ethyl-tyrosine PET imaging on target definition for radiation therapy of high-grade glioma. Neuro Oncol. 2015;17(5):757–63.
12. Muoio B, Treglia G, Reinert M, et al. Diagnostic performance of static 18F-fluoroethyl-L-tyrosine positron emission tomography parameters to differentiate recurrent brain tumours from non-neoplastic treatment-related changes: a meta-analysis. Neuro Oncol. 2016;18.(Suppl 4:iv9.
13. Gempt J, Bette S, Ryang YM, et al. 18F-fluoro-ethyl-tyrosine positron emission tomography for grading and estimation of prognosis in patients with intracranial gliomas. Eur J Radiol. 2015;84(5):955–62.

14. Henriksen OM, Larsen VA, Muhic A, et al. Simultaneous evaluation of brain tumour metabolism, structure and blood volume using [(18) F]-fluoroethyltyrosine (FET) PET/MRI: feasibility, agreement and initial experience. Eur J Nucl Med Mol Imaging. 2016;43(1):103–12.
15. Grosu AL, Astner ST, Riedel E, et al. An interindividual comparison of O-(2-[18F]fluoroethyl)-L-tyrosine (FET)- and L-[methyl-11C]methionine (MET)-PET in patients with brain gliomas and metastases. Int J Radiat Oncol Biol Phys. 2011;81(4): 1049–58.
16. Roelcke U, Bruehlmeier M, Hefti M, et al. F-18 choline PET does not detect increased metabolism in F-18 fluoroethyltyrosine-negative low-grade gliomas. Clin Nucl Med. 2012;37(1):e1–3.
17. Jeong SY, Lim SM. Comparison of 3′-deoxy-3′-[18F] fluorothymidine PET and O-(2-[18F]fluoroethyl)-L-tyrosine PET in patients with newly diagnosed glioma. Nucl Med Biol. 2012;39(7):977–81.
18. Nowosielski M, DiFranco MD, Putzer D, et al. An intra-individual comparison of MRI, [18F]-FET and [18F]-FLT PET in patients with high-grade gliomas. PLoS One. 2014;9(4):e95830.
19. Kratochwil C, Combs SE, Leotta K, et al. Intra-individual comparison of ^{18}F-FET and ^{18}F-DOPA in PET imaging of recurrent brain tumors. Neuro Oncol. 2014;16(3):434–40.
20. Lapa C, Linsenmann T, Monoranu CM, et al. Comparison of the amino acid tracers 18F-FET and 18F-DOPA in high-grade glioma patients. J Nucl Med. 2014;55(10):1611–6.
21. Dunet V, Pomoni A, Hottinger A, et al. Performance of 18F-FET versus 18F-FDG-PET for the diagnosis and grading of brain tumors: systematic review and meta-analysis. Neuro Oncol. 2016;18(3):426–34.

^{18}F-NaF

5

Ferdinando Calabria and Orazio Schillaci

Contents

Abbreviations

^{18}F-FDG	^{18}F-fluorodeoxyglucose
^{99m}Tc-MDP	^{99m}Tc-methyldiphosfonate
CT	Computed tomography
EANM	European Association of Nuclear Medicine and Molecular Imaging
FDA	Food and Drug Administration
MIP	Maximum intensity projection
PET/CT	Positron emission computed tomography/computed tomography
SPECT	Single photon emission computed tomography/computed tomography
SUV	Standardized uptake value

F. Calabria (✉)
Department of Nuclear Medicine and Theranostics, "Mariano Santo" Hospital, Cosenza, Italy
e-mail: ferdinandocalabria@hotmail.it

O. Schillaci
Department of Biomedicine and Prevention, University "Tor Vergata", Rome, Italy

Department of Nuclear Medicine and Molecular Imaging, IRCCS Neuromed, Pozzilli, IS, Italy

F. Calabria, O. Schillaci (eds.), *Radiopharmaceuticals*,
https://doi.org/10.1007/978-3-030-27779-6_5

5.1 Synthesis

The ^{18}F-NaF was synthetized for nuclear imaging since 1962 [1] but was widely replaced by ^{99}Tc-labeled diphosphonate compounds in the 1970s because of their better physical characteristics for imaging with conventional

γ-cameras and SPECT. The ^{18}F-NaF was approved by Food and Drug Administration (FDA) in 1972 for detection of osteogenic activity. However, only the development and commercial availability of PET and hybrid PET/CT scanners allowed the diffusion of ^{18}F-NaF for skeletal system imaging. The ^{18}F can be produced via the ^{18}O-^{18}F nuclear reaction using a cyclotron. Subsequently, the ^{18}F is eluted with sodium chloride into the collection vial. This solution is passed through a sterile filter into a sterile dose vial, before to be released for quality control [2].

5.2 Pharmacokinetics

The ^{18}F-NaF kinetics is quite useful for imaging. After the intravenous injection, the tracer is rapidly cleared out from the blood pool and it forms fluoroapatite crystals by chemo-adsorption to the hydroxyapatite crystals in the extracellular bone matrix. Due to its low molecular weight (see molecular structure in Fig. 5.1), ^{18}F-NaF exhibits a very fast blood clearance with rapid osseous uptake, fast elimination from soft tissues, with high signal to background contrast, and a rapid renal excretion. The tracer uptake is based on the fluoride exchange, forming fluorapatite at the surface of the bone crystals, especially at sites with a high rate of bone remodeling. Subsequently, the fluoride ion migrates to the bone crystalline matrix.

Following suggestions by Hawkins et al. in 1992, a three-compartmental model can display the kinetic of ^{18}F-NaF in the human body: the first constant is the effective ^{18}F-NaF plasmatic fraction, the second is represented by the unbound bone fraction while the third constant is the bound bone mineral fraction [3].

Uptake is higher in osseous sites with physiological processes of remodeling as arthrosis or post-traumatic reparation or in bony neoplastic lesions. In fact, among the diverse stromal cell population, in the presence of a bone metastasis, the osteoblasts are shown to be an important player in the synthesis of a "*wall*" of extracellular bone matrix, to enclose the tumor and limit its growth. Therefore, PET/CT imaging with ^{18}F-NaF "in vivo" allows to track bone metastases, identifying the physiological deposition of extracellular bone crystalline matrix surrounding tumors (Fig. 5.2). This explains the high sensitivity of ^{18}F-NaF PET/CT in detecting bone metastases, even without corresponding morphologic abnormalities on the CT component of

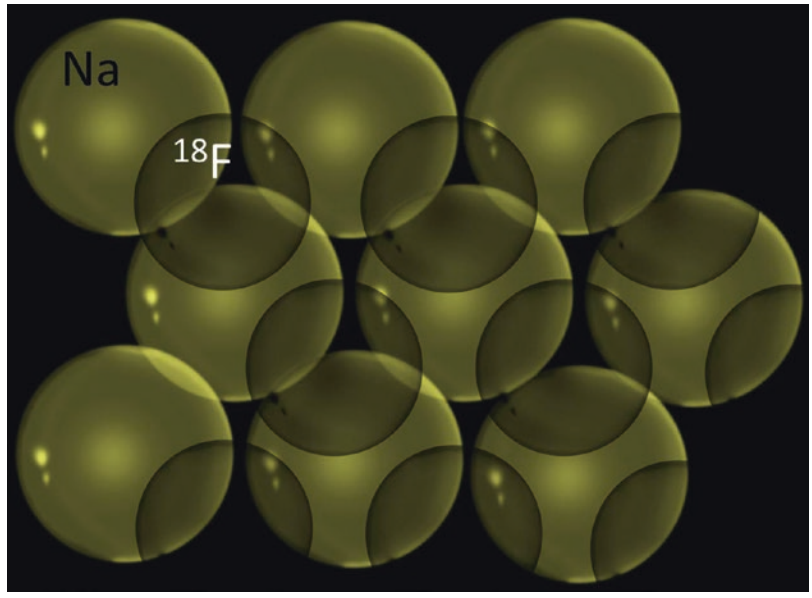

Fig. 5.1 ^{18}F-NaF molecular structure

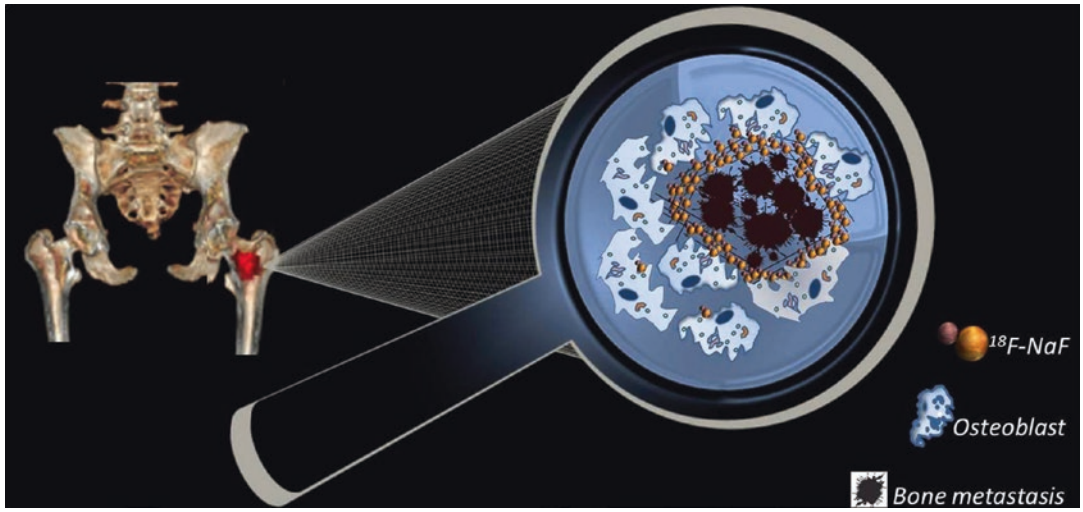

Fig. 5.2 Scheme of ^{18}F-NaF uptake in the remodeling bone tissue surrounding metastases

the exam, rather than bone scan with ^{99m}Tc-Methyldiphosfonate (^{99m}Tc-MDP) or ^{18}F-fluorodeoxyglucose (^{18}F-FDG) [4]. On the other hand, the molecular properties of the ^{18}F-NaF can lead in a lack of specificity and/or render difficult the recognition of the response to therapy. Generally, the tracer uptake depends on increased regional vascularity and increased bone turnover. The sclerotic bone metastases show high uptake while the lytic metastases display uptake around the lesion, due to the peripheral osteoblastic reaction.

5.3 Physiological Distribution

The physiological in vivo distribution of ^{18}F-NaF generally regards the entire skeletal system.

Normally, in the adult, the uptake is more pronounced in the skull, vertebrae, pelvis, and ribs while is evident a lower gradient of uptake in the appendicular skeleton (Fig. 5.3). Due to the renal excretion, kidneys, ureters, and bladder are normally visualized, with some inter-individual variability.

The ^{18}F-NaF distribution in soft tissues and parenchymatous organs is negligible [5]. Extraosseous calcifications can show ^{18}F-NaF uptake, as for calcium deposits in large arteries [6].

5.4 Clinical Indications

5.4.1 Bone Metastases

For the reasons expressed above, PET/CT with ^{18}F-NaF shows high sensitivity in the identification of bone metastases. The diagnostic accuracy is higher for sclerotic lesions rather than lytic ones [7]. Therefore, the main field of applications of this tracer is the diagnosis of bone metastases from prostate cancer, lung carcinoma, and mixed bony lesions of breast cancer.

In breast, prostate, and lung cancer patients, several studies have been elucidated a sensitivity of 100% for ^{18}F-NaF PET/CT in the diagnosis of bone metastases, also superior to bone scan with ^{99m}Tc-MDP and/or PET/CT with ^{18}F-FDG [8]. Regarding conventional bone scan, planar imaging often cannot provide meaningful information about lesion detection or anatomical localization and must be supplemented with SPECT or SPECT/CT to increase the diagnostic accuracy. On the other hand, ^{18}F-NaF PET/CT displays greater spatial resolution and better image quality in a shorter acquisition time, resulting in higher sensitivity [9]. Moreover, the CT component of the exam can accurately depict morphologic features of lesions, allowing a better specificity than planar bone scan. On this topic, we must also

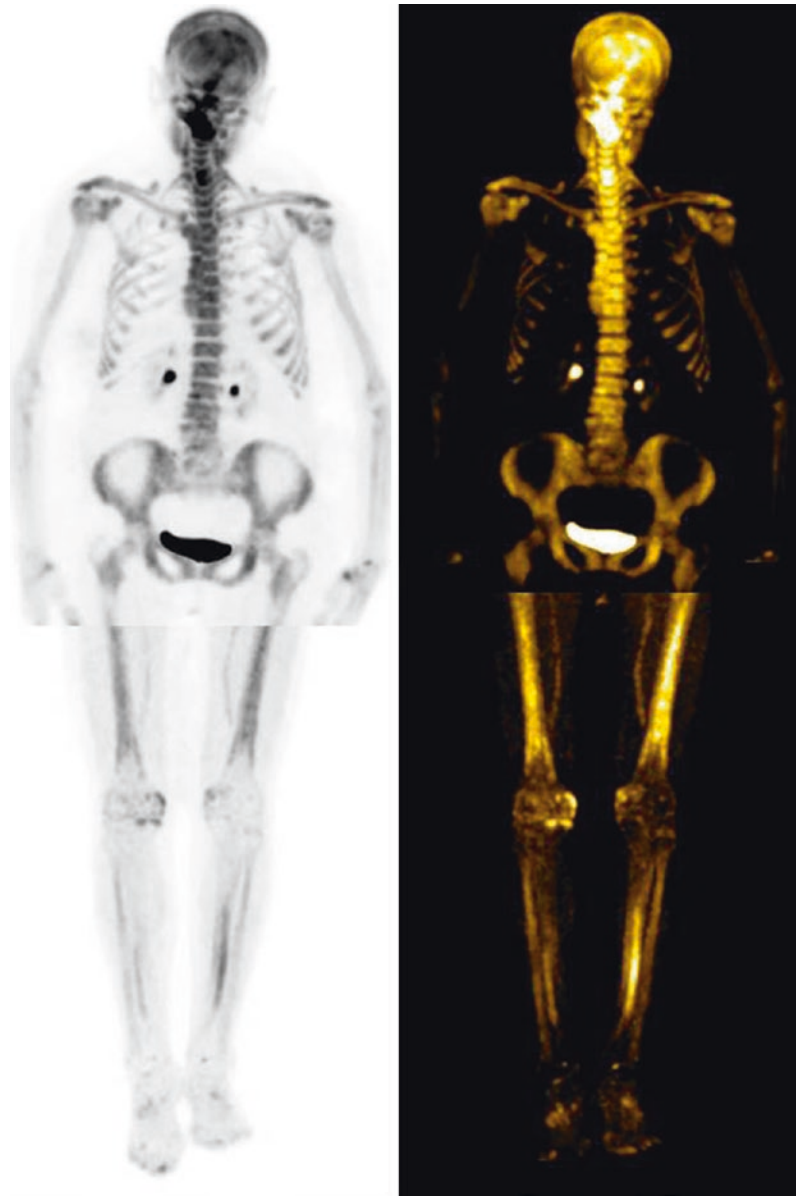

Fig. 5.3 Whole body PET maximum intensity projection of the physiological ^{18}F-NaF bio-distribution

consider the larger availability of hybrid PET/CT rather than SPECT/CT scanners.

PET/CT with ^{18}F-NaF shows superior diagnostic accuracy in detection of bone metastases, also in comparison with other radiopharmaceuticals, as radiolabeled choline in prostate cancer patients [10, 11]: in particular, it is known that, in patients undergoing antiandrogenic therapy, prostate cancer sclerotic lesions can occasionally show faint radiolabeled choline uptake [12] while this feature is not known for ^{18}F-NaF.

Despite a better sensitivity of ^{18}F-NaF in detecting bone metastases, in comparison with the most widely used PET tracers as ^{18}F-FDG and

(^{11}C-^{18}F)-choline, a limit of this tracer is also the inadequacy to depict other findings beyond osseous lesions. In fact, ^{18}F-FDG PET/CT allows to evaluate in a single session soft tissues, parenchymatous organs and bone involvement in patients with high grade of glucose metabolism tumors while radiolabeled choline simultaneously evaluates bone involvement, lymph nodal metastases, and local relapse, in prostate cancer patients. Therefore, the right moment to perform ^{18}F-NaF PET/CT is a matter of discussion. Standing to the current guidelines of the *European Association of Nuclear Medicine and Molecular Imaging* (EANM), ^{18}F-NaF PET/CT can be considered as a valid tool in the evaluation of primary bone malignancies such as osteosarcoma [13], in the assessment of metastatic bone disease, and in the evaluation of abnormal radiographic or laboratory findings [14].

In a recent study, 130 patients with suspicion of bone metastases were examined with ^{18}F-NaF PET/CT: in the large majority of these patients (114/130; 87.7%), at least an extra-skeletal abnormal finding was recorded on the CT component of the studies. In the population were recorded cases of intracranial hemorrhage, pneumothorax, pulmonary fibrosis, pericardial effusion, emphysema, and pulmonary, hepatic, and lymph nodal secondary lesions [15]. Thus, in the clinical practice of nuclear medicine physicians with ^{18}F-NaF PET/CT, it is important to achieve a good skill on the CT component of the exam in order to improve confidence in the differential diagnosis between secondary bone lesions and false positive cases of ^{18}F-NaF uptake in the bones and, in second instance, to globally evaluate extra-skeletal pathologic findings which can be observed at the CT and can occur in a significant minority of the examined patients (5%) [15].

As a future trend, several studies are demonstrating usefulness of ^{18}F-NaF PET/CT in the follow-up of castration resistant prostate cancer with skeletal metastases and in the evaluation of response to therapy with ^{223}Ra-dichloride (see also Chap. 10) [16, 17].

5.4.2 Benign Bone Disease

During the time, due to the specific affinity of ^{18}F-NaF for the skeletal system, a feasible role of this tracer in the management of bony benign lesions has been hypothesized. Several studies proposed the ^{18}F-NaF as a feasible agent in the depiction of bone degenerative or inflammatory diseases and in the evaluation of disease progression, as for spondylo-arthropathy in psoriatic arthritis [18], ankylosing spondylitis [19], avascular osteonecrosis [20], and Paget's disease [21].

Other studies focused the attention on orthopedic diseases as spondylolysis and spondylolisthesis and painful prosthetic joints [22, 23]. Naturally, in benign bone diseases, the physiological processes of bone remodeling are at the basis of tracer uptake. Anyway, the cited clinical indications are related to few studies or reports of a case. A strict collaboration between nuclear medicine physicians and clinicians as orthopedics specialists or rheumatologists should be recommended in order to avoid not useful scans, to verify clinical benefit, and to select patients who can really take advantage by a PET/CT with ^{18}F-NaF.

As future trends, initial reports are suggesting a feasible role of ^{18}F-NaF PET/CT in the evaluation of osteoid-osteoma in pediatric patients and in the sports medicine [24].

5.4.3 Forensic Use

Due to the extreme versatility of this tracer as marker of bone metabolism, recent studies are suggesting its possible role as PET tracer for forensic use, due to accurate diagnosis of injuries in cases of child abuse, especially when injuries are not associated with radiographically evident fractures [25]. In practice, the radiographic skeletal survey is the main diagnostic technique used for imaging suspected infant abuse, and the role of nuclear medicine is less well established. The ^{18}F-NaF PET/CT can potentially allow to detect the presence of bone fractures or injuries not evident on skeletal radiographic surveys [26].

5.5 Clinical Cases

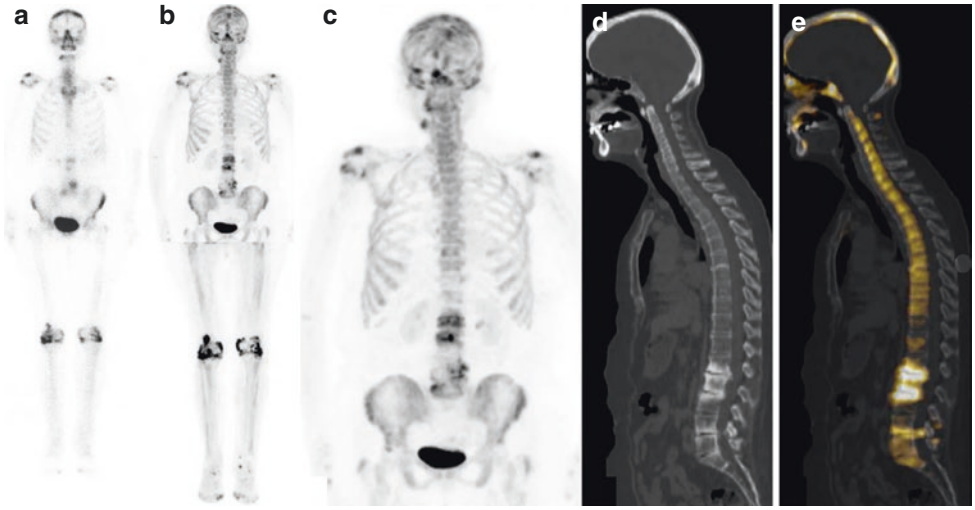

Fig. 5.4 In patient previously treated for breast cancer and submitted to radiotherapy for bone metastases in the lumbar spine, the whole body ^{99m}Tc-MDP bone scan (**a**) displays diffuse tracer uptake in the lumbar tract of the spine and in correspondence of arthrosis in both knees. The whole body 3D, PET maximum intensity projection with ^{18}F-NaF (**b, c**) better shows the uptake in the lumbar vertebrae, in association with vertebral, metastatic sclerotic lesions in sagittal CT (**d**) and PET/CT (**e**) views. In the sagittal PET/CT view is also evident a further lesion, misdiagnosed at bone scan, in the spinous process of the epistropheus

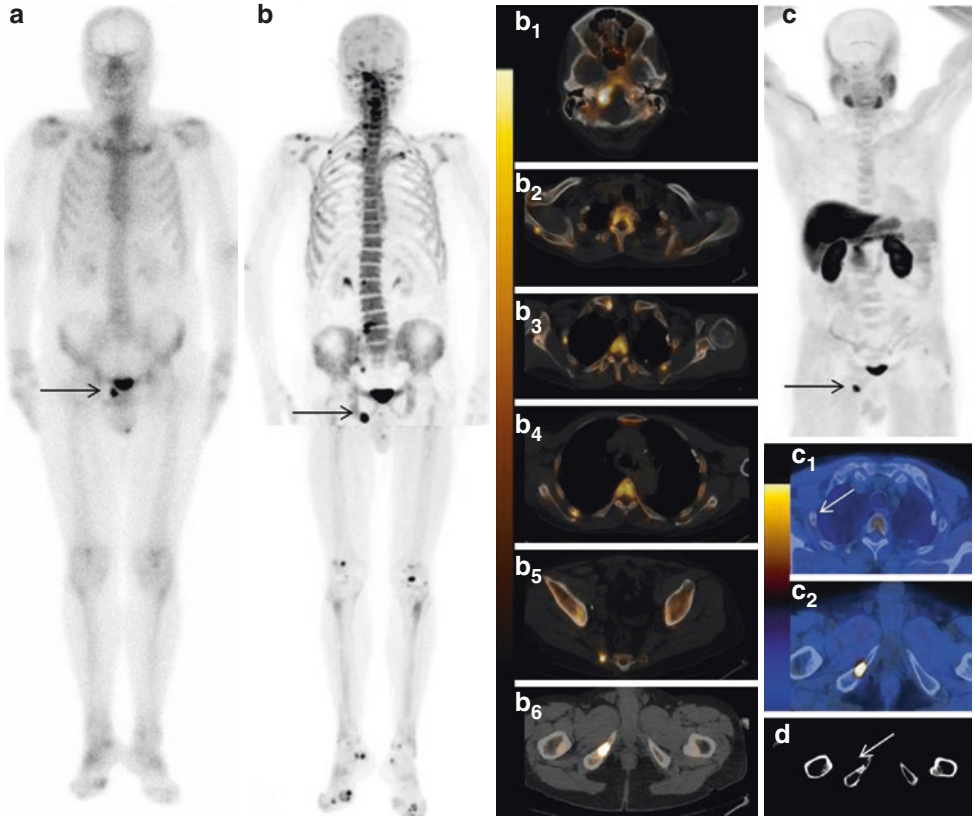

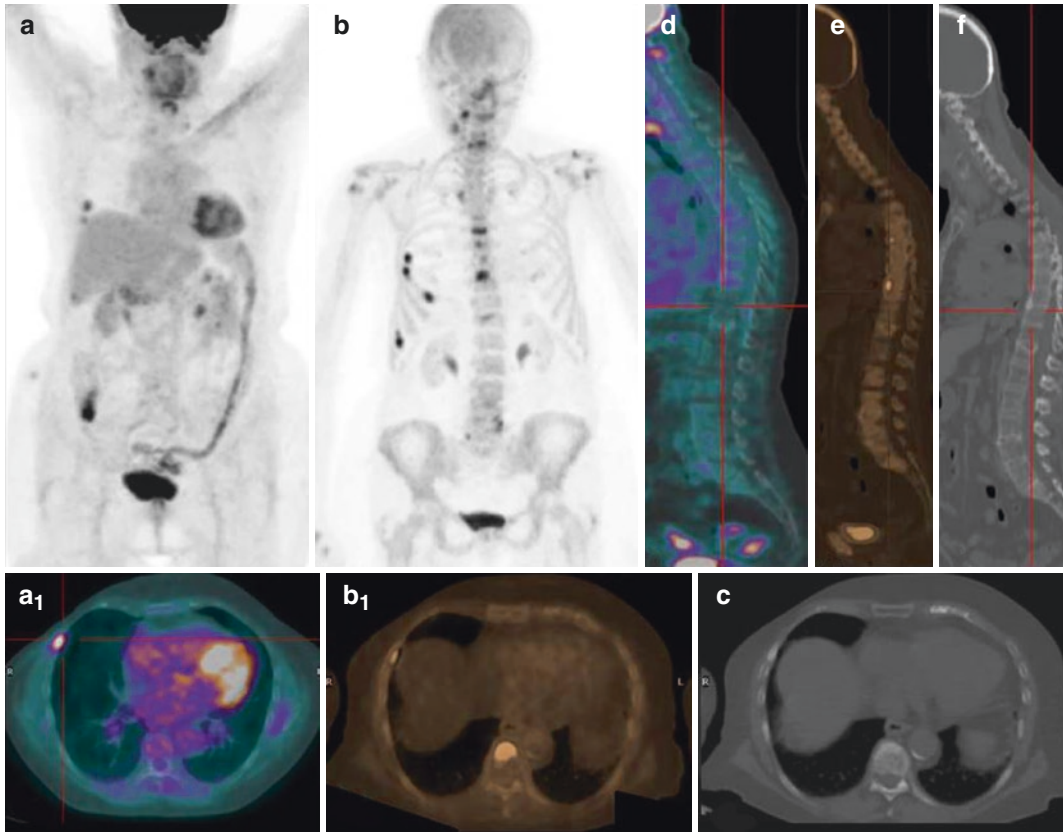

Fig. 5.6 A 64-year-old woman, previously submitted to surgery and chemotherapy for breast cancer, was examined with both ^{18}F-FDG and ^{18}F-NaF PET/CT. ^{18}F-FDG 3D PET maximum intensity projection and axial ^{18}F-FDG PET/CT (**a**, **a$_1$**) shows focal uptake in two ribs in the right hemithorax. ^{18}F-NaF 3D PET maximum intensity projection (**b**) shows more lesions in the right hemithorax, and pathologic uptake in some vertebrae of the dorsal spinal tract, also evident in ^{18}F-NaF axial PET/CT (**b$_1$**). Sagittal ^{18}F-FDG PET/CT view of the spine (**d**) does not show significant findings while the sagittal ^{18}F-NaF PET/CT (**e**) view displays focal uptake in the eighth dorsal vertebra, in association with sclerotic lesion on the CT component of the exam (**f**, **c**)

Fig. 5.5 In a patient examined for early biochemical relapse of prostate cancer (PSA 1.4 ng/mL) 2 years following radical prostatectomy, the whole body ^{99m}Tc-MDP bone scan (**a**) shows a single area of focal uptake in the right pubic bone, suspicion for secondary. Instead, the whole body 3D, PET maximum intensity projection with ^{18}F-NaF (**b**), displays multiple sites of pathologic tracer uptake, in the atlas, right scapula, several vertebrae, ribs, sacrum, and right ileum, evident in ^{18}F-NaF PET/CT views (**b$_1$**–**b$_6$**). The same patient also undergone ^{18}F-choline PET/CT (**c**), confirming as ^{18}F-choline avid only two lesions, respectively, localized in the second right rib (**c$_1$**) and in the right ileum (**c$_2$**). Interestingly, only the two ^{18}F-choline avid lesions were also associated with sclerotic lesions on the CT (**d**)

5.6 PET/CT Acquisition Protocols

Whole body PET/CT: from the vertex of the skull to the feet. The arms may be by the sides for whole body imaging. No fasting or special patient preparation is needed for ^{18}F-NaF PET/CT. Only oral hydration is suggested to obtain a faster renal excretion and to optimize radiation exposure. The dose (185–370 MBq) should be administered as a bolus through a catheter inserted into a large peripheral vein. The whole body imaging starts 45–60 min after the injection (2–5 min per bed position, depending on the PET scanner). A low-dose CT (90 mA) is sufficient for the anatomical localization of bone findings. Being the exam focused on the skeleton, routinely iodinate CT contrast media administration is not necessary [27].

Similar to ^{18}F-FDG PET/CT, maximum intensity projection (MIP) images should be generated to facilitate lesion detection.

5.7 Variants and Pitfalls

An important limit of ^{18}F-NaF in metastatic disease evaluation is the inherent mechanism of tracer uptake, not specific for tumor but primarily marker of an osteoblastic response. Therefore, it is important to consider the uptake in benign lesions, which can simulate malignant diseases.

Normally, the most common site of physiopathological uptake is represented by the osteoarthritis [28]. Nuclear medicine physicians must take into account this feature when approaching ^{18}F-NaF PET/CT for metastatic bone disease evaluation. The optimal knowledge of diagnostic CT criteria helps in this *panorama.* However, the high sensitivity of this tracer allows disease detection before the evidence of morphological lesions that can be radiologically observed. Therefore, the accurate collection of anamnestic data (*in particular for trauma and bone pain*) and a holistic clinical approach to the scan is recommended (Fig. 5.7).

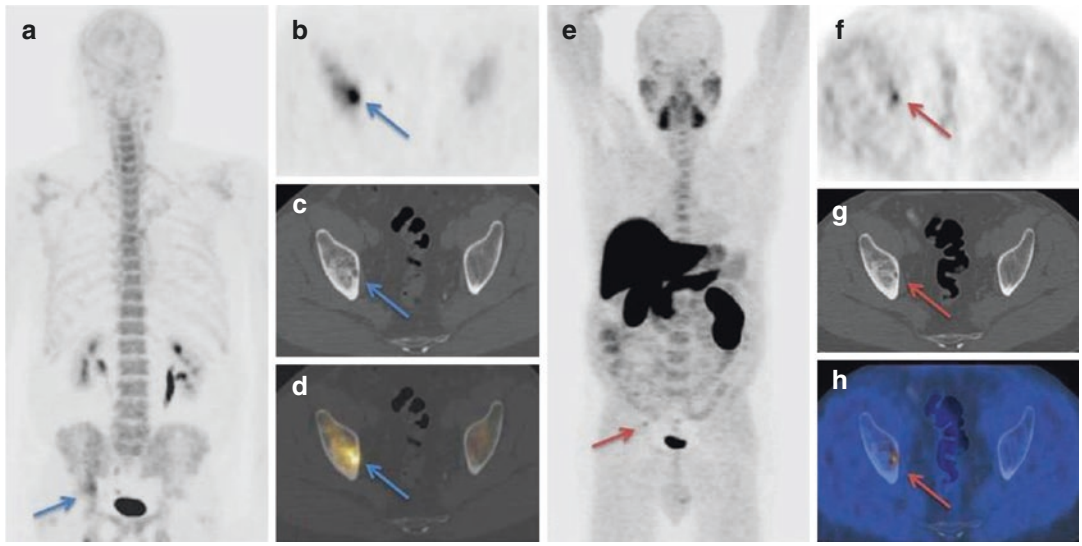

Fig. 5.7 A patient with early biochemical relapse of prostate cancer (PSA 0.8 ng/mL) after radical prostatectomy was examined by means of ^{18}F-NaF PET/CT and ^{18}F-choline PET/CT. The whole body, 3D, ^{18}F-NaF PET maximum intensity projection (**a**) and axial PET view (**b**) show a single area of focal tracer uptake in the right ischium, in association with geodic lesion, evident in corresponding CT (**c**) and PET/CT (**d**) views. The whole body ^{18}F-choline PET maximum intensity projection (**e**) and relative axial ^{18}F-choline PET, CT, and PET/CT views (**f**, **g**, **h**) confirm as ^{18}F-choline-avid the lesion. The low PSA serum level, the peri-articular site of the uptake, and the hypodensity of the lesion were not congruous with a secondary prostate cancer metastasis. The findings of both tracers were considered as false positive in a site of arthrosis. This suspicion was confirmed at clinical follow-up

^{18}F-NaF uptake is frequent in osteoarthritis, as well as for rheumatoid arthritis [29] and inflammation [30]. It has also been considered a possible application of this radiopharmaceutical in the evaluation of atheromatous plaques and in the study of calcific plaque versus the vulnerable carotid atheroma [31] or in study connection between atherosclerotic plaque and trabecular bone degeneration [32].

A possible role of ^{18}F-NaF PET/CT has been hypothesized in the diagnosis and monitoring of osteoporosis. Currently, osteoporosis and other metabolic bone diseases are evaluated primarily through X-rays; ^{18}F-NaF PET/CT can provide a molecular perspective with respect to the underlying metabolic alterations that lead to osseous disorders, by measuring bone turnover through standardized uptake value (SUV). Its sensitivity and ability to examine the entire skeletal system support its superior imaging quality compared to standard structural imaging techniques [33]. However, further studies are needed to assess its accuracy in depicting the efficacy of therapy.

It is also known the possibility of ^{18}F-NaF uptake in calcifications of extra-skeletal tissues: in the brain, it has occasionally depicted ^{18}F-NaF uptake in calcific meningiomas [34] or postischemic lacunar areas [35]. Other sites of uptake can be represented by cardiac amyloidosis [36], lymphomas [37, 38], and myelomatosis [39]. Some authors support the use of ^{18}F-NaF in the evaluation of heterotopic ossification, a benign condition characterized by the abnormal formation of mature lamellar bone in extra-skeletal soft tissues [40].

Generally, we need to keep into consideration the possibility of ^{18}F-NaF uptake in all calcifications that can occur in benign or malignant diseases [41–43].

References

1. Blau M, Nagler W, Bender MA. Fluorine-18: a new isotope for bone scanning. J Nucl Med. 1962;3:332–4.
2. Hockley BG, Scott PJ. An automated method for preparation of [(18)F]sodium fluoride for injection, USP to address the technetium-99m isotope shortage. Appl Radiat Isot. 2010;68:117–9.
3. Hawkins RA, Choi Y, Huang SC, et al. Evaluation of the skeletal kinetics of fluorine-18-fluoride ion with PET. J Nucl Med. 1992;33:633–42.
4. Araz M, Aras G, Küçük ÖN. The role of 18F-NaF PET/CT in metastatic bone disease. J Bone Oncol. 2015;16:92–7.
5. Minamimoto R, Mosci C, Jamali M, et al. Semiquantitative analysis of the biodistribution of the combined ^{18}F-NaF and ^{18}F-FDG administration for PET/CT imaging. J Nucl Med. 2015;56:688–94.
6. Morbelli S, Fiz F, Piccardo A, et al. Divergent determinants of 18F-NaF uptake and visible calcium deposition in large arteries: relationship with Framingham risk score. Int J Cardiovasc Imaging. 2014;30:439–47.
7. Kawaguchi M, Tateishi U, Shizukuishi K, et al. 18F-fluoride uptake in bone metastasis: morphologic and metabolic analysis on integrated PET/CT. Ann Nucl Med. 2010;24:241–7.
8. Damle NA, Bal C, Bandopadhyaya GP, et al. The role of 18F-fluoride PET-CT in the detection of bone metastases in patients with breast, lung and prostate carcinoma: a comparison with FDG PET/CT and 99mTc-MDP bone scan. Jpn J Radiol. 2013;31:262–9.
9. Langsteger W, Rezaee A, Pirich C, et al. 18F-NaF-PET/CT and 99mTc-MDP bone scintigraphy in the detection of bone metastases in prostate Cancer. Semin Nucl Med. 2016;46:491–501.
10. Beheshti M, Rezaee A, Geinitz H, et al. Evaluation of prostate cancer bone metastases with 18F-NaF and 18F-fluorocholine PET/CT. J Nucl Med. 2016;57:55S–60S.
11. Beheshti M, Vali R, Waldenberger P, et al. Detection of bone metastases in patients with prostate cancer by 18F fluorocholine and 18F fluoride PET-CT: a comparative study. Eur J Nucl Med Mol Imaging. 2008;35:1766–74.
12. De Giorgi U, Caroli P, Burgio SL, et al. Early outcome prediction on 18F-fluorocholine PET/CT in metastatic castration-resistant prostate cancer patients treated with abiraterone. Oncotarget. 2014;15:12448–58.
13. Brenner W, Bohuslavizki KH, Eary JF. PET imaging of osteosarcoma. J Nucl Med. 2003;44:930–42.
14. Beheshti M, Mottaghy FM, Payche F, et al. (18)F-NaF PET/CT: EANM procedure guidelines for bone imaging. Eur J Nucl Med Mol Imaging. 2015;42:1767–77.
15. Guo HH, Moradi F, Iagaru A. Clinical significance of extraskeletal computed tomography findings on 18F-NaF PET/CT performed for osseous metastatic disease evaluation. Nucl Med Commun. 2016;37:975–82.
16. Kairemo K, Joensuu T. Radium-223-dichloride in castration resistant metastatic prostate Cancer-preliminary results of the response evaluation using F-18-fluoride PET/CT. Diagnostics (Basel). 2015;13:413–27.
17. Cook G Jr, Parker C, Chua S, et al. 18F-fluoride PET: changes in uptake as a method to assess response in bone metastases from castrate-resistant prostate cancer patients treated with 223Ra-chloride (Alpharadin). EJNMMI Res. 2011;7:4.

18. Tan AL, Tanner SF, Waller ML, et al. High-resolution [18F]fluoride positron emission tomography of the distal interphalangeal joint in psoriatic arthritis-a bone-enthesis-nail complex. Rheumatology. 2013;52:898–904.
19. Strobel K, Fischer DR, Tamborrini G, et al. 18F-fluoride PET/CT for detection of sacroiliitis in ankylosing spondylitis. Eur J Nucl Med Mol Imaging. 2010;37:1760–5.
20. Aratake M, Yoshifumi T, Takahashi A, et al. Evaluation of lesion in a spontaneous osteonecrosis of the knee using 18F-fluoride positron emission tomography. Knee Surg Sports Traumatol Arthrosc. 2009;17:53–9.
21. Chakraborty D, Mittal BR, Kamaleshwaran KK, et al. Urinary bladder carcinoma associated with Paget's disease of skull: imaging findings on Tc99m-MDP bone scintigraphy, F18-fluoride PET/CT and F18-FDG PET/CT. Indian J Nucl Med. 2011;26:42–3.
22. Ovadia D, Metser U, Lievshitz G, et al. Back pain in adolescents: assessment with integrated 18F-fluoride positron-emission tomography-computed tomography. J Pediatr Orthop. 2007;27:90–3.
23. Sterner T, Pink R, Freudenberg L, et al. The role of [18F]fluoride positron emission tomography in the early detection of aseptic loosening of total knee arthroplasty. Int J Surg. 2007;5:99–104.
24. Drubach LA. Pediatric bone scanning: clinical indication of (18)F NaF PET/CT. PET Clin. 2012;7:293–301.
25. Drubach LA, Sapp MV, Laffin S, et al. Fluorine-18 NaF PET imaging of child abuse. Pediatr Radiol. 2008;33(7):776–9.
26. Drubach LA, Johnston PR, Newton AW, et al. Skeletal trauma in child abuse: detection with 18F-NaF PET. Radiology. 2010;255:173–81.
27. Segall G, Delbeke D, Stabin MG, et al. SNM practice guideline for sodium 18F-fluoride PET/CT bone scans 1.0. J Nucl Med. 2010;51:1813–20.
28. Idolazzi L, Salgarello M, Gatti D, et al. 18F-fluoride PET/CT for detection of axial involvement in ankylosing spondylitis: correlation with disease activity. Ann Nucl Med. 2016;30:430–4.
29. Watanabe T, Takase-Minegishi K, Ihata A, et al. (18) F-FDG and (18)F-NaF PET/CT demonstrate coupling of inflammation and accelerated bone turnover in rheumatoid arthritis. Mod Rheumatol. 2016;26:180–7.
30. Quirce R, Martínez-Rodríguez I, Banzo I, et al. New insight of functional molecular imaging into the atheroma biology: 18F-NaF and 18F-FDG in symptomatic and asymptomatic carotid plaques after recent CVA. Preliminary results. Clin Physiol Funct Imaging. 2016;36:499–503.
31. Dweck MR, Chow MW, Joshi NV, et al. Coronary arterial 18F-sodium fluoride uptake: a novel marker of plaque biology. J Am Coll Cardiol. 2012;59: 1539–48.
32. Fiz F, Baucknehtt M, Piccardo A, et al. Metabolic and densitometric correlation between atherosclerotic plaque and trabecular bone: an 18F-Natrium-fluoride PET/CT study. Am J Nucl Med Mol Imaging. 2018;20:387–96.
33. Reilly CC, Raynor WY, Hong AL, et al. Diagnosis and monitoring of osteoporosis with 18F-sodium fluoride PET: an unavoidable path for the foreseeable future. Semin Nucl Med. 2018;48:535–40.
34. Cascini GL, Cuccurullo V, Mansi L. 18FNa-fluoride has a higher extraction with respect to 99mTc-methylene diphosphonate: mismatch in a case of meningioma. Rev Esp Med Nucl Imagen Mol. 2014;33:52–3.
35. Thenkondar A, Jafari L, Sooriash R, et al. 18F-NaF PET demonstrating unusual focal tracer activity in the brain. Clin Nucl Med. 2017;42:127–8.
36. Van Der Gucht A, Galat A, Rosso J, et al. [18F]-NaF PET/CT imaging in cardiac amyloidosis. J Nucl Cardiol. 2016;23:846–9.
37. Zheng W, Chen Y, Huang Z, et al. Burkitt lymphoma presented as acute lower Back pain and revealed by 18F-NaF PET/CT. Clin Nucl Med. 2016;41: e253–4.
38. Shao F, Wu J, Huang Z, et al. Serendipitous detection of Hodgkin lymphoma by 18F-NaF PET/CT. Clin Nucl Med. 2016;41:815–8.
39. Asmar A, Simonsen L, Svolgaard B, et al. Unexpected diffuse 18F-NaF uptake in the lung parenchyma in a patient with severe hypercalcemia due to myelomatosis. Clin Nucl Med. 2017;42:68–9.
40. Seraj SM, Al-Zaghal A, Østergaard B, et al. Identification of heterotopic ossification using 18F-NaF PET/CT. Clin Nucl Med. 2019;44:319–20.
41. Chou YH, Ko KY, Cheng MF, et al. 18F-NaF PET/CT images of cardiac metastasis from osteosarcoma. Clin Nucl Med. 2016;41:708–9.
42. Zou Y, Chen Y, Huang Z, et al. Elevated 99mTc-MDP and 18F-NaF uptake in a bladder stone. Clin Nucl Med. 2016;41:732–3.
43. Calabria F. Fifty shades of meningioma: challenges and perspectives of different PET molecular probes. Clin Transl Imaging. 2017;5:403–405.

6 Somatostatin Receptor Analogs (^{68}Ga-DOTATOC, ^{68}Ga-DOTANOC, ^{68}Ga-DOTATATE)

Luca Filippi, Patrizia Pizzichini, Oreste Bagni, and Francesco Scopinaro

Contents

Abbreviations

CT	Computed tomography
DOTA	1,4,7,10-tetraazacyclododecane-1,4,7,10-tetraacetic acid
FDG	^{18}fluorodeoxyglucose
MRI	Magnetic resonance imaging
NET	Neuroendocrine tumors
PET	Positron emission tomography
PRRT	Peptide receptor radionuclide therapy
SRS	Somatostatin receptor scintigraphy
US	Ultrasonography

L. Filippi (✉) · O. Bagni
Department of Nuclear Medicine, Santa Maria Goretti Hospital, Latina, Italy

P. Pizzichini · F. Scopinaro
Department of Nuclear Medicine, Sant'Andrea Hospital, Rome, Italy

6.1 Synthesis

^{68}Germanium (Ge)/^{68}Gallium (Ga) generators have been developed to allow fast and simple preparation of several ^{68}Ga-labeled radiopharmaceuticals [1]. A variety of monofunctional

F. Calabria, O. Schillaci (eds.), *Radiopharmaceuticals*,
https://doi.org/10.1007/978-3-030-27779-6_6

and bifunctional chelators can be used to obtain stable ^{68}Ga3+ complexes with various ligands. As a matter of fact, ^{68}Ga presents many advantages for imaging: an abundant positron emission, short half-life (i.e., 68 min), no need for on-site cyclotron.

The parent isotope (^{68}Ge) is produced in an accelerator using a variety of nuclear reactions and target materials [2]. The ^{68}Ge is isolated from the irradiated material and then used to load the generator. ^{68}Ge/^{68}Ga generator consists of a column in which ^{68}Ge is absorbed onto the solid matrix. The parent isotope (^{68}Ge) decays to the daughter (^{68}Ga) which is washed off with an appropriate eluent. The ^{68}Ga isotope, in turn, decays to 89% by positron emission with average energy of 740 KeV and 11% by electron capture.

The main drawbacks of ^{68}Ge/^{68}Ga generator are the large volume of the eluate and the amount of metals as Fe, Zn, and Cu [3]. These metals can compete for the ligand and affect the performance during the DOTA-peptides preparation. Several methods have been proposed for concentration and purification of ^{68}Ga. The labeling of ^{68}Ga with peptides can be achieved by using the 1,4,7,10-tetraazacyclododecane-1,4,7,10-tetraacetic acid (DOTA). This bifunctional agent can bind the radiometal (i.e., ^{68}Ga) and still possess a reactive group for the covalent attachment to the peptides (i.e., octreotide) [4]. Initially, the labeling procedures were manually performed; afterwards, the introduction of automated robotic system for the ^{68}Ga-DOTA-peptides labeling has greatly incentivized the routine application of these radiopharmaceuticals. After labeling and quality control (iTLC, HPLC, and pH), the radiopharmaceutical can be directly administered to patients.

Several ^{68}Ga-DOTA-peptides have been obtained; the 3 compounds commonly used for PET imaging are ^{68}Ga-DOTA-Phe1-Tyr3-Octreotide (TOC), ^{68}Ga-DOTA-NaI3-Octreotide (NOC), and ^{68}Ga-DOTA-Tyr3-Octreotate (TATE) [5].

These molecules present few differences in structural formula (Fig. 6.1) but all are characterized by high receptor-mediated uptake in somatostatin receptor (SSTR) positive tumors. SSTRs are G-protein coupled transmembrane receptors and are internalized after binding to the specific ligand. There are five subtypes of SSTRs: SSTR2 are the most common subtype overexpressed in neuroendocrine tumors (NETs) [6]. All ^{68}Ga-DOTA-peptides can bind to SSTR2 but ^{68}Ga-DOTANOC presents an additional affinity for SSTR3. Furthermore, it has been reported that the affinity of DOTATATE in binding SSTR2 is tenfold higher than that of octreotide [7].

6.2 Pharmacokinetics

All the ^{68}Ga-DOTA-peptides present rapid uptake kinetics. During the first 4 h after injection, the 15.6% and 11.9% of injected activity were excreted to urine for ^{68}Ga-DOTATOC and ^{68}Ga-DOTATATE, respectively. It has been reported that 60–180 min after injection, the highest tracer uptake is in the spleen, followed by kidneys and liver. Furthermore, maximal tumor activity accumulation is reached 70+/−20 min post injection, thus allowing a fast imaging protocol in agreement with the short half-life of ^{68}Ga [8]. Clearance from liver and kidneys is rapid for all the ^{68}Ga-DOTA-compounds.

6.3 Physiological Distribution

The biodistribution of ^{68}Ga-DOTA-peptides includes physiological tracer uptake in pituitary gland, spleen, liver, kidneys, and in the urinary tract (Fig. 6.2). Furthermore, ^{68}Ga-DOTATOC

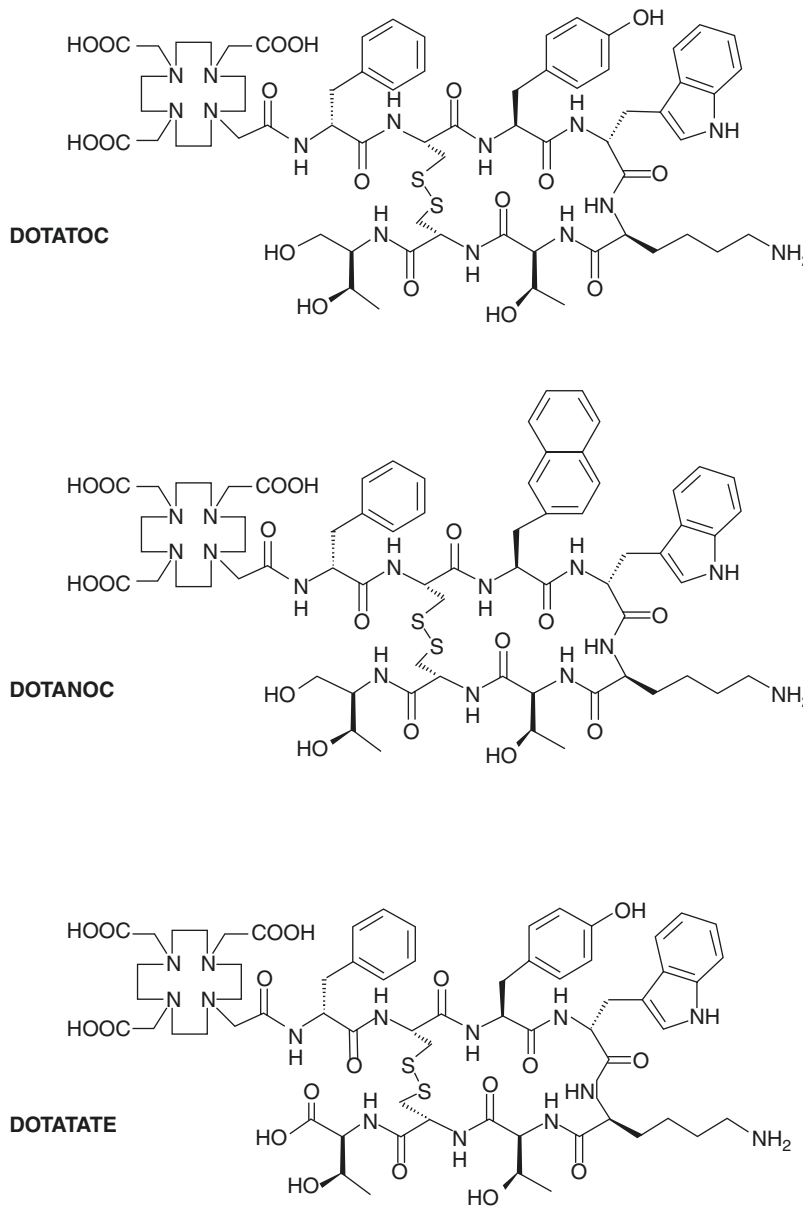

Fig. 6.1 Chemical formula of the three ^{68}Ga-DOTA-compounds

benign uptake has been described in the uncinate process of the pancreas [9]. Variable physiologic uptake is observed in the small and large bowel and in the stomach. Gallbladder, which is often visualized in the ^{111}In-pentetreotide scintigraphy, is rarely evident at PET with ^{68}Ga-DOTA-peptides. It is worthy of note that SSTR2 are expressed by activated lymphocytes and by the macrophages, thus all the ^{68}Ga-DOTA-peptides can be concentrated by the active phlogistic sites [10].

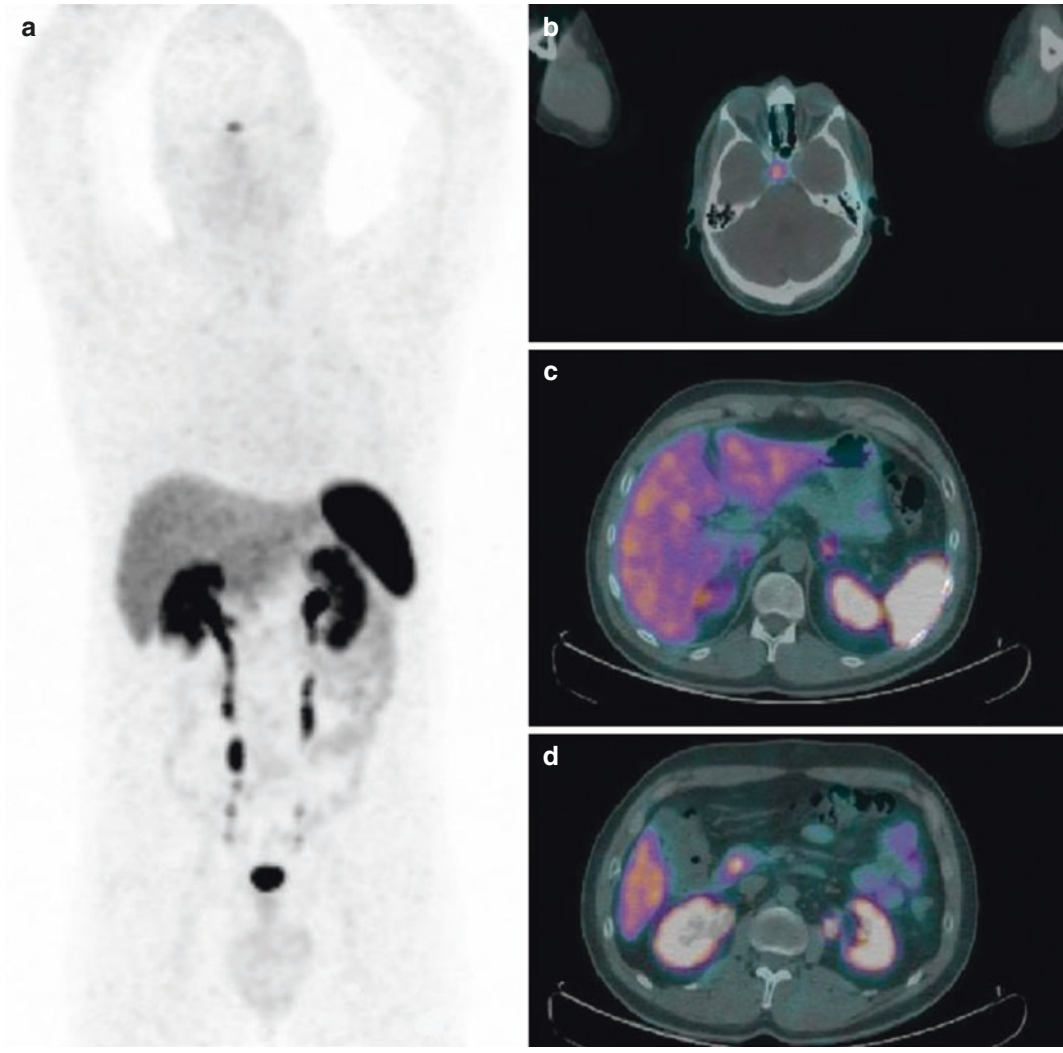

Fig. 6.2 Maximum intensity projection (MIP, **a**) showing the physiological biodistribution of ^{68}Ga-DOTANOC. Note the physiological uptake in the pituitary (**b**) and adrenal glands (**c**) and in the uncinate process of the pancreas (**d**)

6.4 Indications

6.4.1 Diagnosis, Staging, and Restaging of NET

Neuroendocrine tumors (NETs) are a heterogeneous group of rare neoplasms originating from the neural crest. The incidence of these tumors is approximately of 5/100,000 per year and the most frequent sites are the gastrointestinal tract (62–67%) and the lungs (22–27%). More rarely, they may be found in the anterior pituitary gland (pituitary adenomas), thyroid (medullary carcinoma), parathyroid, adrenals (pheochromocytoma), skin, and prostate. According to the classification published by the World Health Organization (WHO) NETs are classified as follows: (1) well-differentiated neuroendocrine tumor; (2) well-differentiated neuroendocrine carcinoma; (3) poorly differentiated neuroendocrine carcinoma; (4) mixed exo-endocrine carcinomas; (5) tumor-like lesions [11].

According to their biological behavior, NETs are usually divided into "functioning" and

"non-functioning" forms; "functioning" NETs produce and release into the blood flow a wide range of biologically active peptides that can cause distinct clinical syndromes. Thus, also very small NET producing hormones can cause an impressive symptomatology. On the contrary, the "non-functioning" NETs often present a late diagnosis since they cause symptoms only due to the mass-effect. The biological mediators (i.e., chromogranin, serotonin, bradykinin, histamine, VIP, gastrin, glucagon, insulin) produced by NETs may also be used as biomarkers for the diagnosis and/or the monitoring of the disease.

The routinely used workflow for diagnosis and staging includes several morphologic imaging modalities: contrast-enhanced computed tomography (CT), magnetic resonance imaging (MRI), transabdominal ultrasound (US), endoscopic US (EUS), and intraoperative US (IOUS). It is worthy of note that specific imaging protocols have been developed for the imaging of NETs with MR: the abdominal organs (i.e., pancreas and liver) should be examined with the "triple-phase scanning" [12]. Furthermore, recently published papers suggest that diffusion-weighted sequences may be of particular usefulness for the detection of small NET tumors and liver metastases [13].

Although ^{18}F-FDG-PET is widely used for diagnosis and staging of many tumors, several reports indicate that this imaging technique might be of limited usefulness in NETs, since they have a low proliferation rate and poor expression of glucose transporter (GLUT) receptors [14].

For many years, somatostatin receptor scintigraphy (SRS) with ^{111}In-pentetreotide has been used for diagnosis and staging of NETs. Nevertheless, it is well known that conventional scintigraphic imaging (i.e., planars and SPECT) presents low spatial resolution. To overcome this drawback, ^{68}Ga-DOTA-compounds have been developed for PET/CT imaging. PET is characterized by a higher spatial resolution; furthermore it allows a single-day procedure and the semiquantitative calculation of the activity in a region of interest with the "SUV" parameter.

An initial report in a limited number of patients suggested that ^{68}Ga-DOTATOC PET was superior to SRS in detecting small tumors or tumors bearing only a low density of SSTRs [15].

In a large cohort of subjects (n = 84) affected by NETs, Gabriel et al. [16] evaluated the role of ^{68}Ga-DOTATOC both for initial diagnosis/staging and follow-up. ^{68}Ga-DOTATOC PET presented a sensitivity of 97%, a specificity of 92%, and an accuracy of 96%; in particular, this imaging modality resulted in usefulness in 5 patients with suspicious of NET in which the unknown primary site was revealed by ^{68}Ga-DOTATOC PET but missed by CT. Moreover, ^{68}Ga-DOTATOC provided additional information that was obtained with none of the other imaging techniques in the 25% (21/84) of the examined subjects. This imaging modality resulted particularly useful to disclose small lesions in bones and lymph nodes. In another published study, in fact, ^{68}Ga-DOTATOC PET/CT was reported to detect secondary bone lesions from NETs better than CT and SRS [17].

PET with ^{68}Ga-DOTA-peptides has been shown to be a useful imaging technique in those patients with clinical or biochemical suspicious of NET but with equivocal or non-conclusive findings at the conventional imaging (contrast-enhanced CT or MRI). Haug et al., in fact, analyzed the role of ^{68}Ga-DOTATATE PET/CT in 104 consecutive patients with biochemical (n = 49), clinical (n = 70), or imaging-based (n = 53) suspicious of NETs [18]. Among the 104 subjects, NET was histologically verified in 36 cases. ^{68}Ga-DOTATATE PET/CT was able to diagnose NET in 29 of these 36 cases, thus having a sensitivity of 81% and specificity of 90%.

There is a growing amount of scientific data confirming the high diagnostic accuracy of PET with ^{68}Ga-DOTA-peptides for the imaging of NETs. In a recently published paper, Treglia et al. performed a meta-analysis of 16 studies including 567 subjects affected by gastroenteropancreatic and thoracic NETs. The sensitivity and specificity of PET imaging with ^{68}Ga-DOTA-compounds resulted of 93% and 91%, respectively [19]. Furthermore, ^{68}Ga-DOTATOC was reported to have the highest value of sensitivity and specificity (92–100% and 83–100%, respectively) when compared to the other ^{68}Ga-DOTA-peptides.

As regards the head-to-head comparison of the different PET tracers, Kasabasakl et al. evaluated the results of ^{68}Ga-DOTATATE and ^{68}Ga-DOTANOC in the same patients' population [20]. On visual evaluation both tracers had similar biodistribution with excellent quality of the images and the diagnostic accuracy for the 2 compounds was comparable although ^{68}Ga-DOTATATE presented higher tumor concentration. Nevertheless, different results were obtained by Wild and colleagues in 18 patients affected by NET and evaluated with ^{68}Ga-DOTANOC and ^{68}Ga-DOTATATE: the lesion-based sensitivity of ^{68}Ga-DOTANOC PET was 93.5%, while that ^{68}Ga-DOTATATE PET was 85.5% (p = 0.005) [21]. In particular, ^{68}Ga-DOTANOC revealed a greater number of liver metastases. It has to be pointed out that no difference was registered as regards tumor differentiation grade; thus, the authors concluded that ^{68}Ga-DOTANOC, having a more wide range of affinity for SSTRs (SSTR2,3,5), may detect more lesions than the SSTR2-specific radiotracer ^{68}Ga-DOTATATE.

These inhomogeneous data gave no clear idea of which ^{68}Ga-DOTA-peptide might have the best performance for PET imaging. It is reasonable to hypothesize that the discordant results reported in literature might be explained by the different subtypes of receptors individually expressed by NETs.

6.4.2 Selection for Therapy

The identification of SSTRs expression by using PET or SPECT tracers represents a crucial step for selecting patients affected by NET and eligible for treatment with somatostatin analogs. It has been demonstrated, in fact, that the grade of ^{68}Ga-DOTA-peptide uptake (SUV max) is strictly correlated with the in vivo SSTRs expression detected by the reverse polymerase-chain reaction [22].

Treatment with somatostatin analogs can be really effective for controlling the symptoms due to the hormones released by NETs (i.e., the so-called "carcinoid syndrome"); furthermore, it has been demonstrated that therapy can also present an antiproliferative effect.

After diagnosis, the grade of uptake of ^{68}Ga-DOTANOC can be considered for predicting patients' outcome. Campana and colleagues have investigated the role of maximum standardized uptake value (SUVmax) as a prognostic factor in 47 patients affected by NETs [23]. At statistical analysis, the authors found that significant well-differentiated NET, a SUVmax of 19.3 or more, and a combined treatment with long-acting somatostatin analogs were all significant prognostic factors.

Patients with positive SSTRs tumors can be enrolled for peptide receptor radionuclide therapy (PRRT) with radiolabeled somatostatin analogs. The rationale of PRRT is to achieve the selective irradiation of tumor cells over-expressing SSTR2 with minimal damaging of the normal parenchyma. Two radiolabeled compounds have been developed to this end: ^{90}Y-DOTATOC and ^{177}Lu-DOTATATE [24]. The selective criterion to enroll patients for PRRT is the demonstration of SSTR2 expression by ^{111}In-pentetreotide scintigraphy or ^{68}Ga-DOTA-compounds PET. PRRT is administered systemically in multiple cycles up to the maximum administrable activity or to the dose limit of 25 Gy to the kidney which is the dose-limiting organ. To reduce the irradiation of the kidneys, patients are usually co-infused with cationic amino acids before and after PRRT [25].

However, PRRT is not the only therapeutic options for NETs. Chemotherapy is also possible, both for high-grade and low-grade tumors, and mTOR inhibition with everolimus has been applied with good antiproliferative effect [26]. Thus, it would be really desirable to identify those patients with higher probability of response to PRRT. In a recently published paper, Kratochwill et al. evaluated if the initial SUV and several other semiquantitative parameters (tumor-to-spleen ratio and tumor-to-liver ratio) are correlated with the objective radiological response

after 3 cycles of PRRT. The authors found that a SUVmax cutoff >16.2 at ^{68}Ga-DOTATOC PET can be considered to select patients suitable for PRRT [27].

6.4.3 Assessment of the Response After Treatment

The potential role of PET with ^{68}Ga-DOTA-peptides for evaluating tumor response after treatment still remains a few explored issues.

Gabriel and colleagues found that PET with ^{68}Ga-DOTATOC provided no additional advantages as compared with conventional imaging (MR/CT) for assessing treatment response in NET after PRRT. In particular, the authors pointed out that SUV analysis of the single lesions was not of additional usefulness for predicting patients' response.

These results are in disagreement with other reports. Haug et al. analyzed the prognostic role of PET with ^{68}Ga-DOTATATE in 33 subjects affected by NET, performing the imaging before and after the first cycle of PRRT [28]. The authors found that the decrease of SUV-derived parameter (i.e., tumor-to-spleen ratio: T/S) strongly correlated with patients' survival. The tumor-to-spleen ratio, calculated on the ^{68}Ga-DOTANOC PET, has been recently found to be a useful predictor in patients affected by NET liver metastases submitted to loco-regional treatment with ^{90}Y-spheres [29].

6.4.4 Tumors Other than Pulmonary and Gastrointestinal NETs

PET/CT with ^{68}Ga-DOTA-compounds can be of great value also for the diagnosis and the follow-up of tumors other than NETs.

In particular, paragangliomas and pheocromocytomas, deriving from neuroectodermal tissue, have been demonstrated to express SSTRs. Although ^{123}I-metaiodo-benzylguanidine (MIBG) scintigraphy has represented a well-established modality of imaging for both these tumors for many years, several published papers indicate that PET with ^{68}Ga-DOTATATE presents higher sensitivity and higher tumor-to-background score in patients with metastases from malignant neural crest tumors [30].

These results were further confirmed with ^{68}Ga-DOTATOC PET: in a series of 10 patients with extra-adrenal paragangliomas, PET presented higher sensitivity as compared to ^{123}I-MIBG scintigraphy, especially in case of lesions located in the head/neck region and in the bones [31].

Furthermore, it has to be pointed out that the assessment of SSTR expression by PET with radiolabeled somatostatin analogs is of utmost importance to identify those subjects who are eligible for PRRT.

6.4.5 Combined Use of ^{18}F-FDG and ^{68}GA-DOTA-Peptides

It is well known that NETs present a wide range of differentiation. While low-grade NETs do not show significant uptake of ^{18}F-FDG, high-grade tumors are often characterized by low SSTR expression and increased glucose turnover.

Several recently published papers suggest that combination of the 2 imaging modalities (i.e., PET with ^{18}F-FDG and ^{68}Ga-DOTA-peptides) can provide important prognostic information [32, 33].

In a series of 38 patients affected by NETs and submitted to both ^{68}Ga-DOTATATE and ^{18}F-FDG PET, the sensitivity of the former diagnostic technique resulted of 82% while that of latter was 66%. It is important to point out that the overall number of detected lesions was greater with the combined use of the 2 tracers [34]. It has been demonstrated, in fact, that in patients with multiple lesions, it may be found variable uptake of the metabolic and receptorial tracer at different lesion sites.

Panagiotidis and colleagues evaluated the clinical impact of the combined imaging in 104 patients affected by histopathologically proven NETs [35]. ^{68}Ga-DOTATATE and ^{18}F-FDG were

discordant in 65 subjects and concordant in 39; the first tracer had the most significant impact on the decision-making, since patients with positive SSTR expression were submitted to PRRT. The most frequent decision based on ^{18}F-FDG was the initiation of chemotherapy. The authors found that ^{18}F-FDG presented no significant impact in the clinical management of G1 NETs and moderate impact in the G2 tumors.

In view of these considerations, the combined functional imaging with the metabolic and receptorial tracers may be of value for the in vivo imaging of NET heterogeneity and to select the more appropriate therapeutic approach.

6.5 Clinical Cases

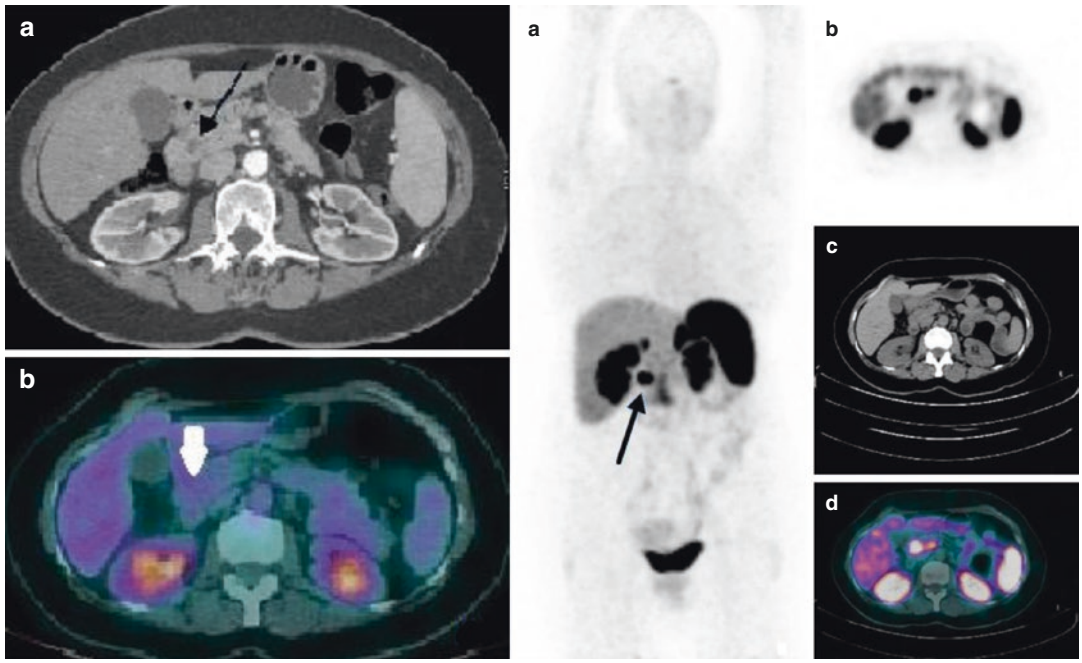

Fig. 6.3 Representative example of a patient with negative ^{18}F-FDG findings and positive ^{68}Ga-DOTANOC PET. (**a**) Patient submitted to multi-slice CT which detected a lesion in the pancreas head with fluid/solid mixed content and maximum diameter = 14 mm (**a**, black arrow). This lesion did not show any significant accumulation of ^{18}F-FDG in the corresponding fused PET/CT transaxial slices (**b**, white arrow). (**b**) In the same patient, PET ^{68}Ga-DOTANOC was performed. MIP imaging (**a**) showed focal and intense tracer uptake in the upper abdomen (black arrow). The corresponding emissive PET (**b**), non-enhanced CT (**c**) and transaxial fused PET/CT slices (**d**) demonstrated that the area of focal uptake was located in the pancreas head. Patient was submitted to US-endoscopy and biopsy that confirmed the presence of pancreatic NET

Fig. 6.5 Representative example of a patient with discordant ^{18}F-FDG and ^{68}Ga-DOTANOC PET findings. (**a**) ^{18}F-FDG PET/CT was performed in a patient with diagnosis of tumor mass of the *right pulmonary hilum* and hepatic lesion in the VIII-VII segment. MIP imaging (**a**) showed intense tracer uptake in the lung tumor (long black arrow) and in the liver (short black arrow), as well demonstrated by the fused PET/CT slices (**c**, **d**). Furthermore, bone localization in the left humerus was detected. Biopsy of the hepatic lesion was positive for metastasis from tumor of neuroendocrine origin. (**b**) Patient was submitted to ^{68}Ga-DOTANOC PET/CT to assess somatostatin receptor expression. MIP (**a**) and fused PET/CT transaxial slices (**c**) demonstrated mild uptake of the tracer in the pulmonary lesion (**c**) while definitely no uptake was detected in the liver metastasis (**d**)

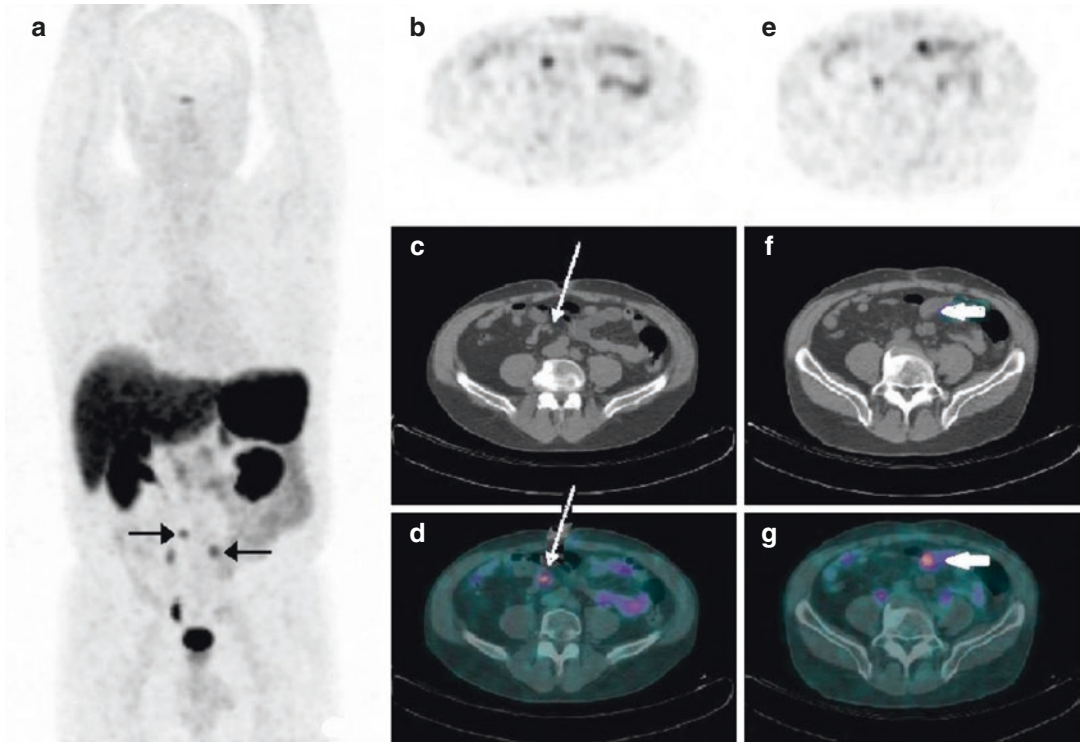

Fig. 6.4 Patient submitted to surgery due to colorectal carcinoma. At post surgery histologic examination, one of the excised nodes resulted positive for NET localization. Preoperative whole body multi-slice CT scan detected the colorectal tumor but missed to identify the site of the primary NET. ^{68}Ga-DOTANOC MIP imaging (**a**) revealed two areas of focal uptake in the abdomen (black arrows); the correspoding emissive PET (**b**, **e**), non-enhanced CT (**c**, **f**) and fused PET/CT transaxial slices (**d**, **g**) revealed focal uptake of the tracer in the small bowel (white short arrow) and in a mesenteric node (white long arrow). New surgery performed after the PET scan confirmed the diagnosis of well-differentiated NET of the ileum with node metastasis

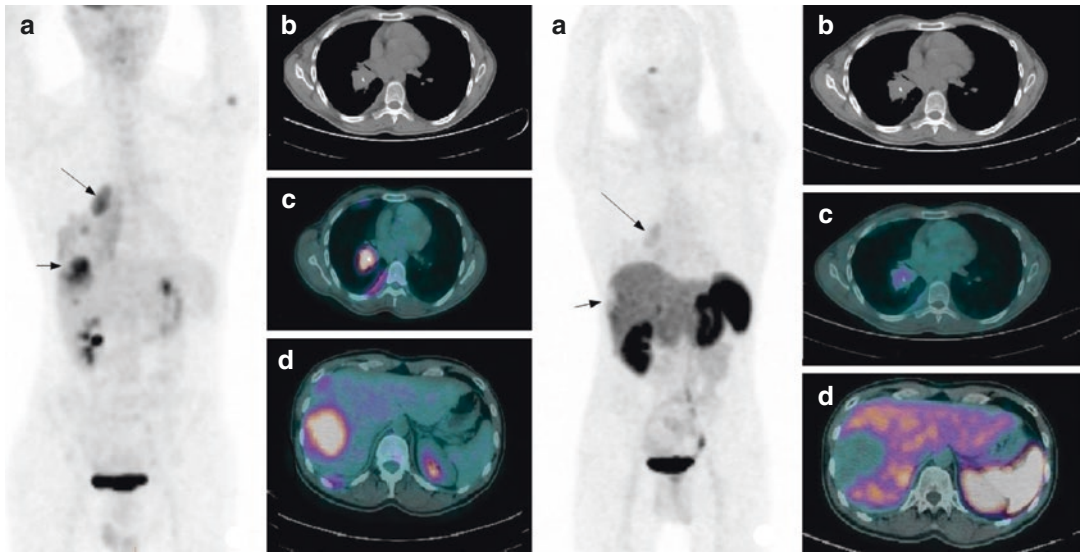

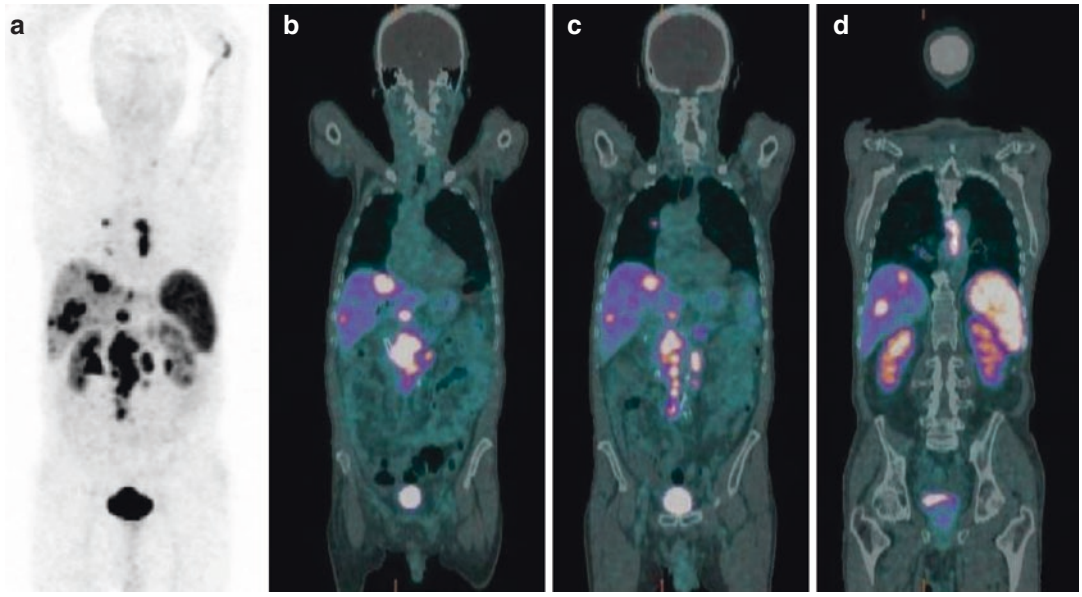

Fig. 6.6 Patient submitted to surgery for ileal NET with subsequent disease progression. ^{68}Ga-DOTANOC PET/CT showed multiple areas of tracer uptake in the liver and in mediastinal and abdominal nodes as evident in the MIP (**a**) and in the fused PET/CT coronal slices (**b**–**d**)

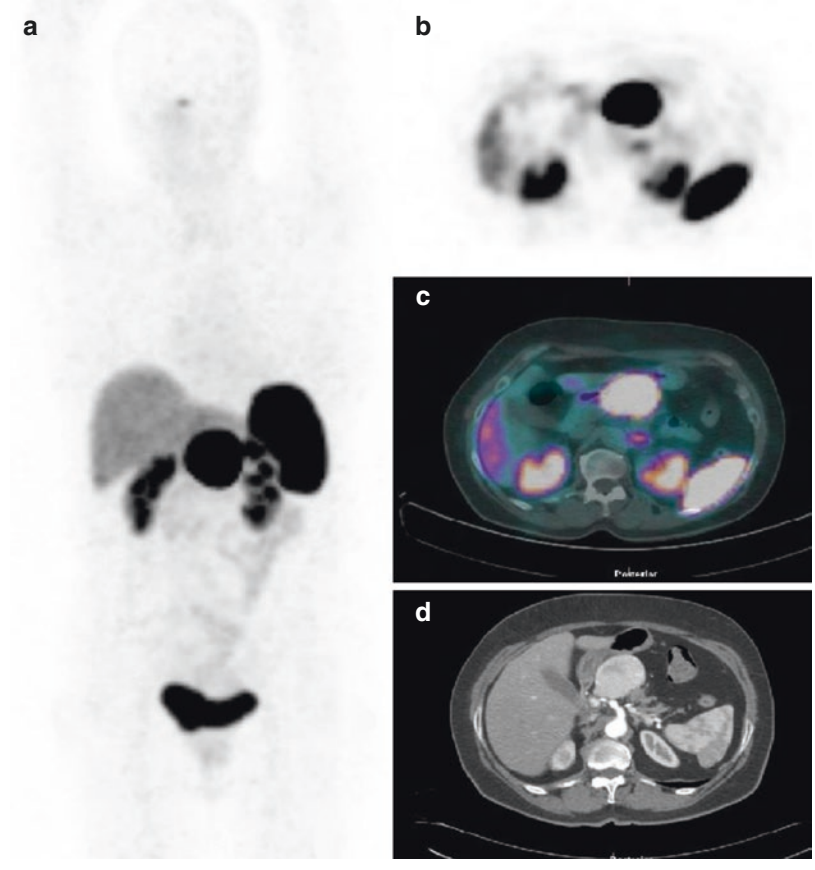

Fig. 6.7 Patient affected by cutaneous melanoma, submitted to preoperative CT scan. CT examination detected a highly vascularized gross tumor mass in the body part of the pancreas. Due to the suspicious of neuroendocrine tumor, ^{68}Ga-DOTANOC PET/CT was performed. MIP (**a**) and transaxial PET (**b**) and PET/CT (**c**) images revealed intense tracer uptake in the pancreas tumor, consistent with the diagnosis of pancreatic NET, also confirmed by contrast-ehanced CT (**d**)

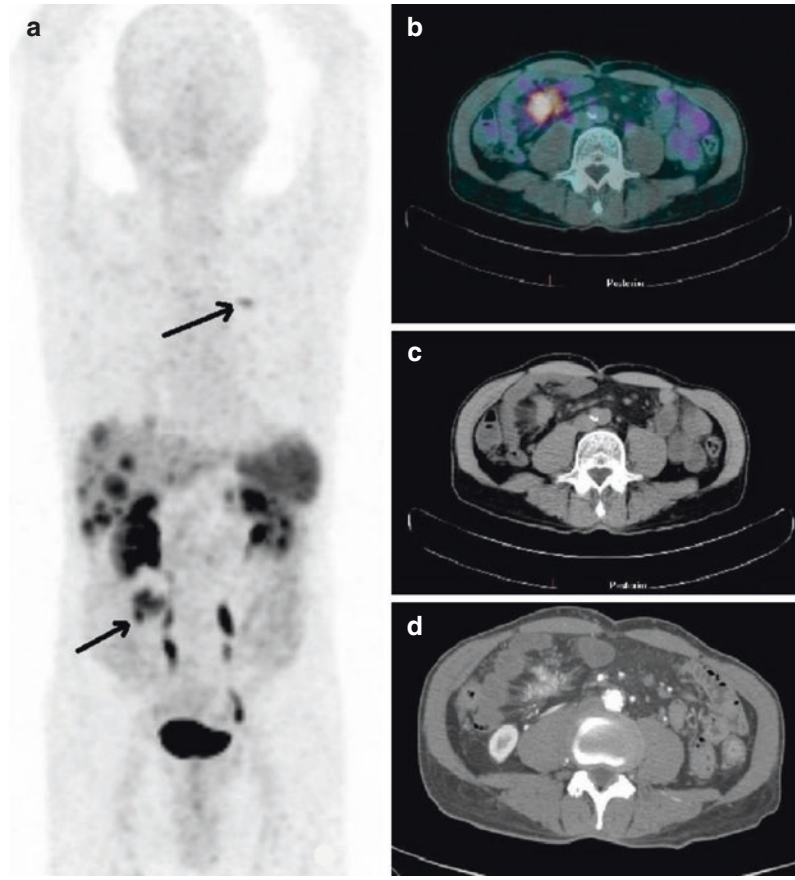

Fig. 6.8 Patient with multiple hepatic lesions submitted to biopsy. Histology was positive for metastases from tumor of neuroendocrine origin. ^{68}Ga-DOTANOC MIP (**a**) showed multiple area of tracer uptake in the liver, furthermore two additional focus of accumulation (black arrows) were detected in the abdomen and in the thorax, respectively. Fused PET/CT transaxial images demonstrated that the area in the abdomen was located in the mesenterial fat tissue next to the small bowel (**b**), while the focus in the thorax resulted to be a rib metastasis. The mesenteric lesion was also confirmed by non-ehanced (**c**) and ehanced (**d**) CT axial slices

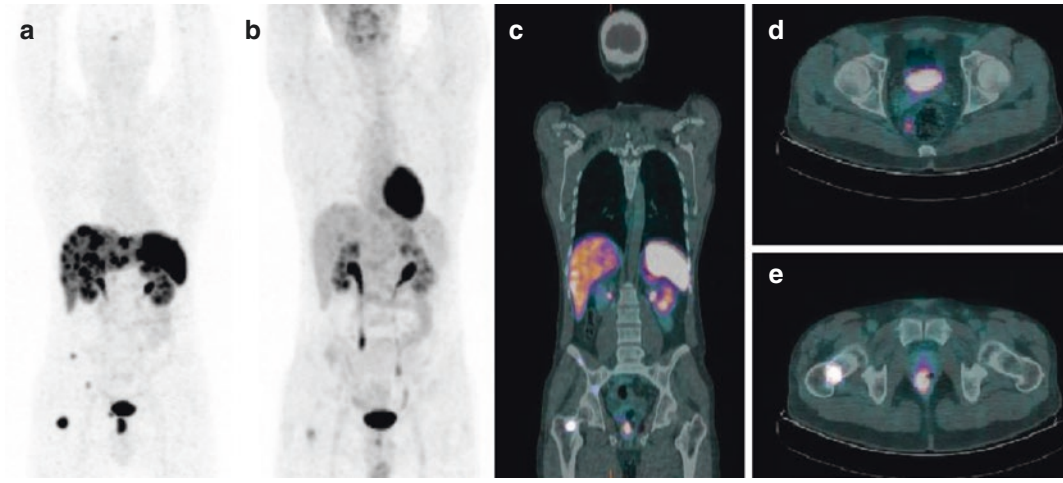

Fig. 6.9 Patient with a gross anal lesion, submitted to biopsy. Histology was positive for neuroendocrine tumor (G2). (**a**) ^{68}Ga-DOTANOC PET/CT was performed: MIP (**a**) showed intense tracer accumulation in the anal lesion along with multiple liver and skeletal (pelvis and right femur) lesions. ^{18}F-FDG PET/CT MIP (**b**) demonstrated mild tracer uptake in the bones with missed visualization of the other localizations detected by the ^{68}Ga-DOTANOC. same patient. ^{68}Ga-DOTANOC PET/CT fused coronal (**c**) and transaxial (**d**, **e**) images

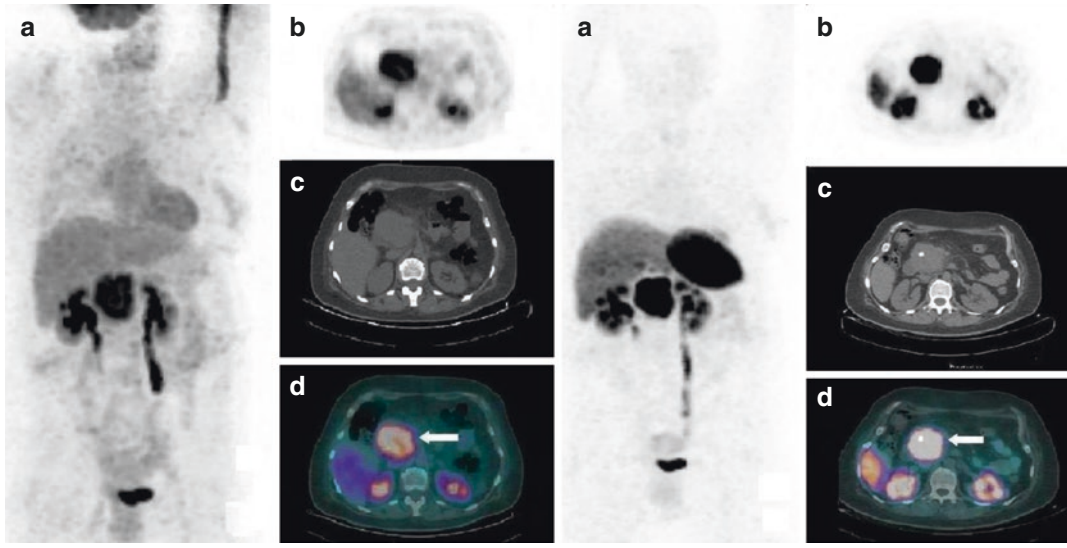

Fig. 6.10 Patient with occasional finding of a gross pancreatic mass during an US examination of the abdomen. (**a**) CT scan demonstrated a pancreatic mass (transverse diameter = 6 cm) containing areas of necrosis and calcifications. Patient was submitted to endoscopic ultrasonography (US)-guided fine-needle aspiration biopsy (FNAB). Cytology resulted positive for adenocarcinoma. ^{18}F-FDG PET/CT MIP (**a**) and fused transaxial images (**d**, arrow) showed intense tracer uptake in the pancreatic tumor. (**b**) The same patient was submitted to ^{68}Ga-DOTANOC PET/CT which demonstrated high somatostatin receptor expression in the pancreatic tumor mass, as shown by the MIP (**a**) and by non-ehanced CT (**c**) and fused PET/CT transaxial images (**d**, arrow). Patient underwent duodenocefalopancreasectomy and definitive histology was positive for NET (G2, pT3, Ki67 = 10%)

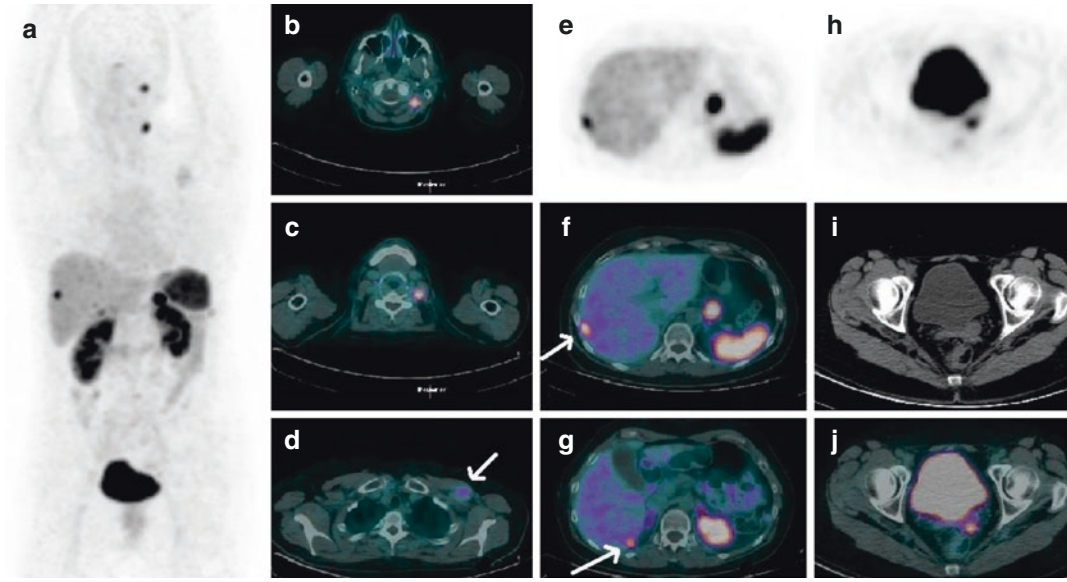

Fig. 6.11 ^{68}Ga-DOTANOC PET/CT in a female patient with metastatic pancreatic NET. MIP (**a**) and fused transaxial PET/CT images of the cervical, thoracic, abdominal, and pelvic regions are shown. Intense tracer accumulation is evident in cervical lymph nodes (**b**, **c**), in the pancreatic tail, in liver metastases (**e**, emissive and **f**, **g**, arrows, fused PET/CT axials), and in a pelvic peritoneal nodule (**h**, emissive; **i**, non-ehanced CT and **j** fused PET/CT axials). Furthermore, patient presented a mass in the left pectoral region which was characterized by mild ^{68}Ga-DOTANOC uptake. She underwent biopsy of one cervical node and of the pectoral mass. Biopsy was positive for NET metastasis in the former site while in the pectoral region histology revealed metastasis from breast cancer

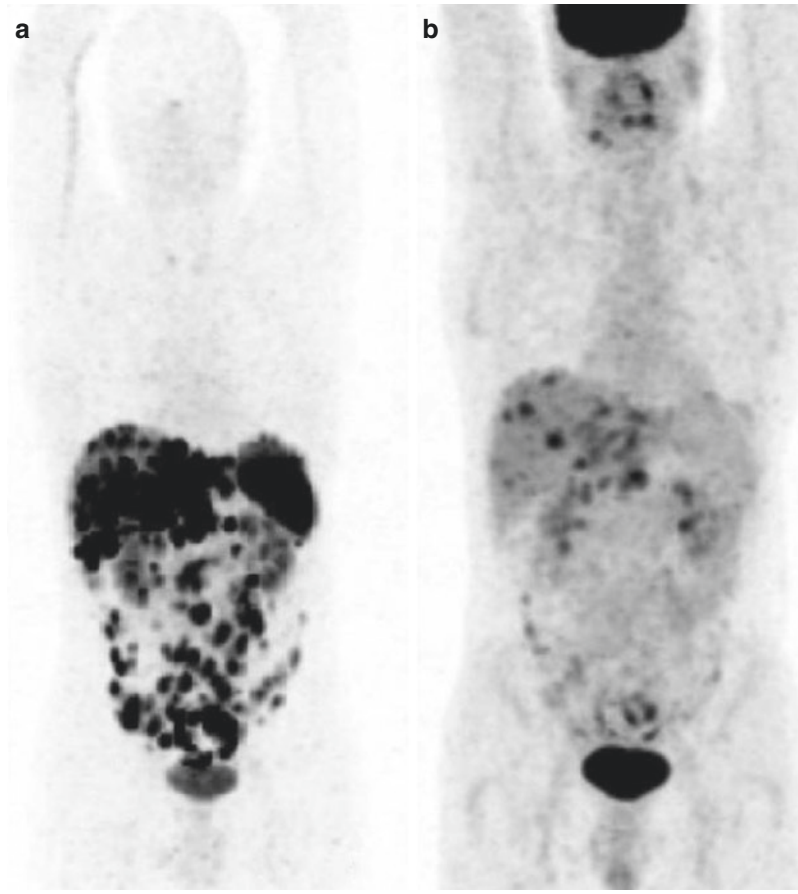

Fig. 6.12 Patient with metastatic NET. ^{68}Ga-DOTANOC PET/CT MIP (**a**), ^{18}F-FDG MIP (**b**). It is well evident that the localizations in liver, lymph nodes, and in the peritoneum are characterized by intense ^{68}Ga-DOTANOC uptake and low glucose turnover

6.6 PET/CT Acquisition Protocols

- **Administered dose**: 150–180 MBq for whole body imaging; 180–230 MBq for segmentary scan.
- **Whole body scan,** 60 min following injection, from vertex of the skull to the proximal femoral tract, 6–7 bed position (3 min per bed position; additional segmentary scans, if requested.
- **Segmentary scan**: a 2–3 bed position (3 min per bed position) focused on the anatomical district under study.

Since short- or long-acting somatostatin analogs can compete with the ^{68}Ga-DOTA-compounds for bioavailability, it is recommended to discontinue short-acting analogs for at least 24 h and perform the PET scan the week before the next administration of the long-acting medications.

6.7 Variants and Pitfalls

In the evaluation of PET scan with ^{68}GA-DOTA-peptides, the observer should pay attention to various physiologic or pathological conditions which can cause an interpretative mistake.

The following possible pitfalls mimicking the presence of neuroendocrine disease should be considered: physiological accumulation of the tracer in the gallbladder, accessory spleens, recent surgery or radiation therapy, with the subsequent lymphoid infiltrate expressing SSTR2.

In more than one-third of patients a prominent uncinate process of the pancreas shows intense uptake; an accurate examination of the corresponding functional and morphological images in fused PET/CT slices may be helpful to gain a correct diagnosis.

Patients affected by pancreatic NETs are usually submitted to splenectomy due to the proximity of spleen to the pancreatic tail, which is a typical site of NET localization. Postsurgical splenosis is a common finding in these subjects: nodular splenosis appears as a focal area of tracer uptake and can be erroneously interpreted as a peritoneal localization.

References

1. Wadas TJ, Wong EH, Weisman GR, et al. Coordinating radiometals of copper, gallium, indium, yttrium, and zirconium for PET and SPECT imaging of disease. Chem Rev. 2010;110(5):2858–902.
2. Antunes P, Ginj M, Zhang H, et al. The renaissance of the Ge/Ga radionuclide generator initiates new developments in Ga radiopharmaceutical chemistry. Curr Top Med Chem. 2010;10(16):1633–68.
3. Breeman WA, De Jong M, Visser TJ, et al. Optimising conditions for radiolabelling of DOTA-peptides with 90Y, 111In and 177Lu at high specific activities. Eur J Nucl Med Mol Imaging. 2003;30(6):917–20.
4. Antunes P, Ginj M, Zhang H, et al. Are radiogallium-labelled DOTA conjugated somatostatin analogues superior to those labelled with other radiometals? Eur J Nucl Med Mol Imaging. 2007;34(7):982–93.
5. Breeman WA, de Blois E, Sze Chan H, et al. (68) Ga-labeled DOTA-peptides and (68)Ga-labeled radiopharmaceuticals for positron emission tomography: current status of research, clinical applications, and future perspectives. Semin Nucl Med. 2011;41(4):314–21.
6. Reubi JC, Waser B, Schaer JC, et al. Somatostatin receptor sst1-sst5 expression in normal and neoplastic human tissues using receptor autoradiography with subtype-selective ligands. Eur J Nucl Med. 2001;28(7):836–46.
7. Poeppel TD, Binse I, Petersenn S, et al. 68Ga-DOTATOC versus 68Ga-DOTATATE PET/CT in functional imaging of neuroendocrine tumors. J Nucl Med. 2011;52(12):1864–70.
8. Hofmann M1, Maecke H, Börner R, et al. Biokinetics and imaging with the somatostatin receptor PET radioligand (68)Ga-DOTATOC: preliminary data. Eur J Nucl Med. 2001;28(12):1751–7.
9. Prasad V, Baum RP. Biodistribution of the Ga-68 labeled somatostatin analogue DOTA-NOC in patients with neuroendocrine tumors: characterization of uptake in normal organs and tumor lesions. Q J Nucl Med Mol Imaging. 2010;54(1):61–7.
10. Reubi JC, Schaer JC, Markwalder R, et al. Distribution of somatostatin receptors in normal and neoplastic human tissues: recent advances and potential relevance. Yale J Biol Med. 1997;70(5–6):471–9.
11. Rindi G, Petrone G, Inzani F. The 2010 WHO classification of digestive neuroendocrine neoplasms: a critical appraisal four years after its introduction. Endocr Pathol. 2014;25(2):186–92.
12. Sommer WH, Zech CJ, Bamberg F, et al. Fluid-fluid level in hepatic metastases: a characteristic sign of metastases of neuroendocrine origin. Eur J Radiol. 2012;81(9):2127–32.
13. Sankowski AJ, Ćwikla JB, Nowicki M, et al. The clinical value of MRI using single-shot echoplanar DWI to identify liver involvement in patients with advanced gastroenteropancreatic-neuroendocrine tumors (GEP-NETs), compared to FSE T2 and FFE T1 weighted image after i.v. Gd-EOB-DTPA contrast enhancement. Med Sci Monit. 2012;18(5): MT33–40.
14. Song YS, Lee WW, Chung JH, et al. Correlation between FDG uptake and glucose transporter type 1 expression in neuroendocrine tumors of the lung. Lung Cancer. 2008;61(1):54–60.
15. Kowalski J, Henze M, Schuhmacher J, et al. Evaluation of positron emission tomography imaging using [68Ga]-DOTA-D Phe(1)-Tyr(3)-octreotide in comparison to [111In]-DTPAOC SPECT. First results in patients with neuroendocrine tumors. Mol Imaging Biol. 2003;5(1):42–8.
16. Gabriel M, Decristoforo C, Kendler D, et al. 68Ga-DOTA-Tyr3-octreotide PET in neuroendocrine tumors: comparison with somatostatin receptor scintigraphy and CT. J Nucl Med. 2007;48(4):508–18.
17. Putzer D, Gabriel M, Henninger B, et al. Bone metastases in patients with neuroendocrine tumor: 68Ga-DOTA-Tyr3-octreotide PET in comparison to CT and bone scintigraphy. J Nucl Med. 2009;50(8):1214–21.
18. Haug AR, Cindea-Drimus R, Auernhammer CJ, et al. The role of 68Ga-DOTATATE PET/CT in suspected neuroendocrine tumors. J Nucl Med. 2012;53(11):1686–92.
19. Treglia G, Castaldi P, Rindi G, et al. Diagnostic performance of Gallium-68 somatostatin receptor PET and PET/CT in patients with thoracic and gastroenteropancreatic neuroendocrine tumours: a meta-analysis. Endocrine. 2012;42(1):80–7.
20. Kabasakal L, Demirci E, Ocak M, et al. Comparison of ^{68}Ga-DOTATATE and ^{68}Ga-DOTANOC PET/CT imaging in the same patient group with neuroendocrine tumours. Eur J Nucl Med Mol Imaging. 2012;39(8):1271–7.
21. Wild D, Bomanji JB, Benkert P, et al. Comparison of 68Ga-DOTANOC and 68Ga-DOTATATE PET/CT within patients with gastroenteropancreatic neuroendocrine tumors. J Nucl Med. 2013;54(3):364–72.

22. Boy C, Heusner TA, Poeppel TD, et al. 68Ga-DOTATOC PET/CT and somatostatin receptor (sst1-sst5) expression in normal human tissue: correlation of sst2 mRNA and SUVmax. Eur J Nucl Med Mol Imaging. 2011;38(7):1224–36.
23. Campana D, Ambrosini V, Pezzilli R, et al. Standardized uptake values of (68)Ga-DOTANOC PET: a promising prognostic tool in neuroendocrine tumors. J Nucl Med. 2010;51(3):353–9.
24. Bodei L, Ferone D, Grana CM, et al. Peptide receptor therapies in neuroendocrine tumors. J Endocrinol Invest. 2009;32(4):360–9.. Review
25. Bodei L, Pepe G, Paganelli G. Peptide receptor radionuclide therapy (PRRT) of neuroendocrine tumors with somatostatin analogues. Eur Rev Med Pharmacol Sci. 2010;14(4):347–51.. Review
26. Falletta S, Partelli S, Rubini C, et al. mTOR inhibitors response and mTOR pathway in pancreatic neuroendocrine tumors. Endocr Relat Cancer. 2016. pii: ERC-16-0329
27. Kratochwil C, Stefanova M, Mavriopoulou E, et al. SUV of [68Ga]DOTATOC-PET/CT predicts response probability of PRRT in neuroendocrine tumors. Mol Imaging Biol. 2015;17(3):313–8.
28. Haug AR, Auernhammer CJ, Wängler B, et al. 68Ga-DOTATATE PET/CT for the early prediction of response to somatostatin receptor-mediated radionuclide therapy in patients with well-differentiated neuroendocrine tumors. J Nucl Med. 2010;51(9):1349–56.
29. Filippi L, Scopinaro F, Pelle G, et al. Molecular response assessed by (68)Ga-DOTANOC and survival after (90)Y microsphere therapy in patients with liver metastases from neuroendocrine tumours. Eur J Nucl Med Mol Imaging. 2016;43(3):432–40.
30. Naji M, Zhao C, Welsh SJ, et al. 68Ga-DOTATATE PET vs. 123I-MIBG in identifying malignant neural crest tumours. Naji Mol Imaging Biol. 2011;13(4):769–75.
31. Kroiss A, Shulkin BL, Uprimny C, et al. (68)Ga-DOTATOC PET/CT provides accurate tumour extent in patients with extraadrenal paraganglioma compared to (123)I-MIBG SPECT/CT. Eur J Nucl Med Mol Imaging. 2015;42(1):33–41.
32. Rinzivillo M, Partelli S, Prosperi D, et al. Clinical usefulness of 18F-fluorodeoxyglucose positron emission tomography in the diagnostic algorithm of advanced Entero-pancreatic neuroendocrine neoplasms. Oncologist. 2018;23(2):186–92.
33. Filippi L, Schillaci O, Cianni R, et al. Imaging neuroendocrine hepatic metastases following 90Y-Radioembolization: is it time to implement routine use of PET molecular/metabolic probes? Cardiovasc Intervent Radiol. 2019;42(6):933–4. https://doi.org/10.1007/s00270-019-02186-w.
34. Kayani I, Bomanji JB, Groves A, et al. Functional imaging of neuroendocrine tumors with combined PET/CT using 68Ga-DOTATATE (Dota-DPhe1Tyr-octreotate) and 18F-FDG. Cancer. 2008;112(11):2447–55.
35. Panagiotidis E, Alshammari A, Michopoulou S, et al. Comparison of the impact of 68Ga-DOTATATE and 18F-FDG PET/CT on clinical management in patients with neuroendocrine tumors. J Nucl Med. 2016. pii: jnumed.116.178095

^{64}Cu-Radiopharmaceuticals

7

Ferdinando Calabria, Antonio Bagnato, Vincenzo Gangemi, Rosina Paonessa, Mario Leporace, Nicoletta Urbano, and Giuseppe Lucio Cascini

Contents

Abbreviations

^{18}F-FDG	^{18}F-fluorodeoxyglucose
^{18}F-MISO	^{18}F-Misonidazole
^{64}Cu-ATSM	Diacetyl-bis-N4-methylthiosemicarbazone
^{64}Cu-DOTANOC	^{64}Cu-tetraazacyclododecane-octreotid
^{64}Cu-DOTATATE	^{64}Cu-tetraazacyclododecane-octreotate
^{64}Cu-PSMA	^{64}Cu-prostate-specific membrane antigen
^{68}Ga-DOTATOC	^{68}Ga-tetraazacyclododecane-octreotide
BFC	Bi-functional-chelator
CTR1	Human copper transporter 1
Cu	Copper
DNA	Deoxyribonucleic acid

Authors declare they have obtained permission for any previously published material used in their chapter.

F. Calabria (✉) · A. Bagnato · M. Leporace
Department of Nuclear Medicine and Theranostics, "Mariano Santo" Hospital, Cosenza, Italy
e-mail: ferdinandocalabria@hotmail.it

V. Gangemi · R. Paonessa · G. L. Cascini
Nuclear Medicine Unit, Department of Diagnostic Imaging, "Magna Graecia" University, Catanzaro, Italy

N. Urbano
Nuclear Medicine Unit, University Hospital "Tor Vergata", Rome, Italy

F. Calabria, O. Schillaci (eds.), *Radiopharmaceuticals*,
https://doi.org/10.1007/978-3-030-27779-6_7

DOTA	Tetraazacyclododecane-tetraacetic acid
GMP	Good manufacture practice
LET	Linear energy transfer
NET	Neuroendocrine tumors
PET/CT	Positron emission tomography/computed tomography
PSMA	Prostate-specific membrane antigen
RRT	Receptors radiation therapy
SPECT/CT	Single photon emission computed tomography/computed tomography
SSTR	Somatostatin receptor

7.1 Copper: Physical and Biological Properties

Copper (Cu) is a transition metal with atomic number 29, involved in several physiological processes, being cofactor for numerous enzymes, such as the "*Cu/Zn superoxide dismutase,*" "*cytochrome-C-oxidase,*" "*tyrosinase,*" "*ceruloplasmin,*" and other proteins. Moreover, the Cu is essential for respiration, iron transport and metabolism, cell growth, and hemostasis [1, 2]. It may also play a role in cancer development and progression, acting as neo-angiogenetic promoter [3, 4].

In fact, the Cu acts on the human cell metabolism through the activity of human copper transporter-1 (CTR1), that is over-expressed in a variety of cancers. On the basis of this evidence, the radioactive Cu isotopes may be potentially used as tracers for the in vivo characterization of copper metabolism in neoplastic tissues, including breast and prostate cancers and malignant cutaneous melanoma, by using PET/CT imaging.

Many copper radionuclides with different biological half-life and decay characteristics have been used in nuclear medicine: ^{60}Cu (23.7 min of half decay), ^{61}Cu (3.32 h), ^{62}Cu (9.76 min), ^{64}Cu (12.7 h), and ^{67}Cu (61.83 h) [5]. These nuclides are particularly interesting for molecular imaging applications (^{60}Cu, ^{61}Cu, ^{62}Cu, ^{64}Cu), and in vivo targeted radiation therapy (^{64}Cu and ^{67}Cu) [1, 6, 7].

The physical features of these nuclides present some similarities to the isotopes of iodine family, joining in particular three aspects:

- *The long half-life, allowing their use in PET centers not provided by a cyclotron*
- *The large availability of molecules to be potentially labeled, as well as the chance to use the nuclides alone, without further complexation*
- *The possibility to select a specific nuclide within a family with similar biological properties, in order to address a specific issue (diagnostic and/or therapeutic), on the basis of the radioactive emission*

All these features well describe the term "*theranostic agent,*" widely used for Cu and iodine radionuclides.

Moreover, the long half-life also permits delayed scans, allowing a dynamic evaluation of the uptake during the time, in comparison to standard PET imaging achievable with ^{18}F- or ^{68}Ga-labeled tracers.

The ^{64}Cu is a versatile nuclide, due to its peculiar decay scheme, combining electron capture (41%), Beta minus (19%) and Beta plus (40%) decays, also resulting in Auger electrons emission with therapeutic potential. Its half-life of 12.7 h is sufficient for synthesis of many ^{64}Cu-labeled radiopharmaceuticals, and is compatible with the in vivo tracking of large and small molecular carriers.

These properties made the ^{64}Cu suitable for applications in PET/CT imaging and targeted radiotherapy, also offering the possibility of an accurate assessment, as part of a quantitatively planned targeted radionuclide therapy regimen.

When using the ^{64}Cu as therapeutic agent, the effects of radiations on tissues are due to the combination of beta minus emission and Auger electrons emission.

Auger electrons show low kinetic energies with short-range penetration but high linear energy transfer (LET); this feature produces high-energy release, exclusively at the site of emission within an extremely small volume, thus preserving normal physiological tissues from

therapeutic effect. For these reasons a predictive dosimetry should be performed in case of ^{64}Cu therapy, but micro (auger electrons) and macro dosimetry (beta minus) need to be simultaneously measured to efficaciously predict the effect of ^{64}Cu on neoplastic tissues during the time. Micro-dosimetry for Auger electron is difficult to measure because its biological effect requires a close distance of emission site to the target (typically DNA). Therefore, the killer effect is manifested only when ^{64}Cu penetrates inside the nucleus within a range of few nanometers. On the other hand, the therapeutic effect may not be successful in case of cytoplasmic deposit [8].

High attention is now paying to the effect of high LET electrons produced by ^{64}Cu, because it binds to DNA and has been suggested to play an important role in DNA repair [9].

The ^{64}Cu production may be either by cyclotron or by nuclear reaction; however, the cyclotron synthesis, using the ^{64}Ni-^{64}Cu reaction, is actually the most widely used method [10]. After separation and purification, a high amount of ^{64}Cu may be available in nuclear medicine units, also far from the site of production, even if high energy cyclotrons (>18 MeV) are used.

7.2 Copper Chemistry

7.2.1 ^{64}Cu Coordination Numbers and Chelators

The water-solution coordination chemistry of ^{64}Cu is limited to three oxidation states (I–III). ^{64}Cu(I) complexes have low stability for radiopharmaceutical applications, while ^{64}Cu(III) is rare. ^{64}Cu(II) favors binding to nitrogen donors like amines, imines, and bidentate-ligands, such as bi-pyridine. The coordination number ranges from 4 to 6, forming complexes that have square planar, square pyramidal, trigonal-bipyramidal, or octahedral geometry [11].

In the development of ^{64}Cu-labeled tracers, chelator-structure is crucial to complex and to bind ^{64}Cu(II) into kinetically and thermodynamically stable biomolecules. Many Cu chelating proteins (e.g., ceruloplasmin, superoxide dismutase, metallothionein, copper transporters, and chaperones) are able to in vivo displace the copper ion from the chelator [12].

7.2.2 Criticisms for Copper Labeling

It is generally accepted that the overall biologic profile of radiolabeled ligands is determined by receptor specific binding as well as by physicochemical features, with particular regard to molecular weight, linkers lipophilicity, charge, stability, and chemical structure of chelators. Consequently, the choice of chelator, as well as its interactions with the radioactive metallic ions, affects the physical-chemical features, especially for smaller molecules like antibodies and nanoparticles.

The stability of the in vivo copper-chelator complex is a critical factor to obtain a useful imaging agent. Ligands with higher kinetic inertness to ^{64}Cu(II) decomplexation (proton-assisted as well as transchelation or transmetallation) should be preferred to complexes with in vivo thermodynamic stability. This aspect is crucial for clinical imaging because it significantly changes the ^{64}Cu bio-distribution: in many cases, the presence of an intense liver uptake with a slow blood clearance may be indicative of free radioactive ^{64}Cu. The phenomenon of ^{64}Cu in vivo de-complexation may be due to two different mechanisms: the transchelation by other competitive molecules and the reduction of ^{64}Cu(II) into ^{64}Cu (I) with a lower affinity to the chelator. In addition, the overall charge modifies the biodistribution because neutral or negative radiopharmaceuticals may exhibit higher kidney and spleen uptake [13].

Furthermore, the physical purity of ^{64}Cu may influence the quality of labeling procedure, because it negatively affects the specific activity (amount of radioactivity per unit mass), which has been reported to be in the range of 94 to 310 mCi/μg. In fact, the purity of the ^{64}Cu produced is influenced by other transition metals (Ni, Zn, Fe, and Co) [12]. The effective specific activity reflects the ability to label a specific ^{64}Cu(II) chelator at particular temperature, pH,

and a specific time. Consequently, the radionuclide purity should be determined before the clinical release in patients.

7.2.3 Copper Chelators

Chelators for radio-metals like copper are generally bi-functional-chelator (BFC), because they are characterized by the capability to bind the metal as well as to covalently link peptides, proteins, and antibodies with a functional group. Ligands may be acyclic, cyclic, and cross-bridged systems.

Classic acyclic Cu chelators such as EDTA are rarely applied for radioactive copper.

The most extensively used class of chelators for ^{64}Cu are the macrocyclic-polyaminocarboxylates and their derivatives (1,4,7,10-tetraazacyclododecane-1,4,7,10-tetraacetic acid, DOTA; 1,4,8,11-tetraazacyclo tetradecane-1,4,8,11-tetraacetic acid, TETA) and cross-bridged cyclic polyaminocarboxylates and derivatives, all with pendant arms to improve stability.

Two of the most studied chelators are DOTA and TETA. DOTA has been extensively used as a BFC for ^{64}Cu due to its ability to bind other metals. Instead, sometimes the TETA can be alternative to DOTA [13].

7.3 Copper-Labeled Radiopharmaceuticals

7.3.1 ^{64}Cu-PSMA

The *Prostate-Specific Membrane Antigen* (PSMA) is a cell-surface protein that shows a significant over-expression on prostate cancer cells, in particular advanced prostate cancer, with lower expression in normal prostate tissue. There are several studies showing that PSMA expression levels increase according to the stage and grade of the tumor. Moreover, in most types of prostate cancers, the majority of primary and metastatic lesions show PSMA expression [14].

Interestingly, the PSMA expression has been also reported in cancer of the colon and breast [15], and in renal carcinoma, in particular in newly originated blood vessels [16].

During the last two decades, many efforts have been undertaken to develop PSMA-ligands. PSMA-11 has become the most clinically used and commercially available molecule. This compound shows a strong binding affinity to PSMA as well as high efficient internalization into prostate cancer cells. Meanwhile, modifications of PSMA-11 have resulted in the development of a novel small molecule PSMA-ligand: PSMA-617. PSMA-617 can be labeled with ^{68}Ga, ^{177}Lu, ^{111}In, ^{90}Y, and, more recently, with ^{64}Cu [17]. Therefore, it can be used for PET/CT imaging and for radionuclide therapy.

Preclinical assays of PSMA-617 showed *Ki* values of 2.3 ± 2.9 nM, demonstrating a significant improvement compared to PSMA-11 (12.0 ± 2.8 nM). PSMA-11 presents a acyclic chelator while PSMA-617 has macrocyclic-chelator (DOTA). In agreement with literature data, PSMA-617 presents more binding affinities to the PSMA receptor than PSMA-11, resulting in higher stability.

Several recent clinical studies have focused the attention on the diagnostic accuracy of PSMA PET/CT in prostate cancer patients, mainly referring to ^{68}Ga-PSMA. In fact, many studies showed that ^{68}Ga-PSMA is very accurate in evaluation of biochemical recurrence of disease, in patients previously submitted to radical prostatectomy and/or radiotherapy, also with low PSA values at the time of the scan [18]. These emerging data support the use of ^{68}Ga-PSMA PET/CT in patients with biochemical recurrence, also for PSA level lower than 1, suggesting a better detection rate than (^{11}C/^{18}F) radiolabeled choline PET-CT [19]. In fact, ^{68}Ga-PSMA is able to detect small lesions of recurrent disease in the prostate bed or in abdominal lymph nodes, also when lesion were < 1 cm in diameter.

Although many nuclear medicine physicians are actually oriented for ^{68}Ga-PSMA as tracer for prostate cancer imaging, several drawbacks concerning availability, regulatory, financial, and specificity are now emerging. ^{64}Cu-PSMA may overcome some of these aspects. In fact, ^{64}Cu is a commercially available tracer, recently authorized for labeling, and can be used without expensive generator. The labeling procedure is simple and may be done in accordance to *Good Manufacture Practice* (GMP) procedures. The long half-life decay of ^{64}Cu warrants an effective management of patients, giving the possibility of repeated scans during the time, also with very delayed acquisitions (*18 h from the injection*). Finally, it is important to consider the high spatial resolution provided by the ^{64}Cu, due to the small range of positron flight. According to the capability of dynamic scans and to images quality, ^{64}Cu-PSMA PET/CT appears as an extremely promising tool in prostate cancer patients.

One of the first published papers has been reported by Grubmüller et al. in a multicenter study examining patients with primary and recurrent prostate cancer. The authors observed in all cases the histologically proven local disease characterized by intense and pathological ^{64}Cu-PSMA uptake. Similar a good detection rates were also reported for lymph node and bone metastases. The ^{64}Cu-PSMA bio-distribution was considered similar to ^{68}Ga-PSMA, with an intense liver uptake during the time. Kidneys, spleen, and salivary glands are also physiologically visualized, whereas bladder and excretory activity is faint [20] (Fig. 7.1).

In our preliminary clinical experience with ^{64}Cu-PSMA PET/CT, developed on prostate cancer patients, we observed high sensitivity and specificity in the disease detection, also for small lesions. In particular, in patients during staging for medium-high risk disease (Gleason Score $\geq$ 7) and patients with biochemical recurrence after primary treatment. Our preliminary results are suggesting a good diagnostic accuracy in the detection of the T component and lymph nodes metastases during the staging of prostate cancer (Fig. 7.2) and in the identification of metastatic lymph

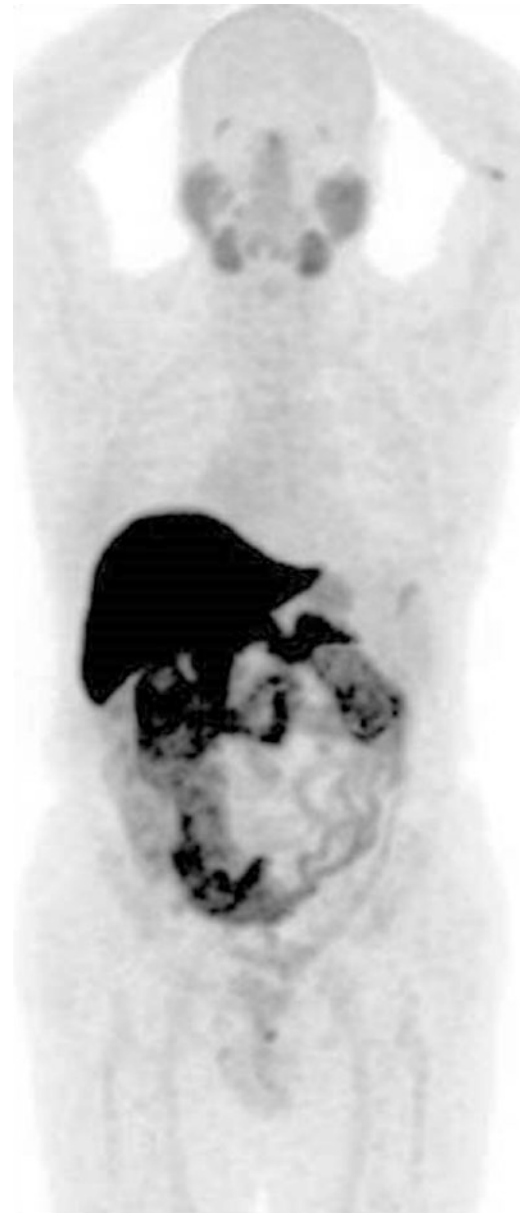

Fig. 7.1 PET 3D maximum intensity projection of the whole physiological bio-distribution of ^{64}Cu-PSMA in male human body

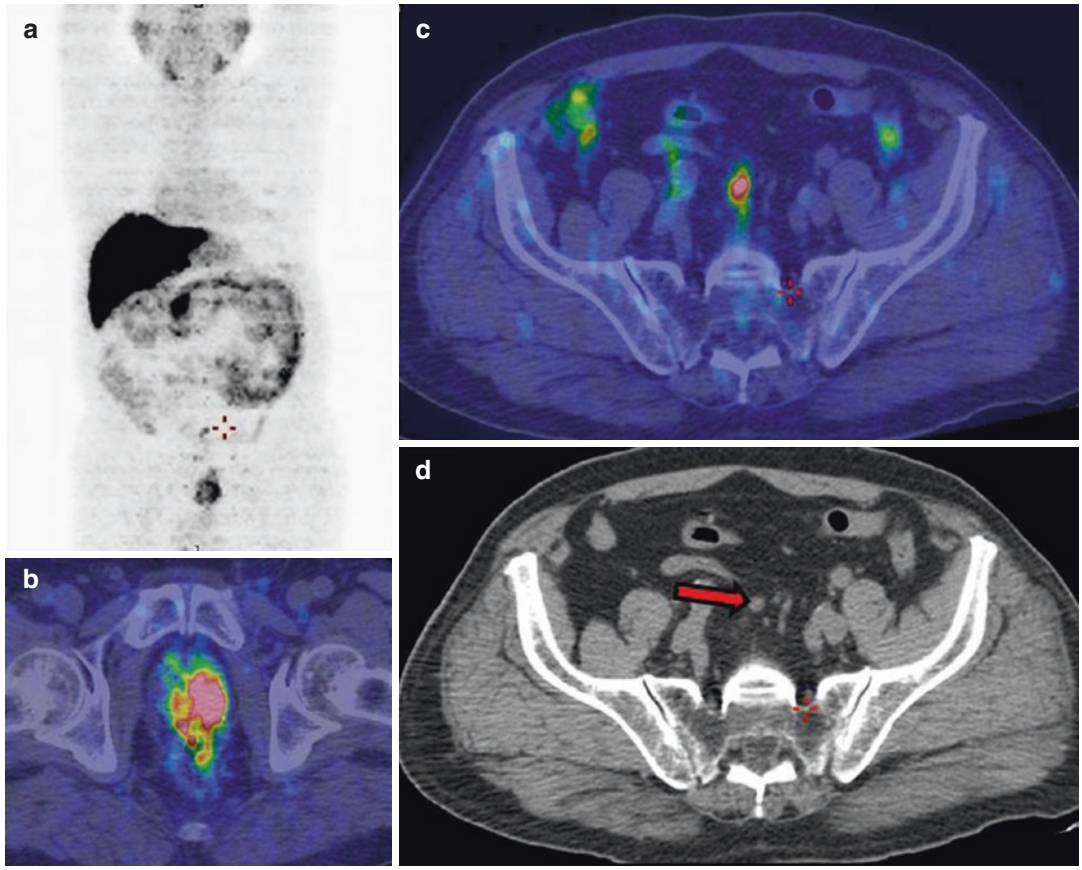

Fig. 7.2 ^{64}Cu-PSMA PET 3D maximum intensity projection (**a**) of a patient examined for staging prostate cancer. Axial PET/CT views show pathologic tracer uptake in the left prostate lobe (**b**) and in a pelvic 8 mm wide lymph node (**c**) not easily recognizable at corresponding CT imaging (**d**, *red arrow*), without contrast administration

nodes (Figs. 7.3 and 7.4) and local relapse during the restaging. In this last clinical setting, the diagnostic accuracy of ^{64}Cu-PSMA PET/CT can be favored by a very low urinary tracer excretion (Fig. 7.5). The urinary excretion is a factor limiting the sensitivity of other PET tracers in detecting local recurrence of prostate cancer [21].

A recent study comparing ^{64}Cu-PSMA and ^{18}F-choline in PET/CT imaging of recurrent prostate cancer demonstrated a better diagnostic performance for ^{64}Cu-PSMA in diagnosing lymph nodes metastases, especially with very low PSA serum levels [22]. However, future studies are needed to ensure these preliminary data. In particular, a direct comparison between ^{64}Cu-PSMA, ^{68}Ga-PSMA, and (^{11}C/^{18}F) radiolabeled choline on large populations is needed to address the best PET tracer for prostate cancer imaging.

Other studies are also needed to effectively verify the impact of false positive cases, linked to the possibility of uptake of (^{64}Cu/^{68}Ga) labeled PSMA in pathological conditions other than prostate cancer, which can lead in a lack of specificity. Initial reports are describing some

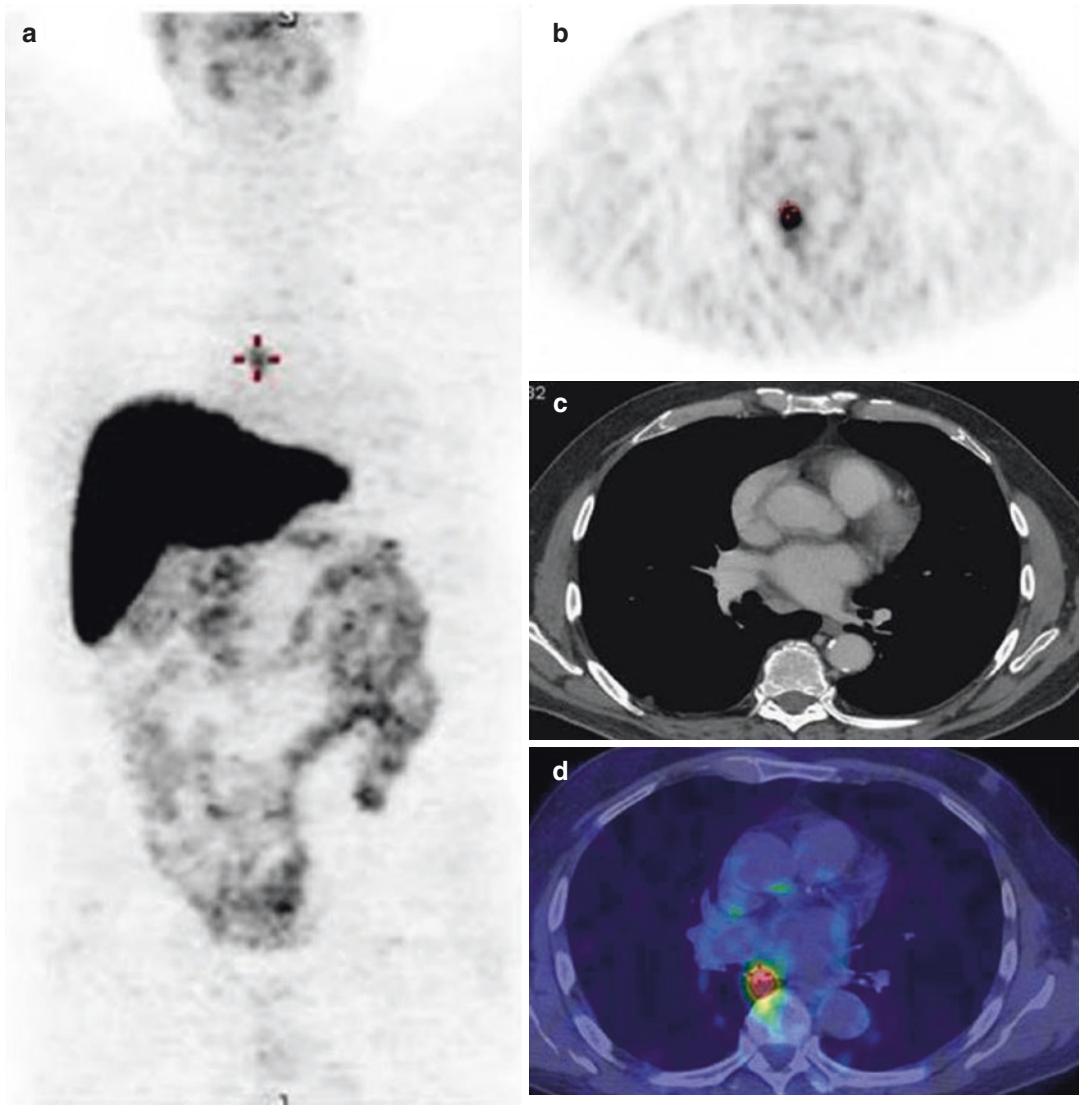

Fig. 7.3 In a patient examined for biochemical relapse (PSA 3.2 ng/ml) three years after radical prostatectomy, ^{64}Cu-PSMA PET 3D maximum intensity projection (**a**) and axial PET (**b**) show focal uptake in the mediastinum, corresponding to 1.4 cm wide metastatic lymph node, evident in CT (**c**) and PET/CT (**d**) views

diagnostic pitfalls linked to the ^{68}Ga-PSMA non-specific uptake [23, 24]; in our experience we also discovered a case of ^{64}Cu-PSMA uptake in meningioma [25] (Fig. 7.6) and other authors also described the possibility of ^{68}Ga-PSMA uptake in meningiomas, potentially mimicking metastases of prostate cancer [26].

The ^{64}Cu/^{68}Ga-PSMA uptake in meningioma could be due to the neo-vasculature of the tumor tissue [27, 28]. The discovery of intracranial ^{64}Cu/^{68}Ga-PSMA uptake during whole body PET/CT scans of patients with prostate cancer may indicate the presence of meningioma, presenting as uncommon diagnostic pitfall [29].

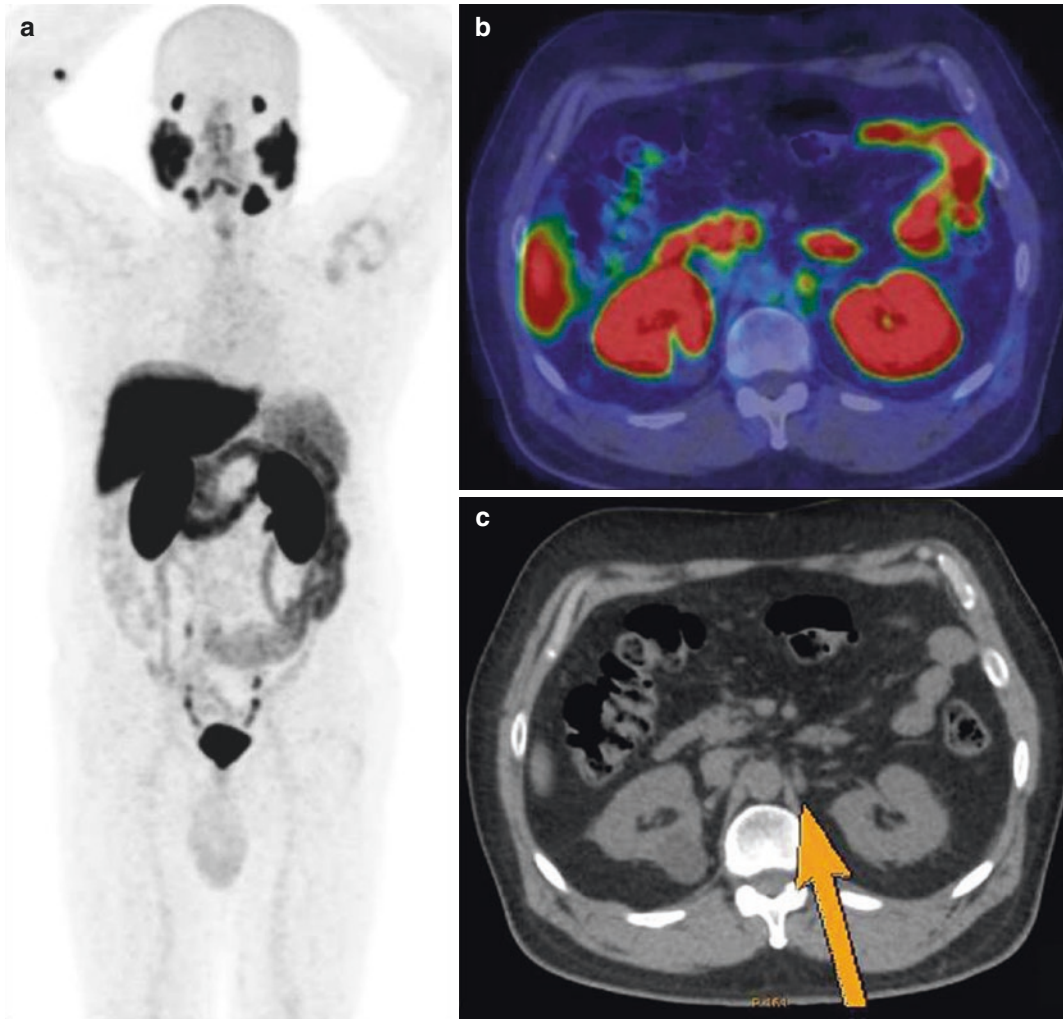

Fig. 7.4 In a patient in biochemical relapse of prostate cancer (PSA 0.6 ng/ml, one year after radical prostatectomy), ^{64}Cu-PSMA PET 3D maximum intensity projection (**a**) and axial PET/CT view (**b**) show pathologic tracer uptake in single abdominal lymph node, not easily recognizable at corresponding CT imaging (**c**, arrow)

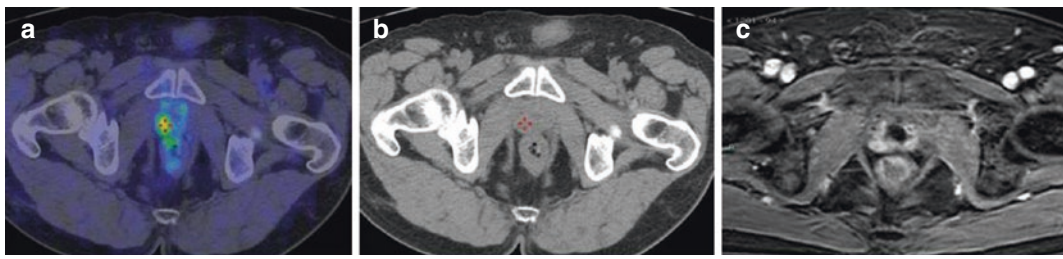

Fig. 7.5 This patient was examined for early biochemical relapse (PSA 0.8 ng/ml), one year after radical prostatectomy for prostate cancer. Axial ^{64}Cu-PSMA PET/CT view (**a**) shows pathologic ^{64}Cu-PSMA uptake in the prostate bed, without corresponding abnormalities on the correlative CT view (**b**). Axial MRI *Short Tau Inversion Recovery* (STIR) confirms the diagnosis of local relapse (**c**). The uptake of ^{64}Cu-PSMA in the bladder is normally faint, helping to detect local relapse of prostate cancer

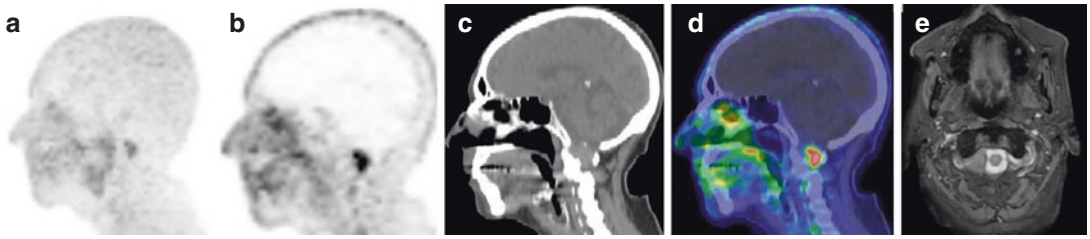

Fig. 7.6 A 64-year-old patient examined by means of ^{64}Cu-PSMA PET/CT for restaging prostate cancer, 2 years after radical prostatectomy. Intense ^{64}Cu-PSMA uptake is documented in the neck, as evident in PET 3D maximum intensity projection (**a**) and in sagittal PET view (**b**). corresponding to a hyperdense area in the foramen magnum in corresponding CT (**c**) and PET/CT (d) views. MRI diagnosed a meningioma with high signal intensity on T2-weighted axial view (**e**)

On the other hand, further false positive cases due to ^{68}Ga-PSMA uptake in conditions other than prostate cancer are already reported (see Chap. 12): reactive lymph nodes, nonmalignant bone lesions, thyroid nodules, ganglions, lung nodes, adrenal glands, and intestinal diverticula can occasionally be ^{68}Ga-PSMA-avid [30–32]. Due to the common molecular structures of both variants of labeled PSMA, we can hypothesize a lack of specificity also for ^{64}Cu-PSMA PET/CT. However, as reported for other tracers in prostate cancer imaging, the majority of diagnostic pitfalls could be due to inflammation [33, 34].

7.3.2 ^{64}Cu-ATSM

Hypoxia is an important marker of the overall tumor response to therapy. In fact, it can result as an expression of tumor aggressiveness, failure of local control, or activation of transcription factors supporting cell survival and migration. The capability to locate and quantify the extent of hypoxia within solid tumors, by using noninvasive nuclear imaging, would facilitate the early diagnosis and help clinicians in selecting the best treatment option, targeted for each patient.

Diacetyl-2,3-bis-N4-methyl-3-thiosemicarbazone (ATSM) seems to be an innovative molecule for hypoxia imaging, which could be labeled with copper isotopes, particularly with ^{64}Cu. In fact, ^{64}Cu is the best compromise between suitable physical properties (sufficient long half-life, better intrinsic image resolution with low β+ maximal energy), good production yield, and reasonable production costs.

^{64}Cu-ATSM displays several advantages in comparison with other PET tracers for hypoxia, including simple and rapid radiolabeling and faster clearance in tissues in *normoxia*, allowing very good image quality.

^{64}Cu-ATSM penetrates trough cell membrane from the blood pool for its suitable molecular size and lipophilicity. ^{64}Cu-ATSM enters and exits unchanged in *normoxic* tissues: in *hypoxic* cells the tracer is progressively retained and metabolized. In *necrotic* tissues the ^{64}Cu-ATSM uptake is faint [35]. Therefore, the ^{64}Cu-ATSM uptake in *hypoxic* tissues is related to the low oxygen tensions and to the subsequent altered redox cellular condition [36].

One of the first preclinical studies on the potential of ^{62}Cu-ATSM as a hypoxia imaging marker has been reported by *Fujibayashi Y et al.* in 1997. The authors described a selective ^{62}Cu-ATSM uptake in rat hearts subjected to ischemia, with a tracer uptake in damaged myocardial cells of 81%, whereas the quote ^{62}Cu-ATSM uptake was only 23% in myocardium of control mice [35]. Subsequently, ^{64}Cu-ATSM has been validated as a valid marker of hypoxia in several preclinical studies, generally comparing PET findings to autoradiography in animal mammary adenocarcinomas, fibrosarcomas, and gliomas [37].

More recently, a strong relationship has been hypothesized between ^{64}Cu-ATSM and multidrug-resistance: Liu et al. have in vitro

demonstrated that cells with a high expression of multidrug resistance show reduced uptake in association with a significant washout during the time. On the other hand, in knockdown cells for multidrug resistance, the ^{64}Cu-ATSM uptake is significantly increased [38].

Interesting data are now emerging on the association of ^{64}Cu-ATSM and stem cells as well as the mitochondrial dysfunction present in different neurological disorders like Parkinson or Alzheimer disease [39, 40], also in preclinical settings.

In clinical human practice, different radiopharmaceuticals have been proposed for hypoxia PET imaging; in particular, ^{18}F-Misonidazole (^{18}F-MISO) has been considered the better choice. However, we must consider that PET/CT with ^{18}F-MISO can often lead to results not easily reproducible, as already demonstrated by in head and neck tumors. In fact, significant differences have been demonstrated in the hypoxic tissues when the ^{18}F-MISO uptake was measured in two different PET scans, performed within a few days interval [41].

In fact, hypoxia volume can change during the time, due to the coexisting quotes of reversible acute hypoxia and irreversible chronic hypoxia in the same cellular neoplastic population. The ^{18}F-MISO is enhanced in both conditions. Due to its longer half-life decay, ^{64}Cu-ATSM allows delayed imaging, even 18–24 h following tracer administration. In our experience on brain lesions, we observed meaningful differences in tracer uptake in brain tumors among early (1 h) and late (24 h) imaging (Fig. 7.7).

These differences may be explained by the predominance of a passive or facilitated diffusion of ^{64}Cu-ATSM in early images. In the early, imaging substantially reflects tumor perfusion while delayed uptake is consistent with ^{64}Cu-ATSM retention during the time, depicting more effectively the grade of cellular hypoxia. These kinetic properties of ^{64}Cu-ATSM have been demonstrated by McCall et al. in an animal model of head and neck tumors by comparing dynamic ^{64}Cu-ATSM imaging and autoradiography. They observed a significant uptake in the tumor, fourfold higher than muscle on 20 min

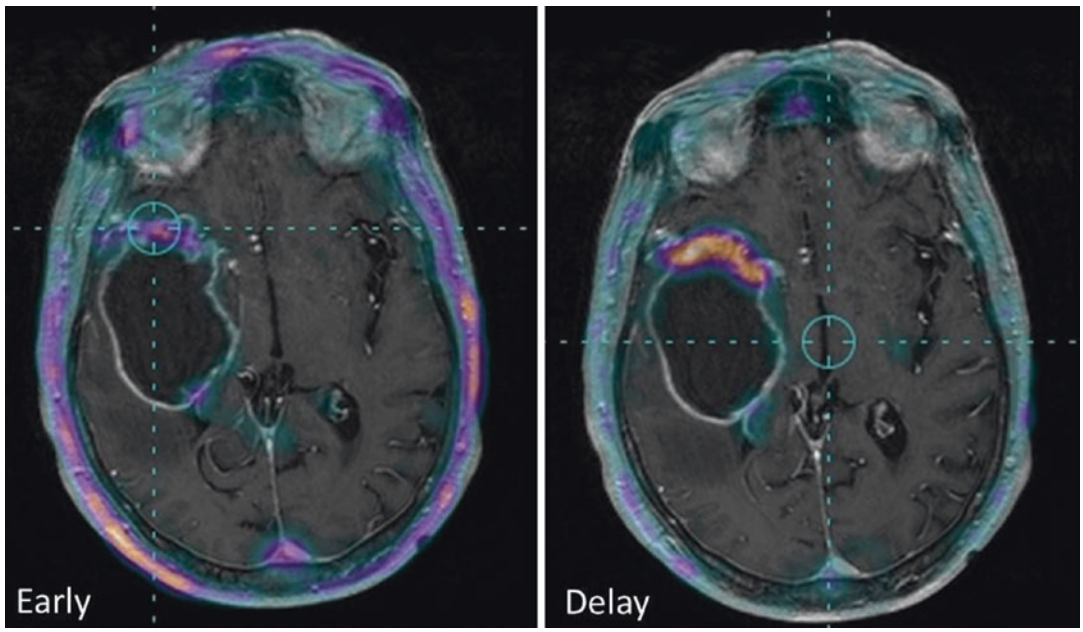

Fig. 7.7 Early (1 h following administration) and delay (24 h following administration) axial ^{64}Cu-ATSM PET/MRI views of the brain, diagnosing tumor relapse in right temporal region in a patient previously treated for glioblastoma. In the late scan is more evident pathologic uptake, significantly higher than surrounding background

images, with progressive increasing during the time, reaching the maximum ratio at 18 h (12:1 tumor/muscle ratio). Autoradiography confirmed the presence of ^{64}Cu-ATSM on late imaging only into the viable part of the tumor [42].

^{64}Cu-ATSM uptake in delayed images however has not completely elucidated, because some further evidences support a lack of selectivity for hypoxic cell fraction within the tumor [43].

These features may be due to low redox potential, potentially influencing the retention of ^{64}Cu-ATSM in *normoxic* and *hypoxic* cells. Moreover, the free ^{64}Cu quote in the blood pool and in the liver may alter the tracer detection at the tumor site.

In clinical practice on humans, many reports have been published to address the ability of ^{64}Cu-ATSM in depicting hypoxia volumes, also for radiotherapy planning. These papers mainly concern gliomas, head and neck cancers, or lung tumors [44–46].

On the basis of these studies, tumor hypoxia may be effectively estimated by ^{64}Cu-ATSM PET/CT, because of the high tumor-to-background ratio and high-quality images. However the cutoff values for tumor depiction as well as technical acquisition details need to be more deeply assessed, also considering the physiological distribution of ^{64}Cu-ATSM in liver, pancreas, kidneys, and intestinal loops (Fig. 7.8).

As a future trend, some studies are actually focused on the role of ^{64}Cu-ATSM as prognostic tumor marker. Lopci et al. [47], in patients affected by lung cancer and head and neck tumors, recently discovered a good correlation between the hypoxic tumor volume and the hypoxic burden of lesions, provided by ^{64}Cu-ATSM PET/CT.

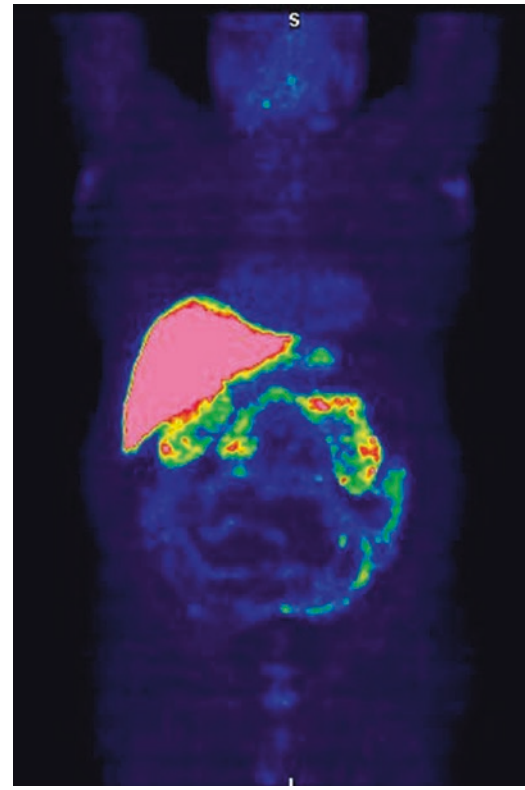

Fig. 7.8 PET 3D maximum intensity projection of the whole physiological bio-distribution of ^{64}Cu-ATSM in the human body

7.3.3 ^{64}Cu-DOTANOC and ^{64}Cu-DOTATATE

Neuroendocrine tumors (NET) are a heterogeneous group of neoplasms, characterized by expression of somatostatin receptors. A large amount of NET originate from the gastro-entero-pancreatic tract (60–70%), followed by NET of the lungs (20–30%) or other parenchymatous organs (10%) as thyroid, parathyroid, and adrenal glands. Somatostatin receptor (*SSTR*) imaging has been used for guiding the management of NET patients, with SPECT, SPECT/CT, and PET/CT.

SSTR PET/CT imaging can change clinical management in 40% of NET patients, also in those patients with a previous SPECT with octreotide analogs [48].

^{68}Ga, labeled with tetraazacyclododecane-octreotide (DOTATOC) or tetraazacyclododecane-octreotate (DOTATATE), is the current widely used radionuclide to track the in vivo behavior of NET. Instead, ^{64}Cu has been recently suggested into clinical practice as an alternative radionuclide for PET/CT imaging of NET. In fact, the chelator DOTA can be used for labeling both ^{68}Ga and ^{64}Cu.

The ^{64}Cu-DOTATATE PET/CT showed a good diagnostic accuracy in detecting NET and it has been proposed for clinical imaging [49]; the peculiar physical features, the long half-life decay as well as the Auger electrons emission make this tracer also potentially useful for receptors radiation therapy (RRT).

The first experience with a ^{64}Cu-labeled somatostatin peptide has been reported by *Anderson et al.* in 1995, in a study comparing the bio-distribution of ^{111}In-Octreotide and two octreotide molecules both labeled with ^{64}Cu but differing in the chelators. In vitro and in vivo analysis, on receptors positive pancreatic tumors in rats, showed a favorable bio-distribution and higher receptor affinity for both ^{64}Cu-labeled molecules, and ^{111}In-Octreotide, whereas significant differences in terms of bio-distribution and tumor uptake were reported between ^{64}Cu-labeled molecules, due to the choice of chelator [50].

In 2012, Pfeifer et al. reported an original human study using ^{64}Cu-DOTATATE PET/CT in 14 patients with NET, aiming to compare PET/CT imaging with standard somatostatin receptor SPECT. They observed high-quality images following 1, 3, and 24 h of the ^{64}Cu-DOTATATE administration, with significant uptake in tumor lesions during the time and a more favorable lesion-to-background ratio 3 h following the injection, due to the reduced renal activity [51].

High physiologic uptake of ^{64}Cu-DOTATATE or ^{64}Cu-tetraazacyclododecane-octreotide (^{64}Cu-DOTANOC) is normally observed in the hypophysis, adrenal glands, kidneys, and bladder; lower uptake can be observed in liver and spleen (Fig. 7.9). Faint uptake is normally detected in thyroid, salivary glands, and brain, with the exception of the hypophysis (Fig. 7.10).

The uptake progressively rises from the early (1 h) imaging to the late (3 h) imaging, as already reported by Pfeifer et al. [51].

Subsequently, the same group also compared the diagnostic accuracy of ^{64}Cu-DOTATATE PET/CT and ^{111}In-Octreotide SPECT/CT in 112 patients: the detection rate and images quality were significantly higher for ^{64}Cu-DOTATATE PET/CT. In particular, the diagnostic sensitivity and accuracy of ^{64}Cu-DOTATATE PET/CT (97% for both) were significantly better than those of ^{111}In-Octreotide SPECT/CT (87% and 88%, respectively). Finally, also the radiation exposure was more favorable for ^{64}Cu-DOTATATE (6.3 mSv vs. 12 mSv of 111In-Octreotide SPECT/CT) [52].

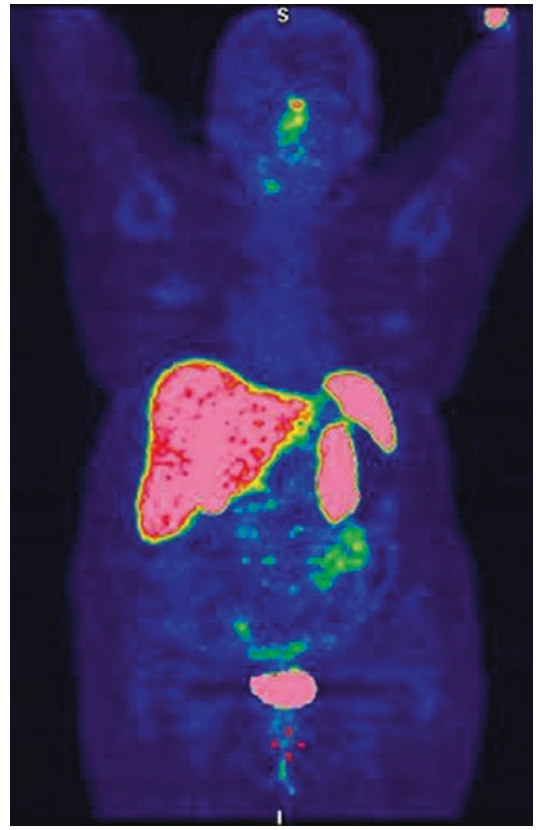

Fig. 7.9 PET 3D maximum intensity projection of the whole physiological bio-distribution of ^{64}Cu-DOTANOC in the human body. Brain uptake is negligible, with the exception of pineal gland

Nevertheless, further studies are needed to ensure these preliminary data. Moreover, only one study compared diagnostic accuracy of ^{68}Ga-DOTATOC and ^{64}Cu-DOTATATE PET/CT; 59 NET patients were examined by means of both tracers. Although patient-based sensitivity was the same for ^{64}Cu-DOTATATE and ^{68}Ga-DOTATOC in this cohort, ^{64}Cu-DOTATATE PET/CT showed a highest diagnostic accuracy on a per lesion analysis, detecting significantly more lesions [53]. No more literature data are actually

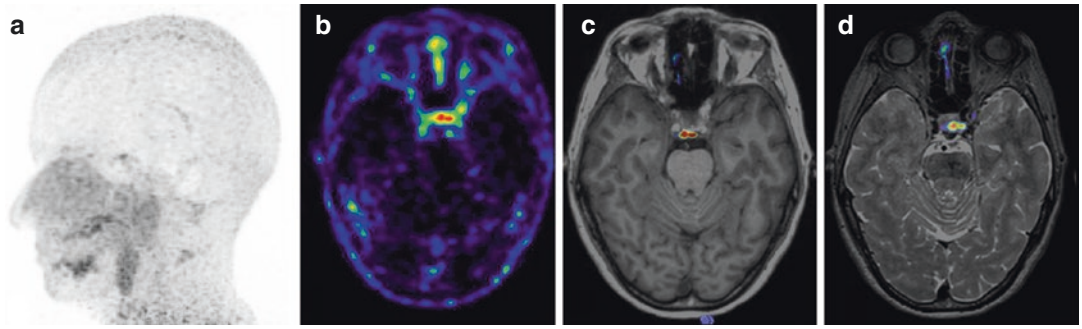

Fig. 7.10 PET 3D maximum intensity projection of the physiological bio-distribution of ^{64}Cu-DOTANOC in the brain (**a**). Axial PET view (**b**) shows focal uptake in the pineal gland, without corresponding abnormalities in T1 (**c**) and T2 (**d**) weighted PET/MRI views, performed on a hybrid PET/MRI scanner

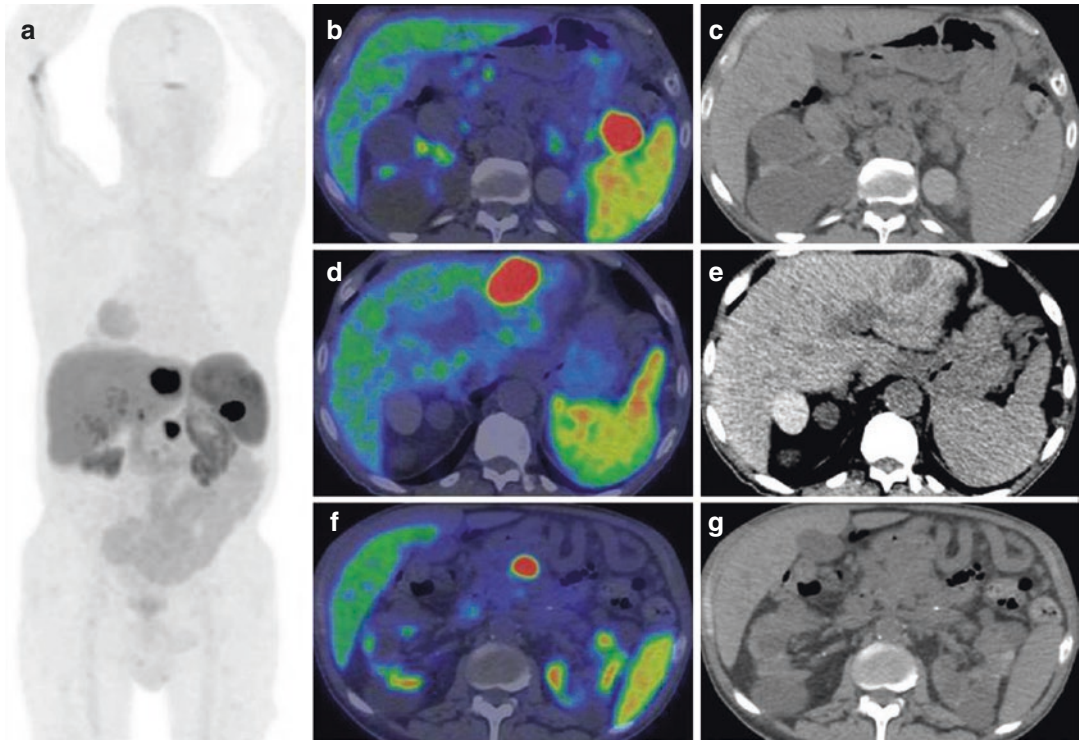

Fig. 7.11 This figure summarizes findings in a 63-year-old patient examined by ^{64}Cu-DOTANOC PET/CT for staging NET of the pancreas. ^{64}Cu-DOTANOC PET 3D maximum intensity projection (**a**) shows three areas of intense uptake in the upper abdomen, corresponding to a lymph node metastasis in the hilum of spleen in axial PET/CT (**b**) and CT (**c**) views, a hypodense hepatic lesion in axial PET/CT (**d**) and CT (**e**) views and the primary NET of the pancreas in PET/CT (**f**) and CT (**g**) views

available, fore the best of our knowledge, concerning potential differences on the direct comparison between ^{68}Ga- and ^{64}Cu-labeled octreotide compounds in imaging NET.

In our preliminary experience, we found a good *signal-to-background ratio* in detecting secondary lesions in NET patients of the pancreas (Fig. 7.11) or intestinal carcinoid (Fig. 7.12) by ^{64}Cu-DOTANOC PET/CT, even in comparison with ^{18}F-FDG PET/CT (Fig. 7.13), which still can be useful in detecting the undifferentiated tumor component [54, 55].

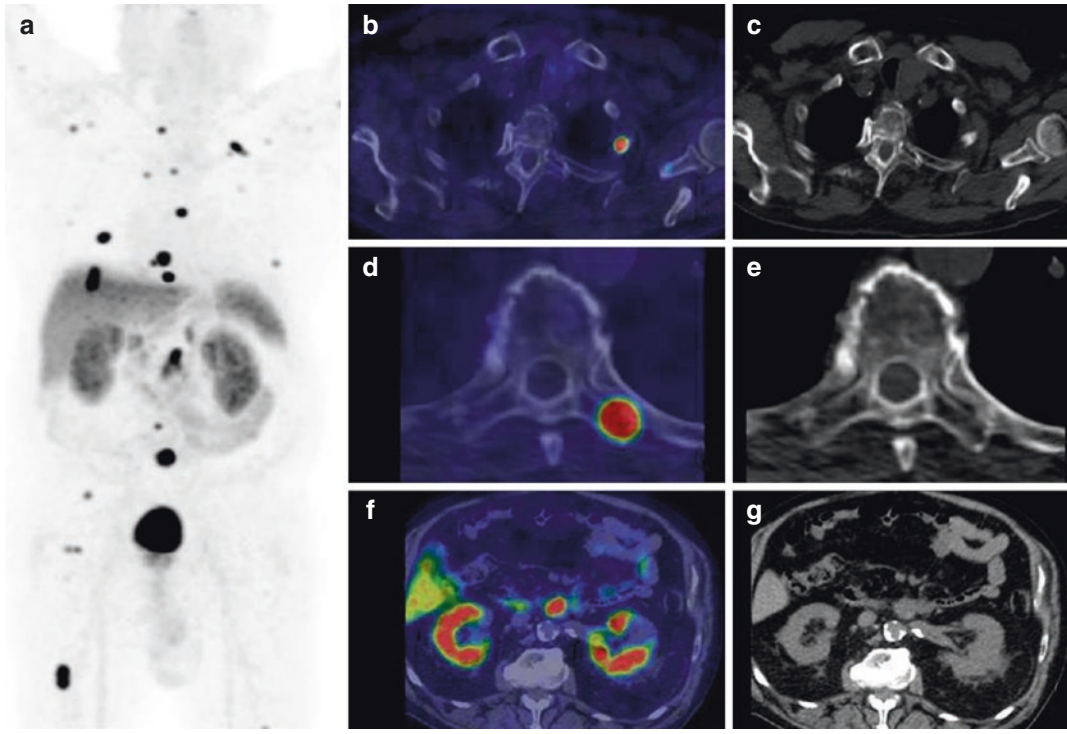

Fig. 7.12 A 58-year-old patient examined by ^{64}Cu-DOTANOC PET/CT due to the rise of *Chromogranin A* (161 U/L) three years after surgical intervention for intestinal carcinoid. ^{64}Cu-DOTANOC PET 3D maximum intensity projection (**a**) shows multiple areas of pathologic tracer uptake in several skeletal localizations, as evident in axial PET/CT (**b**) and CT (**c**) views, also without meaningful corresponding morphological alterations, as evident in axial PET/CT (**d**) and CT (**e**) details of the eighth thoracic vertebra. Axial PET/CT (**f**) and CT (**g**) views show a pre-aortic lymph node metastasis

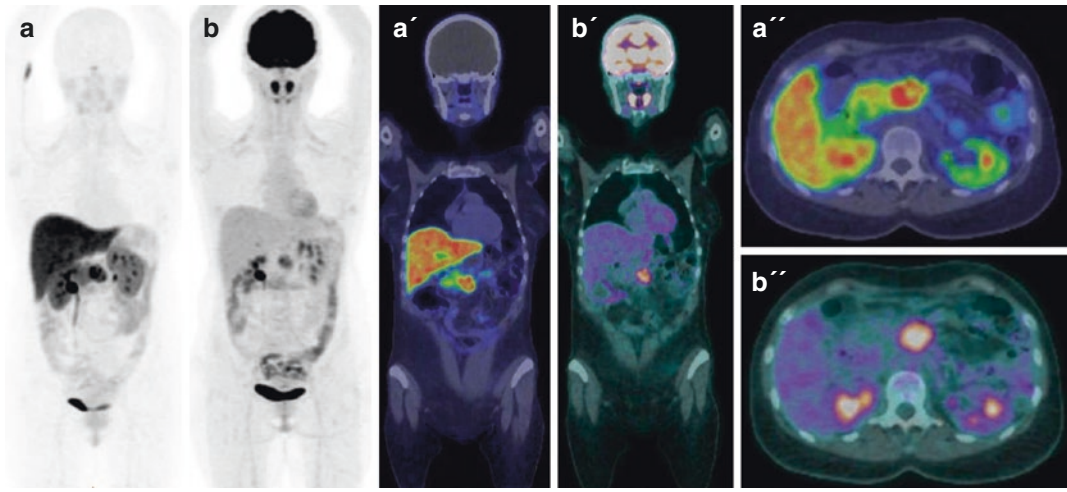

Fig. 7.13 A patient in staging of primary NET of the pancreas. ^{64}Cu-DOTANOC PET 3D maximum intensity projection (**a**), coronal (**a'**) and axial (**a''**) PET/CT views show pathologic tracer uptake in a lesion of the head of the pancreas. ^{18}F-FDG PET 3D maximum intensity projection (**b**), coronal (**b'**) and axial (**b''**) PET/CT views confirm a lesion with high gradient of glucose metabolism. No other pathologic findings were documented in both scans

^{64}Cu-DOTATATE has been lately proposed as imaging marker of atherosclerosis, in order to assess the quote of inflammation inside the plaque and its vulnerability, considering that somatostatin receptors are expressed on membranes of inflammatory cells and macrophages. A recent PET/MRI study demonstrated a significant correlation between the uptake of this tracer and macrophage activation into the atherosclerotic plaques of patients undergoing endarterectomy [56].

References

1. Niccoli Asabella A, Cascini GL, Altini C, et al. The copper radioisotopes: a systematic review with special interest to 64Cu. Biomed Res Int. 2014;2014:786463.
2. Puig S, Thiele DJ. Molecular mechanisms of copper uptake and distribution. Curr Opin Chem Biol. 2002;6:171–80.
3. Reilly W, McAuslan BR. Matrix control of tumor angiogenesis. Adv Exp Med Biol. 1988;242:221–7.
4. Finney L, Vogt S, Fukai T, et al. Copper and angiogenesis: unravelling a relationship key to cancer progression. Clin Exp Pharmacol Physiol. 2009;36:88–94.
5. Blower PJ, Lewis JS, Zweit J. Copper radionuclides and radiopharmaceuticals in nuclear medicine. Nucl Med Biol. 1996;23:957–80.
6. Szymański P, Frączek T, Markowicz M, et al. Development of copper based drugs, radiopharmaceuticals and medical materials. Biometals. 2012;25:1089–112.
7. Evangelista L, Luigi M, Cascini GL. New issues for copper-64: from precursor to innovative PET tracers in clinical oncology. Curr Radiopharm. 2013;6:117–23.
8. Kassis AI, Adelstein SJ. Radiobiologic principles in radionuclide therapy. J Nucl Med. 2005;46:4s–12s.
9. George AM, Sabovljev SA, Hart LE, et al. DNA quaternary structure in the radiation sensitivity of human lymphocytes—a proposed role of copper. Br J Cancer Suppl. 1987;8:141–4.
10. Frindel M, Camus N, Rauscher A, et al. Radiolabeling of HTE1PA: a new monopicolinate cyclam derivative for Cu-64 phenotypic imaging. In vitro and in vivo stability studies in mice. Nucl Med Biol. 2014;41:e49–57.
11. Banerjee SR, Pullambhatla M, Foss CA, et al. ^{64}Cu-labeled inhibitors of prostate-specific membrane antigen for PET imaging of prostate cancer. J Med Chem. 2014;27:6.
12. Cai Z, Anderson CJ. Chelators for copper radionuclides in positron emission tomography radiopharmaceuticals. J Labelled Comp Radiopharm. 2014;57:224–30.
13. Anderson CJ, Ferdani R. Copper-64 radiopharmaceuticals for PET imaging of cancer: advances in preclinical and clinical research. Cancer Biother Radiopharm. 2009;24:379–93.
14. Sweat SD, Pacelli A, Murphy GP, et al. Prostate-specific membrane antigen expression is greatest in prostate adenocarcinoma and lymph node metastases. Urology. 1998;52:637–40.
15. Zhou Y, Li J, Xu X, et al. 64Cu-based Radiopharmaceuticals in Molecular Imaging. Technol Cancer Res Treat. 2019;1:1533033819830758.
16. Eder M, Eisenhut M, Babich J, et al. PSMA as a target for radiolabelled small molecules. Eur J Nucl Med Mol Imaging. 2013;40:819–23.
17. Cui C, Hanyu M, Hatori A, et al. Synthesis and evaluation of [64Cu]PSMA-617 targeted for prostate-specific membrane antigen in prostate cancer. Am J Nucl Med Mol Imaging. 2017;7:40–52.
18. Berliner C, Tienken M, Frenzel T, et al. Detection rate of PET/CT in patients with biochemical relapse of prostate cancer using 68Ga-PSMA;T and comparison with published data of 68Ga PSMA HBED-CC. Eur J Nucl Med Mol Imaging. 2017;44:670–7.
19. Buemel C, Krebs M, Polat B, et al. 68Ga-PSMA-PET/CT in patients with biochemical prostate cancer recurrence and negative 18F-choline-PET/CT. Clin Nucl Med. 2016;41:515–21.
20. Grubmüller B, Baum RP, Capasso E, et al. 64Cu-PSMA-617 PET/CT imaging of prostate adenocarcinoma: first in-human studies. Cancer Biother Radiopharm. 2016;31:277–86.
21. Calabria F, Gallo G, Schillaci O, et al. Biodistribution, imaging protocols and diagnostic accuracy of PET with tracers of lipogenesis in imaging prostate cancer: a comparison between 11C-choline, 18F-fluoroethylcholine and 18F-methylcholine. Curr Pharm Des. 2015;21:4738–47.
22. Cantiello F, Crocerossa F, Russo GI, et al. Comparison between 64Cu-PSMA-617 PET/CT and 18F-choline PET/CT imaging in early diagnosis of prostate cancer biochemical recurrence. Clin Genitourin Cancer. 2018;16:385–91.
23. Huang YT, Fong W, Thomas P. Rectal carcinoma on 68Ga-PSMA PET/CT. Clin Nucl Med. 2016;41:167–8.
24. Krohn T, Verburg FA, Pufe T, et al. [(68)Ga]PSMA-HBED uptake mimicking lymph node metastasis in coeliac ganglia: an important pitfall in clinical practice. Eur J Nucl Med Mol Imaging. 2015;42:210–4.
25. Calabria F, Gangemi V, Gullà D, et al. 64Cu-PSMA uptake in meningioma: a potential pitfall of a promising radiotracer. Rev Esp Med Nucl Imagen Mol. 2017;36:335–6.
26. Bilgin R, Ergül N, Çermik TF. Incidental meningioma mimicking metastasis of prostate adenocarcinoma in 68Ga-Labeled PSMA Ligand PET/CT. Clin Nucl Med. 2016;41:956–8.
27. Calabria F. Fifty shades of meningioma: challenges and perspectives of different PET molecular probes. Clin Transl Imaging. 2017;5:403–5.

28. Calabria F, Pichler R, Leporace M et al. 68Ga/64Cu PSMA bio-distribution in prostate cancer patients: potential pitfalls for different tracers. Curr Radiopharm. 2019 [Epub ahead of print].
29. Fallanca F, Giovacchini G, Picchio M, et al. Incidental detection by [11C]choline PET/CT of meningiomas in prostate cancer patients. Q J Nucl Med Mol Imaging. 2009;53:417–21.
30. Strele-Trieb P, Dunzinger A, Sonnberger M, et al. Uptake of 68Ga-prostate-specific membrane antigen PET in Adrenal Gland: a potential pitfall. Clin Nucl Med. 2017;43:50–1.
31. Keidar Z, Gill R, Goshen E, et al. 68Ga-PSMA PET/CT in prostate cancer patients - patterns of disease, benign findings and pitfalls. Cancer Imaging. 2018;18:39.
32. Jochumsen MR, Bouchelouche K. Intense 68Ga-PSMA uptake in diverticulum of the sigmoid colon. Clin Nucl Med. 2018;43:110–1.
33. Calabria FF, Chiaravalloti A, Jaffrain-Rea ML, et al. 18F-DOPA PET/CT physiological distribution and pitfalls: experience in 215 patients. Clin Nucl Med. 2016;41:753–60.
34. Calabria F, Chiaravalloti A, Cicciò C, et al. PET/CT with 18F-choline: physiological whole biodistribution in male and female subjects and diagnostic pitfalls on 1000 prostate cancer patients: 18F-choline PET/CT bio-distribution and pitfalls. A southern Italian experience. Nucl Med Biol. 2017;51:40–54.
35. Fujibayashi Y, Taniuchi H, Yonekura Y, et al. Copper-62-ATSM: a new hypoxia imaging agent with high membrane permeability and low redox potential. J Nucl Med. 1997;38:1155–60.
36. Padhani AR, Krohn KA, Lewis JS, et al. Imaging oxygenation of human tumours. Eur Radiol. 2007;17:861–72.
37. Yuan H, Schroeder T, Bowsher JE, et al. Intertumoral differences in hypoxia selectivity of the PET imaging agent 64Cu(II)-diacetyl-bis(N4-methylthiosemicarbazone). J Nucl Med. 2006;47:989–98.
38. Liu J, Hajibeigi A, Ren G, et al. Retention of the radiotracers 64Cu-ATSM and 64Cu-PTSM in human and murine tumors is influenced by MDR1 protein expression. J Nucl Med. 2009;50:1332–9.
39. Yoshii Y, Furukawa T, Kiyono Y, et al. Internal radiotherapy with copper-64-diacetyl-bis (N4-methylthiosemicarbazone) reduces CD133+ highly tumorigenic cells and metastatic ability of mouse colon carcinoma. Nucl Med Biol. 2011;38:151–7.
40. Yoshii Y, Yoneda M, Ikawa M, et al. Radiolabeled Cu-ATSM as a novel indicator of overreduced intracellular state due to mitochondrial dysfunction: studies with mitochondrial DNA-less ρ0 cells and cybrids carrying MELAS mitochondrial DNA mutation. Nucl Med Biol. 2012;39:177–85.
41. Nehmeh SA, Lee NY, Schröder H, et al. Reproducibility of intratumor distribution of (18) F-fluoromisonidazole in head and neck cancer. Int J Radiat Oncol Biol Phys. 2008;70:235–42.
42. McCall KC, Humm JL, Bartlett R, et al. Copper-64-diacetyl-bis(N(4)-methylthiosemicarbazone) pharmacokinetics in FaDu xenograft tumors and correlation with microscopic markers of hypoxia. Int J Radiat Oncol Biol Phys. 2012;84:e393–9.
43. Carlin S, Zhang H, Reese M, et al. A comparison of the imaging characteristics and microregional distribution of 4 hypoxia PET tracers. J Nucl Med. 2014;55:515–21.
44. Tateishi K, Tateishi U, Sato M, et al. Application of 62Cu-diacetyl-bis (N4-methylthiosemicarbazone) PET imaging to predict highly malignant tumor grades and hypoxia-inducible factor-1α expression in patients with glioma. AJNR Am J Neuroradiol. 2013;34:98–9.
45. Minagawa Y, Shizukuishi K, Koike I, et al. Assessment of tumor hypoxia by 62Cu-ATSM PET/CT as a predictor of response in head and neck cancer: a pilot study. Ann Nucl Med. 2011;25:339–45.
46. Dehdashti F, Mintun MA, Lewis JS, et al. In vivo assessment of tumor hypoxia in lung cancer with 60Cu-ATSM. Eur J Nucl Med Mol Imaging. 2003;30:844–50.
47. Lopci E, Grassi I, Rubello D, et al. Prognostic evaluation of disease outcome in solid tumors investigated with 64Cu-ATSM PET/CT. Clin Nucl Med. 2016;41:e87–92.
48. Barrio M, Czernin J, Fanti S, et al. The impact of SSTR-directed PET/CT on the management of patients with neuroendocrine tumor: A systematic review and meta-analysis. J Nucl Med. 2017;58:756–61.
49. Hanaoka H, Tominaga H, Yamada K, et al. Evaluation of (64)Cu-labeled DOTA-D-Phe(1)-Tyr (3)-octreotide ((64)Cu-DOTA-TOC) for imaging somatostatin receptor-expressing tumors. Ann Nucl Med. 2009;23:559–667.
50. Anderson CJ, Pajeau TS, Edwards WB, et al. In vitro and in vivo evaluation of copper-64-octreotide conjugates. J Nucl Med. 1995;36:2315–25.
51. Pfeifer A, Knigge U, Mortensen J, et al. Clinical PET of neuroendocrine tumors using 64Cu-DOTATATE: first-in-humans study. J Nucl Med. 2012;53:1207–15.
52. Pfeifer A, Knigge U, Binderup T, et al. 64Cu-DOTATATE PET for neuroendocrine tumors: a prospective head-to-head comparison with 111In-DTPA-octreotide in 112 patients. J Nucl Med. 2015;56:847–54.
53. Johnbeck CB, Knigge U, Loft A, et al. Head-to-head comparison of 64Cu-DOTATATE and 68Ga-DOTATOC PET/CT: a prospective study of 59 patients with neuroendocrine tumors. J Nucl Med. 2017;58:451–7.
54. Bahri H, Laurence L, Edeline J, et al. High prognostic value of 18F-FDG PET for metastatic gastroenteropancreatic neuroendocrine tumors: a long-term evaluation. J Nucl Med. 2014;55:1786–90.
55. Bhatkar D, Utpat K, Basu S, et al. Dual tracer PET imaging (68Ga-DOTATATE and 18F-FDG) features in pulmonary carcinoid: correlation with tumor proliferation index. Indian J Nucl Med. 2017;32:39–41.
56. Pedersen SF, Sandholt BV, Keller SH, et al. 64Cu-DOTATATE PET/MRI for detection of activated macrophages in carotid atherosclerotic plaques: studies in patients undergoing endarterectomy. Arterioscler Thromb Vasc Biol. 2015;35:1696–703.

Amyloid Imaging

8

Agostino Chiaravalloti, Ferdinando Calabria, Antonio Bagnato, and Orazio Schillaci

Contents

Abbreviations

^{18}F-FDG	18F-Fluorodeoxyglucose
AD	Alzheimer's disease
MCI	Mild cognitive impairment
PET/CT	Positron emission tomography/computed tomography
SUV_R	Standardized uptake value ratio

A. Chiaravalloti
Department of Biomedicine and Prevention, University "Tor Vergata", Rome, Italy

F. Calabria (✉) · A. Bagnato
Department of Nuclear Medicine and Theranostics, "Mariano Santo" Hospital, Cosenza, Italy
e-mail: ferdinandocalabria@hotmail.it

O. Schillaci
Department of Biomedicine and Prevention, University "Tor Vergata", Rome, Italy

Department of Nuclear Medicine and Molecular Imaging, IRCCS Neuromed, Pozzilli, IS, Italy

8.1 Synthesis

Among several radiopharmaceuticals for the "*in vivo*" PET/CT imaging of Aβ plaques, ^{18}F-florbetaben is obtained by a diarylethene, which is a hydrocarbon consisting of a trans ethane double bond substituted with a phenyl group on both carbon atoms of the double bond: the (E)-stilbene. A substitution of the (E)-stilbene core with a styryl-pyridine moiety can lead in obtaining ^{18}F-florbetapir, thus potentially reducing the lipophilicity of the molecule and leading

F. Calabria, O. Schillaci (eds.), *Radiopharmaceuticals*,
https://doi.org/10.1007/978-3-030-27779-6_8

in a faster brain kinetics [1]. The automated synthesis of ^{18}F-florbetaben is a two-step reaction, consisting of the nucleophilic displacement of the methane-sulfonic-acid leaving group in the precursor, methanesulfonic acid (Boc-Stilbene-Polyethyleneglycol) with activated ^{18}F-fluoride, followed by acidic hydrolysis to remove the protecting group [2]. More recently, it has been described a one-step automated synthesis of ^{18}F-florbetaben with methane-sulfonic-acid as a precursor, characterized by 50 min of time for synthesis and a purity of 95% [3].

8.2 Pharmacokinetics

Amyloid-imaging agents such as ^{18}F-florbetapir, ^{18}F-flutemetamol, and ^{18}F-florbetaben diffuse across the blood–brain barrier, are taken up in the neuritic plaques, and produce a radioactive signal that is detectable throughout the brain.

Neuritic plaques are mostly represented by a central core of amyloid fibrils surrounded by dystrophic neuritis and active microglia and astrocytes. Aβ peptide is the main constituent of amyloid fibrils. This feature could be at the basis of the "*amyloid hypothesis*" [4], proposed as explanation of the pathological basis of Alzheimer's disease (AD) [5]. On the other hand, another theory considers the neurofibrillary pathology and "*Tau Protein*" deposition as the fundamental problem of AD: in fact, the hyperphosphorylated Tau is found in AD brains.

To date, the relationship between these three molecules in the genesis of disease is not fully understood. Globally, it is generally accepted that Tau and amyloid could represent different features of the same disease.

Standing to these forewords, the PET/CT imaging with amyloid tracers is actually preferred to Tau imaging since a growing amount of literature data shows that Aβ deposition is an earlier molecular marker of AD; moreover, Aβ deposition in human brain represents a potential therapeutic target. However, recent studies are showing encouraging results about Tau tracers, able to accurately and specifically target tau deposits in vivo in the brains of patients [6] (see Chap. 13).

8.3 Physiological Distribution

After the intravenous administration, the brain uptake maximizes within several minutes and then clears rapidly from the circulation during the first 30 min after injection. Clearance slows significantly after 30 min, and by 40–50 min the activity remains in a steady state until 90 min after injection [7].

The highest level of ^{18}F-florbetapir uptake in the normal brain is in regions comprising mostly white matter. The reason for this nonspecific uptake in white matter is still not well established. In healthy subjects, ^{18}F-flutemetamol uptake presents slow uptake in structures such as salivary glands, liver, muscles, and bone marrow (Fig. 8.1) [8]. In our experience, the biodistribution of ^{18}F-florbetapir also shows a significant hepatobiliary and urinary excretion while gastric mucosa can occasionally show mild tracer uptake [7] (Fig. 8.2).

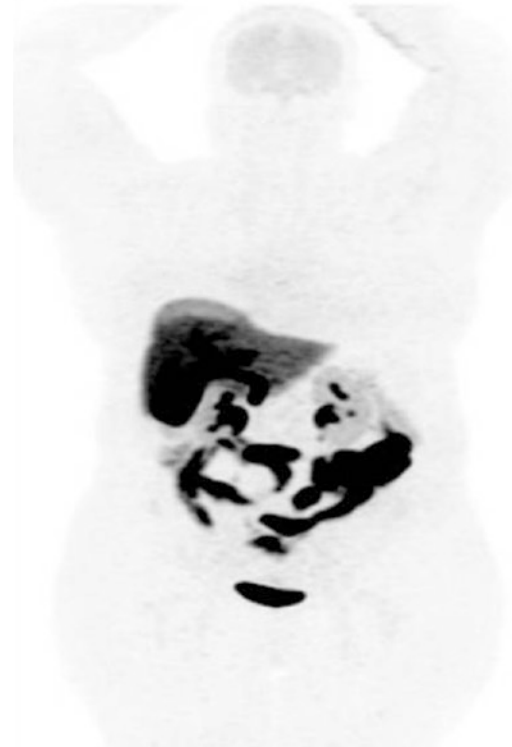

Fig. 8.1 Whole body PET maximum intensity projection of the physiological ^{18}F-flutemetamol in a 63-year-old patient

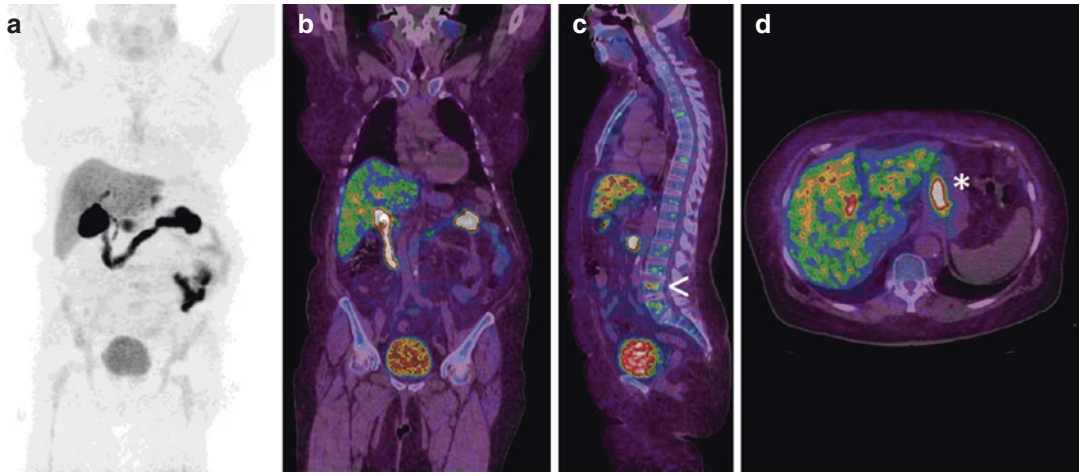

Fig. 8.2 PET maximum intensity projection (**a**) showing the in vivo bio-distribution of ^{18}F-florbetapir in a 63-year-old woman. Fused coronal (**b**) and sagittal (**c**) PET/CT views show a significant hepatobiliary and a mild urinary excretion of the radiolabeled compound. In (**c**) mild uptake is also detectable in bone marrow (<) and in the gastric mucosa (**d**,∗, axial view)

8.4 Clinical Indications

8.4.1 Mild Cognitive Impairment

Amyloid deposition appears early in the development of AD and also in brains of patients with *mild cognitive impairment* (MCI). Therefore, tracking the *in vivo* imaging of amyloid could be of aid for the early diagnosis of the disease especially in those subjects over 65 years old, with short-term or long-term memory impairment, no significant daily functional disability, and subjective complaint of memory loss with global preservation of other cognitive abilities [9] (Fig. 8.3).

In a recent study, 53% of the subjects examined with ^{18}F-florbetaben PET/CT was positive for amyloid burden in brain (in a percentage that is in agreement with that of the MCI subjects that convert to dementia or with that of subjects that show low levels of Aβ amyloid in cerebrospinal fluid) [10]. Therefore, a ^{18}F-florbetapir/^{18}F-florbetaben PET in patients with MCI should be aimed in order to verify the potential progression in AD, which can occur in a significant percentage of patients with MCI. In a recent study, at 2 years, 75% of MCI subjects with a baseline ^{18}F-florbetaben PET positive scan progressed to AD while only 9.5% of the subjects with a negative scan showed disease progression; at 4 years, 87.7% of participants with a positive scan had AD [11]. However, a recent review performed on the role of amyloid PET in management of patients with MCI do not recommend routine use of ^{18}F-flutemetamol PET in this clinical setting, due to the varying sensitivity and specificity for predicting the progression from MCI to AD, considering limited data available in literature and high costs of the exam [12].

8.4.2 Alzheimer Disease and Other Kinds of Dementia

In all the studies comparing AD patients with healthy controls, both visual and semiquantitative analysis (by means of SUV_R) allowed the identification of a meaningfully higher ^{18}F-florbetaben uptake in in Alzheimer's disease patients rather than controls [13–17]. In patients with AD, the PET scan with ^{18}F-florbetaben usually shows higher uptake in frontal, lateral temporal, occipital anterior and posterior cingulate cortex [13].

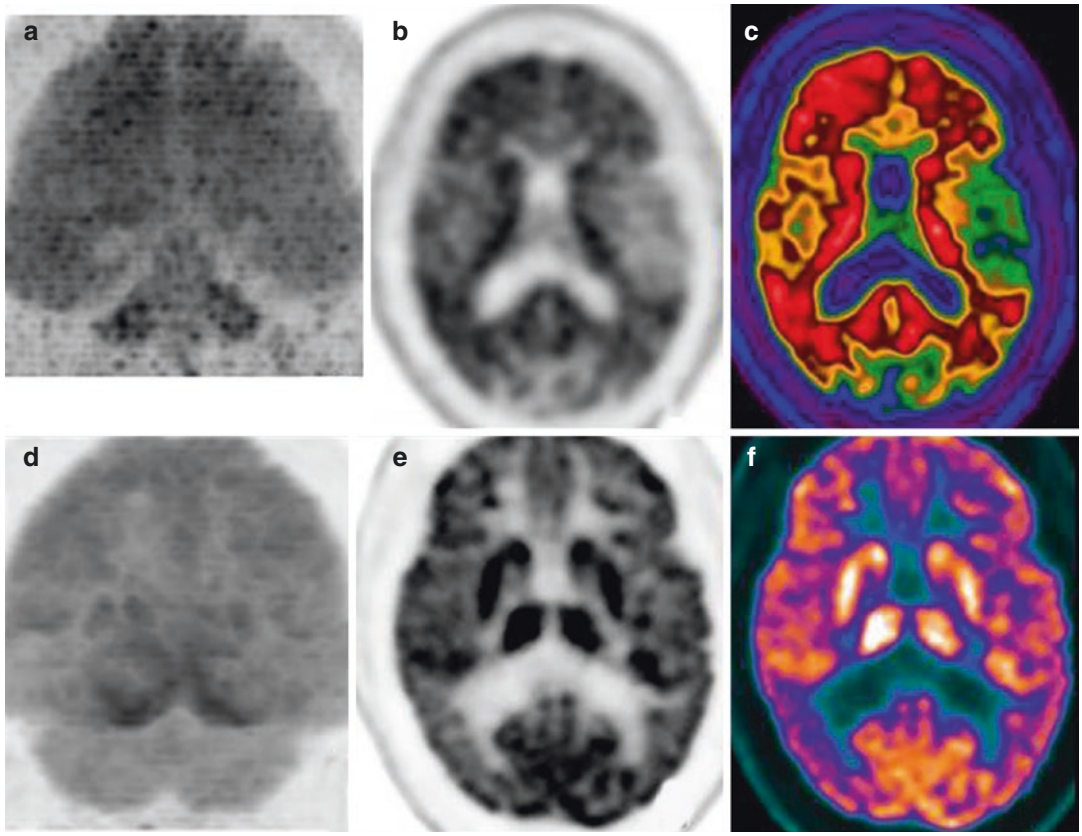

Fig. 8.3 A 61-year-old patient examined for *mild cognitive impairment*. ^{18}F-Flutemetamol maximum intensity projection (**a**) and axial PET views (**b**, **c**) show pathologic amyloid burden in both frontal region and right temporal lobe. ^{18}F-FDG maximum intensity projection (**d**) and axial PET views (**e**, **f**) show deficit of glucose metabolism in right temporal lobe

The diagnostic value of ^{18}F-florbetaben in the differential diagnosis between AD patients and healthy subjects resulted in a sensitivity of 80% and a specificity of 91% [15].

Rowe et al. also demonstrated that PET with ^{18}F-florbetaben is able to discriminate between AD and frontotemporal dementia [18]. In 20 examined patients (15 with AD and 5 with frontotemporal dementia), a higher SUV_R was detectable in AD patients in comparison with subjects with frontotemporal dementia [18].

Regarding a comparison with ^{18}F-FDG, an interesting study examined 19 patients with a clinical diagnosis of Alzheimer's disease and 21 elderly controls with both ^{18}F-florbetapir and ^{18}F-FDG PET. The sensitivity of ^{18}F-florbetapir PET were 95% and 95% while ^{18}F-FDG PET showed lower values, respectively, 89% and 86%. Overall, both scans performed well in the diagnosis of patients with known clinical AD. Moreover, both scans well correlated with cognitive status as assessed by the mini-mental status examination. However, for the intrinsic property of the tracer, only the ^{18}F-FDG PET correlated with the cognitive status [19].

8.5 Clinical Cases

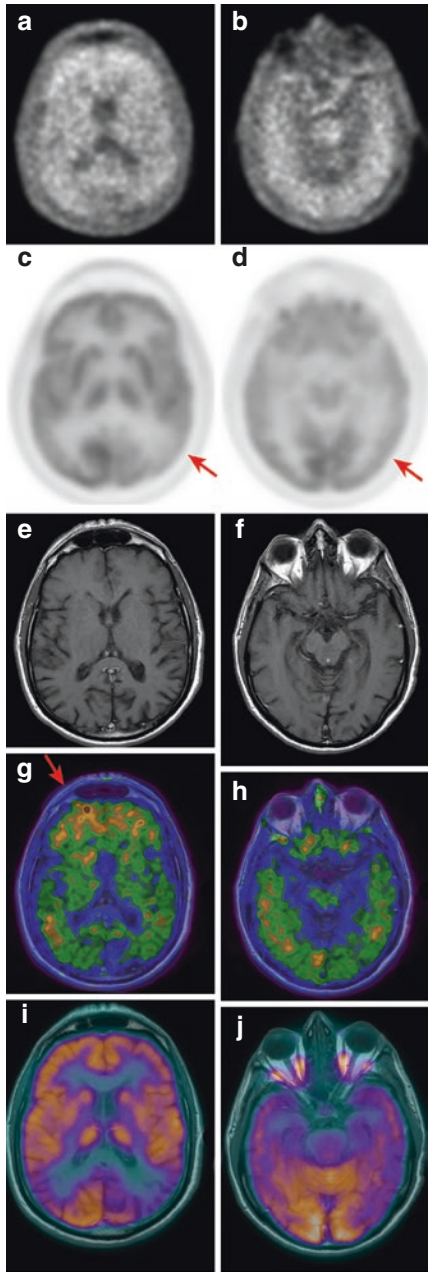

Fig. 8.4 In (**a**) and (**b**) we report the axial views of a ^{18}F-florbetaben PET scan showing a pathological amyloid burden in brain in a 68-year-old male patient with clinical suspect of Alzheimer's disease. In (**c**) and (**d**) we report the axial views of ^{18}F-FDG PET scan in the same subject showing a decrease of brain glucose consumption in the left parietal and temporal lobes (arrows). MRI scans are showed in (**e**) and (**f**) and PET/MR fusion imaging of ^{18}F-florbetaben and ^{18}F-FDG are showed in (**g**, **h**) and (**i**, **j**), respectively. The greatest amyloid burden in brain was detectable in frontal lobes bilaterally (**g**, arrow)

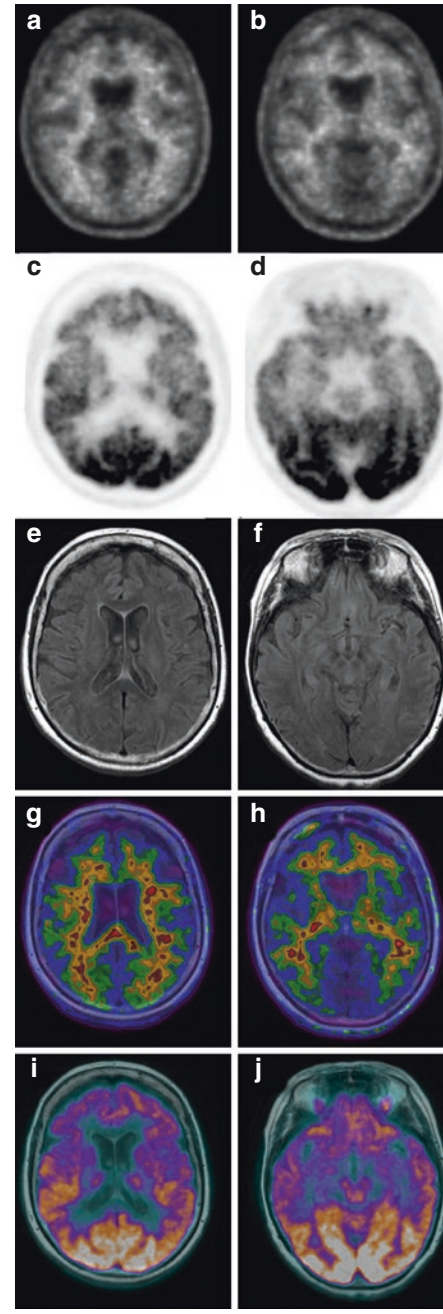

Fig. 8.5 In (**a**) and (**b**) we report the axial views of a ^{18}F-florbetapir PET showing no significant amyloid burden in brain in a 66-year-old female subject with clinical suspect of frontotemporal dementia. In (**c**) and (**d**) we report the axial views of ^{18}F-FDG PET in the same subject, showing a decrease of brain glucose consumption in the frontal and temporal lobes bilaterally. MRI scans are showed in (**e**) and (**f**) and PET/MR fusion imaging of ^{18}F-florbetapir and ^{18}F-FDG are showed in (**g**, **h**) and (**i**, **j**) respectively

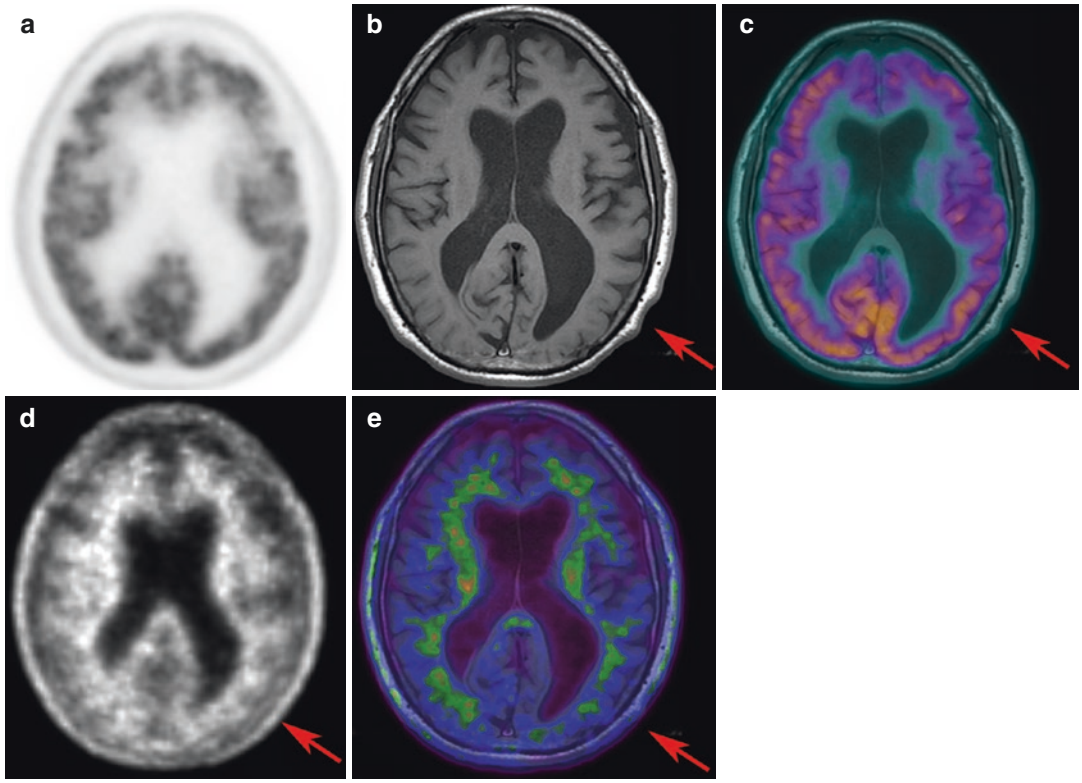

Fig. 8.6 Axial ^{18}F-FDG PET scan in (**a**) in a subject with clinical suspect of frontotemporal dementia. In (**b**) we report the axial MR images showing a significant cortical atrophy involving in particular the left temporal lobe (arrow); in (**c**), ^{18}F-FDG PET/MR fusion imaging showing a significant reduction of brain glucose consumption in the left frontal lobe and a mild decrease of glucose consumption in the left temporal lobe. In (**d**) we report an axial image of ^{18}F-florbetaben PET scan showing no significant amyloid burden in brain. Nevertheless, due to the presence of cortical atrophy, interpretation of PET scan is doubtful in the temporal lobe (arrow). ^{18}F-Florbetaben PET/MR fusion imaging in (**e**) shows no significant amyloid burden in the left temporal lobe

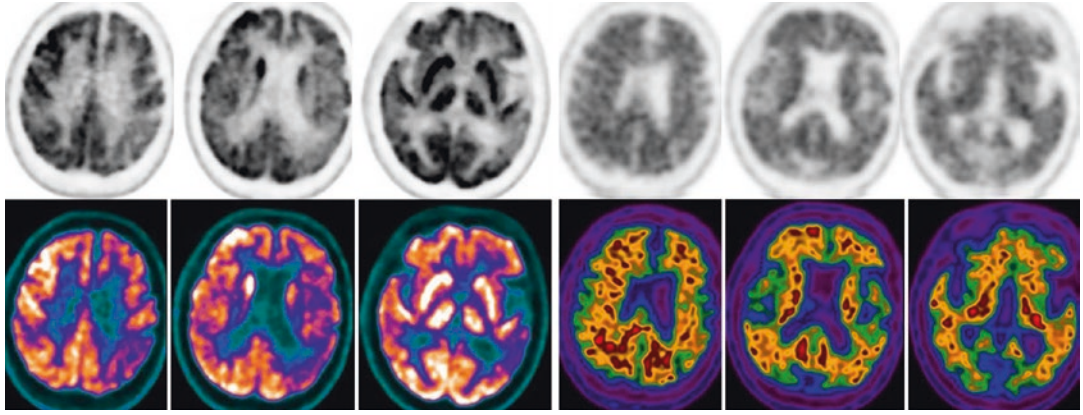

Fig. 8.7 A 66-year-old male patient was examined for clinical suspicion of Alzheimer's disease with ^{18}F-FDG and ^{18}F-flutemetamol PET/CT scans. Both scans confirmed diagnosis. In the left panel, axial ^{18}F-FDG PET views in different color scales show deficit of glucose metabolism in left parietal and temporal regions. In the right panel axial ^{18}F-flutemetamol PET views in different color scales show pathological amyloid burden in frontal and parietal regions bilaterally and in left temporal lobe

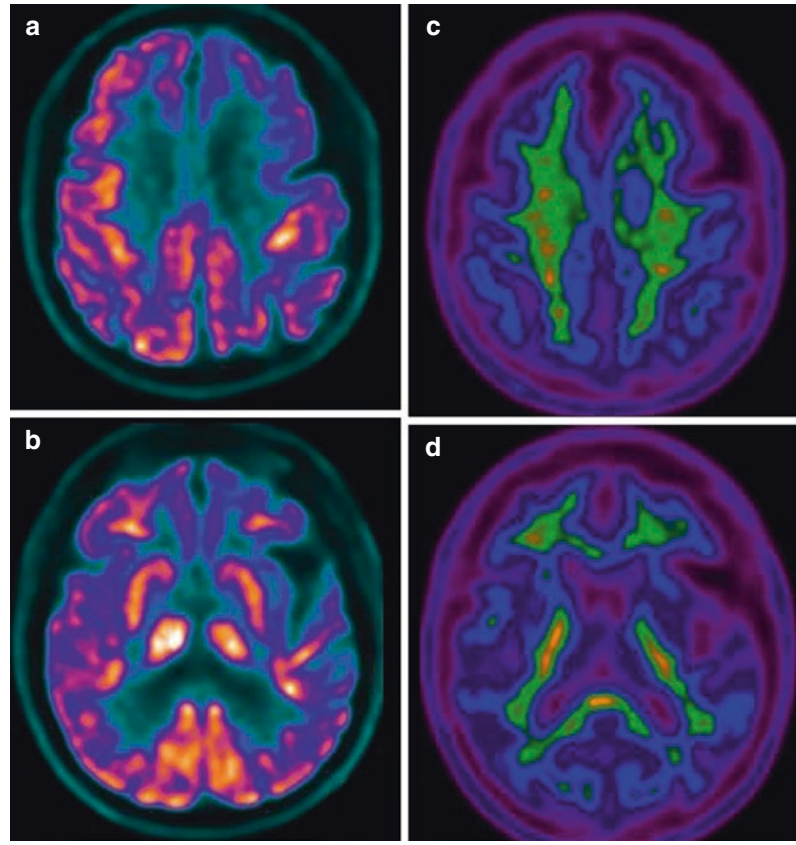

Fig. 8.8 A 62-year-old male patient was examined for clinical suspicion of frontotemporal dementia with ^{18}F-FDG and ^{18}F-flutemetamol PET/CT scans. Axial ^{18}F-FDG PET views (**a**, **b**) show deficit of glucose metabolism in left frontal and temporal lobes, confirming clinical diagnosis. Corresponding axial ^{18}F-flutemetamol PET views (**c**, **d**) show no significant amyloid burden in the same regions

8.6 PET/CT Acquisition Protocols

PET/CT imaging is usually performed 90–110 min after the injection of ~300 MBq of the radiolabeled compound (35, 38, 39, 42) with a PET acquisition time of 20 min [20]. Since movement artifacts may occur during the duration of the scan, especially in less compliant patients, due to the advanced disease, a study has been carried out in order to investigate the influence of scan duration on the evaluation of PET images with ^{18}F-florbetaben: the authors concluded that the agreement among readers of the scans lasting 20, 10, and 5 min, respectively, was good and, in particular, there were not differences in the identification of healthy controls from patients [21].

8.7 Variants and Pitfalls

Due to the rapid brain washout of the tracer it is not uncommon, in late scans following more than 2 h the tracer administration, to obtain low-quality PET images, with a poor count (Fig. 8.9). As already reported, the ideal standard imaging should be performed 90 min following the injection.

No significant diagnostic pitfalls are reported in literature, linked to the distribution of the tracers, with the exception of a certain quote of nonspecific uptake in the skull and in the white matter [22] and the possibility to detect tracer uptake in cardiac amyloidosis. Cardiac amyloidosis is an under-recognized cause of left ventricular hypertrophy and heart failure in the elderly; to date,

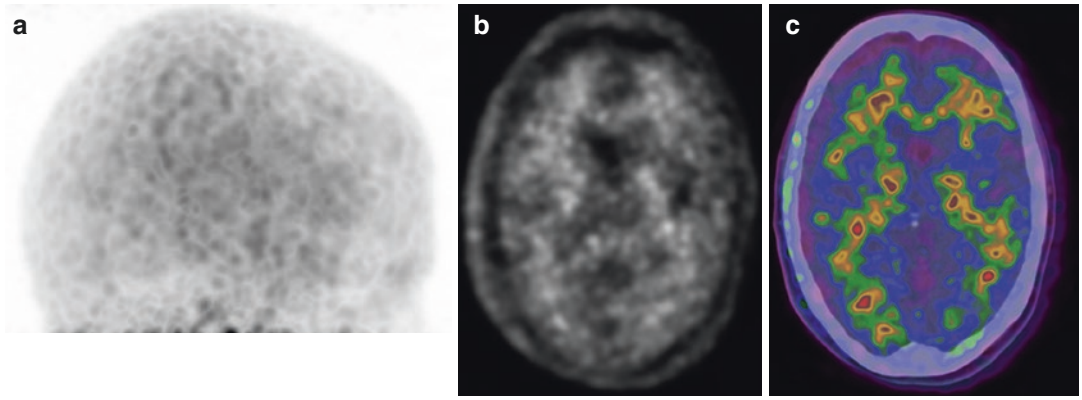

Fig. 8.9 Delayed acquisition (120 min) in a 72-year-old woman showing a poor count in brain PET acquisition due to a significant washout of the radiolabeled compound (^{18}F-florbetaben). PET maximum intensity projection is showed in (**a**) while PET and PET/CT images are showed in (**b**) and (**c**)

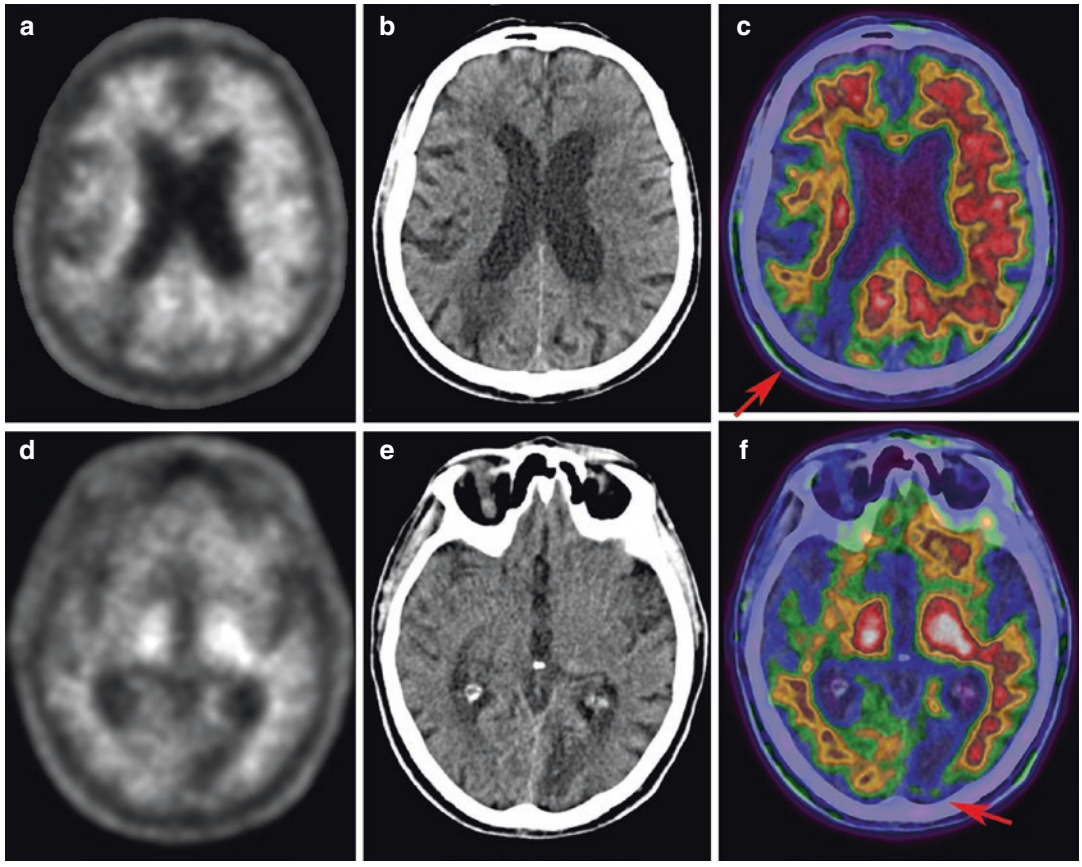

Fig. 8.10 Axial ^{18}F-florbetaben PET (**a**), CT (**b**), and fused PET/CT (**c**) images showing no tracer uptake in a cortical-subcortical area of previous stroke in the right parietal lobe (arrow) in a 70-year-old male subject. In the same subject, another stroke was detectable in the left temporal and parietal lobe (**d**, **e**, **f**) with no significant uptake of the radiolabeled compound (**f**, arrow)

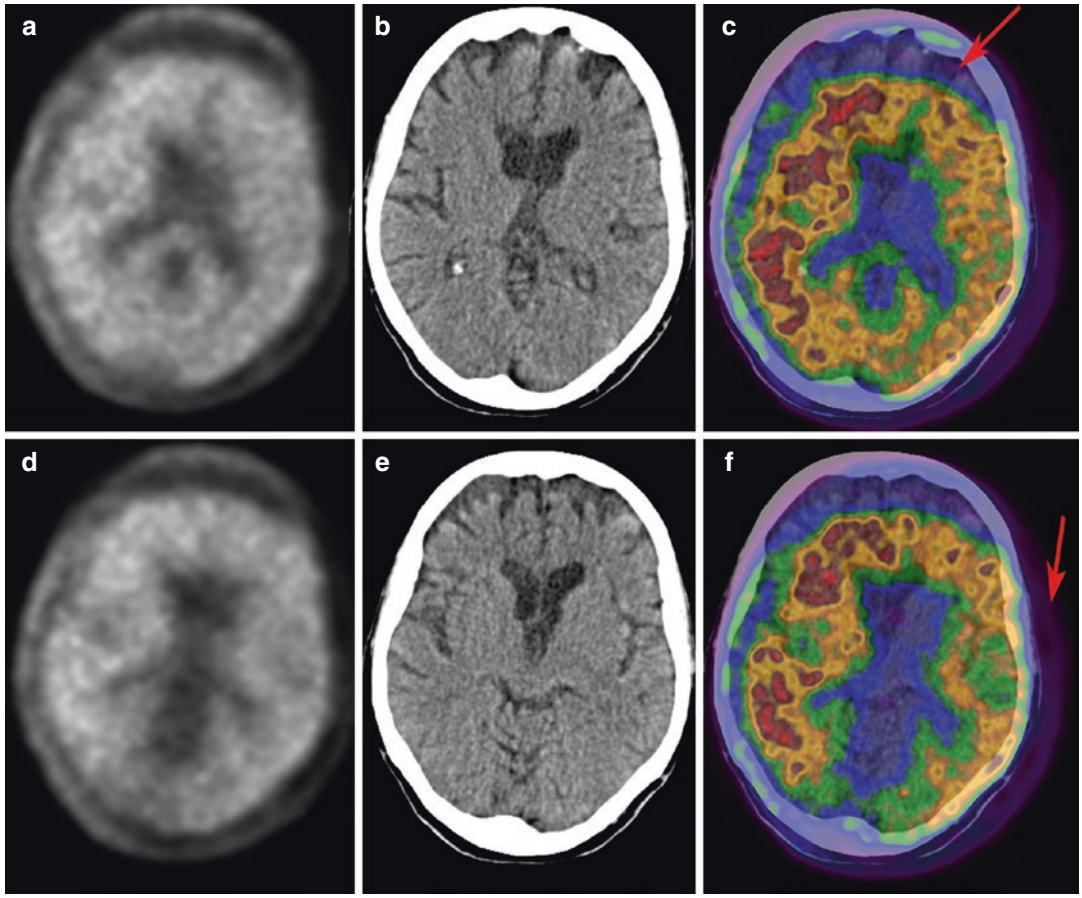

Fig. 8.11 In a patient with Alzheimer's disease, examined with ^{18}F-florbetaben PET/CT, an example of motion artifacts due to the head rotation between PET (**a**, **d**) and CT (**b**, **e**) scans, with abnormal PET/CT fusion imaging (**c**, **f**, arrows)

molecular tracers assessing amyloid plaque burden and sympathetic innervation may be useful for the noninvasive evaluation diagnosis and risk stratification of patients with suspected cardiac amyloidosis [23]. Recently, a pilot study demonstrated constant cardiac uptake with ^{18}F-florbetapir in 15 patients with cardiac amyloidosis [24]. However, studies on larger population are required to establish the role of this tracer in screening patients with amyloidosis for cardiac involvement and in disease monitoring.

In our experience, we documented absent uptake in postischemic lacunar areas (Fig. 8.10). On the other hand, technical artifacts are common to "traditional" PET/CT imaging with ^{18}F-FDG. For the clinical conditions of examined patients in peculiar clinical settings, the most common artifact can be linked to patient movement of the head and neck occurring between PET and CT imaging (Fig. 8.11).

Finally, in patients with negative amyloid tracer PET/CT scan another cause of dementia should be considered. As for vascular dementia, CT component of the exam can lead to few but meaningful information on patient's brain, as in the condition of idiopathic normal pressure hydrocephalus (Fig. 8.12). In this clinical condition, it has already reported the utility of CT while ^{18}F-FDG PET may be associated with preserved cortical metabolism [25]. Similar findings seem to be documented with amyloid PET tracers [26]. In particular, ^{18}F-florbetaben PET/CT can help determine which idiopathic normal pressure hydrocephalus patients will benefit from shunt surgery by discriminating concomitant AD, as reported in a recent study [27].

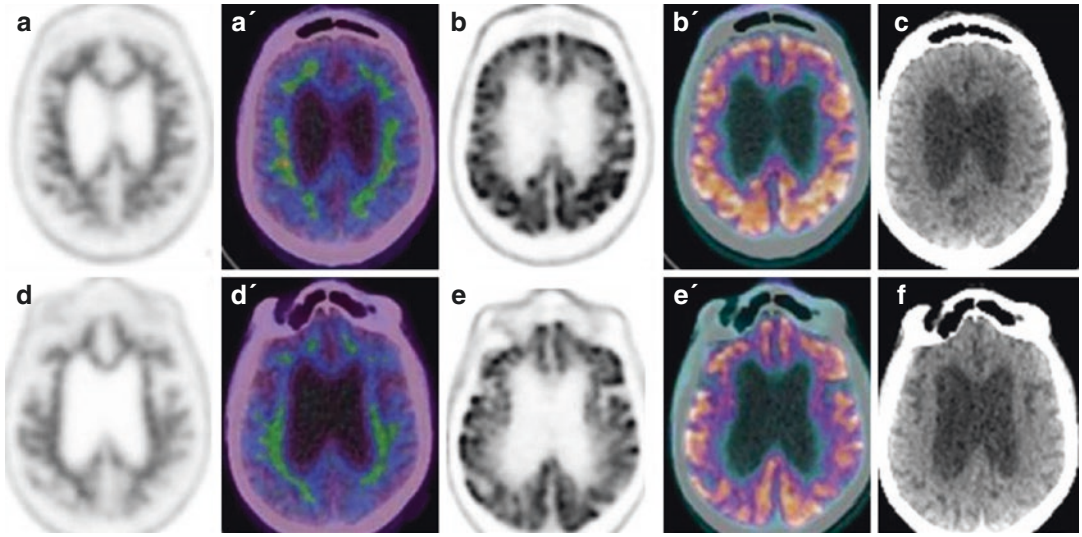

Fig. 8.12 A 59-year-old female patient was examined by ^{18}F-FDG and ^{18}F-flutemetamol PET/CT scans for clinical dementia. Axial ^{18}F-flutemetamol PET (**a**) and PET/CT (**a'**) views show no significant amyloid burden while axial ^{18}F-FDG PET (**b**) and PET/CT (**b'**) do not show deficit of glucose metabolism. In corresponding axial CT view is evident the condition of hydrocephalus (**c**). Subsequently, neurologists diagnosed dementia due to normal pressure hydrocephalus. Axial ^{18}F-flutemetamol PET (**d**) and PET/CT (**d'**) views, axial ^{18}F-FDG PET (**e**) and PET/CT (**e'**) and axial CT (**f**) views of the same patient

References

1. Mason NS, Mathis CA, Klunk WE. Positron emission tomography radioligands for in vivo imaging of Aβ plaques. J Labelled Comp Radiopharm. 2013;56:89–95.
2. Hang W, Oya S, Kung MP, et al. F-18 polyethyleneglycol stilbenes as PET imaging agents targeting Abeta aggregates in the brain. Nucl Med Biol. 2005;32:799–809.
3. Wang H, Guo X, Jiang S, et al. Automated synthesis of [18F]Florbetaben as Alzheimer's disease imaging agent based on a synthesis module system. Appl Radiat Isot. 2013;71:461–46.
4. Hardy JA, Higgins GA. Alzheimer's disease: the amyloid cascade hypothesis. Science. 1992;10:184–5.
5. Priller C, Bauer T, Mitteregger G, et al. Synapse formation and function is modulated by the amyloid precursor protein. J Neurosci. 2006;5:7212–21.
6. Saint-Aubert L, Lemoine L, Chiotis K, Leuzy A, et al. Tau PET imaging: present and future directions. Mol Neurodegener. 2017;20:19.
7. Trembath L, Newell M, Devous MD Sr. Technical considerations in brain amyloid PET imaging with 18F-florbetapir. J Nucl Med Technol. 2015;43:15–184.
8. Thal DR, Beach TG, Zanette M, et al. Estimation of amyloid distribution by [18F]flutemetamol PET predicts the neuropathological phase of amyloid β-protein deposition. Acta Neuropathol. 2018;136:557–67.
9. Petersen RC, Waring SC, Smith GE, et al. Predictive value of APOE genotyping in incipient Alzheimer's disease. Ann New York Acad Sci. 1996;802:58–69.
10. Ong K, Villemagne VL, Bahar-Fuchs A, et al. (18) F-florbetaben Abeta imaging in mild cognitive impairment. Alzheimers Res Ther. 2013;5:4.
11. Ong KT, Villemagne VL, Bahar-Fuchs A, et al. Abeta imaging with 18F-florbetaben in prodromal Alzheimer's disease: a prospective outcome study. J Neurol Neurosurg Psychiatry. 2015;86:431–6.
12. Martínez G, Vernooij RW, Fuentes Padilla P, et al. 18F PET with flutemetamol for the early diagnosis of Alzheimer's disease dementia and other dementias in people with mild cognitive impairment (MCI). Cochrane Database Syst Rev. 2017;(22):CD012884.
13. Barthel H, Sabri O. Florbetaben to trace amyloid-beta in the Alzheimer brain by means of PET. J Alzheimers Dis. 2011;26:117–21.
14. Becker GA, Ichise M, Barthel H, et al. PET quantification of 18F-florbetaben binding to beta-amyloid deposits in human brains. J Nucl Med. 2013;54:723–31.
15. Barthel H, Gertz HJ, Dresel S, et al. Cerebral amyloid-beta PET with florbetaben (18F) in patients with Alzheimer's disease and healthy controls: a multicentre phase 2 diagnostic study. Lancet Neurol. 2011;10:424–35.
16. Sabri O, Sabbagh MN, Seibyl J, et al. Florbetaben PET imaging to detect amyloid beta plaques in Alzheimer disease: phase 3 study. Alzheimers Dement. 2015;28:00060–6.

17. Perani D, Schillaci O, Padovani A, et al. A survey of FDG- and amyloid-PET imaging in dementia and GRADE analysis. Biomed Res Int. 2014;2014:785039.
18. Rowe CC, Ackerman U, Browne W, et al. Imaging of amyloid beta in Alzheimer's disease with 18F-BAY94-9172, a novel PET tracer: proof of mechanism. Lancet Neurol. 2008;7:129–35.
19. Newberg AB, Arnold SE, Wintering N, et al. Initial clinical comparison of 18F-florbetapir and 18F-FDG PET in patients with Alzheimer disease and controls. J Nucl Med. 2012;53:902–7.
20. Barthel H, Gertz HJ, Dresel S, et al. Cerebral amyloid-β PET with florbetaben (18F) in patients with Alzheimer's disease and healthy controls: a multicentre phase 2 diagnostic study. Lancet Neurol. 2011;10:424–5.
21. Tiepolt S, Barthel H, Butzke D, et al. Influence of scan duration on the accuracy of β-amyloid PET with florbetaben in patients with Alzheimer's disease and healthy volunteers. Eur J Nucl Med Mol Imaging. 2013;40:238–44.
22. Arai A, Kaneta T, Okamura N, et al. Pitfalls of voxel-based amyloid PET analyses for diagnosis of Alzheimer's disease: artifacts due to non-specific uptake in the white matter and the skull. Tohoku J Exp Med. 2014;234:175–81.
23. Pelletier-Galarneau M, Abikhzer G, Giraldeau G, et al. Molecular imaging of cardiac amyloidosis. Curr Cardiol Rep. 2019;28:12.
24. Manwani R, Page J, Lane T, et al. A pilot study demonstrating cardiac uptake with 18F-florbetapir PET in AL amyloidosis patients with cardiac involvement. Amyloid. 2018;25:247–52.
25. Townley RA, Botha H, Graff-Radford J, et al. 18F-FDG PET-CT pattern in idiopathic normal pressure hydrocephalus. Neuroimage Clin. 2018;28:897–902.
26. Rinne JO, Suotunen T, Rummukainen J, et al. [11C] PIB PET is associated with the brain biopsy amyloid-β load in subjects examined for Normal pressure hydrocephalus. J Alzheimers Dis. 2019;67:1343–51.
27. Jang H, Park SB, Kim Y, et al. Prognostic value of amyloid PET scan in normal pressure hydrocephalus. J Neurol. 2018;265:63–73.

PET Myocardial Perfusion Imaging: ^{82}Rb

9

Maria Luisa De Rimini and Giovanni Borrelli

Contents

M. L. De Rimini (✉) · G. Borrelli
Nuclear Medicine—PET UNIT, Health Service Department, AO Ospedali dei Colli, Naples, Italy
e-mail: marialuisa.derimini@ospedalideicolli.it

F. Calabria, O. Schillaci (eds.), *Radiopharmaceuticals*,
https://doi.org/10.1007/978-3-030-27779-6_9

9.1 PET Myocardial Perfusion Tracers: Introduction

The most common PET tracers for myocardial perfusion imaging (MPI) and for quantification of myocardial blood flow (MBF) are ^{13}N-labeled ammonia (^{13}NH3), ^{15}O-labeled water (^{15}O-H_2O), and ^{82}Rb [1], they are reported in Table 9.1 showing their main features where, obviously, the common feature for each of them is that the decay.

Positron rapidly looses kinetic energy before colliding with an electron. Both particles annihilate and emit 2 gamma rays with energies of 511 keV in opposite directions. Thus, if in a PET scanner the ring of detectors surrounding the patient detects a coincidence pair of 511 keV gamma rays, it is registered as an event. When many similar events are detected, the activity distribution of the positron-emitting radionuclide may be constructed within the volume of the left ventricle (LV) and cardiac imaging will be obtained.

Reliable attenuation correction (AC) methods for PET require determination of an attenuation map, which represents the spatial distribution of linear attenuation coefficients at 511 keV. Actually PET/CT scanners allow AC for PET images and morpho-functional correlations.

PET MPI is increasingly being used for noninvasive detection of coronary artery disease (CAD), despite its use can be limited by the shortcomings of the current perfusion tracers due to the need of in-house such as ^{15}O-H_2O, or onsite/nearby for ^{13}N-NH3, cyclotron and by commitment to costly generators (^{82}Rb).

Owing to the short half-lives of tracers (Table 9.1), their use with treadmill exercise stress test is not possible (^{82}Rb and ^{15}O-H_2O) and no/or not practical (^{13}N-NH3).

In the recent years, the development of a ^{18}F-labeled PET perfusion tracer has gathered considerable interest. The longer half-life of ^{18}F (109 min) would make the tracer available as a unit dose from regional cyclotrons and allows the use of PET associated with treadmill exercise testing. Furthermore, the short positron range of ^{18}F would result in better image resolution. ^{18}F-Flurpiridaz is by far the most thoroughly studied in animal models and is the only ^{18}F-based PET MPI radiotracer currently undergoing clinical evaluation. Preclinical and clinical experience

Table 9.1 Cardiac PET tracers

PET tracer	Physical half-life (min)	Extraction	Production	Mean positron range	Dose (MBq)	Effective dose (mSv)
^{13}NH3	9.96	80%	Onsite/nearby cyclotron	0.7	370–740	0.7–1.5
$H_2{}^{15}O$	2.05	Diffusible	On-site cyclotron	1.1	700–1500	0.7–1.4
^{82}Rb	1.16	50–60%	Generator	2.6	1100–1500	1.8–3.5 [a]1.26

[a]The use of 3D PET scanners and software allowing to inject half activity of ^{82}Rb with a preserved image quality, the calculated effective dose has been estimated 1.26 mSv for rest and stress scans

with ^{18}F Flurpiridaz demonstrated a high myocardial extraction fraction, high resolution of images and defects, high myocardial uptake, slow myocardial clearance, and high myocardial-to-background contrast stable over time. On this basis ^{18}F-labeled myocardial perfusion tracers could be an ideal PET MPI radiotracer and preclinical data are encouraging [2].

PET MPI provides for accurate diagnosis and has prognostic value in patients affected with CAD, allowing relevant additional advantages such as MBF estimation.

It should be underlined the close correlation between tracer's kinetics and MBF. Differences in the first-pass extraction of PET MPI tracers influence their myocardial uptake relating to regional blood flow and, at the same time, a better first-pass extraction of tracers influences a more effective evaluation of MBF [1].

Note:

- Resting MBF, measured with these tracers in healthy human, is approximately 1.0 mL/(min·g) with increases threefold or higher than 3.0 mL/(min g) under pharmacological stressor/vasodilator: adenosine, dipyridamole, or regadenoson [3]. The techniques for noninvasive flow estimates with compartmental modeling can accurately reflect regional MBF up to 5.0 mL/(min g).

9.1.1 Labeled Water (^{15}O-H_2O)

It is metabolically inert and freely diffusible through capillaries and cell membranes, with high extraction fraction. This feature allows appropriate quantification of MBF, taking advantage of the optimal tracer kinetic going in and out of the compartment in study, without undergoing any change by the system itself. On the other hand, the same feature prevents the uptake in the myocardium, making complex and extremely limited the realization of diagnostic MPI.

The ^{15}O-H_2O PET attractive is in its: Ability to accurately quantify MBF based on high extraction fraction; A short physical half-life making it possible to perform a short stress and rest data acquisition protocol with a lowering radiation exposure [4].

Note:

- ^{15}O-H_2O is not typically used for the assessment of myocardial perfusion alone, but it is the ideal flow tracer, including 100% extraction from blood to tissue, and 100% retention (no washout) allowing a linear relationship between MBF and the measured tracer activity over a wide range of flow rates.
- Currently ^{13}N-NH3 and ^{82}Rb are the two more commonly used tracers in routine clinical environment, with a small number of centers worldwide using ^{15}O-H_2O. Nevertheless they have limited (<100%) extraction and retention, do not exhibit such a linear property between MBF, tracer uptake, and retention rates, indeed roll-off of tracer uptake in the myocardium can underestimate the assessment of regional MBF at high flow.

9.1.2 ^{13}N Ammonia (^{13}N-NH3)

It is characterized by rapid blood disappearance. In the arterial blood it coexists in the neutral form (NH3) in balance with its charged ion (NH4). ^{13}NH3 diffuses rapidly through the plasma and cell membranes, allowing full extraction from the vascular pool and the rapid trapping within the myocytes.

Myocardial retention of ^{13}N-ammonia may be heterogeneous, even in normal subjects, considering that tracer retention in the lateral wall of the LV is about 10% less than that of other segments and the mechanism of this finding is unknown. ^{13}N-NH3 images also may be degraded by occasional intense liver activity, which can interfere with the evaluation of the inferior wall.

As with other nondiffusible tracers, the tissue extraction decreases with the increase of MBF, in linear relation for the flow values up to 2.5 mL/min/g. So, if in the healthy heart the fraction of the myocardial extraction of ^{13}N-NH3 at the first passage is 0.83 for flow = 1 mL/min/g, it drops to 0.60 for flow = 3 mL/min/g. The flow and

perfusion studies (for activity i.v. 370 MBq) are of good quality, with the exception of conditions including patients affected with dysfunctionally LV or chronic lung diseases and occasionally in smokers. Although the sequestration of ^{13}N-ammonia in the lungs is usually minimal, in these selected population of patients it may be necessary to prolong the time between injection and scan for optimizing the myocardium/background ratio [1, 5].

In the assessment of LV contractile function with PET-Gated scan ^{13}N-NH3 and ^{82}Rb provide good quality imaging; however, for evaluating LV function really at peak of stressor test, ^{82}Rb is the preferred one because of the following ^{13}N-NH3 kinetic properties:

Waiting time between injection and scan: 3–4 min; Time for both Rest and Pharmacological stressor acquisitions: ^{13}N-NH3 about 120 min; ^{82}Rb: 35–45 min.

9.2 Rubidium-82

^{82}Rb is a positron emitter tracer used in PET for MPI and MBF studies. It is a monovalent cationic analog of potassium, shows kinetic properties similar to those of Thallium-201, indeed the ^{82}Rb myocardial uptake is conditioned by the coronary flow and requires active transport via the sodium-potassium exchange mechanisms [4–5].

The short physical half-life of ^{82}Rb and the advantage of production via a generator with rapid reconstitution allow fast sequential perfusion imaging and high patient throughput.

After i.v. injection, ^{82}Rb rapidly crosses the capillary membrane, myocardial uptake is dependent on coronary blood flow and requires active transport via the sodium/potassium adenosine triphosphate transporter. ^{82}Rb extraction can be altered by severe acidosis, hypoxia, and ischemia, confirming that ^{82}Rb uptake is both a function of blood flow and myocardial cell integrity [5]. The single-capillary transit extraction fraction of ^{82}Rb exceeds 50%. As ^{13}N-NH3 and other nondiffusible tracers, ^{82}Rb net extraction fraction decreases in a nonlinear fashion with increasing MBF. Between the two ^{82}Rb has a substantially lower extraction fraction (about 35% at peak stress) and tracer retention than does ^{13}N-ammonia; however, quantification of MBF with ^{82}Rb was validated against $H_2{}^{15}O$ and was found to be accurate at high flow rates.

9.2.1 Production and Kinetic

^{82}Rb is produced by nuclear decay of Strontium-82 (^{82}Sr) via a commercially available generator, obviating the need for a cyclotron and allowing the advantage of PET cardiac studies even in those structures without a cyclotron. ^{82}Rb generator can only be used with the calibrated CARDIOGEN-82® infusion system (Fig. 9.1a). The infusion system ensures accurate dosing with minimal operator interface and minimizes the radiation exposure.

The system contains shielding vault for CardioGen-82® Generator and waste container.

^{82}Sr/^{82}Rb generator for producing ^{82}Rb chloride (^{82}RbCl) for intravenous administration use has been provided with initial U.S.—FDA Approval in 1989. Cardiogen can be imported in Italy thanks to the Decree 1997, 11 February.

The ^{82}Rb parent radionuclide is ^{82}Sr that can only be produced efficiently with a high-energy cyclotron (~70 MeV) by proton spallation of molybdenum with a high-energy (800 MeV) accelerator, followed by chemical purification. The ^{82}Sr decays to ^{82}Rb by electron capture, it has a half-life of 25.5 days, which allows the clinical use of the ^{82}Sr/^{82}Rb generator for as long as 4–5 weeks, after which the generator must be replaced.

The main physical characteristics of ^{82}Rb are reported in Table 9.1, it decays into Krypton-82, which is stable, by emitting a positron and a neutrino.

Note:

- Generator can be eluted every 7–10 min in order to obtain the maximum performance

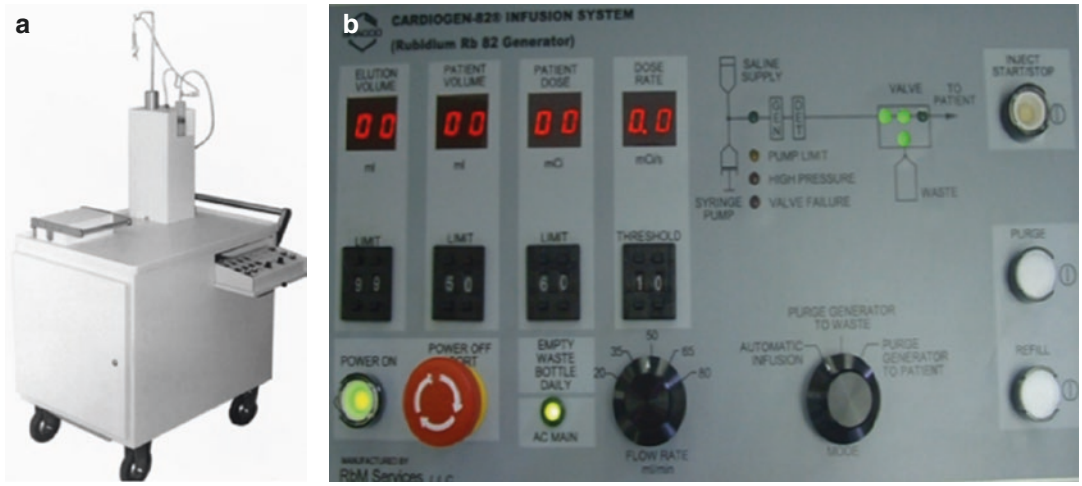

Fig. 9.1 (**a**) CARDIOGEN-82® system—cart containing generator and infusion system. (**b**) CARDIOGEN-82® system—panel to edit elution and monitor infusion

effectiveness. Consequently, the same time (7–10 min) between two consecutive elutions is the minimum time that must elapse between the two phases of ^{82}Rb PET perfusion study: basal and pharmacological stress test.

The ^{82}Sr/^{82}Rb radionuclide generator principle is based on inorganic cation exchange on hydrous tin oxide ($SnO_2 \times H_2O$, where $\times = 1, 2$). The target material is either ^{82}RbCl or ^{82}Rb metal. Chemical processing of ^{82}RbCl is faster, simpler, and much safer than chemical processing of a ^{82}Rb metal target; therefore, the ^{82}RbCl target material is readily available at a high level of purity. The Rubidium atom density is higher in ^{82}RbCl than in the pure metal, so the presence of the chloride atom does not decrease yield compared with the pure metal. Moreover, target fabrication is simpler and safer with ^{82}RbCl than with ^{82}Rb metal. With both ^{82}Rb metal and ^{82}RbCl targets, the buffered ^{82}RbCl solution is filtered and then transferred onto a column containing equilibrated chelating cation exchange resin, whereby the actual ^{82}Sr/^{82}Rb separation is achieved: bivalent $^{82}Sr^{2+}$ is chelated and retained on the column at a high pH, while Rb + is eluted and selected for the automatically infusion into the patient via an automatic injector system incorporated in the console of the Cardiogen system [6].

9.2.2 CardioGen-82® Quality Control Procedures

The short physical half-life of ^{82}Rb, 76 s, requires that the steps for production and infusion occur quite simultaneously via the closed and semiautomatic system which houses the ^{82}Sr-^{85}Sr/^{82}Rb generator. This is the reason why the system should be placed near the patient positioned in the PET machine.

In this system, Strontium-85 (^{85}Sr) is the most important contaminant in the production of ^{82}Sr. It has a longer half-life of 64.8 days. The ratio of ^{85}Sr to ^{82}Sr must not exceed 5.0 for human use. Because the characteristic gamma ray for ^{85}Sr is so close to the annihilation photon energy (514 versus 511 keV), care must be exercised in determining the amount of ^{85}Sr contamination.

Therefore, any procedure will be performed to avoid unintended radiation exposure occurs when the ^{82}Sr and ^{85}Sr levels in ^{82}RbCl injections exceed the specified generator eluate limits, so targeted daily tests and procedures must be obtained as generator eluate tests, before the patients studies, and aseptic techniques should be employed throughout each procedure. The first elution of the day will prepare the generator column for use; this will be a 50 mL elution. Daily procedures start to carry out quality checks as indicated

in the Technical Specifications prepared by the manufacturer and consisting of three different phases summarized in Table 9.2 and briefly commented below.

- *Washing*: This first phase is only for washing the lines belonging to the whole system.

The washing phase is followed by a second elution and the carrying out of **2 Quality Controls**:

(a) *The Breakthrough test*, needed for verifying radionuclide purity. It allows to determine the amount of ^{82}Sr and ^{85}Sr present as impurities in the sample solution of the eluate. The results of these tests are valued at 60 min post the end of elution and affect the feasibility of the study (Fig. 9.2). On this aim, it is **mandatory** that the following values are carefully verified*:*
   - ^{82}Sr content must not be more than 0.02 uCi/mCi of ^{82}Rb
   - ^{85}Sr content must not be more than 0.2 uCi/mCi of ^{82}Rb.

(b) *The Calibration test,* which allows to calibrate the system in order to work at a constant dose for the entire session.

Table 9.2 CardioGen-82®—quality control (QC) procedures steps (Package Insert and Rb-82 Infusion System User's Guide)

Washing	Generator column wash
QC: Breakthrough test	Measurement of Sr-82 and Sr-85 content in the eluate
QC: Calibration test	Compares the infusion system assay of the eluate to a dose calibrator assay of the eluate

The different elutions and administrations of the dose to the patient are managed by an electronic panel (Fig. 9.1b). This system interface allows to set the elution volumes, the activities (according to ALARA principles) and the volume for each dose to be administered to the patient as well as the speed and the type of infusion (Table 9.3). It is well known that the use of automatic injectors will facilitate uniform delivery of the radiotracer and standardize the input function for MBF quantitation; therefore, this infuser system connected to the ^{82}Rb generator

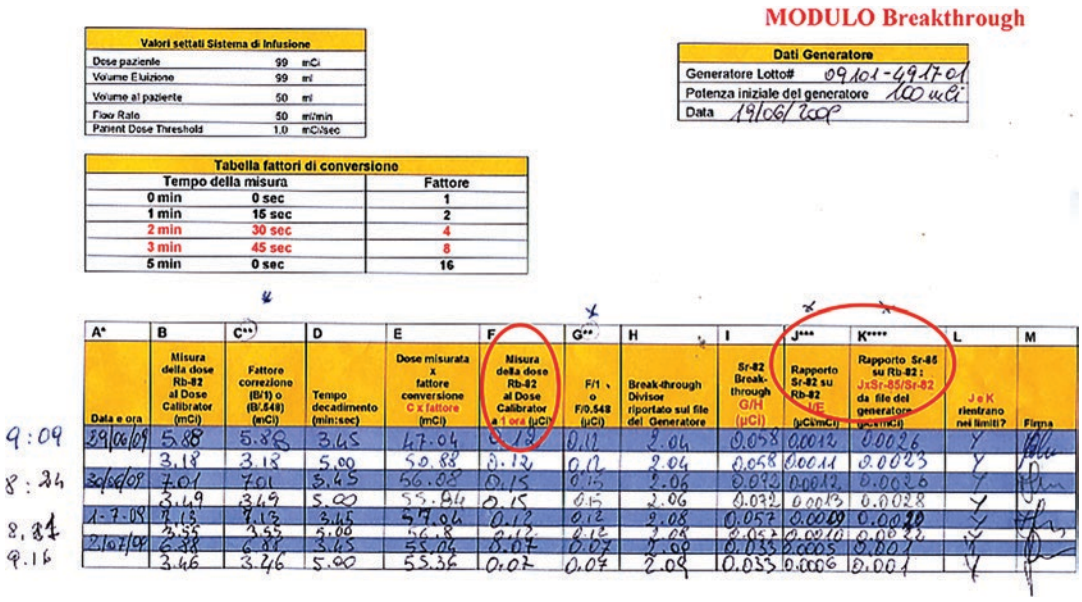
MODULO Breakthrough

Valori settati Sistema di Infusione

Dose paziente	99	mCi
Volume Eluizione	99	ml
Volume al paziente	50	ml
Flow Rate	50	ml/min
Patient Dose Threshold	1.0	mCi/sec

Dati Generatore

Generatore Lotto#	09101-49101
Potenza iniziale del generatore	100 uCi
Data	19/06/2009

Tabella fattori di conversione

Tempo della misura		Fattore
0 min	0 sec	1
1 min	15 sec	2
2 min	30 sec	4
3 min	45 sec	8
5 min	0 sec	16

A* Data e ora	B Misura della dose Rb-82 al Dose Calibrator (mCi)	C** Fattore correzione (B/1) o (B/.548) (mCi)	D Tempo decadimento (min:sec)	E Dose misurata x fattore conversione C x fattore (mCi)	F Misura della dose Rb-82 al Dose Calibrator a 1 ora (uCi)	G** F/1 o F/0.548 (µCi)	H Break-through Divisor riportato sul file del Generatore	I Sr-82 Break-through G/H (µCi)	J*** Rapporto Sr-82 su Rb-82 I/E (µCi/mCi)	K**** Rapporto Sr-85 su Rb-82 : JxSr-85/Sr-82 da file del generatore (µCi/mCi)	L J e K rientrano nei limiti?	M Firma
9:09 29/06/09	5.88	5.38	3.45	47.04	0.12	0.11	2.04	0.058	0.0012	0.0026	Y	
	3.18	3.18	5.00	50.88	0.12	0.11	2.04	0.058	0.0011	0.0023	Y	
8:24 30/06/09	7.01	7.01	3.45	56.08	0.13	0.13	2.06	0.063	0.0012	0.0026	Y	
	3.49	3.49	5.00	55.84	0.15	0.15	2.06	0.072	0.0013	0.0028	Y	
8.34 1-7-09	7.13	7.13	3.45	57.04	0.12	0.12	2.08	0.057	0.0009	0.0020	Y	
	3.55	3.55	5.00	56.8	0.12	0.12	2.08	0.057	0.0010	0.0022	Y	
9.16 2/07/09	6.88	6.88	3.45	55.04	0.07	0.07	2.09	0.033	0.0005	0.001	Y	
	3.46	3.46	5.00	55.36	0.07	0.07	2.09	0.033	0.0006	0.001	Y	

Fig. 9.2 Quality controls phases: daily worksheet for the breakthrough test. It controls for radionuclide purity, allows to determine the amount of ^{82}Sr and ^{85}Sr present as impurities in the sample solution of the eluate. The results of this test are valued at 60 min post the end of elution and they condition the feasibility of the study

Table 9.3 Elution: manual setting general parameters (can be modified relatively to the PET Scanner)

Mode switch	Automatic infusion
Elution volume	99 mL
Patient volume	50 mL
Patient dose	40–60 mCi
Elution volume	99 mL

can be considered an advantage in the determination of MBF [7].

The system is semiautomatic and some settings, as the waste management, loading of raw materials, etc., are manually edited by the operator and are justified by usage over time.

It is mandatory to stop the use of the generator at indicated Expiration Limit.

9.3 ^{82}Rb-PET/CT: Protocols

The short physical half-life of ^{82}Rb allows for an efficient fast protocol, approximately 35–45 min for both baseline and pharmacological stressor phases. It must be underlined that the time for each scan is linked to the physical half-life of the tracer used, respectively: 7–8 min for ^{82}Rb, 20 min for ^{13}N-NH3.

Due to the short physical half-life of tracer, an exercise test cannot be associated, so all stress studies are performed with pharmacologic stressor, dobutamine or vasodilators, with the following features: Adenosine receptors as dipyridamole, adenosine, or regadenoson, a more selectively A2a receptors [3]. Theoretically, vasodilator stressor tests are preferred considering that ^{82}Rb acts as a potassium analogous, allowing a high extraction fraction at high flow rates.

Note:

(a) Myocardial ^{82}Rb-PET/CT: *Patient preparation.*
- The preparation of patient ongoing to myocardial ^{82}Rb-PET/CT is substantially similar to that of routine ^{99m}Tc SPECT MPI one.
- Fast is needed for a minimum of 4 h prior to the scheduled study time. A large stomach volume, in fact, has been found associated with more severe MPI interference, suggesting that sufficient fasting prior to imminent ^{82}Rb PET may be important to reduce aspecific interference from adjacent radiotracer activity and consequently improve the interpretation of MPI results especially in small patients [8].
- Avoid smoking for at least 4 h and avoid caffeine intake for at least 24 h before vasodilator stress.

(b) Myocardial ^{82}Rb-PET/CT: *Pharmacological stressors.*
- Vasodilator stress is chosen in the aim to provide maximal hyperemia. The vasodilator hyperemic stimulus activates specific purinergic receptors on coronary resistive vessels, thereby increasing MBF by direct vasodilation. It can be obtained respectively by the use of:
  – Adenosine (140 mg/Kg/min. i.v. over 4–6 min); dipyridamole (0.56 mg/kg intravenous infusion over 4 min) or regadenoson (0.4-mg rapid intravenous bolus over 10s) which are regularly used as stressor for ^{82}Rb PET stress scan.
  – Among these, regadenoson has been reported as particularly idoneous for ^{82}Rb in terms of strict concordance between stressor and tracer, respectively, related to a rapid pharmacological action and a rapid acquisition scan, due to the kinetics and short half-life of ^{82}Rb [3]. After excluding contraindications, the stress agent can be infused on the basis of standard protocols for each stressor agent.
- Dobutamine (Stepwise increase in infusion from 5 or 10 μg/kg/min up to 40 μg/kg/min to achieve >85% predicted heart rate), or -Dobutamine plus Atropine stress (Atropine boluses may be used to augment heart rate response). Dobutamine, more frequently associated to echocardiographic technique for myocardial viability assessment, is a sympathomimetic amine that acts through α and

β adrenoceptors stimulating both positive inotropic and chronotropic effects and enhancing MBF, mainly through metabolic vasodilatation. In addition, dobutamine increases MBF through direct β2 adrenoceptor-mediated vasodilatation of coronary resistive vessels. It can be associated to ^{82}Rb PET as an alternative to the previously mentioned group of stressors in fact, although vasodilator agents such as adenosine may be more efficient stressors, Dobutamine offers a more physiological approach to assess the demand of ischemia [9].

Today PET scanners let to obtain good quality images. Acquisition and reconstruction parameters can vary between different scanners. The use of 3D PET/CT scanners and upgraded software can allow to inject half activity of ^{82}Rb with a preserved image quality and reduced dose effective to the patient.

For the analysis, the quantification of MBF is the prevalent focus of the study. It requires accurate measurement of the total tracer activity transported by the arterial blood and delivered to the myocardium over time. Some standardization of image acquisition and reconstruction protocols for accurate MBF quantification has been suggested, but it is not universally applied.

In practice, for all data available from a PET myocardial perfusion study, it is recommended: List-mode acquisition because it allows flexibility in the timing and reconstruction of dynamic images for MBF. The List-Mode is the ideal approach for the capability to acquire all the sequences (multiframe, ECG-gated) and allows the reconstruction from the whole set of images or selected portion of it. PET MPI enables images for perfusion study, for LV volumes and ejection fraction thanks to ECG-gated images, and with dynamic images for MBF quantification, by using also a retrospective selection of the onset of the myocardial phase, which can be delayed in low cardiac output conditions or poor bolus quality.

Due to the short half-life of ^{82}Rb, both sets of images, basal and stress scans, can be acquired using the same sized dose.

A post stress CT, useful for photonic attenuation correction (AC-CT), can be associated to avoid motion artifacts due to the patient movement during stressor test or due to changes of the VS silhouette for transient dilation based on ischemic LV dysfunction.

Low-dose (LD) CT, nondiagnostic but useful for photonic attenuation correction (AC-CT), is generally associated in co-registration. The acquisition parameters vary with the configuration of the CT scanner and the number of detectors; however, the settings of an ungated scan, commonly used, include slow rotation speed, high-potential tube, and low amperage. An ECG-gated CT scan perspective for AC and calcium score evaluation can be preferably performed in inspiratory apnea and higher amperage, in which the X-ray input is active only in the diastolic phase of the cardiac cycle, typically 75–80% of the RR. This approach, compared to a gated-scan, increases the dosimetric load to the patient and can translate into more misalignment of CT and PET images (apnea vs. free breathing). Therefore, it is always indispensable to verify the consistency of alignment of the images and use a dedicated software for the realignment of the two data series. In selected patients, it is also possible to combine a diagnostic CT coronary angiography for the evaluation of the coronary lumen.

An example of a dynamic acquisition protocol is reported in Fig. 9.3. It has been selected for a PET/CT tomograph system, 3D, Lutetium oxyorthosilicate (LSO) crystals 13 × 13 × 20 [10].

Typically, basal conditions PET scan is followed by Stress imaging on the same day sequence. An inverse protocol (stress-first) or stress-only imaging are feasible but not recommended in the routine practice for a quantitative PET.

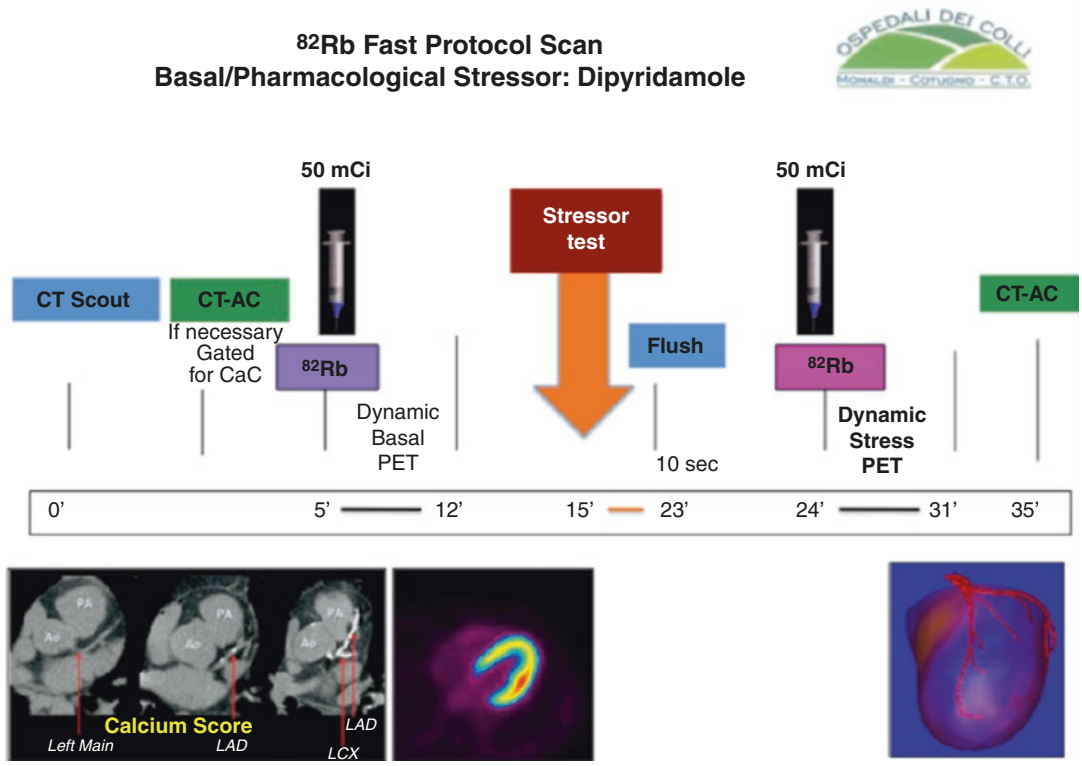

Fig. 9.3 ^{82}Rb PET/CT MPI scan protocol, 7 min/each phase, dynamic list mode acquisition. Proposal used on PET/CT tomograph system, 3D, lutetium oxyorthosilicate (LSO) crystals 13 × 13 × 20

The acquisition steps in Fig. 9.3 are sequentially summarized below:

- CT Scout followed by LD AC-CT
- Rest Scan: 82Rb infusion, Activity: 40–50-mCi; MPI Rest scan, 7 min, dynamic list mode gated Rest acquisition
- Stressor pharmacological test
- At peak stress: 82Rb infusion, Activity 40–50-mCi, followed with dynamic list mode acquisition gated Stress scan, 7 min

Note:

- Focused attention should be paid to the detection and correction of myocardial creep, a technical problem which occurs in more than half of the patients during stressor ^{82}Rb PET and particularly during regadenoson stress test. It occurs a misalignment of the drawn myocardium contour which affects the evaluation of activity in the heart with increased activity in the RCA territory and decreased values in the LAD one's, resulting in unrealistic high MBF values (5 mL/min/g). Proper alignment of the automatically drawn myocardium contours must be obtained for obtaining a correct PET quantitative measure, which decreased after correction to realistic values [11].

9.4 ^{82}Rb-PET/CT MBF—MFR

Filtered back projection with a reconstruction filter and measured AC produces the best myocardial image uniformity, but specific reconstructions details should be checked for each scanner. The

PET reconstruction with iterative methods, in contrast to the filtered backprojection in SPECT, protects from artifacts by subdiaphragmatic high activity, avoiding subtraction of counts in the inferior wall of the LV. Other artifacts should be carefully considered for the PET perfusion scan (without MBF), typically the acquisition still earlier, before the complete clearance of the radiopharmaceutical from the blood pool, adversely affecting the quality of perfusion images, so in healthy subjects it is necessary to start perfusion phase at: 180–240 s for ^{13}N-NH3 and 90–120 s for ^{82}Rb.

Note:

(a) On the reconstructed images, it is mandatory to control the perfect overlapping of CT and PET LV silhouettes for each phase of scans and proceed with images motion correction if necessary. Today, most of the PET/CT systems include dedicated software to correct the misalignment transmission-emission, by operating correction of the sinogram and subsequent reconstruction with proper attenuation map.

(b) PET reconstructed images, gated and ungated, can be displayed using any of the software packages developed for SPECT and adapted for PET.

The largest experience in cardiac quantitative PET is in the measurement of MBF. To estimate MBF, time-activity curves are obtained from dynamic PET images acquisition. Curves are then fit to a mathematic model describing the tracer kinetics over time. Various compartmental models have been proposed for the measurement and many studies have compared their reliability and methodological inequalities that must be considered if the results of diverse laboratories have to be compared.

The two models most commonly used for ^{82}Rb and ^{13}N-ammonia are the one-tissue-compartment model [12] and the simplified retention model [13].

The technical details of these techniques go beyond the aim of this chapter, but it could be useful to underline, among these, the algorithm proposed by Lortie for MBF evaluation [14] which describes a mono-compartmental model preferably used for ^{82}Rb.

Today software for quantization of MBF and myocardial flow reserve (MFR) are available in a user-friendly way**.** Dynamic acquisition is necessary from the beginning, at the time of tracer injection, to be continued until the tracer uptake in the myocardium is completed. Volumes of interest are obtained on the myocardial ventricular cavities, where the activity input is taken on a ROI positioned on LV blood pool [15] and the LV wall are then identified. Time/activity curves are then fitted and the related parameters are calculated to obtain, respectively, the tracer input function and the tracer amount within the myocardium. According to the chosen compartmental model, these values are included in the equations for the calculation of the kinetic parameter that best represents MBF. To ensure accurate estimates of MBF and MFR, it is critical to verify that each dynamic series is acquired and analyzed correctly, with thorough review of quality assurance information including orientation of LV long axis, sampling of myocardium and arterial blood regions, motion detection, dynamic time-activity curves, and kinetic modeling curve-fit [16].

***Note** for MBF evaluation:*

(a) Accurate and reproducible quantification of MBF is possible with both ^{13}N-ammonia and ^{82}Rb (both of which are Food and Drug Administration-approved).

(b) Consistent tracer injection profiles improve the reproducibility of MBF measurements.

(c) The administered dose must be adjusted to avoid detector saturation during the blood pool phase, which can be particularly challenging with ^{82}Rb.

(d) List-mode acquisition enables reconstruction of static, gated, and dynamic datasets. Dynamic datasets are used for blood flow quantification with compartmental modeling [7].

MFR is calculated by the MBF report after baseline and hyperemic stimulus usually induced with dipyridamole, adenosine, or regadenoson.

It may be useful to remember that PET technique doesn't measure volume of blood flow in the epicardial coronary arteries directly but rather blood flow in myocardial tissue. Thus, the term MFR is more appropriate in respect of the largely used definition "Coronary Flow Reserve" (CFR) invasively determined. The standard units of MBF are commonly expressed as mL/min/g. Hyperemic MBF and MFR provide useful information on coronary vasodilator flow capacity and characterization of flow-limiting CAD. Both parameters also share the same limitation for differentiating predominant focal obstructive stenosis from diffuse atherosclerosis and microvascular dysfunction. In 8 studies consisting of 382 healthy subjects MBF -MFR value using ^{82}Rb PET has been evaluated as a weighted mean of:

- Resting MBF: 0.74 mL/g/min (range, 0.69–1.15).
- Stress MBF: 2.86 mL/g/min (range, 2.5–3.82).
- MFR: 4.07 (range, 3.88–4.47) [7].

The young population, or healthy volunteers, or men without coronary risk factors, can limit the overlap of these results in the real life. In an older population with a possible burden of coronary risk factors in fact, it is possible to obtain values below these ranges without any evidence of obstructive epicardial CAD, often due to the effects of diffuse CAD and microvascular disease.

So, while hyperemic MBF and MFR provide useful information on coronary vasodilator flow capacity and characterization of flow-limiting CAD, both of them got the same limit in differentiating predominant focal obstructive stenosis from diffuse atherosclerosis and microvascular dysfunction.

Anyway, for a better understanding of this important tool at our disposal with quantitative PET, we must always keep in mind that in humans resting MBF remains relatively preserved across a wide range of coronary stenosis severity, thanks to the gradual autoregulatory vasodilation of resistive vessels to maintain resting myocardial perfusion in the setting of upstream stenosis. On the other hand, Resting MBF falls only in case of critical subocclusive stenosis with poorly developed collateral blood flow.

Hyperemic MBF and MFR are relatively preserved for coronary lesions with less than 70% angiographic stenosis or with preserved fractional flow reserve, and consistently reduced in lesions with greater than 70% luminal narrowing or those with abnormal FFR.

Hyperemic MBF and MFR can provide useful information on coronary vasodilator flow capacity, addressing the characterization of flow-limiting CAD, but they are not able to distinguish the dominant focal obstructive stenosis from diffuse atherosclerosis and microvascular dysfunction. In this aim invasive coronary angiography (ICA) or coronary CT angiography (CCTA) can differentiate the different categories of patients [17]. For most patients, hyperemic MBF and MFR are concordant both in terms of normal or abnormal responses [18]; however, discordance can be observed in a minority of patients showing abnormalities of MBF, considering that MFR is a ratio between hyperemic and resting MBF. Among the patients mentioned above, showing discordant findings of MBF and MFR, we report for example those one with prior myocardial infarction who may show relatively preserved MFR in infarct-related territories because of low resting MBF.

Coronary stenosis of intermediate severity is associated with significant variability in hyperemic MBF and MFR at PET, whereas their gradual reductions can be due to a progressive loss in maximum vasodilator capacity with increasing stenosis severity, modulated by different agents such as: coronary resistance; development of collateral blood flow; diffuse coronary atherosclerosis; and microvascular dysfunction.

Exceptions to this gradual response are some higher-risk subgroups of patients affected with diabetes, other cardiovascular risk factors and chronic kidney disease where both MBF and MFR can appear reduced even in the absence of overt obstructive stenosis.

These patients show high-risk CAD and CAD complications even in case of relatively low-risk at MPI findings. This poor prognosis is probably due to increased rates of diffuse epicardial CAD and microvascular disease, leading to improved

performance of quantitative PET compared with relative SPECT MPI [19].

Note: Modified from Joint Position Paper of the SNMMI Cardiovascular Council and the ASNC [7].

(a) Preserved stress MBF > 2 mL/min/g and MFR > 2 can exclude the presence of high-risk angiographic disease (negative predictive value 95%);
(b) A severely decreased global MFR (<1.5 mL/min/g) can correlate with adverse cardiac events but the likelihood of multivessel obstructive disease diagnosis requires more studies including ECG, evaluation of LV contractile function and volumes, ICA, or CCTA.
(c) Both regional decreases in stress MBF (<1.5 mL/min/g) and MFR (<1.5) in a vascular territory may indicate regional flow-limiting disease.

9.5 ^{82}Rb PET MPI Versus SPECT MPI

MPI, both PET and SPECT, is highly accurate in detection and risk stratification of CAD, guiding patient outcome and workup. PET and PET/CT seem to be more accurate than SPECT in the diagnosis of obstructive CAD, especially among patients undergoing pharmacological stress.

The high specificity and overall diagnostic accuracy of ^{82}Rb Gated-PET/CT vs. Gated-SPECT reduce the number of false positives even more among women and over-weight patients. Bateman [20] demonstrated that PET MPI is superior to SPECT in: quality image, interpretative certainty, sensibility, specificity and diagnostic accuracy both in men and women, in obese and nonobese patients and for correct identification of multivessel coronary disease (MVD). Same results have also been reported independently of the coronary lumen stenosis (≤50% and ≥70% coronary stenoses) [21]. So, the additional value of PET consists predominantly in the capability, or better capability, of assessing MBF. It is a particularly powerful tool for patient outcome, as it reflects the end result of many processes that lead to atherosclerosis.

Multimodal scanners, combining PET and SPECT with high-resolution multidetector CT, are currently available and offer the ability to assess functional evaluation of transient ischemia or viability associated with LV function and crossed with the anatomy. A systematic review and meta-analysis aimed to assess the diagnostic accuracy of ^{82}Rb PET in patients with known or suspected obstructive CAD in comparison with the reference standard ICA and with contemporary SPECT technology utilizing ECG-gating and AC methods. In the review, including, respectively, 1344 PET and 1755 SPECT patients, ^{82}Rb PET showed sensitivity 90% and specificity 88% in detection of obstructive CAD vs. ICA. Moreover, ^{82}Rb PET showed better accuracy, despite advances in SPECT technology consisting in ECG-gating and AC-CT, and remains superior than SPECT in the workup of patients with CAD [22].

9.6 Clinical Applications

Note: *A sequence of detailed Clinical Cases are attached in the appendix to this paragraph, in order to highlight some of the aspects frequently reported in the diagnostic use of ^{82}Rb PET/CT MPI. The clinical cases will be indicated in numerical sequence in the text, each of them within its own specific clinical context and reported by a brief comment, in order to emphasize the clinical impact of the corresponding information obtained from imaging.*

In the past PET significantly contributed to improve the knowledge of cardiac physiology and to better understand some physiological processes by quantification in vivo. Nevertheless, its clinical applications in cardiac disease were limited, due to high cost and reduced availability of machines and tracer suitable.

In the recent years, PET has reached growing role and now it is widely used in patients with known or suspected CAD and/or dysfunctionally LV, showing high sensibility (93%) and specificity

(92%) in hemodynamically significant stenosis at ICA. It can be due to:

- Tracer availability, thanks to ^{82}Rb for the feasibility of on-site generator for clinical utilization in those structures without a cyclotron.
- The optimal intrinsic characteristics of PET, in terms of spatial and temporal resolution, the latter allowing MBF evaluation.
- The implementation of multimodality technique with hybrid machines.

Although it has been consistently demonstrated the improved diagnostic sensitivity for CAD of PET MBF and MFR evaluation, a potential reduction in the specificity of stress MBF and MFR measurements has been hypothesized on the basis of the possible interference on it of diffuse atherosclerosis or microvascular disease processes [23, 24].

9.6.1 Multimodality Technique PET/CT

On this specific need, the added value of multimodality technique with hybrid machines, equipped with superior AC abilities, has allowed higher accuracy of ^{82}Rb PET MPI-CT in diagnostic efficacy of CAD. It has been demonstrated that the fusion imaging (PET/CT) will optimize precisely ischemic pertaining of the affected vessel, even when ischemia is due to multiple vessels. It allows a stronger clinical impact of ^{82}Rb PET/CT in suggesting targeted coronary arteries revascularizations and can optimize the diagnostic performance of technique, more helpful in RCA and LCX territories, showing that MPI PET/CT "is not only nice to have, but truly needed." Similarly, considering the intrinsic metallic contrast of stenting vessels on CT, the multimodal fusion images can help to match the perfusion map in specific pertaining to the stenting vessel.

This approach may prove useful information in case of MVD, as observed in the Clinical Case Number 1.

- ***Clinical Case N. 1*** *The spontaneous contrast of metallic stent at PET/CT fusion images let better recognize the correct pertinence of ischemia territory between multiple stenting vessels.*

One of the most common additional data of MPI with multimodal technique is the evidence of calcified plaques along the coronary branch path. It is simply evident by spontaneous contrast in co-registration CT or, even better, assessable in terms of calcium score when the CT is conducted with a target Gated technique. It has been reported the prognostic value of calcific atheromasia on the main epicardial coronary artery and even better of the evaluation of coronary artery calcium score (CACS), whereas high score can influence the prognosis of patients both in case of transient ischemia or preserved perfusion at MPI.

- ***Clinical Case N. 2 and N. 3*** *underline the approach of a combined analysis of ^{82}Rb PET/CT MPI and calcium score.*

Evidence of calcific deposit on coronary main vessels is becoming relatively frequent evidence in multimodality studies of MPI/CT.

It doesn't imply necessarily functional matching with ischemia, but the increase of CACS can affect the long-term prognosis with a stronger value when it is associated with perfusion defects. Calcium scoring has been studied extensively over the past decade for predicting outcome in generally asymptomatic subjects at intermediate clinical risk for CAD.

In this purpose, Chang [25] in a large population consisting of 1.126 generally asymptomatic subjects without previous cardiovascular disease, who underwent multimodality MPI techniques, demonstrated that CACS may better estimate longer-term prognosis because of its ability to detect varying degrees of coronary atherosclerosis before the development of stress-induced myocardial ischemia. They showed that CACS and MPI findings are independent and complementary predictors of short- and long-term cardiac events whereas, despite a normal MPI result,

a severe CACS identifies subjects at high long-term cardiac risk.

On this basis the AA support the utility of performing a CACS evaluation in patients at intermediate or high clinical risk for CAD also after a normal perfusion result, to better stratify those who will have a high long-term risk for adverse cardiac events.

On the same aim, it has been demonstrated that quantitative analysis integrating: per-vessel ischemic total perfusion deficit, hyperemic MBF and CFR with CACS, improves the accuracy of ^{82}Rb PET/CT myocardial perfusion imaging for regional prediction of CAD. The combined use of CACS, perfusion data and quantitative coronary vascular function may predict more accurately the presence of obstructive CAD [26].

9.6.2 ^{82}Rb PET/CT in Obstructive and Nonobstructive CAD

The European Society of Cardiology guidelines on myocardial revascularization and management of stable CAD, from 2014 and 2013, stress the role of noninvasive testing including cardiac PET in patients with suspected CAD as follows: after initial pre-testing of CAD likelihood, patients with an intermediate risk of significant CAD are advised to undergo functional testing or CTA, with the purpose of distinguishing between obstructive and nonobstructive CAD. PET is one of the imaging modalities recommended for this purpose.

Thanks to the good quality of images, the diagnostic accuracy over the traditional MPI, and the feasibility of on-site generator for clinical utilization, ^{82}Rb has been widely used to facilitate clinically detection of CAD in subjects at intermediate pretest likelihood and suitable for pharmacological stressor [27].

Still more specific indications, among these group of subjects, are in the obese ones, where the PET AC-CT allows to avoid artifacts, with drastic advantage of diagnostic information, and once again in women, considering the dosimetric advantage of ^{82}Rb PET.

Semiquantitative analysis for MPI has become a major part of nuclear cardiology practice. Current PET software tools are specifically upgraded for ^{82}Rb database and can automatically quantify myocardial function and perfusion maps, by estimating Summed Perfusion Scores, Total Perfusion Defect, overall defect extension, Systolic and Diastolic functionally data, allowing high diagnostic accuracy for detecting CAD and predict outcomes [28]. An extension of perfusion defect $\geq$10% of LV is a poor prognostic factor, it can predict the need and benefit of revascularization and can influence the workup of patients with strong clinical impact in guiding the need of revascularization rather than medical treatment. It is crucial to define the functional significance of a stenosis with MPI, to successfully establish the workup of the patient [29], considering that not all stenoses can induce the same functional significance in terms of transient ischemia as well as in terms of risk. It has been demonstrated, in fact, that the severity of coronary stenosis at angiographic film is a bland predictor of the relevance of the stenosis itself and that the same percentage of vessel stenosis can induce different pathophysiological effects, varying for each patient. The FAME trial, by using the fractional flow reserve (FFR) as cutoff value for myocardial ischemia versus functional severity of coronary artery stenoses, demonstrated that not all coronary stenosis are flow limiting and that severe stenoses by ICA can have completely different functional importance at FFR [30]. On the other hand, it has been well demonstrated that 35% of categories of stenosis ranging between 50 and 70% can induce ischemia.

At the same time though, it has been demonstrated that invasive procedures such as ICA, coronary artery bypass grafting (CABG), and percutaneous transcoronary intervention (PTCI) are overutilized in the US, contributing to unnecessary health care expense without improved patient outcomes. On this basis, several studies investigated on the efficacy of revascularization in addition to optimal medical therapy (OMT) in initial treatment of patients with CAD, but they showed no significant differences in long-term outcome regarding rates of death or major adverse

cardiovascular events (MACE). It seems that only when the invasive strategy is combined with the assessment of significant ischemia from functional imaging, it can lead to a better outcome of CAD patients in respect of OMT.

- ***Clinical Case N. 4*** *shows an extensive transient ischemia evocated during dipyridamole infusion.*

  This case is illustrative of the strong functional significance of a coronary stenosis.
  Clinical impact*: ^{82}Rb PET/CT has high capability in suggesting the need for a quickly revascularization.*

A Multicenter Observational Registry concerning prognostic value of PET MPI was conducted on a total of 7061 patients with clinically indication at rest/stressor ^{82}Rb PET MPI, from 4 centers, with a median follow-up of 2.2 years. The primary outcome of the study was cardiac death and the secondary outcome was all-cause death. The results showed that in patients with known or suspected CAD, the severe degree of scan abnormalities in terms of the extent and severity of ischemia and scar at ^{82}Rb PET MPI provided powerful and incremental risk estimates of cardiac death and all-cause death compared with traditional coronary risk factors [31]. The percent of abnormal myocardium, including the percent of the ischemic and the scarred myocardium, was significant univariable predictor of cardiac death and all-cause death, particularly in case of extension of ischemic perfusion defect equal/more than 20% of LV.

Moreover, hybrid scanners, adding morphological information, get a strong clinical impact in selecting the therapeutic strategy and workup of the patient, as shown in Clinical Case N. 5.

- ***Clinical Case N. 5*** *report an interesting evidence at ^{82}Rb PET/CT MPI of LV pseudoaneurysm with a wide and unknown component of calcific dystrophy in the area of previous necrosis. This case underline the efficacy of multimodality technique and the capability of ^{82}Rb PET/CT in the assessing LVEF in real time with stressor test, as a prognostic factor of main relevance.*
  Clinical Impact*: ^{82}Rb PET/CT MPI can modify the therapeutic strategy of the patient.*

As well known the extension of perfusion defect, in terms of LV percentage, is an effective evaluation tool to establish the progression of disease. It provides a repeatable and reproducible parameter for monitoring patients with known CAD in which it becomes necessary to modify the therapeutic strategy.

- ***Clinical case N. 6*** *underline the capability of perfusion defect extension evaluation at ^{82}Rb PET/CT in estimating and monitoring the therapeutic efficacy/or progression of disease.*
  Clinical impact: ^{82}Rb PET/CT can suggest a shift of treatment in case of ischemic progression disease.

LV transient dysfunction with post-stress impairment of LVEF is a high-risk scintigraphic marker and suggests the need of revascularization. It must be underlined that gating ^{82}Rb PET MPI can be obtained at peak stress, yielding a true stress EF, whereas gated SPECT can offer only post-stress or resting EF, thus alleviating a common source of pitfall of SPECT imaging in case of balanced ischemia. Incremental prognostic value can be obtained if LVEF<45% and post-dipyridamole ESV > 70 mL, considering that these parameters are independent predictors of cardiac death. Similarly, transient ischemic dilation (TID) occurs in the same conditions of transient ischemic dysfunction stress related and is considered a major prognostic marker because it correlates with MACE [32].

- ***Clinical Case N.7*** *report a case of obstructive CAD evolved in dysfunctionally dilatative cardiomyopathy (CMD) with large extension of chronic perfusion defect (35% of LV) and balanced ischemia. This case would underline the strong clinical impact of ^{82}Rb PET/CT in evaluating LVEF dysfunction with LVEF tran-*

sient dilation obtained in real time with stressor test, allowing better evaluation of balanced ischemia.

Typically, vasodilator stressors induce heterogeneity in regional MBF, both in case of normal or coronary stenosis, inducing reduced subendocardial flow reserve, myocardial ischemia, and regional LV dysfunction. On this basis, it can be hypothesized that the LVEF reserve (stressor LVEF—basal LVEF) would be inversely related to the magnitude of jeopardized myocardium and that patients with extensive areas of jeopardized myocardium would not be able to demonstrate a high LVEF reserve. MBF has been proven to add additional prognostic value to the ^{82}Rb PET/CT MPI, as discussed in the previous Sect. 2.4.

Just in case of balanced 3-vessel disease it has been recognized the added role of MFR, whereas the relative assessment of tracer uptake in the LV myocardium alone by semiquantitative MPI may fail to recognize disease, leading to a false negative conclusion. In 120 patients with known or suspected CAD, Ziadi et al. [23] demonstrated the strict correlation between 3-vessel disease and impaired MFR (<2) in respect to patients with preserved MFR. The study is relevant in demonstrating that quantitative global MFR has an advantage in the diagnosis of 3-vessel disease, compared to semiquantitative measurements. It has been demonstrated as an independent predictor of 3-vessel CAD, with a diagnostic sensitivity of 88%, such as in patients without other generally accepted risk factors such as reduced ejection fraction, transient ischemic dilation, and ischemic ECG changes.

Therefore, in patients at higher clinical risk, for whom even a low-risk relative assessment of MPI may be insufficiently reassuring (i.e., those likely to remain at intermediate post-test risk), referral for stress PET with quantification of MBF may be preferable as an initial test over relative MPI alone, such as with SPECT imaging.

PET is the only one technique capable of providing the absolute quantification of MBF in mL/min/g of tissue and MFR, allowing to move the clinical goal from the diagnosis and prognosis of obstructive CAD vs. an early definition of microvascular or endothelial dysfunction in patients without obstructive vessels disease, before clinical evidence of disease.

The MBF assessment represents a prerequisite for further studies to optimize treatment in subjects with anginal pain and normal coronary angiogram. In this way, it can expand the meaning of the imaging moving from the organ damage to the knowledge of biochemical and molecular mechanisms, in the aim to allow to prevent damage.

At this regard, it is important to underline the direct correlation between myocardial oxygen consumption and coronary flow and that, particularly in the myocardium, contrary to what happens in the systemic circulation, the oxygen extraction is already maximal in basic conditions. Therefore, an increase in the oxygen demand can be satisfied only with an increase of MBF that is in dependence of microcirculation, endothelial function, and metabolic factors. Pathological conditions of these elements invalidate the flow and reduce the coronary reserve, thus affecting vasodilation in particular at the subendocardium, which is earlier affected by the ischemia. Flow quantification, from mainly being a research tool, is shifting to clinical practice thanks to different software solutions now available to ensure fast and reproducible flow estimates. On this basis, the clinical use of ^{82}Rb for quantitatively MBF assessment appears to have increased in recent years. ^{82}Rb perfusion has been detected to have high accuracy in CAD assessment and can define flow abnormalities with a similar accuracy to that of ^{13}N-ammonia.

The strongest clinical impact is achieved in patients with MVD or left main artery stenoses and balanced ischemia, where relative assessment of MPI cannot uncover a global reduction in perfusion. Typically, in fact, in relative analysis of perfusion only, the regions supplied with the most severe stenosis are detected. In less severe cases MVD is likely to be underestimated, while PET MBF quantification provides the detection and localization of CAD.

Table 9.4 Quantification of MBF and CFR extends the scope of conventional semiquantitative MPI

1.	Identification of the extent of a multivessel CAD burden
2.	Patients with balanced 3-vessel CAD
3.	Patients with subclinical CAD
4.	Patients with regional flow variance, despite a high global MFR

It has been reported that patients with severely reduced stress MBF and MFR are at higher risk than ones with preserved values. On the other hand, it has been demonstrated both an excellent prognosis versus cardiac mortality for MFR > 2 and a steady increase in cardiac mortality for an MFR < 2 [33]. This allows for more accurate assessment of the CAD burden in individuals with cardiovascular risk than with obtained at semiquantitative PET MPI. The diagnosis of severity and improved identification of patients with MVD and subclinical CAD are interesting advantages of assessing quantitative global MFR and hyperemic MBF with ^{82}Rb PET.

Quantitative PET extends the aim of conventional semiquantitative MPI (Table 9.4) also in case of coronary stenosis, allowing a more accurate assessment of the ischemic burden in patients with intermediate pretest probability of CAD and supporting the clinical decision-making in treatment of CAD patients as a complementary tool to ICA.

The microcirculation controls coronary resistance and MBF, it gets extraordinary importance for the high clinical impact considering that, as well known, only 5% of the coronary circulation is under the control of the main epicardial arteries, while 95% is under the control of the small vessels, arterioles, and exchange vessels [34].

On this basis, the European Sub-Study of EVINCI, the Trial that used Hybrid Technique to rule-out or rule-in revascularization, showed that only 24% of pts. showed ischemia matching with occlusive stenosis [35] and several studies reported the ^{82}Rb PET's long-term prognostic value by a significant association between compromised global MFR and MACE. MFR with ^{82}Rb yields independent and added prognostic information beyond relative MPI. Clinical integration of MFR with relative PET MPI will enhance risk stratification [36] showing that segments supplied by stenotic vessels had significantly lower regional stress MBF and MFR than segments without stenosis. In turn, stenotic segments, showing normal perfusion rated at semiquantitative ^{82}Rb PET, still had reduced hyperemic MBF. These results exemplify, once again, the added diagnostic value of quantitative MPI compared to the semiquantitative one even in areas with significant coronary stenosis.

Ziadi et al. [37] showed that the routine integration of ^{82}Rb MFR with MPI could represent a valuable tool for the clinician to better stratify patients at risk of adverse cardiac events. Abnormal ^{82}Rb MFR means worse outcomes in any category of MPI, from normoperfusion to severe ischemia at MPI, and this could affect management decisions for these patients. Study identifies the capability of MFR of sub-stratify patient's perfusion categories obtained by ^{82}Rb PET MPI with the evaluation of the summed perfusion scores. Even in those patients with mildly abnormal MPI, who may be considered for medical therapy, impaired ^{82}Rb MFR correlated with worse outcome, gaining important impact on decisions for revascularization.

Similarly, in patients with normoperfusion at MPI, reduced ^{82}Rb MFR would also indicate a worse prognosis, and this could also affect management and dictate the need for more aggressive medical therapy and closer follow-up of the patient. On the other hand, patients with reduced MFR and moderate to severe SSS on MPI may already be more likely to undergo ICA and revascularization. The added value of impaired ^{82}Rb MFR may be less in this group but may still affect decisions for those who are at high risk of intervention. In this scene, considering that cardiac deaths occurred in patients with severely reduced ^{82}Rb MFR, AA concluded that MFR may identify a particularly high-risk group [37].

- ***Clinical Case N.8*** *shows an example of impaired MBF in a subject with intact coronary arteries, suggestive for microcirculation abnormalities.*

9.6.3 ^{82}Rb PET/CT: Acute Coronary Syndrome

A growing interest in the last years regards ^{82}Rb PET in the study of suspect acute coronay syndrome (ACS) characterized by atypical onset or doubts for CAD at basal ECG and other instrumental exams, as like as in some emergency departments in the US, thanks to its high diagnostic capability with a very short time of study (35–35 min) and hybrid technique.

- ***Clinical Case N.9*** *shows the added values of ^{82}Rb PET/CT in emergency for evaluating the functionally evidence of culprit lesion, in order to orient stenting revascularization. This condition is especially meaningful of real life in clinical practice, where ^{82}Rb PET/CT, in 35 min, can influence the workup of patients with MVD by identifying the functional significance of stenoses.*

9.6.4 ^{82}Rb PET/CT: Heart Transplant

Chronic immunologic responses appear to be the cause of the occlusive long-term cardiac allograft vasculopathy (CAV) in the heart transplant (HTx) recipients. Despite chronic rejection still being the major drawback of long-term positive outcome after HTx, it remains unclear whether mild, diffuse intimal thickening in the epicardial arteries of HTx recipients affects the functional status of the coronary tree, but it is well known that in these patients' atherosclerosis changes are less likely in respect of chronic rejection. Cardiac allograft vasculopathy is a common complication of HT and one of the main causes of death beyond one year of the transplant. It has been shown the effectiveness of MPI that has a strong predictive value of the clinical outcome in HTx recipients. Abnormal MPI has been reported both as an independent predictor of cardiac death and predictive of 5-year survival and stress-induced ischemia can predict the development of allograft dysfunction [38, 39].

PET, allowing MBF and MFR evaluation, may help to identify CAV abnormalities, considering that the pathophysiological evolution of disease starts just from smaller vessels. It was demonstrated that MBF was higher in transplanted heart at rest in comparison to non-transplanted healthy subjects, probably due to denervation and consequent increase in heart rate [40].

Correlation between ^{82}Rb PET MPI, ICA and intravascular ultrasonography (IVUS), confirmed that ^{82}Rb PET MPI correlates with IVUS and angiograms findings, so ^{82}Rb PET MPI can be suggested to improve HTx patient's management by reducing the frequency of invasive techniques and to establish the functional significance of CAV involvement [41].

9.6.5 Myocardial Viability: A Look to the Past and Directions for the Future with ^{82}Rb PET/CT

PET diagnosis of preserved viability with ischemic (hibernating) myocardium as demonstrated by the "flow-metabolism mismatch" has been shown to be predictive of outcomes after coronary revascularization. On the other hand, a lot of studies showed that there is increased risk of cardiac events in patients with hibernating myocardium who are not revascularized. Historically, ^{18}F-FDG PET is the most sensitive, noninvasive imaging technique for distinguishing necrotic and hibernating myocardium in patients with severe CAD and impaired LV function, but in the clinical routine ^{18}F-FDG PET is expensive and time consuming especially in the structures with high turnover of patients needing PET for oncologic disease. Consequently, ^{82}Rb can target viability assessment in those patients where clinical yield is likely to be highest. Another aspect is that ^{82}Rb, as like as the well-known tracer ^{201}Tl, provides a measure of the myocardial potassium pool. Its washout was previously studied as an indicator of myocardial cell membrane function, so that theoretically it can also be compared with ^{18}F-FDG PET as a clinical marker of impaired myocardial tissue integrity.

Furthermore, ^{82}Rb associates the capability of quantitative assessment of MBF and, looking together to PET technology and kinetic modeling, ^{82}Rb PET/CT may enable consistent viability assessment. Looking at these aspects, recent studies explore the utility of ^{82}Rb in myocardial perfusion assessment in comparison to ^{82}Rb/^{18}F- FDG PET specifically focusing on kinetics of 82Rb as a potential unique alternative to combined perfusion/metabolic assessment for viability [42].

In a pilot study [43] a total of 120 consecutive patients underwent dynamic ^{82}Rb 3D PET. Data were acquired at rest and ^{82}Rb kinetic parameters were estimated in terms of uptake and washout rates (K1 and k2) and ^{82}Rb partition coefficient (also called distribution volume) defined as KP = K1/k2, using a compartmental model commonly used for myocardial blood flow. The results were compared with the relative ones of ^{18}F-FDG and K2 and KP were shown to reliably differentiate hibernating myocardium, metabolically active, and inactive myocardium as scar. This pilot study is very promising considering that current-generation 3D PET/CT systems let reliable dynamic cardiac PET and clinical kinetic modeling. The ^{82}Rb partition coefficient, KP, an index of the myocardial potassium pool, is readily estimated using the same protocol and kinetic model commonly used for myocardial blood flow, and can be obtained at no additional cost, imaging time, or radiation exposure. The AA suggest the partition coefficient, KP as the most suitable ^{82}Rb parameter for distinguishing scar and viable dysfunctional myocardium; however, further studies are necessary to delineate its clinical utility for predicting benefit after revascularization.

9.7 Costs

Theoretic models indicated that increased diagnostic accuracy of PET MPI may reduce costs and improve outcomes. Few years later, it was shown that when PET MPI is used as a routine first-line approach in the management of CAD in patients with intermediate CAD, it is more cost-effective than SPECT MPI and reduces the use of downstream coronary arteriography and CABG by 50% [44].

Comparisons of MPI technologies are so highly relevant for policy makers, practice guidelines and considering that the best diagnostic definition can induce strong repercussions on the cost-effectiveness of the methodology report. To date, there are few economic data available to guide medical decision-making regarding the use of interventions for stable coronary disease patients. Many years ago, the END study provided an observational comparison of diagnostic and follow-up costs for two widely utilized diagnostic strategies, one invasive and the other one noninvasive, for the evaluation of patients with stable angina [45]. AA revealed, by examining practice patterns in seven hospitals, that the initial use of noninvasive stress cardiac imaging decreases the overall costs of patient care during an observational period of nearly 3 years. Composite cost of care was 30–40% less when cardiac catheterization was employed selectively in the diagnostic evaluation of stable angina patients. Further refinement of the estimated cost savings revealed that a conservative management approach may be employed in patients with minimal to no provocative ischemia. These multicenter data provided insight into the advantage of a selective use of cardiac catheterization for patients with inducible myocardial ischemia on noninvasive testing. Moreover, the results of this study should be useful to assist health care providers in defining a broadly applicable clinical pathway for the evaluation of stable angina patients, particularly in our country, considering that the cost of ^{82}Rb generator can justify the higher costs resulting after the ICA (e.g., angioplasty, post-angioplasty coronarographic controls). This results in a 30% reduction in total disease management costs and no deleterious short-term clinical outcome, when compared with the current approach using exercise SPECT, given that globally the demand for ^{82}Rb could grow thanks to the set of clinical information available from its use.

Although ^{82}Rb is now widely used in the US, this tracer has had no commercial success in Europe so far. With this regard, the authors mention in their discussion that ^{82}Rb generator can only be called cheap in relation to a very high number of scans. In fact, ^{82}Rb is not only technically more suitable for high-volume clinical activity but, just in this particular case, its use has a good economic advantage, if compared to the expensive use of a cyclotron, thanks to the use of a generator that allows all the PET MPI needed. The monthly cost of acquiring the ^{82}Sr/^{82}Rb generator was initially considered prohibitive, but it is now clear that it can be amortized by scheduling a number of at least 30 patients for each generator.

9.8 Dosimetry

PET-MPI submits the patients at radiation dosimetry less than the SPECT-MPI. It should be emphasized that the limited dosimetry of ^{82}Rb PET vs. the SPECT one regards both patients and the staff.

Values of effective dose (mSv) are reported respectively for the PET perfusion tracer:

^{13}N-NH3: 0.74–1.48; H^{15}O: 0.65–1.40; 82Rb: 1.8–3.5 but this value can be reduced at 1.26 mSv.

In fact, considering the use of 3D PET scanners and software allowing to inject half activity of ^{82}Rb with a preserved image quality, the calculated effective dose has been estimated 1.26 mSv for rest and stress scans [46].

9.9 Future Directions in Oncology

A new trend of scientific research for ^{82}Rb is emerging in the recent years in the field of oncology. On this purpose ^{82}Rb is a nonspecific radiotracer; therefore, the uptake by the tumor primarily depends on the tumor vascularization. Theoretically, the rationale of use of this radiotracer can be firstly identified in its capability to explore angiogenesis which, in turn, can directly correlate with the aggressiveness of the tumors.

In that case, as induction of angiogenesis is one of the hallmarks of cancer, a noninvasive quantitative estimation of tumor blood flow may assess tumor aggressiveness.

This concept would enable repeated measurements of the tumor's malignant potential, which could make a valuable contribution to the existing panel of diagnostic imaging.

^{82}Rb has been studied in brain tumors, in which high uptake due to the high vascularization both in malignant and benign meningiomas has been demonstrated.

In detail, the level of ^{82}Rb-uptake in cerebral tumor has been directly ascribed respectively to vascularization rate, integrity of blood–brain barrier (BBB), and sodium–potassium pump efficiency, whereas each of them is significantly higher in malignant tumors in comparison with the benign ones. Thus, Rb (as an analog of potassium) penetrates BBB from extracellular fluid and is more easily retained in cells in comparison with benign glioma, especially if the pump functioning is incorrect.

This approach has been observed as simple, reproducible, and provides obtaining exact information on tumor perfusion.

An information obtained with ^{82}Rb PET investigations is especially effective in combination with contrast-enhanced MRI using PET/MRI fusion technique. ^{82}Rb may be an important independent method in PET investigation of brain, or in particular, a complementary method to ordinary approaches using compounds with ^{18}F, typically ^{18}F-FDG, ^{11}C, and ^{13}N [47].

Based on the same theoretical assumption, the ^{82}Rb PET/CT has been reported as additional PET evaluation in non-avid glucose tumors, such as in the evaluation of renal carcinoma metastases [48] and in prostate cancer (PCa) as a diagnostic tool for quantitative tumor blood flow (TBF), in the aim to differentiate between PCa and normal prostate [49].

In PCa another interesting study [50] highlighted the ability of ^{82}Rb PET both in the information relative to TBF and in the synergistic value added to the diagnostic data obtained by different and hybrid techniques as follows:

Study 1, vs. T2 weighted mpMRI images; Study 2, vs. ^{68}Ga-PSMA-PET/CT scans. The AA conclude that: Study 1 shows that ^{82}Rb-PET/CT is a diagnostic tool for quantitative TBF imaging and suggests that ^{82}Rb-SUV is associated with cancer aggressiveness; Study 2 shows that ^{82}Rb uptake is higher in PCa than in normal prostate tissue. Consequently, ^{82}Rb-PET/CT may have potential as a noninvasive tool for evaluation of tumor aggressiveness and monitoring in non-metastatic PCa.

In conclusion, more studies are needed in this aim, but the rationale is particularly interesting not only thinking about the diagnosis, but above all hypothesizing the possible implications that these interactions between methods can guarantee the success of the most up-to-date therapies.

Clinical Case N. 1: Follow-Up of Revascularized MVD: Capability of ^{82}Rb PET/CT in Evaluating Transient ISCHEMIA Target for Vessel

Male, 75 years old with stable chest pain stress induced.

History of chronic CAD (Fig. 9.4a): AMI inferior wall; ICA: MVD, stenting on LDA and RCX; RCA occluded.

Patient underwent ^{82}Rb PET/CT basal/dipyridamole (Figs. 9.4b, 9.4c) (0.56 mg/Kg/4′): fast protocol 35′. Dynamic list-mode acquisition.

Dipyridamole ^{82}Rb PET/CT, from right to left:

(1) CT-AC: metallic Stent (red cross) on LAD and Cx artery; (2) SPECT SA (3) Fusion imaging PET/CT

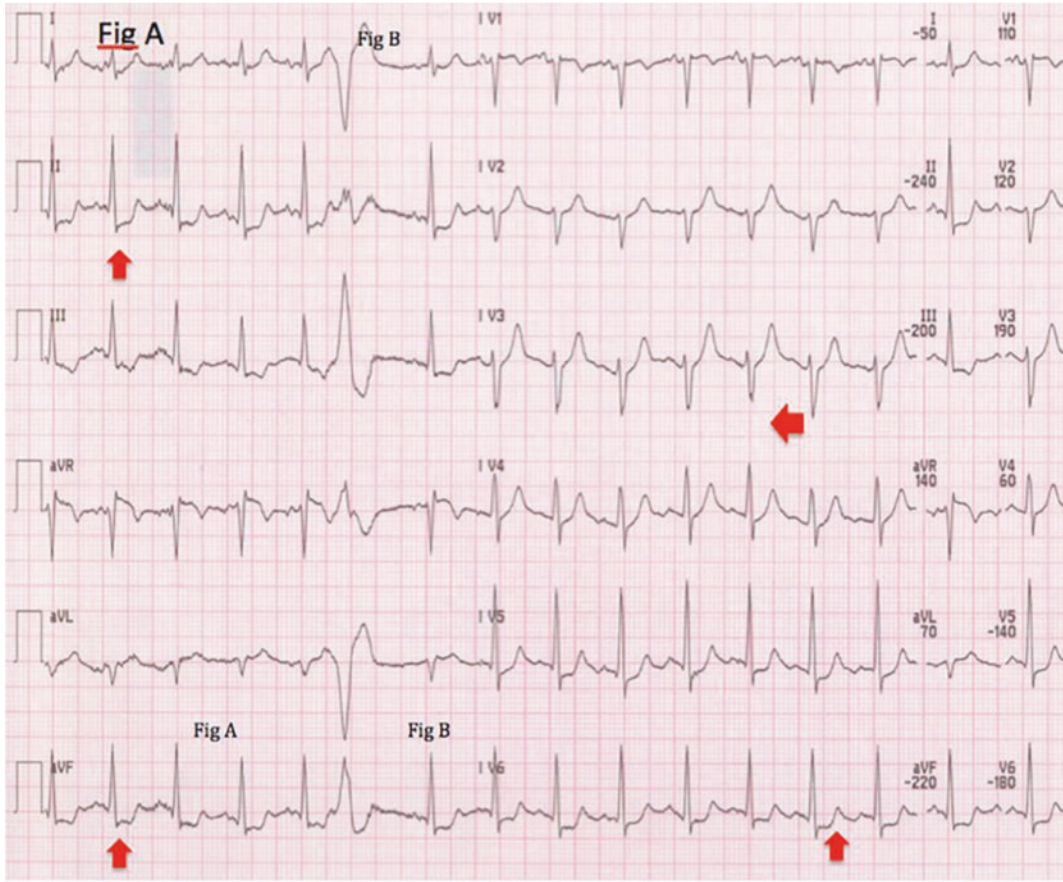

Fig. 9.4a EKG dipyridamole: diffuse abnormality of LV repolarization; ST segment depression in inferior and lateral leads

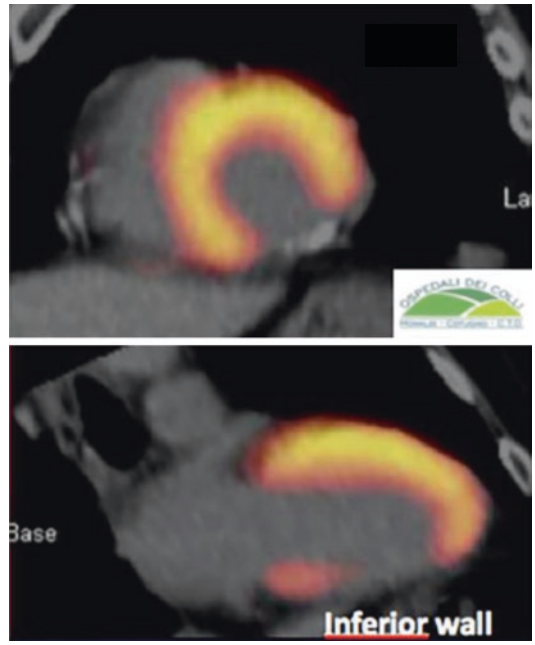

Fig. 9.4b Dipyridamole ^{82}Rb PET MPI/CT Fusion imaging: chronic ischemia with necrosis in inferior wall

Dipyridamole 82Rb PET MPI/CT Fusion imaging:

Chronic ischemia with necrosis in inferior well

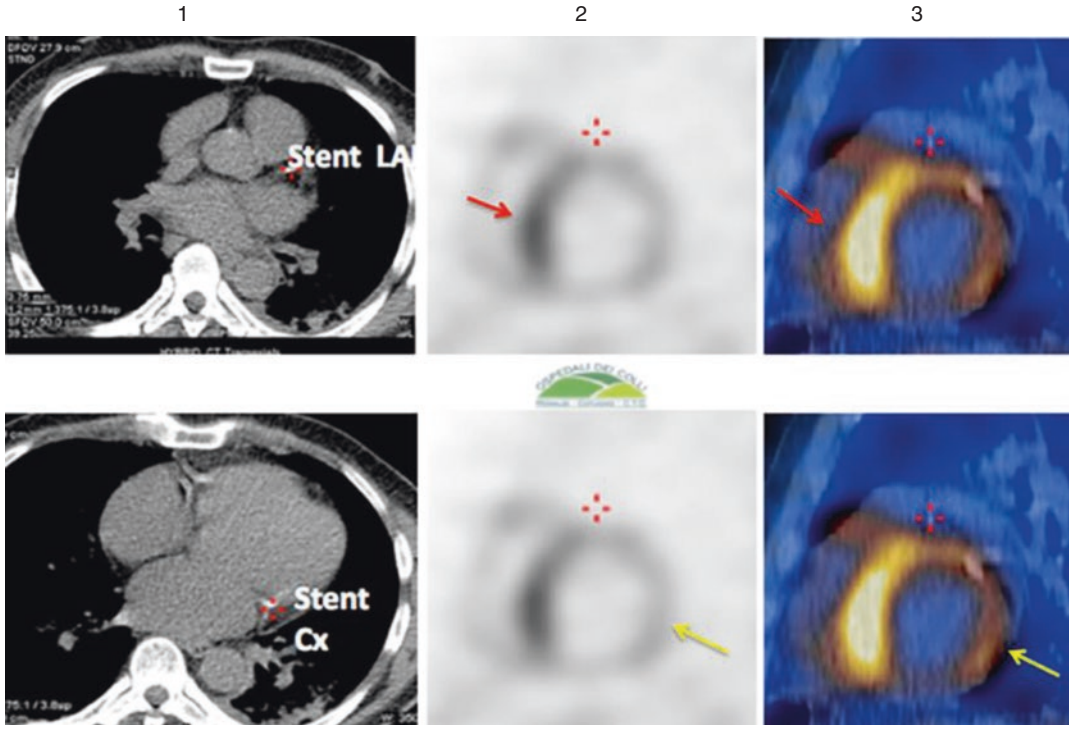

Stent LAD **No Transient Ischemia on Septum (red arrows)**

Stent Cx **Transient Ischemia on Lateral wall (yellow arrows)**

Fig. 9.4c Dipyridamole ^{82}Rb PET/CT, from right to left: (*1*) CT-AC: metallic stent (red cross) on LAD and Cx artery; (*2*) SPECT SA; (*3*) fusion imaging PET/CT

In a patient with revascularized MVD, the evidence of metallic stent at fusion images let better recognize the pertinence of vessel inducing ischemia.

Clinical Case N. 2: Match Normoperfusion, No Significant Calcific Atheromasia

Female, 67 years old, with history of hyperlipidemia and hypertension, referring atypical chest pain.

^{82}Rb PET/CT basal/dipyridamole (Fig. 9.5a), fast protocol: dynamic list-mode acquisition with a total of 35 min for basal and stressor dipyridamole (0.56 mg/Kg/4′). EKG test: No ischemia during vasodilator. Acquisition of CT gated for obtaining calcium score (Fig. 9.5b).

Clinical Case N. 3: Transient Ischemia and Coronary Artery Calcific Atheromasia

Male, 68 years old.

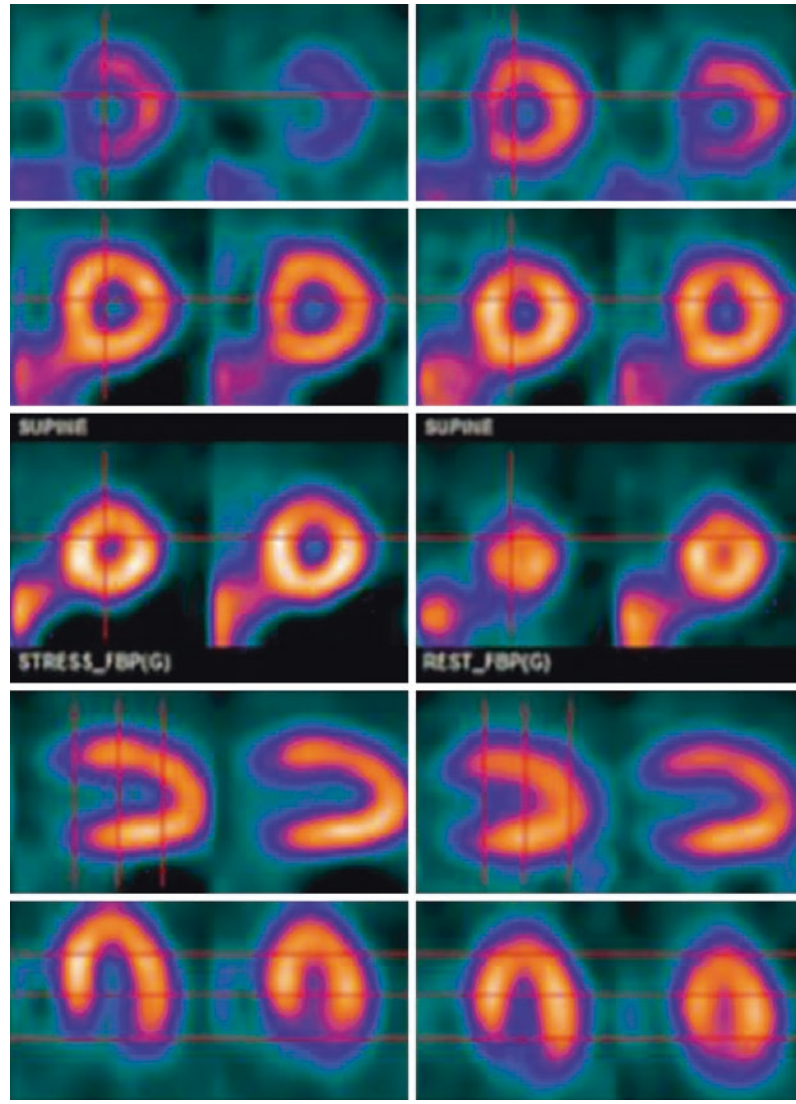

Fig. 9.5a ^{82}Rb PET/TC basal/dipyridamole: normoperfusion

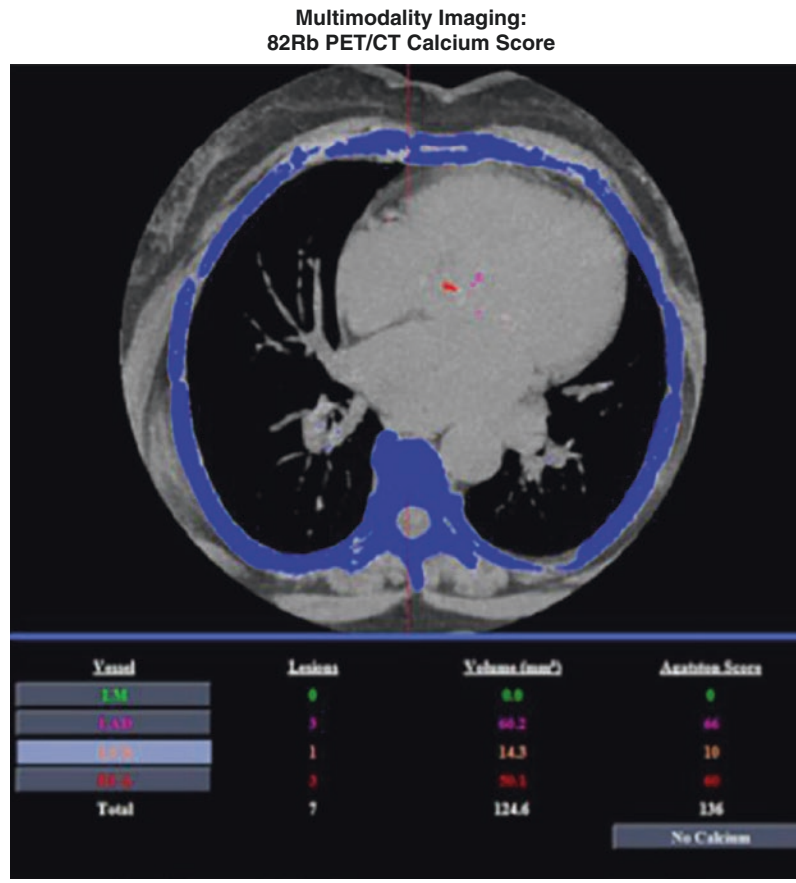

Fig. 9.5b No significant calcium score index

Cardiovascular risk factor: Diabetes type 2 for almost 12 years, smoker.

No history of CAD. The patient referred shortness of breath stress induced.

At baseline 3D transthoracic echocardiography: Preserved LV ejection fraction (LVEF 57%) and LV regional contractile function.

Patient underwent ^{82}Rb PET MPI/CT basal—dipyridamole, showing severe perfusion defect at the apex referring to transient ischemia in regimen of vasodilation by dipyridamole. At CT and fusion PET/CT imaging: Calcific atheromasia diffuse on LAD. High value of CAC score (Fig. 9.6).

Dipyridamole ^{82}Rb PET MPI (QPS Cedars Sinai)	SSS	SDS	% Defect extension
	14	12	12

Calcific atheromasia on coronary main vessels is becoming a relatively frequent evidence in multimodality studies of MPI/CT. It doesn't imply necessarily functional evolution to ischemia, but it can affect the long-term prognosis.

When it is associated with perfusion defects, the prognostic significance gets a stronger value.

According to the literature, report underlined the evidence of transient ischemia corresponding to the LAD calcific atheromasia, as a prognostic tool added to the transient perfusion defect.

Patient underwent coronary-angiography and LAD revascularization (stenting) 1 week after.

Clinical Case N. 4: Obstructive CAD

Male, 63 years old.

Cardiovascular risk factor: History of hyperlipidemia and hypertension.

For about three months, the patient complains of feeling of easy tiredness and chest pain symptoms during sleep.

Basal EKG: Normal. Stress EKG: BEV, also organized in run at the acme of stress.

Patient underwent:

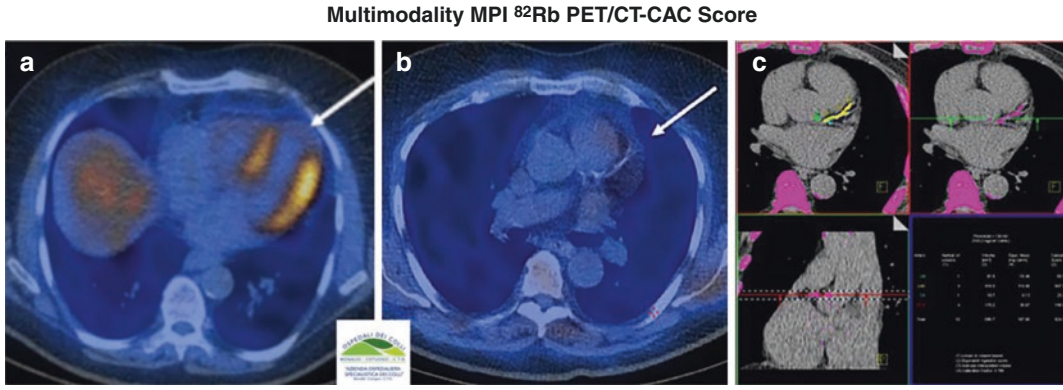

Fig. 9.6 (**a**) ^{82}Rb PET MPI stressor dipyridamole: Transient perfusion defect on antero-apical myocardial segments. (**b**) Extensive calcified plaque on LDA. (**c**) CACS = >400, consistent with ischemia with high risk of future coronary events

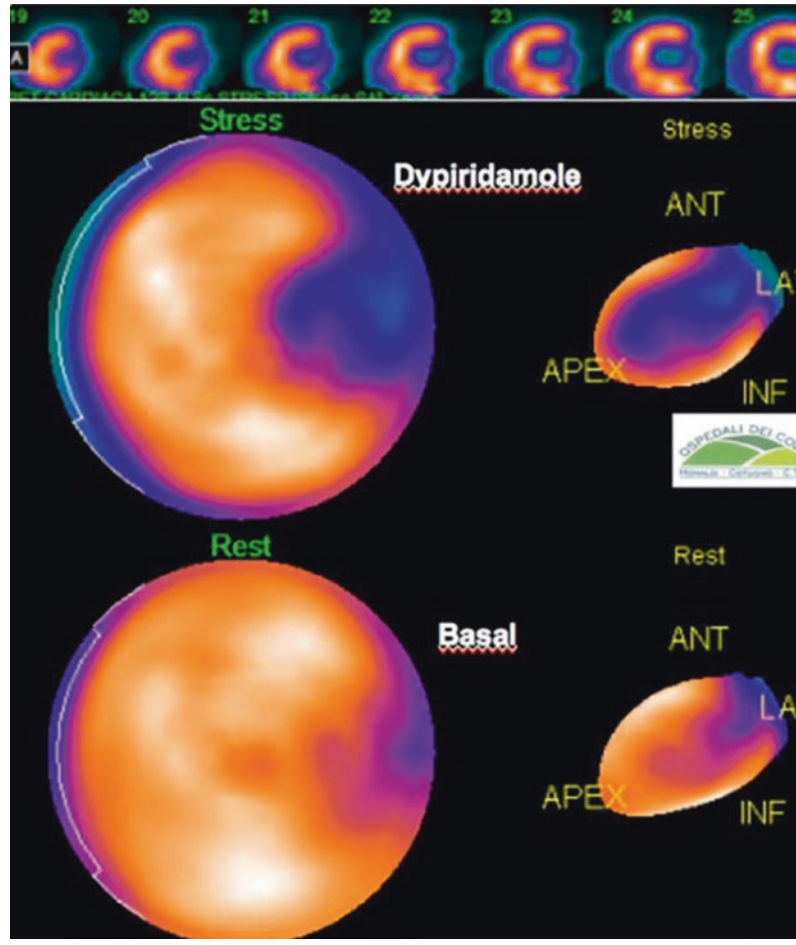

Fig. 9.7a ^{82}Rb PET/TC MPI: Short axis slices dipyridamole slices and polar map: dipyridamole (up); basal (down)

$^{-82}$Rb PET/CT basal/dipyridamole, fast protocol: 35 min for both phases; basal conditions and stressor dipyridamole (0.56 mg/Kg/4′) in dynamic list-mode acquisition.

Report: extensive transient ischemia evocated during dipyridamole infusion (Fig. 9.7a).

LV perfusion summed scores and contractile function indexes are reported, respectively, in Table Clinical Case A and Table Clinical Case B.

Table clinical case A semiquantitative analysis AutoQuant-QPS-(PFQ)		
Scores	Dipyridamole	Rest
Summed scores	SSS 16	SDS 14
	SS% 18	SD% 15
Perfusion defect extension	15% LV	2% LV
TPD	12%	3%

Transient ischemic dilation value (abnormal TID >1.13 (0.98 + 2.5 SD) = 1.1.

Table clinical case B semiquantitative analysis AutoQuant QGS (n.v. LVEF > 46%; EDV < 126 mL; ESV < 68 mL)		
LV contractile function	Dipyridamole	Rest
EF	52%	57%
EDV	138 mL	127 mL
ESV	69 mL	66 mL

Patient underwent ICA, with evidence of RCx occlusion, treated with stenting (Fig. 9.7b).

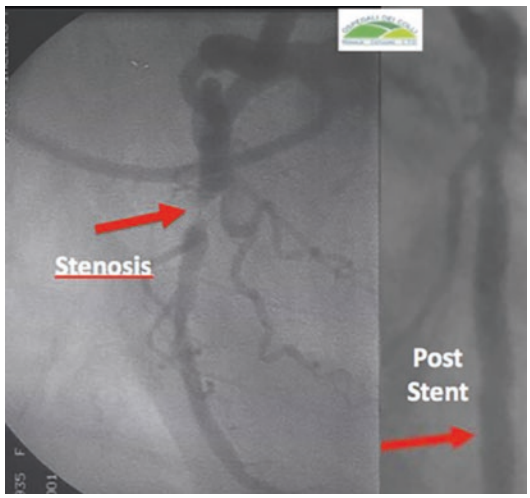

Fig. 9.7b RCx at ICA, red arrows show respecteively: -stenosis (on the left) and -post Stenting Revascularization (on the right)

Clinical Case N. 5: LV Pseudoaneurysm

Male, 54 years old.

Diabetes type 2 for almost 3 years, smoker, abdominal obesity, hypertension.

Known history of chronic CAD with transmural anterior and apex AMI, LDA stenting.

At the time of study, hospital admission for syncopal episode. Baseline Echo: LV dysfunction.

^{82}Rb PET/TC MPI: Dipyridamole/rest was scheduled in the aim to evaluate LV perfusion for transient ischemia and/or viability (Figs. 9.8a, 9.8b), in order to planning new target revascularization.

At CT and PET/CT fusion imaging analysis, clear evidence of pseudoaneurysm at the apex, with a wide and unknown component of calcific dystrophy in the area of previous necrosis (Fig. 9.8c).

Table clinical case A semiquantitative analysis AutoQuant-QPS-(PFQ) – Cedars Sinai LA		
Scores	Dipyridamole	Rest
Summed scores	SSS 24	SD 4
	SS% 25	SD% 5
Perfusion defect extension	27% LV	24% LV
TPD	21%	19%

Transient ischemic dilation value was also obtained: 1.28 (abnormal TID >1.13 (0.98 + 2.5 SD).

(n.v. LVEF > 46%; EDV < 126 mL; ESV < 68 mL)

Image analysis shows: dysfunctionally LV with volumetric overload, associated with extensive chronic CAD.

It is suggestive of:

- Transmural necrosis involving the apex and anterior-septal wall.
- Inferior-septal: chronically hypoperfused but viable myocardium.
- Mild transient ischemia at basal segment of anterior-septal wall and at basal-septum.
- Mild additional impairment of LVEF related to stressor test.
- *Note*: It must be underlined the efficacy of multimodality technique and the capability of 82Rb PET for assessing LVEF in real time with stressor test, as a prognostic factor of main relevance.

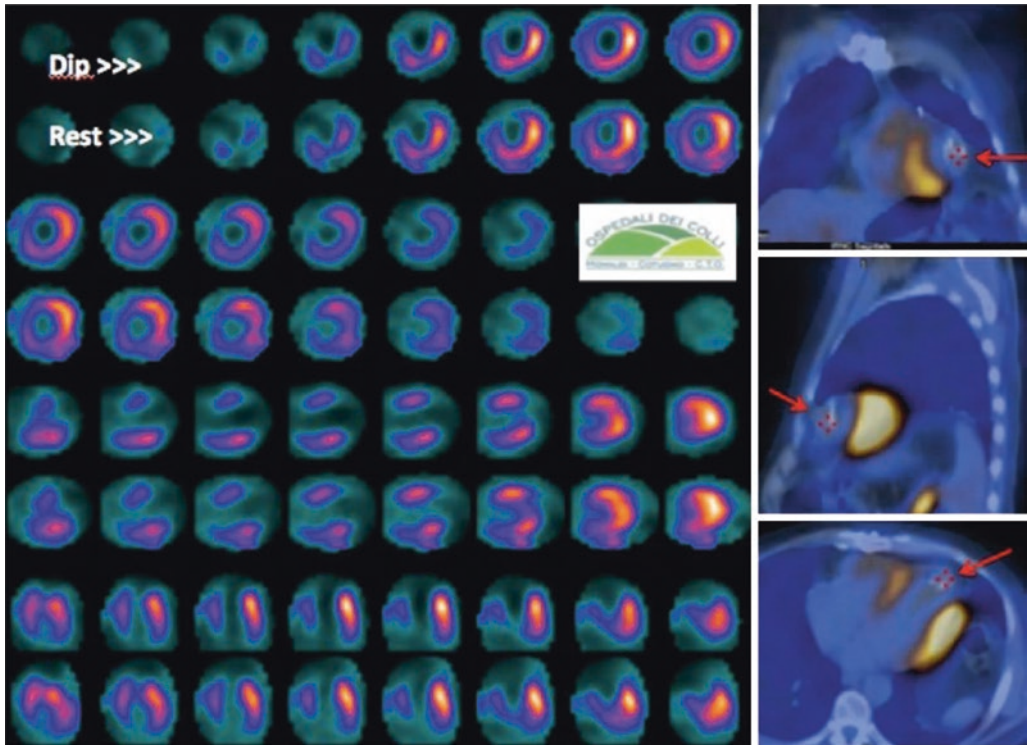

Fig. 9.8a ^{82}Rb PET/TC MPI: dipyridamole/rest. Semiquantitative analysis results are reported in Table Clinical Cases A

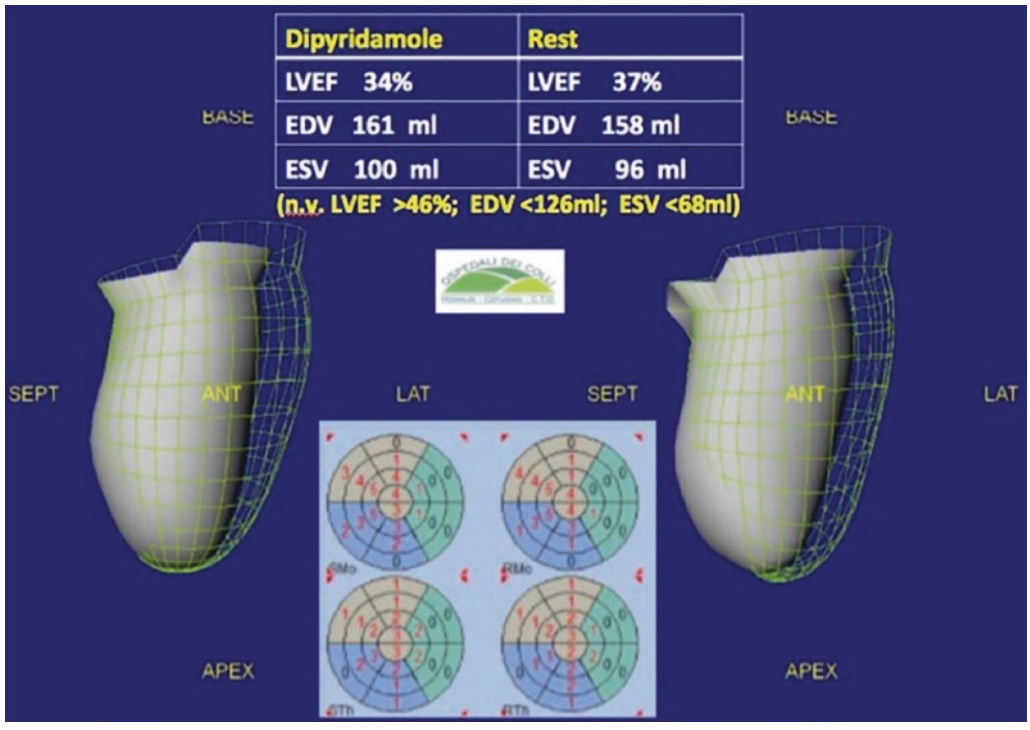

Fig. 9.8b ^{82}Rb gated PET/TC MPI: dipyridamole/rest. LV surface

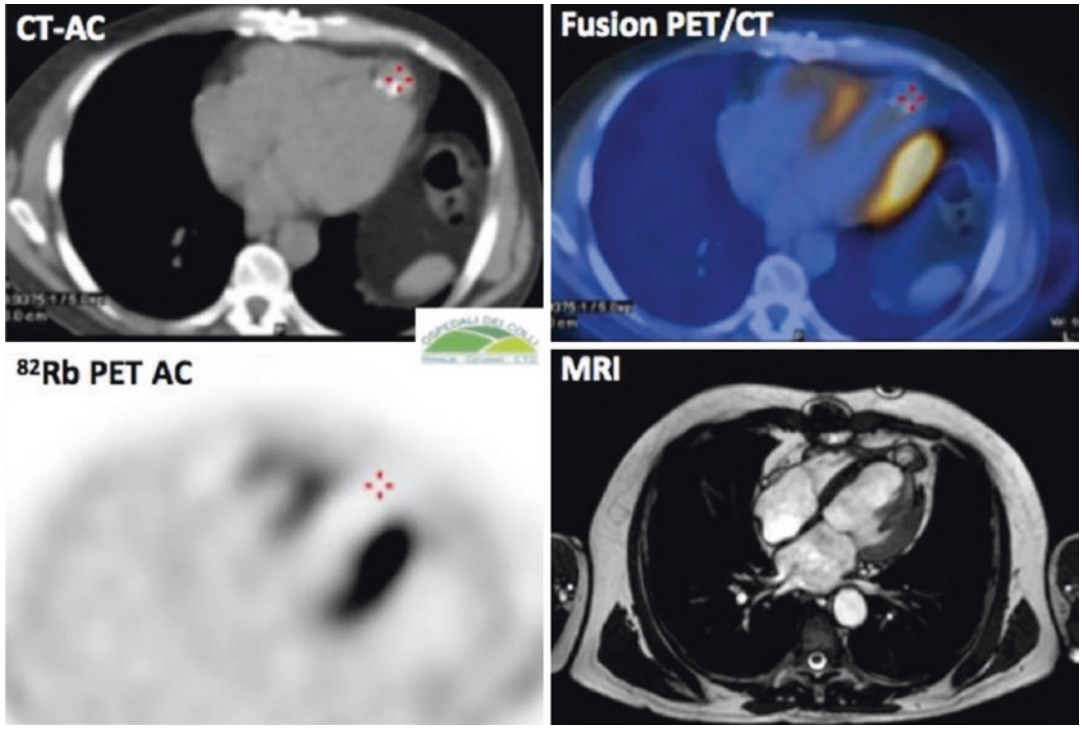

Fig. 9.8c LV Transaxial images show the perfect morphologic overlapping of calcific dystrophy with the transmural perfusion defect

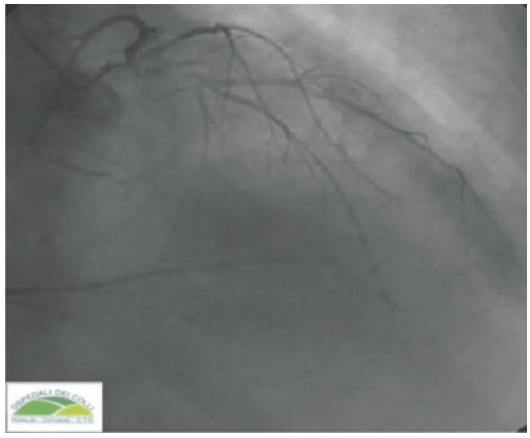

Fig. 9.8d ICA: LDA obstruction

^{82}Rb PET/TC MPI addressed the patient to surgery.

- Clinical Impact: ^{82}Rb PET/CT MPI modified the therapeutic strategy of the patient.

Before surgery patients underwent cardiac MRI and ICA. Images at comparison are shown in Fig. 9.8c.

Clinical Case N. 6: ^{82}Rb PET/CT in the Monitoring the Efficacy of Medical Therapy versus Progression Disease

Male patient, 62 years old. Multiple risk factor for CAD. Atypical chest pain.

A. (1 control) Rest/dipyridamole ^{82}Rb PET/CT (Fig. 9.9a): transient ischemia involving the 7% of LV, pertinent to the apical-medium segments of inferior wall; limited hypoperfusion in anterior wall. Severe calcium score on LDA. Patient underwent medical therapy, but one year later, he referred angina stress induced.

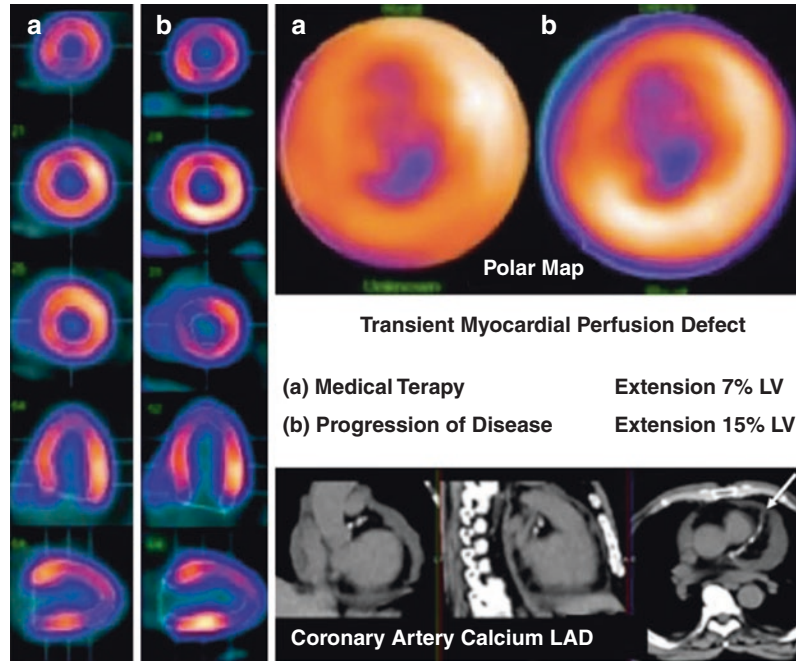

Fig. 9.9a ^{82}Rb PET/CT: The three-standard level of slices and polar map at comparison. At the 2 control, clear evidence of progression of disease extension with the prevalence of territories of LDA pertinence. Severe calcific atheromasia on LDA is also evident

B. (2 control). A new ^{82}Rb PET/CT showed progression of CAD (Fig. 9.9b), involving the 15% of LV, thus doubling the previous extent, pertinent the same region of inferior wall in respect of the previous control, but involving more extensively the LDA territory.

Patient underwent stenting revascularization on LDA and RCA.

Clinical Impact: capability of ^{82}Rb PET/CT in monitoring the efficacy of therapy and in suggesting a shift of treatment when progression disease occurred.

Clinical Case N. 7: Ischemic, Dysfunctional CMD Associated with Balanced Ischemia

Male, 54 years old. Diabetes type 2 for almost 3 years, smoker, abdominal obesity, hypertension.

Known history of chronic CAD: Acute coronary syndrome in anterior wall and apex; LDA stenting (at that time the patient rejected CABG recommended by the clinicians).

New hospital admission because of stress-induced shortness of breath (Fig. 9.10a).

- 3D transthoracic echocardiography: LV ejection fraction (LVEF 40%). Akinesia at apex, anterior wall; septum. Conclusion: dysfunctional CMD.

Patient underwent:

$^{-18}$F-FDG PET/CT (for viability assessment) and MSCT CE coronary angiography (CTA) showing MVD with:

- LDA: Obstructive stenosis distal segment; stenosis 1 diagonal artery 75%.
- RCX: 65% Stenosis.
- RCA: 80% Stenosis distal segment.

$^{-18}$F-FDG PET/CT: main results are shown in the Figure 9.10b.

$^{-82}$Rb PET/CT basal/dipyridamole was also obtained for perfusion analysis (Fig. 9.10c) to better quantify risk stratification and schedule therapeutic strategy.

Protocol: Fast protocol 35 min for basal conditions and stressor dipyridamole (0.56 mg/Kg/4′). Dynamic list-mode acquisition.

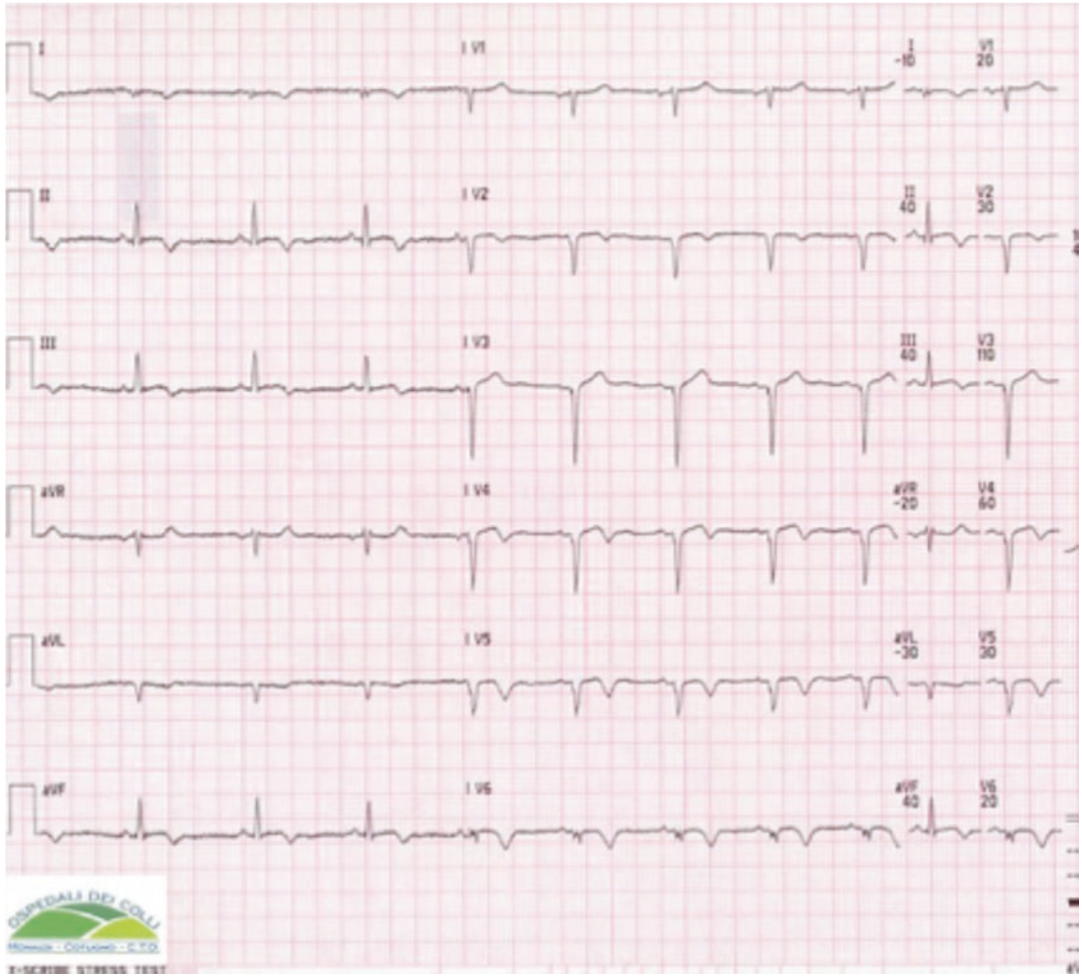

Fig. 9.10a Basal EKG: disappearance of R wave in leads V1–V6

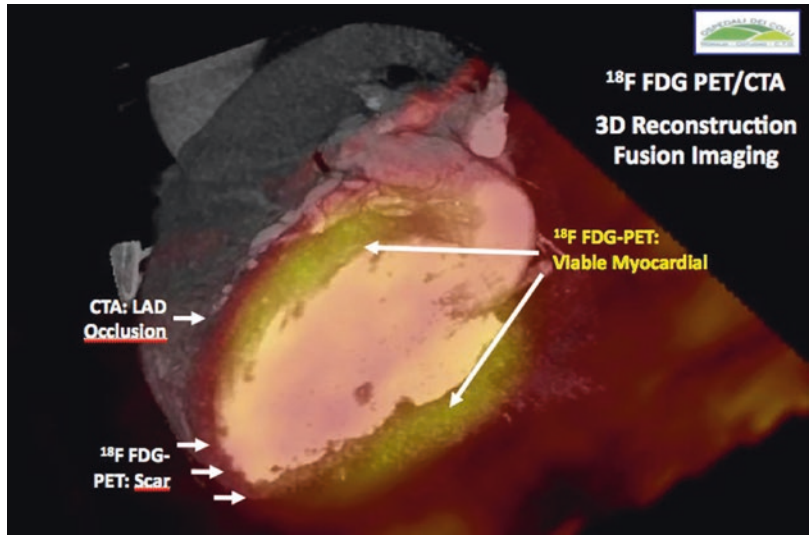

Fig. 9.10b ^{18}F-FDG PET/MSCT coronary angiography fusion imaging

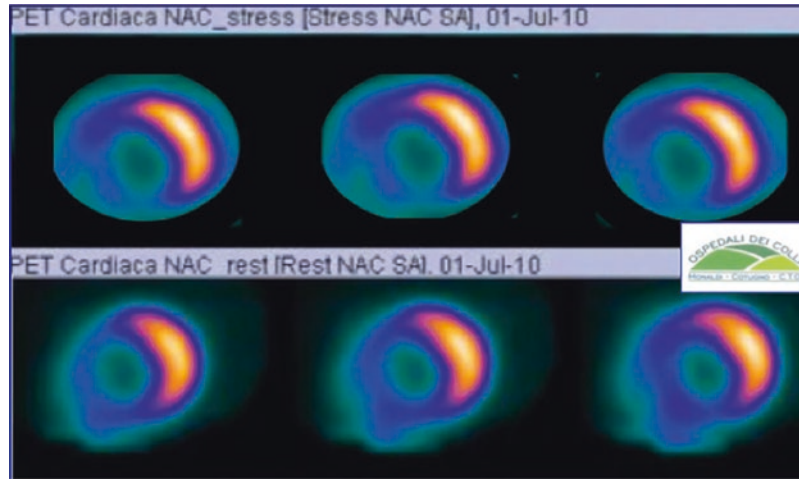

Fig. 9.10c ^{82}Rb PET/TC MPI: short axis slices

SSS	SDS	Perfusion defect extension dipyridamole	Perfusion defect extension basal	LVEF dipyridamole	LVEF basal
27	2	37%	35%	39%	45%

Transient ischemic dilation TID = 1.35 r.v. >1.13 (0.98 + 2.5 SD)
Severe perfusion defect of wide extension involving: Apex, septum, anterior and inferior wall at medio-ventricular level

- Transmural necrosis involving the apex, apical-medium segment of septum, anterior-septal and inferior wall.
- Mild transient ischemia and viable myocardium at medium-basal segment of anterior-septal wall; septum; inferior wall.
- Mild impairment of LVEF related to stressor test.
- Transient ischemic dilation (Fig. 9.10d).

-^{82}Rb PET/TC suggested the need of revascularization. Patient underwent CABG five days after PET-MPI

Clinical Case N. 8: ^{82}Rb PET/CT MPI—Impaired Regional LV MBF

Female, 65 years old.

Cardiovascular risk factor: Diabetes type 2 for almost 12 years, hypertension.

Shortness of breath and chest pain stress induced (Figs. 9.11a, 9.11b).

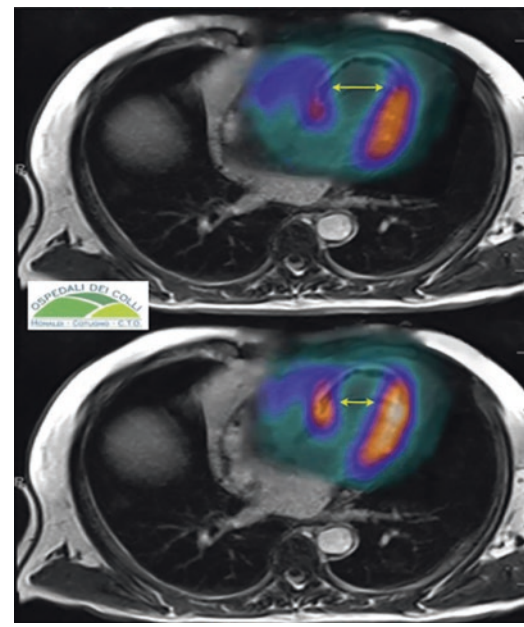

Fig. 9.10d At ^{82}Rb PET/CT MPI: LV Fusion Imaging show Transaxial slices soon after Dipyridamole (up) and at Basal scan (down). The yellow lines show clearly the difference between the maximum diameters of LV soon after Stressor Test in respect of the Basal scan, due to Transient Ischemic Dilation of LV related to Dipyridamole induced ischemia

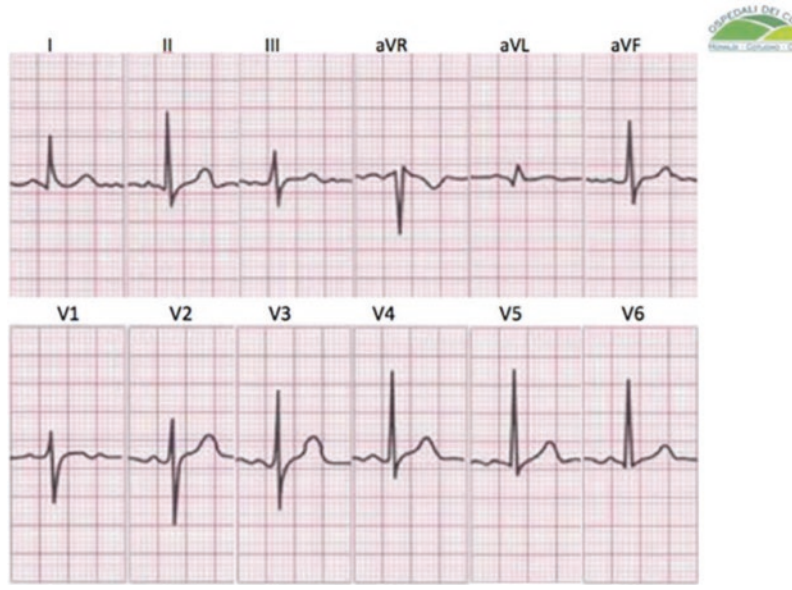

Fig. 9.11a Basal ECK: LV hypertrophy, unspecific abnormalities

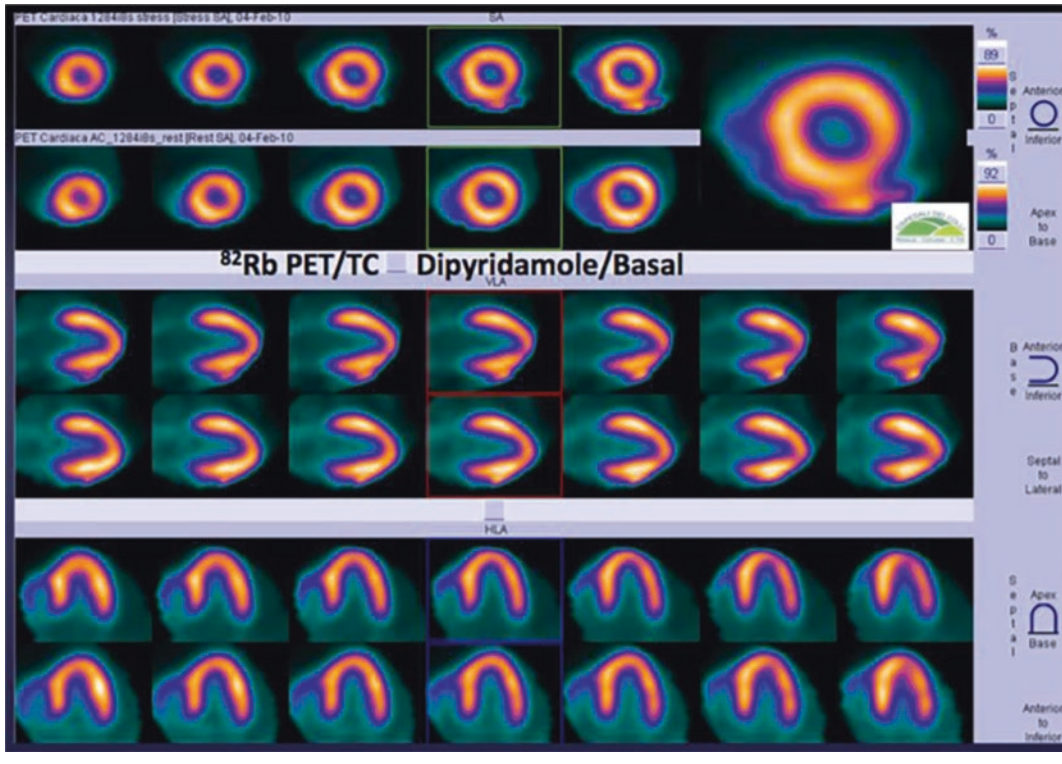

Fig. 9.11b ^{82}Rb PET MPI: No evidence of transient ischemia in response to the vasodilation due to dipyridamole

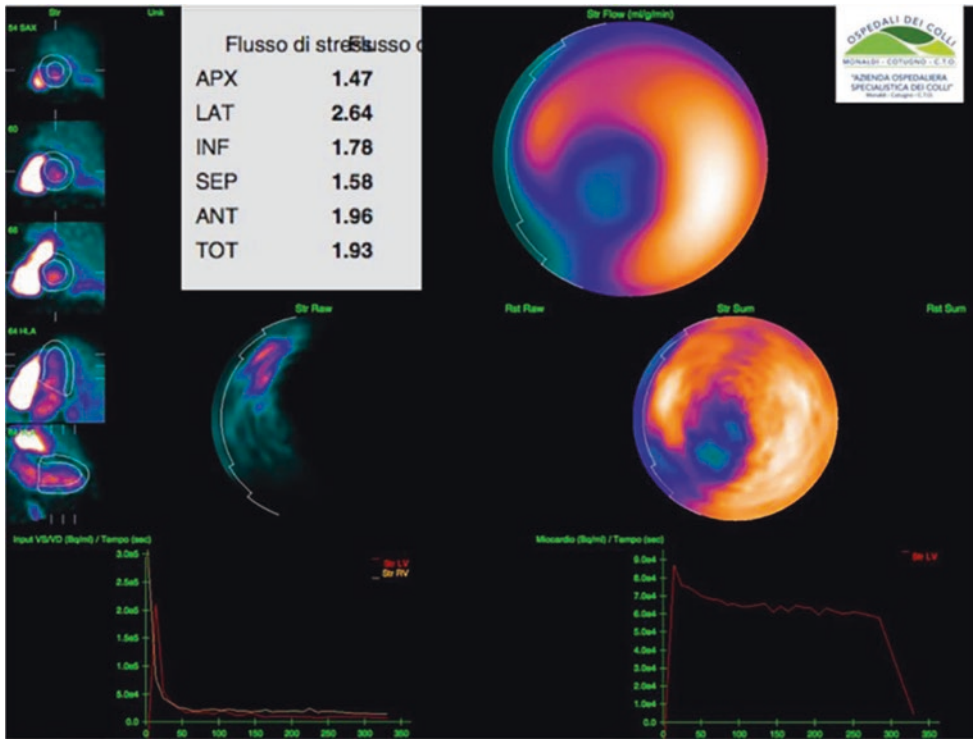

Fig. 9.11c MBF at stressor dipyridamole. Analysis obtained by QPET (G. Germano-Cedars-Sinai Medical Center, LA, CA). Impairment of regional MBF at apex, septal-inferior wall, according with microcirculation impairment

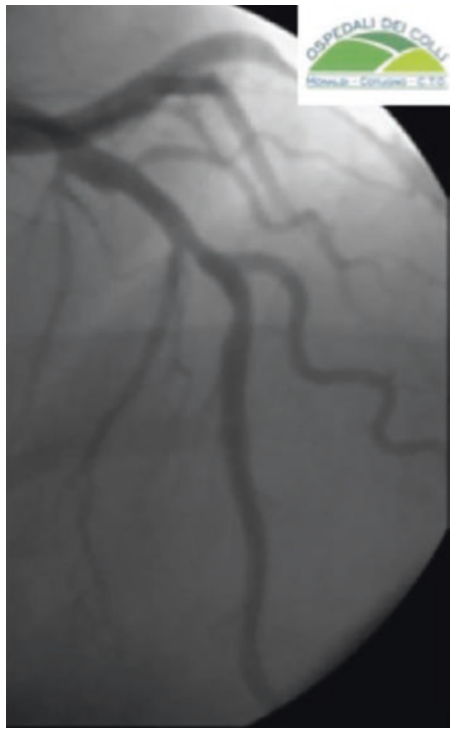

Fig. 9.11d No epicardial coronaries stenosis, FFR impairment on the selected areas

- 3D transthoracic echocardiography: LV ejection fraction (LVEF 55%). No abnormalities of regional wall motion.
- ECK stress test: inconclusive.

$^{-82}$Rb PET/CT dipyridamole/basal (dynamic, list mode, fast protocol: 35 min for both phases) (Fig. 9.11c).

Stressor dipyridamole (0.56 mg/Kg/4′): ECK: N.

Patient underwent ICA that confirmed: No epicardial coronaries stenosis (Fig. 9.11d).

MBF at ^{82}Rb PET/CT dipyridamole/basal was suggestive of microcirculation impairment.

Clinical Case N. 9: ^{82}Rb PET/CT in the Emergency of Cath-lab

Female patient, 77 years old. Two different hospital admission for acute coronary syndrome (ACS), at ICA (48 h post ACS): MVD. LVEF:40%.

At the end of ICA in Cath-lab she underwent rest/dipyridamole ^{82}Rb PET/CT fast protocol, showing:

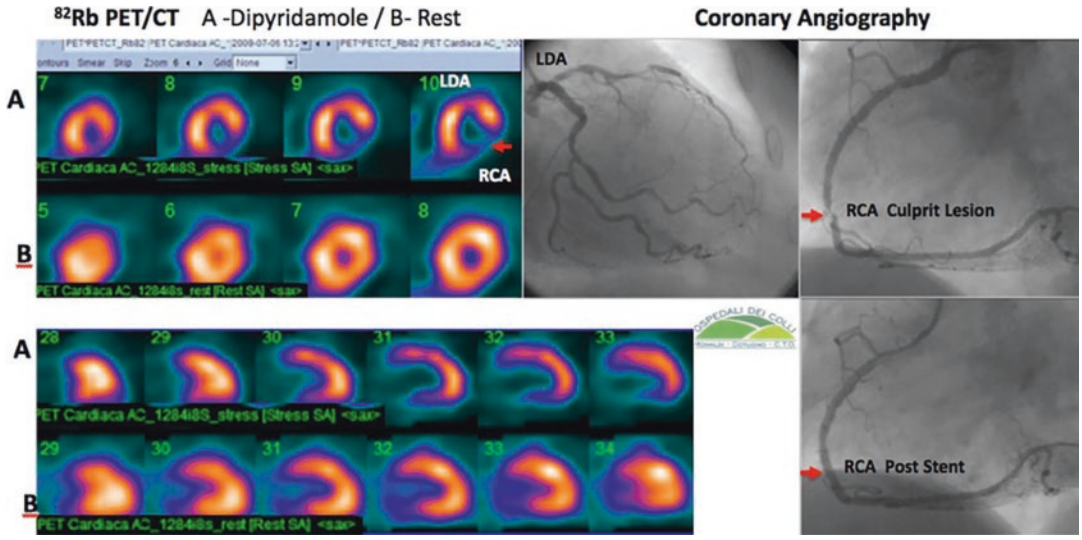

Fig. 9.12 ^{82}Rb PET/CT: transient ischemia at vasodilator test, more severe in infero-lateral, inferior wall. ICA: MVD. Severe stenosis at RCA was treated with stent target on the basis of ^{82}Rb PET evidence of dipyridamole-induced ischemia results

Perfusion defect corresponding to LDA and RCA territories, but more severe at RCA level that was identified as culprit lesion (Fig. 9.12).

Within 35 min of PET scanning, patient was re-addressed in Cath-lab for RCA stenting revascularization.

At 24 h post revascularization, EKG: ST resolution; Echo: improvement of LV compliance. This condition is especially meaningful of real life clinical practice for helping the workup of patients affected with MVD, where MPI with fast protocol can identify the functional significance of stenosis and suggest which one to revascularize, given priority.

Clinical impact: ^{82}Rb PET/CT can address target revascularization of culprit lesion, early out of the beginning of acute coronary syndrome (ACS).

References

1. Hsu B, et al. PET tracers and techniques for measuring myocardial blood flow in patients with coronary artery disease. JBR. 2013;27(6):452–9.
2. Berman DS, et al. Phase II safety and clinical comparison with single-photon emission computed tomography myocardial perfusion imaging for detection of coronary artery disease: flurpiridaz F 18 positron emission tomography. J Am Coll Cardiol. 2013;61(4):469–77.
3. Hsiao E, et al. Detection of obstructive coronary artery disease using regadenoson stress and ^{82}Rb PET/CT myocardial perfusion imaging. J Nucl Med. 2013;54:1748–54.
4. Manabe O, et al. Review article – debate article: which PET flow tracer is the best for MBF quantification? O-15-labeled Water is the best myocardial blood flow tracer for precise MBF quantification. Ann Nucl Cardiol. 2018;4(1):000–00. https://doi.org/10.17996/anc.18-00064
5. Prior JO, et al. Quantification of myocardial blood flow with ^{82}Rb positron emission tomography: clinical validation with ^{15}O-water. Eur J Nucl Med Mol Imaging. 2012;39:1037–47.
6. Iaea Radioisotopes and Radiopaharmaceuticals Series no.2. http://www.iaea.org/Publications/index.html
7. Murthy VL, et al. Clinical quantification of myocardial blood flow using PET: joint position paper of the SNMMI cardiovascular council and the ASNC. J Nucl Med. 2018;59(2):273–93.
8. Rasmussen T, et al. Stomach interference in ^{82}Rb-PET myocardial perfusion imaging. J Nucl Cardiol. 2018; https://doi.org/10.1007/s12350-018-1359-8.
9. Jagathesan R, et al. Dobutamine-induced hyperaemia inversely correlates with coronary artery stenosis severity and highlights dissociation between myocardial blood flow and oxygen consumption. Heart. 2006;92:1230–7.
10. De Rimini ML, et al. Rubidium 82 cardiac PET/CT: the first Italian experience. Eur J Nucl Med Mol Imaging. 2010;(Suppl 2):37.
11. Koenders SS, et al. Impact of regadenoson-induced myocardial creep on dynamic Rubidium-82 PET

myocardial blood flow quantification. J Nucl Cardiol. 2019;26(3):719–28. https://doi.org/10.1007/s12350-019-01649-4.
12. deKemp RA, Yoshinaga K, Beanlands RSB. Will 3-dimensional PET-CT enable the routine quantification of myocardial blood flow? J Nucl Cardiol. 2007;14:380–97.
13. Yoshida K, Mullani N, Gould KL. Coronary flow and flow reserve by PET simplified for clinical applications using rubidium-82 or nitrogen-13-ammonia. J Nucl Med. 1996;37:1701–12.
14. Lortie M, Beanlands RSB, Yoshinaga K, Klein R, Dasilva JN, DeKemp RA. Quantification of myocardial blood flow with 82Rb dynamic PET imaging. Eur J Nucl Med Mol Imaging. 2007;34:1765–74.
15. Slomka PJ, et al. Comparison of clinical tools for measurements of regional stress and rest myocardial blood flow assessed with 13N-ammonia PET/CT. J Nucl Med. 2012;53:171–81.
16. Nagamachi S, Czernin J, Kim AS, et al. Reproducibility of measurements of regional resting and hyperemic myocardial blood flow assessed with PET. J Nucl Med. 1996;37:1626–31.
17. Naya M, Murthy VL, Blankstein R, et al. Quantitative relationship between the extent and morphology of coronary atherosclerotic plaque and downstream myocardial perfusion. J Am Coll Cardiol. 2011;58:1807–16.
18. Johnson NP, Gould KL. Integrating noninvasive absolute flow, coronary flow reserve, and ischemic thresholds into a comprehensive map of physiological severity. JACC Cardiovasc Imaging. 2012;5:430–40.
19. Murthy VL, Naya M, Foster CR, et al. Association between coronary vascular dysfunction and cardiac mortality in patients with and without diabetes mellitus. Circulation. 2012;126:1858–68.
20. Bateman TM, Heller GV, McGhie AI, et al. Diagnostic accuracy of rest/stress ECG-gated Rb-82 myocardial perfusion PET: comparison with ECG-gated Tc99m sestamibi SPECT. J Nucl Cardiol. 2006;(1):24–33.
21. Dorbala S, et al. Incremental prognostic value of gated Rb-82 positron emission tomography myocardial perfusion imaging over clinical variables and rest LVEF. JACC Cardiovasc Imaging. 2009;2(7):846–54.
22. Mc Ardle BA, et al. Does Rubidium-82 PET have superior accuracy to SPECT perfusion imaging for thediagnosis of obstructive coronary disease? JACC. 2012;60(18):1828–37.
23. Ziadi MC, Dekemp RA, Williams K, et al. Does quantification of myocardial flow reserve using rubidium-82 positron emission tomography facilitate detection of multivessel coronary artery disease? J Nucl Cardiol. 2012;19:670–80.
24. Naya M, Murthy VL, Taqueti VR, et al. Preserved coronary flow reserve ef- fectively excludes high-risk coronary artery disease on angiography. J Nucl Med. 2014;55:248–55.
25. Chang SU, et al. The coronary artery calcium score and stress myocardial perfusion imaging provide independent and complementary prediction of cardiac risk. J Am Coll Cardiol. 2009;54(20):1872–82.
26. Zampella E, et al. Combined evaluation of regional coronary artery calcium and myocardial perfusion by ^{82}Rb PET/CT in the identification of obstructive coronary artery disease. Eur J Nucl Med Mol Imaging. 2018;45(4):521–9.
27. Task Force Members 2013 ESC guidelines on the management of stable coronary artery disease: the Task Force on the management of stable coronary artery disease of the European Society of Cardiology. Eur Heart J. 2013;34:2949–3003.
28. Motwani M, et al. Automated quantitative nuclear cardiology methods. Cardiol Clin. 2016;34(1):47–57.
29. Hachamovitch R, et al. Comparison of the short-term survival benefit associated with revascularization compared with medical therapy in patients with no prior coronary artery disease undergoing stress myocardial perfusion single photon emission computed tomography. Circulation. 2003;107(23):2900–7.
30. Tonino PAL, et al. Angiographic versus functional severity of coronary artery stenoses in the FAME study. JACC. 2010;55(25):2816–21.
31. Dorbala S, et al. Prognostic value of PET MPI: a multicenter registry. JACC. 2013;61(2):176–84.
32. Rischpler C, et al. Transient ischemic dilation ratio in ^{82}Rb PET myocardial perfusion imaging: normal values and significante as a diagnostic and prognostic marker. J Nucl Med. 2012;53:723–30.
33. Murthy VL, Lee BC, Sitek A, et al. Comparison and prognostic validation of multiple methods of quantification of myocardial blood flow with 82Rb PET. J Nucl Med. 2014;55:1952–8.
34. Toyota E, et al. Regulation of the coronary vasomotor tone: what we know and where we need to go. J Nucl Cardiol. 2001;8(5):599–605.
35. Liga R, et al. Multicentre multi-device hybrid imaging study of coronary artery disease: results from the evaluation of integrated cardiac imaging for the detection and characterization of ischaemic heart disease (EVINCI) hybrid imaging population. Eur Heart J Cardiovasc Imaging. 2016;17:951–60.
36. Hagemann CE, et al. Quantitative myocardial blood flow with Rubidium-82 PET: a clinical perspective. Am J Nucl Med Mol Imaging. 2015;5(5):457–68.
37. Ziadi MC, et al. Impaired myocardial blood flow reserve on Rubidium-82 positron emission tomography imaging predicts adverse outcomes in patients assessed for myocardial ischemia. JACC. 2011;58(7):740–8.
38. Lovinfosse P. Nuclear medicine techniques in transplantation. Clin Transl Imaging. 2017;5:45–62.
39. Wenning C, et al. Inhomogeneous myocardial stress perfusion in SPECT studies predicts future allograft dysfunction in heart transplant recipients. EJNMMI Res. 2015;5(1):51.

40. Wu YW, et al. PET assessment of myocardial perfusion reserve inversely correlates with intravascular ultrasound findings in angiographically normal cardiac transplant recipients. J Nucl Med. 2010;51(6):906–12.
41. De Rimini ML, et al. Role of cardiac 82Rb PET/CT in heart transplant recipients follow-up. Eur J Nucl Med Mol Imaging. 2010;37(Suppl 2):1963–4.
42. Ananthasubramaniam K, et al. Editorial. Quantitative ^{82}Rb dynamic pet perfusion analysis with kinetic modeling for myocardial viability: can we get away with just ^{82}Rb perfusion kinetics? J Nucl Cardiol. 2019;26(2):387–90. https://doi.org/10.1007/s12350-019-01616-z.
43. Moody JB, et al. The utility of ^{82}Rb PET for myocardial viability assessment: comparison with perfusion-metabolism ^{82}Rb - ^{18}F-FDG PET. J Nucl Cardiol. 2019;26 https://doi.org/10.1007/s12350-019-01615-0.
44. Merhige ME, et al. Impact of myocardial perfusion imaging with PET ^{82}Rb on downstream invasive procedure utilization, costs, and outcomes in coronary disease management. J Nucl Med. 2007;48:1069–76.
45. Shaw LJ, et al. The economic consequences of available diagnostic and prognostic strategies for the evaluation of stable angina patients: an observational assessment of the value of precatherization ischemia. Economics of Noninvasive Diagnosis (END) multicenter study group. JACC. 1999;33(3):661–9.
46. Dorbala S, et al. Approaches to reducing radiation dose from radionuclide myocardial perfusion imaging. J Nucl Med. 2015;56:592–9.
47. Kostenikov NA, et al. Original research application of ^{82}Sr/^{82}Rb generator in neurooncology. Brain Behavior. 2019;9:e01212.
48. Murthy VL, et al. Metastatic renal cell carcinoma avid for ^{82}Rb but not 18F-FDG. Clin Nucl Med. 2014;39(10):908–9.
49. Jochumsen MR, et al. A Proof of concept study of quantitative tumor perfusion imaging with ^{82}Rb OET/CT in Prostate Cancer. J Nucl Med. 2018;59(Suppl 1):1473.
50. Jochumsen MR, et al. Quantitative tumor perfusion imaging with ^{82}Rubidium-PET/CT in prostate cancer – analytical and clinical validation. J Nucl Med. 2019; 60(8):1059–65. https://doi.org/10.2967/jnumed.118.219188.

The Bone Pathway: ^{223}Ra-Dichloride

10

Laura Evangelista and Alessandra Zorz

Contents

Abbreviations

^{153}Sm	Samarium-153
^{186}Re	Rhenium-186
^{223}Ra	Radium-223
^{89}Sr	Strontium-89
ALARA	As low as reasonably achievable
ALP	Alkalinephosphate
ALSYMPCA	ALpharadin in SYMPtomatic Prostate CAncer
CRPC	Castrate-resistant prostate cancer
CT	Computed tomography

The authors declared that they have obtained the permission for any previously published material used in the chapter.

L. Evangelista (✉)
Nuclear Medicine Unit, Veneto Institute of Oncology IOV—IRCCS, Padua, Italy
e-mail: laura.evangelista@iov.veneto.it

A. Zorz
Medical Physic Unit, Veneto Institute of Oncology IOV—IRCCS, Padua, Italy

F. Calabria, O. Schillaci (eds.), *Radiopharmaceuticals*,
https://doi.org/10.1007/978-3-030-27779-6_10

EBRT	External beam radiotherapy
Gy	Gray
LET	Linear energy transfer
MBq	MegaBequerel
MDP	Methyl disphosphonate
Mev	Megaelectronvolt
mSv	Milli-sievert
NIST	National Institute of Standard and Technology
PET	Positron emission tomography

10.1 Background

Radionuclides are an innovative treatment option for neoplasia such as metastasized, castration-resistant prostate cancer. Currently, prostate cancer is the most common cancer in males and one out of seven men develops invasive prostate cancer during his lifetime [1]. Almost 3% of men die from prostate cancer [1].

Several beta-emitting radiopharmaceuticals, including ^{89}Sr-chloride, ^{186}Re-hydroxyethylidene diphosphonate, and ^{153}Sm-ethylene diamine tetramethylene phosphonate, have been developed for palliation of bone pain due to metastases.

^{223}Ra dichloride, known as Alpharadin, is a novel bone-seeking alpha emitter used for treatment of CRPC in patients with bone metastases. It is a calcium-mimetic solution that selectively targets area of increased bone turnover in bone metastases. First clinical studies with ^{223}Ra started in 2012. Nine hundred patients with bone metastases have been treated from castration-resistant prostate cancer in phase I–III clinical trials worldwide [2–7].

10.2 ^{223}Ra and Pharmacokinetic

10.2.1 Isotope

^{223}Ra is predominantly an alpha emitter. It decays via a chain of short-lived alpha and beta emissions into stable lead (Fig. 10.1 shows the complete radium decay chain). Decay products have an average lifetime ranges from 1781 ms and

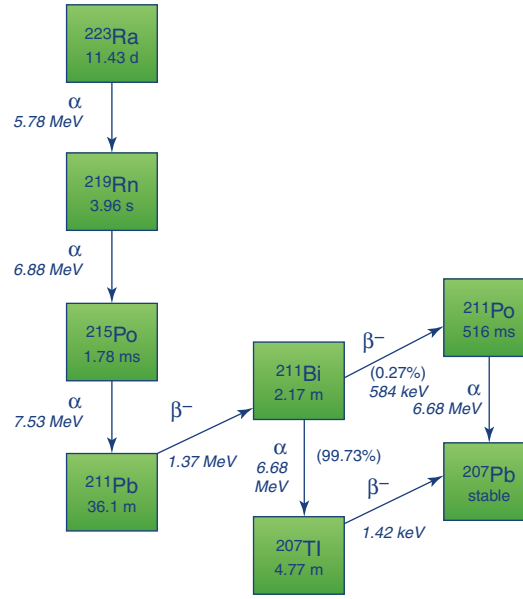

Fig. 10.1 Radium-223 decay scheme

36 min. The isotope half-life is 11,43 days. The total emitted energy is about 28 MeV. On average, four alpha and two beta particles are emitted [8, 9].

On the total decay energy:

- 95.3% is emitted as alpha particles
- 3.6% is emitted as beta particles
- 1.1% is emitted as gamma or X-rays

Although the proportion of gamma emissions from each ^{223}Ra decay is only 1.1%, it allows easily activity measure on standard instruments like dose calibrators. Preliminary studies [8–10] have also shown that quantitative planar images on gamma camera after radium injection is feasible.

The isotope is produced in a reactor, where a target of radium-226 is bombarded with neutron to obtain actinium-227. Actinium-227 decays to radium-223 through thorium-227 (21,77 years).

10.2.2 Advantages of Alpha Particles

Alpha-emitting radiopharmaceuticals are increasingly under evaluation for radionuclide therapy treatment.

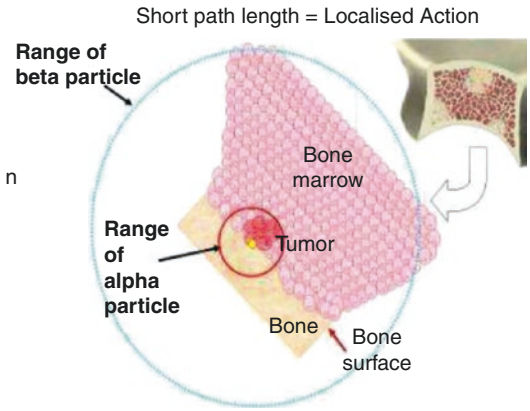

Fig. 10.2 Different range of alpha and beta particles

Alpha particles have a high energy but short path length; physically speaking, they have a high LET, less than 100 keV/μm; thanks to that properties, they release high quantity of energy, so high radiation dose, in a small area (inferior than 100 μm), increasing the biologic effectiveness. If this area corresponds to tumor cells, they provide a highly localized cytotoxic effects and tumor cell killing, minimizing damage to healthy tissue surrounding cancer cells and nontarget toxicity. In other words, alpha emitter has a localized and more effective action compared to beta particles that produces lower energy radiation and longer track length (Fig. 10.2). This high biological effectiveness leads also to a low injected activity if compared to beta particles therapy (70 kg standard man is injected with 3.5 MBq of ^{223}Ra).

Range is sufficiently short that some portion of the trabecular marrow space will experience zero dose from ^{223}Ra distributed on trabecular bone surfaces. Consequently, less hematologic toxicity for a given bone surface dose would be expected in comparison with beta emitters.

10.2.3 Xofigo

Xofigo is a standardized, stable, vial-based product easy to use. It contains a sterile, isotonic aqueous solution of $^{223}RaCl_2$ ready to use: no elution, kit preparation, or chelating is required. It can be directly injected in a patient with a syringe. No particular storage temperature is required. Each vial contains 6 ml of solution with an activity of 6.6 MBq at the reference date (6 MBq before the change in NIST standard reference material on 20th April 2016). The radioactive concentration at reference date is fixed and equal to 1100 kBq/mL. It is possible, after a calibration procedure with a NIST traceable ^{223}Ra reference standard that allows to determine the optimal calibrator dial setting, to measure activity in standard dose calibrator. The drug has a shelf life of 28 days. The administration scheme consists in 6 administrations given at 4 week intervals via intravenous injection. Thanks to the high biological effectiveness of alpha particles, the activity that has to be administered to the patient is much lower with respect to beta particles for bone metastases treatment. The activity that has to be administered is patient specific; it is calculated starting from patient body weight on the day of injection:

$$\text{Abstract} = \text{body weight}\left[\text{kg}\right] \times 55\left[\frac{\text{kBq}}{\text{kg}}\right]$$

Before the administration, it is necessary to calculate the volume of the solution that has to be drawn up from the vial in order to have in a syringe the requested activity. The volume is equal to:

$$\text{Volume to inject}\left(\text{mL}\right) = \frac{\text{Body weight}\left[\text{Kg}\right] \times 55\left[\text{kBq/kg/}\right]}{\text{DK} \times 1100\,\text{kBq/mL}}$$

where DK is the decay factor, calculated to evaluate the physical decay correction between the vial calibration date and the administration date. It is recommended almost to verify the dosage with a dose calibrator.

10.2.4 Radiation Protection Aspects

Radionuclide therapy with ^{223}Ra uses alpha particles, in contrast to established standard treatments with beta or gamma emitters. Therefore, it is necessary to set up standard radiation safety practice for a safe handling. In order to use ^{223}Ra, the center needs a radioactive materials

Table 10.1 Exposure rate of ^{223}Ra without any shielding

	Dose rate [μSv/h · MBq]		
Distance	Vial	Syringe	Average patient activity (3.5 MBq)
1 m	0.05	0	<1
1 cm	~500	54	–

license approved for medical use of this isotope. Moreover, a secure area for drug storage is necessary.

External radiation exposure with alpha emitters is very low. Range of alpha particles in air and in water is equal to several centimeters. These particles are shielded by a tissue or paper, instead of beta (plastic, aluminum foil) or gamma (cm of lead).

Typical exposure rate [11, 12] without any shielding is reported in Table 10.1. Estimated dose to hands during a 5-min handling time is around 116 μSv.

Internalization of alpha emitters poses a greater risk of exposure. This risk can be avoided without unusual safety measures, like manipulation operation in apposite hot cells with ventilation system to avoid inhalation risk and wear protective clothing (gloves..) to avoid contamination incidents. The low gamma emission allows contamination monitoring by standard gamma detectors probes, without the need of alpha-radiation-specific equipment.

Obviously ALARA criteria suggest always to use adequate shielding, maximize distance from the source, and minimize time of exposure.

It is necessary to set up disposal for radioactive waste management (material used in connection with the preparation and administration) because the half-life of this isotope is longer than common isotope used in nuclear medicine department. Decay in secure storage to nonradioactive daughter product. After 10 half-lives, the activity has decayed to minus than 0.1% of starting activity reaching background level. For example, in 8 months a standard 6.6 MBq^{223}Ra vial decays to 3 Bq vial.

Clinical results indicated that ^{223}Ra dichloride goes to the target immediately after the intravenous administration (60% of the injected activity is taken up in the bone by 4 h). The excretion is predominant through the feces (75% is excreted from the body in 1 week mainly by feces, < 5% through urine). The contamination and intake of activity by patient family members or caregivers is unlikely. Estimated dose to family/caregivers is inferior to 1 mSv (a person would have to be standing at 1 m from patient without moving for 119 days to receive 1 mSv). Typical dose rate from patient is 0.35 μSv/h, so radiation exposure to family members is expected to be negligible. It is however recommended to give minimal instructions for standard precautions to dismissed patients in order to prevent direct contact with body fluids, like standard hygiene measures (clean up spilled urine, avoid direct contact with body fluid-contaminated material, gloves, wash hands thoroughly after using toilet, use a condom for 1 week after injection). Due to a possible release of ^{223}Ra in the milk, pregnancy and breast-feeding are contraindicated. Moreover, patients undergoing ^{223}Ra are recommended to use contraceptive devices for 6 months from the end of treatment.

10.2.5 Pharmacokinetic

Pharmacokinetics, biodistribution, and dosimetric data were obtained from a phase I study (Table 10.2).

Nilsson et al. [4] indicated that main clearing was by the hepatobiliary/intestinal route. Accumulation in the soft tissues outside the gut was visualized with a small amount of activity in the kidney and liver of some patients, but only at the very earliest time points. In 2004, Nilsson et al. [13] performed a preliminary phase IB trial, enrolling 6 patients with prostate cancer.

Carrasquillo et al. [14] reported the first study containing the radiopharmacokinetics and biodistribution with escalating doses of ^{223}Ra based on clinical data. Ten patients received either 50, 100, or 200 kBq of ^{223}Ra per kilogram of body weight. Subsequently, six of these ten patients received a second dose of 50 kBq/kg. Pharmacokinetics and biodistribution were assessed by serial blood sampling, planar imaging, and whole-body counting. Safety was also

Table 10.2 Phase I trials with ^{223}Ra

Authors, ref	Journal	N of pts	Population	Dose for ^{223}Ra	End-points
Nilsson et al. [4]	Clinical Cancer Research	31	Prostate and breast cancer patients with bone mets	46 or 93 or 163 or 213 or 250 kBq/kg	Safety and tolerability, efficacy, pharmacokinetics
Nilsson et al. [13]	EJNMMI	6	Prostate cancer patients	250 kBq/kg (in two regimens: 125 kBq/kg or 50 kBq/kg)	Safety profile
Carrasquillo et al. [14]	Meeting Abstract	10	Prostate cancer with bone mets	Increase in dosage: 50, 100, 200 kBq/kg	Safety, tolerability, pharmacokinetics, dosimetry and biodistribution
Chittenden et al. [15]	The Journal of Nuclear Medicine	6	Prostate cancer with bone mets	2 injections 6 weeks apart, at 100 kBq/kg	Biodistribution, pharmacokinetics and dosimetry

assessed. ^{223}Ra is cleared rapidly from the vasculature, with a median of 14% (range 9–34%), 2% (range 1.6–3.9%), and 0.5% (range 0.4–1.0%) remaining in plasma at the end of infusion, after 4 h, and after 24 h, respectively. Biodistribution studies showed early bone uptake and early passage into the small bowel (main excretory organ) with fecal excretion as the major route of elimination, with a median of 52% of administered ^{223}Ra in the bowel at 24 h. In 6–8 days, a median of 76% (2–82%) of the administered ^{223}Ra had been excreted from the body. Urinary excretion was relatively minor (approximately 5% of administered ^{223}Ra). Bone retention was prolonged and no dose limiting toxicity was observed.

Chittenden et al. [15] performed a phase 1 open-label clinical trial to determine the biodistribution, pharmacokinetics, and dosimetry from 2 sequential administrations of ^{223}Ra-dichloride (100 kBq/kg) 6 weeks apart on six patients; data have been determined from activity retention measurements in the whole body, individual organs, blood, urine, and feces beyond whole-body measurements and quantitative gamma camera imaging. Their results confirmed that the injected activity cleared rapidly from blood, with 1.1% remaining at 24 h. Most of the administered activity was taken up rapidly into bone, with 61 ± 10% in the bone after at 4 h. Activity passed rapidly into the intestine. Fecal excretion was the main route of elimination of activity from the body (13 ± 12%), although no significant toxicity was reported. Excretion of activity in the urine was significantly lower than that in feces (2 ± 2%). Specific uptake was seen on the gamma camera images in the whole body, bone, and gut but no specific uptake was observed in kidneys or liver. Table 10.3 reported the most important pharmacokinetic data.

Table 10.3 Comparison of pharmacokinetic results

Authors, Ref	Activity in blood after 24 h	Bone uptake at 4 h	Fecal excretion	Urine excretion
Carrasquillo et al. [2]	0.5%	–	76%	5%
Chittenden et al. [15]	1.1%	61%	13%	2%

To summarize, the pharmacokinetic results demonstrated that the ^{223}Ra-dichloride was rapidly cleared from the blood and taken up into bone. The main route of excretion was via the feces. In Fig. 10.3 is reported the biodistribution of ^{223}Ra limited to the thorax, in patient who underwent 6 cycles of ^{223}Ra (the last scintigraphy scan was not available). As clearly showed, the distribution of ^{223}Ra was always the same, after 24 h, an intense uptake in the intestine was reported, while no uptake in the blood was seen.

10.3 Dosimetric Distribution

The study from Lassmann and Nosske [16] was the first paper that performed a comprehensive dosimetric calculation of normal organ and tissue doses after six intravenous injections of

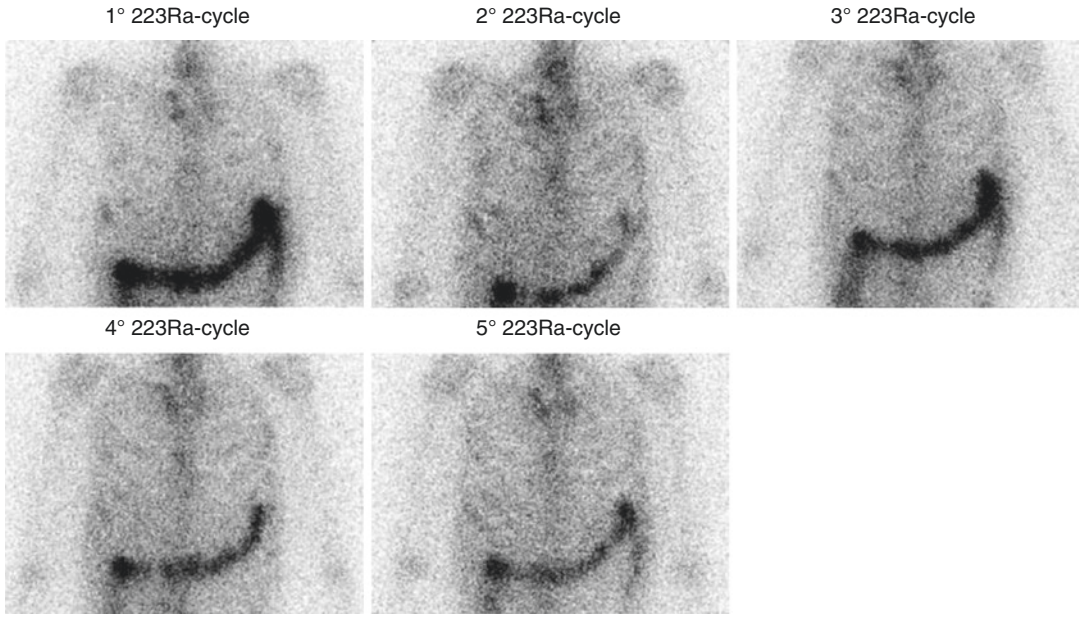

Fig. 10.3 An example of biodistribution across the different ^{223}Ra cycles

0.05 MBq/kg of ^{223}Ra-chloride according to the present International Commission on Radiological Protection (ICRP) model for radium on 25 organs or tissues. In this work, bone endosteum (16 Gy) and red bone marrow (1.5 Gy) show the highest dose coefficients followed by liver, colon, and intestines. It emits gamma useful for imaging. The author suggested that patient-specific dosimetry studies are required.

The drug information sheet reported dosimetric data calculated with Olinda/EXM Software (Organ Level INternal Dose Assessment/EXponential Modeling), based on Medical Internal Radiation Dose (MIRD) methods. The highest dose coefficients were reported for the osteogenic cells (1.152 Gy/MBq) and bone marrow (0.138 Gy/MBq); however, bone marrow adverse reaction observed in clinical studies is less frequent than what can be expected from the value obtained, maybe for the spatial distribution of alpha particles that causes a non-uniform dose distribution.

Several studies addressed the possibility of performing in vivo dosimetry using quantitative planar imaging with gamma camera, for example, the already mentioned Hindorf et al. [10] and Carrasquillo et al. [2], that reported data for in vivo pharmacokinetics and biodistribution of ^{223}Ra. Recently, two further studies published first in vivo image-based dosimetric data.

The first one by Chittenden et al. [15] evaluated the absorbed dose to a range of organs including bone surfaces, red marrow, kidneys, gut, and whole body during the Phase 1 study with Olinda/EXM, in addition to the pharmacokinetic data reported in the previous section. The range of absorbed doses delivered to the bone surfaces was 2331–13,118 mGy/MBq, while to the red marrow were 177–994 and 1–5 mGy/MBq from activity on the bone surfaces and from activity in the blood, respectively. The authors observed a great correlation between dosimetric assessment in the first and second treatment, while interpatient variability in the absorbed dose to normal organs varied from 150% for the liver to nearly 400% for the bone surface and marrow. No gastrointestinal damages were observed, confirmed by the low absorbed dose delivered to the gut wall. The lack of adverse myelotoxicity implies that the absorbed dose delivered from the circulating activity may be a more relevant guide to the potential for marrow toxicity than that due

to activity on the bone surfaces. Doses previous calculated by Lassmann and Nosske [16] fall within these ranges except for the red marrow, bone surfaces (higher), and liver (lower).

Second study was performed by Pacilio et al. [8, 9] who presented a suitable methodology for in vivo dosimetry of bone metastases with quantitative planar imaging; nine patients with 24 lesions affected by osseous metastases from CRPC who were treated with six injections of 50 kBq/kg of ^{223}Ra. The absorbed dose to lesion was assessed after a gamma camera calibration by MIRD approach. In particular, lesions were delineated on 99mTc-MDP whole-body images, and the ROIs superimposed on four ^{223}Ra images acquired at different times after the same administrations. Results indicated that the absorbed dose after the first injection was 0.7 Gy (range 0.2–1.9 Gy) and that the percent uptake of 99mTc and ^{223}Ra were significantly correlated.

A case report of a 70-year-old man affected by CRPC bone metastases who underwent standard Alpharadin therapy is reported from the same authors Pacilio et al. [8, 9]. The inter-fraction variability of the absorbed dose to lesions was evaluated for four out of six injections and the lesion response was monitored in terms of radiopharmaceutical uptake. The mean absorbed dose and standard deviation for 4 lesions were 434 mGy (15%) and 516 mGy (21%) for the right and left humeral head, 1205 mGy (14%) and 781 mGy (8%) for the right and left glenoid. The estimated total absorbed dose after the whole treatment, considering also the relative-biological effectiveness of alpha particles (RBE = 5), yielded a range of 13–36 Gy. The follow-up of the level of uptake of the ^{223}Ra can be efficiently and quantitatively performed by 99mTc-MDP imaging.

Preliminary in vivo dosimetric results indicated that quantification from gamma camera imaging is feasible and that a wide range of absorbed doses are delivered from weight-based administrations of activity. Moreover, the usefulness of dosimetry should be demonstrated. A first attempt to calibrate gamma cameras in the framework of an Italian multicenter study for lesion dosimetry in ^{223}Ra therapy of bone metastases was performed by Pacilio et al. [17] in 2017. Equipment of several manufacturers and different models were used. The option of personalized treatments and the possibility to establish dose-response correlations could be explored.

10.3.1 Adverse Reaction

The main adverse events observed due to the administration of ^{223}Ra are:

1. Gastrointestinal (diarrhea, nausea, and vomiting).
2. Musculoskeletal (bone pain including flare, and fatigue).
3. Hematological (thrombocytopenia and neutropenia).
4. Connective tissue disorders (erythema and bulge).

In the next paragraph, some data about phase II and III clinical trials and the side effects will be reported.

10.4 Clinical Indications

10.4.1 Phase II and III Trial

Between 2007 and 2012, three *phase II trials* were conducted in 317 patients with CRPC who underwent ^{223}Ra treatment with different dose levels (5, 25, 50, and 100 kBq/kg) (Table 10.4).

Nilsson et al. [3] enrolled 95 patients in the first phase II randomized trial. 64 patients received ^{223}Ra and 31 received the placebo. The first end-point of the study was to assess the efficacy of ^{223}Ra in terms of reduction in ALP. As secondary end-point, the effects on skeletal-related events (SRE) and PSA levels were assessed. In the present study, patients were treated with ^{223}Ra (50 kBq/kg every 28 days) for 4 months. ^{223}Ra was well tolerated with a minimum toxicity at the medullary and a significant reduction in ALP levels.

In 2012, Nilsson et al. [5], by including 100 patients with metastatic prostate cancer, evalu-

Table 10.4 Phase II trials

Authors, ref	Journal	N of pts	Population	Dose for ^{223}Ra	End-points
Nilsson et al. [3]	Lancet Oncol	64 (^{223}Ra) vs. 31 (placebo)	Prostate cancer patients with mets	50 kBq/kg every 28 days for 4 months	Efficacy and safety
Nilsson et al. [5]	Eur J Cancer	100	Prostate cancer patients with mets	5, 25, 50 or 100 kBq/kg	Efficacy and safety
[6, 18]	EAU 2012	122	Prostate cancer with mets	25, 50 or 80 kBq/kg per 6 cycles	Efficacy and safety

ated if escalated dose would be useful for improving the efficacy of ^{223}Ra. The authors tested the effect of dose on bone pain, by using a single dose of 5, 25, 50, and 100 kBq/kg of ^{223}Ra. After 8 weeks from the injection, the rate of responders to bone pain were 40%, 63%, 56%, and 71%, respectively. Furthermore, the reduction of bone pain was associated with a reduction in ALP levels.

In the last phase II trial, Parker et al. enrolled 122 patients who received different dosage of ^{223}Ra. 41 patients received 25 kBq/kg, 39 received 50 kBq/kg, and finally 42 had 80 kBq/kg. The treatment was prolonged for 6 months, every 28 days. The reduction of ALP was significantly higher in patients undergoing a dosage of 50 and 80 KBq (67% and 66% respectively vs. 16% with 25 kBq/kg). However, no differences in terms of side effects among the different dosage were reported.

The *pivotal trial ALSYMPCA (the phase III trial)* demonstrated survival benefits for patients with symptomatic bone metastases from CRPC [6, 18]. The inclusion criteria were: symptomatic patients (i.e., regular assumption of analgesic medication (non-opioid or opioid) or pain-free patients who received external-beam radiotherapy (EBRT) for cancer-related bone pain in the 12 weeks before randomization) with at least two bone metastases at bone scan and no visceral disease on computed tomography (CT) scan evaluation; moreover, lymph node was admitted up to 3 cm diameter short axis. Some patients were pretreated with docetaxel, someone else has refused it. Previous chemotherapy, concomitant bisphosphonate use, and ALP baseline level were used for the stratification of patients. For the efficacy evaluation, radium-223 plus best standard of care (BSoC) were compared vs. placebo plus BSoC by checking at the prolonged median overall survival (OS). ^{223}Ra reported an advantage in survival rate of 3.6 months than placebo (hazard ratio [HR] = 0.70; 95% confidence interval [CI]: 0.58–0.83; $p < 0.001$; median 14.9 moths vs. 11.3 months, respectively). Moreover, its effectiveness was documented in all the stratified subgroups. ^{223}Ra also prolonged median time to first symptomatic skeletal event (SSE) by 5.8 mo (HR = 0.66; 95% CI: 0.52–0.83; $p < 0.001$; median 15.6 months vs. 9.8 months, respectively) [6, 7, 18]. Additionally, ^{223}Ra had a favorable safety profile with a low overall incidence of grades 3–4 myelosuppression and fewer adverse events (AE) and severe adverse events (SAE) than placebo arm [6, 18]. The drug was well tolerated regardless of prior docetaxel exposure. No differences were seen in the safety profile between patients who did and did not receive concomitant EBRT for bone pain during the study. Mostly, myelosuppression rates were low regardless of concomitant EBRT. The most important recorded toxicities were minor gastrointestinal side effects and mild neutropenia and thrombocytopenia [6, 18]. Risk for developing a severe neutropenia was related to prior docetaxel therapy, higher WHO pain score, and decreased baseline neutrophil count. The appearance of anemia was mainly related to the extent of bone disease, being higher in patients with ≥6 bone metastases at baseline bone scan or with a super scan pattern, higher level of ALP and PSA, and lower hemoglobin level at enrollment. Platelets were more frequently administered to ^{223}Ra patients, mainly after third cycle, suggesting a cumulative effect and advising clinicians to carefully evaluate the benefit and risk to continue treatment. Before ^{223}Ra initiation, the identification of potential risk factors for hematologic toxicities is very important for monitoring high-risk patients for treatment modifications [19]. However, the best treatment result is associated to completion of 6 injections administration, and

as abovementioned the tolerability is better in case of adequate level of ALP, Hb and platelets, low extension of skeletal disease and mildly pain [6, 18, 20].

A *phase IIIb trial* was conducted after ALSYMPCA. Its endpoints were safety and overall survival. 839 patients with bone metastases (at least two lesions) from CRPC and without visceral disease were enrolled. Lymph nodes were allowed up to 6 cm in diameter, and patients could be treated independently if symptomatic or asymptomatic. Also concomitant anticancer therapies were allowed. 696 patients received at least one dose of ^{223}Ra and were evaluated for safety. Anemia Grade 3–4 occurred in 5% of patients, thrombocytopenia in 2%, and neutropenia in 1%. Median overall survival was 16 months, and it was longer for patients with less than the upper limit of normal ALP than for patients with higher ALP level; for patients with baseline hemoglobin level of 10 g/dl or greater vs. patients with lower Hb; for patients with ECOG PS of 0 compared to ECOG PS 1; and for patients with no reported baseline pain vs. symptomatic patients. Median OS was also better in patients receiving concomitant denosumab and in patients with concomitant administration of ^{223}Ra and new-generation antiandrogens [20]. These observations confirm the data on efficacy and safety observed in the pivotal trial, and reinforce the magnitude of benefit in the early use of the drug. Furthermore, evidence of facticity of combination therapies was showed.

10.4.2 Clinical Issues

The current international guidelines, such as the National Comprehensive Cancer Network (NCCN) and European Society of Medical Oncology (ESMO) recommend ^{223}Ra as an option in both pre- and post-docetaxel settings, although it can be administered also as first-line therapy. In the study by Sartor et al. [21], patients who had received docetaxel prior to the ^{223}Ra treatment did not report different hematological adverse events from those who received chemotherapy. This observation strengthens the possible use of ^{223}Ra as first-line approach when tumor burden is limited, hemoglobin level is adequate, and patient is more likely to complete the planned treatment. In Fig. 10.4 is reported the current utilization of ^{223}Ra in clinical practice.

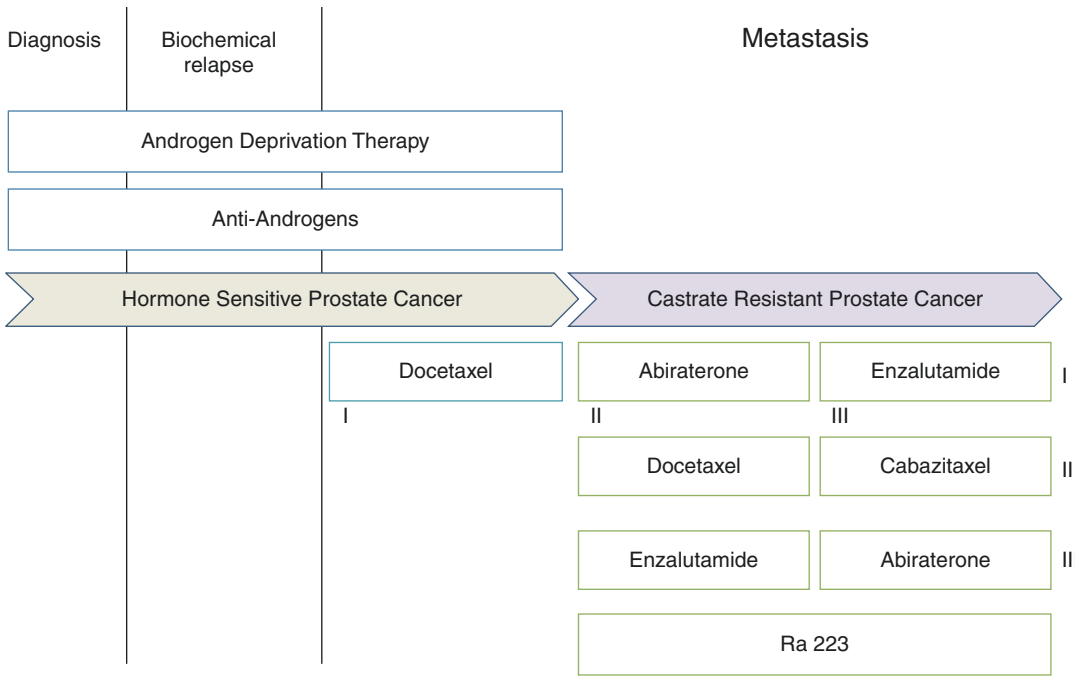

Fig. 10.4 The indication for ^{223}Ra in accordance with current International guidelines

^{223}Ra is often relegated to late-stage metastatic castration-resistant prostate cancer, consistent with the use of beta-emitting and gamma-emitting radionuclides. It is important not to leave treatment with ^{223}Ra for the late phase of disease, to avoid the development of visceral metastases that makes patients ineligible for ^{223}Ra. In Fig. 10.5 are reported two examples of patients treated with ^{223}Ra.

The real information given by 18F-Choline in patients undergoing ^{223}Ra is now unknown, but some preliminary data are encouraging for the assessment of response to therapy. The unique mechanism of action of ^{223}Ra does not potentially overlap with other available treatments and it is suitable for both sequencing and combination studies. The addition of combination therapy may improve outcomes without increasing toxicities [20].

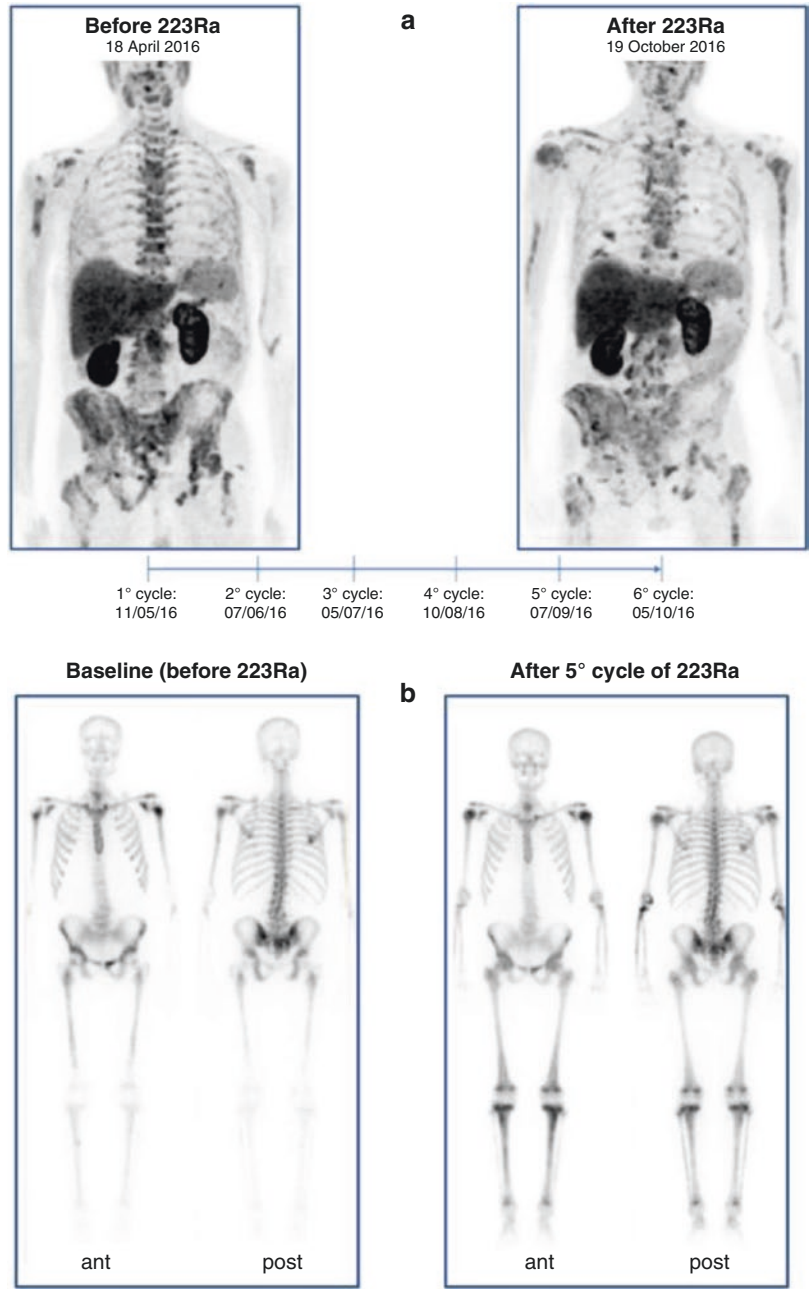

Fig. 10.5 (**a**) A 68-year-old patient with bone-dominant prostate cancer. He underwent 18F-Choline PET/CT before ^{223}Ra for the assessment of bone metastases and for excluding visceral and lymph node disease. The patient received 6 cycles of ^{223}Ra that were well tolerated. At the end of therapy, the patient was sent to a further 18F-Choline PET/CT that showed a potential response to therapy, with the appearance of metabolic activity in the upper limbs. This metabolic behavior was associated with a flare phenomenon, after the injection of ^{223}Ra. (**b**) A 76-year-old patient was treated with ^{223}Ra for 6 cycles. Before and after 5 cycles of therapy, the patient was sent to bone scans that demonstrated a persistent diffuse uptake in the bone (superscan pattern), compatible with no response to treatment

Preliminary results from an ongoing phase I/IIa trial showed that ^{223}Ra in combination with docetaxel is feasible and safe (with lower docetaxel dose at 60 mg/Mq every 3 weeks and Ra223 for 5 cycles every 5 weeks) [22]. Currently, several clinical trials are evaluating safety and efficacy of combination treatments of ^{223}Ra with abiraterone acetate (ERA 223, NCT02043678) and enzalutamide (PEACE III NCT02194842). Another randomized trial compared 50 kBq/kg for 12 cycles vs. 80 kBq/kg for 6 cycles vs. standard dose; this trial completed enrollment, data analysis is ongoing. A potential clinical benefit of ^{223}Ra in the hormone-naïve setting has to be investigated [23].

Moreover, a study exploring the benefit of a re-treatment with ^{223}Ra in patients who have already received 6 cycles of treatment documented a lower number of hematological events than in the ALSYMPCA trial: 44 pts had ^{223}Ra re-treatment, 66% completed all the 6 injections [21].

10.5 Planar Acquisition Protocols

Although the probability of gamma emissions from ^{223}Ra decay is slightly higher than 1%, several studies demonstrated the possibility of gamma camera imaging after injections.

^{223}Ra emitted photons with energies ranging from 12 to 338 keV. Photons emitted at 81 and 84 keV have the highest probability of emission, 15% and 25%, respectively. Further photon energies with high probabilities of emission and within the energy interval suitable for gamma camera imaging are 95 keV (11%), 154 keV (6%), and 270 keV (14%). Also highest energy photons are emitted: 324 and 338 keV (4.0% and 2.8%, respectively).

Hindorf et al. [10] suggested to acquire whole-body scans with medium-energy collimator (necessary to avoid penetration of high-energy photons) at a scan speed of 6 cm/min. Energy windows were set at 82 keV (20%), 154 keV (20%), and 270 keV (20%). With these protocol, the author obtained a sensitivity of 69 cps/MBq for the 82 keV energy window and 31 and 34 cps/MBq for the 154 and 270 keV windows, respectively. The spatial resolution, determined as the FWHM, was found to be 1.1 cm for all the photon energies investigated.

Also Carrasquillo et al. [2] for testing the biodistribution of ^{223}Ra used gamma cameras equipped with a high-energy general purpose collimator with uniformity flood corrections turned off. Images were acquired using five separate 20% energy windows centered on 82, 154, 269, 351, and 402 keV.

Similar experience came from Chittenden et al. [15]. In this work the gamma camera acquisition protocol included the use of medium-energy general-purpose collimator for whole-body and static views; energy window was set at 82 keV with a 20% width. Static images were acquired for approximately 30 min each, using matrix sizes of 256 × 256 pixels.

Pacilio et al. [8, 9, 17] reported patients' images with ^{223}Ra collected acquiring antero-posterior planar static images with double-peak acquisition (two energy windows centered at 82 and 154 keV, 20% wide), MEGP collimator, and an acquisition time of about 30 min. ^{223}Ra images were processed with a Wiener filter to enhance contrast-ratio and signal-to-noise-ratio.

Imaging with radium-223 is feasible. Table 10.5 summarizes the suggested acquisition parameters and Fig. 10.6 shows an example of acquired images with a standard gamma camera.

Table 10.5 Suggested ^{223}Ra gamma camera acquisition protocols

Acquisition Type	Collimator	Energy window	Acquisition time	Scan speed	Matrix size
Static planar images	MEGP	82 keV ± 20% 154 keV ± 20%	30 min	–	256 x 256
Whole-body images	MEGP	82 keV ± 20% 154 keV ± 20%	–	4–6 cm/min	256 × 1024

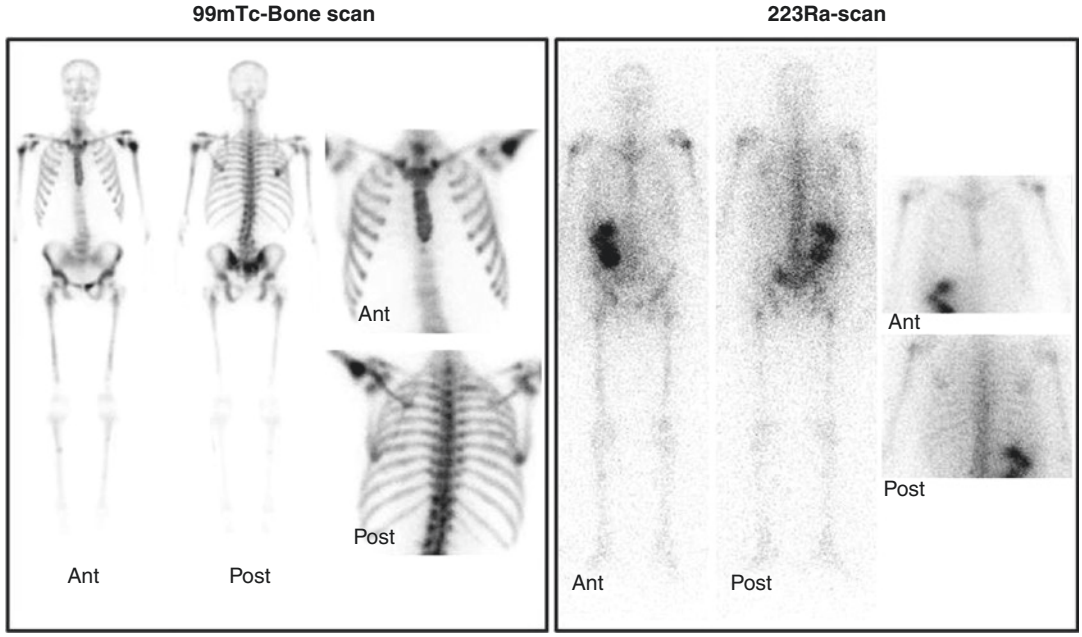

Fig. 10.6 Example of ^{223}Ra whole-body and planar images

In our experience, a static acquisition of 30 min with MEGP collimator, double 20% energy window centered at 82 and 154 keV, matrix size 256x256, zoom 1 was made, by adding a potential whole-body acquisition, scan speed 4 cm/min, matrix size 256 × 1024.

10.6 Last Evidences

In the last European Society for Medical Oncology (ESMO) congress in 2018, the final results of the ERA-223 trial have been presented. The ERA-223 trial (NCT02043678) is a randomized phase III trial in which abiraterone, at the standard dose of 1000 mg daily plus 5 mg of prednisone twice daily, was administered in combination with radium-223 or placebo in asymptomatic or mildly symptomatic men with chemotherapy-naïve CRCP and bone metastases (>2 bone metastatic lesions). The main findings of the trial demonstrated that the addition of ^{223}Ra to abiraterone plus prednisolone was associated with a higher incidence of bone fractures (28.6 vs. 11.4%) and a possible reduction in OS (30.7 vs. 33.3 months; HR 1.195, 95% confidence interval 0.950–1.505; $p = 0.13$). For these results, the Pharmacovigilance Risk Assessment Committee (PRAC) and the European Medicines Agency (EMA) has restricted the use of ^{223}Ra to patients who have had two previous treatments for mCRPC (www.ema.europa.eu/medicines/human/referrals/xofigo). However, a recent opinion by Dalla Volta et al. [24] underlines that the combination of ^{223}Ra, abiraterone, and prednisolone has a synergistic inhibition of osteoblast activity with potentially significant worsening of uncoupled bone remodeling, thus leading to an increase in bone fragility.

However, the interim analysis of the REASSURE study, an observational, global, prospective trial has demonstrated the short-term safety of ^{223}Ra in mCRPC patients, particularly in patients who did not receive a prior chemotherapy [25].

10.7 Future Trends

Given the mechanism of bone targeting of ^{223}Ra, it is likely that it will have activity against other cancers. There is some interest in extending the

treatment indications for ^{223}Ra with a Phase I/II study in patients with osteosarcoma (NCT01833520) and a Phase 2 studies in bone predominant metastatic breast cancer (NCT01070485) and metastatic radioiodine-refractory thyroid cancer (NCT02390934).

Moreover, a growing interest is now available from the literature, about the response to therapy by using some nuclear medicine modalities (i.e., 18F-Choline PET/CT or 68Ga-PSMA PET/CT or 18F-Fluoride PET/CT or Bone scan). Furthermore, molecular biomarkers from bone, other than ALP, are now considered useful for the assessment of response to ^{223}Ra. The data are still preliminary, but the field of research is fervent [26, 27].

By acknowledging the biological characteristics of ^{223}Ra and its efficacy in bone metastases, all cancers that are correlated with skeletal involvement would be potentially treated with ^{223}Ra. Thus, in this way, an additional therapeutic strategy would be included in the armamentarium of war against cancer.

References

1. Siegel RL, Miller KD, Jemal A. Cancer statistics, 2016. CA Cancer J Clin. 2016;66:7–30.
2. Carrasquillo JA, O'Donoghue JA, Pandit-Taskar N. Phase I pharmacokinetic and biodistribution study with escalating doses of ^{223}Ra-dichloride in men with castration-resistant-metastatic prostate cancer. Eur J Nucl Med Mol Imaging. 2003;40:1384–93.
3. Nilsson S, Franzén L, Parker C, et al. Bone-targeted radium-223 in symptomatic, hormone-refractory prostate cancer: a randomised, multicentre, placebo-controlled phase II study. Lancet Oncol. 2007;8:587–94.
4. Nilsson SL, Larsen RH, Foss SD, et al. First clinical experience with a-emitting radium-223 in the treatment of skeletal metastases. Clin Cancer Res. 2005;11:4451–9.
5. Nilsson S, Strang P, Aksnes A, et al. A randomized, dose-response, multicentre phase II study of radium-223 chloride for the palliation of painful bone metastases in patients with castration-resistant prostate cancer. Eur J Cancer. 2012;48:678–86.
6. Parker C, Pascoe S, Chodacki A, et al. A randomized. Double-blind, dose-finding, multicenter phase 2 trial or radium chloride (Ra 223) in patients with bone metastases and castration-resistant prostate cancer. Eur Urol. 2013;63(2):189–97.
7. Sartor O, Coleman R, Nilsson S, et al. Effect of radium-223 dichloride on symptomatic skeletal events in patients with castration-resistant prostate cancer and bone metastases: results from a phase 3, double-blind, randomised trial. Lancet Oncol. 2014;15:738–46.
8. Pacilio M, Ventroni G, Cassano B, et al. A case report of image-based dosimetry of bone metastases with Alpharadin (^{223}Ra-dichloride) therapy: inter-fraction variability of absorbed dose and follow-up. Ann Nucl Med. 2016;30:163–8.
9. Pacilio M, Ventroni G, De Vincentis G, et al. Dosimetry of bone metastases in targeted radionuclide therapy with alpha-emitting ^{223}Ra-dichloride. Eur J Nucl Med Mol Imaging. 2016;43(1):21–33.
10. Hindorf C, Chittenden S, Aksnes A-K, et al. Quantitative imaging of ^{223}Ra-chloride (Alpharadin) for targeted alpha-emitting radionuclide therapy of bone metastases. Nucl Med Commun. 2012;33:726–32.
11. AIFM-AIMN. Linee guida AIFM-AIMN per l'utilizzo terapeutico del 223-Ra. 2014.
12. Stabin S a. Health Phys. 2012;102:271–91.
13. Nilsson S, Balteskard L, Foss SD, et al. Phase I study of Alpharadin2 (^{223}Ra), and a-emitting bone-seeking agent in cancer patients with skeletalmetastases. Eur J Nucl Med Mol Imaging. 2004;31:S290/no 370 [abstract].
14. Carrasquillo JA, J. A. O'Donoghue, Pandit-Taskar N, et al. Phase I pharmacokinetic (PK) and biodistribution study of radium-223 chloride in patients with castration resistant prostate cancer (CRPC) metastatic to bone. 46th annu Meet am Soc Clin oncol (aSCo) (June 4–8, Chicago) 2010, abstratc 4680. 2010.
15. Chittenden S, Hindorf C, Parker C, et al. A phase 1, open-label study of the biodistribution, pharmacokinetics, and dosimetry of ^{223}Ra-dichloride in patients with hormone-refractory prostate cancer and skeletal metastases. J Nucl Med. 2015;56:1304–9.
16. Lassmann M, Nosske D. Dosimetry of ^{223}Ra-chloride: dose to normal organs and tissues. Eur J Nucl Med Mol Imaging. 2013;40:207–12.
17. Pacilio M, Cassano B, et al. Gamma camera calibrations for the Italian multicentre study for lesion dosimetry in ^{223}Ra therapy of bone metastases. Phys Med. 2017 Sep;41:117–23. https://doi.org/10.1016/j.ejmp.2017.04.019.
18. Parker C, Nilsson S, Heinrich D, et al. Alpha emitter radium-223 and survival in metastatic prostate cancer. N Engl J Med. 2013;369:213–23.
19. Vogelzang NJ, Coleman RE, Michalski JM, et al. Hematologic safety of radium-223 dichloride: baseline prognostic factors associated with myelosuppression in the ALSYMPCA trial. Clin Genitourin Cancer. 2017;15(1):42–52.e8.
20. Saad F, Carles J, Gillessen S, et al. Radium-223 and concomitant therapies in patients with metastatic castration-resistant prostate cancer: an international, early access, open-label, single-arm phase 3b trial. Lancet Oncol. 2016;17:1306–16.

21. Sartor AO, Heinrich D., Mariados N, et al. Radium-223 (Ra-223) re-treatment (Re-tx): first experience from an international, multicenter, prospective study in patients (Pts) with castration-resistant prostate cancer and bone metastases (mCRPC). Genitourinary Cancers Symposium 2016. 2016.
22. Morris MJ, HJ Hammers, Sweeney C, et al. Safety of radium-223 dichloride (Ra-223) with docetaxel (D) in patients with bone metastases from castration-resistant prostate cancer (CRPC): a phase I prostate Cancer clinical trials consortium study. ASCO Annual Meeting 2013. 2013.
23. Wilson JM, Parker C. The safety and efficacy of radium-223 dichloride for the treatment of advanced prostate cancer. Expert Rev Anticancer Ther. 2016;16:911–8.
24. Dalla Volta A, Formenti A, Berruti A. Higher risk of fragility fractures in prostate cancer patients treated with combined radium-223 and abiraterone: prednisone may be the culprit. Eur Urol. 2019;75(6):894–5. https://doi.org/10.1016/j.eururo.2019.01.026.
25. Dizdarevic S, Petersen PM, Essler M, Versari A, Bourre J-C, la Fougere C, et al. Interim analysis of the REASSURE (Radium-223 alpha emitter agent in non-intervetional safety study in mCRPC population for long-term evaluation) study: patient characteristics and safety according to prior use of chemotherapy in routine clinical practice. Eur J Nucl Med Mol Imaging. 2019;46:1102. https://doi.org/10.1007/s00259-019-4261-y.
26. Evangelista L, Zorz A. Re: response assessment of ^{223}Ra treatment: should a fluorocholine PET/CT be performed? Clin Nucl Med. 2018;43(11):867–8.
27. García Vicente AM, Soriano Castrejón Á, Alvarez Cabellos R, Sanchez Gil B, Mohedano Mohedano N. Response assessment of ^{223}Ra treatment: should a fluorocholine PET/CT be performed? Clin Nucl Med. 2017;42(10):761–5.

^{11}C-Methionine

11

Sebastiano Cosentino, Fabrizio Scopelliti, Gabriella Murè, Sara Baldari, and Massimo Ippolito

Contents

Abbreviations

^{11}C-CH3I	Methyl iodide
^{11}C-CH3OTf	^{11}C-Methyl triflate
^{11}C-CO2	Carbon dioxide
BBB	Blood brain barrier
BTV	Biological target volume
CT	Computed tomography
FCD	Focal cortical dysplasia
FLAIR	Fluid-attenuated inversion recovery
GTV	Gross tumor volume
HI	Hydriodic acid
HNSCC	Squamous cell head and neck cancer
HPLC	High-performance liquid chromatography
L/N	Lesion-to-normal
LAT	L-type amino acid transporter
MET	Methionine

S. Cosentino · F. Scopelliti · G. Murè · S. Baldari
M. Ippolito (✉)
Division of Nuclear Medicine, Cannizzaro Hospital, Catania, Italy

F. Calabria, O. Schillaci (eds.), *Radiopharmaceuticals*,
https://doi.org/10.1007/978-3-030-27779-6_11

MIBI	99mTc-methoxy-isobutyl-isonitrile
MM	Multiple myeloma
MR	Magnetic resonance
NSCLC	Non-small cell lung cancer
PA	Parathyroid adenoma
PH	Parathyroid hyperplasia
pHPT	Primary hyperparathyroidism
PTH	Parathyroid hormone
RANO	Response assessment in neuro-oncology
SUV	Standardized uptake value
TLC	Thin layer chromatography

11.1 Synthesis

Methionine (MET) is an essential α-amino acid which plays a role in several biochemical processes, such as biosynthesis of proteins. It is made up of an α-amino group (protonated under biological conditions), an α-carboxylic acid group (in the deprotonated form), and a methyl thioether side chain. It exists in two enantiomeric forms: the L-isomer (of which proteins are made) and D-isomer.

L-Methionine labeled with ^{11}C acts as a positron emission tomography tracer, as it is involved in synthesis of proteins in brain tumors.

^{11}C-L-Methionine must be synthetized in a PET Center provided with a cyclotron (particle accelerator) because of the short half-life of the isotope ^{11}C (20 min). In fact either the isotope or the tracer can be used in a very short period of time, so that it is not advisable to distribute them in a department far from production facility [1].

^{11}C is usually produced as carbon dioxide (^{11}C-CO2) as a first step of the tracer synthesis. After trapping this gas into an appropriate device (liquid nitrogen, molecular sieves), it undergoes reduction reactions with lithium aluminum hydride to produce an intermediate ^{11}C-methanol, which finally reacts with hydriodic acid (HI) to produce the radioactive alkylating agent methyl iodide (^{11}C-CH3I).

Less frequently ^{11}C-CH3I is obtained via radical reactions starting from radioactive methane (^{11}C-CH4) which can be produced directly in the cyclotron target or by subsequent radical reactions starting from ^{11}C-CO2 and iodine (I2) inside a loop. The final result of all these steps is however the same compound ^{11}C-CH3I, able to bind an appropriate precursor to produce the desider tracer.

Sometimes ^{11}C-methyl triflate (^{11}C-CH3OTf) instead of ^{11}C-CH3I is used, as it is a more reactive species, produced starting by ^{11}C-CH3I itself.

Cold precursor of methionine (homocysteine thiolactone) is quite sensitive to moisture and temperature, and it is often stored as its more stable salt (homocysteine thiolactone hydrochloride). This precursor must be "prepared" to react with the alkylating agent, so that it is necessary to increase its reactivity towards it. Preparation of the precursor with sodium hydroxide (NaOH) in an appropriate solvent (e.g., acetone) in order to open the lactone ring allows ^{11}C-CH3I to react with it.

Normally ^{11}C-methionine synthesis takes place in liquid solution. Therefore it is necessary to separate the product from other components of the reaction (such as precursor, by-products), i.e., to purify the drug. A semi-preparative HPLC provides a sufficiently pure ^{11}C-L-methionine in reasonable time. To avoid the last step (purification by HPLC) in the last years a solid-phase synthesis has been developed in which ^{11}C-CH3I is sent to a cartridge where precursor was previously loaded. Flushing the cartridge with appropriate buffer solution provides ^{11}C-L-methionine, ready to be injected into patients [2].

Normally a whole synthesis requires around 20–25 min after collecting activity from the cyclotron, time during which radioactivity decays. Before injection, additional time is required to perform quality control tests on the final product. They normally require a HPLC analysis, to verify that at least 95% of ^{11}C is bound to methionine (normally higher values can be easily achieved), and that unreacted precursors and reaction by-products are sufficiently low (limits are indicated into Pharmacopoeia), a Gas Chromatographic analysis, to quantify the amount of residual solvents inside the final formulation, and "simple" tests like pH measurement (between 4.5 and 8.5) appearance (no

particulate matter in the injectable solution). The ratio between L- and D-methionine can be checked after release of the batch, with another chromatographic system (TLC or HPLC).

11.2 Pharmacokinetics

Mechanisms of uptake in brain tumors are not well defined yet. It seems that passive diffusion through damaged BBB (Blood Brain Barrier) and active tumor uptake due to an increased expression of a membrane carrier (as a consequence of active proliferation) can be involved.

Normal brain tissue recognizes only glucose as a metabolic substrate (thus having a very low physiological ^{11}C-methionine uptake), whereas tumoral brain tissues present an increased ^{11}C-methionine uptake. This makes the signal-to-noise ratio quite high, thus helping in reading and interpreting of the PET scans.

^{11}C-Methionine absorption in cells mainly reflects sodium independent trans-membrane transport. This transport is ruled by a concentration gradient and is therefore influenced by intracellular metabolism of amino acids, which, in turn, reflects proliferative activity. Several studies showed how ^{11}C-methionine is rapidly uptaken by different kind of tumors. After injection brain absorption is generally low, according to anatomical district and age. In combination with the high tumoral uptake this provides a good reason to use 11C-methionine to study cerebral tumor imaging, thanks to its high detection rate and good delineation of the lesion. There are several subtypes of amino acid transporters, such as LAT1, 2, and 3. One of these subtypes (LAT2) is expressed in tumoral cells but not in inflammatory cells.

11.3 Physiological Distribution

^{11}C-Methionine transport across plasma membranes occurs via the large amino acid transporter (LAT1), which is overexpressed in malignant cells leading to tracer accumulation within tumors.

Increased uptake of ^{11}C-methionine reflects the increased carrier-mediated transport, vascular permeability, and protein synthesis in malignant tissue (tumor cells require an external supply of methionine).

There is normally low uptake in the brain (gray matter) and in benign conditions as fibrosis, necrosis, or edema because normal brain tissue recognizes only glucose as metabolic substrate (Figs. 11.1 and 11.2).

There are variations in normal ^{11}C-methionine accumulation for each part of the brain and between different ages [3].

The highest accumulation of ^{11}C-methionine was found in pancreas and liver, both of which were readily recognizable as areas of prominent activity on emission images because the exocrine pancreas produces enzymes, such as trypsin and chymotrypsin, for the breakdown of ingested proteins, fats, and carbohydrates, and similarly liver requires amino acids for the synthesis of

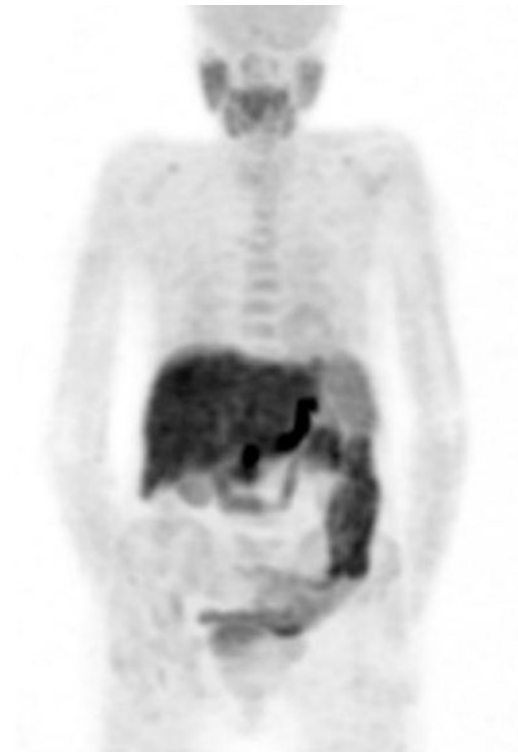

Fig. 11.1 Whole-body anterior maximal intensity projection image of 60-year-old man

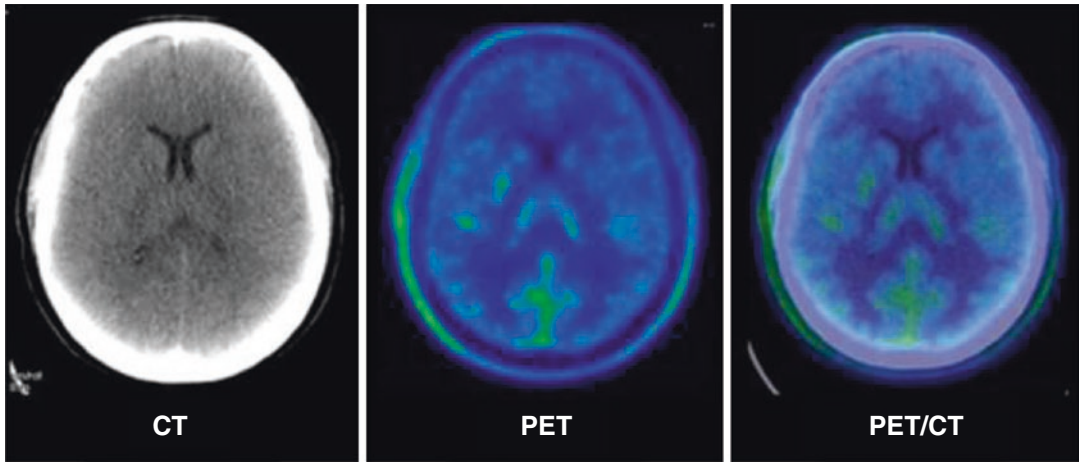

Fig. 11.2 Physiological brain biodistribution

plasma proteins, such as albumin, fibrinogen, and transferrin.

Bone marrow in the axial skeleton is consistently prominent because of the demand for protein synthesis in the replicating cells.

Activity is evident in Waldeyer's ring lymphoid tissue, submandibular glands, bone marrow, and kidneys. Intestinal uptake is quite variable in intensity, extent, and location.

The left ventricle has greater uptake in men than in women. In addition, uptake in the left ventricle increases over the time. This increase could be due to a greater average body mass in men than in women and an increase in body mass over the time.

11.4 Exam technique

^{11}C-Methionine PET is easy and fast to perform. Usually 370–740 MBq of tracer is injected intravenously and, because of the short half-life of ^{11}C-labeled molecules (20 min), the uptake time ranges from only 10–30 min [4].

A segmental static image acquisition is performed on brain for 10–20 min, on body for 20–25 min.

No fasting is usually required and no collateral effects have been described.

You should refer to a recent magnetic resonance (MR) during the evaluation of brain ^{11}C-methionine.

11.5 Indications

^{11}C-Methionine PET is a useful diagnostic and therapeutic tool in neuro-oncology. It has a high sensitivity in identifying brain tumors.

- Primary brain tumors (histologic grading, define the extent of tumor, identify optimal biopsy sites
- Metastases
- Recurrence
- Plan radiotherapy
- Response to therapy

11.5.1 Primary Brain Tumors

Malignant brain tumors are a heterogeneous group of diseases, the most common types of which are metastatic tumors and malignant gliomas (astrocytomas, oligodendrogliomas, and oligoastrocytomas).

These tumors are classified in low grade, or grades I and II, and high grade, or grades III and IV according to the degree of nuclear atypia, mitosis, microvascular proliferation, and necrosis, where anaplasia increases with increasing tumor grade [5, 6].

There are 3 subtypes of low-grade gliomas: pilocytic astrocytoma (grade I), astrocytoma (grade II), and oligodendroglioma (grade II).

High-grade gliomas are the anaplastic tumors (astrocytoma and oligodendroglioma, grade III) and glioblastoma (grade IV).

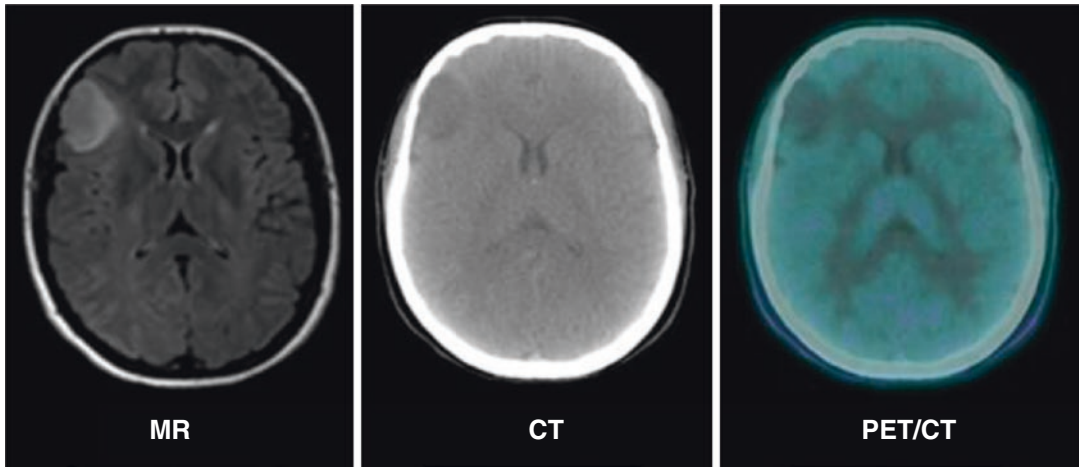

Fig. 11.3 Low-grade glioma. PET/CT highlights an area of reduced uptake of 11C-methionine in right frontal lesion, with tumor-to-normal ratio of 0.8

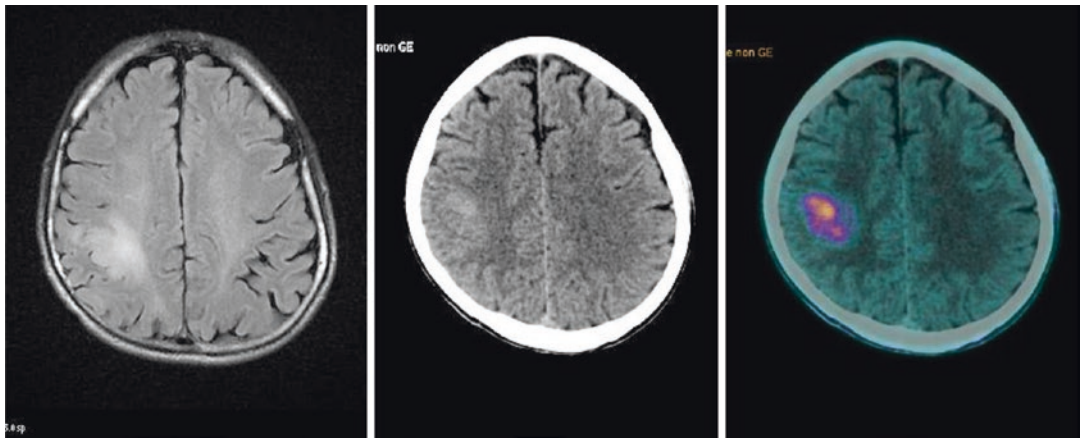

Fig. 11.4 High-grade glioma. MR shows a non-contrast-enhanced lesion indicating low-grade glioma in right parietal lobe where PET demonstrates an area of focal increased uptake, with tumor-to-normal ratio of 5.2. Final diagnosis was high-grade glioma

Glioblastoma is the most malignant and most common glioma, accounting for 45–50% of all gliomas.

Histopathologic examination is still considered the "gold standard" for determination of tumor grading but many brain tumors, especially gliomas, are heterogeneous and contain microscopic areas of necrosis, so there is a probability of underestimating true tumor grading; never the less it is considered as one of the most robust predictors of survival throughout the literature [7].

The visual assessment of [11]C-methionine PET images is simple: each uptake higher than background area (normal gray matter) is considered potentially pathological [8].

Gliomas with high proliferation activity, which correspond to grade III and IV of the WHO classification, are characterized by a higher [11]C-methionine uptake.

Low [11]C-methionine uptake in patients with low-grade glioma is associated with longer survival compared with patients exhibiting higher [11]C-methionine uptake (Fig. 11.3); on the other hand, patients with high uptake tumors seem to receive a benefit from surgery (Figs. 11.4 and 11.5) [9, 10].

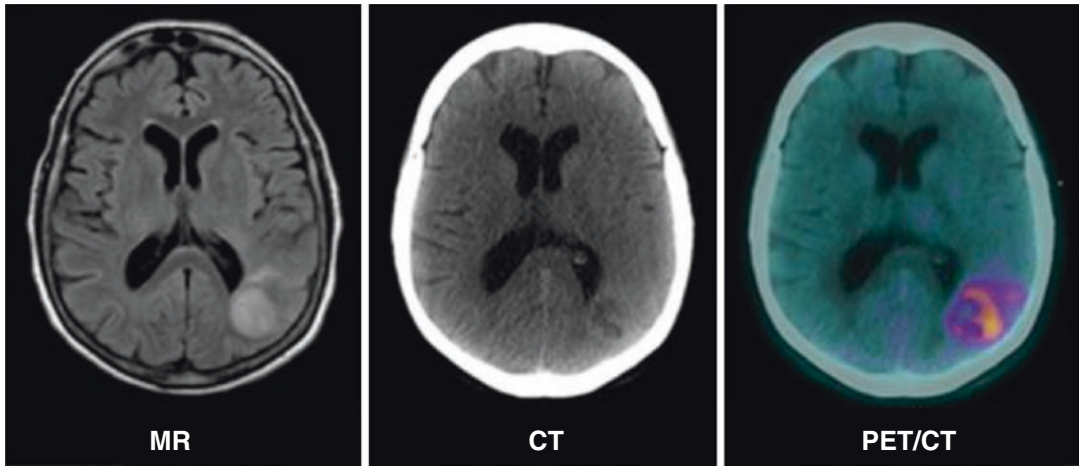

Fig. 11.5 High-grade glioma. MR shows contrast-enhanced lesion in left parietal lobe where PET demonstrates an area of focal increased uptake, with tumor-to-normal ratio of 3.1

The most widely used calculation method is the tumor-to-background ratio (T/N), comparing the tumor uptake to the contralateral frontal lobe or the corresponding contralateral hemisphere.

A cutoff value of target to NT value of 1.47 is a useful parameter to distinguish benign from a malignant lesion on an ^{11}C-methionine scan.

The assessment of biopsy sites using ^{11}C-methionine PET is compared with that using MR because brain tumors are histologically heterogeneous with different cancer grades and necrosis. Biopsy planning depending only on MR can lead to inaccurate diagnosis. Various studies suggest an advantage of ^{11}C-methionine PET for identifying the best target for biopsy or for estimation of the tumor volume.

11.5.2 Metastases

In adults, brain metastases are the most common cause of intracranial mass lesions, accounting for more than 50% of brain tumors. Brain metastases occur in 10–30% of patients with systemic cancer.

In adulthood, the most common sources of brain metastases are lung, breast, skin (malignant melanoma), the gastrointestinal tract, and genitourinary tract; most commonly in young people they originate from sarcomas and germ cell tumors. In selected cases that have been described in autopsy they arise from non-small cell lung cancer (NSCLC, up to 54%) and from melanoma (Fig. 11.6).

The majority of patients with brain metastasis are diagnosed with an adenocarcinoma; the highest numbers of brain metastases arise from the lung; furthermore it has been documented that melanoma has the highest propensity of all malignant tumors to metastasize to the brain.

The distribution of brain metastases correlates with blood flow and tissue volume, with 80% detected in the cerebral hemispheres, 15% in the cerebellum, and 5% in the brainstem.

^{11}C-Methionine PET has the potential for the precise delineation of target volumes in radiotherapy planning for brain metastases.

^{11}C-Methionine PET can distinguish between metastatic and recurrent disease from gliomas and radiation necrosis [11, 12].

11.5.3 Radiation Treatment Planning

Noninvasive imaging techniques are a central component of a radiation treatment planning. Information gained by different imaging modalities are usually given by magnetic resonance imaging and computed tomography (CT) that show only morphological information (GTV).

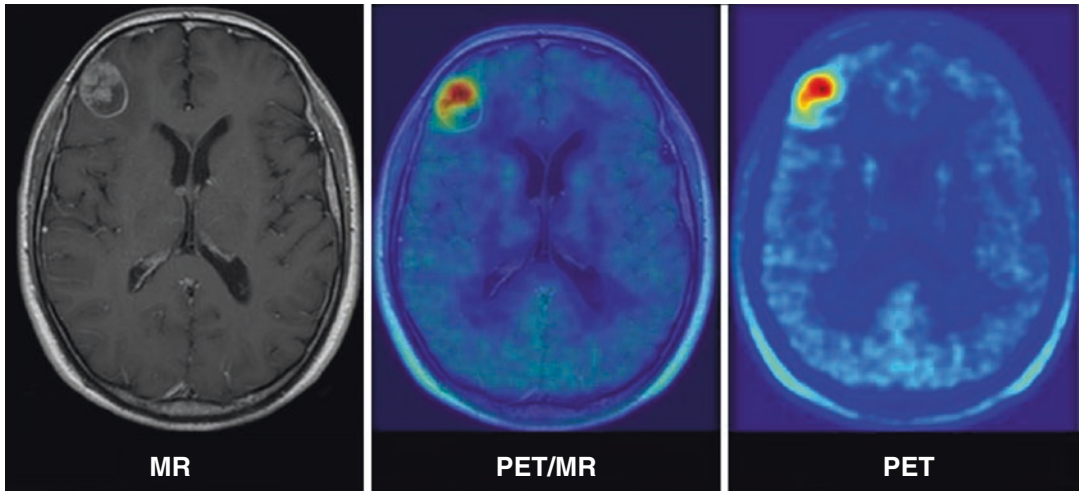

Fig. 11.6 Lung cancer metastasis; MR shows contrast-enhanced lesion in right parietal lobe where PET demonstrates an area of focal increased uptake, with tumor-to-normal ratio of 3.1

A precise delineation of the volumes of interest of each patient is one of the most critical aspects in the preparation of the radiation treatment plan. A significant contribution to this new approach is given by diagnostic imaging systems and to the analysis of images (in particular PET/CT) dedicated to the target definition of radiotherapy and organs at risk.

The use of PET/CT systems in fact is important today in the field of oncologic applications for a more accurate definition of the treatment volume in radiotherapy, which now are also based on the metabolic-functional information provided by PET.

In the field of radiotherapy the development of PET has enabled the introduction of the idea of biological target volume (BTV) that is the part of the biologically active GTV.

The use of ^{11}C-methionine PET for radiation treatment planning is becoming increasingly important in defining the volumes of brain lesions, thanks to the excellent sensitivity that ^{11}C-methionine PET expresses for tumor tissue [13].

In the definition of BTV a key role is played by the contouring method of the lesion that is chosen.

To evaluate the lesion/background ratio we may rely on manual methods or objective and reproducible methods for the segmentation of the PET images, such as semiquantitative or quantitative ones.

Manual methods, though quite simple to perform, have limitations due to the dependence on the operator, the choice of the scale of color, and the consume of time; for this reason, the semiquantitative methods appear the best in use today for the definition of the volume to be treated they can be automatic or semiautomatic. The latter methods are made taking into account SUV values and background activity and are: SUV with method 2.5, fixed threshold method, adaptive threshold method, and the iterative methods.

Treatment planning involves close cooperation between a team made up of nuclear physicians, neurosurgeon physicians, and radiotherapists.

To define a spatial coordinate system, during the acquisition of diagnostic images, PET and MRI, it is necessary to introduce a suitable designed system that landmarks the volume to be treated, to offer a good localization of the regions to be treated. Once the injury to be treated is determined it is possible to proceed with entering coordinates, weight factors and collimation of the fires to be used in the treatment.

A calculation software allows real-time display of the isodose created by various shot set and various shot are designed in such a way that 50% of the isodose perfectly contours the lesion.

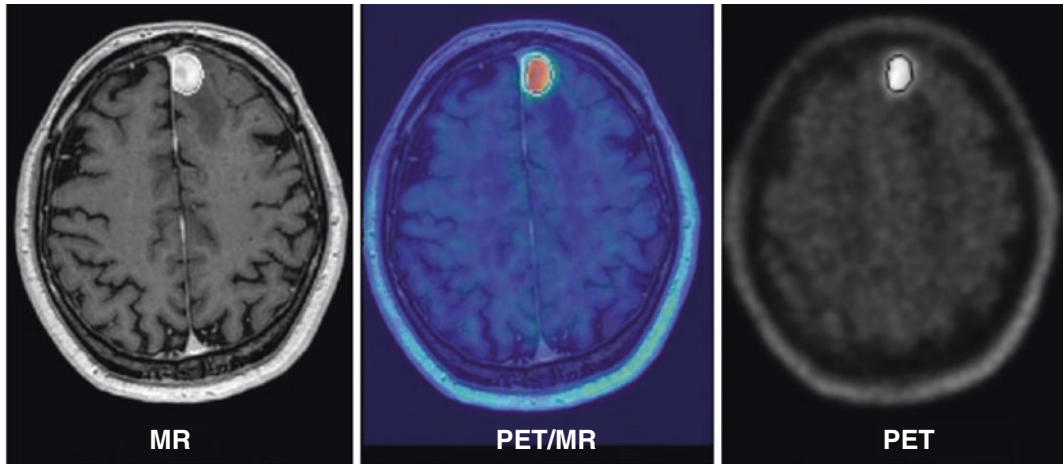

Fig. 11.7 Patient with brain metastasis (melanoma). MR Axial contrast-enhanced image shows clearly enhanced lesion in right frontal lobe; PET demonstrates high uptake corresponding to lesion, with tumor-to-normal ratio of 4.0

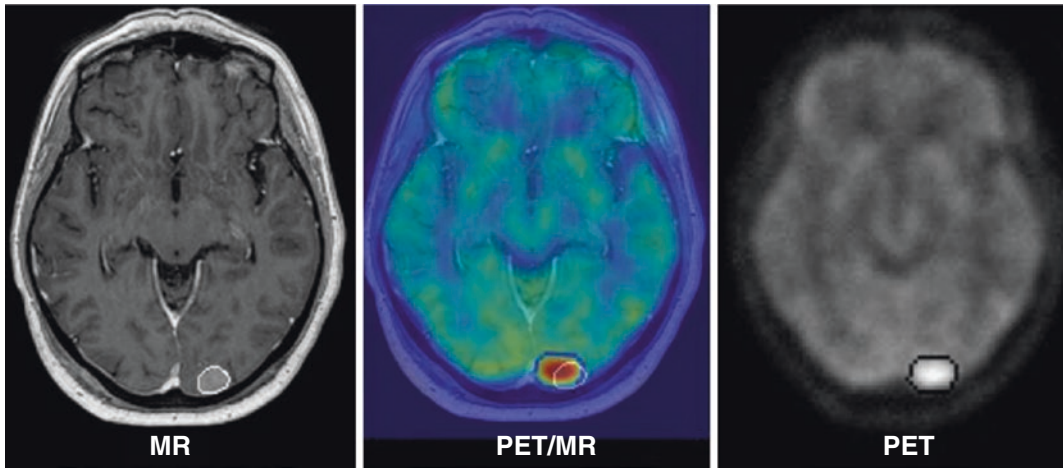

Fig. 11.8 Patient with brain metastasis (lung carcinoma). MR at recurrence time, PET and MR fusion before radiotherapy and PET. PET uptake (blue line) at right occipital area is outside the gross tumor volume (GTV). BTV is bigger than GTV

GTV determined using the diagnostic technique of RM does not always correspond to the biological target volume (BTV) identified using the ^{11}C-methionine PET imaging (Fig. 11.7).

For this reason, the metabolic imaging proved particular value for a more accurate Gamma Knife treatment planning, leading to a redefinition of the diagnostic boundaries of the target volume to be irradiated.

The tumor area showed significant differences between PET and MRI, suggesting that the exact borders of brain localization of disease may not be defined only by MRI; this indicates that treatment planning based on MRI or PET alone could carry a substantial risk of undertreatment of the tumor borders (Figs. 11.8 and 11.9) [14].

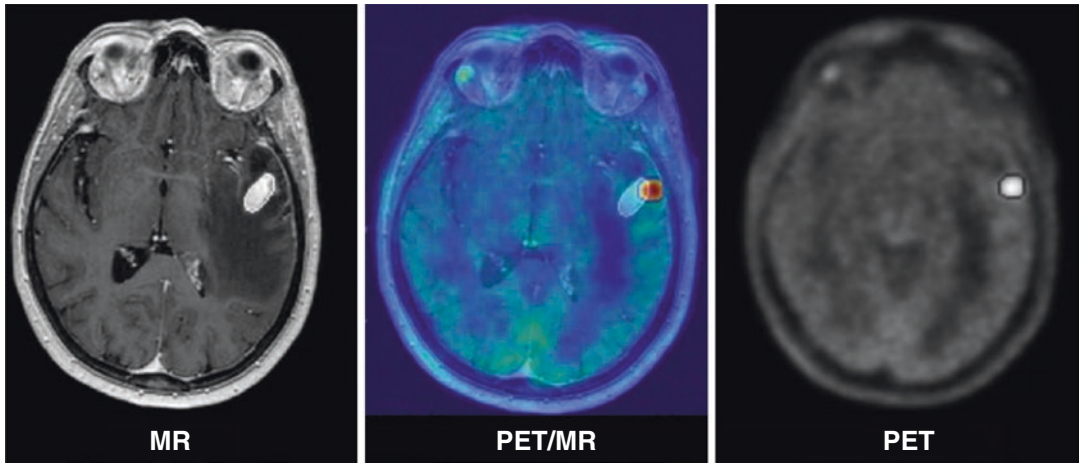

Fig. 11.9 Patient with brain metastasis (lung carcinoma). MR at recurrence time, PET and MR fusion before radiotherapy and PET. PET uptake (blue line) at right temporal area is different to the gross tumor volume (GTV). BTV is different to GTV

11.5.4 Response to Therapy

The evaluation of response to chemotherapy treatment takes into account the radiological image, the patient's condition, and the dosage of steroids according to Macdonald criteria; however some chemotherapy agent as bevacizumab can quickly decrease contrast enhancement after initiation of therapy, producing a falsely high response rate. So Response Assessment in Neuro-oncology (RANO) group proposed new recommendations for evaluating response like fluid-attenuated inversion recovery (FLAIR) or T2 hyperintensity as a surrogate for non-enhancing tumor to help to determine progression.

Nevertheless tumor-related edema or ischemia, radiation effect, demyelination, and infection can all result in increased FLAIR or T2 signal.

Consequently, amino acid PET as an alternative imaging method has been evaluated for the assessment of treatment response to antiangiogenic therapy.

Recent studies and case reports suggest that changes in amino acid PET parameters, such as the metabolically active tumor volume, are useful for determining treatment failure of antiangiogenic treatment with bevacizumab earlier than MR-based RANO criteria (Fig. 11.10).

[11]C-Methionine PET may improve the management of brain tumors by identifying areas of increased metabolic activity beyond the area of contrast enhancement on MRI, which may correspond to the areas at highest risk of recurrence.

Moreover, [11]C-methionine PET may afford additional information need in order to better define the biology of tumors and their response to treatment.

Furthermore uptake of [11]C-methionine correlates with Ki-67 and nuclear antigen expression of proliferating cell and with microvessel count in proliferating cells, suggesting that MET uptake may represent a biological marker for tumor proliferation and neoangiogenesis.

Usually patients with decreased tumor metabolic activity during TMZ chemotherapy below the characteristic threshold of 1.5 had a favorable clinical course.

Numerous studies showed a stability or reduction of amino acid uptake ([11]C-methionine) in the majority of patients with malignant brain tumors treated with chemotherapy, whereas an increase in MET uptake at that early time indicates failure to respond to chemotherapy.

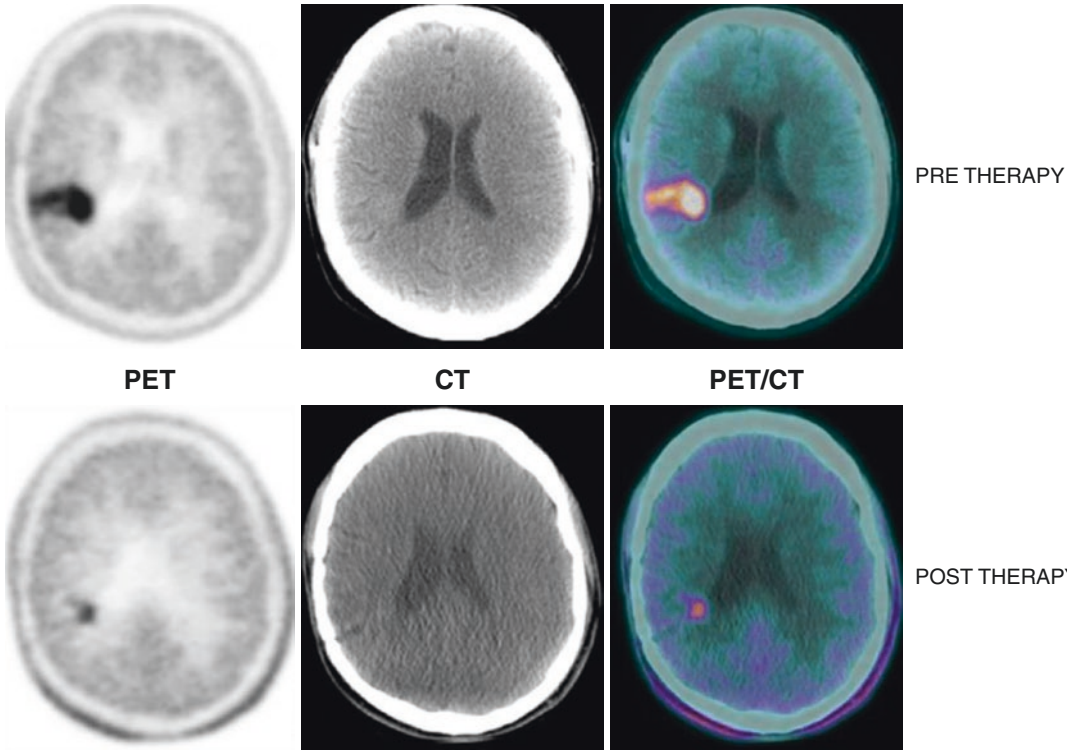

Fig. 11.10 Partial response to radio-chemotherapy; PET demonstrates an area of persistent increased uptake showing an incomplete response to therapy

11.5.5 Brain Tumor Recurrence versus Post-radiotherapy Necrosis

In addition to neurosurgical resection, radiotherapy options, such as brachytherapy, radiosurgery, and whole-brain radiation therapy, are frequently used to treat patients with brain lesions.

Postradiation treatment effects can be divided into acute effects (i.e., immediately after or even during radiotherapy), subacute (early-delayed) effects (i.e., pseudoprogression), or late effects (such as radiation necrosis).

Radiation necrosis occurs in approximately 5–25% of patients receiving standard radiotherapy, high-dose radiation therapies and repeated radiotherapies prolong patient survival, but they also increase the incidence of radiation-induced necrosis.

Depending on the irradiated volume receiving a critical radiation dose, the risk of radiation necrosis may increase up to 47%.

Uptake of ^{11}C-methionine PET in patients with recurrence due to tumor cells is different from the one found in radiation-induced injuries, where only passive diffusion across the broken blood–brain barrier occurs; the main quantitative value for differentiating between tumors, non-tumoral lesions, and tumor recurrence after radiation in ^{11}C-methionine PET studies is the lesion-to-normal (L/N) background ratio [7].

The optimal cutoff value between tumors and non-tumoral lesions was 1.47, providing a sensitivity of 76% and a specificity of 87% but the L/N cutoff ratios used to differentiate recurrence from post-radiotherapy necrosis, as well as the type of standardized uptake value (SUV) used in calculating the ratio (mean or maximum), varies according to the nature of the primary lesion (Fig. 11.11) [15, 16].

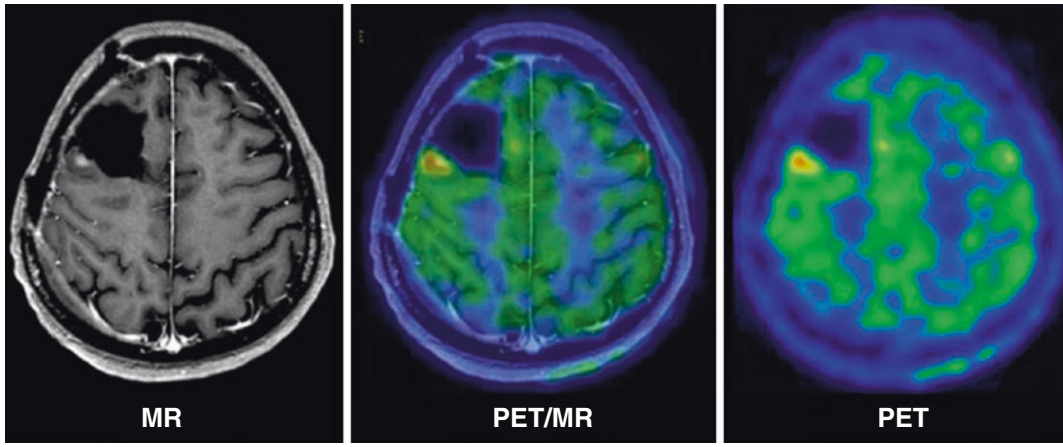

Fig. 11.11 Astrocytoma grade III operated and treated with radio- and chemotherapy. MR axial contrast-enhanced image shows a small enhanced lesion in left parietal lobe in the rear portion of the surgical cavity. PET demonstrates reduced uptake of the surgical cavity with an area of focal increased uptake corresponding to MR lesion, with tumor-to-normal ratio of 2

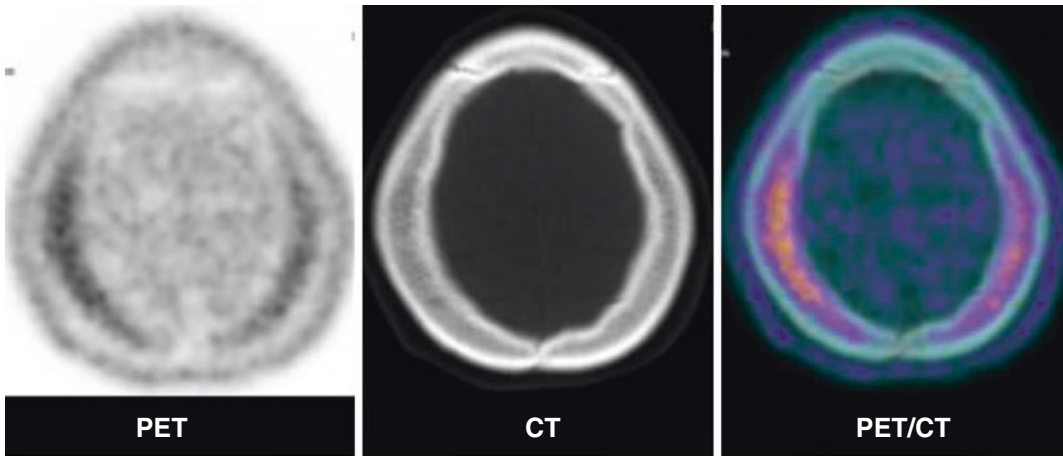

Fig. 11.12 Patient suffering from thalassemia minor. Image showing high uptake of tracer in skullcap due to hyperostosis

[18]F-FET PET scans seem to help to differentiate recurrent brain metastasis tumor from radiation-induced changes, and it is characterized by a high diagnostic accuracy with a sensitivity and specificity of about 90%.

11.6 Variants and Pitfalls

Normal variants, such as hyperostosis or fibrous dysplasia, show relatively high [11]C-methionine uptake, while pineal cysts, choroid plexuses cysts, parahippocampal cysts, and Rathke's cleft cysts show no or low [11]C-methionine uptake (Fig. 11.12) [17].

Vascular lesions may cause false-positive results, because of an increased [11]C-methionine uptake in perivascular mononuclear infiltrate and gliotic reaction in the collagen capsule surrounding hematomas (Fig. 11.13).

[11]C-Methionine uptake in inflammation involves increased metabolism and active amino acid transport as a result of the increased density of inflammatory cells; encephalitis

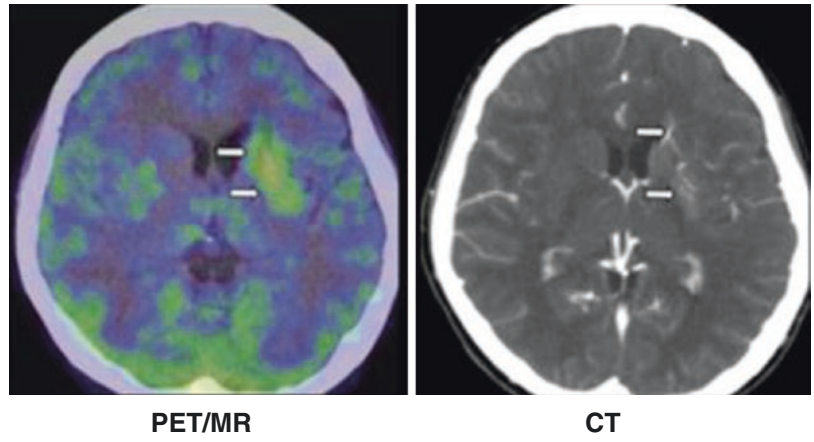

Fig. 11.13 Venous malformation with plugged venous flow. PET showing high uptake at left basal ganglia, with tumor-to-normal ratio of 2.6. B. Axial contrast-enhanced CT image showing vascular anomalies in left basal ganglia (arrows) [17]

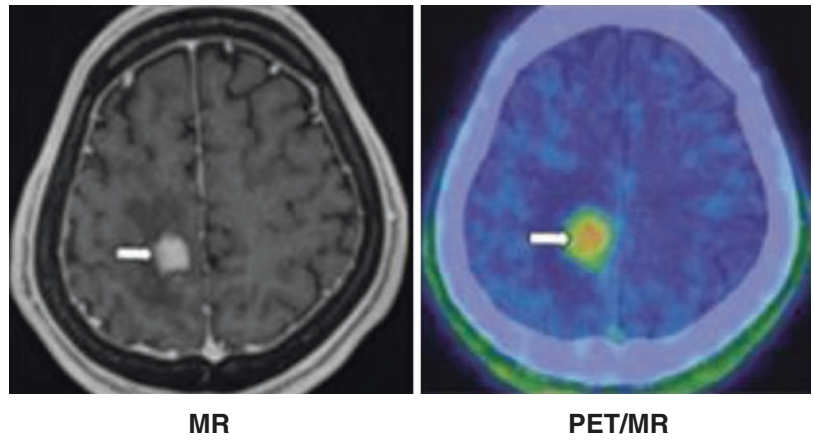

Fig. 11.14 Patient with toxoplasmosis caused by acquired immunodeficiency syndrome. Axial contrast-enhanced T1-weighted image showing clearly enhanced lesion with edema (arrow) in right parietal lobe. PET showing high uptake (arrow) corresponding to lesion, with tumor-to-normal ratio of 4.0 [17]

exhibits various uptake patterns and degrees even in the same pathogens.

Sarcoidosis, brain abscess, progressive multifocal leukoencephalopathy, and tuberculoma are also reported as causes of false positives in ^{11}C-methionine PET.

In patients with AIDS, ^{11}C-methionine uptake may help to distinguish lymphoma from toxoplasmosis; however, several cases of toxoplasmosis show high uptake (Fig. 11.14) similar to the tumor one.

Focal cortical dysplasia (FCD) or cortical tubers are representative of dysplasias having epileptogenic foci. ^{11}C-Methionine uptake of FCD is similar to the uptake of other gray matter; however, some FCD lesions show slightly higher uptake than one of the surrounding cortices.

11.7 New Trend

11.7.1 Myocardial Infarction

Preliminary studies show myocardial uptake of ^{11}C-methionine in acute myocardial infarction patients up to 2 weeks after coronary reperfusion.

Recent ex vivo evidences suggest that ^{11}C-methionine may serve as a potential marker of post-infarct inflammation.

Post-ischemia inflammation could be associated with accumulation in activated macrophages, and could be serially visualized with ^{11}C-methionine and small animal PET.

In vitro studies established a preferential tracer uptake into activated macrophages. In vivo

imaging studies in healthy mice, following permanent ligation of a coronary artery, demonstrate a spatial and temporal pattern of ^{11}C-methionine consistent with leukocyte infiltration of inflamed tissue, sensitive to suppression of inflammation by anti-integrin therapy.

PET imaging with ^{11}C-methionine provides a selective indication of localized tissue inflammation in the acute stages after myocardial infarction, declining over 7d in parallel with activated inflammatory cells. The absence of cardiomyocyte uptake makes ^{11}C-methionine particularly attractive compared to other established inflammation markers.

^{11}C-Methionine molecular imaging may be used to assess efficacy and direct therapy targeted to modulating acute inflammation after myocardial infarction [18].

11.7.2 Hyperparathyroidism

Primary hyperparathyroidism (pHPT) is the third most common endocrine disorder with a prevalence of around 4 per 1000. Diagnosis is established biochemically, with the finding of relatively elevated serum calcium (Ca) level and concomitant inappropriately elevated parathyroid hormone (PTH) level.

Usually, only one of the four glands is abnormal—typically an adenoma—less frequently, there are multiple adenomas (15–25%) and very rarely a carcinoma (1%) [19].

^{99}Tc-Methoxyisobutylisonitrile (MIBI) single photon emission computed tomography (SPECT-CT) has become one of the mainstays in parathyroid imaging but its sensitivity is only 63–84%, so the greater spatial and temporal resolution of PET imaging allows the detection of even the smallest pathological glands which, in theory, could improve sensitivity [20].

Methionine is one of the amino acids comprising parathyroid hormone and it is closely related with biosynthesis of parathyroid hormone so ^{11}C-methionine PET shows higher performance than MIBI scintigraphy in localization of parathyroid tissues; studies show a correct localization rate 87.5% on ^{11}C-methionine PET/CT and 50% on MIBI scintigraphy (Fig. 11.15).

^{11}C-Methionine PET has an overall good sensitivity and PPV and may be considered a reliable second-line imaging modality to enable minimally invasive parathyroidectomy.

Therefore, ^{11}C-methionine PET/CT has a potential to be used for differentiation of parathyroid adenoma (PA) from parathyroid hyperplasia (PH) (Fig. 11.16); SUV can be a useful parameter for the differentiation, PH has the character of low ^{11}C-methionine uptake compared with PA [21].

^{18}F-FCH seems the most promising agent with sensitivity ranging from 80% to 100% and PPV 89% to 100%.

11.7.3 Squamous Cell Head and Neck Cancer

^{11}C-Methionine PET has also been used for characterization of squamous cell head and neck cancer (HNSCC). Sensitivity and specificity of ^{11}C-methionine PET for HNSCC staging are similar to ^{18}F-FDG.

Visualization of HNSCC in ^{18}F-FDG PET images may be impaired because of high ^{18}F-FDG uptake in the tongue and the neck muscles.

^{18}F-FDG and ^{11}C-methionine have different sites of physiological uptake that can cause different tumor-to-background contrast in PET images.

^{18}F-FDG may accumulate in lymphoid tissues like the Waldeyer's ring, in the floor of the mouth, and, in a minor degree, in parotid and submandibular glands and mucosal tissues.

At the opposite, ^{11}C-methionine may accumulate markedly in lacrimal glands, salivary glands, and especially in bone marrow. Thus, facial bones that are photopenic areas in ^{18}F-FDG studies can often be clearly visible in ^{11}C-methionine studies.

Furthermore a relationship between ^{11}C-methionine uptake and cell proliferation of HNSCC, shown in vitro and in vivo, suggests that ^{11}C-methionine could be more specific than ^{18}F-FDG for measuring tumor aggressiveness [22].

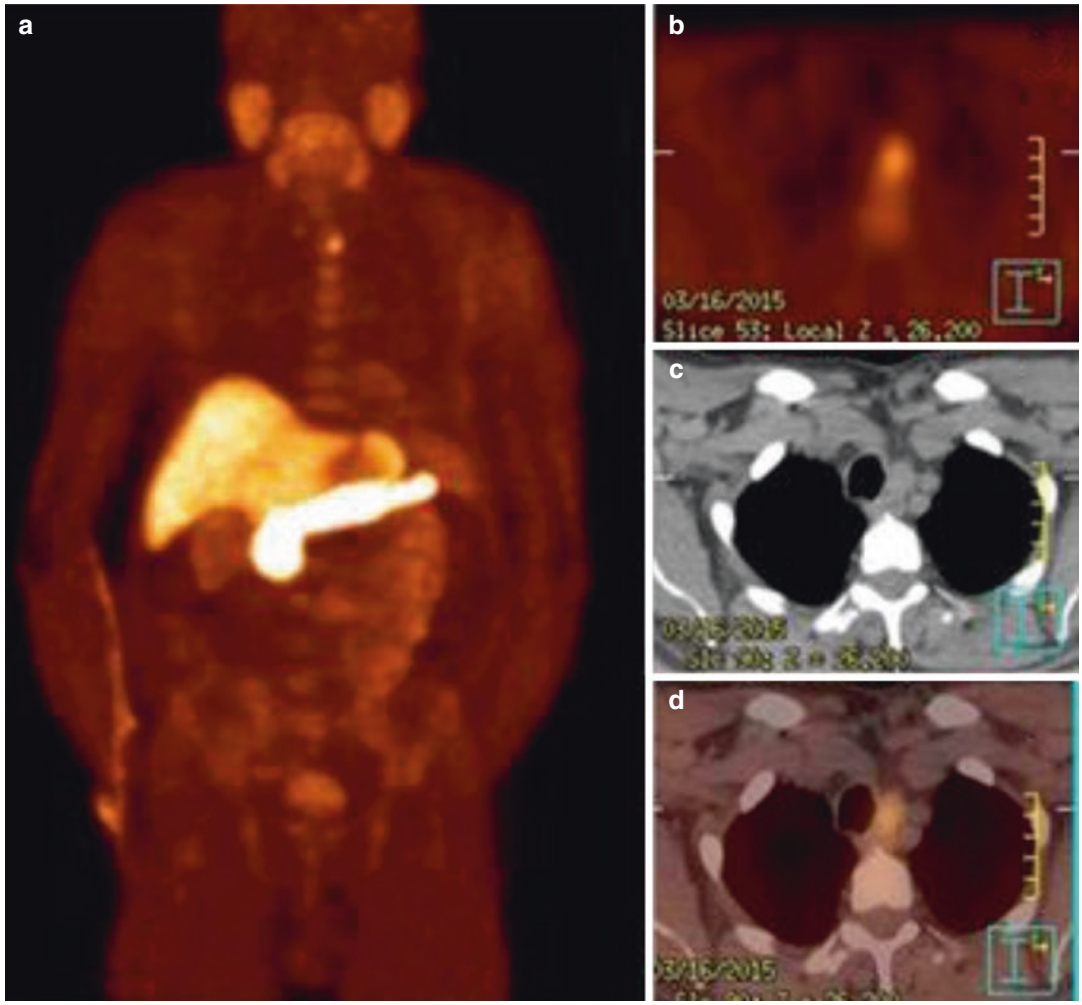

Fig. 11.15 Lymph node metastases from cancer of the parathyroid

^{11}C-Methionine PET provides early useful information about changes in tumor metabolism induced by chemotherapy in hypopharynx cancer.

^{11}C-Methionine PET measurements correlate with end-of-treatment response evaluated with MRI and may thus be helpful to physicians in treatment planning by avoiding unnecessary chemotherapy courses for nonresponding patients [23].

11.7.4 Multiple Myeloma and Lymphoma

Multiple myeloma (MM) accounts for approximately 1% of all cancers and around 10% of hematological malignancies.

Several studies demonstrated the usefulness of molecular imaging using PET and ^{18}F-FDG for diagnosis, staging, and estimation of prognosis. Limitations of ^{18}F-FDG include lack of sensitivity

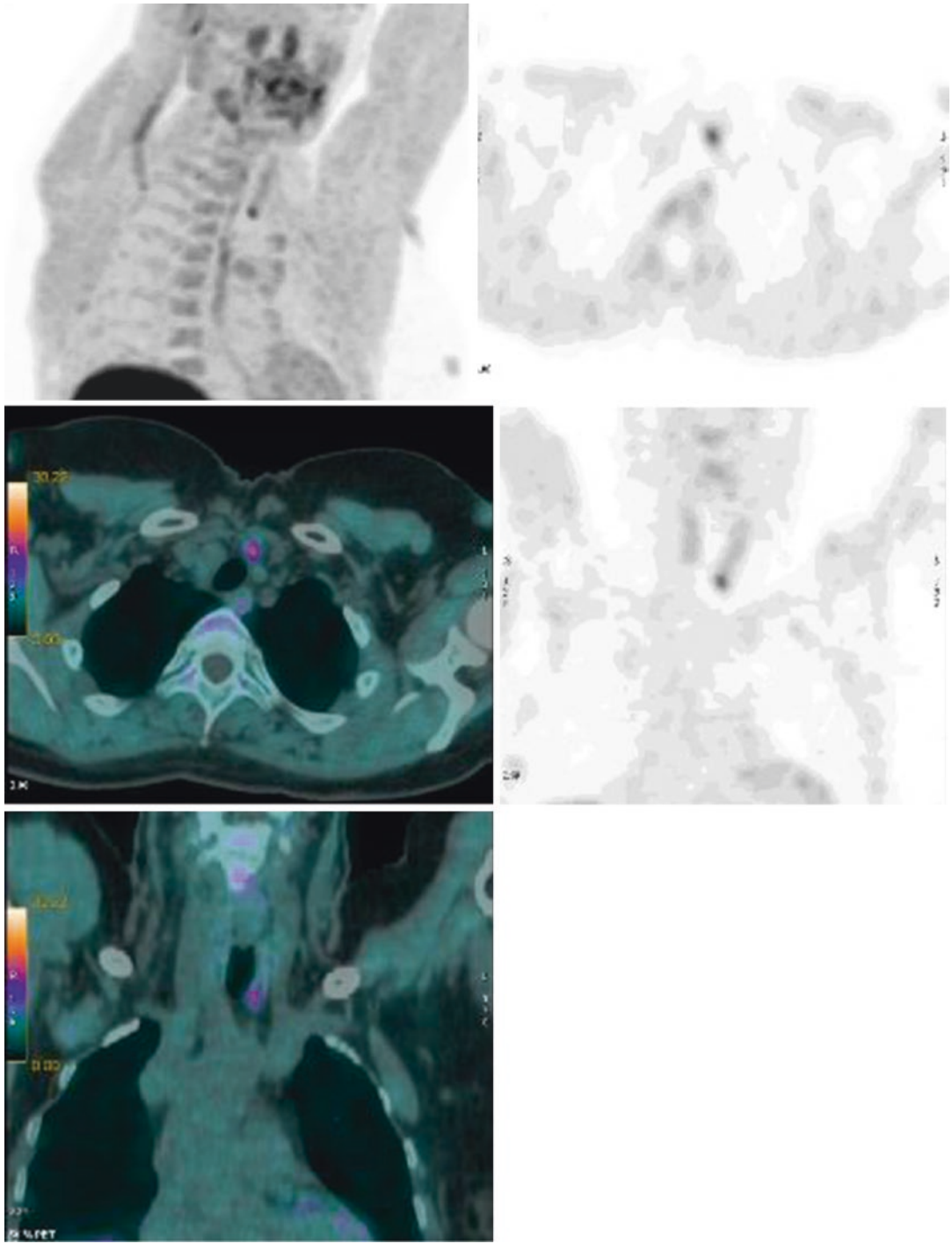

Fig. 11.16 Parathyroid adenoma

and specificity, e.g., in cases with diffuse bone marrow infiltration (false negative) or with inflammatory lesions (false positive).

First human studies suggested a potential for ^{11}C-methionine in MM diagnosis.

^{11}C-Methionine uptake in MM probably reflects increased protein and immunoglobulin synthesis.

^{11}C-Methionine provides more accurate information on both intra- and extramedullary disease and appears to be superior to ^{18}F-FDG in the vast majority of patients.

Due to its potential to reliably reflect MM biology by depicting amino acid metabolism, ^{11}C-methionine served as a superior readout for noninvasive determination of tumor burden.

This finding could be explained because it seems that L-type amino acid transporter 1 (LAT1) as the major uptake mechanism of ^{11}C-methionine was highly expressed by all myeloma cells in almost all samples analyzed [24].

So ^{11}C-methionine might prove a more versatile marker of disease burden, especially as it depicts both low- and high-grade myeloma lesions. In contrast, ^{18}F-FDG might be limited to more aggressive subclones of MM and therefore prone to underestimation of true disease extent.

^{11}C-Methionine is superior to ^{18}F-FDG for staging and re-staging of MM. It is able to detect both intra- and extramedullary MM manifestations. Additionally, tracer uptake correlates with BM involvement and seems to be a more accurate marker of tumor biology [24].

^{11}C-Methionine has also been explored for its potential utility in patients with lymphomas.

Most sites of tumor involvement in children with Hodgkin lymphomas and non-Hodgkin lymphoma are well visualized using ^{11}C-methionine PET/CT; tumor sites in neck and chest are particularly evident due to the low background uptake of ^{11}C-methionine in these areas.

Tumor uptake declines markedly with treatment; this indicates that the activity of LAT1 decreases with effective tumor treatment similarly to glucose transporters [25].

References

1. Saha GB. Fundamentals of Nuclear Pharmacy 2014.
2. Pascali C, Bogni A, Cucchi C, et al. High efficiency preparation of L-[S-methyl-^{11}C]methionine by on-column [^{11}C]methylation on C18 Sep-Pak. J Radioanal Nucl Chem. 1999;288:405–9.
3. Harris SM, James C, et al. Evaluation of the biodistribution of ^{11}C-methionine in children and young adults. J Nucl Med. 2013;54:1902–8.
4. Nakajima R, et al. Optimization of scan ignition timing after ^{11}C methionine administration for the diagnosis of suspected recurrent brain tumors. Ann Nucl Med. 2017;31(2):190–7.
5. Calabria F., Schillaci O. Radiopharmaceuticals Metabolic pathways for PET/CT and PET/ME Moleculr Imaging - Chapter 11: ^{11}C-methionine. 2018.
6. Hoffman RM. L-[Methyl-11C] methionine-positron-emission tomography (MET-PET). Methods Mol Biol. 2019;1866:267–71.
7. Galldiks N, Langen K-J, Pope WB. From the clinician's point of view - What is the status quo of positron emission tomography in patients with brain tumors? Neuro-Oncology. 2015;17(11):1434–44.
8. Minamimoto R, et al. Differentiation of brain tumor recurrence from post-radiotherapy necrosis with ^{11}C-methionine PET: visual assessment versus quantitative assessment. PLoS One. 2015;10(7):e0132515.
9. Ceyssens S, Van Laere K, de Groot T, et al. [^{11}C] Methionine PET, histopathology, and survival in primary brain tumors and recurrence. AJNR. 2006;27(7):1432–7.
10. Galldiks N, Stoffels G, Ruge MI, et al. Role of O-(2–18Ffluoroethyl)- L-tyrosine PET as a diagnostic tool for detection of malignant progression in patients with low-grade glioma. J Nucl Med. 2013;54(12):2046–54.
11. Glaudemans AW, Enting RH, Heesters MA, et al. Value of ^{11}C-methionine PET in imaging brain tumours and metastases. Eur J Nucl Med Mol Imaging. 2013;40(4):615–35.
12. Grosu AL, Astner ST, Riedel E, et al. An interindividual comparison of O-(2-[^{11}F]fluoroethyl)-L-tyrosine (FET)- and L-[methyl-^{11}C]methionine (MET)-PET in patients with brain gliomas and metastases. Int J Radiat Oncol Biol Phys. 2011;81:1049–58.
13. Grègoire V, Haustermans K, Geets X, et al. PET-based treatment planning in Ra-diotherapy: a new standard? J Nucl Med. 2007;48:68S–76S.
14. Lohmann P, Werner J-M, Jon Shah N, Langen GRFK-J, Galldiks N. Combined amino acid positron emission tomography and advanced magnetic resonance imaging in glioma patients. Cancer. 2019;11:153.

15. Kawasaki T, Miwa K, Shinoda J, Asano Y, Takei H, Ikegame Y, Yokoyama K, Yano H, Iwama T. Dissociation between 11C-methionine-PET and Gd-MRI in the longitudinal features of Glioblastoma after postoperative radiotherapy. World Neurosurg. 2019. pii: S1878-8750(19)30229-3
16. Qiao Z, Zhao X, Wang K, Zhang Y, Fan D, Yu T, Shen H, Chen Q, Ai L. Utility of dynamic susceptibility contrast perfusion-weighted MR imaging and 11C-methionine PET/CT for differentiation of tumor recurrence from radiation injury in patients with high-grade gliomas. AJNR Am J Neuroradiol. 2019;40(2):253–9.
17. Ito K, Matsuda H, Kubota K. Imaging spectrum and pitfalls of ^{11}C-methionine positron emission tomography in a series of patients with intracranial lesions. Korean J Radiol. 2016;17(3):424–34.
18. Thackeray JT, Bankstahl JP, Wang Y, et al. Targeting amino acid metabolism for molecular imaging of inflammation early after myocardial infarction. Theranostics. 2016;6(11):1768–79.
19. Phitayakorn R, McHenry CR. Incidence and location of ectopic abnormal parathyroid glands. Am J Surg. 2006;191:418–23.
20. Wei WJ, Shen CT, Song HJ, et al. Comparison of SPET/CT, SPET and planar imaging using ^{11}mTc-MIBI as independenttechniques to support minimally invasive parathyroidectomy in primary hyperparathyroidism: a meta-analysis. Hell J Nucl Med. 2015;18:127–35.
21. In KC, Gi JC, et al. Detection and characterization of parathyroid adenoma/hyperplasia for preoperative localization: comparison between ^{11}C-methionine PET/CT and ^{99}mTc-sestamibi scintigraphy. Nucl Med Mol Imaging. 2013;47(3):166–72.
22. Leskinen-Kallio S, Lindholm P, Lapela M, et al. Imaging of head and neck tumors with positron emission tomography and ^{11}C-methionine. Int J Radiat Oncol Biol Phys. 1994;30(5):1195–9.
23. Chesnay E, Babin E, Constans JM, et al. Early response to chemotherapy in hypopharyngeal cancer: assessment with ^{11}C-methionine PET, correlation with morphologic response, and clinical outcome. J Nucl Med. 2003;44(4):526–32.
24. Lapa C, Knop S, Schreder M, et al. ^{11}C-methionine-PET in multiple myeloma: correlation with clinical parameters and bone marrow involvement. Theranostics. 2016;6(2):254–61.
25. Kaste SC, Snyder SE, Metzger ML, et al. Comparison of ^{11}C-methionine and 18F-FDG PET-CT for staging and follow-up of pediatric lymphoma. J Nucl Med. 2017;58(3):419–24.

^{68}Ga-PSMA

12

Robert Pichler, Johannes Wolfsgruber, Ferdinando Calabria, Orazio Schillaci, and Andreas Dunzinger

Contents

R. Pichler (✉)
Institute of Nuclear Medicine, Kepler University Hospital, Neuromed Campus, Linz, Austria

Institute of Nuclear Medicine, General Hospital Steyr, Steyr, Austria

Department of Radiology, Clinic of Nuclear Medicine, Medical University Graz, Graz, Austria
e-mail: robert.pichler@ooeg.at

J. Wolfsgruber
Department of Urology, General Hospital Steyr, Steyr, Austria

F. Calabria
Department of Nuclear Medicine and Theranostics, "Mariano Santo" Hospital, Cosenza, Italy

O. Schillaci
Department of Biomedicine and Prevention, University "Tor Vergata", Rome, Italy

Department of Nuclear Medicine and Molecular Imaging, IRCCS INM Neuromed, Pozzilli, IS, Italy

A. Dunzinger
Institute of Nuclear Medicine, Kepler University Hospital, Neuromed Campus, Linz, Austria

F. Calabria, O. Schillaci (eds.), *Radiopharmaceuticals*,
https://doi.org/10.1007/978-3-030-27779-6_12

Abbreviations

^{18}F-DCFBC	(N-[N-[(S)-1,3-dicarboxypropyl] carbamoyl]-4-F-fluorobenzyl-L-cysteine)
^{18}F-DCFPyL	2-(3-{1-carboxy-5-[(6-[(18)F] fluoro-pyridine-3-carbonyl)-amino]-pentyl}-ureido)-pentanedioic acid
^{18}F-FDG	^{18}F-Fluorodeoxyglucose
^{18}F-FET	^{18}F-Fluoroethylthirosine
^{68}Ga-PSMA	^{68}Ga-prostate-specific membrane antigen
DOTAtaGA	(1,4,7,10-tetraazacyclododecane-1-(1-carboxy-3-carbo-tertbutoxypropyl)-4,10 (carbotertbutoxymethyl)-7-acetamide)
PET/CT	Positron emission tomography/computed tomography
PET/MRI	Positron emission tomography/magnetic resonance imaging
PSA	Prostate-specific antigen

12.1 Synthesis

^{68}Ga-PSMA (^{68}Ga-prostate-specific membrane antigen) with high radiochemical and radionuclidic purity is conveniently prepared by using a ^{68}Ge/^{68}Ga generator and manual synthesis module. This production is limited by the availability of the parent nuclide ^{68}Ge. The radiochemical yields are very high, and activity sufficient for 3–4 patients can be prepared in a single batch; multiple batches can be done on the same day and when needed after a gap of 1.5-2 h [1]. Alternatively, the use of a ^{68}Zn salt solution in a liquid target has been proposed. With this process, ^{68}Ga can be produced in a cyclotron, but this concept has not reached relevant propagation yet.

12.2 Pharmacokinetics

Imaging prostate cancer and metastases either by morphologic radiological approach or nuclear medicine methods has not fulfilled the expectations of the clinicians until several years. PSMA—which can be labeled with positron-emitting isotopes mostly ^{68}Ga—changed this setting substantially. PSMA, identical to glutamate carboxypeptidase II, is a type II 750 amino acid integral transmembrane glycoprotein (100–120 kDa) belonging to the M28 peptidase family [2]. The term can be considered a misnomer as PSMA is not related to PSA and is not an antigen; strictly spoken PSMA is not even specific to prostate tissue. Anyhow, PSMA is considered to be the best established target antigen in prostate cancer because it is highly expressed on the surface of prostate cancer cells at all tumor stages (Fig. 12.1) [3]. PSMA expression is associated with prostate cancer aggressiveness and has been shown to have prognostic relevance [4]. In normal prostatic tissue it is found within the apical epithelium of secretory ducts, the physiological role remaining unclear [5]. Benign prostate cells contain PSMA in the cytosol; in prostate cancer cells PSMA switches to a membrane-bound protein. Older agents targeting the intracellular domain of PSMA showed disappointing results with low sensitivity, whereas targeting the extracellular domain by small specific inhibitors that are internalized after ligand binding overcome these limitations [6]. The recently developed PET radiotracers target the extracellular moiety of the PSMA of viable prostate cancer cells and include ^{11}C, ^{18}F, ^{68}Ga, ^{89}Zr, ^{64}Cu, and ^{86}Y labeled agents that involve antibodies, antibody fragments, aptamers, and PSMA inhibitors [7]. ^{68}Ga is the most frequently used isotope for PSMA imaging and became available in 2013 [5]. Hundreds of publications on PSMA-targeted PET are now available [8].

Fig. 12.1 ^{68}Ga labelled PSMA binds to the extracellular domain by small specific inhibitors that are internalized after ligand binding. A high level of accumulation can be reached even in small metastases of prostate cancer

12.3 Physiological Distribution

Intense physiological distribution can be observed in secretory glands, especially the pancreas, salivary, and lachrymal glands (Fig. 12.2). Moderate physiological uptake can be registered in liver, gallbladder, and intestinal loops, to a less degree in spleen, bone marrow, thyroid, and testicles. In respect to the thyroid it has to be stressed that in areas like central Europe where thyroid disease is of high prevalence, benign and malignant nodules as well as autoimmune inflammatory conditions may be associated with accentuated tracer uptake. The same is true for pulmonary inflammatory disease, which can be considerably intense in sarcoidosis. The renal parenchyma itself accumulates PSMA, additionally the excretory pathway by urine unfavorably is present by high tracer accumulation also in renal pelvis, ureters, and urinary bladder—in a time-dependent manner. Urine caused uptake in the prostate gland because of activity in urine—in case the prostate gland has not been extirpated—can also be misleading.

12.4 Clinical Indications

Prostate cancer is the most common tumor entity in men worldwide and the third leading cause of cancer-related death in men in Europe and the USA [9]. Biochemical relapse is a frequent event after primary therapy and occurs in 20–30% of patients after radical prostatectomy and even more frequently after primary external beam radiotherapy [10]. There is no place for PSMA-PET in screening persons at risk for prostate

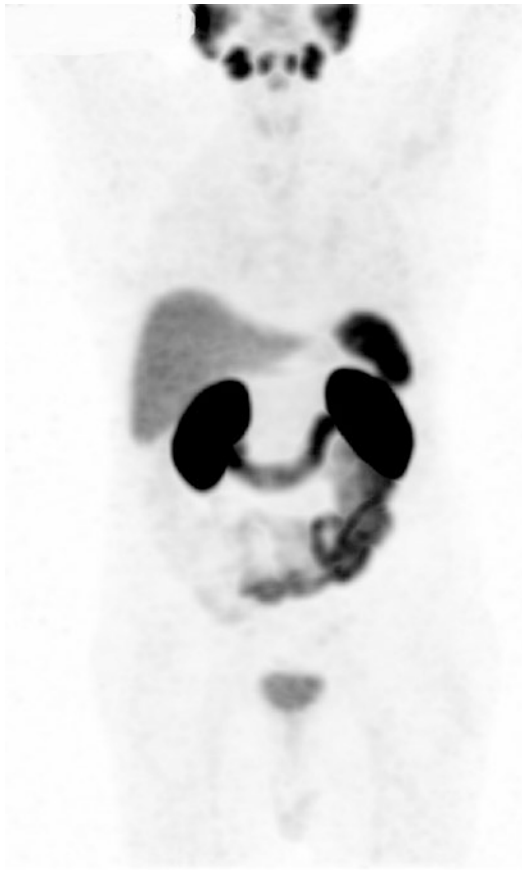

Fig. 12.2 Physiological distribution of ^{68}Ga-PSMA in salivary glands, liver, and spleen. A diffuse bowel uptake can be observed. Marked uptake is also present in the kidneys and the urinary tract

cancer. Abundant data are available for primary staging, patients with biochemical recurrence and for radiotherapy planning. Moreover, evaluation for alpha- or beta-emitting isotope-labeled PSMA therapy is feasible.

^{68}Ga-PSMA PET/CT has been investigated for its potential in staging of primary prostate cancer and has been shown to be superior to standard imaging modalities as CT alone [11]. At its best it is considered to perform equally to MRI. It has also to be considered that up to 10% of prostate cancers do not overexpress PSMA at this stage of disease [11]. Also the clinical impact for detection of (small) pelvic lymph nodes has been questioned, so pre-therapeutic use of PSMA PET has not gained broad propagation. This scenario might change with the availability of PET/MRI, as ^{68}Ga-PSMA PET/MRI has been shown by a Viennese investigator group to correctly identify prostate cancer in 97.5% of 122 patients. The accuracy for T staging was 82.5% and 93% for N1 stage. This hybrid modality was found to change the therapeutic strategy in 29% of the patients [12].

A large body of evidence is available for restaging of prostate cancer patients with biochemical recurrence. In most cases, recurrence after initial therapy is diagnosed either by two consecutive PSA values of ≥0.2 μg/L after prostatectomy or external beam radiation therapy [13]. A PSA doubling time < 6 months can predict a relapse and is a predictor of pathological PSMA PET findings [9]. In this indication a substantial impact on clinical management can be expected. After potential salvage treatment options, patients are usually treated with androgen-deprivation therapy. Typically, after 2–8 years PSA begins to rise again, indicating castration-resistant prostate cancer [14]. A review paper from 2016 is available: sixteen articles involving 1309 patients were analyzed. The overall percentage of positive ^{68}Ga-PSMA PET among patients was 76% for biochemical recurrence. Positive ^{68}Ga-PSMA PET scans increased with pre-PET PSA. For the PSA categories 0–0.2, 0.2–1, 1–2, and > 2 ng/ml, 42%, 58%, 76%, and 95% scans, respectively, were positive. Shorter PSA doubling time also increased ^{68}Ga-PSMA PET positivity. On per-patient analysis, the summary sensitivity and specificity were both 86%. Pooled data indicate favorable sensitivity and specificity profiles [15].

Considering the clinical impact related to patients referred for an increase in PSA level in a

large Swiss study ^{68}Ga-PSMA identified recurrence in 74% of 223 patients, with a detection rate of 50% for recurrent disease at low PSA values of <0.5 ng/mL. PSMA-PET directed metastasis-targeted treatment led to a complete response after 6 months in 45% of patients [16]. ^{68}Ga-PSMA PET/CT demonstrates high detection rates in patients with biochemical recurrence of prostate cancer after primary radiation therapy [17] as well as after radical prostatectomy [6].

^{68}Ga-PSMA PET has also been used for radiotherapy planning. Compared to conventional CT, PSMA PET/CT had a remarkable impact on radio-therapeutic approach especially in postoperative patients [18]. Salvage radiotherapy for prostate cancer after prostatectomy offers long-term biochemical control in about 50–60% of patients. Hopefully an ongoing randomized prospective trial with about 200 patients will quantify an expected improved outcome using PSMA PET/CT for radiotherapy planning [19, 20].

PSMA is an ideal structure for both imaging and targeted therapy for prostate cancer, therefore enabling a theranostic approach—the same ligand is used for both in vivo imaging and therapy [21]. ^{68}Ga-PSMA shows potential for high contrast PET imaging of metastatic prostate cancer, whereas its ^{177}Lu-labeled counterpart exhibits suitable targeting and retention characteristics for successful endoratiotherapeutic treatment [22]. Alternatively, radionuclide therapy with the alpha emitter ^{225}Ac PSMA has been developed [23]. Although PSMA-based radionuclide therapy has not entered urologic guidelines successfully, its efficacy and safety in routine practice have already been shown [24].

12.5 PET Radioligands for Prostate Cancer Imaging

PET with choline tracers—labeled with ^{11}C or ^{18}F—has historically found widespread use for the diagnosis of (metastatic) prostate cancer. However, choline metabolism is not increased in a substantial number of cases. When compared head-to-head ^{68}Ga-PSMA PET/CT outperforms standard ^{18}F-choline PET/CT, especially at low PSA levels [25].

Considering ^{68}Ga-labeled PSMA a variety of agents is available with presumable very similar clinical value. ^{68}Ga-HBED-CC-PSMA or ^{68}Ga-PSMA-11 [26], and ^{68}Ga-DOTAtaGA-FFK, termed PSMA I&T [22] are frequently used. Variants labeled with ^{64}Cu are available, especially considered if the supply with ^{68}Ga is logistically demanding. ^{18}F-labeled PSMA PET tracers have already been evaluated, as ^{18}F-DCFBC [26], but are not yet on the market in most European countries. Newer ^{18}F-labeled agents are ^{18}F-DCFPyL and ^{18}F-PSMA-1007 [14].

A different approach related to amino acid metabolism—the tracer mirrors the upregulation of transmembrane amino acid transport [27]—is applied by the use of ^{18}F Fluciclovine (^{18}F-FACBC) to image prostate cancer tissue. One advantage is that kidney uptake of fluciclovine is negligible and no relevant activity in the urinary tract can be observed. As the method is relatively new, clinical usefulness and superiority to choline PET have already been demonstrated [11, 28, 29], but the clinical value compared head-to-head to ^{68}Ga-PSMA still has to be demonstrated.

12.6 Clinical Cases

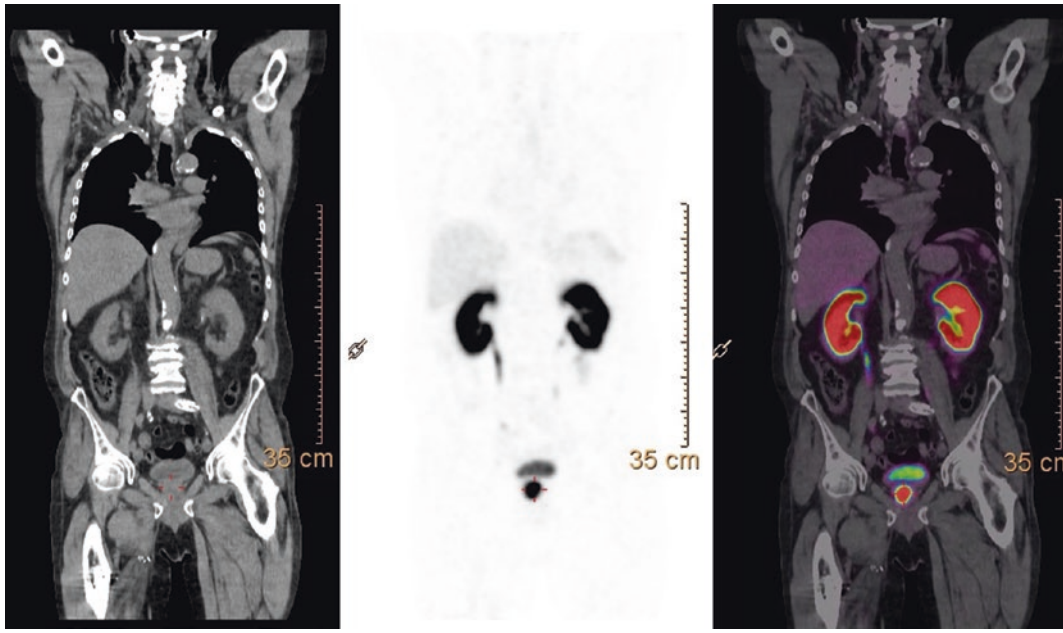

Fig 12.3 The images of this prostate cancer patient before prostatectomy show a marked uptake in the prostate primary. No metastases were observed by ^{68}Ga-PSMA PET/CT

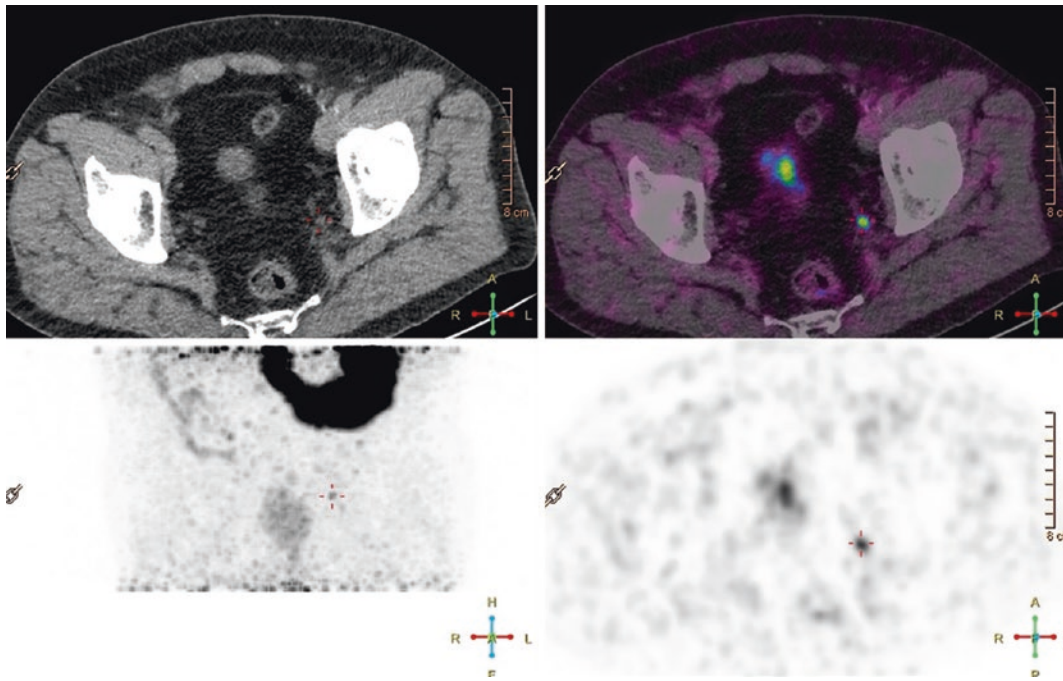

Fig 12.4 This patient presented with PSA rise after radical prostatectomy and limited extended lymphadenectomy. A singe small lymph node metastasis in the left pelvis could be observed

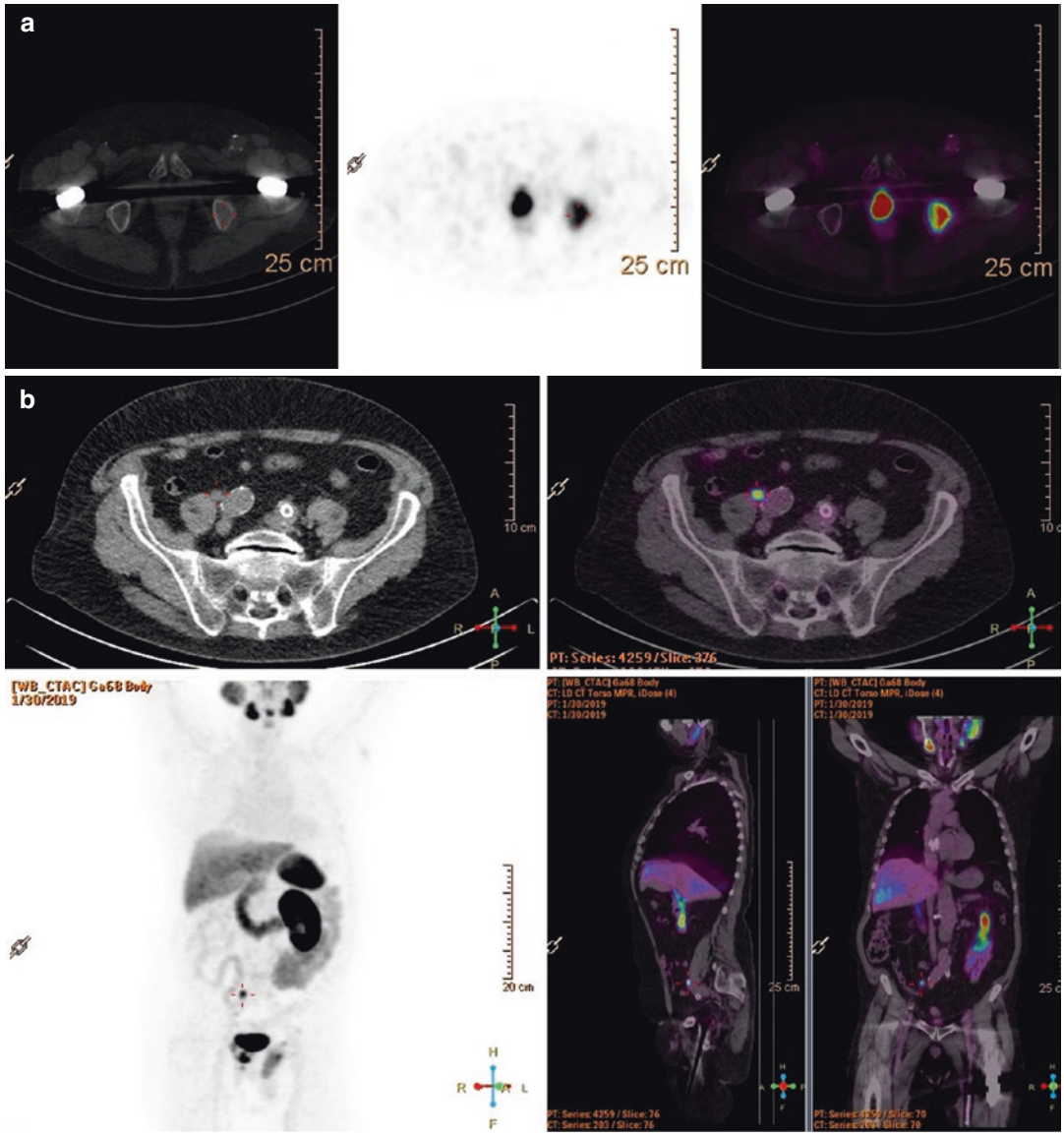

Fig 12.5 Single bone metastasis in the left os pubis and at least one pelvic lymph node with marked ^{68}Ga-PSMA uptake – new findings in respect to a PET/CT three years before. A local relapse in the prostate bed was also present

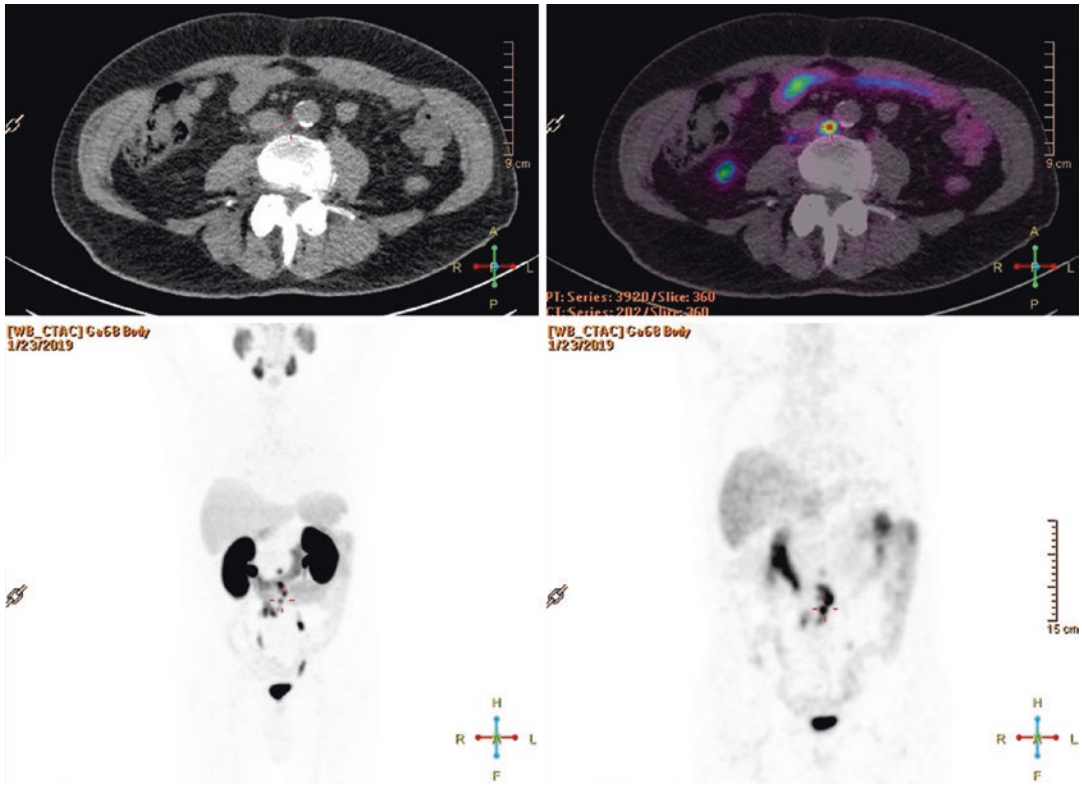

Fig 12.6 After prostatectomy, external beam radiation therapy and androgen-deprivation therapy this patient presented a relapse with multifocal paraaortal lymph node metastases observed by ^{68}Ga-PSMA. This high lumbar level had not been covered by radiation planning before. The findings are new in respect to a ^{68}Ga-PSMA PET/CT two years before

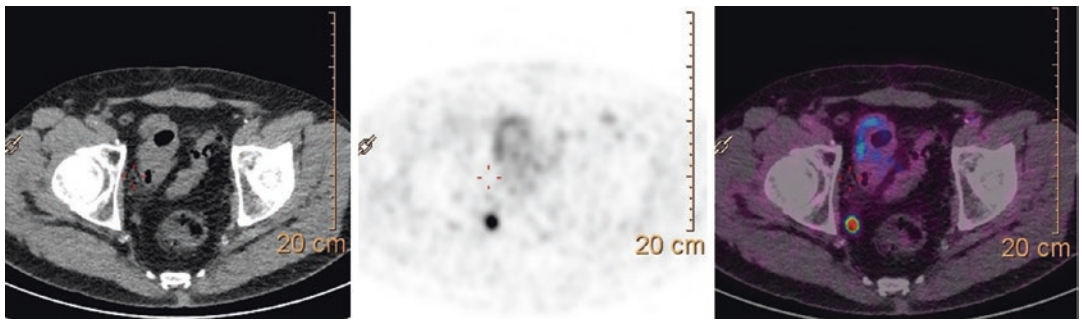

Fig 12.7 This patient had radical prostatectomy in 1999, followed by pelvic radiation in 2015 when he had his first relapse. In 2019 when an asymptomatic PSA rise occured the only finding in ^{68}Ga-PSMA was a single pelvic lymph node metastasis

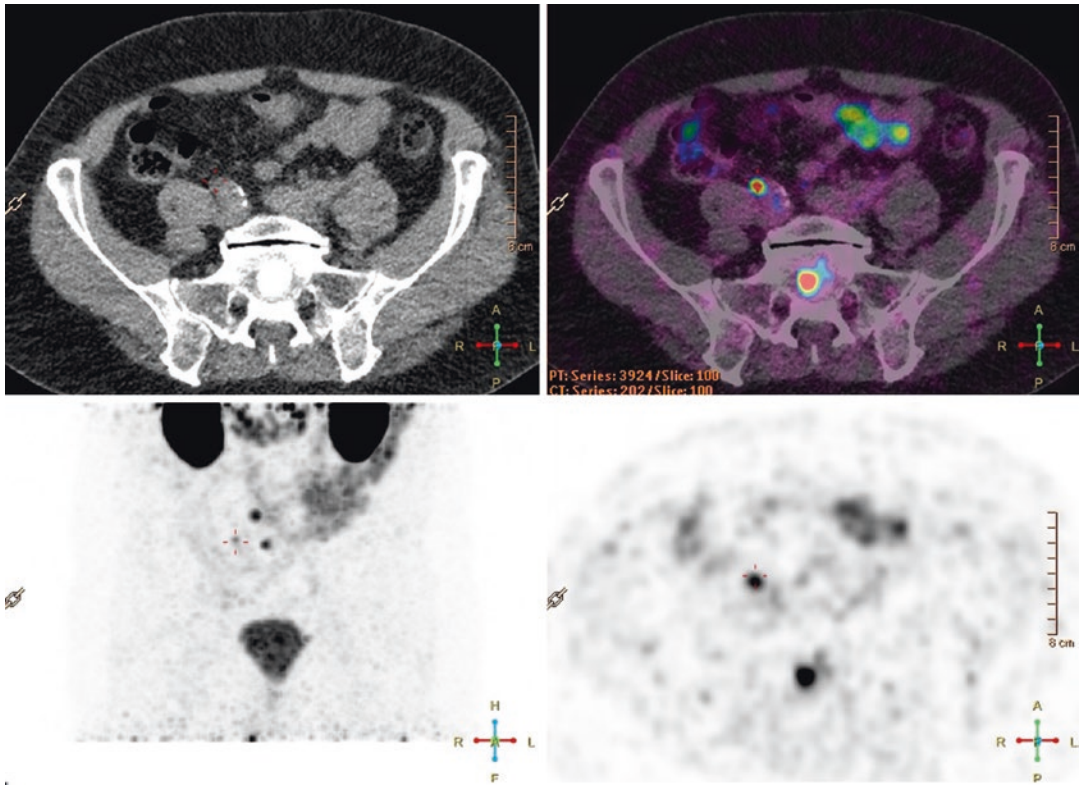

Fig 12.8 In these images multifocal pelvic lymph node metastases and a sacral bone metastasis are presented by ^{68}Ga-PSMA

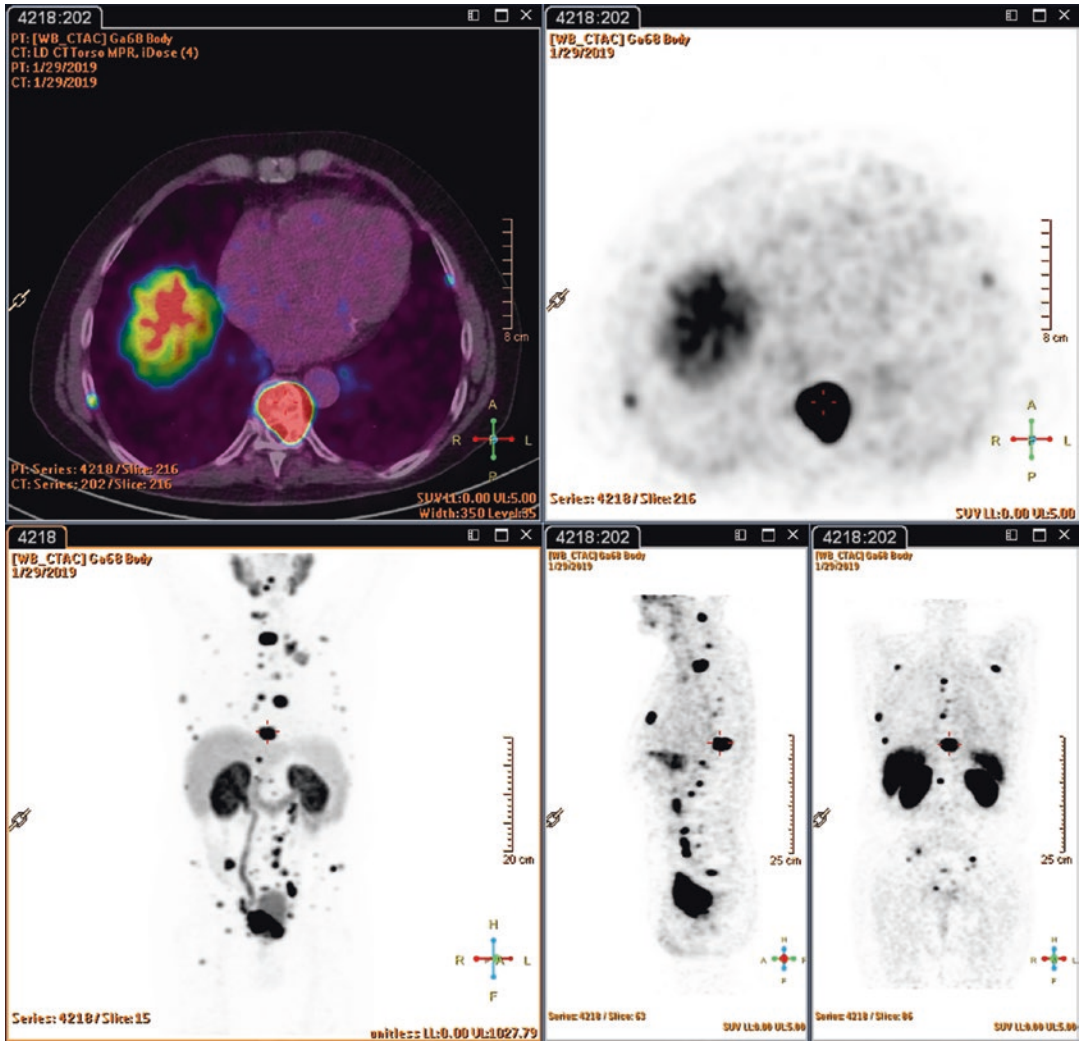

Fig 12.9 This patient presented multifocal osseous and lymph node metastases with high uptake of ^{68}Ga-PSMA. A therapeutic option with ^{177}Lu-PSMA was suggested

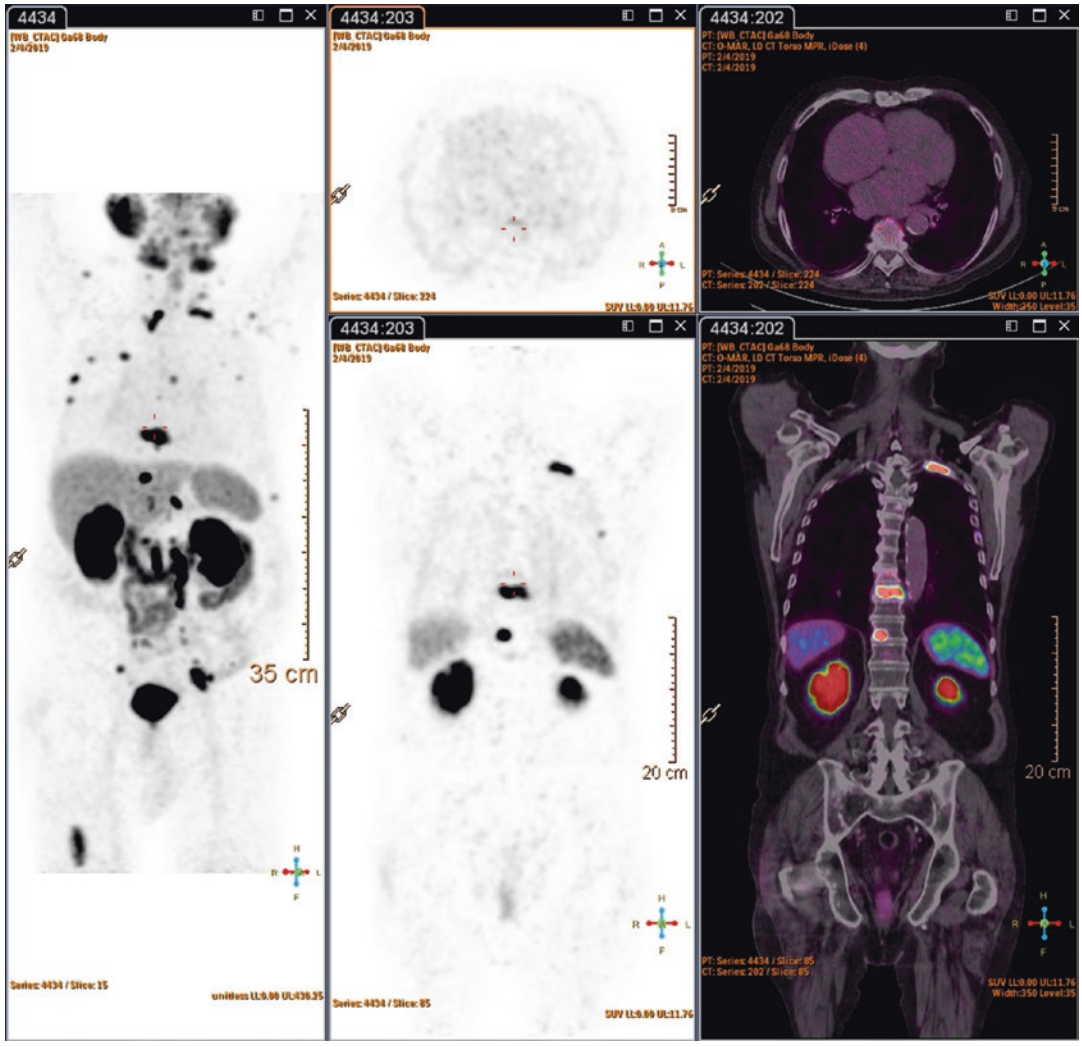

Fig 12.10 Massive osseous metastasis is presented here by ^{68}Ga-PSMA, some positive lymph node metastases were observed as well

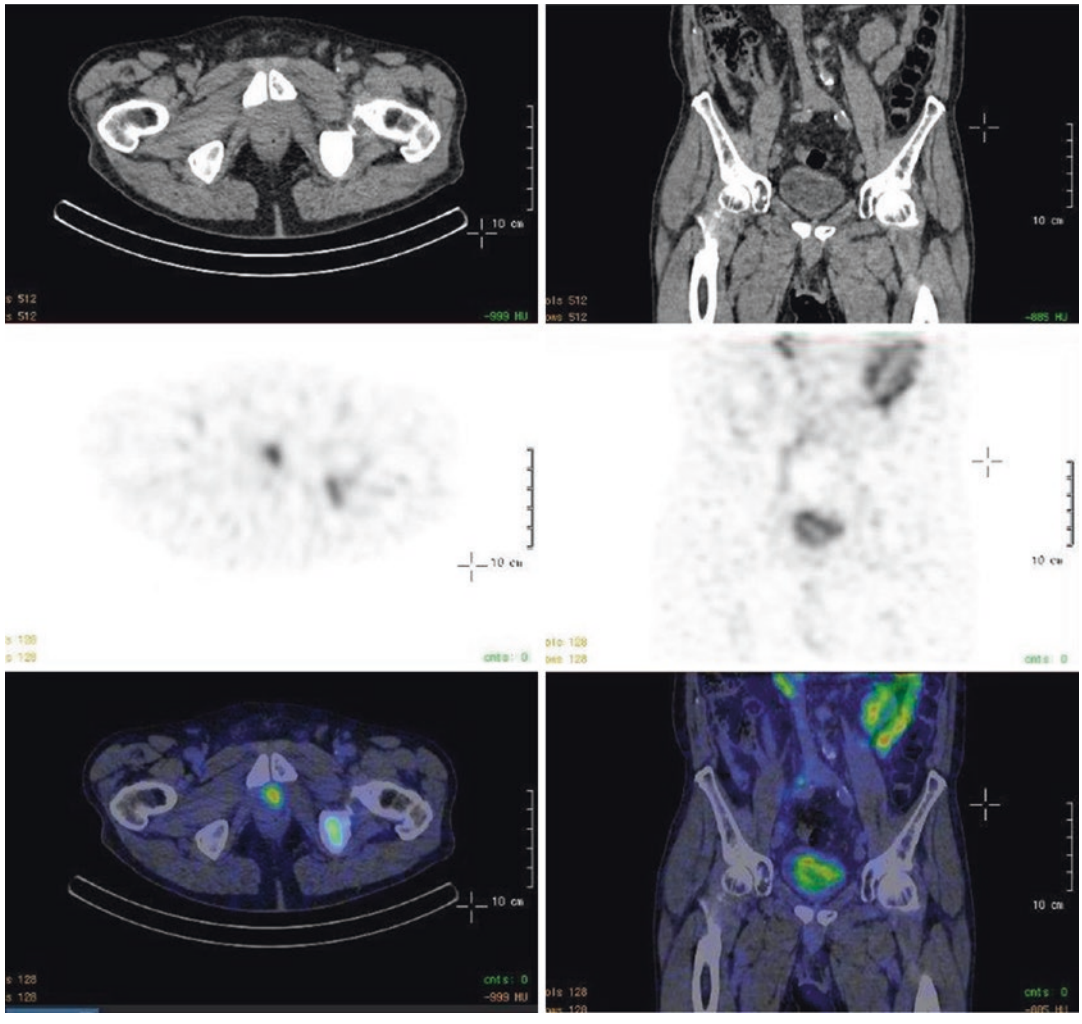

Fig 12.11 SPECT/CT images of Tc99m-PSMA show clearly a local relapse and bone metastasis in the pelvis, a small lymph node right to the aortal bifurcation is hardly visible on the fusion images. This method is an alternative when a PET scanner or a gallium generator are not available

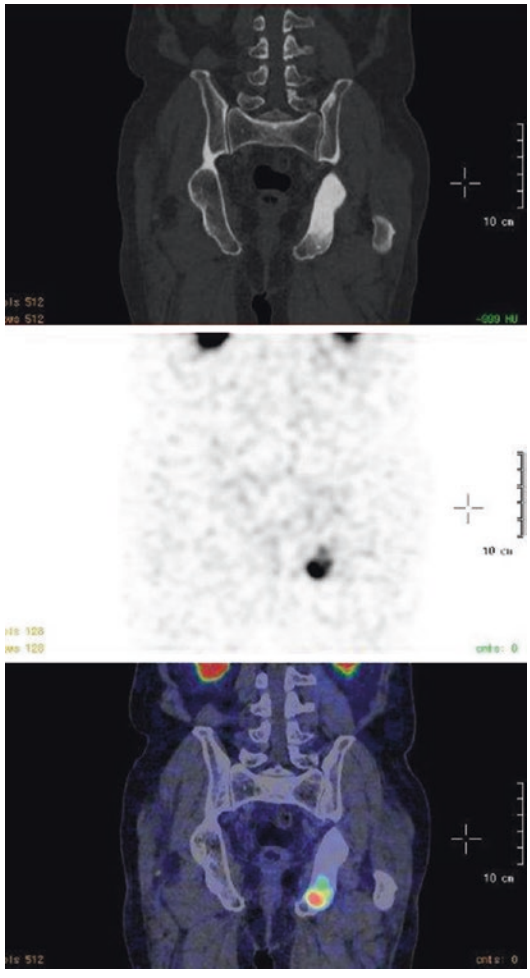

Fig. 12.11 (continued)

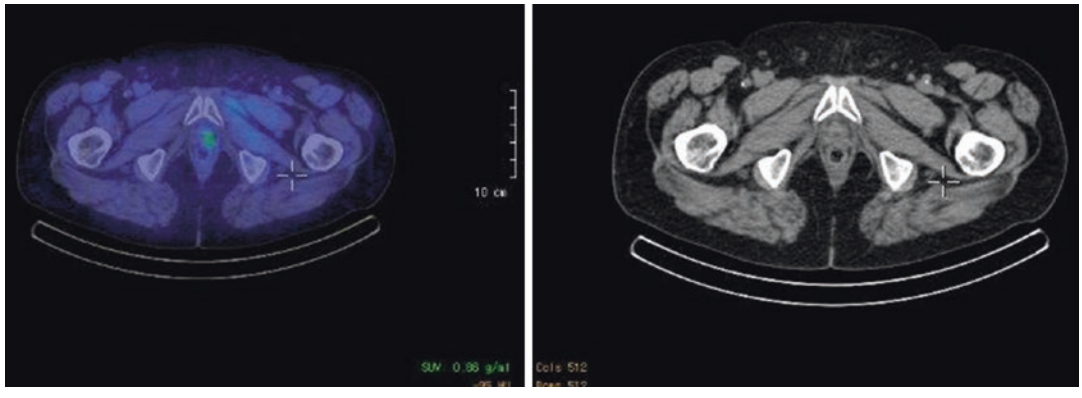

Fig 12.12 ^{18}F-Fluciclovine PET/CT had been helpful to identify a local relapse of prostate cancer—due to the fact that there is no relevant uptake of this tracer in urine

12.7 PET/CT Acquisition Protocols

In general, PET/CT images are obtained about 60 minutes after i.v. bolus application of an activity of 200–250 MBq ^{68}Ga-PSMA [30] or 1.8–2.2 per kilogram bodyweight [31]. Sufficient hydration is recommended, the administration of diuretics—e.g., furosemide 20 mg—is frequently used [31]. It has been shown that imaging 3 h after injection can reveal more lesions characteristic for prostate cancer with a higher uptake and contrast [32]. Anyhow, practical considerations as patient management and the half-life of the tracer have to be kept in mind.

A diagnostic or low-dose CT scan is generally performed from the skull base to midthigh [31], followed by acquisition of PET images according to the specific scanner and the manufacturer's instructions. In our institution in Linz, we frequently perform additional late regional images, e.g., of the pelvis approximately 1 h later when indicated after evaluation of the PET/CT images already acquired before.

12.8 Variants and Pitfalls

Comparable to the experience with ^{18}F-FDG and ^{18}F-FET the usage of ^{68}Ga-PSMA revealed a growing body of evidence for pathological or marked uptake in diverse anatomical structures, in this case unrelated to prostate cancer. As a major goal of PSMA imaging is the detection of lymph node metastases, unspecific uptake in celiac ganglia was among the first reported pitfalls [33]. The uptake of active granulomatous lesions in sarcoidosis, especially in the lung, can appear quite impressive [4]. Paget's disease has also been suggested as a potential clinical mimicker of bone metastasis on PSMA-targeted PET imaging [4]. In general terms augmented bone metabolism might be detected by moderate tracer uptake, as in postfracture healing. A variety of benign etiologies for focal intense PSMA PET uptake has been published mostly in form of case reports [34, 35].

A potential for specific oncologic imaging of different malignancies has also been presented, as for renal cell carcinoma [8] and hepatocellular carcinoma [36]. Of special interest is the marked uptake in endothelium in angiogenesis, which has been proven by immune-histochemical staining. Thereby the imaging of primary brain gliomas and brain metastases can be enabled [37, 38].

References

1. Nanabala R, Anees MK, Sasikumar A, et al. Preparation of [(68)Ga]PSMA-11 for PET-CT imaging using a manual synthesis module and organic matrix based (68)Ge/(68)Ga generator. Nucl Med Biol. 2016;43:463–9.
2. Giovacchini G, Giovannini E, Riondato M, et al. PET/CT with 68Ga-PSMA in prostate cancer: radiopharmaceutical background and clinical implications. Curr Radiopharm. 2018;11:4–13.
3. Afshar-Oromieh A, Babich JW, Kratochwil, et al. The rise of PSMA ligands for diagnosis and therapy of prostate cancer. J Nucl Med. 2016;57:79S–89S.
4. Sheikhbahaei S, Afshar-Oromieh A, Eiber M, et al. Pearls and pitfalls in clinical interpretation of prostate-specific membrane antigen (PSMA)-targeted PET imaging. Eur J Nucl Med Mol Imaging. 2017;44:2117–36.
5. Lenzo NP, Meyrick D, Turner JH, et al. Review of gallium-68 PSMA PET/CT imaging in the management of prostate cancer. Diagnostics (Basel). 2018;11, 8
6. Eiber M, Maurer T, Souvatzoglou M, et al. Evaluation of hybrid 68Ga-PSMA ligand PET/CT in 248 patients with biochemical recurrence after radical prostatectomy. J Nucl Med. 2015;56:668–74.
7. Jadvar H. PSMA PET in prostate cancer. J Nucl Med. 2015;56:1131–2.
8. Salas Fragomeni RA, Amir T, Sheikhbahaei S, et al. Imaging of nonprostate cancers using PSMA-targeted radiotracers: rationale, current state of the field, and a call to arms. J Nucl Med. 2018;59:871–7.
9. Ceci F, Uprimny C, Nilica B, et al. 68Ga-PSMA PET/CT for restaging recurrent prostate cancer: which factors are associated with PET/CT detection rate? Eur J Nucl Med Mol Imaging. 2015;42:1284–94.
10. Freedland SJ, Presti JC Jr, Amling CL, et al. Time trends in biochemical recurrence after radical prostatectomy: results of the SEARCH database. Urology. 2003;61:736–41.
11. Rayn KN, Elnabawi YA, Sheth N. Clinical implications of PET/CT in prostate cancer management. Transl Androl Urol. 2018;7:844–54.
12. Grubmüller B, Baltzer P, Hartenbach S, et al. PSMA ligand PET/MRI for primary prostate cancer: staging performance and clinical impact. Clin Cancer Res. 2018;24:6300–7.
13. Afshar-Oromieh A, Avtzi E, Giesel FL, et al. The diagnostic value of PET/CT imaging with the (68)

Ga-labelled PSMA ligand HBED-CC in the diagnosis of recurrent prostate cancer. Eur J Nucl Med Mol Imaging. 2015;42:197–209.
14. Schwarzenboeck SM, Rauscher I, Bluemel C, et al. PSMA ligands for PET imaging of prostate cancer. J Nucl Med. 2017;58:1545–52.
15. Perera M, Papa N, Roberts M, et al. Gallium-68 prostate-specific membrane antigen positron emission tomography in advanced prostate cancer-updated diagnostic utility, sensitivity, specificity, and distribution of prostate-specific membrane antigen-avid lesions: a systematic review and meta-analysis. Eur Urol. 2019;. [Epub ahead of print]
16. Müller J, Ferraro DA, Muehlematter UJ, et al. Clinical impact of 68Ga-PSMA-11 PET on patient management and outcome, including all patients referred for an increase in PSA level during the first year after its clinical introduction. Eur J Nucl Med Mol Imaging. 2019;6:889–900.
17. Einspieler I, Rauscher I, Düwel C, et al. Detection efficacy of hybrid 68Ga-PSMA ligand PET/CT in prostate cancer patients with biochemical recurrence after primary radiation therapy defined by phoenix criteria. J Nucl Med. 2017;58:1081–7.
18. Schmidt-Hegemann NS, Fendler WP, Ilhan H, et al. Outcome after PSMA PET/CT based radiotherapy in patients with biochemical persistence or recurrence after radical prostatectomy. Radiat Oncol. 2018;13:37.
19. Calais J, Czernin J, Cao M, et al. 68Ga-PSMA-11 PET/CT mapping of prostate cancer biochemical recurrence after radical prostatectomy in 270 patients with a PSA level of less than 1.0 ng/mL: impact on salvage radiotherapy planning. J Nucl Med. 2018;59:230–7.
20. Calais J, Czernin J, Fendler WP, et al. Randomized prospective phase III trial of 68Ga-PSMA-11 PET/CT molecular imaging for prostate cancer salvage radiotherapy planning [PSMA-SRT]. BMC Cancer. 2019;19:97.
21. Heinzel A, Boghos D, Mottaghy FM, et al. 68Ga-PSMA PET/CT for monitoring response to 177Lu-PSMA-617 radioligand therapy in patients with metastatic castration-resistant prostate cancer. Eur J Nucl Med Mol Imaging. 2019;46:1054–62.
22. Weineisen M, Schottelius M, Simecek J, et al. 68Ga- and 177Lu-labeled PSMA I&T: optimization of a PSMA-targeted theranostic concept and first proof-of-concept human studies. J Nucl Med. 2015;56:1169–76.
23. Sathekge M, Bruchertseifer F, Knoesen O, et al. 225Ac-PSMA-617 in chemotherapy-naive patients with advanced prostate cancer: a pilot study. Eur J Nucl Med Mol Imaging. 2019;46:129–38.
24. Kesavan M, Turner JH, Meyrick D, et al. Salvage radiopeptide therapy of advanced castrate-resistant prostate cancer with lutetium-177-labeled prostate-specific membrane antigen: efficacy and safety in routine practice. Cancer Biother Radiopharm. 2018;33:274–81.
25. Afshar-Oromieh A, Zechmann CM, Malcher A, et al. Comparison of PET imaging with a (68)Ga-labelled PSMA ligand and (18)F-choline-based PET/CT for the diagnosis of recurrent prostate cancer. Eur J Nucl Med Mol Imaging. 2014;41:11–20.
26. Lütje S, Heskamp S, Cornelissen AS, et al. PSMA ligands for radionuclide imaging and therapy of prostate cancer: clinical status. Theranostics. 2015;5:1388–401.
27. Parent EE, Schuster DM. Update on 18F-fluciclovine PET for prostate cancer imaging. J Nucl Med. 2018;59:733–9.
28. England JR, Paluch J, Ballas LK, et al. 18F-fluciclovine PET/CT detection of recurrent prostate carcinoma in patients with serum PSA $\leq$ 1 ng/mL after definitive primary treatment. Clin Nucl Med. 2019;44:e128–32.
29. Andriole GL, Kostakoglu L, Chau A, et al. The impact of positron emission tomography with 18F-fluciclovine on the treatment of biochemical recurrence of prostate cancer: results from the LOCATE trial. J Urol. 2019;201:322–31.
30. Koerber SA, Will L, Kratochwil C, et al. 68Ga-PSMA-11 PET/CT in primary and recurrent prostate carcinoma: implications for radiotherapeutic management in 121 patients. J Nucl Med. 2019;60(2):234–40.
31. Rauscher I, Maurer T, Fendler WP, et al. (68) Ga-PSMA ligand PET/CT in patients with prostate cancer: how we review and report. Cancer Imaging. 2016;16:14.
32. Afshar-Oromieh A, Sattler LP, Mier W, et al. The clinical impact of additional late PET/CT imaging with 68Ga-PSMA-11 (HBED-CC) in the diagnosis of prostate cancer. J Nucl Med. 2017;58:750–5.
33. Krohn T, Verburg FA, Pufe T, et al. [(68)Ga]PSMA-HBED uptake mimicking lymph node metastasis in coeliac ganglia: an important pitfall in clinical practice. Eur J Nucl Med Mol Imaging. 2015;42:210–4.
34. Strele-Trieb P, Dunzinger A, Sonnberger M, et al. Uptake of 68Ga-prostate-specific membrane antigen pet in adrenal gland: a potential pitfall. Clin Nucl Med. 2018;43:50–1.
35. Calabria F, Gangemi V, Gullà D, et al. 64Cu-PSMA uptake in meningioma: a potential pitfall of a promising radiotracer. Rev Esp Med Nucl Imagen Mol. 2017;36:335–6.
36. Kesler M, Levine C, Hershkovitz D, et al. 68Ga-PSMA is a novel PET-CT tracer for imaging of hepatocellular carcinoma: a prospective pilot study. J Nucl Med. 2018;. [Epub ahead of print]
37. Backhaus P, Noto B, Avramovic N, et al. Targeting PSMA by radioligands in non-prostate disease-current status and future perspectives. Eur J Nucl Med Mol Imaging. 2018;45:860–77.
38. Nomura N, Pastorino S, Jiang P, et al. Prostate specific membrane antigen (PSMA) expression in primary gliomas and breast cancer brain metastases. Cancer Cell Int. 2014;14:26.

PET Biomarkers for Tau Pathology

13

Antoine Leuzy, Kerstin Heurling,
and Michael Schöll

Contents

13.1 Tau PET Tracers

The protein tau was first described in 1975 as a neuronal factor associated with the assembly and stability of microtubules [1]. Though additional functions have since been recognized for tau [2], its role in maintaining the microtubule-based cytoskeleton via binding to tubulin is regarded as its primary function. In this respect, the activity of tau is mediated by its degree of phosphorylation, with tau containing 2–3 mol of phosphate per mol of the protein under physiological conditions [3]. Hyperphosphorylation of tau, however, decreases its ability to bind to microtubules [4]

A. Leuzy
Clinical Memory Research Unit, Department of Clinical Sciences, Lund University, Malmö, Sweden

Wallenberg Centre for Molecular and Translational Medicine and The Department for Psychiatry and Neurochemistry, The Sahlgrenska Academy, University of Gothenburg, Gothenburg, Sweden

K. Heurling
Wallenberg Centre for Molecular and Translational Medicine and The Department for Psychiatry and Neurochemistry, The Sahlgrenska Academy, University of Gothenburg, Gothenburg, Sweden

M. Schöll (✉)
Clinical Memory Research Unit, Department of Clinical Sciences, Lund University, Malmö, Sweden

Wallenberg Centre for Molecular and Translational Medicine and The Department for Psychiatry and Neurochemistry, The Sahlgrenska Academy, University of Gothenburg, Gothenburg, Sweden

Department of Neurodegenerative Disease, Dementia Research Centre, UCL Institute of Neurology, London, UK
e-mail: michael.scholl@neuro.gu.se

F. Calabria, O. Schillaci (eds.), *Radiopharmaceuticals*,
https://doi.org/10.1007/978-3-030-27779-6_13

resulting in an increase in its cytosolic levels [5]. Following a shift from axonal to somatodendritic compartments, hyperphosphorylated tau, being an amyloid, then self-assembles into, among other aggregates, paired helical filaments (PHFs) [6] and, subsequently neurofibrillary tangles (NFTs). The accumulation of these pathological forms of tau is a common feature of a several neurodegenerative disorders collectively referred to as tauopathies, of which Alzheimer's disease (AD) is the most common. Recently, high affinity positron emission tomography (PET) tracers selective for tau aggregates were introduced, enabling the visualization, mapping, and quantification of tau pathology in vivo [7].

The challenges inherent to imaging tau notwithstanding, considerable progress has been made over the past years with respect to the development of tau selective PET tracers. Though the first PET tracer capable of binding tau aggregates—2-(1-(6-[(2-^{18}F-fluoroethyl)(methyl)amino]-2-naphthyl)ethylidene)malononitrile (^{18}F-FDDNP), a tracer with nanomolar affinity for amyloid-β shown also to bind to NFTs [8]—was first reported nearly 20 years ago, the development of tracers selective and specific for tau is a comparatively recent development. Initial tracers include ^{18}F-THK5317, ^{18}F-THK5351, ^{18}F-flortaucipir (also known as ^{18}F-AV1451 and ^{18}F-T-807), and ^{11}C-PBB3. Used extensively in research studies, these compounds are now properties, including ^{18}F-MK-6240, ^{18}F-RO948 (previously referred to as ^{18}F-RO69558948), ^{18}F-PI-2620, ^{18}F-GTP1, ^{18}F-PM-PBB3, ^{18}F-JNJ64349311 (^{18}F-JNJ311), and its derivative ^{18}F-JNJ-067 [7].

13.1.1 Synthesis

Given the number of tau PET tracers under development covered in this chapter, specifics regarding synthesis strategies for all of these will not be covered. For ^{18}F-flortaucipir, the by far most used tau tracer to date, several alternative methods for synthesis have been suggested and subsequently optimized, including synthesis from the N-Boc-protected nitro precursor [9], which eliminated the need for the reduction of the nitro precursor prior to purification that the original report required to facilitate purification of ^{18}F-flortaucipir [10]. Holt et al. demonstrated ^{18}F-fluorination of N-Boc-protected trimethylammonium precursor by microwave irradiation [11] and recently an optimized fully automated synthesis of ^{18}F-flortaucipir was developed which uses an unmodified LIGANDLab FX_{FN} synthesis module [12]. As novel compounds become more used, similar optimization efforts will surely follow as has recently been the case for ^{18}F-MK-6240 [13].

13.1.2 Pharmacokinetics

Initial tau tracers have been subject to extensive characterization using in vitro autoradiography and tau immunostaining, on both paraffin and frozen AD brain tissue. Flortaucipir, THK5117, THK5351, and PBB3 (with the absence of labels reflecting the use of different approaches—unlabeled as well as ^{11}C, ^{18}F, and ^{3}H labeled—across studies) have all been shown to bind to neurofibrillary tangles (intracellular and extracellular "ghost tangle" variants) as well as to neuritic plaques [14]. Contradictory findings, however, have been reported for pretangles. In vitro binding assays using tau fibrils or human brain homogenates and brain sections have shown current tau tracers to have favorable binding properties (nanomolar range) and point to several binding sites. In vitro autoradiography studies in non-AD tauopathies [15, 16], most involving direct comparison with tau immunostaining, suggest that PBB3 and tracers of the THK family may be better able to detect non-AD tau, relative to flortaucipir.

Binding of tau PET tracers to non-tau targets (so-called "off-target" binding) stands as an important and as yet unresolved challenge. Off-target binding of ^{18}F-flortaucipir, ^{11}C-PBB3, and the ^{18}F-THK compounds has been reported predominantly in the choroid plexus, the basal ganglia, and the meninges [17]. While iron and neuromelanin have been proposed to underlie

the signal from the basal ganglia [18, 19], binding in the choroid plexus has been attributed to the presence of calcifications, "on-target" binding to tangle-like structures (Biondi ring tangles), and melanocytes [17]. Other studies point to off-target binding to monoamine oxidase A (MAO-A; ^{18}F-flortaucipir) [20] and B (MAO-B; ^{18}F-flortaucipir and ^{18}F-THK5317) [21]. Though novel tau tracers appear to be less affected, uptake in the ethmoid sinus, clivus, the meninges, and substantia nigra has been reported with ^{18}F-MK-6240 and ^{18}F-RO948 in a small sample of AD patients and older cognitively unimpaired adults [22, 23].

Initial studies of the different tau PET tracers have shown that binding kinetics of tracer binding to tau are well described by the two-tissue compartment model (2TCM) for most tracers [24–26]. While compartmental modeling provides detailed insights into the binding characteristics, it is sensitive to noise and requires arterial blood sampling as well as long, fully dynamic PET acquisitions. More robust estimates of tracer retention can be achieved for the tau tracers using the plasma input Logan graphical model, and—alleviating the need for arterial sampling—the reference input Logan graphical model using cerebellar cortex as reference region [22, 24, 25]. For ^{11}C-PBB3, tracer kinetics could not be described by the 2TCM, attributed to the fact that radioactively labeled metabolites also crossed the blood–brain barrier, but binding to tau could still be accurately quantified using the multilinear reference tissue model [27]. Utility in large-scale cohort studies, clinical trials, or clinical settings by means of shorter acquisition protocols and simplified semiquantitative estimates of tracer retention such as late-phase standardized uptake value ratios (SUVR) has been shown for ^{18}F-flortaucipir, ^{18}F-RO948, ^{18}F-MK-6240, and ^{18}F-THK5317 with strong agreement between the SUVR and quantitative estimates [22, 25, 26, 28], even though a time dependency of SUVR and nonlinear associations between SUVR values and reference-tissue model-derived parameters for ^{18}F-flortaucipir calls for caution [28–30].

13.1.3 Physiological Distribution

Though most tau PET imaging studies use standard region-of-interest (ROI) based quantification, a number have used ROIs that approximate the Braak staging scheme for tau pathology [31, 32]. While the number of longitudinal tau imaging studies is as yet limited, a recent follow-up study in a large cohort showed that positive rates of change in ^{18}F-flortaucipir uptake were seen beyond the expected medial temporal areas (i.e., Braak stage I and II) in amyloid-β positive, cognitively unimpaired individuals (CU) [33]. This suggests that the distribution and spread of tau pathology does not invariably follow the patterns outlined by Braak. The conclusion from this study was rather that tau accumulation may be reliably obtained using composite ROIs that sample from areas showing both early (e.g., posterior cingulate) and late (e.g., orbitofrontal cortex) changes in AD. A similar study reached the same conclusion, where tau pathology seemed to emerge through the cortex, instead of following the stepwise Braak stages [34]. Findings from an additional study, however, showed patterns of tau accumulation in AD consistent with the Braak staging model and an association between tau pathology in higher Braak stages and severity of cognitive impairment [35]. Though awaiting *post-mortem* confirmation, these observations suggest that the global burden of tau, as opposed to its topography, may be more important to disease progression. In contrast to the use of a priori defined ROIs, however, several studies have employed data-driven methods [36–38] including clustering approaches that showed greater discrimination between CU subjects showing high and low levels of tau PET signal [39] and better captured both typical and atypical variants of AD [40].

13.1.4 Indications

Tau imaging in CU elderly individuals using ^{18}F-flortaucipir, ^{11}C-PBB3, and ^{18}F-THK tracers has consistently shown tracer retention to be largely restricted to the medial temporal lobe

(MTL), with neocortical findings variable and dependent on the presence of amyloid-β [7]. This pattern of MTL limited uptake is consistent with an age-related process (primary age-related tauopathy), which has been shown to result in atrophy of the hippocampus and amnestic deficits that are independent from amyloid-β [41]. Among AD dementia patients, higher levels of tau tracer retention have been consistently reported throughout the brain, including in regions known to be characterized by tau pathology, such as the posterior cingulate and inferior lateral temporal cortex, but also involving occipital, parietal, and frontal cortical areas. Differences have also been reported between early onset (EOAD) (<65 years) and late onset AD (LOAD), with EOAD showing greater uptake within prefrontal and premotor cortices, as well as in the inferior parietal lobe [42]. Studies that have compared CU and individuals with mild cognitive impairment (MCI) have shown differences restricted to regions of the MTL (Cho [32]) and parietal and lateral temporal areas when comparisons were restricted to amyloid-β-positive MCI (i.e., prodromal AD) patients [43]. While few in number, studies published to date using novel tau tracers show findings consistent with those for earlier tracers [44].

The majority of studies using tau imaging have been performed in AD patients; however, there is hope that tau PET may prove of value in other neurodegenerative disorders associated with tau pathology such as corticobasal syndrome (CBS) and progressive supranuclear palsy (PSP) [45, 46]. Though studies performed in patients with these disorders have shown regional uptake patterns consistent with expected distribution of tau pathology based on the neuropathology literature, many of these areas also coincide with areas known to be affected by off-target binding (e.g., within the basal ganglia). Additional disorders associated with the presence of tau pathology include Down syndrome (DS), Parkinson's disease (PD), and dementia with Lewy bodies (DLB). While preliminary findings show an AD-like pattern of uptake with ^{18}F-flortaucipir in DS [47], findings have been more varied in PD and DLB, often overlapping with CU subjects [48]; this may, in part, reflect the varying degree of tau pathology seen in these diseases, as well as the as yet unknown specificity of current tau tracers towards α-synuclein, the pathological hallmark of both PD and DLB. In a recent large-scale multicentric study, ^{18}F-flortaucipir PET was shown to provide very good differential diagnostic properties to differentiate between AD dementia and other neurodegenerative disorders, discrimination, however, was less good in MCI due to AD due to less pronounced uptake [49].

In patients with AD, a close correspondence has been shown between tau PET and hypometabolism within the neocortex [50]. Further, tau imaging findings related more closely to metabolic findings with ^{18}F-FDG PET than to MRI-based atrophy or levels of amyloid-β, with the strength of this association positively correlated to global tau burden [51]. Longitudinal findings suggest the existence of a spatio-temporal offset, however, between tau pathology and synaptic impairment [52]. Studies addressing the link between tau and cognition within CU elderly without amyloid-β pathology have shown that this association is strongest between measures of episodic memory and MTL tau (more specifically, the entorhinal cortex) [31]. Importantly, the deleterious effect of tau in this region on episodic memory performance within this population do not seem to be mediated by global amyloid-β levels, suggesting that the accumulation of tau in the MTL is itself not a benign event. Additional work points to tau having both direct and indirect—via gray matter loss—effects on cognition [53]. Overall, studies support an empirical model in which cognitive decline follows the accumulation of tau beyond the MTL into cortical association areas already affected by amyloid-β pathology [54].

13.1.5 Clinical Cases

The rapid development of tau PET imaging has been accompanied by questions pertaining to its potential usefulness from a clinical standpoint. Though the body of evidence thus far available indicates that currently available tau tracers bind

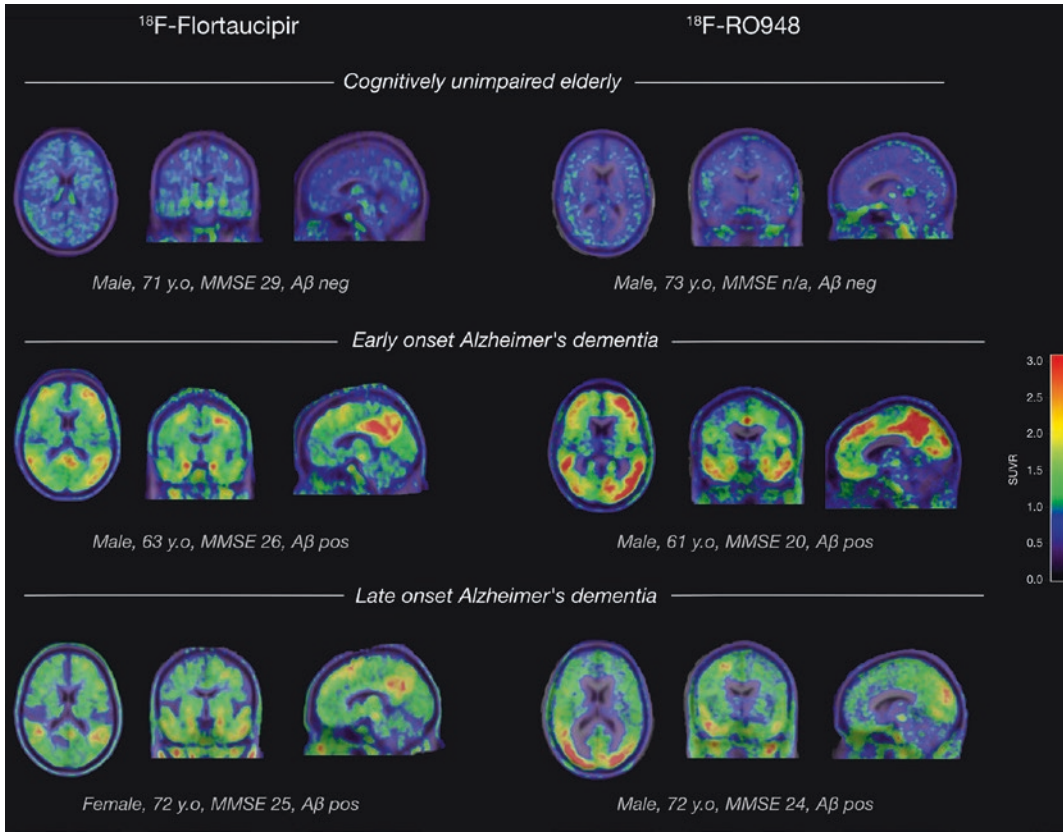

Fig. 13.1 Representative ^{18}F-flortaucipir (80–100 min) and ^{18}F-RO948 (60–90 min) PET SUVR images in cognitively unimpaired older individuals (upper row) and patients with early-onset Alzheimer's disease (EOAD) (<65 years) and late onset AD (rows two and three, respectively). ^{18}F-Flortaucipir images (80–100 min SUVR) are courtesy of the Alzheimer's disease neuroimaging initiative (ADNI); ^{18}F-RO948 images were kindly provided by Roche (Drs. Gregory Klein and Edilio Borroni) and Drs. Dean Wong and Hiroto Kuwabara from Johns Hopkins University, Baltimore, Maryland. Following co-registration of PET images to their corresponding T1-weighted magnetic resonance imaging (MRI) scan, PET images were spatially normalized to the Montreal Neurological Institute (MNI) template space; standardized uptake value ratio (SUVR) images were created using the inferior cerebellum cortex as reference region. *Aβ pos/neg* Amyloid status, positive/negative, based on ^{11}C-Pittsburgh Compound B Aβ PET scans; *MMSE* Mini Mental State Examination

primarily to AD-type PHF tau (Fig. 13.1), tau PET remains a promising technique with respect to the differential diagnosis of tauopathies as well as in the workup of diagnostically challenging cases of atypical AD. Though studies using novel compounds in non-AD disorders have yet to be published, the seemingly reduced off-target binding in the basal ganglia seen with these tracers suggest that these may be of value when it comes to characterizing such disorders. An open question remains, however, as to whether or not multiple tracers will eventually prove interchangeable, similar to tracers for amyloid-β. Further studies addressing the ability of tau imaging to help resolve clinically complex, diagnostically uncertain cases, are crucial, as are studies comparing tau PET to other established PET- and CSF-based biomarkers [55, 56]. At a broader level, tau imaging is also expected to help with disease staging and to resolve long-standing questions surrounding the contributions of amyloid-β and tau to cognitive decline, as well as their interplay with other pathological features, such as α-synuclein and TAR DNA-binding protein 43, once tracers are available for these targets. Lastly, tau PET may prove valuable in the

context of clinical trials as a means of population enrichment, proof of target engagement, and as an outcome measure.

13.1.6 Acquisition Protocols

Given the multitude of tau PET tracers under development, there is not yet one fixed acquisition protocol to be used for all of them. However, for ^{18}F-flortaucipir, with the largest collective experience to date, a dose of 370 MBq followed by a 20-min acquisition 80 min post tracer injection is most commonly used.

13.1.7 Variants and Pitfalls

Imaging tau deposits using PET is a task complicated by several obstacles. To begin with, tau aggregates are primarily located intracellularly; as such, a tracer must cross not only the blood–brain barrier but also the cell membrane to reach its target. Further, six tau isoforms are expressed in the brain; functionally categorized based on the number of repeats (i.e., 3R or 4R) in the microtubule-binding domain, these isoforms are differentially manifested across tauopathies and result in distinct morphological and ultrastructural tau conformations [57]. Posttranslational modifications, including acetylation, glycosylation, ubiquitination, and truncation, are known to affect the ultrastructural conformation adopted by aggregates [57]. An additional issue is the co-localization of tau and other misfolded proteins having a secondary beta-sheet structure, such as amyloid-β, which also demonstrates 5- to 20-fold higher concentration levels [57].

The advent of tau PET imaging over the past several years has substantially advanced the field, allowing for the in vivo visualization, mapping, and quantification of a known characteristic pathogenic feature of AD. Though technical and methodological challenges remain, optimized compounds now entering the field will further our understanding of the role of tau pathology in AD and related disorders, including its link to both amyloid-β and neurodegeneration, and its relationship with cognitive decline. As the number of tau tracers increases, however, new methods to ensure appropriate quantitative comparison will be needed, similar to approaches developed for amyloid-β imaging. Moreover, while existing tracers are useful for the assessment of AD-related tau pathology, tracers binding to tau isoforms underlying other tauopathies are still needed. Lastly, it is important to situate tau pathology within a broader context of misfolded proteins; once PET tracers for α-synuclein and TDP-43, for example, become available, multi-ligand studies will be a key strategy to achieve a more complete understanding of what differentiates the brain in aging from dementia.

References

1. Weingarten MD, Lockwood AH, Hwo SY. A protein factor essential for microtubule assembly. Proc Natl Acad Sci U S A. 1975;72(5):1858–62.
2. Sotiropoulos I, Galas MC, Silva JM, et al. Atypical, non-standard functions of the microtubule associated tau protein. Acta Neuropathol Commun. 2017;5(1):91.
3. Kopke E, Tung YC, Shaikh S, et al. Microtubule-associated protein tau. Abnormal phosphorylation of a non-paired helical filament pool in Alzheimer disease. J Biol Chem. 1993;268(32):24374–84.
4. Lindwall G, Cole RD. Phosphorylation affects the ability of tau protein to promote microtubule assembly. J Biol Chem. 1984;259(8):5301–5.
5. Maas T, Eidenmuller J, Brandt R. Interaction of tau with the neural membrane cortex is regulated by phosphorylation at sites that are modified in paired helical filaments. J Biol Chem. 2000;275(21):15733–40.
6. Hernandez F, Avila J. Tauopathies. Cell Mol Life Sci. 2007;64(17):2219–33.
7. Schöll M, Maass A, Mattsson N, et al. Biomarkers for tau pathology. Mol Cell Neurosci. 2019;97:18–33.
8. Shoghi-Jadid K, Small G, Agdeppa E, et al. Localization of neurofibrillary tangles and beta-amyloid plaques in the brains of living patients with Alzheimer disease. Am J Geriatr Psychiatry. 2002;10:24–35.
9. Shoup TM, Yokell DL, Rice PA, et al. A concise radiosynthesis of the tau radiopharmaceutical, [(18) F]T807. J Labelled Comp Radiopharm. 2013;56(14):736–40.
10. Xia CF, Arteaga J, Chen G, et al. [(18)F]T807, a novel tau positron emission tomography imaging agent for Alzheimer's disease. Alzheimers Dement. 2013;9(6):666–76.

11. Holt DP, Ravert HT, Dannals RF. Synthesis and quality control of [(18) F]T807 for tau PET imaging. J Labelled Comp Radiopharm. 2016;59(10):411–5.
12. Mossine AV, Brooks AF, Henderson BD. An updated radiosynthesis of [(18)F]AV1451 for tau PET imaging. EJNMMI Radiopharm Chem. 2017;2(1):7.
13. Collier TL, Yokell DL, Livni E, et al. cGMP production of the radiopharmaceutical [(18) F]MK-6240 for PET imaging of human neurofibrillary tangles. J Labelled Comp Radiopharm. 2017;60(5):263–9.
14. Saint-Aubert L, Lemoine L, Chiotis K, et al. Tau PET imaging: present and future directions. Mol Neurodegener. 2017;12(1):19.
15. Ono M, Sahara N, Kumata K, Ji B, Ni R, Koga S, et al. Distinct binding of PET ligands PBB3 and AV-1451 to tau fibril strains in neurodegenerative tauopathies. Brain. 2017;140:764–80.
16. Marquie M, Normandin MD, Meltzer AC, Siao Tick Chong M, Andrea NV, Anton-Fernandez A, et al. Pathological correlations of [F-18]-AV-1451 imaging in non-Alzheimer tauopathies. Ann Neurol. 2017;81:117–28.
17. Lemoine L, Leuzy A, Chiotis K, et al. Tau positron emission tomography imaging in tauopathies: the added hurdle of off-target binding. Alzheimers Dement (Amst). 2018;10:232–6.
18. Choi JY, Cho H, Ahn SJ, et al. Off-Target (18) F-AV-1451 binding in the basal ganglia correlates with age-related iron accumulation. J Nucl Med. 2018;59:117–20.
19. Marquie M, Normandin MD, Vanderburg CR, et al. Validating novel tau positron emission tomography tracer [F-18]-AV-1451 (T807) on postmortem brain tissue. Ann Neurol. 2015;78:787–800.
20. Vermeiren C, Motte P, Viot D, et al. The tau positron-emission tomography tracer AV-1451 binds with similar affinities to tau fibrils and monoamine oxidases. Mov Disord. 2018;33(2):273–81.
21. Lemoine L, Gillberg PG, Svedberg M, et al. Comparative binding properties of the tau PET tracers THK5117, THK5351, PBB3, and T807 in postmortem Alzheimer brains. Alzheimers Res Ther. 2017;9(1):96.
22. Betthauser TJ, Cody KA, Zammit MD, et al. In vivo characterization and quantification of neurofibrillary tau PET radioligand (18)F-MK-6240 in humans from Alzheimer disease dementia to young controls. J Nucl Med. 2019;60(1):93–9.
23. Wong DF, Comley RA, Kuwabara H, et al. Characterization of 3 novel tau radiopharmaceuticals, (11)C-RO-963, (11)C-RO-643, and (18)F-RO-948, in healthy controls and in Alzheimer subjects. J Nucl Med. 2018;59(12):1869–76.
24. Hahn A, Schain M, Erlandsson M, et al. Modeling strategies for quantification of in vivo (18)F-AV-1451 binding in patients with tau pathology. J Nucl Med. 2017;58(4):623–31.
25. Jonasson M, Wall A, Chiotis K, et al. Tracer kinetic analysis of (S)-(1)(8)F-THK5117 as a PET tracer for assessing tau pathology. J Nucl Med. 2016;57(4):574–81.
26. Kuwabara H, Comley RA, Borroni E, Honer M, Kitmiller K, Roberts J, et al. Evaluation of (18) F-RO-948 PET for quantitative assessment of tau accumulation in the human brain. J Nucl Med. 2018;59(12):1877–84.
27. Kimura Y, Ichise M, Ito H, et al. PET quantification of tau pathology in human brain with 11C-PBB3. J Nucl Med. 2015;56(9):1359–65.
28. Barret O, Alagille D, Sanabria S, et al. Kinetic modeling of the tau PET tracer (18)F-AV-1451 in human healthy volunteers and Alzheimer disease subjects. J Nucl Med. 2017;58(7):1124–31.
29. Baker SL, Lockhart SN, Price JC, et al. Reference tissue-based kinetic evaluation of 18F-AV-1451 for tau imaging. J Nucl Med. 2017;58(2):332–8.
30. Heurling K, Smith R, Strandberg OT, et al. Regional times to equilibria and their impact on semi-quantification of [(18)F]AV-1451 uptake. J Cereb Blood Flow Metab. 2018:271678X18791430.
31. Schöll M, Lockhart SN, Schonhaut DR, et al. PET imaging of tau deposition in the aging human brain. Neuron. 2016;89(5):971–82.
32. Cho H, Choi JY, Hwang MS, et al. In vivo cortical spreading pattern of tau and amyloid in the Alzheimer disease spectrum. Ann Neurol. 2016;80(2):247–58.
33. Jack CR Jr, Wiste HJ, Schwarz CG, et al. Longitudinal tau PET in ageing and Alzheimer's disease. Brain. 2018;141(5):1517–28.
34. Jones DT, Graff-Radford J, Lowe VJ, et al. Tau, amyloid, and cascading network failure across the Alzheimer's disease spectrum. Cortex. 2017;97:143–59.
35. Cho H, Choi JY, Lee HS, et al. Progressive tau accumulation in Alzheimer's disease: two-year follow-up study. J Nucl Med. 2019. pii: jnumed.118.221697
36. Brier MR, Gordon B, Friedrichsen K, et al. Tau and Abeta imaging, CSF measures, and cognition in Alzheimer's disease. Sci Transl Med. 2016;8(338):338ra66.
37. Lowe VJ, Wiste HJ, Senjem ML, et al. Widespread brain tau and its association with ageing, Braak stage and Alzheimer's dementia. Brain. 2018;141(1):271–87.
38. Sepulcre J, Sabuncu MR, Li Q, et al. Tau and amyloid beta proteins distinctively associate to functional network changes in the aging brain. Alzheimers Dement. 2017;13(11):1261–9.
39. Mishra S, Gordon BA, Su Y, et al. AV-1451 PET imaging of tau pathology in preclinical Alzheimer disease: defining a summary measure. Neuroimage. 2017;161:171–8.
40. Whitwell JL, Graff-Radford J, Tosakulwong N, et al. [(18) F]AV-1451 clustering of entorhinal and cortical uptake in Alzheimer's disease. Ann Neurol. 2018a;83(2):248–57.
41. Jack CR Jr. PART and SNAP. Acta Neuropathol. 2014;128(6):773–6.

42. Schöll M, Ossenkoppele R, Strandberg O, et al. Distinct 18F-AV-1451 tau PET retention patterns in early- and late-onset Alzheimer's disease. Brain. 2017;140(9):2286–94.
43. Chiotis K, Saint-Aubert L, Savitcheva I, et al. Imaging in-vivo tau pathology in Alzheimer's disease with THK5317 PET in a multimodal paradigm. Eur J Nucl Med Mol Imaging. 2016;43(9):1686–99.
44. Leuzy A, Chiotis K, Lemoine L, et al. Tau PET imaging in neurodegenerative tauopathies-still a challenge. Mol Psychiatry. 2019;
45. Smith R, Schöll M, Honer M, et al. Tau neuropathology correlates with FDG-PET, but not AV-1451-PET, in progressive supranuclear palsy. Acta Neuropathol. 2017a;133(1):149–51.
46. Smith R, Schöll M, Widner H, et al. In vivo retention of (18)F-AV-1451 in corticobasal syndrome. Neurology. 2017b;89(8):845–53.
47. Rafii MS, Lukic AS, Andrews RD, et al. PET imaging of tau pathology and relationship to amyloid, longitudinal MRI, and cognitive change in down syndrome: results from the down syndrome biomarker initiative (DSBI). J Alzheimers Dis. 2017;60(2):439–50.
48. Smith R, Schöll M, Londos E, et al. (18)F-AV-1451 in Parkinson's disease with and without dementia and in dementia with Lewy bodies. Sci Rep. 2018;8(1):4717.
49. Ossenkoppele R, Rabinovici GD, Smith R, et al. Discriminative accuracy of [18F]flortaucipir positron emission tomography for Alzheimer disease vs other neurodegenerative disorders. JAMA. 2018;320(11):1151–62.
50. Ossenkoppele R, Schonhaut DR, Baker SL, et al. Tau, amyloid, and hypometabolism in a patient with posterior cortical atrophy. Ann Neurol. 2015;77(2):338–42.
51. Whitwell JL, Graff-Radford J, Tosakulwong N, et al. Imaging correlations of tau, amyloid, metabolism, and atrophy in typical and atypical Alzheimer's disease. Alzheimers Dement. 2018b;14(8):1005–14.
52. Chiotis K, Saint-Aubert L, Rodriguez-Vieitez E, et al. Longitudinal changes of tau PET imaging in relation to hypometabolism in prodromal and Alzheimer's disease dementia. Mol Psychiatry. 2018;23(7):1666–73.
53. Bejanin A, Schonhaut DR, La Joie R, et al. Tau pathology and neurodegeneration contribute to cognitive impairment in Alzheimer's disease. Brain. 2017;140(12):3286–300.
54. Jacobs HIL, Hedden T, Schultz AP, et al. Structural tract alterations predict downstream tau accumulation in amyloid-positive older individuals. Nat Neurosci. 2018;21(3):424–31.
55. Mattsson N, Schöll M, Strandberg O, et al. (18) F-AV-1451 and CSF T-tau and P-tau as biomarkers in Alzheimer's disease. EMBO Mol Med. 2017;9(9):1212–23.
56. Mattsson N, Smith R, Strandberg O, et al. Comparing (18)F-AV-1451 with CSF t-tau and p-tau for diagnosis of Alzheimer disease. Neurology. 2018;90(5):e388–e95.
57. Villemagne VL, Fodero-Tavoletti MT, Masters CL. Tau imaging: early progress and future directions. Lancet Neurol. 2015;14(1):114–24.